

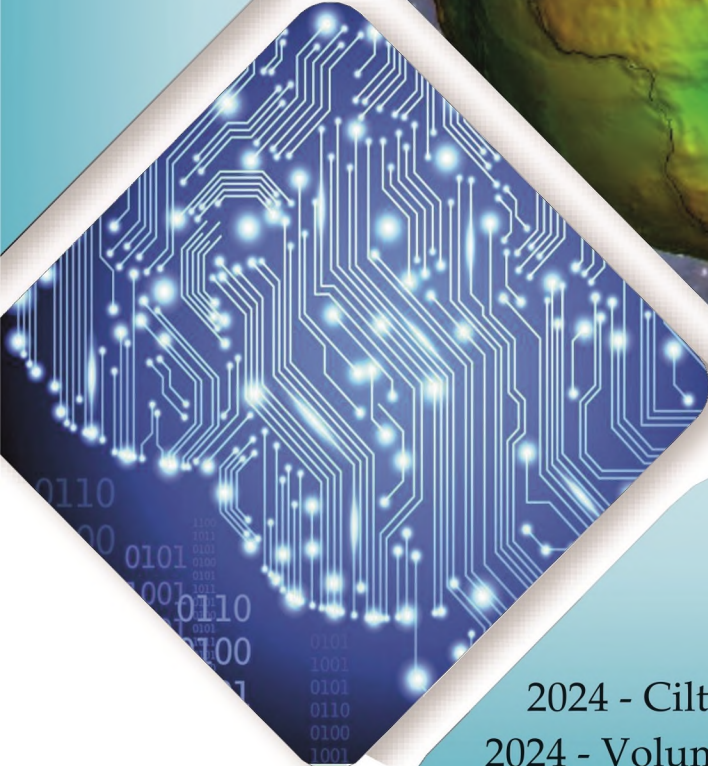


Konya Mühendislik Bilimleri Dergisi

Konya Journal of Engineering Sciences



(KONJES)
E-ISSN: 2667-8055



2024 - Cilt : 12 - Sayı : 1
2024 - Volume : 12 - Issue :1

KONYA JOURNAL OF ENGINEERING SCIENCES (KONJES)
KONYA MÜHENDİSLİK BİLİMLERİ DERGİSİ

HAKEMLİ DERGİDİR

OWNER/SAHİBİ

Owner on Behalf of Engineering and Natural Sciences Faculty of Konya Technical University **Prof. Dr. Ali KÖKEN** Konya Teknik Üniversitesi Mühendislik ve Doğa Bilimleri Fakültesi Adına Dekan **Prof. Dr. Ali KÖKEN**

Editor-in-Chief/Şef Editör

Prof. Dr. Mustafa TABAKCI

Editors/Editörler

Prof. Dr. Halife KODAZ

Assoc. Prof. Dr. Ömer Kaan BAYKAN

Section Editors/Alan Editörleri

Prof. Dr. Niyazi B L M

Prof. Dr. Volkan KALEM

Assoc. Prof. Dr. Farabi TEMEL

Assoc. Prof. Dr. smail NCE

Assoc. Prof. Dr. Ömer Kaan BAYKAN

Assoc. Prof. Dr. Selim DO AN

Assoc. Prof. Dr. Sercan BÜLBÜL

Assist. Prof. Dr. Alper DÖYEN

Assist. Prof. Dr. Cihangir KÖYCE Z

Assist. Prof. Dr. Kemal ERDO AN

Assist. Prof. Dr. Muhammed Arif EN

Assist. Prof. Dr. Muharrem Hilmi AKSOY

Advisory Board/Danışma Kurulu

Prof.Dr. Ferruh YILDIZ, Konya Technical University

Prof.Dr. Reşat ULUSAY, Hacettepe University

Prof.Dr. Ibaraki SOICHI, Kyoto University

Prof.Dr. Matchavariani LIA, Tbilisi State University

Prof.Dr. Seref SAGIROGLU, Gazi University

Prof.Dr. Vijay P. SINGH, Texas A and M University

Prof.Dr.-Ing. Rudolf STAIGER, Bochum University of Applied Sciences

Prof.Dr. Chryssy POTSIU, National Technical University of Athens

Prof.Dr. Lena HALOUNOVA, Czech Technical University

Prof.Dr. Petros PATIAS, The Aristotle University

Prof.Dr. Sitki KULUR, Istanbul Technical University

Language Editing/Yabancı Dil Editörü

Prof. Dr. Ali BERKTAY

Secretary/Sekreter

Assist. Prof. Dr. Emel Zeray ÖZTÜRK

Composition and Printing/Baskı ve Dizgi

Assist. Prof. Dr. smail KOÇ

Res. Assist. Emir Ali D NSEL

Res. Assist. Aybüke BABADA

Correspondance Address/ Yazışma Adresi

Konya Teknik Üniversitesi Mühendislik ve Doğa Bilimleri Fakültesi Dekanlığı
42075-Kampüs, Selçuklu, Konya-TURKEY

Tel : 0 332 223 88 18

Fax : 0 332 241 06 35

E-mail : konjes@ktun.edu.tr

Web : <http://dergipark.org.tr/konjes>

Editorial Board/Yayın Kurulu

Ahmet Afsin Kulaksiz, Konya Technical University, TURKEY

Alla Anohina-Naumeca, Riga Technical University, LATVIA

Ashok K. Mishra, Clemson University, USA

Baris Binici, Middle East Technical University, TURKEY

Coskun Bayrak, University of Arkansas, USA

Demetrio Fuentes Ferrera, University of Castilla-La Mancha, SPAIN

Fahrettin Ozturk, The Petroleum Institute, UAE

Haci Murat Yilmaz, Aksaray University, TURKEY

Heinz Ruther University of Cape Town, SOUTH AFRICA

Homayoun Moghimi, Payame Noor University, IRAN

Ihsan Ozkan, Konya Technical University, TURKEY

John Trinder, The University of New South Wales, AUSTRALIA

Kerim Kocak, Konya Technical University, TURKEY

Loredana Judele, Technical University of Iasi, ROMANIA

Mohamed Bouabaz, Université 20 août 1955-Skikda, ALGERIA

Mohd Arif Wani, California State University, USA

Mortaza Yari, University of Tabriz, IRAN

Ömer Aydan, University of the Ryukyus, JAPAN

Sanchoy K. Das, New Jersey Institute of Technology, USA

Selim Dogan, Konya Technical University, TURKEY

Spase Shumka, Agricultural University of Tirana, ALBANIA

Tahira Geroeva, Baku State University, AZERBAIJAN

Vladimir Androkhonov, Novosibirsk Soil Research Institute, RUSSIA

Ali Kocak, Yildiz Technical University, TURKEY

Alpaslan Yarar, Konya Technical University, TURKEY

Ataur Rahman, University of Western Sydney, AUSTRALIA

Cihan Varol Sam Houston State University, USA

Dan Stumbea, Alexandru Ioan Cuza University of Iasi, ROMANIA

Eva Burgetova, Czech Technical University, CZECH REPUBLIC

Georgieva Lilia, Heriot-Watt University, UNITED KINGDOM

Halil Kursad Ersoy, Konya Technical University, TURKEY

Hi-Ryong Byun, Pukyong National University, SOUTH KOREA

Huseyin Devenci, Konya Technical University, TURKEY

Iraida Samofalova, Perm University, RUSSIA

Juan Maria Menendez Aguado, University of de Oviedo, SPAIN

Laramie Vance Potts, New Jersey Institute of Technology, USA

Mila Koeva, University of Twente, NETHERLANDS

Mohamed Metwaly Abu Anbar, Tanta University, EGYPT

Moonis Ali Khan, King Saud University, KSA

Murat Karakus, University of Adelaide, AUSTRALIA

Saadettin Erhan Kesen, Konya Technical University, TURKEY

Selcuk Kursat Isleyen, Gazi University, TURKEY

Shukri Maxhuni, Prizen University, KOSOVA REPUBLIC

Syed Tufail Hussain Sherazi, University of Sindh, PAKISTAN

Thomas Niedoba, AGH University of Science and Technology, POLAND

Zoran Sapuric, University American College Skopje, MACEDONIA

KONYA MÜHENDİSLİK BİLİMLERİ DERGİSİ
Konya Journal of Engineering Sciences
(KONJES)

ISSN 2667 – 8055 (Elektronik/Electronic)

Cilt	12	Mart	2024	Sayı	1
Volume	12	March	2024	Issue	1

İÇİNDEKİLER (CONTENTS)

Araştırma Makalesi (Research Article)

OPTIMIZING ENERGY HUB SYSTEM OPERATION WITH ELECTRICAL AND THERMAL DEMAND RESPONSE PROGRAMS

Özge Pınar AKKAŞ, Yağmur ARIKAN YILDIZ 1-13

EFFECT OF BASALT FIBER ASPECT RATIO ON MECHANICAL AND WORKABILITY PROPERTIES OF SELF-COMPACTING CONCRETE

Mehmet UZUN, Mehmet Akif ARSLAN 14-21

FAILURE ANALYSIS OF A BASE SUPPORT PLATE OF A SEMOLINA PURIFIER MACHINES SUBJECTED TO FATIGUE LOADING

Yunus DERE, Hakkı EKEM, Ömer Sinan ŞAHİN, Hasan Hüsnü KORKMAZ 22-36

EFFECTIVE POLYMER DECORATION ON NICKEL-IMINE COMPLEX TO ENHANCE CATALYTIC HYDROGEN EVOLUTION

Dilek KILINÇ, Ömer ŞAHİN 37-52

LEAN ENERGY EFFICIENCY: SCENARIO ANALYSIS OF A REFRIGERATOR PLANT APPLICATION

Irem DUZDAR, Kazım ALBAYRAK, Gulgun KAYAKUTLU, M. Ozgur KAYALICA 53-68

EFFECT OF HEAT TREATMENT ON CORROSION RESISTANCE OF Al-Ni-Mn EUTECTIC ALLOY IN 3.5% NaCl SOLUTION *

Yusuf KAYGISIZ 69-83

PERFORMANCE ANALYSIS OF P&O AND PSO MPPT ALGORITHMS FOR PV SYSTEMS UNDER PARTIAL SHADING

Mustafa Sacid ENDİZ 84-99

ESTIMATING THE POWER DRAW OF GRIZZLY FEEDERS USED IN CRUSHING-SCREENING PLANTS THROUGH SOFT COMPUTING ALGORITHMS

Ekin KÖKEN 100-108

A COMMERCIAL TURBOFAN ENGINE MODELING AND EXERGY ANALYSIS

Orhan KALKAN 109-122

ENERGY, ENVIRONMENTAL, AND EXERGOCHEMICAL (3E) ANALYSIS OF TRANSCRITICAL CO₂ BOOSTER AND PARALLEL COMPRESSION SUPERMARKET REFRIGERATION CYCLES IN CLIMATE ZONES OF TÜRKİYE Oğuz ÇALIŞKAN, H. Kürşad ERSOY	123-137
ESTIMATIONS OF GREEN HOUSE GASES EMISSIONS OF TURKEY BY STATISTICAL METHODS Suat ÖZTÜRK, Ahmet EMİR	138-149
ADSORPTION OF MALACHITE GREEN INTO POTATO PEEL: NONLINEAR ISOTHERM AND KINETIC İlhan KÜÇÜK, Halil BİÇİÇİ	150-161
ASSESSMENT OF URBAN FLOOD RISKS OF THE CITIES USING ENTROPY-VIKOR METHODS IN TÜRKİYE Onur DERSE, Elifcan GÖÇMEN POLAT	162-176
COMPARISON OF CLASSICAL AND FUZZY EDGE DETECTION METHODS Gülcihan ÖZDEMİR	177-191
ENCAPSULATION OF VITAMIN D IN THE EXINE-ALGINATE-CHITOSAN MICROCAPSULE SYSTEM Gülnur DUYSAK, Idris SARGIN	192-204
ESTIMATING THE HARDNESS AND ABRASION PROPERTIES OF IGNEOUS ROCKS FROM CERCHAR INDENTATION DEPTH (CID) Ahmet TEYMEN	205-220
PRODUCTION OF CuO/ZrO₂ NANOCOMPOSITES IN POWDER AND FIBER FORMS Zeynep ÇETİNKAYA	221-230
DETERMINATION BY NUMERICAL MODELING OF STRESS-STRAIN VARIATIONS RESULTING FROM GALLERY CROSS-SECTION CHANGES IN A LONGWALL TOP COAL CAVING PANEL Mehmet MESUTOĞLU, İhsan ÖZKAN, Alfonso RODRIGUEZ-DONO	231-250
MACHINE WHEEL EDGE DETECTION MORPHOLOGICAL OPERATIONS Pınar KARAKUŞ	251-262
GIS-AHP APPROACH FOR A COMPREHENSIVE FRAMEWORK TO DETERMINE THE SUITABLE REGIONS FOR GEOTHERMAL POWER PLANTS IN İZMİR, TÜRKİYE Kemal KOCA, Fatih KARİPOĞLU, Emel Zeray ÖZTÜRK	263-279



OPTIMIZING ENERGY HUB SYSTEM OPERATION WITH ELECTRICAL AND THERMAL DEMAND RESPONSE PROGRAMS

^{1,*} Özge Pınar AKKAŞ , ² Yağmur ARIKAN YILDIZ 

¹ Kırıkkale University, Engineering and Natural Sciences Faculty, Electrical-Electronics Engineering Department, Kırıkkale, TÜRKİYE

² Sivas Cumhuriyet University, Şarkışla School of Applied Sciences, Information Systems and Technologies Department, Sivas, TÜRKİYE

¹ ozgepinarakkas@kku.edu.tr, ² yagmurarikan@cumhuriyet.edu.tr

Highlights

- The study focuses on EH optimization, including renewable energy systems, combined heat and power, and more, to minimize costs.
- Demand response programs (DRP) play a crucial role in adjusting electricity consumption in response to price fluctuations.
- The article incorporates Electrical Demand Response Program (EDRP) and Thermal Demand Response Program (TDRP) into the EH.
- The optimization problem is addressed through Mixed Integer Linear Programming (MILP) and CPLEX solver in GAMS.
- The effectiveness of the model is validated by comparing results from various case studies.



OPTIMIZING ENERGY HUB SYSTEM OPERATION WITH ELECTRICAL AND THERMAL DEMAND RESPONSE PROGRAMS

^{1,*} Özge Pınar AKKAŞ , ² Yağmur ARIKAN YILDIZ 

¹ Kırıkkale University, Engineering and Natural Sciences Faculty, Electrical-Electronics Engineering Department, Kırıkkale, TÜRKİYE

² Sivas Cumhuriyet University, Şarkışla School of Applied Sciences, Information Systems and Technologies Department, Sivas, TÜRKİYE

¹ ozgepinarakkas@kku.edu.tr, ² yagmurarikan@cumhuriyet.edu.tr

(Received: 18.10.2023; Accepted in Revised Form: 04.12.2023)

ABSTRACT: Electricity consumption is increasing rapidly and many countries are looking for ways to cope with the energy crisis. Moreover, the world is facing the problem of global warming caused by emissions. Therefore, it is of great importance to operate power systems efficiently. Energy Hub (EH) represents a versatile energy system capable of providing efficient and optimal solutions for the operation of power systems across multiple carriers. This paper examines the optimization of an EH encompassing renewable energy systems (RES) like wind and photovoltaic, combined heat and power (CHP), transformer, absorption chiller, energy storage system (ESS) and furnace with aiming at minimizing the cost. Demand response is an energy sector strategy that entails modifying electricity consumption patterns in reaction to fluctuations in electricity supply or pricing. The objective of demand response programs (DRP) is to curtail or shift electricity consumption during periods of elevated electricity prices. Therefore, Electrical Demand Response Program (EDRP) for electrical demand and the Thermal Demand Response Program (TDRP) for heating demand are incorporated into the EH. The optimization problem is formulated as Mixed Integer Linear Programming (MILP) and solved with CPLEX solver in GAMS. The outcomes of various case studies are compared to ascertain the model's efficiency.

Keywords: Demand response program, Energy Hub, Optimization, Renewable energy systems

1. INTRODUCTION

The rise in energy demand in the world is followed closely. There are reports from various organizations that the amount of electricity consumption has increased by almost four times over the last half century. When global warming, environmental problems and energy needs are evaluated together, the importance of using clean, reliable, abundant and renewable alternative energy sources is increasing. The contribution of renewable energy sources (RES) is expected to be significant in meeting global targets for reducing greenhouse gas emissions. It is foreseen that technological energy harvesting alternatives will increase and costs will decrease rapidly with technological developments. The Energy Hub (EH) is a recently developed technology that aims to optimize the operations of energy systems. EH systems use the energy sources efficiently and convert a set of different energy carriers such as electricity, heat, natural gas and so on in its input into a set of energy demands such as electricity, cooling and heating. They achieve the generation, distribution, conversion, and retention of diverse interconnected energy carriers. [1, 2]. EH reduces costs and emissions and improves the system reliability with combining RES as the distributed generation (DG) [1, 3]. The most countries are expected to use EH systems as a robust tool for the optimal planning and operation of multiple energy carriers [3].

There are many studies on EH in several aspects such as optimal modeling, scheduling, load dispatch, operation and energy management. Lu et al. [2] have developed a computational model to optimize the allocation of energy in an EH system, which includes an energy storage system (ESS) and a demand response program (DRP). The primary goal is to minimize the overall cost associated with electricity consumption. Eladl et al. [3] have proposed a model that aims to optimize the operation and configuration

*Corresponding Author: Özge Pınar AKKAŞ, ozgepinarakkas@kku.edu.tr

of EH in order to minimize costs, reduce emissions, and maximize profits. Rakipour and Barati [4] have developed a mixed-integer linear programming (MILP) model aimed at optimizing the operation of an EH that incorporates heating, cooling, electrical storage systems, RES and DRPs. The goal is to maximize the profitability of the EH. Tian et al. [5] have introduced a stochastic model based on risk for optimizing the operation of an EH that encompasses storage systems, a wind energy system (WES), the electricity and heating markets and DRP, all with the objective of cost minimization. Additionally, they have incorporated downside risk constraints (DRC) to mitigate the uncertainties and associated risks. Nasir et al. [6] have investigated the day-ahead scheduling of an electric-hydrogen integrated energy system, considering various components such as wind and photovoltaic energy systems, electric storage, thermal storage, hydrogen storage systems, combined heat and power (CHP), biomass units, boilers, solar heaters and hydrogen electrolyzer. The main objective is to optimize the operational cost of the system while establishing connections with demand response aggregators. Davatgaran et al. [7] have proposed a model aimed at determining the most efficient bidding strategy for an EH's involvement in the day-ahead market, with the main goal of reducing costs. Vahid-Pekdel et al. [8] have proposed a comprehensive model for the optimal operation of an EH. The model incorporates various components such as WES, storage systems, DRPs and participation in energy markets. The main objective of this model is to minimize the operational costs associated with operating the EH while ensuring efficient utilization of resources. Shahrabi et al. [9] have presented a model for the strategic planning and optimal operation of an EH system, which addresses both electrical and thermal demands to minimize the overall cost. Cao et al. [10] have proposed a multi-energy hub system model that focuses on minimizing carbon emissions and operational expenses. The study has also integrated real-time DRPs, resulting in cost and emission reductions. Jamalzadeh et al. [11] have proposed a MILP model for an EH. Their objective is to minimize costs while considering the thermal energy market and incorporating both thermal and electrical DRPs. Dolatabadi and Mohammadi-Ivatloo [12] have presented a smart EH scheduling model under DRP. They have also integrated the conditional value-at-risk (CVaR) method into the model for risk measurement. Pazouki et al. [13] have proposed a model for optimal operation of the EH with consideration of cost, emission and reliability. Pazouki and Haghiham [14] have proposed a mathematical formulation including costs related to operation, emission, reliability and investment of the EH for optimal planning. Thang et al. [15] have presented a stochastic scheduling framework aiming to minimize the cost and emission for multi EH systems. Majidi et al. [16] have presented a model considering both economy and environment for operation of the EH in the presence of DRP.

The use of RES is a promising way to decrease emission and cost and increase reliability. Therefore, in this paper, the proposed EH system includes wind and PV energy systems from RES. Demand Response Programs (DRP) are valuable tools that facilitate efficient load shifting for the management of EH system to minimize cost. The Electrical Demand Response Program (EDRP) for electrical demand and the Thermal Demand Response Program (TDRP) for heating demand are included in the system. The other components of the EH system are transformer, CHP, furnace, absorption chiller and ESS. The study makes a significant contribution to addressing the contemporary challenges associated with the escalating electricity consumption and the global energy crisis. In light of the pressing issue of global warming attributed to emissions, the study emphasizes the critical importance of enhancing the efficiency of power systems. It introduces the concept of an EH as a versatile energy system with incorporating RES such as wind and solar, as well as energy storage technology to efficiently meet the demands for electricity, heating and cooling and with incorporating DRPs to provide a strategic approach to changing electricity consumption patterns in response to changes in supply or pricing. The optimization problem with the aim of minimizing the cost of EH with consideration of EDRP and TDRP in three case studies have been analyzed. The problem is solved using CPLEX solver in GAMS software.

2. THE STRUCTURE OF THE ENERGY HUB SYSTEM

The EH proposed in this study incorporates various components that are specifically designed to generate, convert, and store different forms of energy. These components allow for the harnessing and

storage of energy to meet the required demands efficiently. The EH system is powered by a combination of natural gas, electricity from the external grid and RES such as wind and solar. The output of the system includes energy needs for electricity, heating, and cooling. The presented EH contains a wind energy system (WES), a photovoltaic energy system (PVES), a furnace, a CHP, a transformer, an ESS, an absorption chiller, an EDRP unit and a TDRP unit. Figure 1 illustrates the schematic diagram of the proposed model for the EH system.

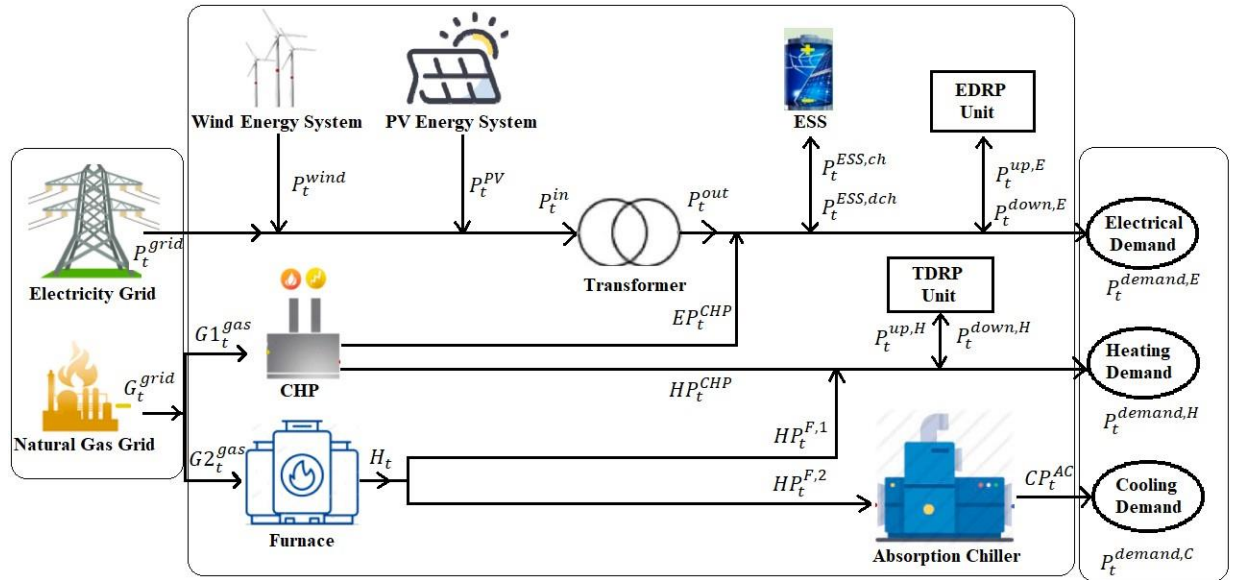


Figure 1. The suggested EH system

The electricity demand within the described system is met through a combination of solar and wind systems, the CHP unit and the main grid. The heating demand is fulfilled by both the CHP unit and the furnace, while cooling needs are catered for by an absorption chiller. The wind and solar energy systems generate environmentally friendly energy. The CHP utilizes natural gas to generate both heat and electricity. The absorption chiller takes the heat and converts it into cooling demand. The furnace uses natural gas to meet heating demand. The transformer is used to adjust the voltage levels of electricity. The ESS is also incorporated within the system to charge and discharge electricity as required.

3. MATHEMATICAL FRAMEWORK FOR THE PROPOSED PROBLEM FORMULATION

Here, a comprehensive explanation of the mathematical portrayal of the components in the EH are provided. Additionally, the objective function and constraints pertaining to this problem are elaborated.

3.1. Wind Energy System Modeling

The electricity generated by a WES depends on numerous factors, such as wind speed, the number and characteristics of turbines in the system. This calculation can be expressed using Equation 1 [17,18,19].

$$P_t^{wind} = N^{WT} \times \begin{cases} P_{rated}^{wind}, & v_t^{wind} < v_{in}^{wind} < v_t^{wind} < v_{out}^{wind} \\ 0, & v_t^{wind} < v_{in}^{wind} \text{ or } v_t^{wind} > v_{out}^{wind} \\ P_{rated}^{wind} \times \left(\frac{v_t^{wind} - v_{in}^{wind}}{v_{rated}^{wind} - v_{in}^{wind}} \right)^3, & v_{in}^{wind} < v_t^{wind} < v_{rated}^{wind} \end{cases} \quad (1)$$

where P_t^{wind} is the output power of the WES at hour t , N^{WT} is the number of wind turbines, P_{rated}^{wind} is the rated power of the wind turbine (MW), v_t^{wind} is the wind speed in the region at hour t (m/s), v_{out}^{wind} ,

v_{in}^{wind} and v_{rated}^{wind} are the cut-out, cut-in and rated wind speeds (m/s) that are specific values for the wind turbine.

3.2. Photovoltaic Energy System Modeling

The electricity generated by a PVES is dependent on numerous factors including the temperature and sunlight intensity of the surroundings, as well as the number and specifications of the PV panels used in the system. This calculation can be expressed using Equations 2a-2e [3, 20].

$$P_t^{PV} = N^{PV} \times FF^{PV} \times V_t^{PV} \times I_t^{PV} \quad (2a)$$

$$FF^{PV} = \frac{V_{MPP}^{PV} \times I_{MPP}^{PV}}{V_{OC}^{PV} \times I_{SC}^{PV}} \quad (2b)$$

$$V_t^{PV} = V_{OC}^{PV} - C_{VT}^{PV} \times T_t^C \quad (2c)$$

$$I_t^{PV} = S_t \times [I_{SC}^{PV} + C_{CT}^{PV} \times (T_t^C - 25)] \quad (2d)$$

$$T_t^C = T_t^A + S_t \times \left(\frac{T^B - 20}{0.8} \right) \quad (2e)$$

where P_t^{PV} is the power output of the PVES at hour t, N^{PV} is the number of PV panels within the system, FF^{PV} is the filling factor of the panel, V_t^{PV} and I_t^{PV} are the voltage and current characteristic of the panel at hour t, respectively, V_{MPP}^{PV} and I_{MPP}^{PV} denote the maximum power point voltage and current, respectively, V_{OC}^{PV} and I_{SC}^{PV} are the open circuit voltage and short circuit current of the panel, respectively, C_{VT}^{PV} and C_{CT}^{PV} represent the voltage and current temperature coefficient of the panel, respectively, T_t^A and T_t^C are the temperature of the ambient and panel at hour t, respectively, S_t is the solar radiation level at hour t, T^B indicates the nominal operating temperature of the panel.

3.3. Combined Heat and Power Modeling

The CHP system receives the natural gas and converts it into electricity, by considering the efficiency of converting gas to electricity as shown in Equation 3a, as well as into heat, considering the efficiency of converting gas to heat as shown in Equation 3b [4].

$$EP_t^{CHP} = \eta_{GE}^{CHP} \times G1_t^{gas} \quad (3a)$$

$$HP_t^{CHP} = \eta_{GH}^{CHP} \times G1_t^{gas} \quad (3b)$$

where EP_t^{CHP} is the output electrical power of the CHP system at hour t, η_{GE}^{CHP} is the efficiency for gas to electricity conversion for CHP, $G1_t^{gas}$ is the input of natural gas to the CHP at hour t, HP_t^{CHP} is the output heat power of the CHP system at hour t, η_{GH}^{CHP} is the efficiency for gas to heat conversion for CHP.

3.4. Furnace Modeling

The heat output of the furnace in the EH is determined by assessing the natural gas input and its conversion efficiency. This calculation, detailed in Equation 4, mathematically represents the heat power generated.

$$H_t = HP_t^{F,1} + HP_t^{F,2} = \eta_{GH}^F \times G2_t^{gas} \quad (4)$$

where H_t is the output heat power of the furnace at hour t, η_{GH}^F is the efficiency of natural gas to heat

power conversion for the furnace, $G2_t^{gas}$ is the input of the natural gas to the furnace at hour t. A portion of H_t is used to meet the heating demand that is represented as $HP_t^{F,1}$, while another portion is utilized as input for the absorption chiller that is represented as $HP_t^{F,2}$.

3.5. Absorption Chiller Modeling

It operates by converting heat into cooling capacity. The calculation of the cooling capacity produced by the absorption chiller is determined by the input heat power and the efficiency of the conversion process from heat to cooling, as depicted in Equation 5 [4].

$$CP_t^{AC} = \eta_{HC}^{AC} \times HP_t^{F,2} \quad (5)$$

where CP_t^{AC} is the output cooling power of the absorption chiller at hour t, η_{HC}^{AC} is the efficiency of heat to cooling conversion for the absorption chiller, $HP_t^{F,2}$ is the heat power input to absorption chiller at hour t.

3.6. Transformer Modeling

A transformer is installed in the EH for voltage transformation. The calculation of the power output from the transformer relies on both the input power provided to the transformer and its efficiency, as described in Equation 6a [4]. The input power to the transformer consists of the electrical power from grid and the output power of WES and PVES as shown in Equation 6b.

$$P_t^{out} = \eta_{EE}^T \times P_t^{in} \quad (6a)$$

$$P_t^{in} = P_t^{grid} + P_t^{wind} + P_t^{PV} \quad (6b)$$

where P_t^{in} is the input power of the transformer, η_{EE}^T is the efficiency of the transformer, P_t^{out} is the output power of the transformer, P_t^{grid} is the electrical power taken from electrical grid at hour t.

3.7. Energy Storage System Modeling

The ESS is utilized to charge and discharge the electricity. The constraints of the ESS are given in Equations 7a-7e [2, 17].

$$SOC_t^{ESS} = SOC_{t-1}^{ESS} + (P_t^{ESS,ch} \times \eta_{ch}) - (P_t^{ESS,dch} / \eta_{dch}) \quad (7a)$$

$$P_{min}^{ESS,ch} \leq P_t^{ESS,ch} \leq P_{max}^{ESS,ch} \quad (7b)$$

$$P_{min}^{ESS,dch} \leq P_t^{ESS,dch} \leq P_{max}^{ESS,dch} \quad (7c)$$

$$SOC_{min}^{ESS} \leq SOC_t^{ESS} \leq SOC_{max}^{ESS} \quad (7d)$$

$$I_t^{ESS,ch} + I_t^{ESS,dch} \leq 1, \quad I_t^{ESS,ch} \text{ and } I_t^{ESS,dch} \in \{0,1\} \quad (7e)$$

where SOC_t^{ESS} is the state of charge (SoC) of the ESS at hour t, $P_t^{ESS,ch}$ is the charging power of the ESS at hour t, η_{ch} is the charging efficiency of the ESS, $P_t^{ESS,dch}$ is the discharging power of the ESS at hour t, η_{dch} is the discharging efficiency of the ESS, $P_{min}^{ESS,ch}$ and $P_{max}^{ESS,ch}$ are the minimum and maximum charging power of the ESS, respectively, $P_{min}^{ESS,dch}$ and $P_{max}^{ESS,dch}$ are the minimum and maximum discharging power of the ESS, respectively, SOC_{min}^{ESS} and SOC_{max}^{ESS} are the minimum and maximum capacity of SoC of the ESS at hour t. $I_t^{ESS,ch}$ and $I_t^{ESS,dch}$ represent the binary variables that show the charging and discharging

situation of the ESS, respectively. The battery must be in either charging or discharging state as described in Equation 7e.

3.8. Electrical Demand Response Program Constraints

The constraints of the EDRP are given in Equations 8a-8d [2, 4].

$$\sum_{t=1}^T P_t^{up,E} = \sum_{t=1}^T P_t^{down,E} \quad (8a)$$

$$0 \leq P_t^{up,E} \leq MRT_E^{up} \cdot P_t^{demand,E} \cdot I_t^{up,E} \quad (8b)$$

$$0 \leq P_t^{down,E} \leq MRT_E^{down} \cdot P_t^{demand,E} \cdot I_t^{down,E} \quad (8c)$$

$$0 \leq I_t^{down,E} + I_t^{up,E} \leq 1 \quad (8d)$$

where $P_t^{up,E}$ and $P_t^{down,E}$ are the shifted up and shifted down electrical power demand at hour t , respectively, MRT_E^{up} and MRT_E^{down} are the maximum ratio of the shifted up and shifted down electrical power demand, $P_t^{demand,E}$ is the electrical power demand at hour t , $I_t^{up,E}$ and $I_t^{down,E}$ are the binary variables that show the shifting up and shifting down situation of electrical demand at hour t , respectively.

Equation 8a provides the balance between shifted up and shifted down electrical demands. Equation 8b and 8c express the limits for allowed shifted up and shifted down electrical power demands with respect to the maximum ratio of related electrical power demand, respectively. Equation 8d prevents to shift up and shift down the electrical power demand at the same time.

3.9. Thermal Demand Response Program Constraints

The constraints of the TDRP are given in Equations 9a-9d [2].

$$\sum_{t=1}^T P_t^{up,H} = \sum_{t=1}^T P_t^{down,H} \quad (9a)$$

$$0 \leq P_t^{up,H} \leq MRT_H^{up} \cdot P_t^{demand,H} \cdot I_t^{up,H} \quad (9b)$$

$$0 \leq P_t^{down,H} \leq MRT_H^{down} \cdot P_t^{demand,H} \cdot I_t^{down,H} \quad (9c)$$

$$0 \leq I_t^{down,H} + I_t^{up,H} \leq 1 \quad (9d)$$

where $P_t^{up,H}$ and $P_t^{down,H}$ are the shifted up and shifted down heating power demand at hour t , respectively, MRT_H^{up} and MRT_H^{down} are the maximum ratio of the shifted up and shifted down heating power demand, $P_t^{demand,H}$ is the heating power demand at hour t , $I_t^{up,H}$ and $I_t^{down,H}$ are the binary variables that show the shifting up and shifting down situation of heat demand at hour t , respectively.

Equation 9a provides the balance between shifted up and shifted down heat demands. Equation 9b and 9c express the limits for allowed shifted up and shifted down heating power demands with respect to the maximum ratio of related heat demand, respectively. Equation 9d prevents to shift up and shift down the heating power demand at the same time.

3.10. Objective Function

The main objective of the problem is to minimize the overall cost. This total cost is determined by considering both the amount and price of electricity and natural gas, as described in Equation 10.

$$Cost = \sum_{t=1}^T \lambda_t^{el} \times P_t^{grid} + \lambda_t^{ng} \times G_t^{grid} \quad \text{where} \quad G_t^{grid} = G1_t^{gas} + G2_t^{gas} \quad (10)$$

where λ_t^{el} is the price of electricity from electrical grid at hour t , λ_t^{ng} is the price of natural gas from natural gas grid at hour t and G_t^{grid} is the natural gas taken from natural gas grid at hour t . G_t^{grid} is utilized for both input to CHP ($G1_t^{gas}$) and input to furnace ($G2_t^{gas}$).

3.11. Energy Balance Constraints

Equations 11a, 11b, and 11c represent the energy equilibrium between power generation and consumption in terms of electricity, heating, and cooling requirements.

$$P_t^{demand,E} = P_t^{out} + P_t^{ESS,dch} - P_t^{ESS,ch} + EP_t^{CHP} + P_t^{down,E} - P_t^{up,E} \quad (11a)$$

$$P_t^{demand,H} = HP_t^{CHP} + HP_t^{F,1} + P_t^{down,H} - P_t^{up,H} \quad (11b)$$

$$P_t^{demand,C} = CP_t^{AC} \quad (11c)$$

where $P_t^{demand,E}$ is the electrical demand at hour t , $P_t^{demand,H}$ is the heating demand at hour t and $P_t^{demand,C}$ is the cooling demand at hour t .

Equation 11a gives the energy balance for the electrical demand. The sum of the output power of the transformer that receives the electrical power from grid and the output power of WES and PVES as an input, the discharging power of the ESS, the output electrical power of the CHP system and shifted down electrical power demand at hour t must be equal to the sum of electrical demand, the charging power of the ESS and shifted up electrical power demand at hour t .

Equation 11b gives the energy balance for the heating demand. The sum of the output heat power of the CHP system, the heat power generated by the furnace and not used in the absorption chiller and shifted down heating power demand at hour t must be equal to the sum of heating demand and shifted up heating power demand at hour t .

Equation 11c gives the energy balance for the cooling demand. The cooling requirement during hour t should be satisfied by the absorption chiller's cooling capacity during that same hour.

4. CASE STUDIES AND RESULTS

4.1. Input Data

The parameter values of the WES are taken from the study [21]. There are 50 wind turbines in the WES. The parameter values of PVES are taken from the study [22]. There are 100 PV panels in the PVES. The data regarding wind speed, solar radiation, and ambient temperature have been taken from meteorological sources. The parameter values of the CHP [4], the absorption chiller [4], the furnace [23], the transformer [23], the ESS [23], the maximum ratios of shifted electrical and heat demand, both upwards and downwards [5], are provided in Table 1.

Table 1. The parameter values

Parameter	Value	Parameter	Value	Parameter	Value
η_{GE}^{CHP}	0.40	η_{ch}	0.90	MRT_E^{up}	0.20
η_{GH}^{CHP}	0.35	η_{dch}	0.90	MRT_E^{down}	0.20
η_{HC}^{AC}	0.92	SOC_{min}^{ESS}	120	MRT_H^{up}	0.20
η_{GH}^F	0.90	SOC_{max}^{ESS}	600	MRT_H^{down}	0.20
η_{EE}^T	0.98	$SOC(t=0)$	120		

Figure 2 displays the data pertaining to the electricity, heating, and cooling requirements, while Figure 3 illustrates the hourly rates for electrical energy. The natural gas price is fixed for each hour and taken as 12 \$/MWh [23].

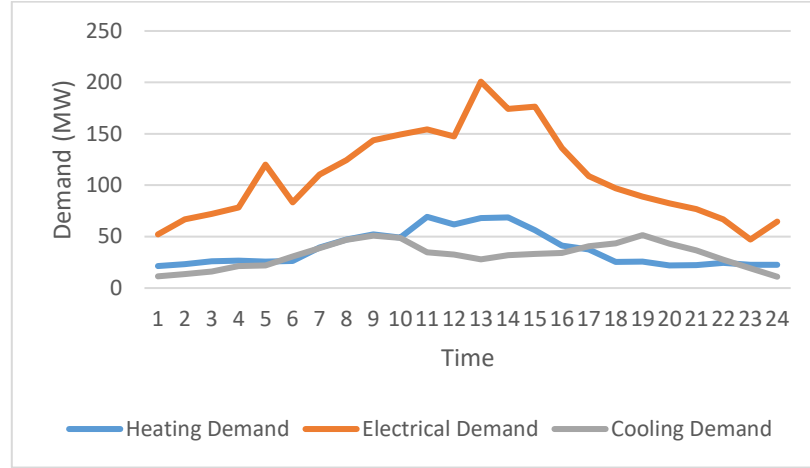


Figure 2. The electrical, heating and cooling demand

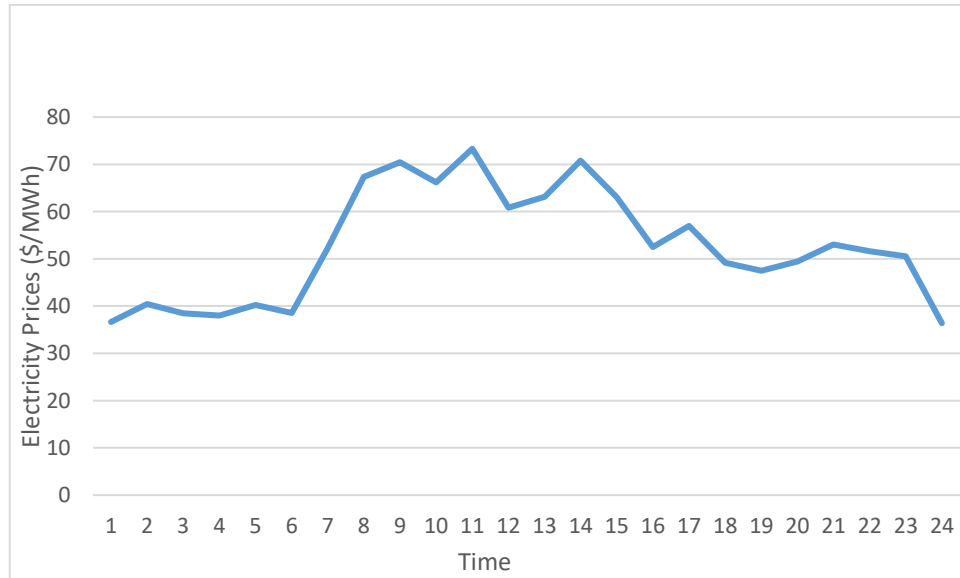


Figure 3. The electrical energy prices

4.2. Case Studies

The optimal operation of the EH is investigated for three different cases:

Case 1: Both EDRP and TDRP are not considered.

Case 2: EDRP is considered and TDRP is not considered.

Case 3: Both EDRP and TDRP are considered.

The proposed optimization is formulated as MILP and solved under GAMS software using CPLEX solver. GAMS serves as a robust tool for modeling a spectrum of optimization problems, encompassing linear, nonlinear, and combinatorial scenarios [24]. It provides a range of solvers that are designed to handle optimization problems based on mathematical programming. One such solver is CPLEX, known for its advanced capabilities in solving complex optimization problems [4]. The CPLEX solver is widely recognized as a powerful and efficient tool that enhances the optimization capabilities of GAMS software. This robust solver excels in determining optimal values for complex optimization problems, surpassing alternative solutions successfully. The CPLEX solver applies various algorithms such as the primal simplex, dual simplex, interior point barrier and mixed-integer methods to effectively tackle a diverse

range of optimization problems [6].

The results of the cases are explained below.

4.2.1. Case 1

In Case 1, EDRP and TDRP are not incorporated into the model. The total cost of the EH operation is found as 109787.3993 \$. The results for Case 1 are presented in Table 2.

Table 2. Case 1 results

Time	P_t^{grid}	G_t^{grid}	SOC_t^{ESS}	$P_t^{ESS,ch}$	$P_t^{ESS,dch}$
1	148.127	75.032	228.000	120.000	-
2	38.573	82.832	228.000	-	-
3	163.727	93.895	336.000	120.000	-
4	168.478	102.131	444.000	120.000	-
5	142.971	99.713	492.000	53.333	-
6	169.502	112.627	600.000	120.000	-
7	55.338	159.838	600.000	-	-
8	-	191.665	539.896	-	54.094
9	-	210.451	468.118	-	64.600
10	-	199.344	387.897	-	72.199
11	-	240.029	330.729	-	51.451
12	54.928	216.636	330.729	-	-
13	-	227.861	220.102	-	99.565
14	-	234.647	133.986	-	77.504
15	88.040	201.239	120.000	-	12.587
16	83.341	159.184	120.000	-	-
17	62.491	156.133	120.000	-	-
18	67.009	125.228	120.000	-	-
19	59.094	135.627	120.000	-	-
20	56.810	114.625	120.000	-	-
21	50.349	108.082	120.000	-	-
22	37.393	103.740	120.000	-	-
23	19.781	87.925	120.000	-	-
24	37.265	77.856	120.000	-	-

As shown in Table 2, the electricity has not been purchased from the grid during the hours 8-11 and 13-14 that electricity price is high. During these hours, the discharging power of the ESS is utilized to fulfill the electrical demand, while in other hours, electricity is procured from the grid due to favorable, low electricity prices. The ESS is charged in hours 1, 3-6 due to extremely low electricity prices. In these hours, more electricity has been purchased from the grid to charge the ESS and use it when electricity prices are high.

4.2.2. Case 2

In Case 2, the EDRP is incorporated into the EH system in Case 1 and its impact on EH operation has been analyzed. The total cost of the EH operation is found as 106332.5618 \$. A decrease in cost has been observed when compared to the Case 1. The results for Case 2 are presented in Table 3.

Table 3. Case 2 results

Time	P_t^{grid}	G_t^{grid}	SOC_t^{ESS}	$P_t^{ESS,ch}$	$P_t^{ESS,dch}$	$P_t^{up,E}$	$P_t^{down,E}$
1	158.760	75.032	228.000	120.000	-	10.420	-
2	52.185	82.832	228.000	-	-	13.340	-
3	178.462	93.895	336.000	120.000	-	14.440	-
4	184.478	102.131	444.000	120.000	-	15.680	-
5	167.502	99.713	492.000	53.333	-	24.040	-
6	186.543	112.627	600.000	120.000	-	16.700	-
7	77.869	159.838	600.000	-	-	22.080	-
8	-	191.665	567.518	-	29.234	-	24.860
9	-	210.451	527.651	-	35.880	-	28.720
10	-	199.344	480.608	-	42.339	-	29.860
11	-	240.029	432.685	-	43.131	-	8.320
12	-	216.636	405.608	-	24.369	-	29.460
13	-	227.861	339.580	-	59.425	-	40.140
14	-	234.647	292.220	-	42.624	-	34.880
15	-	201.239	182.368	-	98.867	-	-
16	111.117	159.184	182.368	-	-	27.220	-
17	-	156.133	138.477	-	39.502	-	21.740
18	-	125.228	138.477	-	-	19.380	-
19	77.278	135.627	138.477	-	-	17.820	-
20	73.647	114.625	138.477	-	-	16.500	-
21	17.686	108.082	120.000	-	16.629	-	15.380
22	51.026	103.740	120.000	-	-	13.360	-
23	29.414	87.925	120.000	-	-	9.440	-
24	50.469	77.856	120.000	-	-	12.940	-

As depicted in Table 3, similar to Case 1, electricity has not been procured from the ESS during hours with high electricity prices. Instead, during hours with lower electricity prices, electricity has been purchased and a portion of it has been stored in the ESS. At the same time, owing to the impact of the EDRP, the load is adjusted downward during the hours when electricity prices are high, effectively curbing costs. Conversely, during hours with lower electricity prices, the load is shifted upward.

4.2.3. Case 3

In Case 3, both the EDRP and the TDRP units are incorporated into the EH system in Case 1 and their impacts on EH operation have been analyzed. The total cost of the EH operation is found as 105675.7576 \$. A decrease in cost has been observed when compared to the Case 1 and Case 2. The results for Case 3 are presented in Table 4.

Table 4. Case 3 results

Time	P_t^{grid}	G_t^{grid}	SOC_t^{ESS}	$P_t^{ESS,ch}$	$P_t^{ESS,dch}$	$P_t^{up,E}$	$P_t^{down,E}$	$P_t^{up,H}$	$P_t^{down,H}$
1	163.751	62.803	228.000	120.000	-	10.420	-	-	4.280
2	57.597	69.574	228.000	-	-	13.340	-	-	4.640
3	184.549	78.981	336.000	120.000	-	14.440	-	-	5.220
4	190.705	86.874	444.000	120.000	-	15.680	-	-	5.340
5	173.473	85.084	492.000	53.333	-	24.040	-	-	5.120
6	192.700	97.541	600.000	120.000	-	16.700	-	-	5.280
7	87.081	137.266	600.000	-	-	22.080	-	-	7.900
8	-	218.693	551.909	-	43.282	-	-	9.460	-
9	-	210.451	512.042	-	35.880	-	28.720	-	-
10	-	199.344	464.999	-	42.339	-	29.860	-	-
11	-	279.629	459.697	-	4.771	-	30.840	13.860	-
12	-	216.636	432.620	-	24.369	-	29.460	-	-
13	-	227.861	366.593	-	59.425	-	40.140	-	-
14	-	267.619	295.131	-	64.316	-	-	11.540	-
15	-	233.468	227.683	-	60.703	-	25.273	11.280	-
16	51.415	182.784	227.683	-	-	-	21.847	8.260	-
17	-	177.504	169.136	-	52.693	-	-	7.480	-
18	92.708	110.714	169.136	-	-	19.380	-	-	5.080
19	83.272	120.941	169.136	-	-	17.820	-	-	5.140
20	78.755	102.110	169.136	-	-	16.500	-	-	4.380
21	-	120.882	120.000	-	44.222	-	-	4.480	-
22	56.763	89.683	120.000	-	-	13.360	-	-	4.920
23	34.708	74.953	120.000	-	-	9.440	-	-	4.540
24	55.741	64.942	120.000	-	-	12.940	-	-	4.520

As seen in Table 4, similar to cases 1 and 2, the ESS has not been used for electricity procurement or consumption during periods of high electricity prices. Conversely, when electricity prices are low, some amount of electricity is acquired and stored in the ESS. Moreover, similar to Case 2, the load is adjusted downward during the hours of high electricity prices and it is shifted upward during hours of lower electricity prices, aiming to minimize costs through the influence of the EDRP. In addition, with the effect of the EDRP, the heating demand is elevated during high electricity price hours, leading to an increased procurement of natural gas from the grid. The purpose of this is to ensure that CHP receives more heat and generates more electricity. Thus, when the electricity price is high, the purchase of electricity from the grid is reduced and it causes the cost to decrease. During hours of low electricity prices, the heating demand is adjusted downward, leading to a decrease in the procurement of natural gas from the grid. Consequently, this reduction in heating demand also results in decreased heat generation by the CHP system and an increased reliance on purchasing electricity from the grid.

5. CONCLUSION

In this paper, a MILP model has been developed for the optimal operation of the EH. This model incorporates components such as WES, PVES, CHP, furnace, absorption chiller, ESS, transformer, EDRP and TDRP units. In the simulation studies, the impact of EDRP and TDRP units on cost has been analyzed by considering 3 different cases. The model is implemented in GAMS software and CPLEX is used, which is an efficient and powerful solver for MILP problems. In Case 1, EDRP and TDRP are not added to the model and minimum cost is tried to be obtained. In Case 2, EDRP is added to the model and 3.15% reduction has been observed compared to the Case 1. In Case 3, both EDRP and TDRP are added to the model and the cost is decreased by 3.75% compared to the cost in Case 1. According to the results obtained,

it is seen that the proposed problem provides significant cost reduction when the long-term operation planning of the EH is also considered.

To build upon this research, it is recommended to investigate the feasibility of integrating additional RES like geothermal, biomass or hydrogen into the EH system with including Hydrogen Storage System and hydrogen demand. Furthermore, it would be beneficial to analyze the uncertainties related to output from RES, electricity prices and demand. In addition to cost minimization, an objective function could be developed that reduces risks associated with these uncertainties as well as emissions resulting from thermal resources.

Declaration of Ethical Standards

Authors declare to comply with all ethical guidelines including authorship, citation, data reporting, and publishing original research.

Credit Authorship Contribution Statement

Ö. P. AKKAŞ: Methodology, Conceptualization, Resources, Investigation, Writing - review & editing, Supervision.

Y. ARIKAN YILDIZ: Methodology, Conceptualization, Resources, Investigation, Writing -review & editing, Supervision.

Declaration of Competing Interest

The authors declared that they have no conflict of interest.

Funding / Acknowledgements

The author(s) received no financial support for the research.

Data Availability

The data that support the findings of this study are available from the corresponding author upon reasonable request.

REFERENCES

- [1] M. Geidl and G. Andersson, "A modeling and optimization approach for multiple energy carrier power flow," in Proc. IEEE 2005 Power Tech Conference, Russia, 27-30 June 2005.
- [2] X. Lu, H. Li, K. Zhou, and S. Yang, "Optimal load dispatch of energy hub considering uncertainties of renewable energy and demand response," *Energy*, vol. 262, pp. 125564, 2023.
- [3] A. A. Eladl, M. I. El-Afifi, M. A. Saeed, and M. M. El-Saadawi, "Optimal operation of energy hubs integrated with renewable energy sources and storage devices considering CO₂ emissions," *Electrical Power and Energy Systems*, vol. 117, p. 105719, 2020.
- [4] D. Rakipour and H. Barat, "Probabilistic optimization in operation of energy hub with participation of renewable energy resources and demand response," *Energy*, vol. 173, pp. 384-399, 2019.
- [5] M. Tian, A. G. Ebadi, K. Jernsittiparsert, M. Kadyrov, A. Ponomarev, N. Javanshir, and S. Nojavan, "Risk-based stochastic scheduling of energy hub system in the presence of heating network and thermal energy management," *Applied Thermal Engineering*, vol. 159, p. 113825, 2019.
- [6] M. Nasir, A. R. Jordehi, M. Tostado-Veliz, V. S. Tabar, S. A. Mansouri, and F. Jurado, "Operation of energy hubs with storage systems, solar, wind and biomass units connected to demand

- response aggregators," *Sustainable Cities and Society*, vol. 83, p. 103974, 2022.
- [7] V. Davatgaran, M. Saniei, and S. S. Mortazavi, "Optimal bidding strategy for an energy hub in energy market," *Energy*, vol. 148, pp. 482-493, 2018.
- [8] M. J. Vahid-Pakdel, S. M. Nojavan, B. Mohammadi-ivatloo, and K. Zare, "Stochastic optimization of energy hub operation with consideration of thermal energy market and demand response," *Energy Conversion and Management*, vol. 145, pp. 117-128, 2017.
- [9] E. Shahrabi, S. M. Hakimi, A. Hasankhani, G. Derakhshan, and B. Abdi, "Developing optimal energy management of energy hub in the presence of stochastic renewable energy resources," *Sustainable Energy, Grids and Networks*, vol. 26, p. 100428, 2021.
- [10] Y. Cao, Q. Wang, J. Du, S. Nojavan, K. Jermsttiparsert, and N. Ghadimi, "Optimal operation of CCHP and renewable generation-based energy hub considering environmental perspective: An epsilon constraint and fuzzy methods," *Sustainable Energy, Grids and Networks*, vol. 20, p. 100274, 2019.
- [11] F. Jamalzadeh, A. H. Mirzahosseini, F. Faghihi, and M. Panahi, "Optimal operation of energy hub system using hybrid stochastic-interval optimization approach," *Sustainable Cities and Society*, vol. 54, p. 101998, 2020.
- [12] A. Dolatabadi and B. Mohammadi-Ivatloo, "Stochastic risk-constrained scheduling of smart energy hub in the presence of wind power and demand response," *Applied Thermal Engineering*, vol. 123, pp. 40-49, 2017.
- [13] S. Pazouki, M. Haghifam, and A. Moser, "Uncertainty modeling in optimal operation of energy hub in presence of wind, storage and demand response," *Electrical Power and Energy Systems*, vol. 61, pp. 335-345, 2014.
- [14] S. Pazouki and M. Haghifam, "Optimal planning and scheduling of energy hub in presence of wind, storage and demand response under uncertainty," *Electrical Power and Energy Systems*, vol. 80, pp. 219-239, 2016.
- [15] V. V. Thang, T. Ha, Q. Li, and Y. Zhang, "Stochastic optimization in multi-energy hub system operation considering solar energy resource and demand response," *Electrical Power and Energy Systems*, vol. 141, p. 108132, 2022.
- [16] M. Majidi, S. Nojavan, and K. Zare, "A cost-emission framework for hub energy system under demand response program," *Energy*, vol. 134, pp. 157-166, 2017.
- [17] M. H. Shams, M. Kia, M. Heidari, A. Lotfi, M. Shafie-khah, and J. P. S. Catalao, "Optimal operation of electrical and thermal resources in microgrids with energy hubs considering uncertainties," *Energy*, vol. 187, p. 115949, 2019.
- [18] S. A. Mansouri, A. Ahmarinejad, M. Ansarian, M. S. Javadi, and J. P. S. Catalao, "Stochastic planning and operation of energy hubs considering demand response programs using Benders decomposition approach," *Electrical Power and Energy Systems*, vol. 120, p. 106030, 2020.
- [19] W. Jiang, X. Wang, H. Huang, D. Zhang, and N. Ghadimi, "Optimal economic scheduling of microgrids considering renewable energy sources based on energy hub model using demand response and improved water wave optimization algorithm," *Journal of Energy Storage*, vol. 55, p. 105311, 2022.
- [20] A. Soroudi, M. Aien, and M. Ehsan, "A probabilistic modeling of photovoltaic modules and wind power generation impact on distribution networks," *IEEE Systems Journal*, vol. 6, no. 2, pp. 254-259, 2012.
- [21] B. Ozerdem, S. Ozer, and M. Tosun, "Feasibility study of wind farms: A case study for Izmir, Turkey," *Journal of Wind Engineering and Industrial Aerodynamics*, vol. 94, no. 10, pp. 725-743, 2006.
- [22] S. Hadayeghparast, A. S. Farsangi, and H. Shayanfar, "Day-ahead stochastic multi-objective economic/emission operational scheduling of a large scale virtual power plant," *Energy*, vol. 172, pp. 630-646, 2019.
- [23] A. Soroudi, *Power System Optimization Modeling in GAMS*. Springer, 2017.
- [24] GAMS. [Online]. Available: <http://www.GAMS.com>. [Accessed Feb. 26, 2024].



EFFECT OF BASALT FIBER ASPECT RATIO ON MECHANICAL AND WORKABILITY PROPERTIES OF SELF-COMPACTING CONCRETE

¹ Mehmet UZUN , ^{2,*} Mehmet Akif ARSLAN 

¹Karamanoğlu Mehmetbey University, Engineering Faculty, Civil Engineering Department, Karaman, TÜRKİYE

²Konya Technical University, Engineering and Natural Sciences Faculty, Civil Engineering Department, Konya, TÜRKİYE

¹mehmetuzun@kmu.edu.tr, ²maarslan@ktun.edu.tr

Highlights

- Basalt fiber improved flexural and splitting tensile strength of Self- Compacting Concrete
- Aspect ratio is an important parameter that effects the mechanical performance of fiber reinforced concrete.
- Increasing aspect ratio increases the mechanical and workability performance of fiber reinforced SCC.



EFFECT OF BASALT FIBER ASPECT RATIO ON MECHANICAL AND WORKABILITY PROPERTIES OF SELF-COMPACTING CONCRETE

¹ Mehmet UZUN , ^{2,*} Mehmet Akif ARSLAN 

¹Karamanoğlu Mehmetbey University, Engineering Faculty, Civil Engineering Department, Karaman, TÜRKİYE

²Konya Technical University, Engineering and Natural Sciences Faculty, Civil Engineering Department, Konya, TÜRKİYE

¹ mehmetuzun@kmu.edu.tr, ² maarslan@ktun.edu.tr

(Received: 15.11.2023; Accepted in Revised Form: 12.12.2023)

ABSTRACT: Self-compacting concrete (SCC) has become widely used thanks to its various advantages. SCC is also fiber reinforced, similar to conventional concrete. However, studies on SCC with fiber addition are limited. In this study, the effect of basalt fibers at different aspect ratios on the mechanical and workability properties of SCC was examined. Slump flow, V-funnel, compressive, flexural and splitting tensile strength tests were carried out within this study. Results showed that, although increasing the aspect ratio causes improvement in the workability properties of concrete, workability decreases compared to the reference SCC. Increases were observed in flexural and splitting tensile strengths with increasing aspect ratio. The compressive strength of the specimens that contains BF decreased compared to the reference sample because of the agglomeration effect. The results obtained were examined and discussed in detail.

Keywords: Aspect ratio, Basalt, Fiber, Self compacting concrete

1. INTRODUCTION

Concrete is the most significant and used building material, with its advantages such as high durability and strength, low cost, strong bond with reinforcement steel and plasticity [1], [2]. Besides these advantages, studies have shown a trend towards self-compacting concrete (SCC) to improve the workability of conventional concrete. SCC settles into concrete molds with its own weight and viscosity, without requiring any vibration or placement process. It is especially suitable for pouring concrete in places where vibration is difficult and at night. Low labor costs and less energy used for compaction are also advantages over conventional concrete [3]. SCC is produced similar to conventional concrete and is produced with a mixture of aggregates, binders, water, mineral, chemical additives and natural additives [4]–[6]. Although concrete is the most used building material with a good performance in terms of compressive strength, its tensile strength and brittleness are problems that need to be solved.

Researchers found that adding fiber to concrete mixtures improved the mechanical performance (Flexural and tensile strength, crack resistance, ductility, toughness) of concrete [7]. Basalt, steel, carbon, glass, polypropylene and natural fibers are mostly studied fiber types in the literature [8], [9]. Basalt fiber (BF) is produced from basalt rock with molting in high temperature. BF has high tensile strength, fire and impact resistance. Compared to commonly used glass and carbon fibers, BF has higher tensile strength than glass fibers and higher elongation at break than carbon fibers [10]. There are various studies carried out for BF usage in conventional concrete, however, studies about SCC with BF are limited. *Algin & Ozen* investigated properties of SCC reinforced with BF. Researchers examined different lengths and dosages of BF in SCC and concluded that 0.5% fiber content and 24 mm fiber length provided a 19% increase in flexural strength [11]. *Rohilla et al.* studied on different fibers for reinforcing SCCs. It was reported that %0.25 content of BF improved the mechanical properties of SCC. At 28th day, compressive, flexural and split tensile strength are increased at the rate of %50.16, %61.74 and %24.56, respectively. [12]. *Ponikiewski and Katzer* investigated steel, basalt and polypropylene fiber reinforced SCCs. Authors reported that fibers are useful solutions for improving performance of SCC. However, 5 and 12 mm basalt fibers cause

*Corresponding Author: Mehmet Akif ARSLAN, maarslan@ktun.edu.tr

decrease on compressive strength at the rate of %11.5 and %31.1, respectively [13]. Studies show that while BF provides improvement on the mechanical properties of SCC, it causes a decrease in its workability properties. Changes in workability and mechanical properties occur depending on the dosage, aspect ratio and other properties of the fiber.

In this study, the effect of the change in aspect ratio of the commonly used basalt fiber on the mechanical and workability properties of SCC was examined. SCC samples prepared with 4 different aspect ratios were compared with the reference sample. Slump flow, V funnel, compression, flexure and split tensile tests were carried out and result were discussed. While various studies on the use of BF in conventional concrete were presented, there are deficiencies regarding the use of SCC with basalt fiber. Therefore, this study aims to fill this gap.

2. MATERIAL AND METHODS

2.1. Materials and Mixture Design

CEM I 42.5 R Portland cement was utilized in mixture design in compliance with TS EN 197/1 standard [14]. The chemical, mechanical and physical features of used cement (CEM I 42.5 R) were listed in Table 1. The water-cement ratio was constant at 0.4 in the reference sample and other samples with basalt fiber additives. 1.6% superplasticizer were used in all specimens. basalt fiber was used with the ratio of 0.75% of total volume. The mixing ratios of reference and fiber samples are presented in Table 2. "R" represents reference specimen, other SCC specimens numbered with their aspect ratios (AR). For each type of experimental parameter, 3 samples were prepared and tested. Their averages were calculated and evaluated as results.

Table 1. Properties of CEM I 42.5 R Portland Cement

Chemical properties (%)		Physical and mechanical properties	
SO ₃	2.84	Initial setting time (min.)	137
MgO	3.76	Final setting time (min.)	179
CaO	62.96	2-days compressive strength (MPa)	25.4
SiO ₂	17.99	28-days compressive strength (MPa)	51.8
K ₂ O	0.35	Specific gravity (g/cm ³)	3.12
Na ₂ O	0.17	Specific surface (cm ² /g)	3674
Al ₂ O ₃	4.43		
Fe ₂ O ₃	3.35		
Cl-	0.0211		

Table 2. Mix Design Proportions

Mixture Codes	Cement (kg/m ³)	Water (kg/m ³)	FA (kg/m ³)	CA (kg/m ³)	W/C	Superplasticizer (%)	BF Fiber Volume (%)
R	480	192	690	470	0.4	1.6	0
SCC-AR-430	480	192	690	470	0.4	1.6	0.75
SCC-AR-560	480	192	690	470	0.4	1.6	0.75
SCC-AR-855	480	192	690	470	0.4	1.6	0.75
SCC-AR-1145	480	192	690	470	0.4	1.6	0.75

In this study, the effect of fiber aspect ratio in SCC was examined. Basalt fibers with different lengths were used in the prepared samples, while keeping the fiber diameter constant. Since basalt fiber is added to the concrete volumetrically, as the aspect ratio increases, the volumetric fiber amount in the concrete remains constant, but the amount of fiber per unit volume decreases. The tensile strength of the basalt fiber is 4840 MPa. The fiber lengths and aspect ratios of basalt fiber added specimens were presented in Table 3, and an image of the fiber is presented in Figure 1.

Table 3. Fiber Lengths and Aspect Ratios of Mixtures

Mixture Code	Fiber length (mm)	Aspect Ratio
SCC-AR-430	6	430
SCC-AR-560	8	560
SCC-AR-855	12	855
SCC-AR-1145	16	1145



Figure 1. Basalt fibers

2.2. Methods

2.2.1. Slump flow and V funnel tests

Fresh concrete properties were tested with slump flow and V funnel tests. Slump flow test carried out according to standard of TS EN 12350-8 [15], V funnel test carried out according to TS EN 12350-9 [16].

2.2.2. Compressive, flexural and splitting tensile strength

Hardened concrete tests (compression, flexural and splitting tensile) were carried out in accordance with TS EN 12390-3[17],12390-5 [18] and 12390-6 [19] standards respectively. Cube samples with dimensions of 150x150x150 mm were prepared for compression and splitting tensile tests, and 40x40x160 mm rectangular samples were prepared and tested at the age of 28 days. The experimental setups are presented in Figure 2.



Figure 2. Compression and flexural test

3. RESULTS AND DISCUSSION

3.1. Fresh Concrete Properties

V – funnel and slump flow tests were performed for investigate fresh concrete properties of specimens. Slump flow tests results were presented in Figure 3. Spread diameter of reference specimen was 269 mm. Basalt fiber addition decreases the spread diameter of SCC compared with the conventional SCC. The increase in basalt fiber aspect ratio also increases the spreading diameter. When the aspect ratio is increased by keeping the fiber volume constant in the mixture, the amount of fiber per unit volume decreases. Therefore, as the aspect ratio increases, workability and concrete consolidation increases.

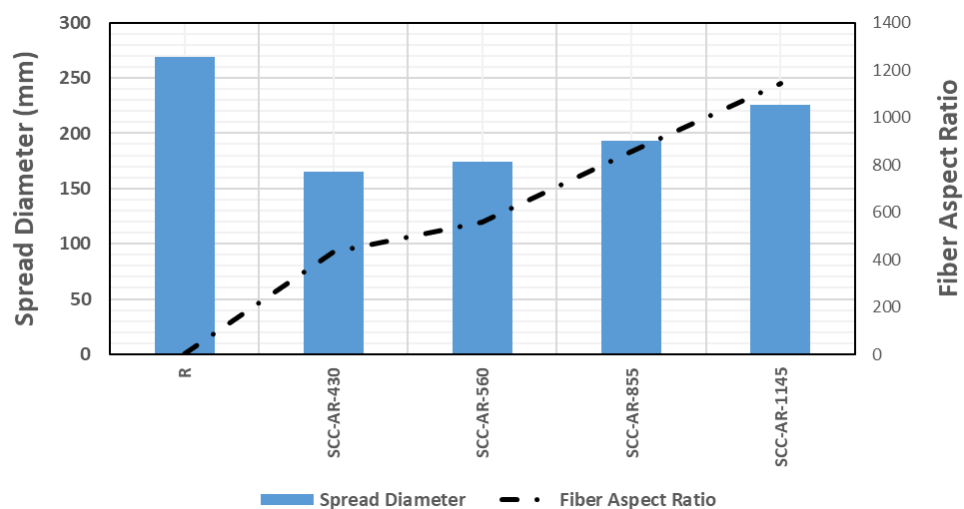


Figure 3. Slump Flow Test Results

Results of V funnel test are shown in Table 4. The results observed in the V funnel test are at an acceptable level between 9-25 seconds according to TS - EN 12350-9. For this reason, the results obtained in this work are acceptable. Increasing the fiber aspect ratio decreases the flow time. The SCC-AR-1145

sample provided a flow time (12.4 s) value close to the reference sample (11.6). This can be explained by the increase in workability as a result of the decrease in the amount of fiber per unit volume as the aspect ratio increases.

Table 4. V – Results of V Funnel Test

Specimens	V-Funnel (s)
R	11.6
SCC-AR-430	19.2
SCC-AR-560	17.3
SCC-AR-855	14.7
SCC-AR-1145	12.4

3.2. Hardened Concrete Properties

In this section, compressive, flexural, and splitting tensile strengths are presented. Compressive strength test results are presented in Figure 4. The compressive strength of the reference sample is higher than all other samples on the 7th and 28th days. The addition of basalt fiber caused decrease in compressive strength in comparison with the reference sample. However, increasing the aspect ratio also caused an increase in compressive strength. The 28th day compressive strength of the SC-AR-1145 sample decreased by 3.24% in comparison with the reference sample.

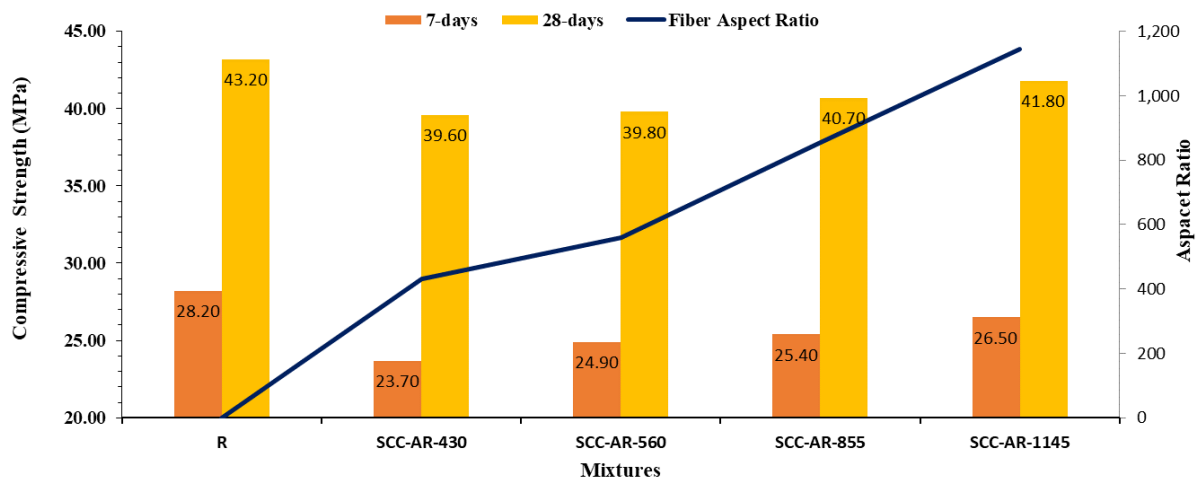


Figure 4. Results of Compressive Strength Test

Flexural strength results were presented in Figure 5. It is expected that adding fiber to concrete will affect the flexural strength more than the compressive strength. When the results were examined, the flexural strengths of all samples increased comparison with the reference sample. Additionally, increasing the aspect ratio also increased the flexural strength. As the aspect ratio increases, the interaction surface of basalt fibers with cement increases, so the flexural strength also increases due to increased adherence.

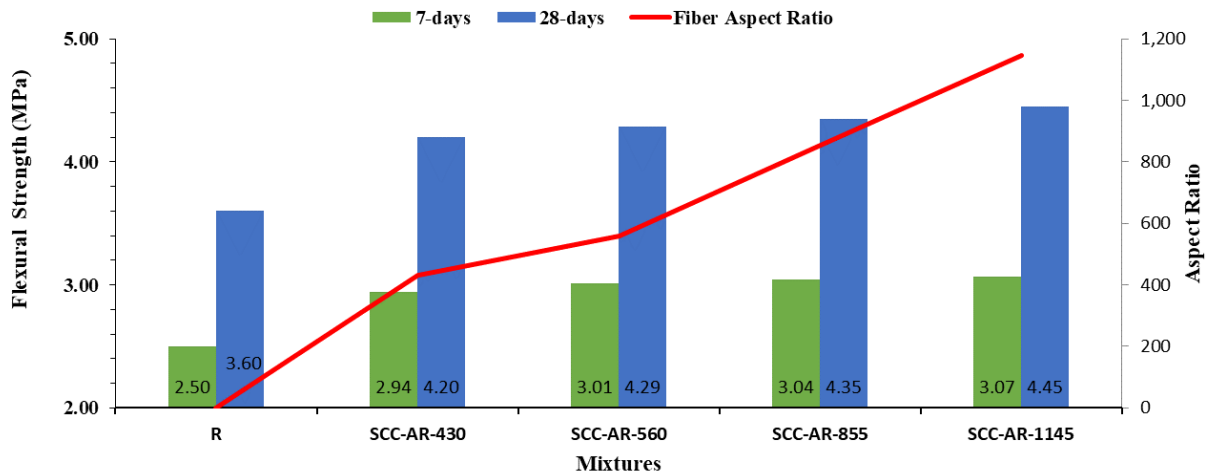


Figure 5. Flexural Strength Test Results

Splitting tensile strength results were presented in Figure 6. The splitting tensile strength of all samples with added basalt fiber is higher than the reference sample. The increase in aspect ratio had a slight effect on the increase in splitting tensile strength. While the reference sample has a strength of 3.65 MPa, the SCC-AR-430 sample has a strength of 4.17 MPa and the increase rate is 14.25%. While the strength of the SCC - AR - 430 sample is 4.17 MPa, the strength of the SCC - AR - 1145 sample is 4.41 MPa and the increase rate is 5.76%.

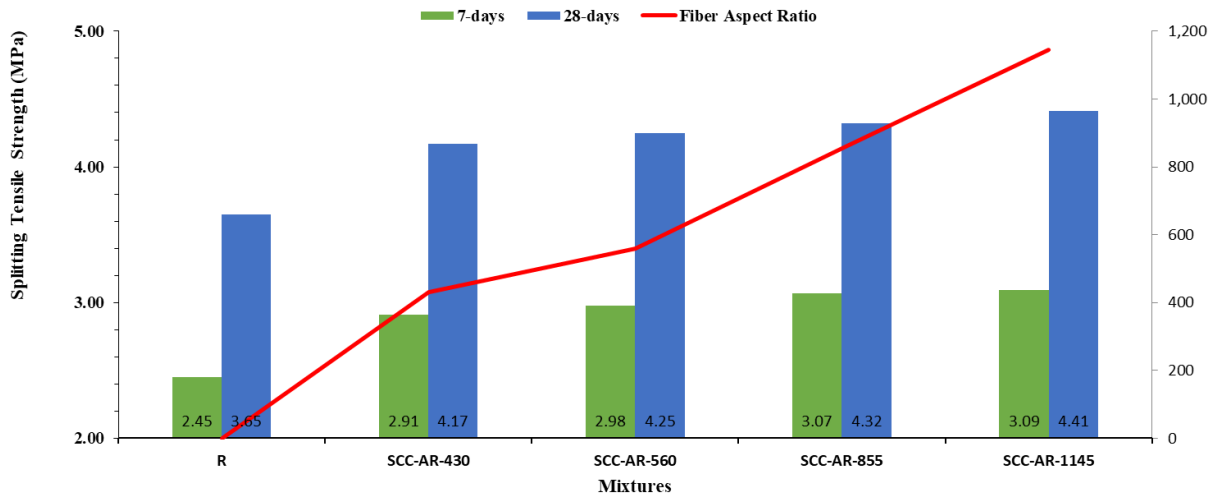


Figure 6. Splitting Tensile Strength Test Results

4. CONCLUSIONS

In this study, the effect of the aspect ratio of basalt fibers on the workability and mechanical properties of SCC was investigated. The SCC prepared as a reference and basalt fiber added SCCs with different aspect ratios were examined comparatively. Basalt fibers with 4 different aspect ratios were used, and these values are 430,560,855,1145. Slump flow, V tunnel, compression, flexural and splitting tensile strength tests were carried out. The results can be drawn as follows:

- Adding fiber to the SCC will increase the adherence and thus reduce the slump spread diameter values. SCC-AR-1145 sample has the closest slump value to the reference sample, while its spreading diameter is 15.99% lower than the reference sample. It is 36.97% higher than the SCC-

AR- 430 sample. Since basalt fiber is added to the concrete volumetrically, as the aspect ratio increases, the volumetric fiber amount in the concrete remains constant, but the amount of fiber per unit volume decreases. Therefore, as the aspect ratio increases, workability and concrete settlement increases. However, the compressive strength decreased in all samples compared to the reference.

- Increasing the basalt fiber aspect ratio caused an increase in compressive strength. However, in all BF added SCCs, concrete compressive strengths decreased in t comparison with the reference SCC. The compressive strength at 28th day of the SCC - AR -1145 sample has the closest value to the reference sample. SCC-AR-1145 specimen's compressive strength was 3.2% lower than the reference sample. Agglomeration had an effect on the lower compressive strength of all fiber-added samples compared to the reference sample.
- Flexural strength increased with increasing fiber aspect ratio. From the sample with the lowest aspect ratio to the highest, there was an increase of 16.67%, 19.17%, 20.83%, 23.61%, respectively, compared to the reference sample at 28th day. As the aspect ratio increases, the interaction surface of basalt fibers with concrete increases, so the bending strength also increases due to increased adherence.
- The tensile strength in splitting increased depending on the increase of the aspect ratio. The highest increase was recorded in the SCC-AR-1145 sample, with a 20.82% increase compared to the reference sample.
- Since studies examining the effects of basalt fiber and aspect ratio on the mechanical properties of SCC are limited, this study plays an important role for future studies and more effective usage of fiber to enhance performance of concrete.

Declaration of Ethical Standards

Authors declare that all ethical standards have been complied with.

Declaration of Competing Interest

The authors declare no conflict of interest.

Funding / Acknowledgements

No funding is available for this research.

Data Availability

No data was used within this study.

REFERENCES

- [1] L. Yu, X. J. Li, L. S. Bao, Z. X. Zhang, and Z. B. Zhou, "Experimental study on basic properties of basalt fiber reinforced concrete," *Green Intell. Technol. Sustain. Smart Asph. Pavements - Proc. 5th Int. Symp. Front. Road Airpt. Eng. IFRAE 2021*, pp. 548–553, 2022, doi: 10.1201/9781003251125-87.
- [2] M. T. Çöğürçü and M. Uzun, "Effects of accelerator type and dosage on the mechanical and durability properties of rapid-setting precast concrete," *Sigma J. Eng. Nat. Sci.*, vol. 40, no. 4, pp. 685–694, 2022, doi: 10.14744/sigma.2022.00084.
- [3] H. J. H. Brouwers and H. J. Radix, "Self-compacting concrete: Theoretical and experimental study," *Cem. Concr. Res.*, vol. 35, no. 11, pp. 2116–2136, 2005, doi: 10.1016/j.cemconres.2005.06.002.
- [4] F. Türk, M. Kaya, M. Saydan, and Ü. S. Keskin, "Environmentally friendly viscosity-modifying agent for self-compacting mortar: *Cladophora* sp. cellulose nanofibres," *Eur. J. Environ. Civ. Eng.*, vol. 27, no. 5, pp. 2015–2030, 2023, doi: 10.1080/19648189.2022.2108502.

- [5] F. Türk, M. Saydan, and Ü. S. Keskin, "The effect of different viscosity modifying additives on the mechanical and flow properties of self-compacting mortars," *Niğde Ömer Halisdemir Univ. J. Eng. Sci.*, vol. 11, no. 3, pp. 752–757, 2022, doi: 10.28948/ngmuh.1048632.
- [6] S. Biçici and Y. Tola, "Mechanical Properties and Durability of Steel Fiber Self-Compacting Concrete," *Kocaeli Üniversitesi Fen Bilim. Derg.*, vol. 6, no. 1, pp. 57–67, 2023.
- [7] Y. Li *et al.*, "A review on durability of basalt fiber reinforced concrete," *Compos. Sci. Technol.*, vol. 225, no. May, p. 109519, 2022, doi: 10.1016/j.compscitech.2022.109519.
- [8] Y. Zheng, Y. Zhang, J. Zhuo, Y. Zhang, and C. Wan, "A review of the mechanical properties and durability of basalt fiber-reinforced concrete," *Constr. Build. Mater.*, vol. 359, no. September, p. 129360, 2022, doi: 10.1016/j.conbuildmat.2022.129360.
- [9] M. Tolga Cogurcu, "Investigation of mechanical properties of red pine needle fiber reinforced self-compacting ultra high performance concrete," *Case Stud. Constr. Mater.*, vol. 16, 2022, doi: 10.1016/j.cscm.2022.e00970.
- [10] M. Oltulu and H. Oktan, "Farklı Görünüm Oranlı Bazalt Liflerin Betonun Mekanik Özelliklerine Etkisi," *Iğdır Üniversitesi Fen Bilim. Enstitüsü Derg.*, vol. 9, no. 2, pp. 870–879, 2019, doi: 10.21597/jjst.450272.
- [11] Z. Algin and M. Ozen, "The properties of chopped basalt fibre reinforced self-compacting concrete," *Constr. Build. Mater.*, vol. 186, pp. 678–685, 2018, doi: 10.1016/j.conbuildmat.2018.07.089.
- [12] C. Rohilla, K. Sharma, and . K., "A Study on Behavior of Chopped Fiber Reinforced Self-Compacting Concrete," *Eng. Technol. J.*, vol. 1, no. 01, pp. 33–38, 2016.
- [13] T. Ponikiewski and J. Katzer, "Fresh mix characteristics of self-compacting concrete reinforced by fibre," *Period. Polytech. Civ. Eng.*, vol. 61, no. 2, pp. 226–231, 2017, doi: 10.3311/PPci.9008.
- [14] TS-EN-197-1, "Cement—Composition, Specifications and Conformity Criteria— Part 1: Common Cements, TS EN 197, TSE, Ankara, Turkey," 2012.
- [15] TS EN 12350-8, "Concrete - Fresh concrete tests - Part 8: Self-compacting concrete - Slump flow test." TSI, Ankara, 2019.
- [16] TS EN 12350 - 9, "Concrete - Fresh concrete tests - Part 9: Self-compacting concrete - V funnel test." TSI, Ankara, 2011.
- [17] TS EN 12390-3, "Testing hardened concrete-Part 3: Compressive strength of test specimens." TSI, Ankara, 2019.
- [18] TS EN 12390-5, "Testing hardened concrete- Part 5: Flexural strength of test specimens." TSI, Ankara, 2019.
- [19] TS EN 12390 - 6, "Concrete - Hardened concrete tests - Part 6: Determination of splitting tensile strength of test specimens." TSI, Ankara, 2010.



FAILURE ANALYSIS OF A BASE SUPPORT PLATE OF A SEMOLINA PURIFIER MACHINES SUBJECTED TO FATIGUE LOADING

¹Yunus DERE , ^{2*}Hakkı EKEM , ³Ömer Sinan ŞAHİN , ⁴Hasan Hüsnü KORKMAZ 

¹Necmettin Erbakan University, Engineering Faculty, Civil Engineering Department, Konya, TÜRKİYE

²IMAS Integrated Machines Co. Research and Development Center, Konya, TÜRKİYE

³Konya Technical University, Engineering and Natural Sciences Faculty, Mechanical Engineering Department,
Konya, TÜRKİYE

¹ydere@erbakan.edu.tr, ²hakki.ekem@imas.com.tr, ³ossahin@ktun.edu.tr,

⁴hasanhusnukorkmaz@gmail.com

Highlights

- The design of the semolina purifier machine, which is frequently used in the milling industry and is subject to fatigue, was examined.
- Finite element method was used in design improvements.
- Similarly, approaches that will be essential in the design of machines subject to fatigue have been tried to be put forward.



FAILURE ANALYSIS OF A BASE SUPPORT PLATE OF A SEMOLINA PURIFIER MACHINES SUBJECTED TO FATIGUE LOADING

¹Yunus DERE , ^{2*}Hakkı EKEM , ³Ömer Sinan ŞAHİN , ⁴Hasan Hüsnü KORKMAZ 

¹Necmettin Erbakan University, Engineering Faculty, Civil Engineering Department, Konya, TÜRKİYE

²IMAS Integrated Machines Co. Research and Development Center, Konya, TÜRKİYE

³Konya Technical University, Engineering and Natural Sciences Faculty, Mechanical Engineering Department,
Konya, TÜRKİYE

¹ydere@erbakan.edu.tr, ²hakki.ekem@imas.com.tr, ³ossahin@ktun.edu.tr,

⁴hasanhusnukorkmaz@gmail.com

(Received: 13.09.2023; Accepted in Revised Form: 12.12.2023)

ABSTRACT: The semolina purifier is a machine used in the production phase in flour factories and is exposed to fatigue loads. In this study, the reason for the damage when a semolina purifier machine breaks during use and the improvements that need to be made in the design are discussed. For this purpose, a finite element model (FEM) was created using ABAQUS software. As a result of the analysis, it was determined that the design of the machine support platform should be improved. A two-stage strengthening alternative is designed. The cyclic loads applied by the twin motors that move the machine screens are applied in the FEM model. The deformations and stresses occurring in the reinforced and existing design machine base plate were compared. The results showed that, the maximum equivalent stress level can be reduced from 86 MPa to 35 MPa by design improvements made on the base plate.

Keywords: Failure, Fatigue, Semolina purifier machine, Strengthening

1. INTRODUCTION

Maintenance of critical equipment to ensure high levels of reliability, availability, and performance is one of the major concerns on today's industrial sector especially for rotation machines [1-4] and other conventional type machines [5-8] subjected to cyclic loading. Unexpected failures can lead to substantial losses, either from the maintenance procedure itself or from the resulting production halts [9-12]. In order to proactively prevent failure of components, failure modes in functional component's caused by the damage/fracture modes of the materials should be comprehensively determined. Failure analysis is a process performed in order to determine the root causes or factors that led to an undesired loss of functionality. The immediate objective is to find the root causes of the failure in order to obtain the compensation for the induced damage even if the really important is to prevent similar failures in new components [3]. Literature review revealed that fatigue and Failure analysis of various machines and machine parts such as anti-return valve of a high pressure machine [13], yarn twisting machine [14], diesel engine injector [15], excavator buckets [16], welded steel plates for conveyor belts [17], aluminum alloy elastic coupling [18], friction-stir welded joints [19, 24], bridge conveyor [20], cutting blades [21] and gear and transmission shafts [22, 23]. The subject of fatigue damage development and design according to fatigue damage is a subject that has been studied extensively in the literature. However, there are no studies on fatigue damage and fatigue-based design in special purpose machines such as semolina purification machines. This study will fill this gap.

Semolina is a type of flour made only from durum wheat. It is obtained by grinding and sieving durum wheat. In English, semolina is an extract from the word "coarsely ground wheat flour. The term semolina is also used to designate coarse middlings from other varieties of wheat. It is expressed by the words "semola" in Italian, "simil" in Latin and "semidalis" in ancient Greek. Semolina is divided into 5 groups according to its grain size (Figure 1). Semolina between 125-300 microns is used for pasta production and 1120 microns and above is "whole wheat" semolina. Semolina is yellow in color, bright and angular.

*Corresponding Author: Hakkı EKEM, hakki.ekem@imas.com.tr



Figure 1. Types of semolina

Durum wheat is grown mainly in the Middle East and accounts for about 5-8% of the world's cultivated wheat amount. Semolina contains 73% carbohydrates. There is approximately 360 kcal of energy in 100 grams of semolina.

Semolina contains high amount of gluten and for this reason it is preferred to make pasta. The semolina helps to maintain the shape of the pasta during cooking. The main difference between semolina and flour is that semolina can be a better coarse and darker shade and more yellow than traditional flour. It is important to carefully clean and grind the wheat to prevent the presence of stains in the semolina. Semolina quality directly affects the pasta quality.

Semolina purifiers are machines used in flour and semolina factories to purify, classify and clean semolina from crushing rolls and lyso rolls. (Figure 2). The purifier consists of four main parts (Figure 3):

- A fixed main frame
- Oscillating body containing sieves
- One suction channel
- Exhaust chamber,

The machine is produced as a monolithic moving body with two vibro motors and a three-layer sieve system. The three sieve layers are angled according to the ground. These sieves oscillate on the fixed main chassis. The oscillation of the sieves is provided by two eccentric motors at the end of the machine (Figure 3). The product coming from the inlet is evenly distributed on the sieve surface with the adjustable valves and the vibration effect of the machine. In three-row boxes, the desired amount and type of product is obtained according to its shape.



Figure 2. Semolina purifier machine

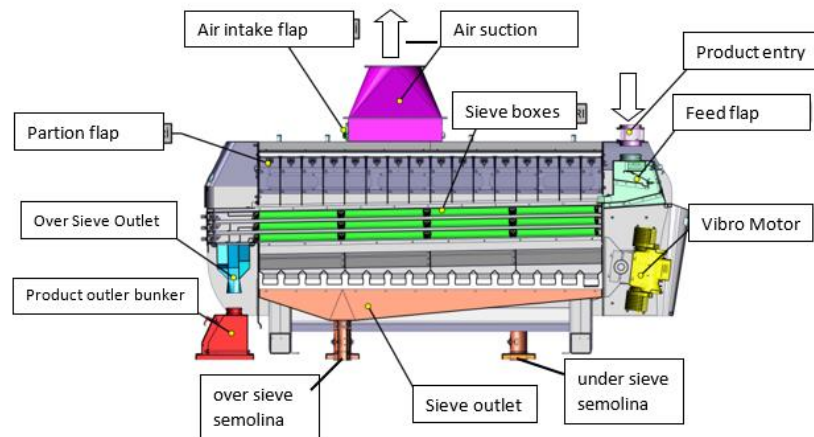


Figure 3. Main components of purifier machine

The product enters the machine from the top in a way that the flow rate can be adjusted. It should be homogeneously distributed over the whole screen surface. The purifier provides mobility to the semolina by moving the tray with the sieves thanks to its vibration motor. The motors that make an upward angle with the horizontal make the particles an inclined projection motion (Figure 4). Thus, the surface of the products is expanded. Air, which enters from the bottom of the sieves and goes upwards, creates a vacuum effect. The particles, whose adhesion surface is expanded, are separated and pushed to the outlet channel by keeping them suspended with vacuum. It is then moved to the collection box below. Due to more than one sieve, the product can be separated according to the particle size. The air entering the machine leaves the machine from the top by passing through the air ducts after passing through the sieves (Figure 5).

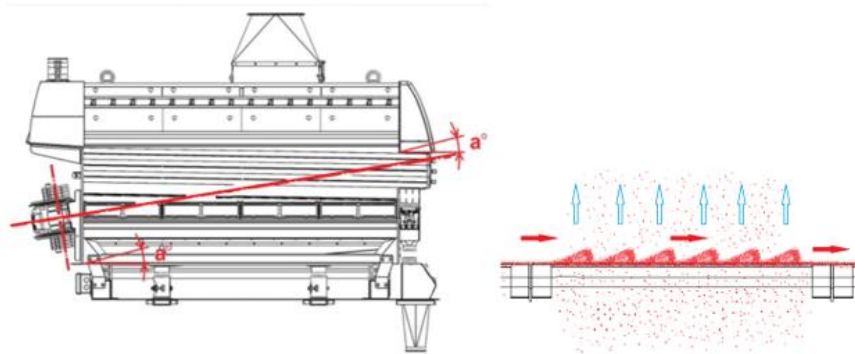


Figure 4. Inclined projection of particles in purifier machine

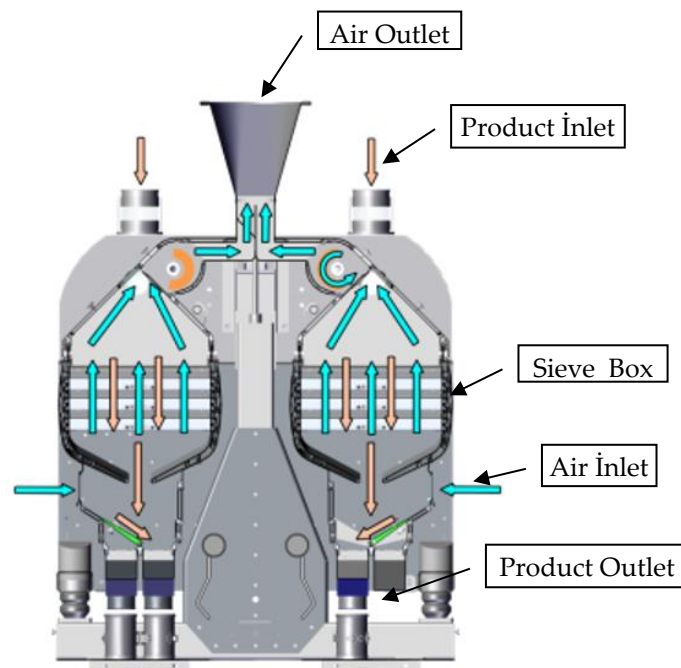


Figure 5. Air flow chart in purifier machine

2. MATERIAL AND METHODS

The design of the traditional semolina purifier machine, which is exposed to variable loads, is examined. The fracture surface examined by optical microscopy and evaluation revealed that the base plates fractured under fatigue failure.

As a result of the examination, it was determined that the design of the machine support platform should be improved and two different reinforcement alternatives were designed. The conventional design and new design alternatives were modelled by using ABAQUS finite elements software. The strengthened and current design is compared through the deformations and stresses occurring in the machine base plate.

The cyclic loads applied by the twin motors that move the machine screens are applied in the FEM model. The deformations and stresses occurring in the reinforced and existing design machine base plate were compared. The analysis-review and update procedure is conducted in accordance with methodology shown in Figure 6.

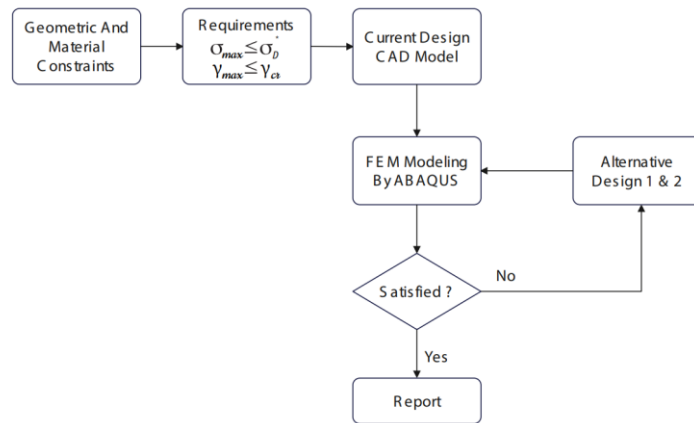


Figure 6. Flowchart of the analysis procedure

A three-dimensional finite element model of the machine was created in order to investigate the cause of the fatigue failure in the sub-frame of the purifier machine and to evaluate the strengthening alternatives. Numerical study was carried out in the ABAQUS software (Figure 10). Mechanical properties of materials used in analysis is given in Table 1.

Table 1. Mechanical properties of machine components

Material	Young Modulus (GPa)	Poisson's ratio	Density (kg/m ³)
AISI-430	200	0.28	7850
AL-5083	71	0.33	2650
AL-6061	69	0.33	2690
C-1010	200	0.28	7850
ST-37	200	0.3	7850
ST-42	200	0.3	7850

The elastomeric bearings on the machine base are modeled as springs in the FE model. Spring constants were supplied by the manufacturer of the elastomeric bearings. For the vertical and lateral movement, different values are defined. The vertical spring constant was defined as 328 N/mm and the lateral spring constant was defined as 340 N/mm.

3. RESULTS AND DISCUSSIONS

3.1. Description of Fracture Failure

In the semolina purifier, the moving body is obtained with two vibro motors (Figure 8). The movable sieve part is placed on the fixed chassis. The fixed chassis is placed on four elastomeric supports. The chassis rests on two 20 mm thick plates (Figure 9).

These are the machines produced and sold by the manufacturer company. Breakage problems in the support plates have been reported after prolonged use of the machines. Said plates are shown in green in Figure 8. Fracture occurred at the corners where the plates were attached to the elastomeric support (Figure 9). The manufacturer contacted the authors to determine the cause of the damage to the support sheet of the machine and to determine the strengthening methods. It is desired that the retrofit to be developed can also be applied to machines that have been sold before and are still in use.

is examined, it is seen that the displacement value of the support leg in the $-Z$ direction is 2.08 mm. Here the relative displacement was obtained as 5.35 mm. The von Mises equivalent stress distribution on the support plate is given in Figure 12-a. As seen in this figure, the maximum equivalent stress was obtained as 35 MPa.

In the second stage of the study, in addition to the machine weight, the sinusoidal variable force created by the twin vibromotors on the side of the machine was applied to the model. The time-dependent variation of periodic loading is shown in Figure 13. There are rubber vibration damping elements at four points where the machine chassis is connected to the ground. The mechanical properties of these components are defined in the software. The distribution of horizontal displacements obtained under dynamic loading on the support plate is given in Figure 14-a. Here the relative displacement was obtained as 23.4 mm. The von Mises stress distribution obtained in the support plate under dynamic loads is given in Figure 15-a. As seen in this figure, the maximum equivalent stress was obtained as 86 MPa.

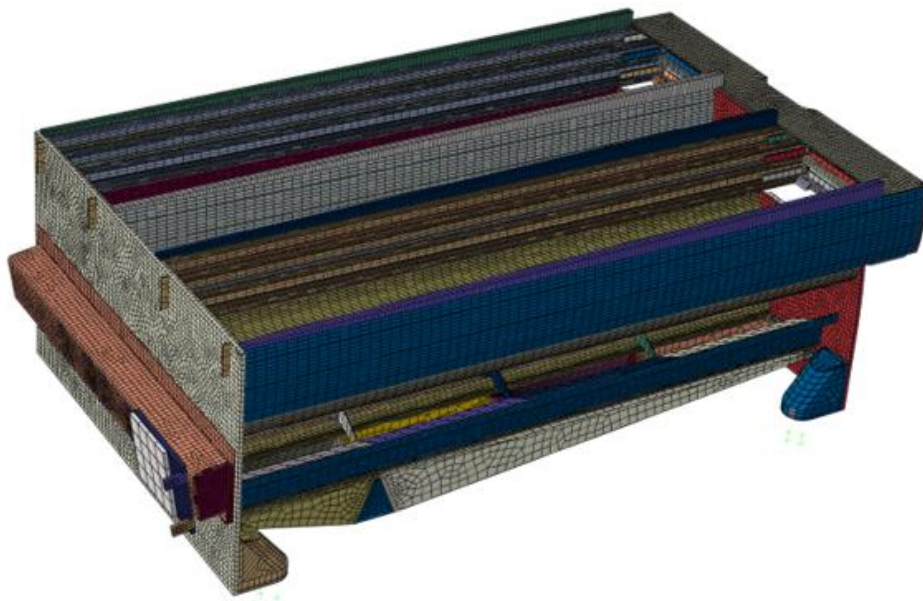


Figure 10. Finite element model of purifier machine

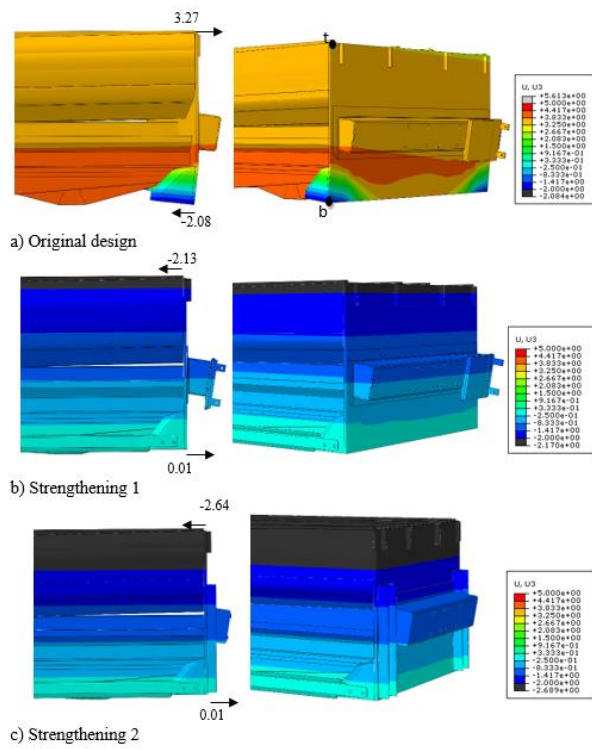


Figure 11. Lateral displacement distribution of purifier machine under self-weights (mm)

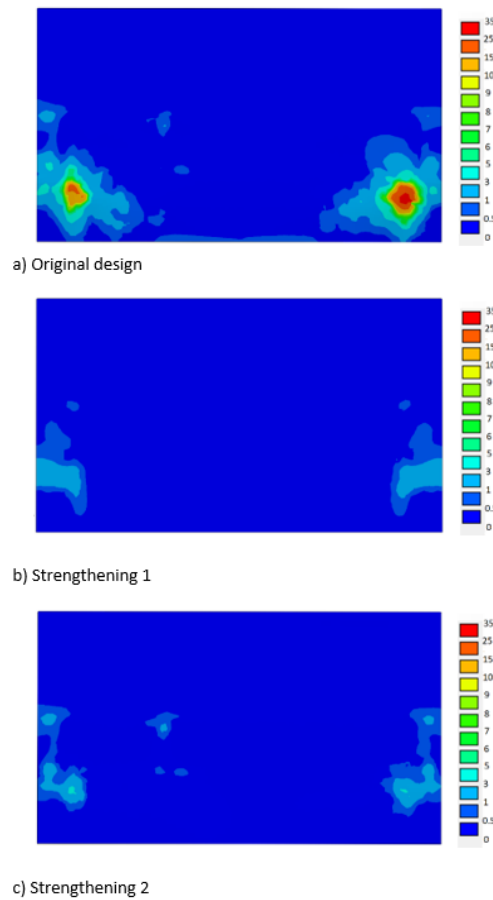


Figure 12. Von Misses stress distribution of side support plate (motor side) (self-weight) (MPa)

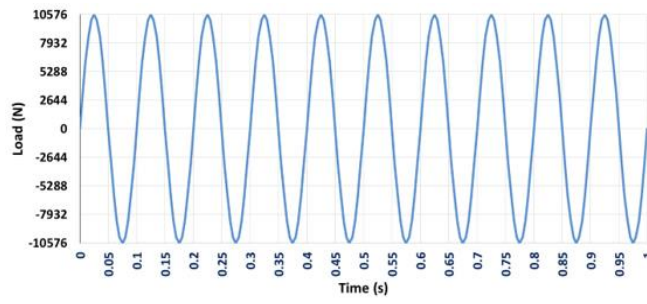


Figure 13. Cyclic loading of twin motors

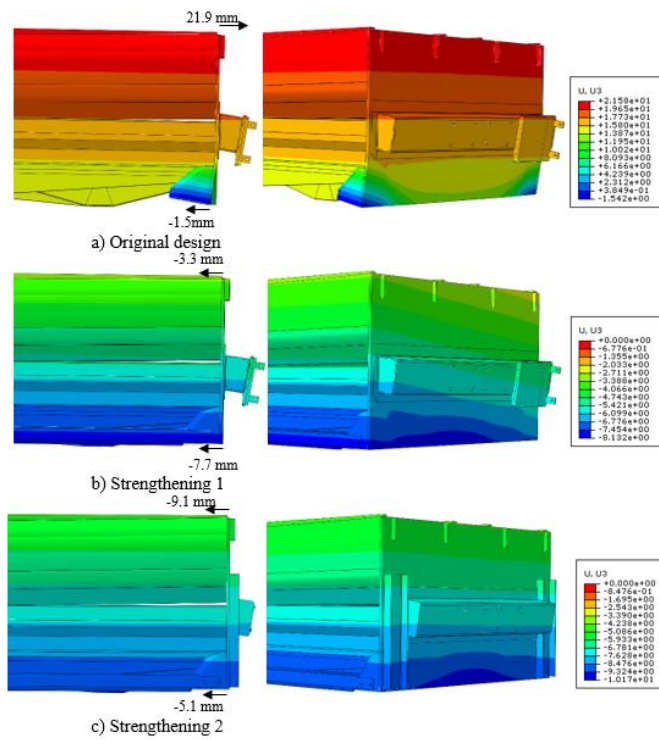


Figure 14. Lateral displacement distribution of support plate region under dynamic loading (mm)

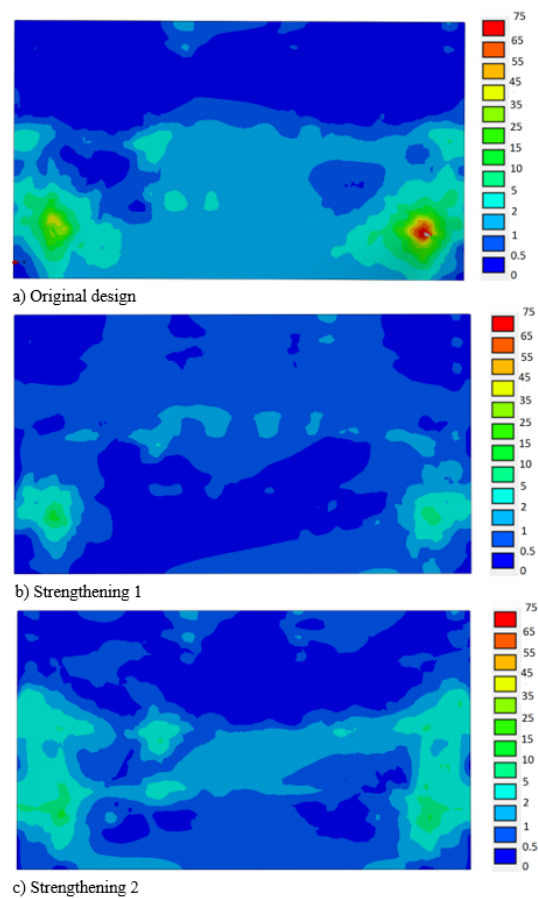


Figure 15. Von Mises stress distribution of side support plate (motor side) (MPa) (cyclic loading)

3.3. Retrofit Alternatives and FEM Results

When the fatigue damages observed on the motor plate (Figure 9) and the FEM analysis results were evaluated, it was concluded that the motor support plate was insufficient against fatigue loads. So, it was concluded that a design improvement is needed to eliminate this negativity. However, the machine consists of many components and has complex connections. So, design improvements must not seriously affect the production and assembly process of the machine. In this context, two different reinforcement alternatives are planned.

In the first alternative, the lower support legs of the machine are connected to each other horizontally with 2 U-shaped steel elements (Figure 16). This alternative is called “First alternative strengthening”. The second alternative was called “First alternative strengthening”. Here, in addition to the steel elements mentioned in the first alternative, U-shaped reinforcement elements were mounted upwards from both sides of the support plate. (Figure 17). Later, reinforcement elements were included in the FEM model and the analyzes were repeated. Figure 11-b-c shows the lateral displacement distributions of reinforcement alternatives. Here, the relative displacements of the upper (“t”) and lower (“b”) points of the support plate were also obtained. Table 2 shows the relative displacement values. Compared to the relative displacement of 5.35 mm in the original design, it was obtained 2.14 mm displacement in the first strengthening alternative and 2.64 mm in the second alternative.

Table 2. Relative displacements of the models

		Displacement (mm)	Decrease (%)
Self-Weight	Current Design	5.35	-
	1 st Alternative Strengthening	2.14	-60
	2 nd Alternative Strengthening	2.65	-50.4
Dynamic Loading	Current Design	23.46	-
	1 st Alternative Strengthening	4.44	-81
	2 nd Alternative Strengthening	4.06	-82.7

In Figure 14-b and c, under cyclic dynamic loading, lateral displacement distributions for the 1st and 2nd strengthening alternatives are presented. The top and bottom points of the vibromotor side plate is marked as "t" and "b" in Figure 11-a. The relative displacement (Z direction) of the "t" and "b" points are calculated and given in Figure 18. Maximum relative displacement is calculated as 23.46 mm for original design, 4.44 mm for first strengthening alternative and 4.06 mm for second strengthening alternative. The relative displacements of the "t" and "b" points under cyclic loadings are given in Figure 18.

The bearing plate on the side where the twin vibromotors are connected has been examined. The obtained stresses, under the machine's dead weight (on the support plate) are given in Figure 12-a-c for original design, 1st strengthening alternative and 2nd strengthening alternative, respectively. A maximum stress of 6.24 MPa occurred in the 1st alternative application and a maximum of 3.7 MPa in the 2nd alternative application. Also, in Figure 15 a-b-c, corresponding stresses under dynamic loading are depicted.

The time dependent variation of the maximum equivalent stress formed under cyclic loading in the support plate is given in Figure 18. In this graph, the stress variation obtained from the original design and the models with strengthening alternatives is also given. The maximum values are tabulated in Table3.

Table 3. Maximum equivalent stress values

		Stress (MPa)	Decrease (%)
Self-Weight	Current Design	34	-
	1 st Alternative Strengthening	6.24	-81.6
	2 nd Alternative Strengthening	3.7	-89.1
Dynamic Loading	Current Design	86	-
	1 st Alternative Strengthening	20	-76,7
	2 nd Alternative Strengthening	15.4	-82.1

Considering the above listed design and analysis results, the production of the machine is revised, and the final design of the machine is shown in Figure 20.

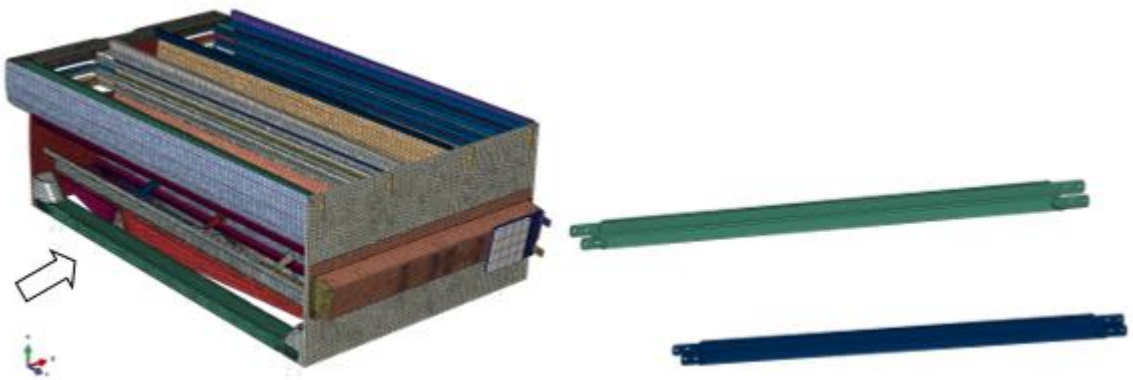


Figure 16. First alternative strengthening steel rods connecting machine bottom legs

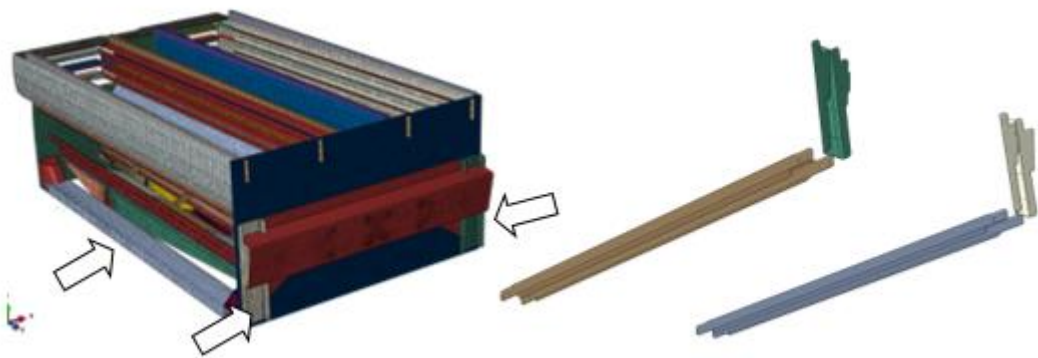


Figure 17. Second alternative strengthening

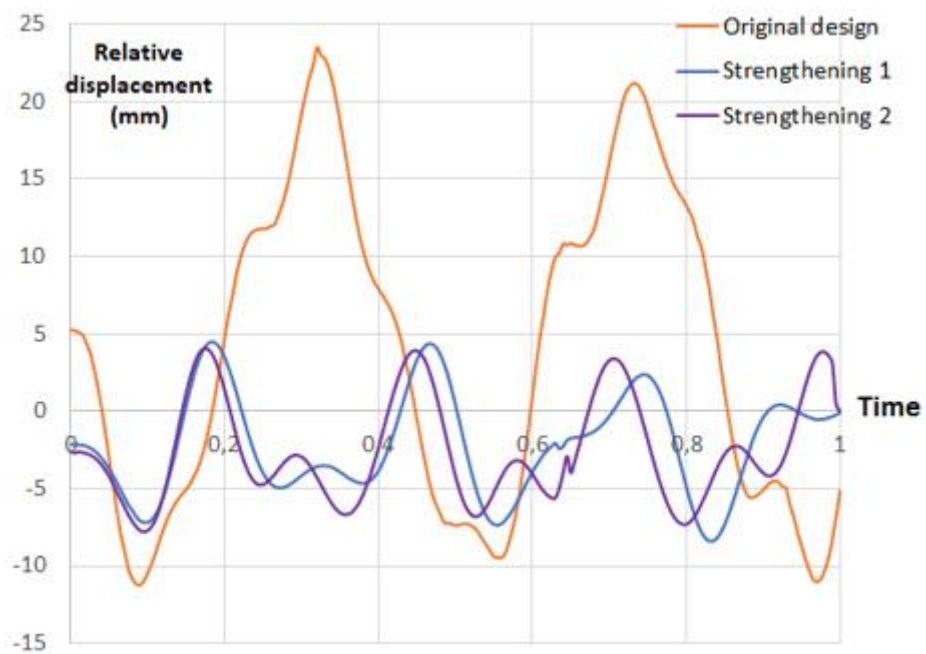


Figure 18. Relative displacement of side plate under cyclic loading

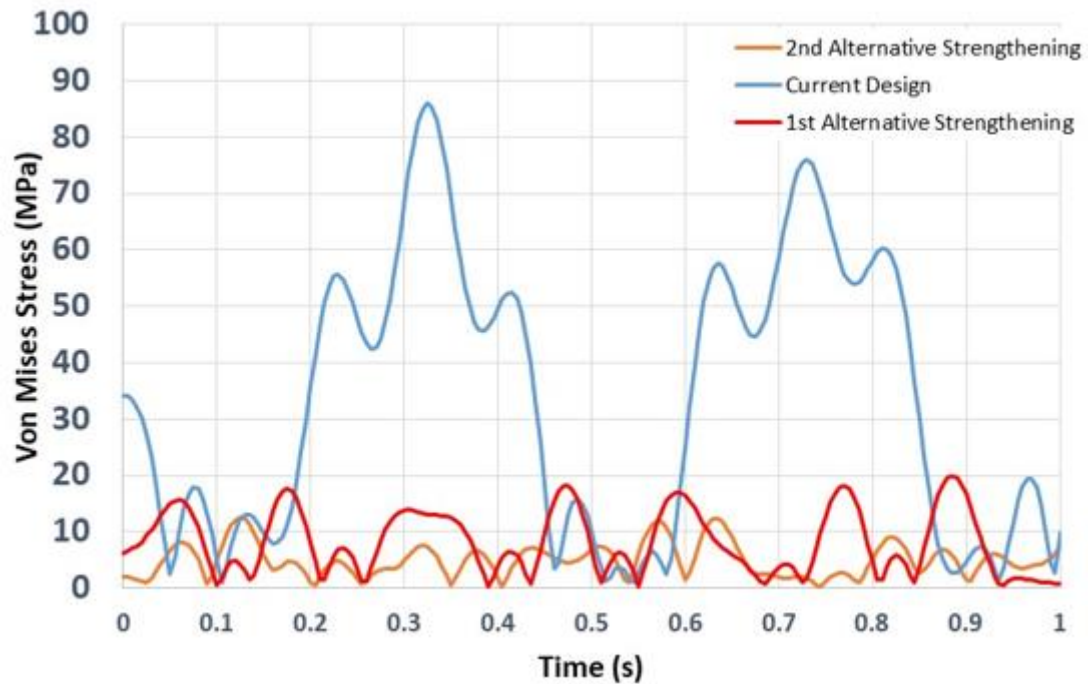


Figure 19. Maximum stress on bearing plates during cyclic loading



a) Rear view

b) Front view

Figure 20. Final design of the machine

4. CONCLUSIONS

It was concluded that the base support plates of the original design of the machine were insufficient for fatigue loading and susceptible to high cycle fatigue. Under cyclic loading, the initially displaced plate breaks under the effect of bending due to fatigue damage and the fatigue crack starts from one edge and proceeds to the other edge, passing through the nearest screw hole.

In this study, different strengthening alternatives have been proposed and analyzed in order to limit the deformations of the base support plates under static and dynamic loads and to prevent fatigue failure. The effectiveness of the proposed strengthening alternatives was evaluated according to the relative displacement of the upper and lower edges of the base support plate and the maximum Von Mises stresses occurring on the plate.

The 1st strengthening alternative decreased the relative displacement by -%60 for the self-weight case and -%50,4 for the dynamic case while the 2nd strengthening alternative decreased the relative displacement by -%81 for the self-weight case and -%82.7 for the dynamic case. On the other hand, the 1st

strengthening alternative decreased the maximum stress by -%81.6 for the self-weight case and -%89.1 for the dynamic case. The 2nd strengthening alternative decreased the maximum stress -%76,7 for the self-weight case and -%82,1 for the dynamic case. It is concluded that, reducing the stress and strain levels about %70 can result in considerable increase in fatigue life of constituents made of aluminum.

It is concluded that the stresses formed in the support plates after the strengthening remain well below the elastic limits. Static and dynamic analysis of computer models of the strengthening alternatives showed that the 2nd strengthening alternative was more effective in reducing the relative displacements between the edges of the support plate and the maximum Von Mises stresses. Therefore, alternative 2 was adopted as a preventative solution to a possible breakage failure in the support plate. Retrofit can be applied to existing treatment machines without too many changes to the structural system. It is also an economical solution as it requires additional steel elements that can be easily produced and shipped to worldwide demanded locations.

Acknowledgement

We would like to thank to the Imas Machinery Co. (Konya/TURKEY) for supporting the current work.

Conflict of Interest

Authors declare no conflicts of interest.

Author Contributions

Author contributions are as follows:

- 1st Author FEM Modelling and evaluation
- 2nd Author FEM Modelling and evaluation
- 3rd Author: Performing design studies, manuscript preparation
- 4th Author: FEM results evaluation, manuscript preparation

REFERENCES

- [1] M. A. Marins, F. M. L. Ribeiro, S. L. Netto, and E. A. B. Silva, "Improved similarity-based modeling for the classification of rotating-machine failures," *Journal of the Franklin Institute*, vol. 355, ss. 1913–1930, 2018.
- [2] T. Okabea and Y. Otsuka, "Proposal of a Validation Method of Failure Mode Analyses based on the Stress-Strength Model with a Support Vector Machine," *Reliability Engineering and System Safety*, vol. 205, 2021.
- [3] A. M. Irisarri, and E. Silveira, "Study of the failure of one machining tool," *Engineering Failure Analysis*, vol. 17, pp. 380–386, 2010.
- [4] F. Delgado, J. J. Coronado, and S. A. Rodríguez, "Failure analysis of a machine support for fique fibre processing," *Engineering Failure Analysis*, vol. 56, pp. 58-68, 2015.
- [5] X. Zhao, W. Ke, S. Zhang, and W. Zheng, "Potential failure cause analysis of tungsten carbide end mills for titanium alloy machining," *Engineering Failure Analysis*, vol. 66, pp. 321-327, 2016.
- [6] S. Papadopoulou, I. Pressas, A. Vazdirvanidis, and G. Pantazopoulos, "Fatigue failure analysis of roll steel pins from a chain assembly," *Engineering Failure Analysis*, vol. 101, pp. 320-328, 2019.
- [7] P. V. Krot, and R. Zimroz, "Failure analysis and modernization of high-pressure hydraulic press for drilling tubes testing," *Engineering Failure Analysis*, vol. 117, 2020.
- [8] Y. Li, P. Lu, B. Wang, Q. Xiang, and B. Ma, "Failure analysis of bolts on fatigue test bench for excavator stick," *Engineering Failure Analysis*, vol. 118, 2021.
- [9] T. Saraçyakupoglu, "Fracture and failure analysis of the trainer aircraft rudder pedal hanger,"

- Engineering Failure Analysis*, vol. 122, 2021.
- [10] M. Caliskan, "Evaluation of bonded and bolted repair techniques with finite element method," *Materials and Design*, vol. 27, pp. 811–820, 2006.
- [11] A. J. Wanga, Z. Guoa, X. Y. Jiaoa, L. Songc, W. X. Huc, J. C. Lic, and S. M. Xionga, "On the failure mechanism for high pressure die casting A390 hypereutectic alloy in low cycle and high cycle fatigue," *Materials Science and Engineering*, vol. 723, pp. 48-55, 2018.
- [12] C. Sasikumar, S. Srikanth, and S. K. Das "Analysis of premature failure of a tie bar in an injection molding machine," *Engineering Failure Analysis*, vol. 13, pp. 1246–1259. 2006.
- [13] J. M. Alegre, M. Preciado, and O. Ferren, "Study of the fatigue failure of an anti-return valve of a high pressure machine," *Engineering Failure Analysis*, vol. 14, pp. 408–416, 2007.
- [14] B. Tadic, P. M. Todorovic, Dj. Vukelic, and B. M. Jeremic, "Failure analysis and effects of redesign of a polypropylene yarn twisting machine," *Engineering Failure Analysis*, vol. 18, pp. 1308-1321, 2011.
- [15] X. Xu, Z. Yu, and Y. Gao, "Micro-cracks on electro-discharge machined surface and the fatigue failure of a diesel engine injector," *Engineering Failure Analysis*, vol. 13, pp. 124-133, 2013.
- [16] S. M. Bošnjaka, M. A. Arsićb, N. B. Gnjatovića, ILJ. Milenovića, and D. M. Arsićc, "Failure of the bucket wheel excavator buckets," *Engineering Failure Analysis*, vol. 84, pp. 247-261, 2018.
- [17] M. A. Khattaka, S. Zamana, S. Kazic, H. Ahmed, H. M. Habibe, H. M. Alie, and M. N. Tamina, "Failure investigation of welded 430 stainless steel plates for conveyor belts," *Engineering Failure Analysis*, vol. 116, 2020.
- [18] R. Guo, S. Xue, L. Zheng, A. Deng, and Lv. Liu, "Fracture failure analysis of DY08 Aluminum alloy elastic coupling," *Engineering Failure Analysis*, vol. 104, pp. 1030-1039, 2019.
- [19] H. R. Majidia, A.R. Torabib, M. Zabihia, S. M. J. Razavic, and F. Bertoc, "Energy-based ductile failure predictions in cracked friction-stir welded joints," *Engineering Failure Analysis*, vol. 102, pp. 327-337, 2019.
- [20] P. Moczko, D. Pietrusiak, and J. Wieckowski, "Investigation of the failure of the bucket wheel excavator bridge conveyor," *Engineering Failure Analysis*, vol. 106, 2019.
- [21] J. S. Rodrígueza, J. F. Duranb, Y. Aguilara, G. A. P. Alcázarb, and O. A. Zambranoa, "Failure analysis in sugar cane cutter base blades," *Engineering Failure Analysis*, vol. 112, 2020.
- [22] G. Vukelica, D. Pastorcicb, G. Vizentina, and Z. Bozic, "Failure investigation of a crane gear damage," *Engineering Failure Analysis*, vol. 115, 2020.
- [23] Q. Xiaofenga, L. Jie, Z. Xingguod, F. Lia, and P. Ruiqiang, "Fracture failure analysis of transmission gear shaft in a bidirectional gear pump," *Engineering Failure Analysis*, vol. 118, 2020.
- [24] R. Rajasekaran, A. K. Lakshminarayanan, R. Damodaram, and V. Balasubramanian, "Stress corrosion cracking failure of friction stir welded nuclear grade austenitic stainless steel," *Engineering Failure Analysis*, vol. 120, 2021.



EFFECTIVE POLYMER DECORATION ON NICKEL-IMINE COMPLEX TO ENHANCE CATALYTIC HYDROGEN EVOLUTION

^{1,*}Dilek KILINÇ^{ID}, ²Ömer ŞAHİN^{ID}

¹Harran University, Pharmacy Faculty, Pharmaceutical Chemistry Department, Şanlıurfa, TÜRKİYE
²Istanbul Technical University, Chemical and Metallurgical Engineering Faculty, Chemical Engineering Department, Istanbul, TÜRKİYE

¹dkilinc@harran.edu.tr, ²sahinomer2002@yahoo.com

Highlights

- Preparation of polymer decorated Ni@EC, Ni@EC-250, Ni@ECM catalysts.
- Effectively enhanced catalytic NaBH₄ hydrolysis activity by polymer decoration.
- Excellent catalytic activity of Ni@EC-250 with 28689 mL H₂/g_{cat}.min HGR at 50 °C.
- High stability of catalyst in 5th recycles with 100 % conversion.
- Obtaining low activation energy of 39.255 kJ·mol⁻¹



EFFECTIVE POLYMER DECORATION ON NICKEL-IMINE COMPLEX TO ENHANCE CATALYTIC HYDROGEN EVOLUTION

^{1,*}Dilek KILINÇ^{ID}, ²Ömer ŞAHİN^{ID}

¹Harran University, Pharmacy Faculty, Pharmaceutical Chemistry Department, Şanlıurfa, TÜRKİYE
²Istanbul Technical University, Chemical and Metallurgical Engineering Faculty, Chemical Engineering Department, Istanbul, TÜRKİYE

¹dkilinc@harran.edu.tr, ²sahinomer2002@yahoo.com

(Received: 27.10.2023; Accepted in Revised Form: 18.12.2023)

ABSTRACT: Since fossil fuels are rapidly depleting, finding alternative energy sources is becoming increasingly important. Among these alternatives, hydrogen (H₂) is the most viable option. In hydrogen evolution systems, supported metal catalysts enhance the catalytic activity in the hydrolysis reaction by increasing the surface area. Therefore, this research focuses on preparing three different polymer-decorated Nickel-Imine complex catalysts (Ni@EC, Ni@EC-250, Ni@ECM) to improve their efficiency. To achieve the catalysts, a Nickel-Imine complex [1] was supported on three different polymers (EC, EC-250, and ECM). The catalysts (Ni@EC, Ni@EC-250, Ni@ECM) were then utilized to generate hydrogen from NaBH₄ hydrolysis. The hydrogen evolution rates for Ni@EC, Ni@EC-250, and Ni@ECM catalysts were found as 6879; 15576; 8830 and 15459; 28689; 23417 mL H₂ gcat⁻¹.min⁻¹, respectively at 30 °C and 50 °C. Results indicate that the Ni@EC-250 catalyst exhibited the best activity. Consequently, the subsequent steps of the catalytic hydrolysis reaction were studied using Ni@EC-250. The activation energy of the Ni@EC-250 catalyst was estimated at 39.255 kJ.mol⁻¹. The reusability tests demonstrate that Ni@EC-250 remains active in sodium borohydride hydrolysis even after five runs. Technical abbreviations are defined upon first use. This study elucidates the reaction mechanism and kinetic data of catalytic sodium borohydride hydrolysis at various temperatures.

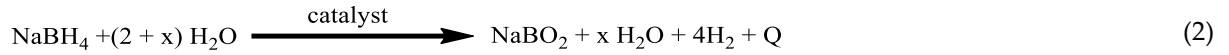
Keywords: Catalyst, Hydrogen evolution, NaBH₄, Ni-Imine, Polymer

1. INTRODUCTION

Hydrogen evolution is a prominent renewable energy concern [2,3]. Hydrogen represents an environmentally friendly energy source and stands out as a favorable substitute for fossil fuels due to its non-toxic emissions, long-term viability, and energy security benefits [4]. As a safe and efficient source of clean energy carriers [5,6], chemical hydrides are advantageous hydrogen storage materials due to their high hydrogen densities [7,8]. Among the different chemical hydrides, sodium borohydride stands out as the preferred material due to its high H₂ capacity, stability, recyclability, non-flammability, and non-toxic chemistry [9, 10]. H₂ is produced from sodium borohydride through hydrolysis or thermolysis [11, 12]. However, since thermolysis reactions are not an economically feasible process and cannot be practically used, hydrolysis is the preferred reaction. Eq. 1 provides the general hydrolysis reaction of sodium borohydride.



In the presence of water, the reaction is expressed as shown in Eq. 2.



In this case, x is referred to as the "hydration factor".

In hydrolysis, slow and controllable reactions with higher rates of H_2 evolution are obtained in objective systems using metal catalysts [13]. Numerous studies concerning the catalytic hydrolysis of sodium borohydride have been conducted by scientists for decades. Metal salts, alloys [14, 15], acids [16], or support materials [17] have been studied for this purpose. Due to the cost of noble metal catalysts, the usage of comparatively inexpensive non-noble metal catalysts is desired. Generally, the catalytic performance diminishes after each cycle in the hydrogen evolution reaction [18-20]. To counter this issue, incorporating a metal catalyst into a support material enhances the catalytic performance by expanding the catalyst surface area [21-23]. The chief issue remains to extract the metal catalyst from the reaction medium [24, 25], which can be effectively and practically addressed by using a supported catalyst [26, 27]. In the literature, various catalysts that support hydrolysis of sodium borohydride have been documented, including resin bead-supported Ru [26], poly-*p*-xylene supported Co [28], polymer-modified Co [29], Cu-ZrO₂ films [27], magnetically supported catalyst [24], Ni-Al₂O₃ [30, 31].

Polymers are widely used as support materials due to their high surface area, thermal stability, mechanical strength, and easy modification [32]. Furthermore, polymer-supported catalysts offer more environmentally friendly methods for various synthesis reactions than traditional methods. They have also enabled catalyst recycling [32, 33]. The polymer-supported catalytic system comprises robust polymer support and physical interactions. In recent years, imines and their compounds have received extensive research attention for their outstanding optical, thermal, electronic, and mechanical properties [34]. Furthermore, due to their straightforward synthesis and high electrical conductivity, imines and their metal complexes demonstrate remarkable photovoltaic effects [35].

Imines containing azomethine ($-\text{C}=\text{N}-$) bonds [36] exhibit an impressive ability to chelate with transition metals, lanthanide, or actinide ions forming imine complexes [35, 36]. Due to its versatile coordination compounds, with flexible and stereo-electronic structures, imine complexes have emerged with several applications such as plastic, aircraft, agriculture, cancer chemotherapy, drug production, antifungal, anti-inflammatory, antibacterial, and antiviral reactions, space, and electronics industries [37]. However, only a few studies exist about Imine complexes used in catalytic hydrogen evolution systems [38, 39].

In this paper, we examine the impact of three varied polymer-decorated Nickel-Imine catalysts (Ni@EC, Ni@ECM, and Ni@EC-250). Our study had two goals: (i) to enhance the catalytic activity of the Nickel-Imine complex by utilizing distinct polymer decoration in sodium borohydride hydrolysis reaction, which would lead to better interaction between the catalysts and sodium borohydride, and (ii) to determine the most efficient polymer-decorated catalyst for this reaction. The hydrogen evolution rates for Ni@EC, Ni@EC-250, and Ni@ECM catalysts were calculated from the experimental results. At 30 °C and 50 °C, they were found as 6879; 15576; 8830 and 15459; 28689; 23417 mL H₂ gcat⁻¹.min⁻¹, respectively. In comparison, the pure Nickel-Imine complex exhibited only 2240 and 10983 mL H₂ gcat⁻¹.min⁻¹ at the same temperatures [1]. Therefore, it can be concluded that the polymer decoration significantly increased the hydrogen evolution rate. Between the three catalysts, Ni@EC-250 demonstrated superior activity compared to the others under identical conditions. Henceforth, the other stages of catalytic hydrolysis reaction were examined using Ni@EC-250. The activation energy of the Ni@EC-250 catalyst was estimated at 39.255 kJ.mol⁻¹. The recycle tests revealed that Ni@EC-250 remains active in sodium borohydride hydrolysis even after five cycles. This report presents the reaction mechanism and kinetic data of catalytic hydrolysis of sodium borohydride at varying temperatures.

2. MATERIAL AND METHODS

2.1. Materials

All chemicals and solvents used were supplied by Merck, without undergoing any purification.

All samples were subjected to XPS studies to analyze the chemical states of the polymer-decorated nickel complex catalysts, using a Flex Specs electron spectrometer.

The Perkin-Elmer model FT-IR spectrometer was used to record Fourier Transform Infrared (FT-IR) spectra of the samples in the 4000-400 cm⁻¹ range.

The Ni@EC, Ni@EC-250, and Ni@ECM samples underwent measurement of their surface areas using the Brunauer-Emmett-Teller (BET) theory by BET surface area measurement.

To identify their crystal structures, X-ray diffraction (XRD) patterns were measured for Ni@EC, Ni@EC-250, and Ni@ECM with Rigaku Cu K α (λ = 154.059 pm) radiation at a scanning rate of 5 °C min⁻¹ within the range of 2 θ =0-80°.

The electronic behavior of the catalysts Ni@EC, Ni@EC-250, and Ni@ECM was investigated through the use of a Perkin-Elmer model UV-Vis spectrometer, ranging between 250 and 800 nm.

To examine the microstructure and morphology of these catalysts, a JEOL JSM 5800 model scanning electron microscope (SEM) was utilized.

2.2. Synthesis of the Catalyst

Step1: Synthesis of the Imine ligand

The ligand was synthesized by adding 1 mmol of 3,5-ditertbutylsalicylaldehyde (30 ml of ethanol) to 5-Amino-2,4-dichlorophenole (20 ml of ethanol) and refluxing the mixture at 80 °C for 5-6 h, as described in our earlier study [1].

Step 2: Synthesis of the Nickel-Imine complex

The Nickel-Imine complex was synthesized under mild conditions using 40 mM of 5-Amino-2,4-dichlorophenol-3,5-di-tertbutyl salicylalimine ligand and 20 mM of NiCl₂.6H₂O in 20 mL of ethanol, following the procedures outlined in our previous study [1].

Step 3: Preparation of the polymer-decorated Nickel-Imine complex catalysts

Ni@EC, Ni@EC-250, and Ni@ECM catalysts were prepared using a precipitation technique with Nickel-Imine complex [1] and EC, ECM, and EC-250 polymers. Technical abbreviations are explained on first use. To do this, 100 mg of the polymer was added to an ethanolic solution of Nickel-Imine complex at different concentrations (1 %, 5%, 10 %, 15 %, and 20 %) and stirred for approximately 72 hours at room temperature. The obtained catalysts, Ni@EC, Ni@ECM, and Ni@EC-250, were filtered, washed with ethyl alcohol, and finally dried at 70°C. The diagrammatic representation of catalysts comprising nickel complexes coated with polymers (Ni@EC, Ni@ECM, and Ni@EC-250) is depicted in Figure 1.

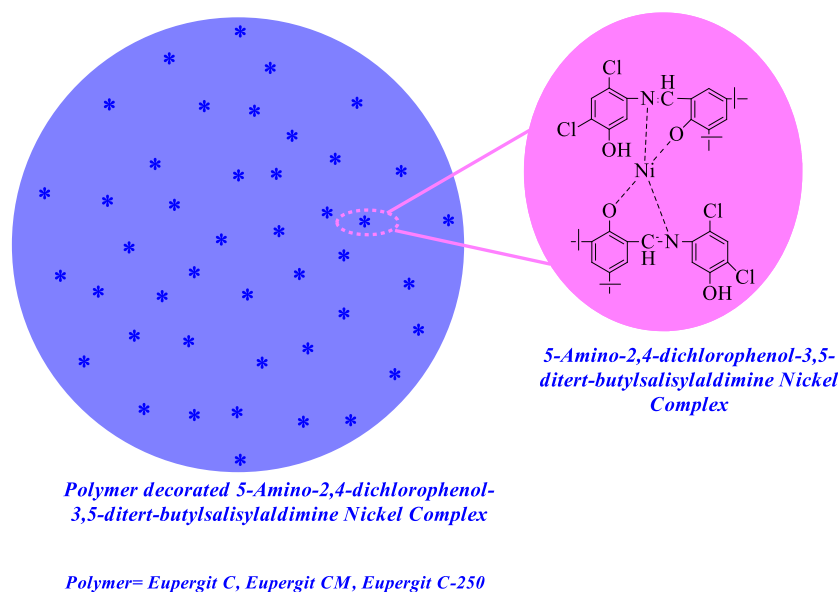


Figure 1. Schematic illustration of polymer decorated Nickel-Imine complex (Ni@EC, Ni@EC-250, Ni@ECM)

2.3. Catalytic Hydrogen Evolution Performance

Various experiments were conducted on hydrogen evolution using Nickel-Imine catalysis with different polymers. The experiments took place at 30°C in an aqueous solution containing 2 % NaBH₄, 10 % NaOH, and 15 mg catalyst. The concentration of Nickel-Imine complex varied for each experiment. The hydrogen evolution system was implemented through the water-gas displacement method. For various Nickel-Imine catalysts decorated with different polymers (Ni@EC, Ni@EC-250, and Ni@ECM), comparative experiments were conducted to determine the hydrogen evolution rates. The most effective catalyst was selected and further tested.

3. RESULTS AND DISCUSSION

3.1. Catalytic Studies

3.1.1. Hydrogen evolution activities

Several experiments were conducted to identify the most effective polymer-decorated Nickel-Imine with the highest catalytic activity for the hydrolysis of NaBH₄ to release hydrogen. As a result, the catalytic hydrolysis of NaBH₄ was examined under the same reaction conditions using 5 % Ni complex, 15 mg catalyst (Ni@EC, Ni@EC-250, and Ni@ECM), 10 % NaOH, and 2 % NaBH₄ at 30 °C. In this reaction medium, hydrogen evolution rates of 6,879 mL H₂ gcat⁻¹.min⁻¹, 15,576 mL H₂ gcat⁻¹.min⁻¹, and 8,830 mL H₂ gcat⁻¹.min⁻¹ were calculated, as shown graphically in Figure 2. It is evident that, under the same reaction

conditions, Ni@EC-250 exhibited the highest catalytic activity, compared to Ni@EC and Ni@ECM. The catalytic activity increased in the order of Ni@EC-250 > Ni@ECM > Ni@EC, with the inclusion of polymer into the Nickel-Imine complex structure. Therefore, other catalytic hydrolysis experiments were conducted using the Ni@EC-250.

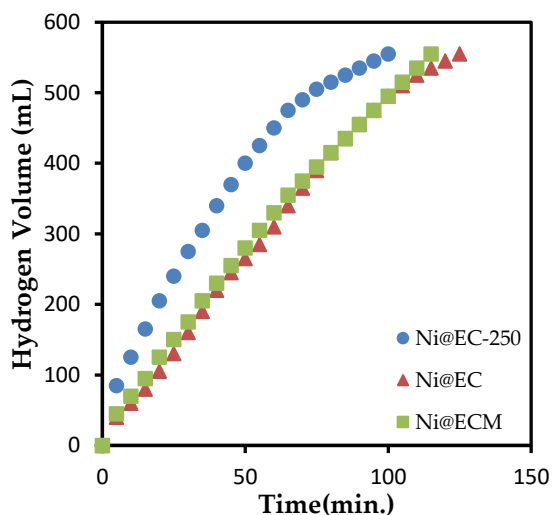


Figure 2. Plot of hydrogen volume versus time with different Ni catalysts

To determine the extent of Ni@EC-250 catalyzed hydrolysis reaction, the first step was to establish the quantities of their Ni complexes. To achieve this, the catalytic activity of Ni@EC-250 was investigated with varying concentrations of Ni complexes (1 %, 5 %, 10 %, 15 %, and 20 %) loaded onto 15 mg polymer-decorated nickel complex catalysts, as shown in Figure 3. To assess the impact of different Ni complex concentrations (1 %, 5 %, 10 %, 15 %, 20 %), the rates of hydrogen evolution were determined as 28,907; 15,576; 9,905; 7,708; 5,401 mL H₂ gcat⁻¹.min⁻¹, respectively. While 1 % Ni complex exhibited the highest catalytic activity, the hydrolysis reaction was incomplete resulting in a lower H₂ volume (only 370 mL H₂) than the calculated value (560 mL). According to the results, the use of a 5 % nickel complex produced faster hydrogen evolution rates than excessive concentrations for Ni@EC-250 catalyst. However, using over 5% nickel-imine complex caused a decrease in hydrogen evolution rates and catalytic activities. This reduction is due to the saturation of the catalyst surface with 5 % Ni complex, which occurs as the concentration of nickel complex increases.

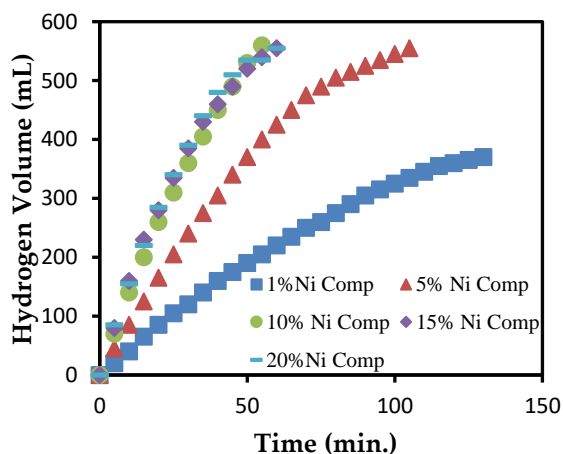


Figure 3. Plot of hydrogen volume versus time with various nickel complex concentrations in Ni@EC-250 catalyst

The impact of sodium hydroxide concentration on Ni@EC-250 catalyzed sodium borohydride hydrolysis is illustrated in Figure 4. The reaction mixture was prepared using 5% Nickel-Imine complex and 15 mg Ni@EC-250 in a 2 % sodium borohydride solution at 30°C. The rates of hydrogen evolution were determined through the addition of 0 %, 3 %, 5 %, 7 % and 10 % NaOH concentrations, resulting in respective rates of 7514; 7403, 9204; 14161 and 15576 mL H₂ gcat⁻¹.min⁻¹. According to the results, hydrogen evolution rates catalyzed by Ni@EC-250 increased as the sodium hydroxide concentration increased from 0 % to 10 %. At higher NaOH concentrations, the interaction of hydroxyl ions with free water molecules made the required water for the hydrolysis reaction easily accessible, increasing hydrogen evolution rates. In addition, the increase in sodium hydroxide concentrations led to shorter completion times of the hydrolysis reaction.

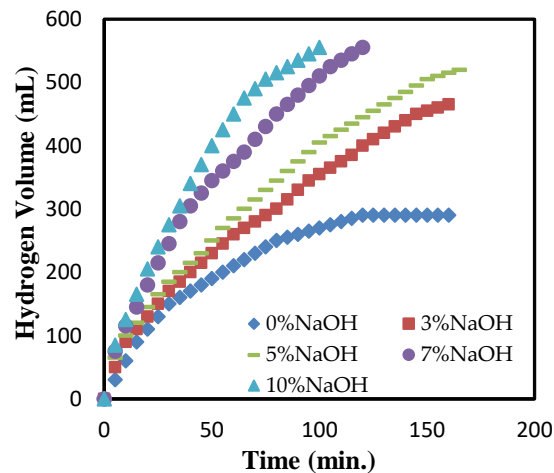


Figure 4. Plot of hydrogen volume versus time with various NaOH concentrations with Ni@EC-250 catalyst

In the sodium borohydride hydrolysis process, the influence of the Ni@EC-250 catalyst amount was presented in Figure 5. The reaction mixture resulted from a 5 % Nickel-Imine complex in a 2 % sodium borohydride solution at 30 °C. To apply 5mg, 15mg, 25mg, and 50mg of the catalyst, hydrogen evolution rates were determined as 10622; 15576; 26095 and 27284 mL H₂ gcat⁻¹.min⁻¹, respectively. According to the outcomes, the increment in the catalyst amount led to a reduction in reaction times. Ni@EC-250 catalyzed hydrogen evolution rates increased as the amount of catalyst increased from 5 mg to 50 mg. With more catalysts, the reactants were exposed to a larger reaction area, and the residence time in the reactor was reduced, accelerating the hydrolysis process.

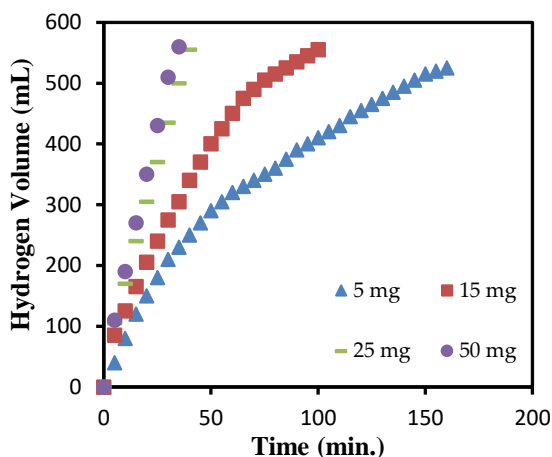


Figure 5. Plot of hydrogen volume versus time with various catalyst amounts with Ni@EC-250 catalyst

In Figure 6, the plot displays the relationship between hydrogen volume and time for a range of NaBH_4 concentrations. The reaction medium consisted of 5 % Nickel-Imine complex and 15 mg Ni@EC-250 catalyst in a 10 % sodium hydroxide solution at a temperature of 30°C. The hydrogen evolution rates catalyzed by Ni@EC-250 were calculated as 15576; 23089; 25415 and 26571 $\text{mL H}_2 \text{ g}_{\text{cat}}^{-1} \cdot \text{min}^{-1}$ correspondingly, using 2 %, 5 %, 7 %, and 10 % sodium borohydride. An increase in gas volume was observed by increasing NaBH_4 concentration in the hydrolysis solution. The hydrogen evolution rates gradually increased with the increasing Ni@EC-250 catalyst and NaBH_4 concentration from 2 % to 10 %, as expected.

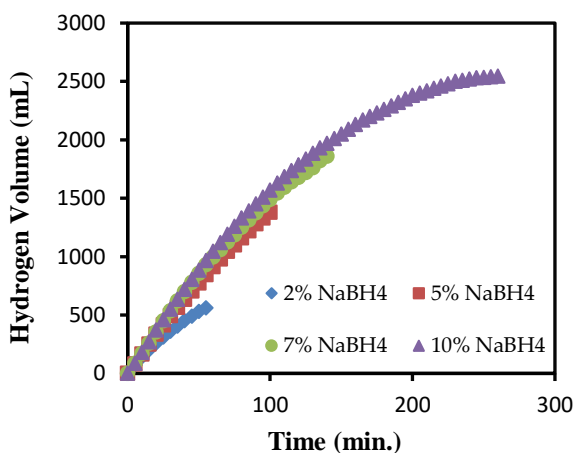


Figure 6. Plot of hydrogen volume versus time with various NaBH_4 concentrations with Ni@EC-250 catalyst

For the optimization of temperature effects, four different temperatures (20–50 °C) were studied. The reaction medium occurred from 5% Nickel-Imine complex, 15 mg Ni@EC-250 catalyst in 10 % sodium hydroxide-2 % NaBH_4 solution. Figure 7a displays the plot of hydrogen volume versus time with various temperatures with Ni@EC-250, catalyst in the range 20–50 °C. According to the experimental results, Ni@EC-250 catalyzed hydrogen evolution rates were calculated as 9329; 15576; 24740 and 28689 $\text{mL H}_2 \text{ g}_{\text{cat}}^{-1} \cdot \text{min}^{-1}$ respectively. The reaction temperature increases positively affected the hydrogen evolution rates in this system. Four different temperatures (20-50 °C) were studied to optimize the temperature effects. The reaction medium consisted of 5 % nickel-imine complex, 15 mg Ni@EC-250 catalyst in 10 % sodium hydroxide-2 % NaBH_4 solution. Figure 7a shows the plot of hydrogen volume versus time with

different temperatures with Ni@EC-250, catalyst in the range 20-50 °C. According to the experimental results, the Ni@EC-250 catalyzed hydrogen evolution rates were calculated as 9329; 15576; 24740 and 28689 mL H₂ g_{cat}⁻¹.min⁻¹, respectively. Increasing the reaction temperature had a positive effect on the hydrogen evolution rates in this system.

3.1.2. Kinetic studies

The kinetic calculations for the hydrolysis of sodium borohydride, catalyzed by Ni@EC-250, can be determined using the equation for an nth-order reaction as seen in Eq. 3-6.

$$-r_{\text{NaBH}_4} = -\frac{dC_{\text{NaBH}_4}}{dt} = k \cdot C_{\text{NaBH}_4}^n \quad (3)$$

Separating and integrating, we get

$$-\int_{C_{\text{NaBH}_4 0}}^{C_{\text{NaBH}_4}} \frac{dC_{\text{NaBH}_4}}{C_{\text{NaBH}_4}^n} = k \int_0^t dt \quad (4)$$

$$\frac{1}{(n-1)} \left(\frac{1}{C_{\text{NaBH}_4}^{n-1}} - \frac{1}{C_{\text{NaBH}_4 0}^{n-1}} \right) = kt \quad (5)$$

$$\frac{1}{C_{\text{NaBH}_4}^{n-1}} = (n-1)k \cdot t + \frac{1}{C_{\text{NaBH}_4 0}^n} \quad (6)$$

According to Eq. 6, the hydrolysis reaction catalyzed by Ni@EC-250 had a reaction order (n) value of 0.2. The rate constants were determined from the linear portion of H₂ generation versus time between 20-50 °C, as shown in Figure 7b. The activation energy for Ni@EC-250 in the NaBH₄ hydrolysis reaction was also calculated from the slope of the Arrhenius plot and found to be E_a = 39.255 kJ.mol⁻¹, as presented in Figure 7c. The reaction appears to be unaffected by changes in temperature due to its relatively low activation energy, and the catalyst's performance at low temperatures is adequate.

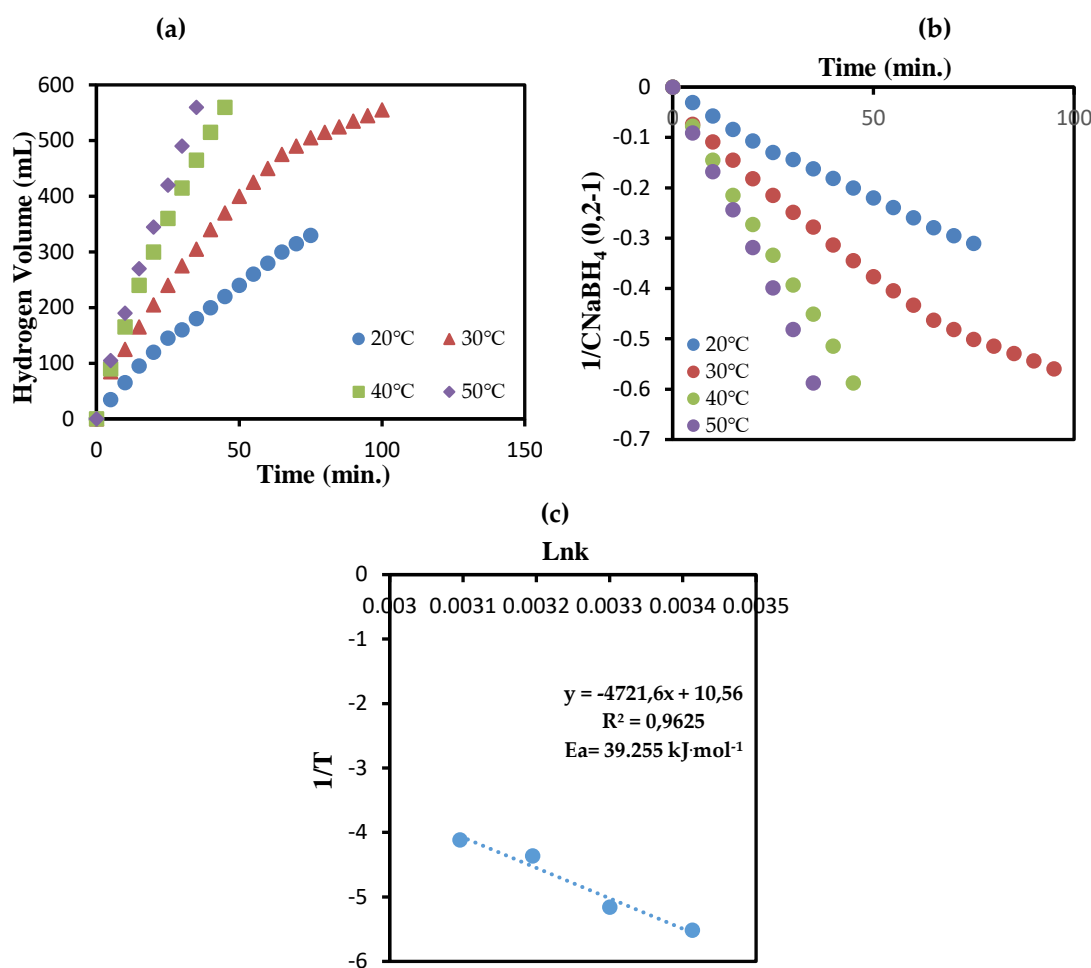


Figure 7. The plot of hydrogen volume versus time with various temperatures with Ni@EC-250 catalyst (a), Linear regression based on n-order at different temperatures (b) and apparent activation energy for Ni@EC-250 catalyst (c)

Table 1 presents a comparison of hydrogen evolution activities between various nickel catalysts. According to the data in Table 1, it is evident that polymer decoration has substantially enhanced the hydrogen evolution rate.

Table 1. The comparison of the hydrogen evolution activities of Nickel catalysts

Catalyst	Hydrogen evolution rate($\text{mLH}_2\cdot\text{g}_{\text{cat}}^{-1}\cdot\text{min}^{-1}$)	Activation Energy($\text{kJ}\cdot\text{mol}^{-1}$)
Ni metal	772	-
Nickel-Imine complex	2240	18.160
Ni@EC	6879	16.633
Ni@EC-250	15576	39.255
Ni@ECM	8830	28.766

3.1.3. Reusability tests of Ni@EC-250 in sodium borohydride hydrolysis reaction

For the catalyst, reusability is essential to determine the catalytic performance. In sodium borohydride hydrolysis, to determine the reusability performance of Ni@EC-250 catalyst, five catalytic cycles were experienced. For this purpose, the reusability tests were performed at 30 °C with 10 % NaOH in 2 % NaBH₄ solution and the results were shown in Figure 8. Before each hydrolysis study, the Ni@EC-250 catalyst was washed and dried several times for the next catalytic cycle in the sodium borohydride hydrolysis reaction. Even if small decreases were observed in the catalytic activity, the reactions resulted with 100 %

conversion in five hydrolysis cycles. These small decreases may have arisen from both by-product filling into the catalyst's pores and the increasing viscosity of the solution. Thus, they caused a decrease in the active sites of the catalyst surface.

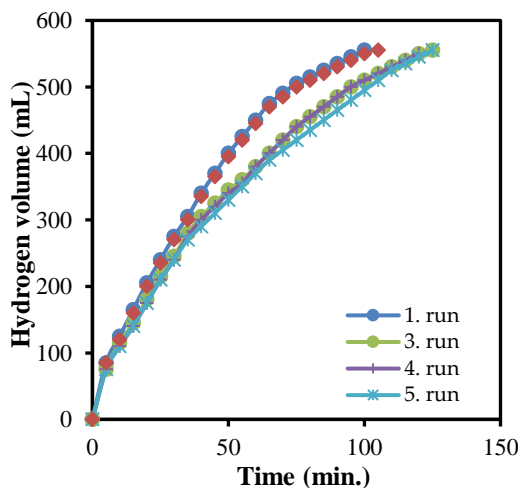


Figure 8. Reusability test results for Ni@EC-250 catalyst in hydrolysis of sodium borohydride reaction

3.2. Characterization

The synthesized polymer-decorated nickel-imine complex catalysts (Ni@EC, Ni@EC-250, and Ni@ECM) characterization occurred using FT-IR, BET, SEM, XRD, XPS, and UV-Vis. Table 2 displays the characteristic infrared spectral values of the nickel complex and the Ni@EC, Ni@EC-250, and Ni@ECM catalysts. The azomethine ($-C=N-$) group [40], represented by a band at 1621 cm^{-1} in the nickel-imine complex, shifted to 1628 ; 1632 and 1629 cm^{-1} in Ni@EC, Ni@EC-250, and Ni@ECM catalysts, respectively. The changes in observed bands from 2958 cm^{-1} to 2960 ; 2964 and 2959 cm^{-1} for the free $-OH$ vibrations [41] were seen in Ni@EC, Ni@EC-250, and Ni@ECM catalysts, respectively. The Ni@EC, Ni@EC-250, and Ni@ECM catalysts exhibited $-C-O$ vibrations, characterized by shifts in the 1020 cm^{-1} band to 1047 ; 1056 and 1051 cm^{-1} respectively. The FT-IR band related to $-CH_3$ vibrations remained unaltered in both the nickel-imine complex and the three-polymer-adorned nickel-imine complex catalysts, with a band spotted at $2750\text{-}2950\text{ cm}^{-1}$. The key bands verifying the coordination between metals and ligands (Ni-O and Ni-N) demonstrated certain shifts [42, 43], as displayed in Table 2.

Table 2. Characteristic FT-IR bands of catalysts (cm^{-1})

Catalyst	$\nu(\text{CH}_3)$	Free $\nu(\text{OH})$	$\nu(\text{C}=\text{N})$	$\nu(\text{C}-\text{O})$	$\nu(\text{M}-\text{O})$	$\nu(\text{M}-\text{N})$
Nickel-Imine complex	2750-2950	2958	1621	1020	495	430
Ni@EC	2750-2950	2960	1628	1047	498	426
Ni@ECM	2750-2950	2964	1632	1056	501	432
Ni@EC-250	2750-2950	2959	1629	1051	496	428

Figure 9 illustrates the electronic spectra of Ni@EC, Ni@EC-250, and Ni@ECM. The three polymer-decorated nickel-imine complexes display comparable electronic behavior. A broad electronic band at 397.55 nm was observed in all three samples, which can be attributed to Ni \rightarrow Ni charge transfer. Additionally, small bands detected at 316.27 nm were assigned to the $n-\pi^*$ transition of the azomethine group ($-C=N-$). Furthermore, two different electronic bands were observed, although this was not very apparent. They are located at 324.56 nm (due to the ligand-to-metal charge transfer (LMCT) resulting from the O \rightarrow Ni charge transfer) and 492.23 nm (due to the d-d transitions (${}^1A_{1g} \rightarrow {}^1A_{2g}$) of the Ni ion), respective.

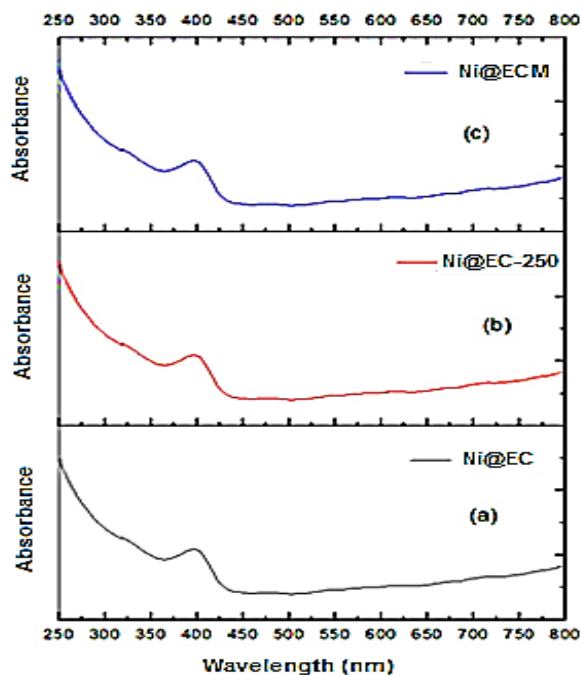


Figure 9. The UV-Vis spectrum of Ni@EC, Ni@EC-250, Ni@ECM

Fig.10a displays the XRD patterns for Ni@EC, Ni@EC-250 and Ni@ECM. The patterns reveal that the crystalline phase was present in the synthesized polymer-decorated nickel-imine complex catalysts. The polymer-decorated nickel complex catalysts exhibit sharp crystalline XRD patterns, which are caused by the natural crystalline properties of the nickel complex. The size of the crystallites for Ni@EC, Ni@EC-250, and Ni@ECM were assessed using Scherrer's formula, by measuring the full width at half maximum of the corresponding XRD peaks. The obtained data indicates that the synthesized nickel-imine complexes decorated with polymer are monocrystalline. Specifically, the crystallite sizes of the Ni@EC, Ni@EC-250 and Ni@ECM samples are 29°, 38°, and 59° respectively.

X-ray photoelectron spectroscopy (XPS) was used to determine the electronic properties of the species on the catalyst surface. A clear presence of Ni@EC, Ni@EC-250 and Ni@ECM, which confirm the respective oxidation states of the elements, is shown in Figure 10b. The XPS traces of Ni@EC, Ni@EC-250 and Ni@ECM were determined to be around 885 eV for Ni (II) (2p), which confirms the diamagnetic structure of the nickel-imine complex. X-ray photoelectron spectroscopy traces of Ni@EC, Ni@EC-250, and Ni@ECM demonstrated binding energy values of 862.1 eV and 879.9 eV for the $2p^{3/2}$ and $2p^{1/2}$ conditions, respectively.

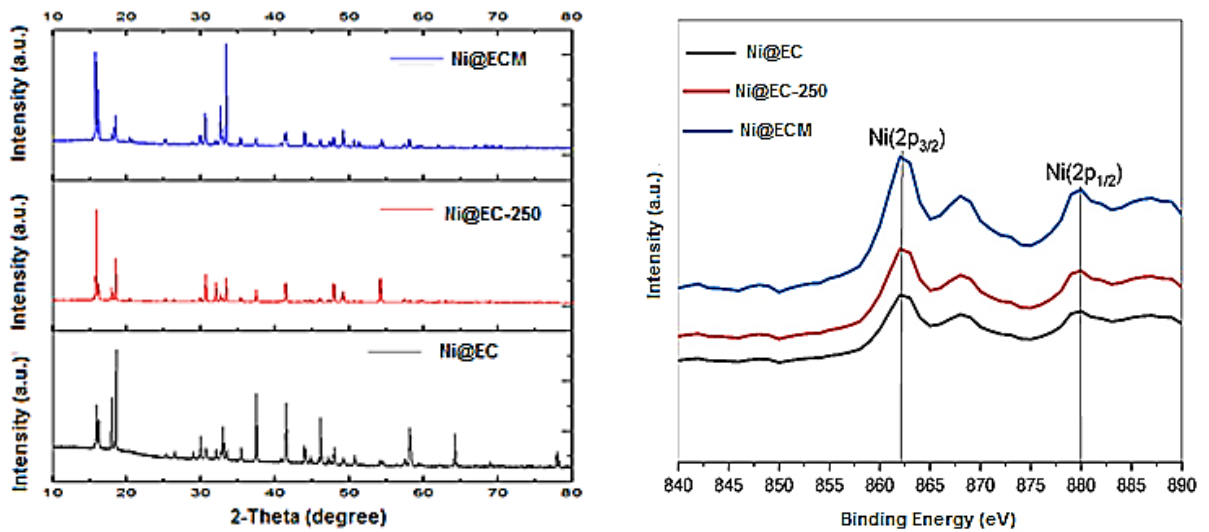


Figure 10. The XRD patterns Ni@EC, Ni@EC-250, and Ni@ECM (a) and XPS traces of Ni@EC, Ni@EC-250 and Ni@ECM (b)

Figure 11a shows the recorded SEM image of the Ni@EC sample. As can be seen from the figure, there is an agglomerated spherical image. It seen that the Nickel-Imine complex was well distributed on polymers. Based on the size scale given in the SEM image, the average crystallite size of the Ni@EC sample is less than 100 nm. It shows a similar image in the Ni@EC-250 example given in Figure 11b. Unlike the Ni@EC sample, the particles are separated from each other in the Ni@EC-250 sample. Rather than a spherical structure, a bar image is observed. The SEM image shown in Figure 11c is from the Ni@ECM sample. The sample synthesized in the figure has been observed to be in the form of nanoscale wire. When examined dimensionally, the crystallite size of the Ni@ECM sample was less than 100 nm. Thus, it was realized that the crystallite size obtained for all three samples coincided with the crystallite size data obtained from XRD measurements.

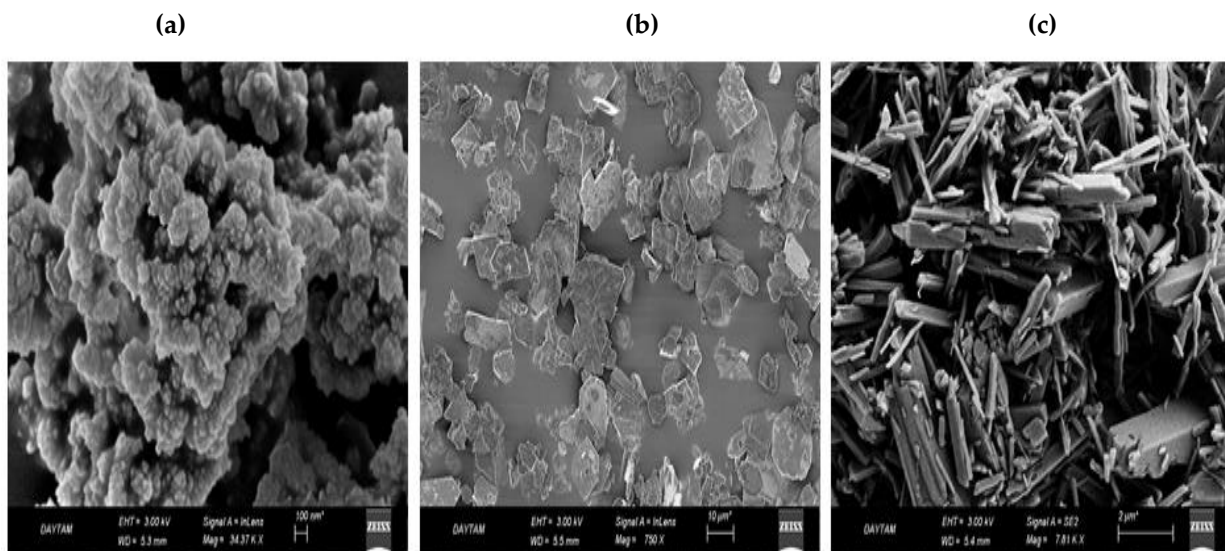


Figure 11. The SEM images of Ni@EC (a), Ni@EC-250 (b) and Ni@ECM (c)

The specific surface areas, total pore volumes, and average pore sizes of the nickel-imine complex, Ni@EC, Ni@EC-250, and Ni@ECM catalysts are presented in Table 3. The polymer-decorated nickel-imine complex catalysts had surface areas of 58.721; 56.365 and 52.849 m²/g for Ni@EC, Ni@EC-250 and Ni@ECM catalysts, respectively. Technical term abbreviations were explained upon the first usage. In contrast, the

surface area of the nickel complex was measured to be 48.456 m²/g. It can be observed that the Ni@EC, Ni@EC-250, and Ni@ECM catalysts exhibit larger surface areas compared to the nickel-imine complex. The pore volume of the nickel-imine complex was found to be smaller at 0.178 cm³.g⁻¹ as opposed to the Ni@EC, Ni@EC-250 and Ni@ECM catalysts which had pore volumes of 0.253; 0.211 and 0.230 cm³.g⁻¹ respectively. These outcomes suggest that the larger surface area of the catalysts is attributed to the presence of larger active sites leading to enhanced hydrogen evolution performance.

Table 3. BET analysis results of catalysts

Catalyst	S _{BET} (m ² .g ⁻¹)	Average pore	Pore volume
Nickel-Imine complex	48.456	14.743	0.178
Ni@EC	58.210	21.194	0.253
Ni@EC-250	56.365	18.296	0.211
Ni@ECM	52.849	17.885	0.230

4. CONCLUSIONS

In this study, the initial objective was to synthesize three new and effective catalysts for the hydrolysis of sodium borohydride to produce hydrogen. To achieve this, a Nickel-Imine complex was combined with three distinct polymers (EC, EC-250, and ECM) to enlarge the surface area of Nickel-Imine and enhance the catalytic interaction with sodium borohydride. According to the experimental results, the catalysts obtained, i.e., Ni@EC, Ni@EC-250, and Ni@ECM, exhibited exceptional performance in hydrolysis of sodium borohydride with hydrogen evolution rates of 6879; 15576; 8830 mL H₂ gcat⁻¹.min⁻¹ and 15459; 28,689; 23,417 mL H₂ gcat⁻¹.min⁻¹ at 30 °C and 50 °C, respectively. It is evident that the polymer decoration remarkably enhances the hydrogen evolution rate. Whereas the pure Nickel-Imine complex showed lower activity, with 2240 mL H₂ gcat⁻¹.min⁻¹, compared to Ni metal which was only 772 mL H₂ gcat⁻¹.min⁻¹ at the same temperatures, the decoration of the Ni-Imine complex with polymers on its surface area increased the catalyst's surface area, resulting in improved hydrogen evolution rates. The activation energies of the Ni@EC, Ni@EC-250, and Ni@ECM catalysts were calculated to be 16.633 kJ.mol⁻¹, 39.255 kJ.mol⁻¹, and 28.766 kJ.mol⁻¹, respectively. In the second step, the objective was to determine the catalyst with the best catalytic performance among the three options. Out of all the decorated catalysts, Ni@EC-250 catalyst showed the best activity under the same conditions compared to Ni@EC and Ni@ECM. With the addition of the polymer, the catalytic activity increased in the order of Ni@EC-250 > Ni@ECM > Ni@EC. As a result, Ni@EC-250 was selected for the remaining steps of the catalytic hydrolysis reaction. The results of the reusability tests indicate that Ni@EC-250 remains active in sodium borohydride hydrolysis even after the fifth run, achieving 100 % conversions.

Declaration of Ethical Standards

The authors declare that all ethical guidelines including authorship, citation, data reporting, and publishing original research are followed.

Credit Authorship Contribution Statement

Dilek KILINÇ: Investigation, Experimental Section, Data curation, Methodology, Original draft preparation, Writing- Reviewing-Editing, Validation. **Ömer ŞAHİN:** Methodology, Validation

Declaration of Competing Interest

The authors declare that they have no known competing financial interests or personal relationships that could have appeared to influence the work reported in this paper.

Funding / Acknowledgements

This work was supported by the Research Centre of Siirt University (Project number 2017-SIUFED-67).

REFERENCES

- [1] D. Kılınç, O. Sahin, C. Saka, "Investigation on salicylaldimine-Ni complex catalyst as an alternative to increasing the performance of catalytic hydrolysis of sodium borohydride," *International Journal of Hydrogen Energy*, vol. 42, pp. 20625-20637, 2017.
- [2] S. Santra, D. Das, N.S. Das, K.K. Nanda, "An efficient on-board metal-free nanocatalyst for controlled room temperature hydrogen production," *Chemical Science*, vol. 8, pp.2994-3001, 2017.
- [3] L. Semiz, N. Abdullayeva, M. Sankir, "Nanoporous Pt and Ru catalysts by chemical dealloying of Pt-Al and Ru-Al alloys for ultrafast hydrogen generation," *Journal of Alloys Compounds*, vol. 744, pp. 110-115, 2018.
- [4] M.Z. Jacobson, W.G. Colella, D.M. Golden, "Cleaning the air and improving health with hydrogen fuel-cell vehicles," *Science*, vol. 308, pp. 1901-1905, 2005.
- [5] D. Huang, P. Zhao, F. Fu, J. Wie, X. Yang, D. Astruc, C. Wang, J. Zhu, C. Luo, "Highly efficient and selective Co@ZIF-8 nanocatalyst for hydrogen release from sodium borohydride hydrolysis, *ChemCatChem*," vol. 11, pp. 1643-1649, 2019.
- [6] M. Sankir, L. Semiz, R.B. Serin, N.D. Sankir, "Hydrogen generation from nanoflower platinum films," *International Journal of Hydrogen Energy*, vol. 40, pp. 8522-8529, 2015.
- [7] S.C. Li, F.C. Wang, "The development of a sodium borohydride hydrogen generation system for proton exchange membrane fuel cell," *International Journal of Hydrogen Energy*, vol. 41, pp. 3038-3051, 2016.
- [8] M. Sankir, R.B. Serin, L. Semiz, N.D. Sankir, "Unusual behavior of dynamic hydrogen generation from sodium borohydride," *International Journal of Hydrogen Energy*, vol. 39, pp. 2608-2613, 2014.
- [9] F. Ali, S.B. Khan, A.M. Asiri, "Chitosan coated cellulose cotton fibers as catalyst for the H₂ production from NaBH₄ methanolysis," *International Journal of Hydrogen Energy*, vol. 44, pp. 4143-4155, 2014.
- [10] C. Huff, T. Dushatinski, T.M. Abdel-Fattah, "Gold nanoparticle/multi-walled carbon nanotube composite as novel catalyst for hydrogen evolution reactions," *International Journal of Hydrogen Energy*, vol. 42, pp. 18985-18990, 2017.
- [11] D. Kılınç, "Effect of Al₂O₃-supported Cu-Schiff base complex as a catalyst for hydrogen generation in NaBH₄ hydrolysis," *Energy Sources Part A-Recovery Utilization and Environmental Effects*, vol. 40, pp. 873-885, 2018.
- [12] E. Fangaj, A.A. Ceyhan, "Apricot Kernel shell waste treated with phosphoric acid used as a green, metal-free catalyst for hydrogen generation from hydrolysis of sodium borohydride," *International Journal of Hydrogen Energy*, vol. 45, pp. 17104-17117, 2020.
- [13] D. Kılınç, O. Sahin, "Effective TiO₂ supported Cu-Complex catalyst in NaBH₄ hydrolysis reaction to hydrogen generation," *International Journal of Hydrogen Energy*, vol. 44: pp. 18858-18865, 2019.
- [14] O. Akdim, U.B. Demirci, D. Muller, P. Miele, "Cobalt (II) salts, performing materials for generating hydrogen from sodium borohydride," *International Journal of Hydrogen Energy*, vol. 34, pp. 2631-7, 2019.
- [15] J. Andrieux, D. Swierczynski, L. Laversenne, A. Garron, S. Bennici, C. Goutaudier, et al., "A multifactor study of catalyzed hydrolysis of solid NaBH₄ on cobalt nanoparticles: thermodynamics and kinetics," *International Journal of Hydrogen Energy*, vol. 34, pp. 938-51, 2019.
- [16] O. Akdim, U.B. Demirci, P. Miele, "Acetic acid, a relatively green single-use catalyst for hydrogen

- generation from sodium borohydride," *International Journal of Hydrogen Energy*, vol. 34, pp. 7231-8, 2009.
- [17] Y. Kojima, K.I. Suzuki, K. Fukumoto, M. Sasaki, T. Yamamoto, Y. Kawai, et al., "Hydrogen generation using sodium borohydride solution and metal catalyst coated on metal oxide," *International Journal of Hydrogen Energy*, vol. 27, pp. 1029-34, 2002.
- [18] D. Xu, X. Lai, W. Guo, X. Zhang, C. Wang, P. Dai, "Efficient catalytic properties of SO₄²⁻ / MxO_y (M = Cu, Co, Fe) catalysts for hydrogen generation by methanolysis of sodium borohydride," *International Journal of Hydrogen Energy*, vol. 43, pp. 6594-6602, 2018.
- [19] X. Zhang, X. Sun, D. Xu, X. Tao, P. Dai, Q. Guo, X. Liu, "Synthesis of MOF-derived Co@C composites and application for efficient hydrolysis of sodium borohydride, *Applied Surface Science*, vol. 469, pp. 764-769, 2019.
- [20] D. Kılınç, Ö. Şahin, "Ruthenium-Imine Catalyzed KBH₄ Hydrolysis as an Efficient Hydrogen Production System, *International Journal of Hydrogen Energy*, vol. 46, pp. 20984-20994, 2021.
- [21] D. Kılınç, O. Sahin "Highly active and stable CeO₂ supported nickel complex catalyst in hydrogen generation," *International Journal of Hydrogen Energy*, vol. 46, pp. 499-507, 2022.
- [22] J. Lee, H. Shin, K.S. Choi, J. Lee, J.Y. Choi, H.K. Yu, "Carbon layer supported nickel catalyst for sodium borohydride (NaBH₄) dehydrogenation," *International Journal of Hydrogen Energy*, vol. 44 pp. 2943-2950, 2019.
- [23] A.A. Ceyhan, S. Edebali, E. Fangaj, "A study on hydrogen generation from NaBH₄ solution using Co-loaded resin catalysts," *International Journal of Hydrogen Energy*, vol. 45, pp. 45:34761-34772, 2020.
- [24] A. Pozio, M. De Francesco, G. Monteleone, R. Oronzio, S. Galli, C. D'Angelo, et al., "Apparatus for the production of hydrogen from sodium borohydride in alkaline solution," *International Journal of Hydrogen Energy*, vol. 33, pp. 51-56, 2008.
- [25] N. Patel, R. Fernandes, N. Bazzanella, A. Miotello, "Co-P-B catalyst thin films prepared by electroless and pulsed laser deposition for hydrogen generation by hydrolysis of alkaline sodium borohydride: a comparison," *Thin Solid Films*, vol. 518, pp. 4779-4785, 2010.
- [26] S.C. Amendola, S.L. Sharp-Goldman, M. Saleem Janjua, N.C. Spencer, M.T. Kelly, P.J. Petillo, et al., "A safe, portable, hydrogen gas generator using aqueous borohydride solution and Ru catalyst," *International Journal of Hydrogen Energy* vol. 25, pp. 969-75, 2010.
- [27] J.P. Holgado, J. Morales, A. Caballero, A.R. Gonza' lez-Elipse, "Plate reactor for testing catalysts in the form of thin films," *Applied Catalysis B: Environment and Energy*, vol. 31, pp. 31-36, 2001.
- [28] N. Malvadkar, S. Park, "Urquidi-MacDonald M, Wang H, Demirel MC. Catalytic activity of cobalt deposited on nanostructured poly(p-xylylene) films," *Journal of Power Source*, vol. 182, pp. 323-8, 2008.
- [29] D. Kılınç, "Co complex modified on Eupergit C as a highly active catalyst for enhanced hydrogen production," *International Journal of Hydrogen Energy*, vol. 47, pp. 11894-11903, 2022.
- [30] D. Kılınç, O. Sahin, C. Saka, "Salicylaldimine-Ni complex supported on Al₂O₃: Highly efficient catalyst for hydrogen production from hydrolysis of sodium borohydride," *International Journal of Hydrogen Energy*, vol. 43, pp. 251-261, 2018.
- [31] D. Kılınç, Ö. Şahin, "Synthesis of polymer supported Ni (II)-Schiff Base complex and its usage as a catalyst in sodium borohydride hydrolysis," *International Journal of Hydrogen Energy*, vol. 43, pp. 10717-10727, 2018.
- [32] G.P. Rachiero, U.B. Demirci, P. Miele, "Bimetallic RuCo and RuCu catalysts supported on γ-Al₂O₃. A comparative study of their activity in hydrolysis of ammonia-borane," *International Journal of Hydrogen Energy*, vol. 36, pp. 7051-7065, 2011.
- [33] J.Q. Wu, D.L. Wang, X.M. Xu, N.B. Long, R.F. Zhang, "Efficient synthesis of DHA/EPA-rich phosphatidylcholine by inhibition of hydrolysis reaction using immobilized phospholipase A1 on macroporous SiO₂/cationic polymer nano-composited support," *Molecular Catalysis*, vol. 499, pp. 111278, 2021.

- [34] M. Grigoras, C.O. Catanescu, "Imine oligomers and polymer," *Journal of Macromolecular Science, Part C: Polymer Reviews*, vol. 44, pp. 131-173, 2004.
- [35] D. Kılınç, O. Sahin, S. Horoz, "Use of low-cost Zn (II) complex efficiently in a dye-sensitized solar cell device," *Journal of Materials Science: Materials in Electronics*, vol. 30, pp. 11464-11467, 2019.
- [36] A. Xavier, N. Srividhya, "Synthesis and study of Schiff base ligands," *Journal of Applied Chemistry*, vol. 7, pp. 6-15, 2014.
- [37] M.S. Karthikeyan, D.J. Prasad, B. Poojary, K.S. Bhat, B.S. Holla, N.S. Kumari, "Synthesis and biological activity of Schiff and Mannich bases bearing 2, 4-dichloro-5-fluorophenyl moiety," *Bioorganic & Medicinal Chemistry*, vol.14, pp. 7482-7489, 2006.
- [38] D. Kılınç, O. Sahin "High volume hydrogen evolution from KBH₄ hydrolysis with palladium complex catalyst," *Renewable Energy*, vol. 161, pp. 257-264, 2019.
- [39] D. Kılınç, O. Sahin "Development of highly efficient and reusable Ruthenium complex catalyst for hydrogen evolution," *International Journal of Hydrogen Energy*, vol. 47, pp. 3876-3885, 2022.
- [40] K. Nejati, Z. Rezvani, "Syntheses, characterization and mesomorphic properties of new bis(alkoxyphenylazo)- substituted N, N' salicylidene diiminato Ni (II), Cu (II) and VO(IV) complexes," *New J Chem*, vol. 27, pp. 1665, 2003.
- [41] K. Naresh Kumar K, R. Ramesh, "Synthesis, luminescent, redox and catalytic properties of Ru (II) carbonyl complexes containing 2N₂O donors," *Polyhedron*, vol. 24, pp. 1885-92, 2005.
- [42] T. Rosu, E. Pahontu, C. Maxim, R. Georgescu, N. Stanica, A. Gulea, "Some new Cu (II) complexes containing an on-donor Schiff base: synthesis, characterization and antibacterial activity," *Polyhedron*, vol. 30, pp. 154-62, 2011.
- [43] M.R.P. Kurup, B. Varghese, M. Sithambaresan, S. Krishnan, S.R. Sheeja, E. Suresh, "Synthesis, spectral characterization and crystal structure of copper (II) complexes of 2- benzoyl pyridine-N (4)-phenyl semicarbazone," *Polyhedron*, vol.30, pp. 70-8, 2011.



LEAN ENERGY EFFICIENCY: SCENARIO ANALYSIS OF A REFRIGERATOR PLANT APPLICATION

^{1,*} Irem DUZDAR , ² Kazım ALBAYRAK ,
³ Gulgun KAYAKUTLU , ⁴ M. Ozgur KAYALICA 

¹ Duzce University, Engineering Faculty, Industrial Engineering Department, Duzce, TÜRKİYE
^{2,3,4} Istanbul Technical University, Energy Institute, Istanbul, TÜRKİYE

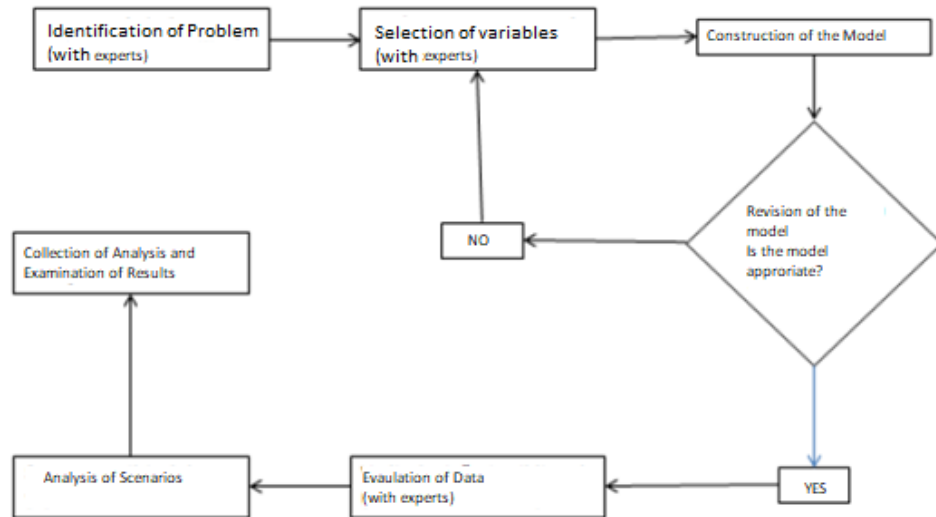
¹ iremduzdar@duzce.edu.tr, ² albayrakka@itu.edu.tr, ³ gkayakutlu@gmail.com, ⁴ kayalica@itu.edu.tr

(Received: 03.03.2023; Accepted in Revised Form: 19.12.2023)

Highlights

- This study aimed to reveal the emerging techniques for energy efficiency management and to promote the implementation of value stream mapping (VSM) to increase the efficiency of flexible operations.
- The relevance of energy consumption in a production process was demonstrated by applying a specific value stream map to appliance manufacturing.
- The main objectives of this study were to determine the energy bottlenecks for a sample refrigerator production plant and construct strategies to eliminate them, as support for future decisions to be taken by the management.

Graphical Abstract (Optional)



Flowchart of the proposed method.



LEAN ENERGY EFFICIENCY: SCENARIO ANALYSIS OF A REFRIGERATOR PLANT APPLICATION

^{1,*} Irem DUZDAR , ² Kazım ALBAYRAK ,
³ Gulgun KAYAKUTLU , ⁴ M. Ozgur KAYALICA 

¹ Duzce University, Engineering Faculty, Industrial Engineering Department, Duzce, TÜRKİYE
^{2,3,4} Istanbul Technical University, Energy Institute, Istanbul, TÜRKİYE

¹ iremduzdar@duzce.edu.tr, ² albayrakka@itu.edu.tr, ³ gkayakutlu@gmail.com, ⁴ kayalica@itu.edu.tr

(Received: 03.03.2023; Accepted in Revised Form: 19.12.2023)

ABSTRACT: Energy concern is increasing in the manufacturing companies implementing the most recent technologies. Energy is a major input for many industries and therefore, within the definition of Industry 4.0 new energy efficiency strategies are defined. Energy flexible processes and waste-to-energy are well-known strategies since they are easily implemented in any manufacturing site. Reduction in energy consumption is also facilitated by the preventive maintenance and renewal of the technologies using energy resources. This study aims to apply a lean production method Value Stream Maps (VSM) on energy consumption levels of the processes to evaluate the decision of technology and/or process change. Processes which use energy excessively when compared with the industry average, will be considered as a bottleneck. Using the value stream maps for energy use is accepted as “Lean Energy Efficiency”. Parameters determined by the preparation of these maps will be enriched by interdependencies determined using the Bayesian Belief Network, which will support finding the priorities among the new efficiency activities. This technique will facilitate the decision of repair or buy through priority scenarios showing the possibility of a decision in each scenario. The combination of the Lean Energy Efficiency Method and the Bayesian Belief Network Method will assist the decision-makers in developing more informed and knowledge-based strategies. The case study is realized in a refrigerator factory handling the energy consumption of different departments. Consequently, these findings could be used as a roadmap for the technology renewal investment decisions made by the firm.

Keywords: Bayesian network, Lean energy efficiency, Value stream mapping

1. INTRODUCTION

Energy demand and consumption are rapidly increasing together with technological developments. Industries are surveying energy consumption and seeking the safest manner of supplying energy. Energy is the basic input for many profitable manufacturing sites. Consequently, because of the desire to reduce production costs and to receive green certification, the number of lean energy efficiency applications is increasing. The two terms “energy efficiency” (EE) and “lean manufacturing” are combined in the new term “lean energy efficiency” (LEE), defined as energy used in the most efficient way to reduce energy consumption per unit product [1].

Energy consumption in the EU-28 according to the sector is listed as transport 33.9%, industry 25,3 %, residential 24.7%, commercial and public services 14.53%, agriculture, forestry and fishing 2.43%, and others 0.3% in 2018. Hence, industrial sectors with heavy energy use in manufacturing need to apply energy-saving policies [2]. Most governments are implementing energy efficiency policies to fight against climate change, to balance payments and improve the competitive edge.

To create momentum for the decrease in energy consumption by the manufacturing sites, the Environmental Protection Agency (EPA) has introduced a series of energy efficiency guidelines. These industry-specific guides, currently available for 14 manufacturing industries, report that the top five metal products and machinery industries are responsible for 92% of industrial pollutants. Since refrigerator

production belongs to both the metal and machinery sectors, it is listed among the promoted industries [3]. Since machine parts have erosion and corrosion, both the energy consumption and the waste increase. The production losses caused by old machine parts can be removed by using lean production tools [4]. Hence, the implementation of lean energy efficiency can avoid the increase in energy consumption.

The Turkish government follows the global approaches and supports efficiency strategies for industrial energy consumption [5]. One of the objectives is to take preventive action and promote the usage of clean energy resources. Other objectives of the program include ensuring the rational use of energy resources, promoting the diversification of energy resources, and introducing the usage of electricity and hydrogen in transportation. Moreover, it involves a credit system designed for use in financing resource efficiency and energy investments for potential investors such as industrial organizations, commercial entrepreneurs, or residence owners. The fact that the manufacturing sector has been at the top of the energy-consumption lists [6], clearly demonstrates the importance of energy projects in manufacturing. It is also well known in this sector that energy has always constituted an important percentage of operational costs. The manufacturing companies therefore look for the direct and indirect benefits created by EE.

Lean production is implemented by completing operations in the shortest time and by reducing waste, thereby increasing efficiency and quality, reducing costs, and providing flexible operations for companies. Energy is one of the most important resources in the production process; hence, companies need the concept of lean energy efficiency. Lean energy efficiency (LEE) is a lead for lean production. Here, the main target is to reduce the energy consumed per unit of product. In the production process, there are clear links between energy use and waste, such as the use of electricity to heat, cool, and light underutilized inventory spaces [7].

When the literature on lean energy is examined [8-13], no study focusing on the lean energy efficiency scenario has been encountered, especially in refrigerator manufacturing. The most recent study that can be mentioned on the subject is Verma et al. (2021) [14]. Verma et al. (2021) emphasized that sustainable value stream mapping (VSM) is an evolving research theme. In order to organize how sustainable VSM can be applied to lean energy, it aimed to reduce non-value-added processes in energy consumption with the Lean-Energy-Six Sigma Value Stream Mapping model.

This study aims to reveal the emerging techniques for energy efficiency management and to promote the implementation of value stream mapping (VSM) to increase the efficiency of flexible operations. The relevance of energy consumption in a production process is demonstrated by applying a specific value stream map to appliance manufacturing. The main objectives of this study are to determine the energy bottlenecks for a sample refrigerator production plant and construct strategies to eliminate them, as support for future decisions to be taken by the management. Energy shortages in refrigerator production facilities may be caused by factors such as inefficient use of resources or insufficient availability. In such facilities, power outages can result from inefficient operation of equipment or from the use of energy-inefficient equipment. For example, old or technologically outdated production equipment may consume more energy. Inadequate maintenance and inadequate working conditions can also prevent the efficient use of energy resources. Additionally, HVAC (Heating, Ventilation, and Air Conditioning) systems are major energy consumers in refrigerator manufacturing plants. Power outages can occur due to incorrect sizing of HVAC systems, the use of low-efficiency equipment, or ineffective control of systems. Unnecessary energy consumption based on heating or cooling needs can lead to wastage of energy resources. In addition, energy shortages can result from ineffective energy management practices or inadequate implementation of energy-saving measures in operational processes. For example, unnecessary energy consumption during working hours or not implementing energy-saving methods can contribute to power cuts. Addressing these energy deficiencies includes developing energy efficiency scenarios, monitoring and analysing energy consumption, using energy-efficient equipment, adopting low-energy lighting systems, using effective HVAC systems and implementing energy-saving measures in operational processes.

The Bayesian Belief Network method is applied to determine the interrelation among the criteria that

will be handed as a result of the Lean Energy Efficiency application so that the decision of investment or maintenance could be given by applying the probabilities. Alternative scenarios are created by implementing the Bayesian Belief Network in Netica software, where applying the LEE possibilities according to the probabilities achieved, will change the decision of investment. Bayesian Belief network created according to the preferences of the decision-makers will eliminate the uncertainties caused by subjectivity. This method will assist decision-makers by showing the causal relationship among the LEE parameters and estimating the probabilities of investment accordingly.

In the next section of the study, more information is given on LEE. In the third section, VSM and Bayesian network methods are explained. The fourth section is reserved for the implementation of the methods and discussion of the results followed by a scenario analysis. In the last section, concluding remarks and recommendations are given.

2. MATERIAL AND METHODS

2.1. Lean Approach and Lean Energy Efficiency (LEE)

The lean manufacturing concept is generally associated with Toyota, a Japanese automotive company. In the 1950s, Taiichi Ohno designed a new system based on eliminating unnecessary activities, eliminating waste, and improving efficiency [15]. The lean manufacturing concept was first written up and published in 1990 by Womack et al. [16]. Statistical data published in North America in 2006 showed that Toyota had reached the top of the list of automotive manufacturers, demonstrating the company's significant progress in lean manufacturing. The manufacturing establishments will intensely focus on both service and lean manufacturing at the same time [17]. Lean manufacturing is defined in various ways, including: "An important concept that increases productivity and quality, reduces costs, and provides flexible operation for firms" [18], "a concept that ensures the continuous increase of the system efficiency and aims to eliminate waste" [19], "the production of the item requested by the customer at the most affordable price, in the shortest time, and by reducing waste" [20], "an important parameter that provides a competitive advantage over other organizations" [21], and "production of the item requested by the customer using all elements most properly, with the fewest resources, with the least error, without waste, and by eliminating all functions that do not add value in production" [22]. Thus, lean manufacturing is a concept related to all the parameters in the production system and supply chain management. In the business model of a circular economy, the suppliers employ a technician to superintend the repair operations of improper goods to make them reusable with the help of lean tools [4]. The main values of lean manufacturing are 'must' parameters. These can be summarized as flexibility, elimination of faults, optimization, process control, and effective usage of the workforce [23].

In lean manufacturing, there are five main principles involving the processes between customer demand and the delivery of the product [24] (Fig. 1). The first is 'Value' as identified by the end customer. The demand of the customer is a requisite. The value is produced according to customer demand. The second, the 'Value Stream' principle, is defined as the operations necessary to produce the items. The third one is the 'Flow', the formation of the production for the needed quantity in the required time. 'Pull' is the production of items just at the time the customer needs them. The last principle, 'Perfection', seeks the perfect product. One of the goals is to minimize the amount in stock because, in lean manufacturing, these items are seen as waste (Fig. 1).

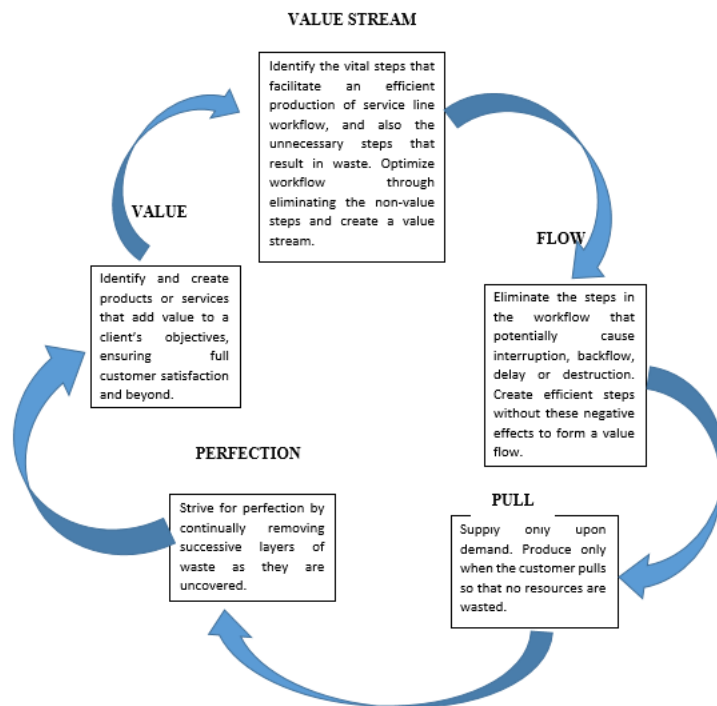


Figure 1. Basic principles of lean manufacturing [25]

Applying lean manufacturing concepts to energy efficiency created the lean energy (LE) concept [26]. The basic goal is to reduce the energy consumption per unit produced by identifying the maximum energy-consuming points and energy bottlenecks and finding the optimal solution by using energy efficiency methods.

In a worldwide survey, studies performed to improve energy efficiency have included methods such as applying various motor driver speeds, reusing scrap heat, using higher-efficiency electric motors, and reducing pressure to reduce losses from compressor leaks [27]. Examples of the benefits of these approaches can be found in [28].

In 2011, the Turkish government introduced a regulation to raise energy efficiency. This regulation, prepared under the leadership of the Ministry of Energy and Natural Resources, serves as an example for boosting EE in the industrial sector [29]. The projects to promote EE carried out by industries have mainly involved steam, boilers, and thermal operations [30], a detailed literature review was performed for this study. The basic relation between lean energy and manufacturing is EE [31]. Kiss proposed the Kaizen principles as an ideal tool for preventing energy losses [32]. In a study on work standardization, Deming's PDCA circle, and 5S were introduced as important tools for saving energy. Gogula et al. simultaneously applied the pull system, cellular manufacturing, poka-yoke, work standardization, visual control, and workload balancing methods to reduce the energy bills in a valve regulator production facility [33]. In the study performed by Rivas Duarte et al., the interrelations of energy consumption and manufacturing operations were successfully demonstrated by employing methods depending on lean manufacturing principles [34]. The main objective of LE can be defined as reducing the energy bills of production by controlling the energy stream to prevent unnecessary energy consumption in the production processes. Value stream maps (VSMs) are used to improve the search for energy efficiency at various types of production plants. In their 2008 study, Fraizer et al. determined that VSMs could be used to determine the energy consumption characteristics of production processes [35]. In another study, an easy and quick technique was proposed to analyze the flow of material and energy [36].

2.2. Value Stream Mapping

Value stream mapping (VSM) is a dynamic and customer-focused method that plays an important

role in eliminating production system waste. The flow of information is shown by using certain symbols to produce the desired product and service. All the necessary and unnecessary activities are visualized during the processes. The concept of VSM is one of the indispensable parameters of production.

The process of VSM consists mainly of four steps: gathering the data, presenting the status map, applying VSM tools, and preparing the future status map [37]. In the first step of VSM, answers are sought to questions in terms of customer demands, information flow, and material flow. After gathering the required information, the present status map can be prepared. At this step, the customer demands, the process flow, the information flow, and the material flow are mapped respectively. By using tools like process mapping, pairing, and a value-added time profile, the end status is then formed, and the VSM is carried out. The VSM is analyzed in detail, and the bottlenecks and improvement potentials are determined. The prescribed future status map is prepared together with the improvement potentials. The result of the study by Dağ and Kara (2020) shows that the VSM application can be considered an important starting point in terms of simplifying the operation of the enterprise [38].

To use VSM for EE projects (E-VSM), some studies must be carried out within the firm. These include a lean analysis, an energy survey for E-VSM, and scenario studies for a Bayesian network. The E-VSM is a graphical method that shows energy consumption and indicates the potential energy-saving points in each process of the production line [26].

In one study, Shadid et al. combined total productive maintenance, process mapping, and VSM for use in EE projects [39]. The value-adding and non-adding operations are defined after the application of the process map. These outcomes are useful for reducing energy consumption. In another study, Rivas introduced a practical process mapping methodology that combined energy management with VSM [34]. The methodology, based on lean manufacturing principles, was applied to industrial use cases and was shown to successfully illustrate the relationship between energy usage and production activities for a particular value stream.

The present study presents an E-VSM perspective combined with Bayesian networks that enables bottlenecks to be depicted and potential results to be analyzed in future scenarios.

2.3. Bayesian Networks

In this study, future-study scenarios were implemented using Bayesian networks (BNs). Around the 1960s, statisticians realized that graphical models were the best and easiest way to analyze statistical conditions involving uncertainties and probabilities [40]. In recent years, artificial intelligence and expert probability systems have been used, especially to solve the problems of various industries in an integrated structure. Nowadays, BNs are frequently used for surveys on data mining and for artificial intelligence-oriented solutions.

Some features of BNs are found to be very useful for solving problems involving the analysis and management of real data. Deterministic modeling is very effective when there is not enough data or the control mechanisms are insufficient [41]. When the amount of data is insufficient for sampling, the BN technique for estimation when used together with analytical decision-making tools can be helpful for decision-makers [42]. The interdependent associations between variables are found presuming they have conditional probability distribution employing the cause and result effects of existing variables in the parameter learning of the Bayesian belief network [43].

A Bayesian probability approach provides the chance for inference where there is no past data, or when the data contain uncertainties. If event A has occurred and there is no uncertainty, then $P(A) = 1$. However, if event A is in the future and involves uncertainty, expert advice is necessary to determine the probability of the occurrence of A. In light of this expert advice, some assumptions can be made, as seen in the form of Equation (1).

$$A = \{a_1, a_2, a_3, \dots, a_n\} \quad (1)$$

Here, a_1 and a_2 represent the variables of event A. When all the variables are evaluated in a common

denominator, the result is $\sum p(a_i) = 1$. This implies that the probability of event A is related to the probability of the occurrence of its variables. In general, the expression $P(A|B)$ means that with the probability of occurrence of event A, event B has already happened. The expression $P(A|B,K)$ is derived at the point where the basic logic of the Bayesian approach and networks are taken into account. This means that K represents all of the variables of A [44]. The mathematical expression of the Bayesian rule is seen in Equation (2) below.

$$P(A|B) = \frac{P(A,B)}{P(B)} \quad (2)$$

$P(A)$: Probability of occurrence of event A

$P(B)$: Probability of occurrence of event B

$P(A|B)$: Event B has already happened and the probability of occurrence of event A.

In Equation (2), two different events can be represented as A and B, with P representing the probability.

The Bayesian Belief Network (BBN) facilitates understanding the causal relations among the parameters or activities by using a graphical representation [45]. The literature covers several studies that apply BBNs as decision-support tools in different areas. One detailed evaluation showed the use of BBNs in the industry for risk and reliability analyses, health and mechanical diagnoses, and financial risk management [46]. One of these studies was performed by Neil et al. [47] and involved the modelling of real decision-making problems and situations including uncertainties. All the potential results and the analyses of interactions between all variables were revealed to the experts and decision-makers. Aktaş et al. used a BBN in a proposed decision-support system in the healthcare field [48]. Gupta and Kim developed an integrated model combining BBNs and structural equation modelling for decision-making in customer management [49]. Dereli used a BBN to evaluate the risks from factors that negatively affected the efficiency of a supply chain [50]. Çınar and Kayakutlu proposed an overview of building scenarios for energy policies using BBN models [51]. In the study of Jones et al., a BBN model was applied to a maintenance and inspection department. That study aimed to construct a BBN model whereby various parameters were responsible for the failure rate of the system. One study was able to apply BBNs to a delay-time analysis. The BBN modelling allowed certain influencing events that affected the parameters to be used in determining the failure rate of a system under consideration [52]. As demonstrated by these studies, the outcomes of BBNs are graphical, descriptive, and easy to understand for decision-makers [26].

A BBN has been used in this study to facilitate the technology investment decisions during the implementation of the energy efficiency strategies. By using this method the investment decision will be tested by different priorities of energy efficiency activities. Since the achievement will allow observing the activity priorities with the smallest probability of investment based on the beliefs of a group of decision-makers, economic benefits will be protected during energy efficiency investments.

2.4. Proposed Model and Application

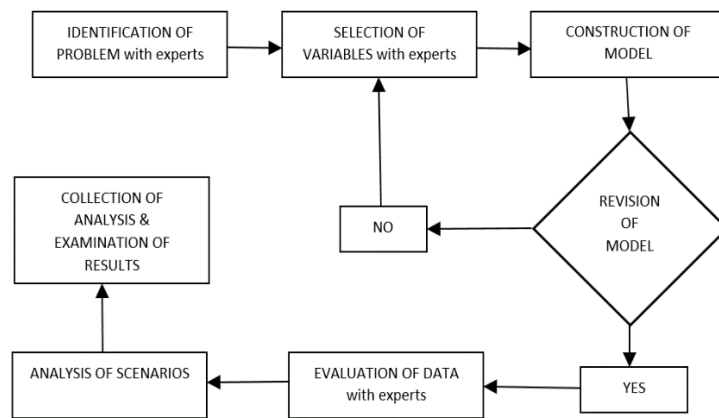


Figure 2. Bayesian network process used in the study

First, to evaluate the current energy situation, meetings were conducted with experts who defined energy efficiency conditions in the factory by taking energy, production, manufacturing, and maintenance dynamics into account. Because of the many fields that had been included, the results were more realistic. Next, the energy consumption of the factory was analyzed. This enabled the processes that were consuming more energy to be identified. This information was combined using E-VSM. Moreover, the combined information enabled the bottlenecks of the factory to be determined from an energy point of view. After the resources of the factory had been evaluated and the bottlenecks determined, alternative solutions for the bottlenecks were set.

In order to understand the relations between these three stages of the process, a relation matrix was formed and evaluated by the experts. After forming the model, a three-step survey was administered to the experts to determine the probability values. The first step was to evaluate factory resources in terms of probability values, the second was to evaluate factory resources and alternative solutions at the same time, and the last step was to evaluate alternative solutions and bottlenecks at the same time. After collecting all probability values, using NETICA software, these values were applied to a BN. This software enabled the determination of the probability values of the bottlenecks within the context of acquiring the solution. After receiving the results for the current energy status of the factory, scenarios were developed to determine the future status.

A flowchart showing the Bayesian network used in the study is presented in Figure 2. Re-evaluations may be required in some parts of this generation process. At this point, a cyclic structure can be seen, and the same operations can be repeated. When constructing the optimal model, the process is turned back and the same operations are executed again [53].

3. RESULTS AND DISCUSSION

3.1. Energy Value Stream Mapping

VSM is implemented for the manufacturing processes in a refrigerator production plant. The manufacturing process in the plant consists of three steps: preproduction, assembly, and packaging. A sketch of the process is shown in Figure 3.

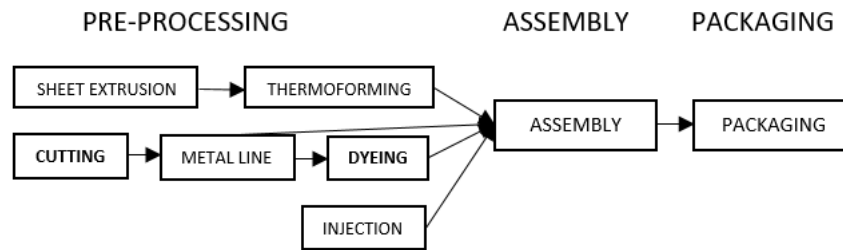


Figure 3. Plant manufacturing process

VSM for the manufacturing processes already existed in the plant. We used the existing maps to structure energy value maps (E-VSM) on the three groups of processes. In this way, energy bottlenecks are specified. The map given in Figure 4 shows a section of the energy value stream map of the current processes of the plant. The main processes and the job allocations to the departments can be seen on this map. In Figure 5 E-VSM of the factory is shown. On this map, the high-energy-consuming areas are coloured with red and the lower-energy-consuming areas are coloured with light red or orange. The 'High' and 'Medium' notes at the bottom of the map represent the general evaluation of energy consumption in the related departments. These measures are determined by comparing the plant values with the local industry average. High means higher than the industry average, Medium means very close or similar to the industry average and Low means lower than the industry averages. Obviously, points determined as 'High' are the potential energy bottlenecks in the factory's basic focus.

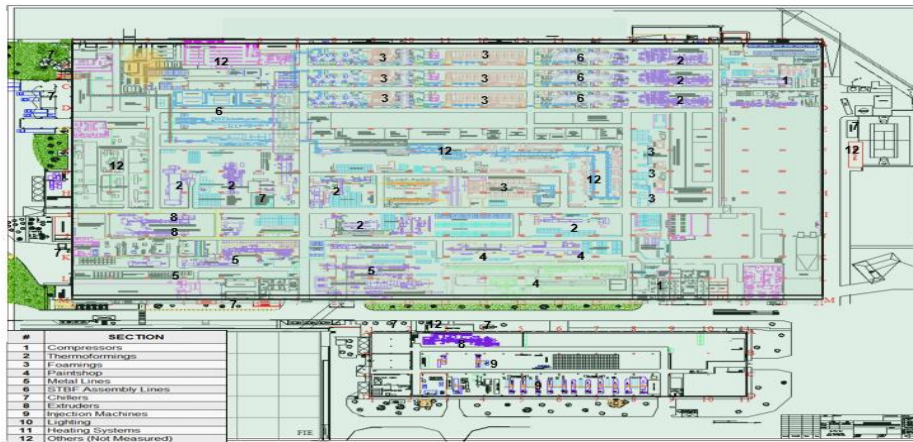


Figure 4. Section of plant value stream map

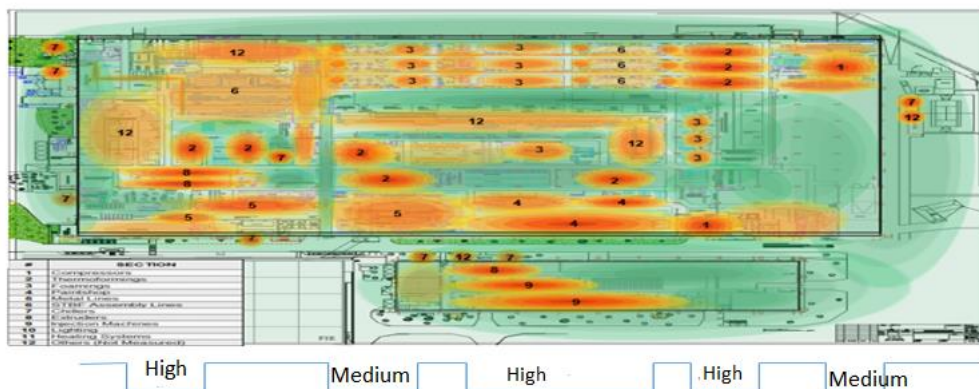


Figure 5. Plant energy value stream map

Considering the expert recommendations and the annual energy consumption, the energy bottlenecks of the factory were identified as the Machine Injection, Thermoforming, and Painting Departments.

3.2. Establishing the Bayesian Network Model

Bayesian Belief Network will be used to model future activities to dissolve the bottlenecks defined by using the VSM. However, the investment or activity decisions are very much affected by the resources of the plant and BBN will be defined according to those resources based on the preferences of the decision makers of the Plant. The resource variables obtained via expert recommendations and the literature survey are listed in Table 1. The alternatives for dissolving the bottlenecks are also presented in the same table as solution alternatives.

Table 1. Resource variables and alternative solutions for the firm

RESOURCE VARIABLES	Definition
Budget	Budget is one of the most important parameters as a resource variable. In many cases, it directly affects the decision to be made. It allows the company to evaluate whether an investment should be made or not.
Total Production	If more products are produced, more energy is consumed, and thus, annual period planning affects consumption.
Equipment	The industry needs a great deal of equipment to produce the requested products. The number of equipment items varies depending on the planning. Therefore, the amount of equipment has been chosen as a resource variable.
Quality	Quality is not considered directly as a resource, yet, it is one of the most important resource variables. In particular, the case plant has quality as the top priority of a German branch. The quality standards are above the industry limits That is why quality is chosen as the fourth source variable.
Market Share	The position of the company in the market affects many operations. Changes in the market share affect energy consumption at the factory.
Number of employees	The number of employees in the enterprise is an important resource for the company. Many employees are needed to continue production in the best possible way.
SOLUTION ALTERNATIVES	Definition
Investment in New Energy-Efficient Machinery	To solve the consumption problem, the purchase of new energy-efficient machinery is proposed, which will certainly reduce energy consumption by using the most recent technology, thereby reducing consumption in the related bottlenecks.
Change to Energy-Efficient Processes	An energy-efficient process is proposed to replace the current on-going process. Here the focus is on process modification to realize the predicted reduced consumption.
Energy-Efficient Automation / Usage of Robots	Plans are made to purchase energy-efficient automation/robot systems to be used during production in the factory. In this way, it is predicted that consumption will be reduced.
Energy-Efficiency Projects	Energy efficiency projects at the factory will be studied and carried out in an appropriate process.
Increase in Energy Efficiency of Machines	Energy efficiency studies will be carried out on the machines owned by the company to reduce consumption.
Energy Efficiency Conscious Employees	As part of the planned reduction of energy use efforts will be made to raise the energy efficiency awareness of the employees. Energy-efficiency training is to be carried out in the company.

The initial structure, in which the determined variables are arranged in accordance with the BBN structure, is given in Figure 6. At the top of the structure, the business resources are seen, in the middle, the solution alternatives, and at the bottom, the bottlenecks. A dual evaluation was performed using a BBN model. The business resources were evaluated with solution alternatives creating alternative solutions for the bottlenecks which structured the scenarios. The relation matrix is used to evaluate the cause and result relations, and then the BBN model is designed according to the opinions of the experts.

This section includes the business resource variables analysed by the experts. When evaluating each variable, the present status of the factory is conceptualised. After the evaluation of the relation matrix, the final structure of the model is loaded in NETICA software as shown in Figure 7. The questionnaire to determine the probabilities is given to the decision-makers.



Figure 6. Variable Relations

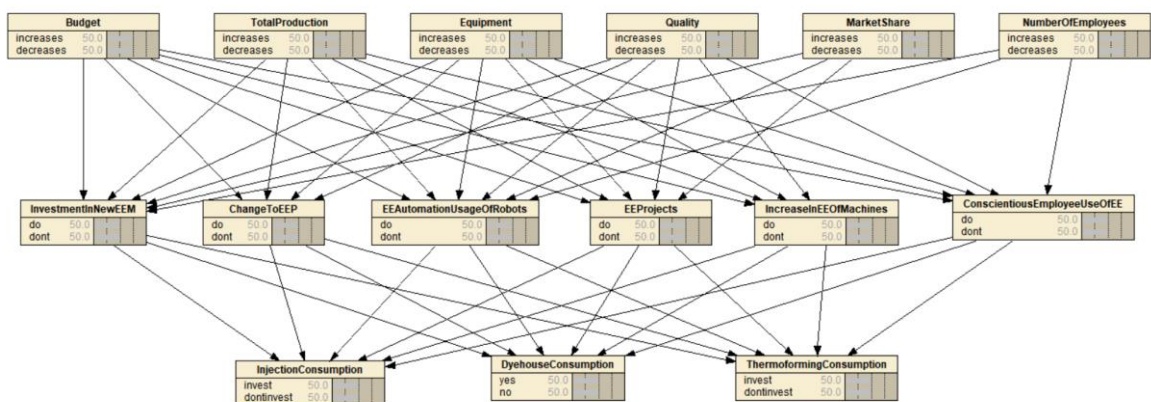


Figure 7. BBN Model in NETICA

The decision-makers gave two alternatives for all the resource variables as increasing or decreasing, with equal probabilities. The values of the alternative solutions are also evaluated by the decision makers as do and do not with different probabilities. For example, in the budget/purchasing section, there is an investment for a new energy-efficient machine, for which there were more than two probability combinations, including alternatives for the budget ('increases' and 'decreases') and for purchasing the energy-efficient new machine ('do' and 'do not'). For instance, Budget Decrease with investment becomes 100%.

Although the resources budget, production volume, equipment, and quality concepts are evaluated under the alternative solutions, the market share and the number of employees are evaluated independently as process change and the increase in the number of EE machines. The market share was not related to EE-trained personnel as a resource, and the personnel number was not related to EE projects. All of the alternative solutions were affecting the three bottlenecks determined by the application of the E-VSM.

3.3. Scenario Analysis

Once the BBN model is structured, three basic scenarios are designed: the 'as-is' case changing nothing in the current situation, 'the worst' case, and 'the best' case. These scenarios will allow observing the future indication of activities of using all the resources or not. The general evaluation results in further investment strategies for EE improvement.

The impacts of the three EE scenarios on investment are explored. The first scenario is stable, based on the current conditions. The second scenario is optimistic, where all resource variables were evaluated as 100% in the positive direction. The third and last scenario was reserved for a pessimistic condition where all resource variables are evaluated as 100% in the negative direction. Figures 8, 9, and 10 show the results obtained for the current situation, the optimistic, and the pessimistic scenarios.

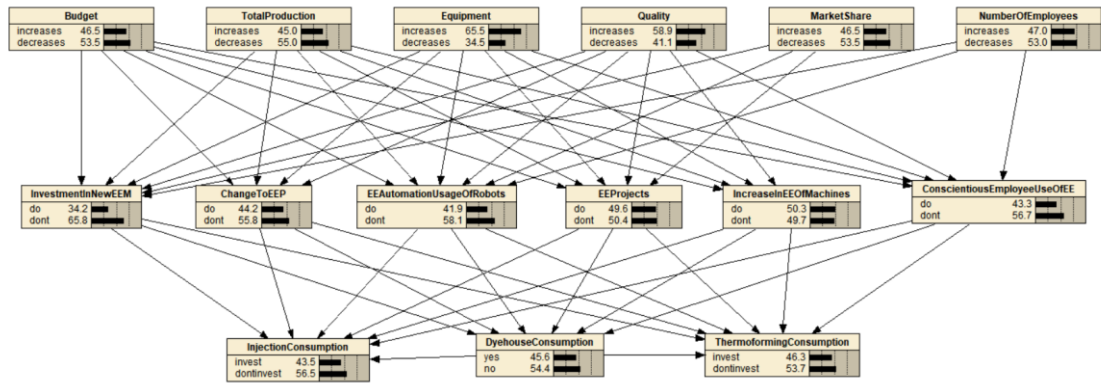


Figure 8. As-Is Scenario in NETICA

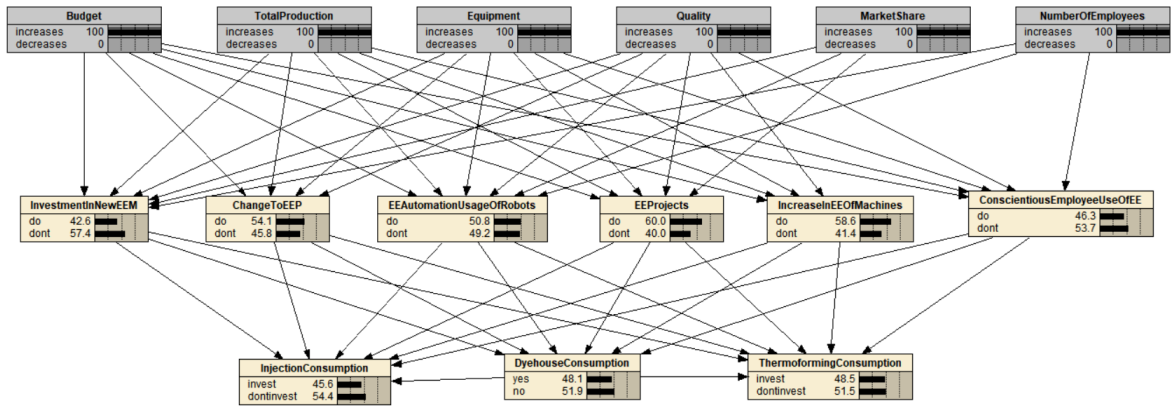


Figure 9. Best Case Scenario in NETICA

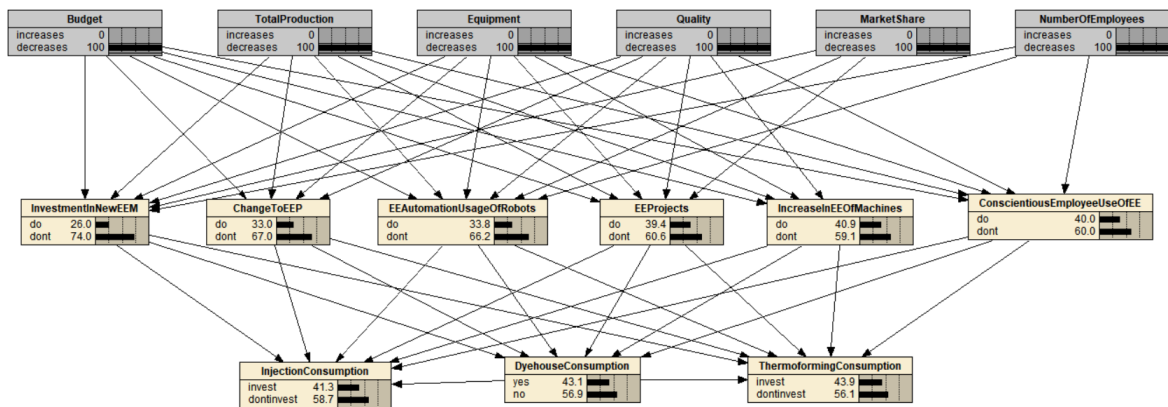


Figure 10. Worst Case scenario in NETICA

When the current situation scenario is evaluated, energy efficiency projects are preferred to be considered as future activities. The best ('optimistic') scenario shows that the EE process could be changed by investing in energy-efficient automation or robots, and by increasing the number of EE machines (Fig. 9). The worst ('pessimistic') scenario is kind of about doing nothing, so no efficiency improvement can be observed (Fig. 10). This application shows that if energy efficiency strategies are given full priority, then new investments in energy-efficient technologies are unavoidable. If budget is concerned to have the first priority, then no energy efficiency can be expected. Hence, as a German company, this case cannot afford the alternative "don't invest" in energy-efficient technologies (based on the scenarios – see, Figures 7 to 9).

In the white goods sector, this could mean addressing inefficiencies in the manufacturing process that hinder energy efficiency and lean production goals. Investment scenario analysis helps prioritize which bottlenecks to address, based on their impact on energy efficiency and overall production performance. Moreover, investment scenario analysis assists in aligning short-term investments with long-term objectives. It allows companies to plan for continuous improvement in energy efficiency and lean production, ensuring sustainability and competitiveness in the white goods sector.

4. CONCLUSIONS AND DISCUSSION

The energy efficiency improvement of an electronic home equipment producer is analysed in three steps. First, a Lean Manufacturing technique, Value Stream Mapping is implemented in end-to-end processes of manufacturing and the bottlenecks in terms of energy use are determined. In the second step, a basic framework has been designed for energy consumption policies with the focus of providing solutions. The Bayesian method facilitates the links among the variables by giving the impact probabilities. Hence in the third and last step, a refrigerator plant with high energy consumption is analysed referring to the energy expert beliefs in the factory. The current energy status of the plant is determined considering the company resources. Yet, only three departments of bottlenecks are considered in this study giving more space to the detailed processes of each department as part of the future studies. In the three chosen departments company's resources are evaluated to support the decision to repair existing equipment or invest in replacement with the improved technologies. Budget, Production, Equipment, Quality, Market Share and Number of Employees are the resources evaluated to design the Bayesian Map given in Figure 7.

After designing the conditions for the current energy status of the manufacturing site, scenarios are developed to determine future strategies. In addition to the current energy evaluation, the best and the worst scenarios are developed. In the best scenario, it was assumed that all of the factory resources were maximal in terms of probability values. With this scenario, we achieved an increasing reduction in the electricity budget flow over the years. As is, the scenario reflects the current situation, hence, gives no differences. However, in the worst scenario, it is assumed that all of the factory resources are minimal in

terms of probability values. With this scenario, investments are increased. After evaluating the current energy status and the best and the worst scenarios, the bottlenecks that are identified by VSM are focused to realise investment. This is because the current scenario and the worst-case scenario were both aiming for the repair of the current equipment which led to increasing energy costs. In the Optimistic scenario, the investment in new technologies is foreseen to solve the bottleneck. It is observed that the probability of investing in thermoforming machines is more effective than that of investing in injection machines. Investment in the thermoforming machines is to given priority (Figure 11).

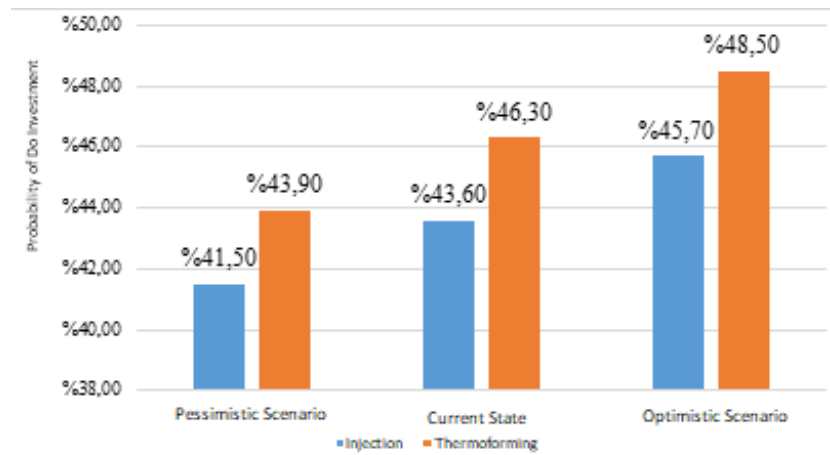


Figure 11. Probability of doing investment based on different scenarios

Bayesian Belief Network supports the managerial decision with respect to the status of different company resources. In this analysis, energy consumption is evaluated with the Lean manufacturing techniques to determine the points of interest to be changed with different scenarios caused by expert beliefs. An additional benefit of the BBN application is not creating a need for sensitivity analysis, since the scenarios cause changes in probabilities and take the role of sensitivity analysis. As an example, we can see the increase in budget decrease probability almost 50% when energy efficiency projects are given priority. It is observed that the biggest increase in energy efficiency will be achieved by investments in energy-efficient technologies of thermoforming.

In the future, this study will be expanded by raising the number of variables in the Bayesian network with the addition of opinions from a new set of decision-makers and considering the details of each process. It is further recommended that a time-based dynamic Bayesian network be designed to predict short-term, middle-term, and long-term strategies.

Declaration of Competing Interest

There is no conflict of interest in this study.

Funding / Acknowledgements

There is no funding for this study.

Declaration of Ethical Standards

The study is conducted in accordance with ethical standards.

Credit Authorship Contribution Statement

I.D.: Writing – review, Original draft & editing, Supervision, Validation, K.A.: Conceptualization,

Investigation, Methodology, Software, Writing - review, Software, Original draft & editing, G.K.: Conceptualization, Supervision, Methodology, Writing – review, M.O.K.: Conceptualization, Supervision, Methodology, Writing – review.

Data Availability

Data will be made available on request.

REFERENCES

- [1] A. Koç, H. Yağlı, K. Yıldız, and İ. Uğurlu, "Dünyada ve Türkiye’de enerji görünümünün genel değerlendirilmesi," *Mühendis ve Makina*, 59(692), pp.86-114, 2018.
- [2] L. Castellazzi, T. Serrenho, M. Economidou, and P. Zangheri, "Energy Consumption and Energy Efficiency trends in the EU-28. 2000-2018", 2020.
- [3] (EPA) Environmental Protection Agency, "Final Effluent Guidelines Program Plan 14 Documents. Final Effluent Guidelines Program Plan 14 – Overview," Jan. 2021.
- [4] M.K. Lim, M. Lai, C. Wang, and Y. Lee, "Circular economy to ensure production operational sustainability: A green-lean approach," *Sustainable Production and Consumption*, 30, pp.130-144, 2022.
- [5] Middle Black Sea Development Agency, "Guide to Incentives and Supports Provided in Turkey," <https://www.oka.org.tr/assets/upload/dosyalar/turkiyede-saglanan-tesvik-ve-destekler-25-78.pdf> Accessed 28.10.2019
- [6] O. Türkyılmaz, and C. Özgiresun, "Türkiye Enerji Görünümü 2013," *Türkiye Makine Mühendisleri Odası Birliği*, 2013,
- [7] M. Sciortino, S. Watson, and R. Presnar, "The importance of energy efficiency in lean manufacturing: declaring energy the ninth waste," *Proceedings of the 2009 Summer Study on Energy Efficiency in Industry*, 3, pp.113-122.R, 2009.
- [8] C. Tian, G. Feng, S. Li, and F. Xu, "Scenario analysis on energy consumption and CO2 emissions reduction potential in building heating sector at community level," *Sustainability*, 11(19), 5392, 2019.
- [9] M. Haragovics, and P. Mizsey, "A novel application of exergy analysis: Lean manufacturing tool to improve energy efficiency and flexibility of hydrocarbon processing," *Energy*, 77, 382-390, 2014.
- [10] S. Yang, L. Zhang, N. Xie, Z. Gu, and Z. Liu, Z, "Thermodynamic analysis of a semi-lean solution process for energy saving via rectisol wash technology," *Energy*, 226, 120402, 2021.
- [11] U. Kumar, and R. Shankar, "Application of Value Stream Mapping for Lean Operation: An Indian Case Study of a Dairy Firm," *Global Business Review*, 09721509221113002, 2022.
- [12] A. Trubetskaya, O. McDermott, & S. McGovern, "Implementation of an ISO 50001 energy management system using Lean Six Sigma in an Irish dairy: a case study," *The TQM Journal*, 35(9), 1-24 2023.
- [13] X. Wen, H. Cao, B. Hon, E. Chen, and H. Li, "Energy value mapping: A novel lean method to integrate energy efficiency into production management," *Energy*, 217, 119353, 2021.
- [14] N. Verma, V. Sharma, and M.A. Badar, "Entropy-based lean, energy and six sigma approach to achieve sustainability in manufacturing system" *Arabian Journal for Science and Engineering*, 46(8), pp.8105-8117, 2021.
- [15] R. Shah, and P.T. Ward, "Defining and Developing Measures of Lean Production. Journal of Operations Management," 25(4), 785-805, 2007.
- [16] P. J. Womack, J. T. Daniel, and D. Ross, "Dünyayı Değiştiren Makine" Çeviri Osman Kabak, İstanbul, Panel Matbaacılık, 1990.
- [17] E.B. Sarı, "Yalın üretim uygulamaları ve kazanımları" *Uluslararası İktisadi ve İdari İncelemeler Dergisi*, 17, pp.585-600, 2018.

- [18] Z. Hao, C. Liu, and M. Goh, "Determining the effects of lean production and servitization of manufacturing on sustainable performance," *Sustainable Production and Consumption*, 25, pp.374-389, 2021.
- [19] A. Kiliç, and B. Ayvaz, "Türkiye otomotiv yan sanayinde yalin üretim uygulaması/a lean manufacturing application in Turkish automotive industry," *Istanbul Ticaret Universitesi Fen Bilimleri Dergisi*. 15(29), p.29, 2016.
- [20] J. Bhamu, A. Khandelwal, and K.S. Sangwan, "Lean manufacturing implementation in an automated production line: a case study," *International Journal of Services and Operations Management*, 15(4), pp.411-429, 2013.
- [21] A. Gurumurthy, and R. Kodali, "Design of lean manufacturing systems using value stream mapping with simulation: a case study," *Journal of manufacturing technology management*, 22(4), pp. 444-473, 2011.
- [22] E. Yılmaz, "Siparişe göre üretim yapan sistemlerde yalin üretim uygulamaları" (Doctoral dissertation, Fen Bilimleri Enstitüsü) ,2013.
- [23] S.M. James-Moore, and A. Gibbons, "Is lean manufacture universally relevant? An investigative methodology," *International Journal of Operations & Production Management*, 17(9), pp.899-911, 1997.
- [24] J.P. Womack, and D.T. Jones, "Lean thinking—banish waste and create wealth in your corporation," *Journal of the Operational Research Society*, 48(11), pp.1148-1148, 1997.
- [25] R. Balocco, A. Cavallo, A. Ghezzi, and J. Berbegal-Mirabent, "Lean business models change process in digital entrepreneurship," *Business Process Management Journal*, 25(7), pp.1520-1542, 2019.
- [26] C. Keskin, U. Asan, and G. Kayakutlu, "Value stream maps for industrial energy efficiency," *In Assessment and simulation tools for sustainable energy systems*, pp. 357-379, Springer, London, 2013.
- [27] E.A. Abdelaziz, R. Saidur, and S. Mekhilef, "A review on energy saving strategies in industrial sector," *Renewable and sustainable energy reviews*, 15(1), pp.150-168, 2011.
- [28] İ. Kavaz, "Sürdürülebilirlik Politikaları Çerçevesinde Enerji Verimliliği," *SETA Analiz*. 287, pp.1-8, 2019.
- [29] R. Gazete, "Enerji Kaynaklarının ve Enerjinin Kullanımında Verimliliğin Artırılmasına Dair Yönetmelik", 2011.
- [30] Productivity Enhancing Projects, "Renewable Energy General Directorate" http://www.yegm.gov.tr/verimlilik/d_VAP.aspx | Accessed 28.10.2019
- [31] P.J. Martínez-Jurado, and J. Moyano-Fuentes, "Lean management, supply chain management and sustainability: a literature review," *Journal of Cleaner Production*. 85, pp.134-150, 2014.
- [32] D. Kiss, "Using kaizen to reduce energy consumption," 2009.
- [33] V. Gogula, H.D. Wan, and G. Kuriger, "Impact of lean tools on energy consumption," *Sistemas & Telemática*, 9(19), pp.33-53, 2011.
- [34] M.J. Rivas Duarte, J. Cosgrove, and F. Hardiman, "A Methodology for Process and Energy Mapping In Production Operations," *InImpact: The Journal of Innovation Impact*, 8(2), p.412, 2016.
- [35] E.V. Fraizer, and S. Mitra, "Methodological and interpretive issues in posture-cognition dual-tasking in upright stance," *Gait & posture*, 27(2), pp.271-279, 2008.
- [36] M. Schmidt, C. Raible, R. Keil, and M. Gräber, "Energy and material stream mapping. Recovery of Materials and Energy for Resource Efficiency," *Davos*. 7, pp.3-5, 2007.
- [37] N. Patel, N. Chauhan, and M.P. Trivedi, "Benefits of value stream mapping as a lean tool implementation manufacturing industries: a review," *Int. J. Innov. Res. Sci. Technol.*, 1(8), pp.53-57, 2015.
- [38] H. İ. Dağ, and K. A. R. A. Yakup, "Yalin Üretime Geçişte Değer Akışı Analizi Ve Haritalandırma İle İsrif Kaynaklarının Belirlenmesi: Güneş Enerjisi Kollektörleri Üreten Bir İşletmede Uygulama," *Konya Journal of Engineering Sciences*, 8(3), 652-665, 2009.
- [39] S. Shahid, S. Chacko, and C.M. Shukla, "Energy conservation for a paint company using lean manufacturing technique," *Universal J. Ind. Bus. Manag.*, 1(3), pp.83-89, 2013.

- [40] J. Pearl, Probabilistic reasoning in intelligent systems: networks of plausible inference. Morgan kaufmann, 1988.
- [41] O. Varis, and S. Kuikka, "Learning Bayesian decision analysis by doing: lessons from environmental and natural resources management," *Ecological Modelling*, 119(2-3), pp.177-195, 1999.
- [42] O. Varis, "Bayesian decision analysis for environmental and resource management," *Environmental Modelling & Software*, 12(2-3), pp.177-185, 1997.
- [43] M.A. Orzechowski, "Measuring housing preferences using virtual reality and Bayesian belief networks," 2002.
- [44] P. Goyal, and U. Chanda, "A Bayesian Network Model on the association between CSR, perceived service quality and customer loyalty in Indian Banking Industry," *Sustainable Production and Consumption*, 10, pp.50-65, 2017.
- [45] E. Alpaydın, "Introduction to Machine Learning", The MIT Press, Cambridge, London, England, 2004.
- [46] L. Oteniya, "Bayesian belief networks for dementia diagnosis and other applications: a comparison of hand-crafting and construction using a novel data driven technique", 2008.
- [47] M. Neil, P. Krause, and N. Fenton, "Software quality prediction using Bayesian networks," *In Software engineering with computational intelligence*, pp. 136-172. Springer, Boston, MA., 2003.
- [48] E. Aktaş, F. Ülengin, and Ş.Ö. Şahin, "A decision support system to improve the efficiency of resource allocation in healthcare management," *Socio-Economic Planning Sciences*, 41(2), pp.130-146, 2007.
- [49] S. Gupta, and H.W. Kim, "Linking structural equation modeling to Bayesian networks: Decision support for customer retention in virtual communities," *European Journal of Operational Research*, 190(3), pp.818-833, 2008.
- [50] A. Dereli, "Tedarik riskleri altında tedarikçi seçiminin Bayes ağlarıyla modellenmesi" (Doctoral dissertation, Fen Bilimleri Enstitüsü), 2014.
- [51] D. Cinar, and G. Kayakutlu, "Scenario analysis using Bayesian networks: A case study in energy sector," *Knowledge-Based Systems*, 23(3), pp.267-276, 2010.
- [52] B. Jones, I. Jenkinson, Z. Yang, and J. Wang, "The use of Bayesian network modelling for maintenance planning in a manufacturing industry," *Reliability Engineering & System Safety*, 95(3), pp.267-277, 2010.
- [53] J.G Caballero, "Measuring the effect of organisational factors using Bayesian Networks" (Doctoral dissertation, PhD thesis, Queen Mary University, part of the University of London, 2005. draft) ,2005.



EFFECT OF HEAT TREATMENT ON CORROSION RESISTANCE OF Al-Ni-Mn EUTECTIC ALLOY IN 3.5% NaCl SOLUTION

* Yusuf KAYGISIZ 

*Aksaray University, Technical Vocational School of Sciences, Electricity and Energy Department, Aksaray,
TÜRKİYE*
yusufkaygisiz@aksaray.edu.tr

Highlights

- The corrosion performance of the heat treated sample at 570°C is the highest.
- The matrix (M) phase is in equilibrium with the gray (G), White (W) and eutectic (E) phases.
- Open circuit potential of the samples that were heat treated at 570°C and 600°C and non-heat treated samples were found to be -685 mV, -693 mV and -761 mV, respectively.
- α -Al Matrix phase in the Al-Ni-Mn alloy is preferentially dissolved in the non-heat treated and heat treated samples.



EFFECT OF HEAT TREATMENT ON CORROSION RESISTANCE OF Al-Ni-Mn EUTECTIC ALLOY IN 3.5% NaCl SOLUTION

*Yusuf KAYGISIZ 

Aksaray University, Technical Vocational School of Sciences, Electricity and Energy Department, Aksaray,
TÜRKİYE
yusufkaygisiz@aksaray.edu.tr

(Received: 19.09.2023; Accepted in Revised Form: 22.12.2023)

ABSTRACT: In this study, the effects of solution heat treatment (SHT) on how the Al-Ni-Mn eutectic alloy reacts to corrosion were looked into. The composition of the Al-Ni-Mn eutectic alloy was chosen as Al-5.3%Ni-1.3%Mn (wt). In solution heat treatment, firstly, the samples were kept at 570°C and 600°C for 2 hours and quenched with water at room temperature. Then, artificial aging was carried out by keeping 0-2-4 and 8 hours at 180°C. The corrosion behavior of the alloy was investigated by immersion tests in a 3.5% NaCl solution and electrochemical methods such as Tafel polarization curves and Electrochemical Impedance Spectroscopy (EIS). According to the immersion test results, the heat treatment applied at 600°C took the alloy to the more noble side and further increased its corrosion resistance. The α -Al matrix phase in the Al-Ni-Mn alloy system preferentially dissolves in untreated and heat-treated samples, and SEM images reveal the presence of corrosion pits. The corrosion performance of the heat-treated sample at 570°C is the highest. Heat treatment reduced the corrosion current density, indicating a lower corrosion rate and higher corrosion resistance. Also, the open circuit potential of the Tafel polarization curves of heat-treated and unheat-treated samples at 570°C and 600°C was found to be -685 mV, -693 mV and -761 mV, respectively. Similarly, the corrosion resistance of heat-treated and untreated samples at 570°C and 600°C was found to be 58 k Ω , 433 k Ω and 408 k Ω , respectively.

Keywords: Aluminium alloys, $Al_3(Mn,Ni)_2$ phase, Corrosion resistance, Heat treatment

1. INTRODUCTION

Aluminum alloys have found use in many areas, from automotive to aircraft. The electrochemical properties and corrosion potential of aluminum alloys are as important as knowing and developing their mechanical properties. Similarly, the components of the alloy, the intermetallic phases occurring in the microstructure, and the sizes and distributions of these phases are as important as the potential difference of aluminum alloys with other metals, and these affect both the structure and morphology of the resulting corrosion [1]. The corrosion resistance of aluminum increases as the metal's purity increases. The use of 99.8% and 99.9% pure aluminum is generally limited to applications requiring very high corrosion resistance or ductility [1].

The microstructure of aluminum alloys varies depending on the composition, casting methods and processes, and applied heat treatment processes. In terms of corrosion properties, the grain structure in the microstructure, the presence of intermetallic phases, dispersides, and precipitates are the dominant features [1]–[7]. Al-Ni eutectic alloys exhibit excellent fluidity, excellent feedability, and low susceptibility to hot tearing [8]. However, it exhibits high mechanical properties at high temperatures thanks to its thermally stable Al_3Ni intermetallic phase [9]–[11]. It is stated that in Al-Ni alloys, depending on sample processing and annealing conditions, the first phase to be formed will be Al_3Ni [12]–[14], AlNi [15] or Al_3Ni_2 [11], [14], [16]. Zuogui Zhang et al. [2], in their study on the corrosion behavior of Al-5.4%Ni (wt) alloy, it was stated that preferential corrosion pits were formed in the Al phase area and that the more homogeneous and thinner Al/ Al_3Ni structure played a vital role in improving the corrosion resistance of the alloy. Similarly, Wislei R. Osório et al. [17], in their study on the electrochemical corrosion behavior of Al-5%Ni(wt) alloy powders in 0.05 M NaCl solution, they stated that samples with a finer structure

*Corresponding Author: Yusuf KAYGISIZ, yusufkaygisiz@aksaray.edu.tr

approached the positive side more and had higher corrosion resistance. In another study, Engelbert H. Padilla et al. [18], in their study on the corrosion behavior of NiAl and Ni₃Al intermetallic in acid rain, stated that both intermetallic phases have similar corrosion potential.

Although manganese has a low solubility in aluminum, it increases the corrosion resistance of the alloy and can reduce the possible harmful effects of ferrous intermetallic phases. Additions of up to 1% manganese provide good corrosion resistance as well as high formability in the structure [1], [19], [20]. Junwei Fu and Kai Cui [3] examined the effect of different amounts of Mn addition and heat treatment on the corrosion resistance of the Al-Cu-Mg alloy in 3.5% NaCl solution and stated that the Mn content increased the corrosion resistance of the alloy. They found the E_{corr} and values to be -1.536 and -1.143 V for the additions of 0.6 Mn and 1.2 Mn, respectively.

Within the scope of this information, the aim of this study is to examine the corrosion behavior of the Al-Ni-Mn eutectic alloy formed using high purity Al, Ni and Mn elements in 3.5% NaCl solution and its changes according to heat treatment processes. The solution heat treatment process will be carried out in two stages at different temperatures of 570°C and 600°C. Electrochemical methods such as immersion tests and Tafel polarization curves and Electrochemical Impedance Spectroscopy will be used to determine the corrosion properties of the heat treatment process.

2. MATERIALS AND METHODS

2.1. Heat Treatment Process and Microstructure Observation

With the help of the phase diagram [21] of the Al-Ni-Mn alloy system, the composition of the eutectic point was determined as Al-5.3%Ni-1.3%Mn (wt). Mondolfo stated that according to this phase diagram, the eutectic reaction should be in the form: $L \rightarrow (Al) + Al_3Ni + Mn_3NiAl_{16}$ [22].

The schematic representation of the Solution heat treatment (SHT) process steps in this study is given in Figure 1. First, the formed samples were kept at temperatures below the eutectic temperature, at 570°C and 600°C for 2 hours, and quenched in water at room temperature. Then, artificial aging was carried out by keeping 0-2-4 and 8 hours at 180°C (Figure 1.).

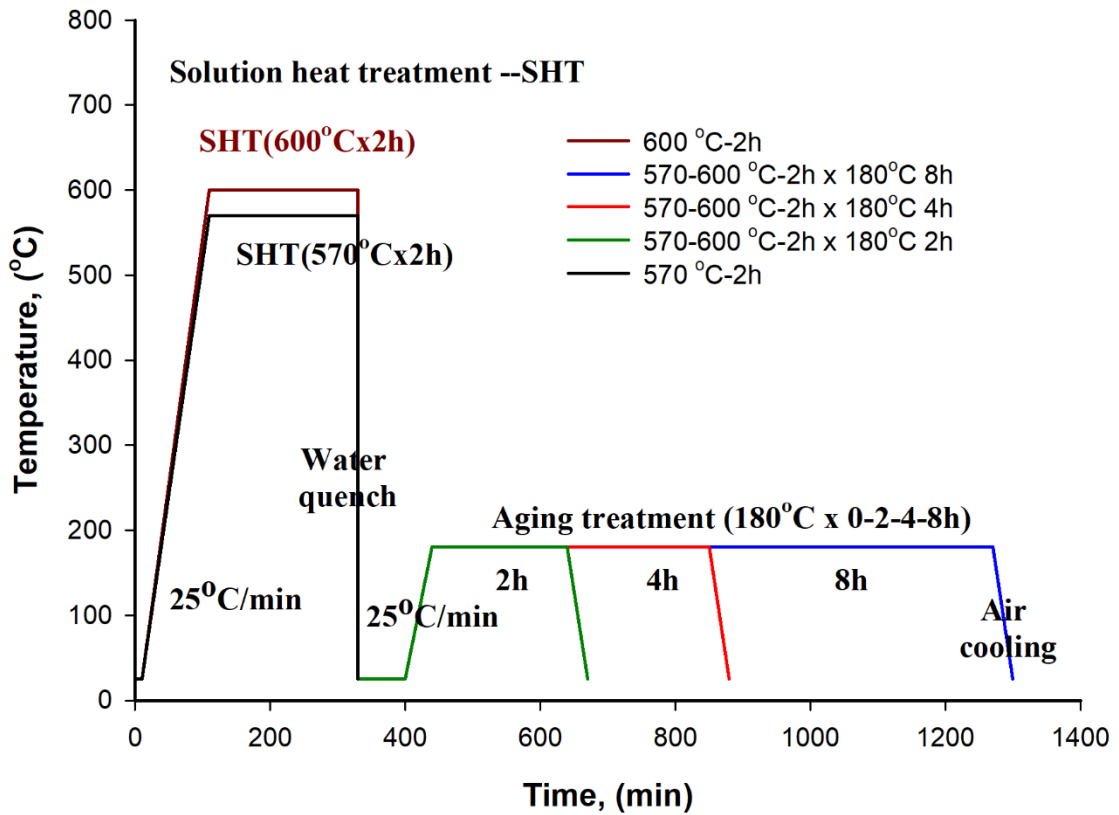


Figure 1. Schematic representation of solution heat treatment steps for Al-Ni-Mn alloy.

The typical SEM images of growth morphologies for eutectic Al-5.3wt%Ni-1.3wt.%Mn alloy are shown in Figure 2. As can be seen from Figure 2, the matrix (M) phase is in equilibrium with the gray (G), white (W) and eutectic (E) phases. According to the Energy dispersive spectroscopy (EDS) results given in Table 1, the α -Al phase of the Matrix (M) phase, the gray phase's binary intermetallic $Al_9(Mn,Ni)_2$ phase and the white phase is Al_3Ni intermetallic phase. Different from the phases indicated in the phase diagram [22], $Al_9(Mn,Ni)_2$ phase was observed. This metastable Al_9Ni_2 or $Al_9(Mn,Ni)_2$ phase was first described by Li and Kuo[23] in rapidly solidifying Al4Ni and Al6Ni alloys. Subsequently, precipitates were observed in the rapidly solidified Al-rich Al-Ni alloys[24], [25] and the annealed Al-rich Al/Ni alloys[26]. However, it should be noted that the Al_9Ni_2 phase does not occur in all Al-Ni alloys. We can say that the Al_9Ni_2 phase is the primary intermetallic phase at high solidification temperatures [27].

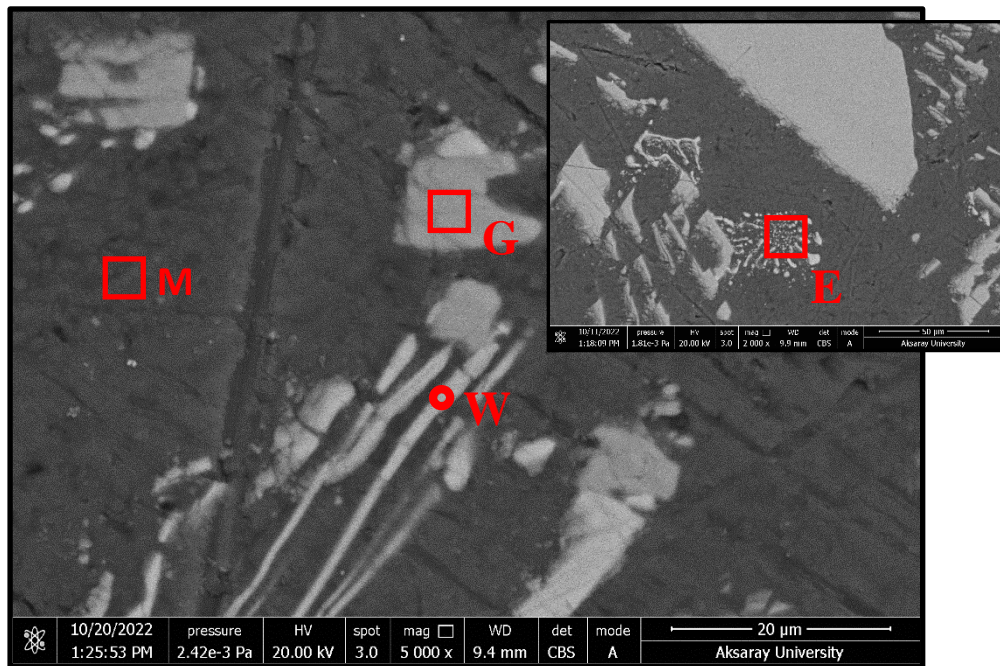


Figure 2. SEM image of longitudinal section of non-heat-treated Al-Ni-Mn alloy and, marked phase areas (M: Matrix phase, G: Gray phase, W: White phase, E: Eutectic area).

Table 1. EDS analysis results of the phases of Al-5.3Ni-1.3Mn (wt%) alloy before heat treatment.

Process	Test area	Specific position	Al		Ni		Mn	
			wt. %	at. %	wt. %	at. %	wt. %	at. %
Non-heat treated	White	W	61.48	77.63	37.87	21.97	0.65	0.40
	Gray	G	71.32	84.35	27.05	14.70	1.64	0.95
	Matrix	M	98.95	99.50	0.58	0.27	0.47	0.23
	Eutectic	E	88.50	94.36	11.15	5.46	0.35	0.18

2.2. Immersion Tests

Chlorides cause serious problems in metals or alloys due to their presence in many environments such as sea water and road salt, and in the chemical industry[28]. Therefore, in this study, mass loss measurements of Al-5.3%Ni-1.3%Mn (wt) alloy system prepared in eutectic composition were carried out in 3.5% NaCl solution at 25°C room temperature. Firstly, samples measuring 25 x 5 x 5 mm were cut, then they were mechanically polished using 360-600-1200-2000 and 4000 grit sandpaper and cleaned with deionized water. For mass loss measurement of heat treated and untreated alloy samples, they were kept in 3.5% NaCl solution at 25°C for 6-240 hours and the mass difference was measured with the help of precision balance. In order to remove the oxide layer and particle residues on the samples before weighing, they were kept in 10% silver nitrate (AgNO₃) prepared with distilled water for 30 seconds and then in 20% nitric acid (HNO₃) prepared with distilled water for 30 seconds.

The material removal rate or corrosion rate, which is an important corrosion parameter, can be expressed as the corrosion penetration rate (CPR) or the thickness loss of the material per unit time[29]. CPR can be formulated [29] as follows;

$$CPR = \frac{K \cdot \Delta W}{\rho \cdot A \cdot t} \quad (1)$$

where ΔW value is weight loss in mg, ρ is the density of the sample (calculated as $\rho = 2.67 \text{ g/cm}^3$), A is the total surface area of the sample (cm^2), h is the immersion time (hours). Since CPR is expressed in millimeters per year (mm/year), the K coefficient was taken as 87.6 [29].

2.3. Electrochemical Measurements

Corrosion measurements of Al-Ni Mn alloy were investigated using Tafel polarization curves and Nyquist diagrams obtained from Electrochemical Impedance Spectroscopy (EIS). Experimental studies were carried out using a conventional three-electrode cell in a 3.5% NaCl solution at room temperature. The Tafel polarization curves of the alloy samples were obtained at a scanning rate of 1mV/s (v). Nyquist diagrams obtained by EIS method were measured in the range of 0.1 Hz to 100 kHz and at 10mV AC voltage amplitude.

3. RESULTS AND DISCUSSIONS

3.1. Effect of Heat Treatment on Corrosion Behaviors

3.1.1. Analysis of immersion test results

Mass loss measurements of heat-treated and non-heat-treated samples were performed by immersing them in 3.5% NaCl solution between 6 and 240 hours, and the graph showing the variation of corrosion rate/mass loss with immersion time is given in Figure 3. As can be seen from Figure 3, it can be said that for all samples, the corrosion progression rate progresses rapidly during the first 24 hours of immersion, while it progresses steadily (horizontal speed) in the subsequent processes. In other words, the corrosion kinetics (progression rate) in the first 24 hours decreased from 0.8520 to 0.2982, from 1.086 to 0.3054 and from 0.3208 to 0.1604 (mm/year) for the untreated samples and the samples heat treated at 570 and 600°C, respectively.

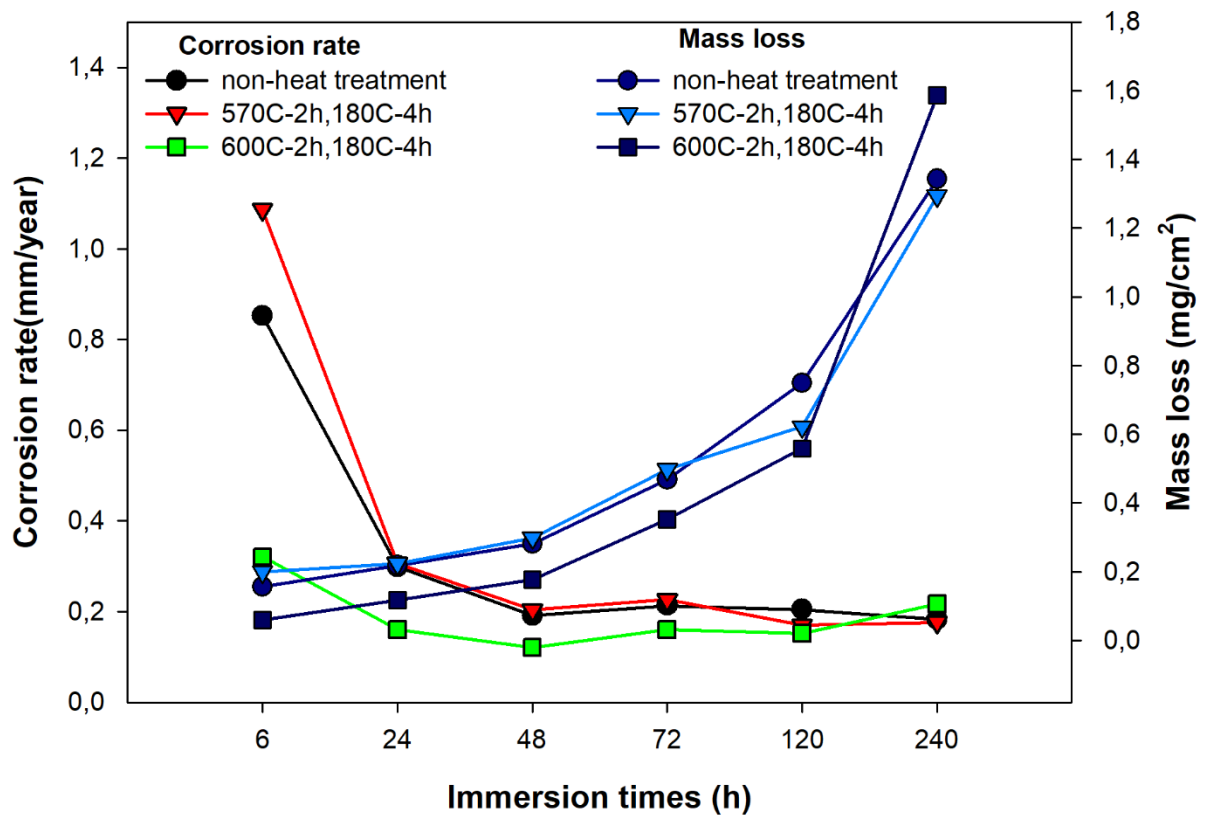


Figure 3. Immersion time & Corrosion rate and Mass loss curve for heat-treated and non-heat-treated Al-Ni-Mn alloy in 3.5% NaCl solution at 25°C.

Again from Figure 3, it can be seen that the corrosion progression rate of the samples heat treated at 600°C is lower than the corrosion progress rate of the samples that were non-heat treated and heat treated at 570°C. Similarly, looking at the mass loss graph given in Figure 3, the mass loss increases exponentially with increasing immersion times for heat treated and non-heat treated samples. We can say that the heat treatment process applied at 600°C takes the alloy to the more noble side and increases the corrosion resistance more.

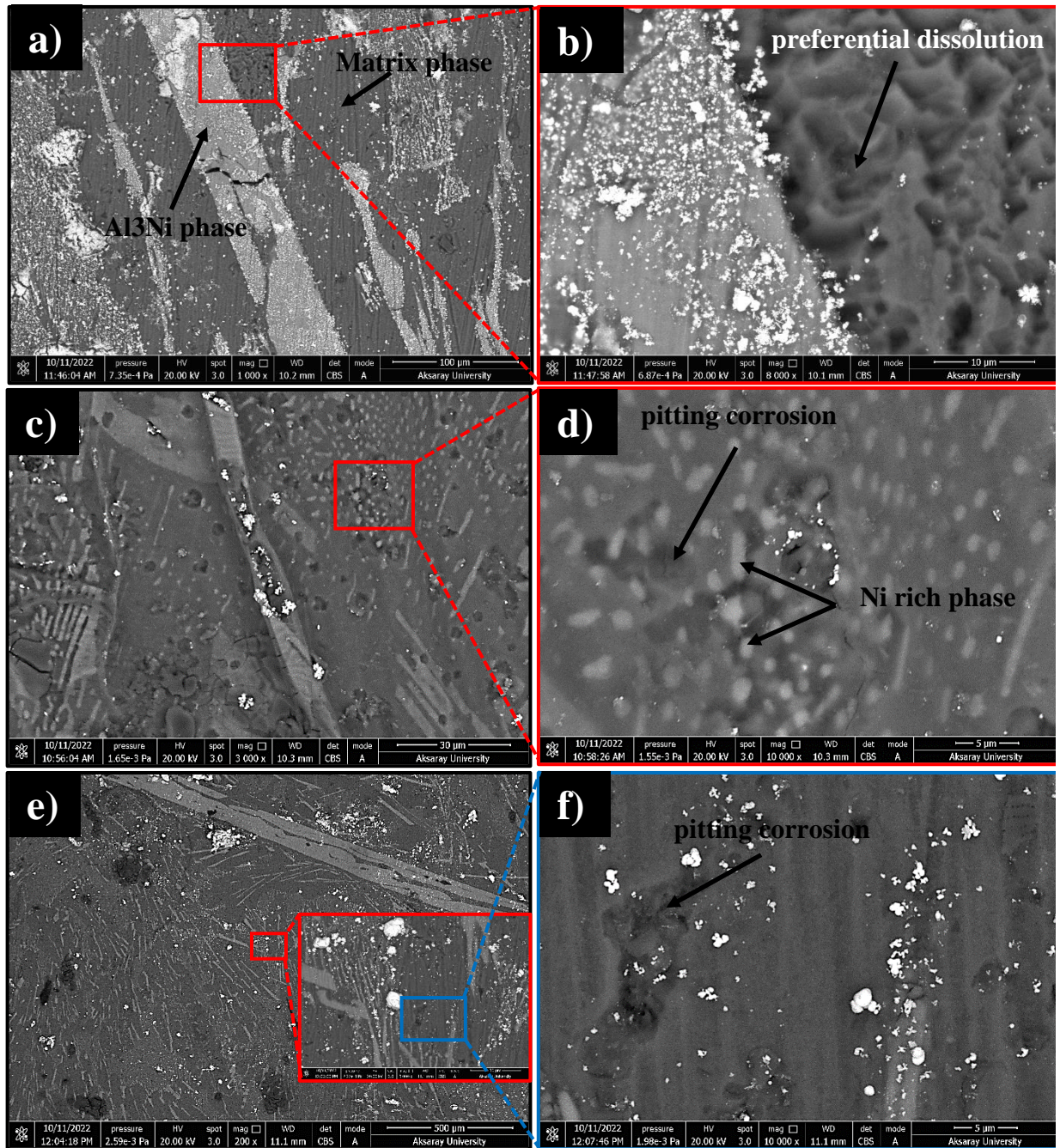


Figure 4. SEM images and corrosion types of samples immersed in 3.5% NaCl solution (a) not heat treated and immersed for 48 hours, (c) 2 hours at 570°C solution heat treated, then 4 hours at 180°C artificially aged and immersed for 48 hours, (e) 2 hours at 600°C solution heat treated, then 4 hours at 180°C artificially aged and immersed for 4 hours.

For determine the corrosion types after the immersion tests for corrosion progression rate/mass loss measurement, as shown in Figure 4, SEM images were taken from the heat treated and non-heat treated samples. As seen from the SEM images, the α -Al Matrix phase in the Al-Ni-Mn alloy system is preferentially dissolved in the non-heat treated and heat-treated samples. The SEM images given in Figure 4.d-f of the samples heat treated at 570°C and 600°C and immersed in NaCl solution for 48 hours reveal the presence of corrosion pits. It is worth noting that as can be seen from Figure 4.c-e, the heat treatment processes lead to a smaller Al matrix attack and corrosion pits.

Pitting corrosion [1], [30], [31] progression steps can be divided into several steps. In the 1st stage there are processes that lead to the breakdown of passivity. In stages 2 and 3, the early and late stages of pit growth and the final stage are repassivation. In stages 2 and 3, aluminum is oxidized to aluminum ions at the bottom of the pits. The reduction of water or hydrogen occurs in contact with the metal outside the pit. In both reduction reactions, the pH will increase outside the pit, giving an alkaline pH. The aluminum ions will create a film of aluminum chloride or aluminum oxychloride in the pit and stabilize it. After some time, aluminum chloride hydrolyzes to aluminum hydroxide. This causes the pH value to drop to a more acidic environment, which increases the corrosion rate in the furnace. Aluminum hydroxide precipitates at the edge of the pit and closes the opening, eventually inhibiting ion exchange and slowing down the corrosion process [28].

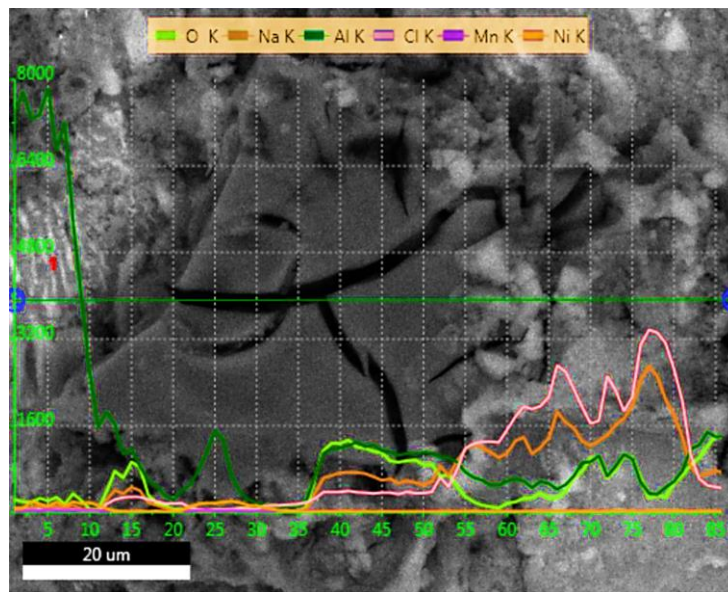


Figure 5. Line EDS image taken from the heat treated sample (solution heat treatment at 570°C for 2 hours, then artificial aging at 180°C for 4 hours) after immersion in 3.5% NaCl solution for 48 hours.

Line EDS and Mapping images taken from the sample (solution at 570°C for 2 hours, artificial aging at 180°C for 4 hours) immersed in 3.5% NaCl solution for 48 hours are shown in Figure 5 and Figure 6. These line EDS and mapping images also support preferential dissolution of the Al matrix phase. Shape. As can be clearly seen from the results of the line EDS given in Figure 5, an oxide layer has formed on the surface of the corrosion zone and Cl⁻ ions have accumulated around this oxide layer.

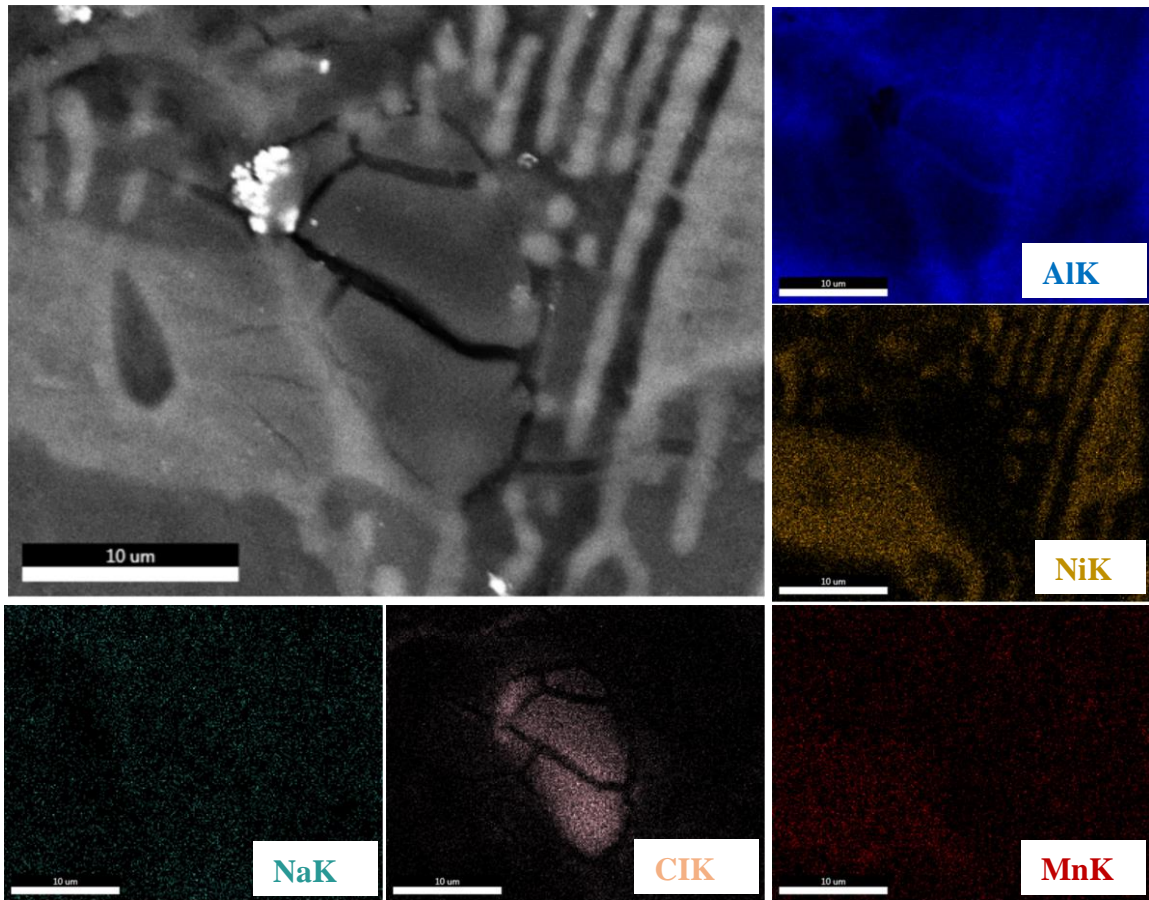


Figure 6. Mapping images of the heat treated sample (solution heat treatment at 570°C for 2 hours, then artificial aging at 180°C for 4 hours) immersed in 3.5% NaCl solution for 48 hours.

3.2. Analysis of electrochemical measurement results

Tafel polarization curves of heat treated and non-heat treated samples of Al-Ni-Mn eutectic alloy are given in Figure 7, and Nyquist diagrams obtained by Electrochemical Impedance Spectroscopy (EIS) method are given in Figure 8.

The corrosion characteristics of the alloys were determined by calculating the anodic and cathodic potentials in the Tafel area, together with their corresponding current densities. The corrosion current density (i_{corr}), which is directly related to the corrosion rate, was determined using the extrapolation of the cathodic and anodic Tafel lines to the corrosion potential (E_{corr}). The data shown in Figure 7 demonstrates that the non-heat-treated sample exhibits the greatest corrosion rate and a larger negative corrosion potential. Following the heat treatment conducted at temperatures of 570°C and 600°C, significant reductions in the corrosion rate were observed, accompanied by a change in the corrosion potential towards more positive values. The heat-treated sample exhibits the maximum corrosion performance when subjected to a temperature of 570°C. Furthermore, it can be seen that the application of heat treatment resulted in a decrease in the corrosion current density, so suggesting a reduction in the corrosion rate and an enhancement in the overall corrosion resistance.

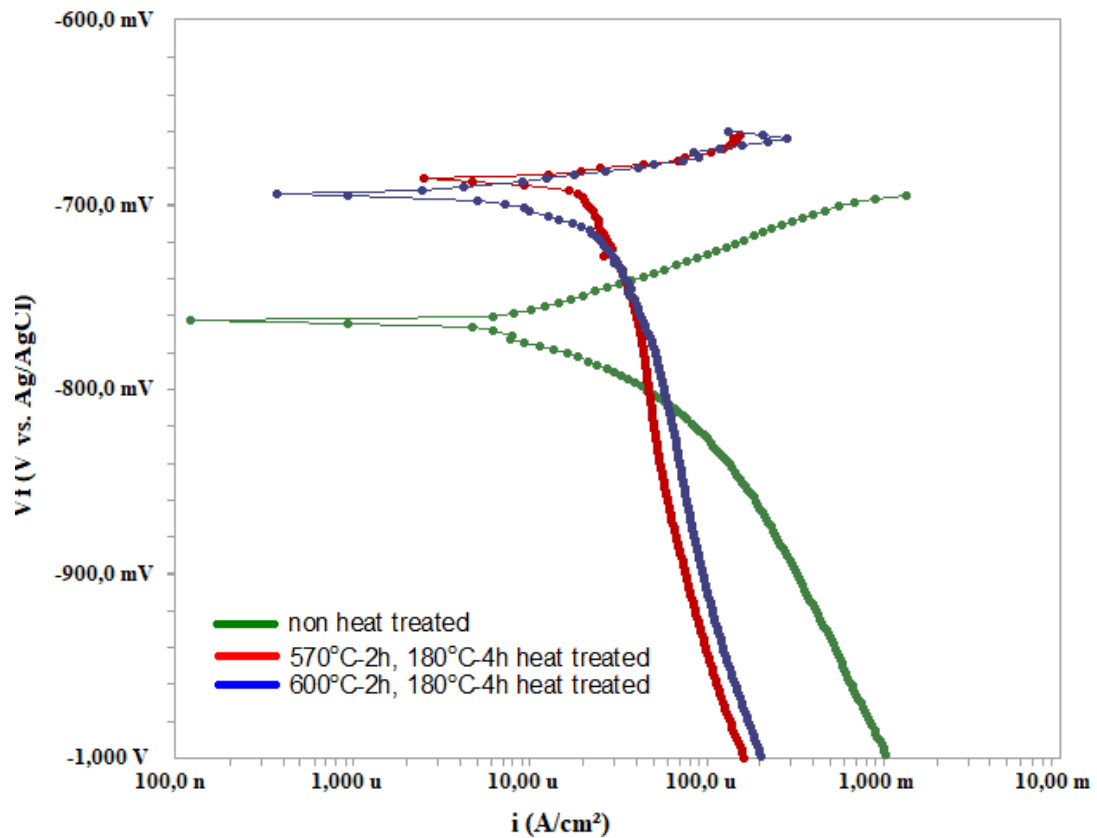


Figure 7. Current-Potential (Tafel polarization) curves recorded in 3.5% NaCl solution of Al-Ni-Mn eutectic alloys at a scanning rate of $\varnothing=1$ mV/s.

In addition, the open circuit potential of the Tafel polarization curves of the samples that were heat treated at 570°C and 600°C (2 hours in solution, then artificially aged at 180°C for 4 hours) and non-heat treated samples were found to be -685 mV, -693 mV and -761 mV, respectively.

Nyquist diagrams obtained using EIS are given in Figure 8. The impedance data of the alloys were analyzed using Nyquist plots plotted against the imaginary part of the impedance ($-Z_{imag}$) versus the real part (Z_{reel}). Nyquist plots consist of a semicircle for all non-heat-treated and heat-treated samples. The magnitude of the semicircle represents the value of the charge transfer resistance (R_{ct}) [32], [33] existing between the electrode material and the corrosive ions present in the electrolyte. The broader semicircle denotes a favored corrosion tendency or increased impedance.

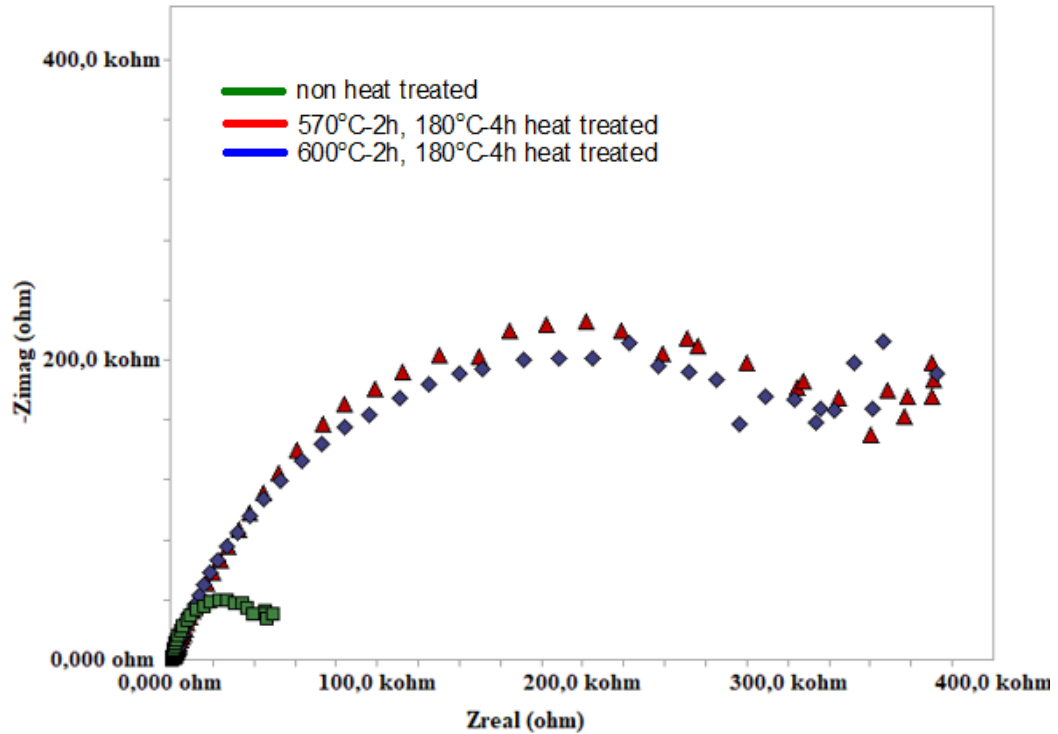


Figure 8. Nyquist plots obtained in 3.5% NaCl solution of Al-Ni-Mn eutectic alloy at -1.3V, frequency range: 0.1Hz-100kHz.

As can be seen from Figure 8, the non-heat treated sample has the lowest semicircular diameter (58k Ω) compared to the heat treated samples. This result shows that a homogeneous structure is formed during the heat treatment process and this leads to a better corrosion resistance. With solution heat treatment at 570°C and 600°C, the corrosion resistance of Al-Ni-Mn alloy samples increased to 433 k Ω and 408 k Ω , respectively. These results are consistent with those from the Tafel curves.

The findings derived from the implementation of Nyquist diagrams by the electrochemical impedance spectroscopy (EIS) technique and Tafel polarization curves have been consolidated and presented in Table 2. The findings demonstrate that heat treatment facilitated an increase in the corrosion potential, resulting in more positive values, and concurrently reduced the corrosion current density. As a result, the heat treatment process increased the corrosion resistance and decreased the corrosion rate.

Table 2. Corrosion potentials, corrosion current density and corrosion resistance of Al-Ni-Mn alloy

Samples	Electrochemical measurement results		
	E_{corr}/mV	$i_{corr}/mA.cm^{-2}$	$R_{ct}/k\Omega$
Non-heat treated	-764	1.12×10^{-1}	58
Heat treated (570°C)*	-682	1.63×10^{-3}	433
Heat treated (600°C)**	-793	2.01×10^{-3}	408

R_{ct} : charge transfer resistance, *570°C-2h-180°C-4h, **600°C-2h-180°C-4h

The immersion test results and electrochemical measurement results performed to determine the corrosion behavior of Al-Ni-Mn eutectic alloy were compared with the experimental results of similar studies in the literature [2], [3], [36]–[38], [6], [17]–[20], [28], [34], [35]. Zuogui Zhang et al.[2], in their study investigating the corrosion behavior of Al-5.4%Ni (wt) alloy produced by equal channel angular pressing (ECAP), they stated that preferential corrosion pits were formed in the Al phase area. It has also been stated that the more homogeneous and thinner Al/Al₃Ni structure plays a vital role in improving the

corrosion resistance of the Al-5.4% Ni (wt.) alloy. Wislei R. Osório et al. [17], in their study investigating the electrochemical corrosion behavior of Al-5%Ni(wt) alloy powders in 0.05 M NaCl solution, they stated that samples with finer microstructure approached the positive side more and had higher corrosion resistance. In the same study, the open circuit potentials of Tafel polarization curves were found to be -647 mV and -729 mV. These results are in full agreement with the open circuit potentials (685 mV, -693 mV and -761 mV) found in our study. Engelbert H. Padilla et al.[18], in their study investigating the corrosion behavior of NiAl and Ni₃Al intermetallics in acid rain, stated that both intermetallic phases have similar corrosion potential. They found the E_{corr} and I_{corr} values for Ni₃Al intermetallic to be -339.21 mV/SCE and 0.54×10^{-3} mA/cm², respectively. These values are approximately half of the E_{corr} and I_{corr} values given in Table 2, which we found in our study for samples heat treated at 570°C and 600°C. This may be due to the difference in the immersed solution. Junwei Fu and Kai Cui[3], examined the effects of different amounts of Mn addition and heat treatment on the corrosion resistance in 3.5% NaCl solution on the Al-Cu-Mg alloy. In their study, they found that the addition of Mn to the Al-Cu-Mg alloy had a significant effect on the electrochemical corrosion parameters. The addition of Mn increased the corrosion resistance of the alloy. For the additions of 0.6 Mn and 1.2 Mn, they found the E_{corr} and values to be -1.536 V and -1.143 V, respectively. Similarly, they measured I_{corr} values as 3.388×10^{-4} A/cm² and 7.197×10^{-6} A/cm² for 0.6 Mn and 1.2 Mn additions, respectively. They reported that they observed that corrosion resistance increased with the heat treatment process in the precipitation hardening heat treatment, in parallel with the results obtained in our study. In another study, Donghui Zhang and Dejun Kong[38], in their study investigating the effect of Al-Ni coating on S355 steel in 3.5% NaCl solution on corrosion resistance, stated that increasing the Ni ratio in Al increases the corrosion resistance of the alloy. In the amorphous Al-Ni coating with a 4:1 mass ratio of Al and Ni, the E_{corr} and I_{corr} values were found to be -0.727 V and 0.0028 A/m², respectively. This value is in full agreement with the experimental results obtained in our study for the sample heat treated at 600 °C

4. CONCLUSIONS

The typical SEM images of growth morphologies for eutectic Al-5.3wt%Ni-1.3wt.%Mn alloy are shown in Figure 2. As can be seen from Figure 2, the matrix (M) phase is in equilibrium with the gray (G), white (W) and eutectic (E) phases. According to the Energy dispersive spectroscopy (EDS) results given in Table 1, the α -Al phase of the Matrix (M) phase, the gray phase's binary intermetallic Al₉(Mn,Ni)₂ phase and the white phase is Al₃Ni intermetallic phase. Different from the phases indicated in the phase diagram [22], Al₉(Mn,Ni)₂ phase was observed. Despite these observed phases, the Mn₃NiAl₁₆ (Q) phase, which is one of the phases in the reaction expected in the eutectic composition, was not found in the SEM and EDS images. It is thought that the Mn₃NiAl₁₆ (Q) phase, which Mondolfo's claims to be in the eutectic reaction, is due to the solidification rate not allowing this phase to form.

According to the SEM images taken from the samples after the immersion tests in 3.5% NaCl solution, it is clearly seen that the α -Al Matrix phase in the Al-Ni-Mn alloy system is preferentially dissolved in the non-heat treated and heat treated samples.

In the immersion test results, it is seen that the corrosion progression rate of the samples heat treated at 600°C is lower than the corrosion progress rate of the samples that were not heat treated and heat treated at 570°C. In contrast, for heat-treated and non-heat-treated samples, the mass loss increases exponentially with increasing immersion times.

The Tafel curves reveal that the non-heat-treated sample exhibits the greatest corrosion rate and has greater negative corrosion potential. Following the application of heat treatment at temperatures of 570°C and 600°C, a significant reduction in the corrosion rate was seen, accompanied with a change in the corrosion potential towards more positive values. The open circuit potential of the Tafel polarization curves of the samples that were heat treated at 570°C and 600°C (2 hours in solution, then artificially aged at 180°C for 4 hours) and non-heat treated samples were found to be -685 mV, -693 mV and -761 mV, respectively.

Nyquist diagrams drawn by Electrochemical Impedance Spectroscopy and Tafel curves were observed to be consistent. The non-heat treated sample has the lowest semicircular diameter (58k Ω) compared to the heat treated samples. The obtained outcome demonstrates the formation of a homogenous structure by the heat treatment procedure, resulting in increased corrosion resistance. The corrosion resistance of the samples was enhanced to 433 k Ω and 408 k Ω , respectively, after heat treatment at temperatures of 570°C and 600°C.

According to the findings obtained from Nyquist diagrams and Tafel polarization curves and summarized in Table 2, it shows that heat treatment increases the corrosion potential and reaches more positive values. The heat treatment process also reduced the corrosion current density. As a result, the heat treatment process increased corrosion resistance and reduced the corrosion rate.

Declaration of Competing Interest

The authors declare that they have no known competing financial interests or personal relationships that could have appeared to influence the work reported in this paper.

Funding / Acknowledgements

This project was supported by Aksaray University Scientific Research Project Unit, Contract No: 2021-010. The authors are obliged to Aksaray University for their financial contribution.

REFERENCES

- [1] G. M. Scamans, N. Birbilis, and R. G. Buchheit, "Corrosion of aluminum and its alloys," in *Corrosion of Aluminum and its Alloys*, 2010, pp. 1974–2010.
- [2] Z. Zhang, E. Akiyama, Y. Watanabe, Y. Katada, and K. Tsuzaki, "Effect of α -Al/Al₃Ni microstructure on the corrosion behaviour of Al-5.4 wt% Ni alloy fabricated by equal-channel angular pressing," *Corros. Sci.*, vol. 49, no. 7, pp. 2962–2972, 2007.
- [3] J. Fu and K. Cui, "Effect of Mn content on the microstructure and corrosion resistance of Al-Cu-Mg-Mn alloys," *J. Alloys Compd.*, vol. 896, p. 162903, 2022.
- [4] M. C. Reboul, T. J. Warner, H. Mayet, and B. Baroux, "A ten-step mechanism for the pitting corrosion of aluminium," *Mater. Sci. Forum*, vol. 217–222, no. PART 3, pp. 1553–1558, 1996.
- [5] R. G. Buchheit, "A Compilation of Corrosion Potentials Reported for Intermetallic Phases in Aluminum Alloys," *J. Electrochem. Soc.*, vol. 142, no. 11, pp. 3994–3996, 1995.
- [6] Yusuf Kaygısız and Didem Balun Kayan, "Effect of Heat Treatment on the Mechanical Properties and Corrosion Behaviour of Al-Si-Mg Alloy Systems," *Phys. Met. Metallogr.*, vol. 123, no. 14, pp. 1499–1508, 2022.
- [7] Ş. Candan, S. Çim, S. Emir, and E. Candan, "AZ91 Mg Alaşımlarında Korozyon Davranışı-Fe Tolerans Sınırı Arasındaki İlişkinin Araştırılması," *Konya J. Eng. Sci.*, vol. 7, no. 3, pp. 654–662, 2019.
- [8] N. A. Belov, A. N. Alabin, and D. G. Eskin, "Improving the properties of cold-rolled Al-6%Ni sheets by alloying and heat treatment," *Scr. Mater.*, vol. 50, no. 1, pp. 89–94, 2004.
- [9] C. Suwanpreecha, P. Pandee, U. Patakham, and C. Limmaneevichitr, "New generation of eutectic Al-Ni casting alloys for elevated temperature services," *Mater. Sci. Eng. A*, vol. 709, no. September 2017, pp. 46–54, 2018.
- [10] J. T. Kim, S. H. Hong, J. M. Park, J. Eckert, and K. B. Kim, "Microstructure and mechanical properties of hierarchical multi-phase composites based on Al-Ni-type intermetallic compounds in the Al-Ni-Cu-Si alloy system," *J. Alloys Compd.*, vol. 749, pp. 205–210, 2018.
- [11] F. Yousefi, R. Taghiabadi, and S. Baghshahi, "Effect of Partial Substitution of Mn for Ni on Mechanical Properties of Friction Stir Processed Hypoeutectic Al-Ni Alloys," *Metall. Mater. Trans. B Process Metall. Mater. Process. Sci.*, vol. 49, no. 6, pp. 3007–3018, 2018.
- [12] E. Ma, M. A. Nicolet, and M. Nathan, "NiAl₃ formation in Al/Ni thin-film bilayers with and

- without contamination," *J. Appl. Phys.*, vol. 65, no. 7, pp. 2703–2710, 1989.
- [13] E. Ma, C. V. Thompson, and L. A. Clevenger, "Nucleation and growth during reactions in multilayer Al/Ni films: The early stage of Al₃Ni formation," *J. Appl. Phys.*, vol. 69, no. 4, pp. 2211–2218, 1991.
- [14] A. S. Edelstein, R. K. Everett, G. R. Richardson, S. B. Qadri, J. C. Foley, and J. H. Perepezko, "Reaction kinetics and biasing in Al/Ni multilayers," *Mater. Sci. Eng. A*, vol. 195, no. C, pp. 13–19, 1995.
- [15] R. B. and K. B. C. Michaelsen, S. Wohler, "The Early Stages of Solid-State Reactions In Ti/Al Multilayer Films," *Eff. Partial Substit. Mn Ni Mech. Prop. Frict. Stir Process. Hypoeutectic Al-Ni Alloy.*, vol. 398, pp. 245–250, 1996.
- [16] M. H. Da Silva Bassani, J. H. Perepezko, A. S. Edelstein, and R. K. Everett, "Initial phase evolution during interdiffusion reactions," *Scr. Mater.*, vol. 37, no. 2, pp. 227–232, 1997.
- [17] W. R. Osório, J. E. Spinelli, C. R. M. Afonso, L. C. Peixoto, and A. Garcia, "Electrochemical corrosion behavior of gas atomized Al-Ni alloy powders," *Electrochim. Acta*, vol. 69, pp. 371–378, 2012.
- [18] E. H. Padilla, A. M. Flores, C. A. Ramírez, I. A. López, and L. B. Gómez, "Electrochemical corrosion characterization of nickel aluminides in acid rain," *Rev. Mater.*, vol. 23, no. 2, 2018.
- [19] C. Cao, D. Chen, J. Ren, J. Shen, L. Meng, and J. Liu, "Improved strength and enhanced pitting corrosion resistance of Al-Mn alloy with Zr addition," *Mater. Lett.*, vol. 255, p. 126535, 2019.
- [20] H. Mraied, W. Cai, and A. A. Sagüés, "Corrosion resistance of Al and Al-Mn thin films," *Thin Solid Films*, vol. 615, pp. 391–401, 2016.
- [21] V. S. Zolotarevsky, N. A. Belov, and M. V. Glozoff, *Plating Aluminium Alloys*. Amsterdam: Elsevier Ltd., 2007.
- [22] Mondolfo L. F., *Aluminum Alloys-Structure and Properties*. 1976.
- [23] X. Z. Lit and K. H. Kuo, "Decagonal quasicrystals with different periodicities along the tenfold axis in rapidly solidified al-ni alloys," *Philos. Mag. Lett.*, vol. 58, no. 3, pp. 167–171, 1988.
- [24] J. F. Nie and B. C. Muddle, "Microstructure in rapidly solidified Al-Ti-Ni alloys," *Mater. Sci. Eng. A*, vol. 215, no. 1–2, pp. 92–103, 1996.
- [25] C. Pohla and P. L. Ryder, "Crystalline and quasicrystalline phases in rapidly solidified Al-Ni alloys," *Acta Mater.*, vol. 45, no. 5, pp. 2155–2166, 1997.
- [26] A. Yamamoto and H. Tsubakino, "Al₉Ni₂ precipitates formed in an Al-Ni dilute alloy," *Scr. Mater.*, vol. 37, no. 11, pp. 1721–1725, 1997.
- [27] M. A. Martínez-Villalobos *et al.*, "Microstructural evolution of rapid solidified Al-Ni alloys," *J. Mex. Chem. Soc.*, vol. 60, no. 2, pp. 67–72, 2016.
- [28] J. Tao, "Surface composition and corrosion behavior of an Al-Cu alloy," Docteur De L'université Pierre Et Marie Curie, 2016.
- [29] J. A. D. G. R. William D. Callister, *Materials Science and Engineering an Introduction*, 9th ed. Wiley, 2013.
- [30] T. Suter and R. C. Alkire, "Microelectrochemical Studies of Pit Initiation at Single Inclusions in Al 2024-T3," *J. Electrochem. Soc.*, vol. 148, no. 1, p. B36, 2001.
- [31] R. L. Cervantes, L. E. Murr, and R. M. Arrowood, "Copper nucleation and growth during the corrosion of aluminum alloy 2524 in sodium chloride solutions," *J. Mater. Sci.*, vol. 36, no. 17, pp. 4079–4088, 2001.
- [32] D. Balun Kayan, D. Koçak, and M. İlhan, "Electrocatalytic hydrogen production on GCE/RGO/Au hybrid electrode," *Int. J. Hydrogen Energy*, vol. 43, no. 23, pp. 10562–10568, 2018.
- [33] D. B. Kayan, M. İlhan, and D. Koçak, "Chitosan-based hybrid nanocomposite on aluminium for hydrogen production from water," *Ionics (Kiel)*, vol. 24, no. 2, pp. 563–569, 2018.
- [34] Y. Yang *et al.*, "Improved corrosion behavior of ultrafine-grained eutectic Al-12Si alloy produced by selective laser melting," *Mater. Des.*, vol. 146, pp. 239–248, 2018.
- [35] D. S. Carvalho, C. J. B. Joia, and O. R. Mattos, "Corrosion rate of iron and iron-chromium alloys in CO₂ medium," *Corros. Sci.*, vol. 47, no. 12, pp. 2974–2986, 2005.

- [36] M. jia Li *et al.*, "Improved intergranular corrosion resistance of Al-Mg-Mn alloys with Sc and Zr additions," *Micron*, vol. 154, no. December 2021, p. 103202, 2022.
- [37] M. Mirzaee-Moghadam *et al.*, "Dry sliding wear characteristics, corrosion behavior, and hot deformation properties of eutectic Al-Si piston alloy containing Ni-rich intermetallic compounds," *Mater. Chem. Phys.*, vol. 279, no. January, p. 125758, 2022.
- [38] D. Zhang and D. Kong, "Microstructures and immersion corrosion behavior of laser thermal sprayed amorphous Al-Ni coatings in 3.5 % NaCl solution," *J. Alloys Compd.*, vol. 735, pp. 1-12, 2018.

PERFORMANCE ANALYSIS OF P&O AND PSO MPPT ALGORITHMS FOR PV SYSTEMS UNDER PARTIAL SHADING

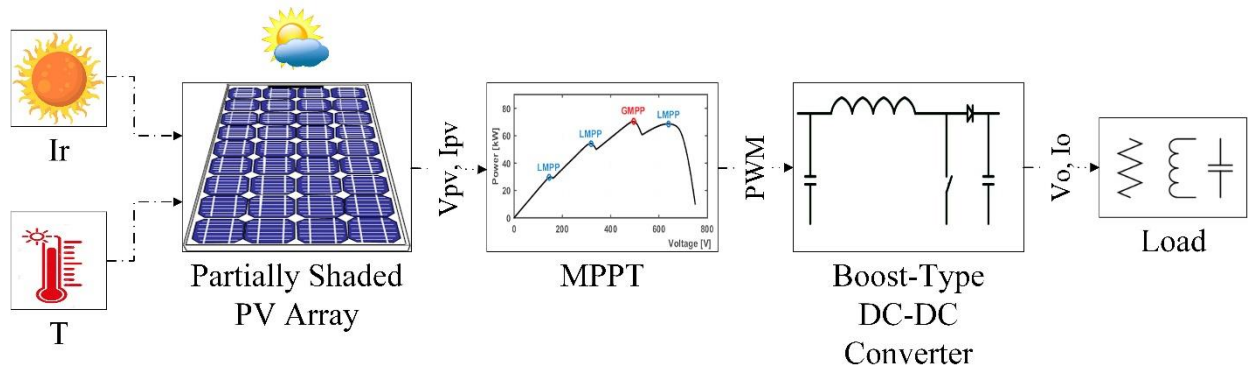
*Mustafa Sacid ENDİZ 

Necmettin Erbakan University, Engineering Faculty, Electrical-Electronics Department, Konya, TÜRKİYE
[msendiz@erbakan.edu.tr](mailto:mSENDIZ@ERBAKAN.EDU.TR)

Highlights

- Modeling and simulation of the designed PV system applying P&O and PSO MPPT strategies.
- Performance analysis under uniform and two different partial shading configurations.
- Discussing the results based on tracking efficiency and convergence speed of the MPPT system.

Graphical Abstract



Graphical abstract of the proposed system.



PERFORMANCE ANALYSIS OF P&O AND PSO MPPT ALGORITHMS FOR PV SYSTEMS UNDER PARTIAL SHADING

*Mustafa Sacid ENDİZ 

Necmettin Erbakan University, Engineering Faculty, Electrical and Electronics Department, Konya, TÜRKİYE
[msendiz@erbakan.edu.tr](mailto:mSENDIZ@ERBAKAN.EDU.TR)

(Received: 12.09.2023; Accepted in Revised Form: 22.12.2023)

ABSTRACT: Photovoltaic (PV) modules are devices that transform photon energy into electrical energy. The output power of the PV modules is influenced by the intensity of solar radiation and the ambient temperature. Non-uniform shading can cause variations in the extent of sunlight absorbed by PV modules, resulting in a decrease in power output. Maximum power point tracking (MPPT) techniques are employed to optimize the power output of PV modules by operating them at their maximum power point (MPP). The main objective of the study is to investigate the performance analysis of Perturb and Observe (P&O) and Particle Swarm Optimization (PSO) MPPT strategies in uniform and partially shaded conditions with equally and unequally different irradiance differences. Simulation studies were conducted on the PV circuit model using Matlab/Simulink, and the results were evaluated. MPPT algorithms are compared based on their tracking efficiency and convergence speed when solar radiation conditions vary. The findings of the simulation indicate that the P&O is unable to determine global MPP and gets trapped in one of the local MPPs. However, the PSO is very effective in tracking MPP under different partial shading patterns with more than 96% tracking efficiency. In the first partial shading configuration where the sunlight intensity of the PV modules is uniformly distributed, the PSO technique has reduced steady-state oscillations around the MPP. However, the P&O technique demonstrates superior response time and convergence speed in comparison to the PSO technique.

Keywords: MPPT, P&O, Partial shading, Photovoltaic, PSO

1. INTRODUCTION

The global demand for energy generation is experiencing a significant increase due to population and economic growth, with fossil fuels emerging as the dominating source. The environmental impact of greenhouse gas emissions from burning fossil fuels and the fact that these fuels will be depleted in the near future due to the limited reserves increase the need for clean and infinite energy sources [1]. Countries are turning to the use of renewable energy resources that produce very low or near zero greenhouse gas emissions to respond to increasing energy demands and prevent global warming. Therefore, the significance of environmentally friendly and cost-effective renewable energy sources is growing rapidly [2-4].

Due to its low cost, ease of use, and ecologically beneficial characteristics, the use of solar power in electricity production has grown rapidly in recent years. Solar energy can be directly transformed into direct current (DC) electricity using photovoltaic (PV) technology [5]. PV modules are composed of PV cells that are interconnected in series and parallel, and a PV array consists of PV modules. PV cells are the smallest part of a solar power system and are made up of semiconductor material. In a PV cell, sunlight is converted into electrical energy by absorbing the energy in the photon particles, which is commonly referred to as the photovoltaic effect. When a PV cell is subjected to solar radiation, it causes electron movement, resulting in the generation of a voltage potential across the front and back surfaces of the cell. Thus, a solar cell can produce an electric current [6, 7].

The solar radiation value reaching the Earth's atmosphere is accepted as approximately 1000W/m² due to the losses and reflections of the photon particles. PV modules used today provide energy conversion

*Corresponding Author: Mustafa Sacid ENDİZ, [msendiz@erbakan.edu.tr](mailto:mSENDIZ@ERBAKAN.EDU.TR)

with an efficiency between 15% and 20% depending on the cell structure despite all current technological developments. Therefore, it is significant to use PV modules with the highest possible efficiency. PV module output power varies depending on the solar radiation intensity and ambient temperature during the day [8]. The current of a PV module exhibits a proportionate change in response to an increase in solar radiation intensity. Consequently, the module's output power experiences a rise. As the ambient temperature rises, there is a corresponding increase in the current value of the PV module, while the voltage value decreases. Since the change in PV voltage value is greater than the current change, the overall power output of the PV module decreases. The technique known as maximum power point tracking (MPPT) refers to the process of maintaining the output power of a PV module at its highest achievable level [9]. The achievement of the highest power output in PV systems occurs at a specific operating point referred to as the Maximum Power Point (MPP). Independent of environmental conditions, with MPPT techniques the PV module is continuously operated at the maximum available power point. The position of this point varies continually in response to changes in environmental conditions.

1.1. Literature Review

Several MPPT methods are discussed in literature studies, however, they all have their drawbacks when it comes to PV applications in terms of efficiency, cost, and usability [10, 11]. MPPT techniques use two different methods, direct and indirect search, to obtain the MPP. The direct methods depend on variations in current and voltage values, while the indirect methods search the MPP with solar radiation, temperature, and certain mathematical expressions. In the last few years, metaheuristic optimization MPPT algorithms have been proposed which can dynamically track the real MPP [12]. Due to the bypass diodes, in addition to the global MPP, the power-voltage curve of a PV module exhibits many local MPPs as a result of the non-uniform shading effect. In the presence of a non-uniform shading effect, in addition to a global MPP, there are multiple local MPPs in the power-voltage curve of the PV module due to the bypass diodes. The commonly used MPPT techniques are not sufficient to track the MPP in normal conditions as well as in conditions of partial shading. However, metaheuristic optimization algorithms can effectively track the MPP in both cases, so that they can avoid getting trapped in local MPPs [13]. The PV array must always operate at the global MPP to maximize energy generation. A study presents a hybrid MPPT technique using Particle Swarm Optimization (PSO) and Perturb and Observe (P&O) methods for PV systems. Simulations show the proposed technique can track global MPP under uniform and partial shading conditions, with a 50% shorter tracking time and 0.3% more electricity extraction [14]. Another study introduces a logarithmic PSO method for MPPT, reducing power oscillations and accelerating convergence without search space reduction. In the steady-state process, the swarm is reduced to a single particle, which slightly changes to detect local variations [15]. A study compares P&O and PSO algorithms for MPPT in PV power systems. The results show that P&O is faster but generates significant energy losses due to constant oscillations. PSO is slower but less energy-intensive, and only PSO ensures convergence to the MPP under partial shading conditions [16]. Three MPPT algorithms, P&O, Incremental Conductance (INC), and PSO are compared to show the effectiveness in PV systems. While the P&O and INC are simple to implement, the PSO is more effective in optimizing the output power [17]. This study investigates the performance analysis of P&O and PSO MPPT techniques in uniform and partially shaded conditions with equally and unequally different irradiance differences based on the tracking efficiency and convergence speed on the designed PV circuit model developed in Matlab/Simulink. The rest of the paper is structured as follows: Section 2 explains a single-diode PV cell model with mathematical expressions, the details of the P&O and PSO algorithms, and the boost-type DC-DC converter respectively. Section 3 describes the parameters of the developed PV system and discusses the simulation results. Section 4 outlines conclusions and suggestions for further study.

2. MATERIAL AND METHODS

2.1. A Single-diode PV Cell Model

The solar cell, consisting of P-type and N-type semiconductor materials, is the smallest unit in PV systems that directly transforms the absorbed solar radiation into electricity. Photons of varying energy levels make up solar radiation, and part of these photons are absorbed in the p-n junction. Solar energy is transformed into DC electricity by combining photons with energies higher than the band gap of semiconductor material to the electrons in the atoms. PV modules are formed at the desired power values by combining solar cells appropriately. The PV cell's single-diode model, which is used more frequently than the two-diode model because of its ease of usage and reasonable accuracy, is shown in Figure-1. On the equivalent circuit model of the PV cell, I_{ph} is the current generated by the PV cell, I_d is the diode current, I_p is the current of the parallel resistance, I_{pv} is the output current of the PV cell, D is the diode, R_p is the resistance parallel to the current source, R_s is the series connected resistance, and R_L is the output load resistance [18].

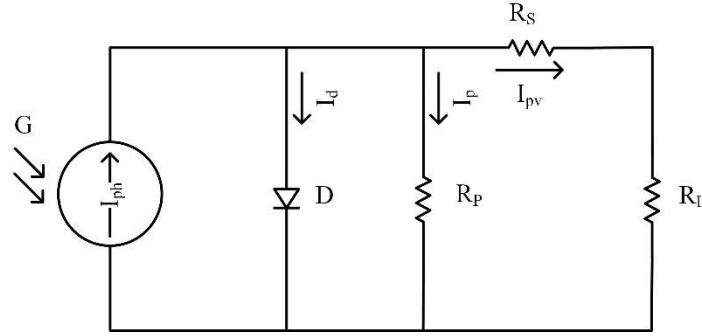


Figure 1. The single-diode model of the PV cell

Solar radiation (G) and cell temperature (T) are directly related to the production of electricity from sunlight. Equation 1 and Equation 2 indicate the generated current I_{ph} and the output current I_{pv} respectively. In the below equations; I_{sc} is the short circuit current at 25 °C and 1000W/m², K_i is the temperature coefficient of the short circuit current, and ΔT is the difference between reference temperature and PV cell temperature.

$$I_{ph} = [I_{sc} + K_i * \Delta T] \frac{G}{G_r} \quad (1)$$

$$I_{pv} = I_{ph} - I_d - I_p \quad (2)$$

2.2. Perturb and Observe (P&O) MPPT Technique

MPPT algorithms are employed to regulate the operating point of the PV array at its MPP. The complexity, tracking speed, accuracy, oscillations, and hardware implementation of these techniques differ among themselves. Many different algorithms have been proposed in recent years as potential approaches to MPP tracking. One of the most frequently employed MPPT strategies among the traditional MPPT techniques is the P&O technique. The fundamental concept underlying this methodology is to track the changes in module output power. The operating point is determined by checking the module's power-voltage curve and slope (dP/dV) variation as shown in Figure-2. A positive derivative of power to voltage indicates that the operating point is to the left of the MPP. Conversely, a negative slope shows that the operating point is to the right of the power-voltage curve. By adjusting the duty ratio, the P&O continually changes the voltage level of the PV array to approach the MPP [19].

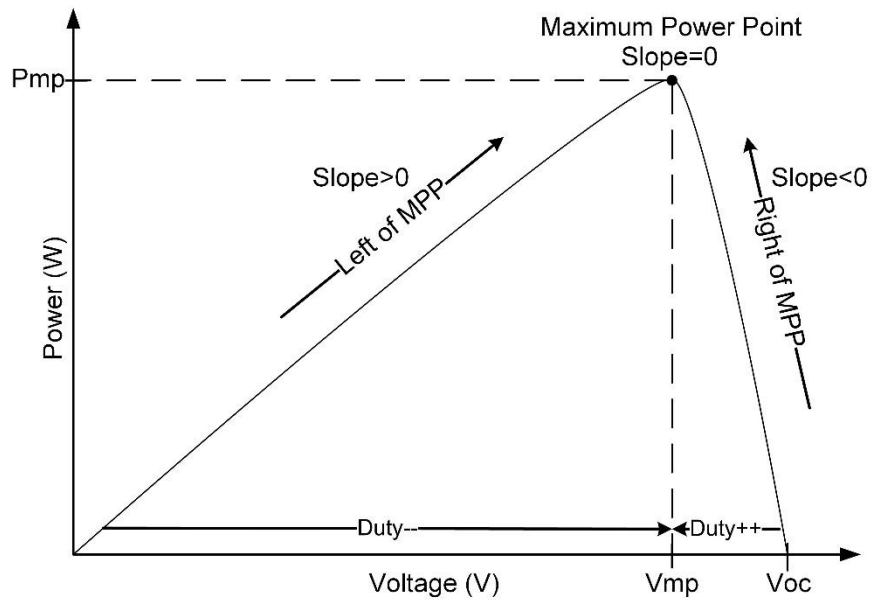


Figure 2. Behavior of the P&O MPPT with P-V curve

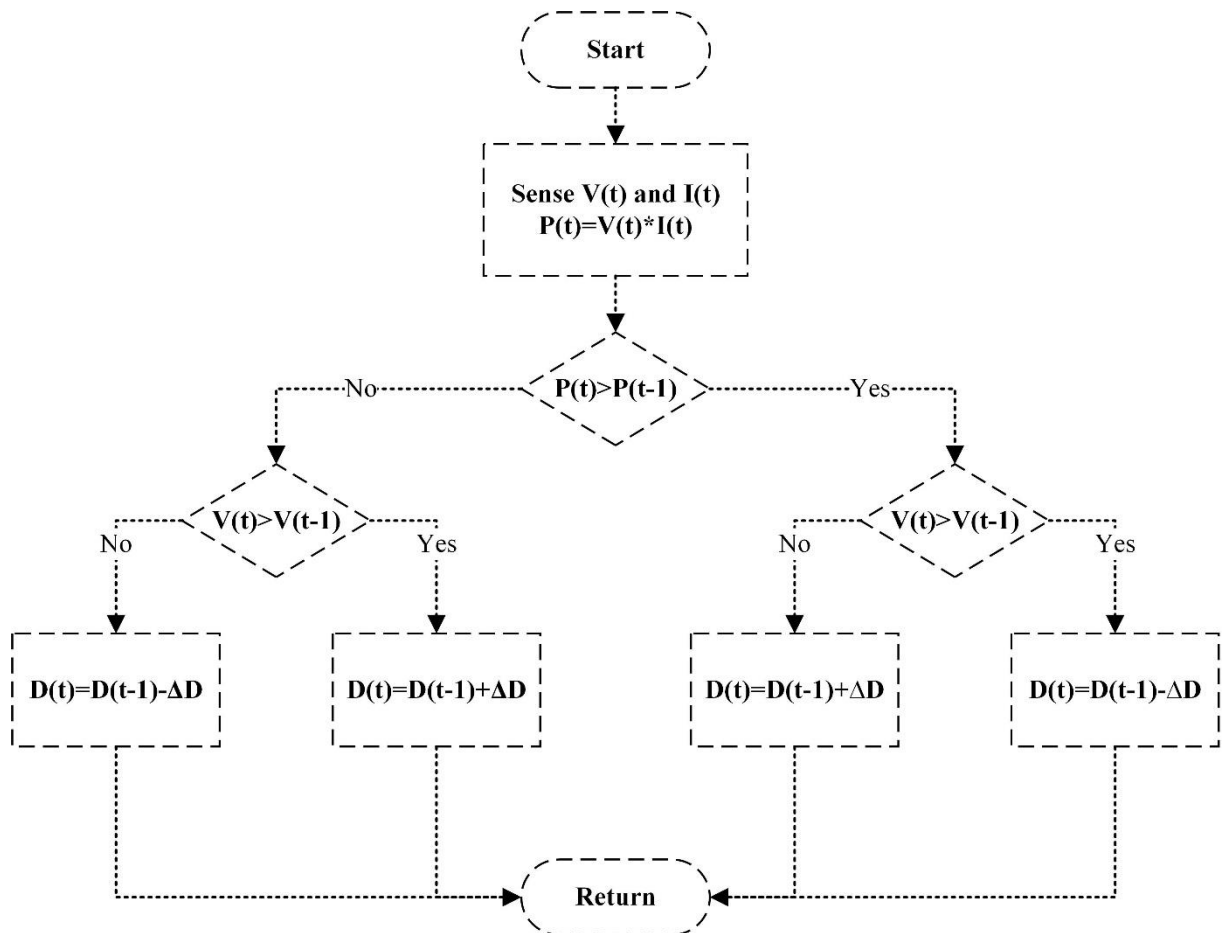


Figure 3. Flowchart of the P&O MPPT algorithm

In Figure-3, the flowchart of the P&O MPPT is demonstrated. The P&O technique's primary limitations are its inefficiency in quickly changing air conditions and its significant steady-state oscillations around the MPP due to the continual repetition of the perturbation process in both directions. For PV module operation, the P&O typically uses a constant step size interval. However, using a constant

step size speeds up tracking but causes high steady-state oscillations at the MPP. This can be solved by damping the oscillations, which slows tracking. Variable step sizes can be used in the algorithm to improve tracking performance and reduce high steady-state oscillations. The P&O based on the variable step-size algorithm can improve the tracking performance. Because of its simple structure and potential for improvement, P&O MPPT is widely used [19].

2.3. Particle Swarm Optimization (PSO) MPPT Technique

In recent years, metaheuristic optimization algorithm based MPPT approaches have become increasingly popular due to their many advantages over conventional MPPT algorithms. Especially, under partial shade conditions, the MPP is not tracked by conventional approaches due to the existence of several power peaks in the P-V characteristics curve. The PSO algorithm was introduced by Eberhart and Kennedy in 1995 as a population-based metaheuristic intelligent optimization approach which is characterized by its simplicity and effectiveness [20]. The basic idea of the algorithm was based on how groups of birds move together to solve problems in the search process and optimization. The flowchart of the PSO MPPT is depicted in Figure-4.

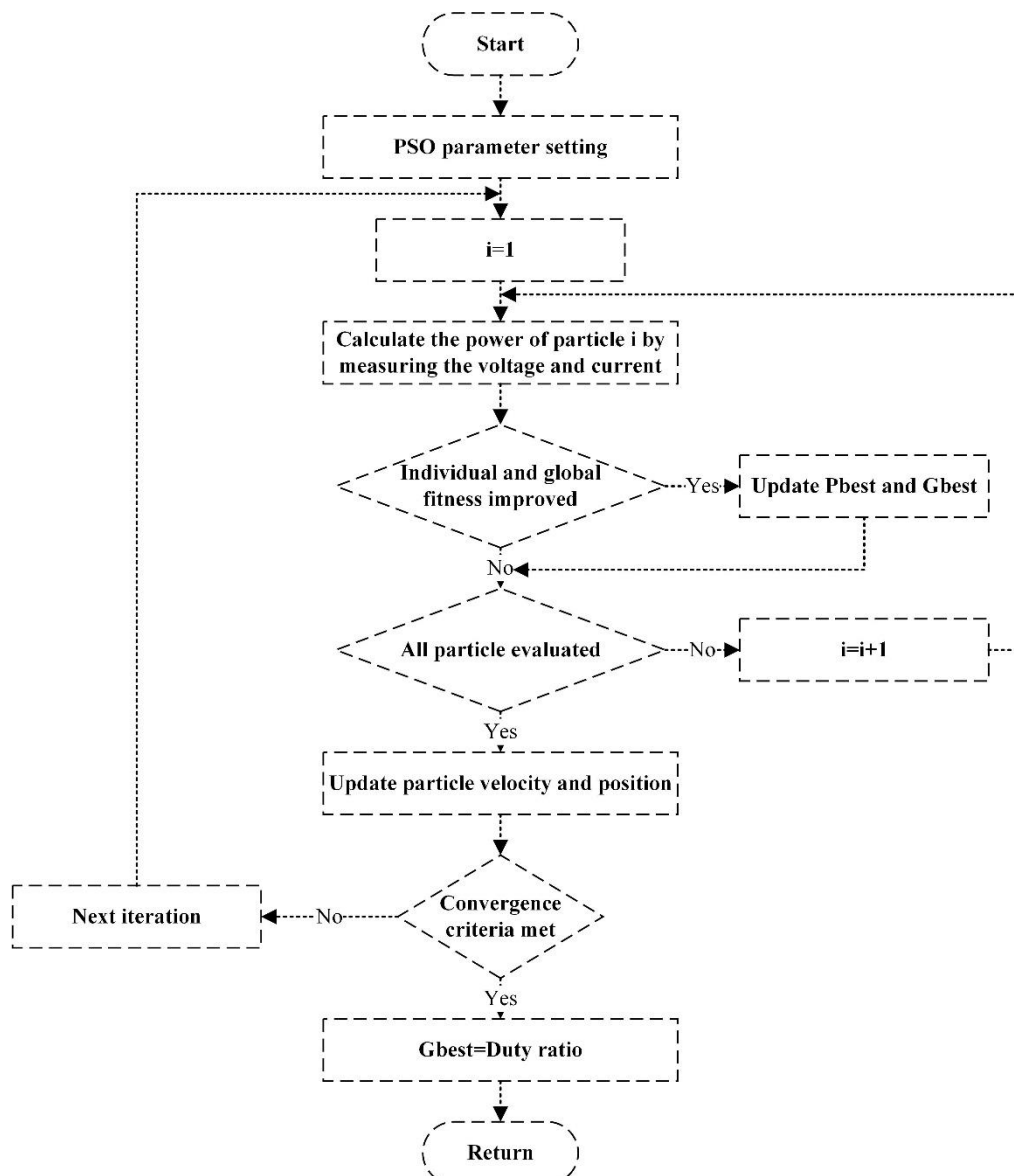


Figure 4. Flowchart of the PSO MPPT algorithm

Each particle in the PSO algorithm's population represents a distinct approach to the optimization issue. During the search process of the algorithm, the particles in the swarm continuously update their velocity and position to iteratively determine the optimal solution. Each particle communicates with its neighbors, evaluates points in a D-dimensional search space, and moves according to its best individual position (P_{best}) and the global best position (G_{best}). Thus, P_{best} and G_{best} have a role in determining where each particle is located. This leads to the swarm converging rapidly on the best possible solution. The position and velocity for each article are updated using the following equations:

$$x_i^{k+1} = x_i^k + \Phi_i^{k+1} \quad (3)$$

$$\Phi_i^{k+1} = w\Phi_i^k + c_1r_1\{P_{best} - x_i^k\} - c_2r_2\{G_{best} - x_i^k\} \quad (4)$$

Where x_i and Φ_i are the position and velocity of each particle (i) respectively, k is the iteration counter, w is the inertia weight, c_1 and c_2 are acceleration factors, r_1 and r_2 are random values that are evenly spread between 0 and 1. The fitness value of each particle is determined using the output voltage and output current of the PV array, which is denoted as the power of the PV array. The highest produced power is considered the best in the population. The PSO search process terminates after the maximum number of iterations has been achieved. In particular, when facing non-uniform solar irradiation, the use of the PSO MPPT improves the performance of the PV array and offers the greatest available amounts of power [21].

2.3. Boost-type DC-DC Converter

To maximize the output power of the PV module in a wide range of conditions, MPPT algorithms regulate the duty ratio of the PWM signal that is sent to the switch of the power conversion stage. As a high-frequency power conversion circuit between the PV array and the load, a boost-type converter is employed to increase the input voltage to higher values [22, 23].

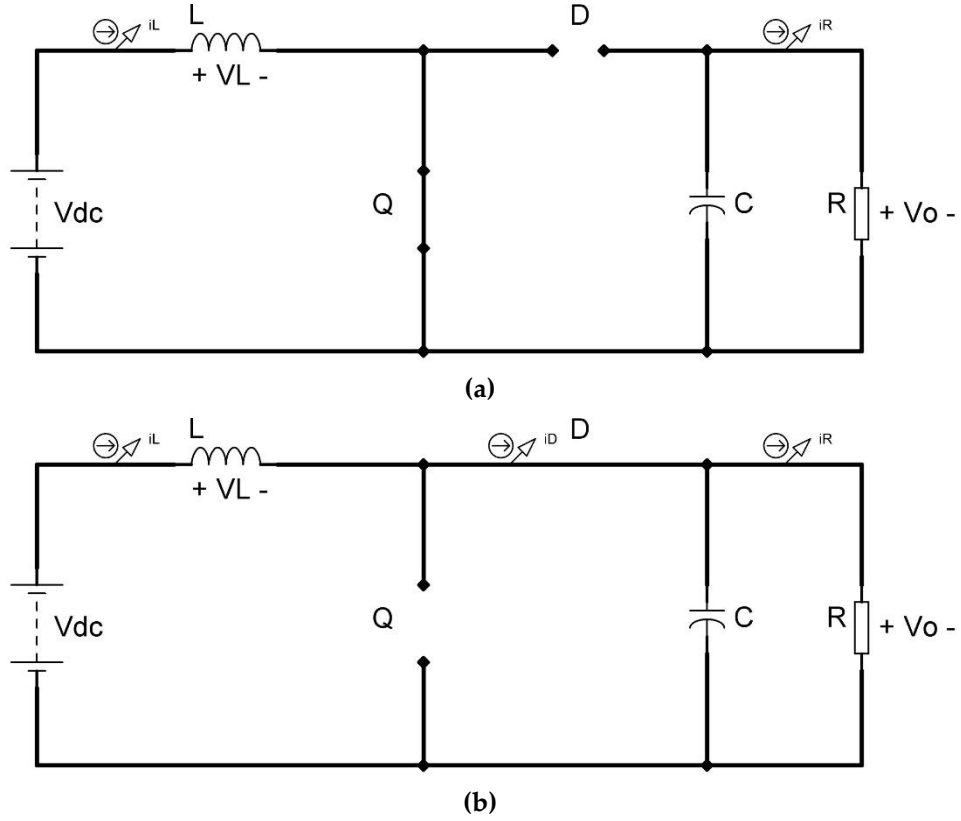


Figure 5. A boost-type DC-DC converter a) On state b) Off state

As illustrated in Figure-5, a boost-type converter consists of circuit components including a diode, an inductor, a capacitor, and a semiconductor switch. To step up DC voltage from its input, a boost-type converter has the capability of being operational in either a continuous or discontinuous conduction mode during the switching process. Because of the switching device's lower peak current and conduction losses, continuous conduction mode operation is more widely used. This can be achieved by selecting the appropriate inductor and capacitor values. During switching states, the output load receives a higher voltage because of the energy stored in the inductor's magnetic field. By adjusting the duty ratio of the PWM signal, the output voltage of the boost-type converter can be determined [22]. As given in Equation (5), the output voltage of the boost converter is proportional to its duty ratio. Equation (6) and Equation (7) are used to determine minimum inductor (L_{min}) and capacitor (C_{min}) values for the desired ripple current and output voltage ripple [24, 25]. In the below equations, V_{dc} is input voltage, V_o is output voltage, ΔD is duty ratio, ΔV_o is output voltage ripple, i_o is output current, Δi_L is inductor ripple current, and f is the switching frequency.

$$\frac{V_o}{V_{dc}} = \frac{1}{1-\Delta D} \quad (5)$$

$$L_{min} = \frac{V_{dc}(V_o - V_{dc})}{\Delta i_L f V_o} \quad (6)$$

$$C_{min} = \frac{i_o \Delta D}{f \Delta V_o} \quad (7)$$

3. RESULTS AND DISCUSSION

PSO and P&O MPPT techniques are compared based on tracking efficiency and convergence speed. Simulations are conducted on the developed Matlab/Simulink model, which is shown in Figure-6. The PV circuit model consists of a partially shaded PV array comprised of four series-connected PV modules of

250 W, a boost-type DC-DC converter with MPPT controller, and a DC load. Figure-7 depicts the PV array current-voltage curve for different solar radiations. Table 1 and Table 2 list the irradiance-temperature data, and the parameters of the selected PV module respectively. In Table 3, the specifications of the designed boost-type converter are listed for the required inductor ripple current and output voltage ripple at the switching frequency of 5 kHz.

At standard test conditions (1000 W/m² of sunlight; 25 °C cell temperature), for the boost-type converter the input voltage is 122.8 V, the output voltage is 225 V, the input current is 8.75 A, the output current is 4.25 A, and the output power is 955 W. The initial duty ratio of the boost-type converter for P&O and PSO MPPT is set to 0.1 and 0.5 respectively. Using Equation (5), Equation (6), and Equation (7), the maximum available duty ratio is 0.45, and minimum inductor (L_{min}) and capacitor (C_{min}) values are 1 mH and 470 uF respectively. The effectiveness of the PSO algorithm is dependent on the settings of its various parameters. In the swarm, the number of particles is 4, the number of iterations $k=300$, the inertia weight $w=0.4$, the acceleration factors $c1=1.2$, and $c2=2$.

In terms of performance analysis, P&O and PSO MPPT approaches are compared with uniform and two different partial shading configurations. In Figure-8, the PV array configurations under partial shading are depicted. Figure-9 shows the P-V curve under uniform and partial shading conditions. Both MPPT techniques are tested first at standard test conditions and then at two different partial shading conditions. While the solar radiation levels of the first pattern are 400 W/m², 600 W/m², 800 W/m², and 1000 W/m², the second pattern consists of 1000 W/m², 900 W/m², 700 W/m², and 400 W/m² at constant temperature (25 °C). When comparing the two different patterns for the partial shading conditions, it can be noticed that the irradiance difference of the PV modules in the first pattern is equally different from each other (200 W/m²) while it is variable in the second pattern.

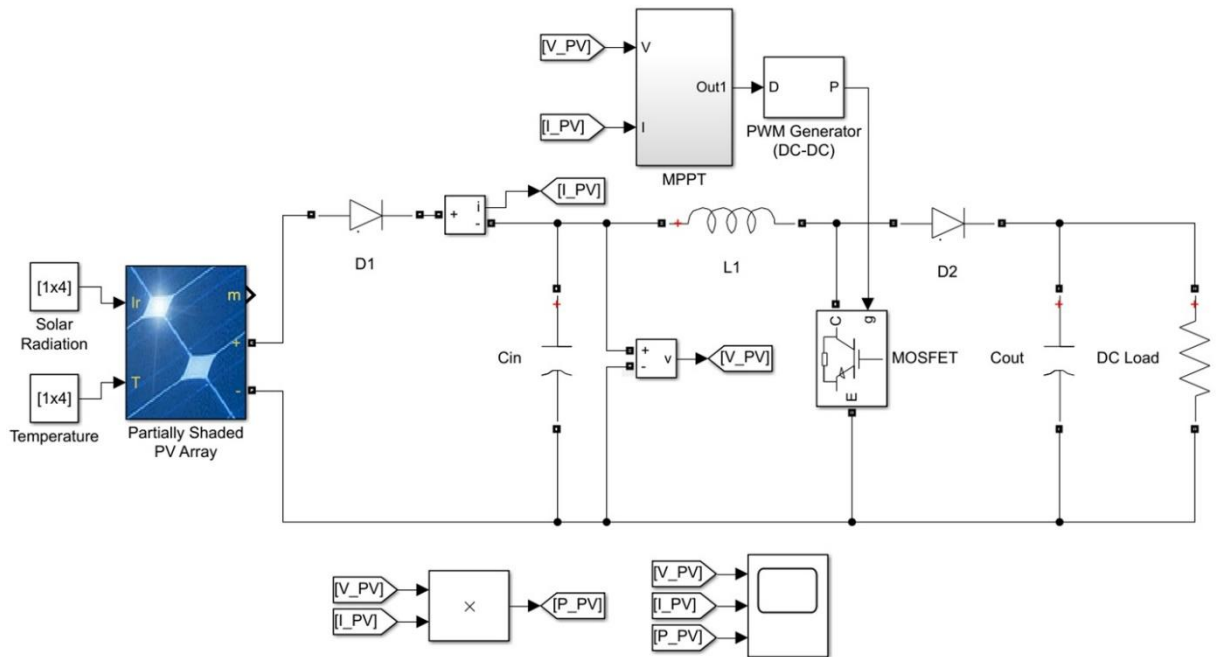
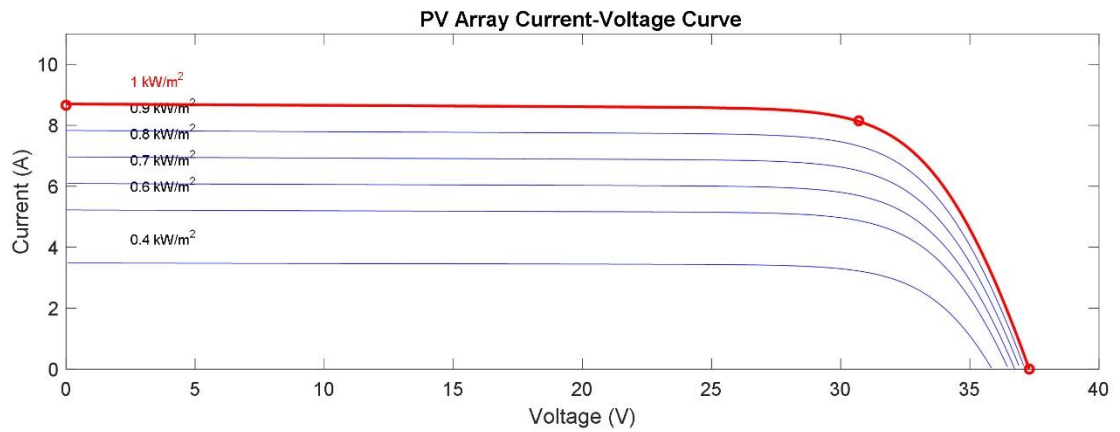


Figure 6. Matlab/Simulink model of the presented system

Table 1. The irradiance-temperature data

Irradiance (W/m ²)	Temperature (°C)
First pattern	
400 W/m ²	25 °C
600 W/m ²	25 °C
800 W/m ²	25 °C
1000 W/m ²	25 °C
Second pattern	
1000 W/m ²	25 °C
900 W/m ²	25 °C
700 W/m ²	25 °C
400 W/m ²	25 °C

**Figure 7.** PV array current-voltage curve for different solar radiations

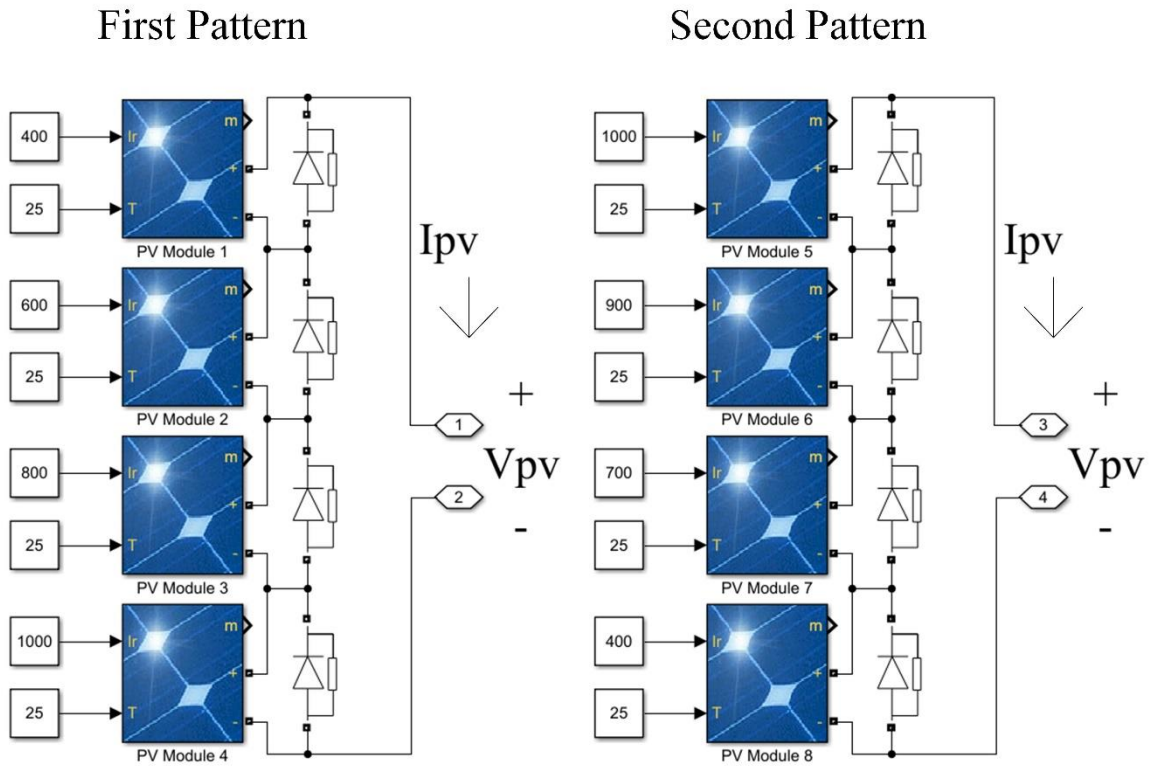


Figure 8. Patterns for partial shading conditions

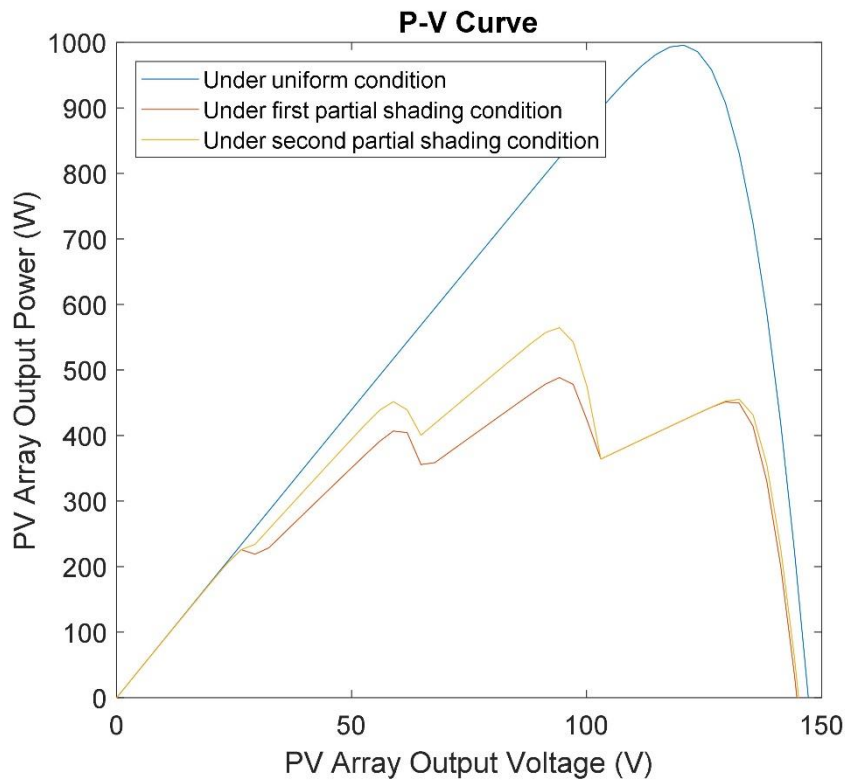


Figure 9. P-V Curve under uniform and partial shading conditions

Table 2. PV module parameters

Parameters	Values
Series-connected modules per string	4
Parallel strings	1
Cells per module (Ncell)	60
Maximum power (W)	250
Voltage at maximum power point V_{mp} (V)	30.7
Current at maximum power point I_{mp} (A)	8.15
Open circuit voltage V_{oc} (V)	37.3
Short-circuit current I_{sc} (A)	8.66
Temperature coefficient of V_{oc} (%/deg.C)	-0.36901
Temperature coefficient of I_{sc} (%/deg.C)	0.086998

Table 3. Boost-type converter specifications

Parameters	Values
Load resistance (Ω)	50
Inductance (mH)	1
Capacitance (μ F)	470
Switching frequency (kHz)	5
Inductor current ripple Δi_L	%10
Capacitor voltage ripple ΔV_o	%2

**Figure 10.** Duty cycle change for the P&O and PSO

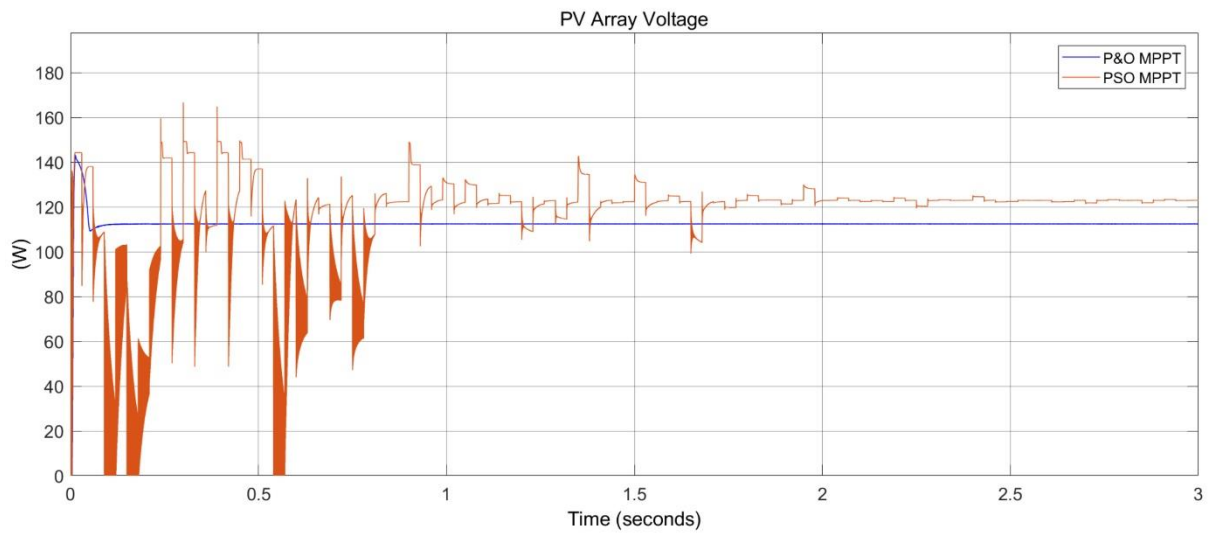


Figure 11. PV array voltage for the P&O and PSO

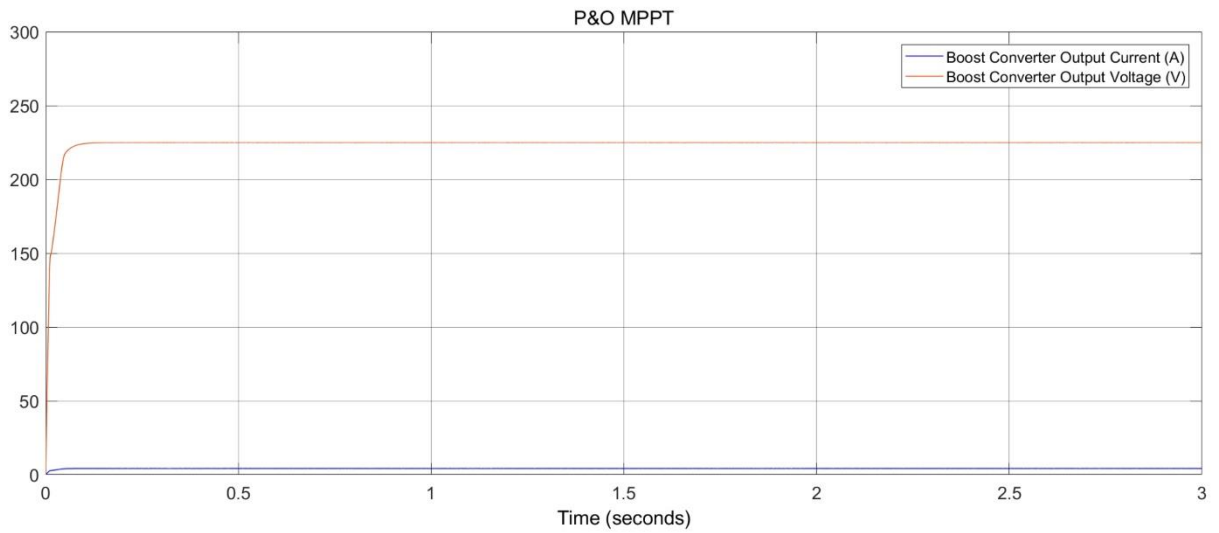


Figure 12. Boost-type DC-DC converter output current and voltage for the P&O

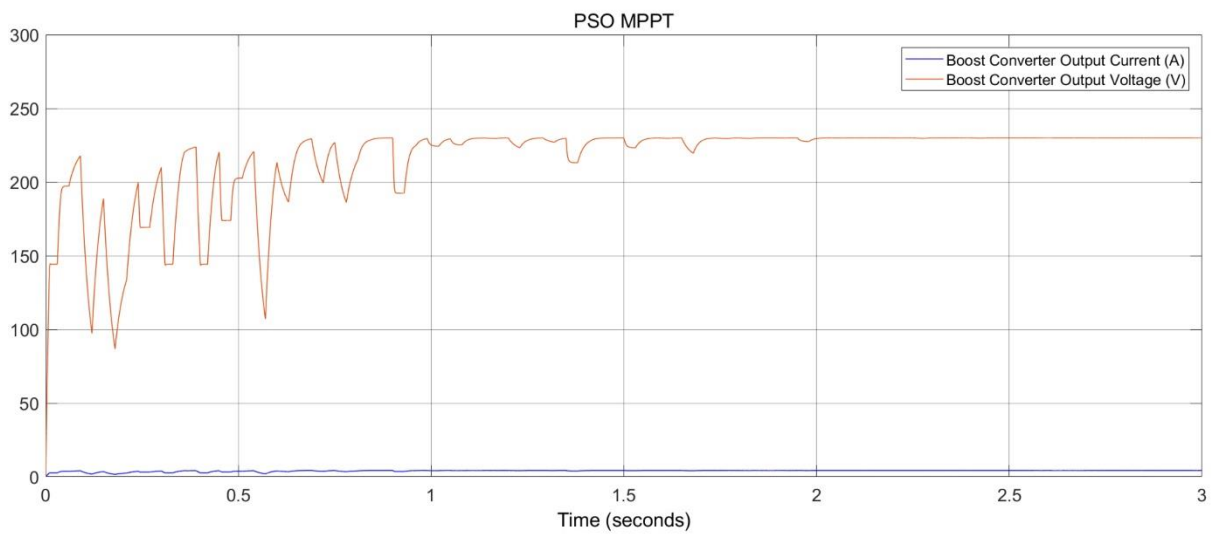


Figure 13. Boost-type DC-DC converter output current and voltage for the PSO

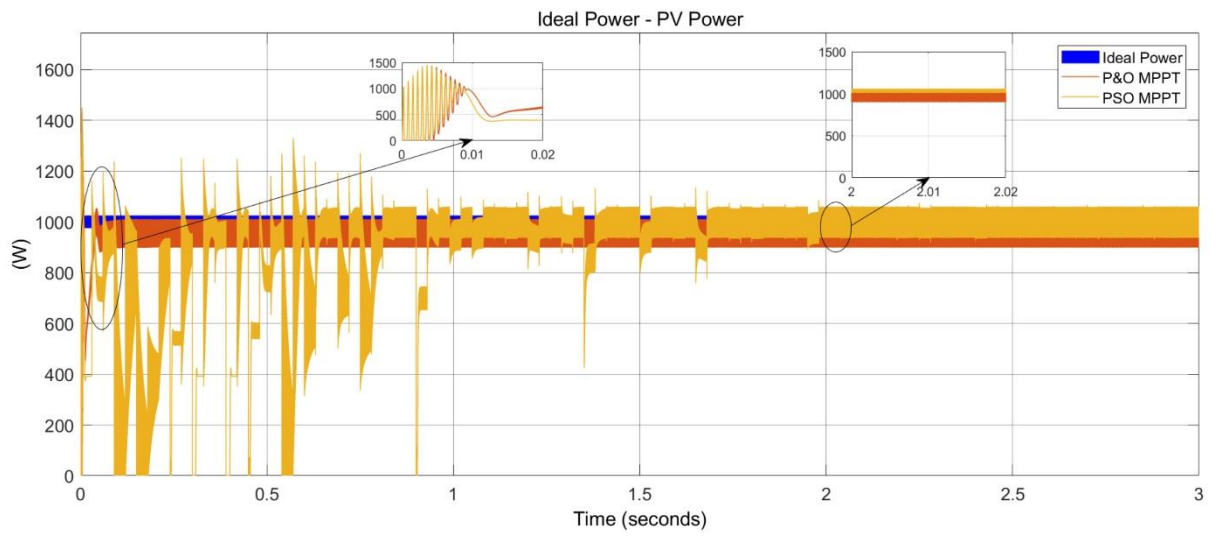


Figure 14. PV array power for the P&O and PSO at standard test conditions

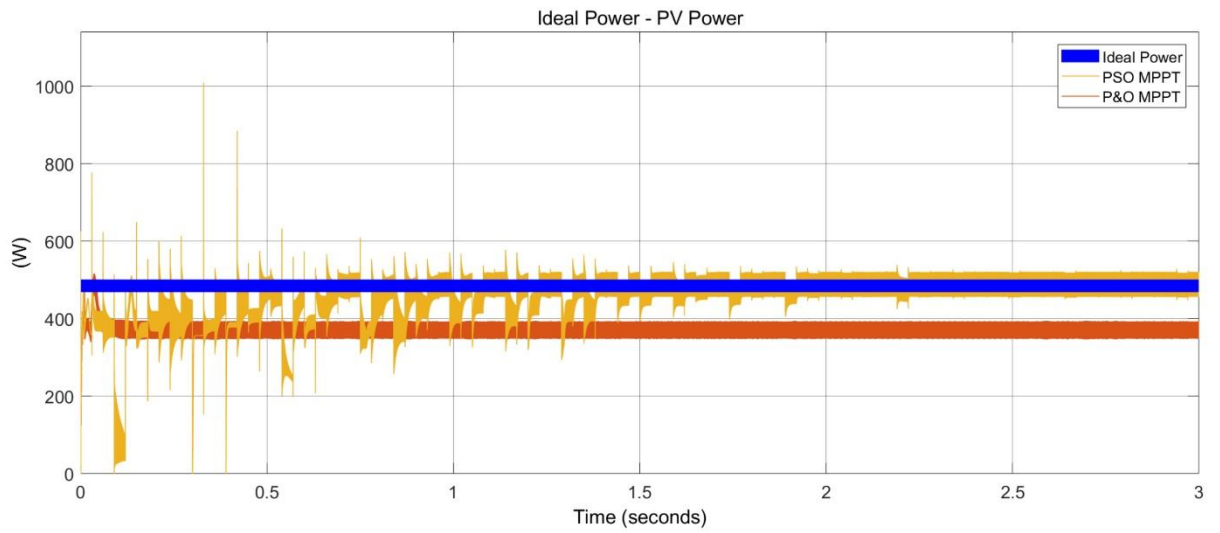


Figure 15. PV array power for the P&O and PSO at the first partial shading condition

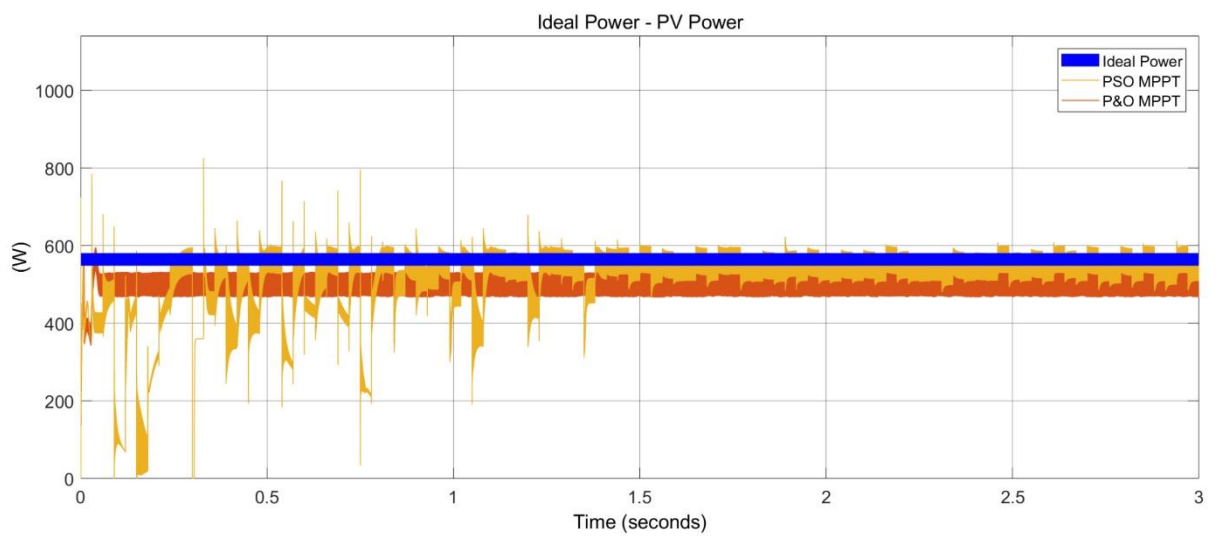


Figure 16. PV array power for the P&O and PSO at the second partial shading condition

PSO and P&O MPPT techniques are tested for 3 seconds on the Matlab/Simulink-based PV circuit model. Duty cycle change, PV array voltage, boost-type DC-DC converter output current and voltage, and PV array power for the P&O and PSO in uniform and partially shaded conditions with equally and unequally different irradiance differences are given in between Figures-10-16 respectively. As shown in Figure-14, both MPPT techniques are capable of tracking MPP under standard test conditions. However, while the PO technique stays at 980 W, the PSO technique reaches a power of 986 W during the search process. On the other hand, PSO is relatively slow in reaching the MPP compared to the P&O. The PSO algorithm caught the MPP in 1.65 seconds, while the P&O algorithm reached this in 0.2 seconds. Although the PSO is a widely used optimization algorithm for tracking the global MPP, it has power ripple and slow convergence speed due to its unique characteristics such as large search space and huge computing efforts during the search process.

Partial shading conditions cause non-uniform shading and different irradiance levels in PV arrays. The decrease in solar radiation on the surface of the PV module leads to a corresponding reduction in the total power output of the PV array. When the simulation results of the first partial shading configuration are examined as shown in Figure-15, P&O is trapped in one of the local MPPs but PSO has demonstrated considerable performance in finding the global MPP. The P&O algorithm stays at 380 W, while the PSO algorithm has a power output of 478 W.

In the second partial shading configuration as shown in Figure-16, P&O again failed to track global MPP and gets trapped in one of the local MPPs. PSO, on the other hand, is quite successful in finding the global MPP. Both MPPT techniques reach 485 W and 545 W MPP values respectively. Similar to the results of the standard test condition, P&O reveals a superior response time with 0.2 seconds and fast convergence in the presence of partial shading too. The PSO technique reaches the global MPP in 1.8 seconds and 1.5 seconds for two different partial shading conditions respectively. Compared to the previous studies, the main difference of this study is that, it observes partially shaded conditions with equal and unequal irradiance differences. When comparing the two different patterns for the partial shading conditions, it can be seen that the PSO technique has lower steady-state oscillations at the MPP in the first configuration where the sunlight intensity of the PV modules is equally different from each other. Based on the simulation results, the mean values of PV array power, tracking efficiency, and convergence speed for P&O and PSO are listed in Table 4.

Table 4. PV array power, tracking efficiency, convergence speed, and response time for P&O and PSO

Condition	MPPT	PV Array Power (W)	Tracking Efficiency (%)	Convergence Speed	Response Time (s)
Standard Test Condition	P&O	980	98	Fast	0.2
	PSO	986	98.6	Moderate	1.65
First Partial Shading Condition	P&O	380	76.5	Fast	0.2
	PSO	478	96.5	Moderate	1.8
Second Partial Shading Condition	P&O	485	85.8	Fast	0.2
	PSO	545	96.4	Moderate	1.5

4. CONCLUSIONS

The tracking efficiency and convergence speed of the P&O and PSO MPPT algorithms are compared on the designed PV circuit model built in Matlab/Simulink. Under uniform and two different partial shading configurations, the simulations are conducted. P&O and PSO techniques are successful in finding the MPP under uniform solar radiation. Under partial shading configurations, however, P&O gets trapped in the local MPP, where PSO has approached the global MPP. Regarding convergence speed, the P&O

technique is quite fast in uniform and partially shading conditions while the PSO technique takes more time to converge to global MPP. Furthermore, it can be seen that the PSO technique has reduced steady-state oscillations around the MPP in the first partial shading configuration where the irradiance difference of the PV modules is uniformly distributed. Future studies can be conducted to overcome the main limitations of the PSO technique such as longer response time to reach the maximum power and higher transient and steady-state oscillations around the MPP.

Declaration of Ethical Standards

The author declares to comply with all ethical guidelines, including authorship, citation, data reporting, and original research publication.

Declaration of Competing Interest

The author declares that he has no known competing financial interests or personal relationships that could have appeared to influence the work reported in this paper.

Funding / Acknowledgements

The author declares that he has not received any funding or research grants during the review, research, or assembly of the article.

Data Availability

Data will be made available on request.

REFERENCES

- [1] X. Zheng, D. Streimikiene, T. Balezentis, A. Mardani, F. Cavallaro, and H. Liao, "A review of greenhouse gas emission profiles, dynamics, and climate change mitigation efforts across the key climate change players," *Journal of Cleaner Production*, vol. 234, pp. 1113-1133, 2019.
- [2] A. Qazi *et al.*, "Towards sustainable energy: a systematic review of renewable energy sources, technologies, and public opinions," *IEEE access*, vol. 7, pp. 63837-63851, 2019.
- [3] S. R. Sinsel, R. L. Riemke, and V. H. Hoffmann, "Challenges and solution technologies for the integration of variable renewable energy sources—a review," *renewable energy*, vol. 145, pp. 2271-2285, 2020.
- [4] C. Gao and H. Chen, "Electricity from renewable energy resources: Sustainable energy transition and emissions for developed economies," *Utilities Policy*, vol. 82, p. 101543, 2023.
- [5] E. Kabir, P. Kumar, S. Kumar, A. A. Adelodun, and K.-H. Kim, "Solar energy: Potential and future prospects," *Renewable and Sustainable Energy Reviews*, vol. 82, pp. 894-900, 2018.
- [6] B. Parida, S. Iniyar, and R. Goic, "A review of solar photovoltaic technologies," *Renewable and sustainable energy reviews*, vol. 15, no. 3, pp. 1625-1636, 2011.
- [7] N. Sharma and V. Puri, "Solar energy fundamental methodologies and its economics: A review," *IETE Journal of Research*, vol. 69, no. 1, pp. 378-403, 2023.
- [8] A. Karafil, H. Ozbay, and M. Kesler, "Temperature and solar radiation effects on photovoltaic panel power," *Journal of New Results in Science*, vol. 5, pp. 48-58, 2016.
- [9] S. Motahhir, A. El Hammoumi, and A. El Ghzizal, "The most used MPPT algorithms: Review and the suitable low-cost embedded board for each algorithm," *Journal of cleaner production*, vol. 246, p. 118983, 2020.
- [10] N. Karami, N. Moubayed, and R. Outbib, "General review and classification of different MPPT Techniques," *Renewable and Sustainable Energy Reviews*, vol. 68, pp. 1-18, 2017.

- [11] F. A. Omar, G. Gökkuş, and A. A. KULAKSIZ, "ŞEBEKEDEN BAĞIMSIZ FV SİSTEMDE MAKSİMUM GÜÇ NOKTASI TAKİP ALGORİTMALARININ DEĞİŞKEN HAVA ŞARTLARI ALTINDA KARŞILAŞTIRMALI ANALİZİ," *Konya Journal of Engineering Sciences*, vol. 7, no. 3, pp. 585-594, 2019.
- [12] Z. Salam, J. Ahmed, and B. S. Merugu, "The application of soft computing methods for MPPT of PV system: A technological and status review," *Applied energy*, vol. 107, pp. 135-148, 2013.
- [13] H. Rezk, A. Fathy, and A. Y. Abdelaziz, "A comparison of different global MPPT techniques based on meta-heuristic algorithms for photovoltaic system subjected to partial shading conditions," *Renewable and Sustainable Energy Reviews*, vol. 74, pp. 377-386, 2017.
- [14] S. Figueiredo and R. N. A. L. e Silva, "Hybrid mppt technique pso-p&o applied to photovoltaic systems under uniform and partial shading conditions," *IEEE Latin America Transactions*, vol. 19, no. 10, pp. 1610-1617, 2021.
- [15] S. Makhloufi and S. Mekhilef, "Logarithmic PSO-based global/local maximum power point tracker for partially shaded photovoltaic systems," *IEEE Journal of Emerging and Selected Topics in Power Electronics*, vol. 10, no. 1, pp. 375-386, 2021.
- [16] O. M. Elbadri, K. M. Mohammed, and Z. I. Saad, "Comparison of P&O and PSO Algorithms using Matlab/Simulink," in *The 7th International Conference on Engineering & MIS 2021*, 2021, pp. 1-7.
- [17] H. El Hammedi, J. Chroua, H. Khaterchi, and A. Zaafouri, "Comparative study of MPPT algorithms: P&O, INC, and PSO for PV system optimization," in *2023 9th International Conference on Control, Decision and Information Technologies (CoDIT)*, 2023: IEEE, pp. 2683-2688.
- [18] A. M. Humada, M. Hojabri, S. Mekhilef, and H. M. Hamada, "Solar cell parameters extraction based on single and double-diode models: A review," *Renewable and Sustainable Energy Reviews*, vol. 56, pp. 494-509, 2016.
- [19] D. Sera, L. Mathe, T. Kerekes, S. V. Spataru, and R. Teodorescu, "On the perturb-and-observe and incremental conductance MPPT methods for PV systems," *IEEE journal of photovoltaics*, vol. 3, no. 3, pp. 1070-1078, 2013.
- [20] J. Kennedy and R. Eberhart, "Particle swarm optimization," in *Proceedings of ICNN'95-international conference on neural networks*, 1995, vol. 4: IEEE, pp. 1942-1948.
- [21] A. Khare and S. Rangnekar, "A review of particle swarm optimization and its applications in solar photovoltaic system," *Applied Soft Computing*, vol. 13, no. 5, pp. 2997-3006, 2013.
- [22] K. V. G. Raghavendra *et al.*, "A comprehensive review of DC-DC converter topologies and modulation strategies with recent advances in solar photovoltaic systems," *Electronics*, vol. 9, no. 1, p. 31, 2019.
- [23] R. B. Gonzatti, Y. Li, M. Amirabadi, B. Lehman, and F. Z. Peng, "An overview of converter topologies and their derivations and interrelationships," *IEEE Journal of Emerging and Selected Topics in Power Electronics*, vol. 10, no. 6, pp. 6417-6429, 2022.
- [24] R. Ayop and C. W. Tan, "Design of boost converter based on maximum power point resistance for photovoltaic applications," *Solar energy*, vol. 160, pp. 322-335, 2018.
- [25] H. Tarzamni, H. S. Gohari, M. Sabahi, and J. Kyyrä, "Non-isolated high step-up dc-dc converters: comparative review and metrics applicability," *IEEE Transactions on Power Electronics*, 2023.



ESTIMATING THE POWER DRAW OF GRIZZLY FEEDERS USED IN CRUSHING–SCREENING PLANTS THROUGH SOFT COMPUTING ALGORITHMS

*Ekin KÖKEN 

Abdullah Gül University, Engineering Faculty, Nanotechnology Engineering Department, Kayseri, TÜRKİYE
ekin.koken@agu.edu.tr

Highlights

- The power draw (P) of grizzly feeders is investigated based on their common working conditions.
- Soft computing analyses are performed to build predictive models by considering the collected data.
- The most reliable predictive model is found to be based on the adaptive neuro-fuzzy inference system methodology.



ESTIMATING THE POWER DRAW OF GRIZZLY FEEDERS USED IN CRUSHING–SCREENING PLANTS THROUGH SOFT COMPUTING ALGORITHMS

*Ekin KÖKEN 

Abdullah Gül University, Engineering Faculty, Nanotechnology Engineering Department, Kayseri, TÜRKİYE
ekin.koken@agu.edu.tr

(Received: 14.10.2023; Accepted in Revised Form: 02.01.2024)

ABSTRACT: In this study, the power draw (P) of several grizzly feeders used in the Turkish Mining Industry (TMI) is investigated by considering the classification and regression tree (CART), random forest (RF) and adaptive neuro-fuzzy inference system (ANFIS) algorithms. For this purpose, a comprehensive field survey is performed to collect quantitative data, including power draw (P) of some grizzly feeders and their working conditions such as feeder width (W), feeder length (L), feeder capacity (Q), and characteristic feed size (F_{80}). Before applying the soft computing methodologies, correlation analyses are performed between the input parameters and the output (P). According to these analyses, it is found that W and L are highly associated with P. On the other hand, Q is moderately correlated with P. Consequently, numerous soft computing models were run to estimate the P of the grizzly feeders. Soft computing analysis results demonstrate no superiority between the performances of RF and CART models. The RF analysis results indicate that the W is necessary for evaluating P for grizzly feeders. On the other hand, the ANFIS-based predictive model is found to be the best tool to estimate varying P values, and it satisfies promising results with a correlation of determination value (R^2) of 0.97. It is believed that the findings obtained from the present study can guide relevant engineers in selecting the proper motors propelling grizzly feeders.

Keywords: *Adaptive neuro-fuzzy inference system, Classification and regression tree, Grizzly feeder, Power draw, Random forest*

1. INTRODUCTION

Conveyor belts and feeders are among the most critical components in handling a wide range of bulk materials from meter to millimeter scale. In this context, they should ensure accurate and uniform discharge from storage to the upcoming system. Regarding mining engineering applications such as crushing-screening and ore-dressing plants, feeders are of prime importance to maintaining plant sustainability [1]. In crushing–screening plants, grizzly and apron-type feeders are commonly used to increase the capacity and efficiency of primary crushing equipment [2–6].

Primary considerations in deciding which type of feeder to use are the properties of the bulk material being handled (e.g., cohesiveness, maximum particle size, particle friability, propensity for dust generation) [7]. Based on this approach, grizzly feeders may be an alternative to apron feeders when handling bulk materials with high amounts of dust.

Grizzly feeders are typically located before primary crushing equipment in most crushing-screening plants [5, 8, 9]. The main advantage of using grizzly feeders in crushing–screening plants is that grizzly feeders can feed the crushing equipment and remove the undesired particles from the feeding material by sieving simultaneously. In addition, when considering engineering economics, grizzly feeders are cheaper than apron feeders.

In most cases, the selection of proper grizzly feeders is based on the capacity of the primary crushing equipment [10]. For jaw crushers, the geometric properties (i.e., width and length) and the fill factor of grizzly feeders are also important parameters for the suitability and adaptation of these feeders [11]. It is worth reminding that to diminish the undesired effects of vibration arising from primary crushing equipment, Lyashenko et al. [12] proposed a novel design for the bars of grizzly feeders that improved

*Corresponding Author: Ekin Köken, ekin.koken@agu.edu.tr

their efficiency. On the other hand, the power draw (P) of grizzly feeders is highly affected by the vibration of rock-crushing equipment. Since the vibration is associated with the geometric properties and engine power of grizzly feeders, a true determination of power draw propelling grizzly feeders is necessary. However, there is a lack of literature directly focusing on some predictive models that estimate varying P values based on different working conditions.

In this study, the P of grizzly feeders is investigated in a detailed manner. For this purpose, a comprehensive field survey is conducted to collect quantitative data from several crushing–screening plants in Turkey. Soft computing analyses are performed using the collected data to obtain feasible predictive models for estimating the P for different grizzly feeders.

2. MATERIAL AND METHODS

A comprehensive field survey was conducted to collect quantitative data on grizzly feeders operating in several crushing–screening plants in Turkey. Based on the field survey including 44 mining companies, quantitative data were collected on the working conditions (e.g., conveyor speed (V), the height of the material being conveyed (H), capacity (Q), and characteristic feed size (F_{80})) geometric features (feeder width, (W) and feeder length (L)) and power draw (P) of some grizzly feeders. A working grizzly feeder is shown in Fig 1.

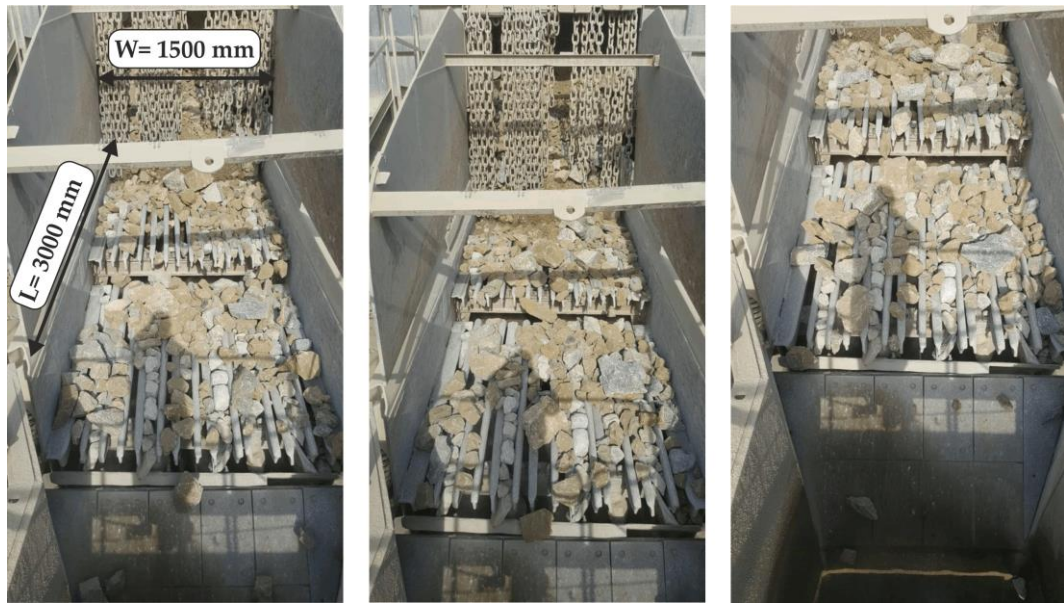


Figure 1. Illustration of a working grizzly feeder.

The Q of grizzly feeders was calculated using Eq 1 [11].

$$Q = 3600 \otimes V \otimes W \otimes H \otimes t_1 \otimes t_2 \quad (1)$$

Where V is conveyor speed (m/s), W is feeder width (m), H is the average material height on feeder (m), t_1 is the size factor ($t_1 = 1$, for sands, $t_1 = 0.80$ to 0.90 for crushed stones up to 152 mm and $t_1 = 0.60$ for crushed stoned over 152 mm) and t_2 is the moisture factor ($t_2 = 1$ for dry material, $t_2 = 0.8$ wet material and $t_2 = 0.6$ for adhesive material like clays).

Furthermore, it should be mentioned that F_{80} was calculated based on detailed sieve analyses using the particles directly flowing on grizzly feeders. The H was determined by measuring the average height of materials transported on grizzly feeders. The quantitative information on the geometric (W , L) and working conditions (e.g., V and P) of grizzly feeders was obtained by considering the catalogues of installed grizzly feeders.

2.1. Soft Computing Methods

In this study, three well-established soft computing methods are adopted. These are based on adaptive neuro-fuzzy inference system (ANFIS), classification and regression tree (CART) and random forest (RF) methodologies. The CART is a machine-learning method for establishing classification and predictive models. Decision trees are represented by a set of questions which splits the learning sample into smaller and smaller parts [13]. A regression tree is similar to a classification tree, except that the dependent variable takes ordered values, and a regression model is fitted to each node, giving some outputs [14].

For the last decades, the CART methodology has been used in different mining engineering disciplines. For example, Hasanipanah et al. [15] employed the CART method to estimate blast-induced ground vibration. Their findings demonstrated that the performance of the CART method is better than that of conventional regression models. By adopting the CART method, Salimi et al. [16] proposed a robust predictive model to evaluate the performance of tunnel boring machines (TBM). Last but not least, Bharti et al. [17] performed detailed slope stability analyses using the CART methodology.

Random Forest (RF) is also a machine-learning method developed by Breiman [18]. Compared with conventional decision trees, RF is more accurate and runs efficiently on large datasets [19]. Based on modern mining engineering approaches, RF has been successfully employed to solve many problems. For example, Matin et al. [20] adopted RF to select exact variables for evaluating rock strength properties. Zhao and Wu [21] proposed a predictive model to estimate the height of the fractured water-conduction zone of coal strata. Gu et al. [22] also used RF to monitor the deformations of a concrete dam in China.

Considering many advantages, researchers have also used an adaptive neuro-fuzzy inference system (ANFIS) to build predictive models used in many engineering problems [23–26]. The main advantage of ANFIS is that it practices a hybrid learning process to estimate the premise and consequent parameters [27].

2.2. Data Documentation

In this study, CART, RF and ANFIS methodologies were adopted to establish some predictive models to estimate the P of grizzly feeders. The CART and RF analyses were performed using Salford Predictive Modeler software. On the other hand, ANFIS analyses were performed in the MATLAB environment. Table 1 shows descriptive statistics of the variables considered in this study.

Table 1. Descriptive statistics of the variables.

Variable	Mean	Std. dev.	Min	Max
F ₈₀ (mm)	426.6	128.7	135	731
H (m)	0.295	0.087	0.09	0.48
V (m/s)	0.294	0.076	0.12	0.47
W (m)	1.21	0.33	0.6	2.1
L (m)	4.40	1.33	1.8	6.0
Q (t/h)	784.5	470.2	116.6	1827.4
P (kW)	21.26	12.36	3.00	55.00

**Note: the number of samples (n) is 44 for each parameter.*

Correlation analyses were also conducted before soft computing analyses to reveal the factors affecting the P of grizzly feeders. Accordingly, the W and L are highly associated with the P. The Q and F₈₀ have moderate and minor effects on the P, respectively (Table 2). Although H has a more significant impact than F₈₀ on the P, H was not considered an input parameter due to a close relationship between H and Q.

Table 2. Correlation analysis results.

Parameter	W	L	F ₈₀	Q	H	V	P
W	1						
L	0.710	1					
F ₈₀	-0.277	0.126	1				
Q	0.469	0.691	0.175	1			
H	0.242	0.353	0.066	0.858	1		
V	-0.101	0.008	0.296	0.419	0.010	1	
P	0.822	0.819	-0.124	0.558	0.322	0.027	1

Note: Bolded values (e.g., **0.822**) indicate the parameters used in soft computing analyses.

3. RESULTS AND DISCUSSION

As a result of soft computing analyses, three robust predictive models were obtained. When considering the CART model, L, W, and F₈₀ were input parameters. Average values in red boxes in Figure 2 were assumed to be estimated P values. The estimated P values were obtained based on the if-then rules summarized in Figure 2. In the RF analyses, mean squared error (MSE) was assumed to be the fitness function. The number of trees in the RF analyses was 200. The database (n=44) was divided into training (70/100) (Figure 3a) and testing (30/100) parts (Figure 3b). As a result of the RF analyses, another robust predictive model was obtained. The W was found to have the most significant influence on the P (Figure 3c).

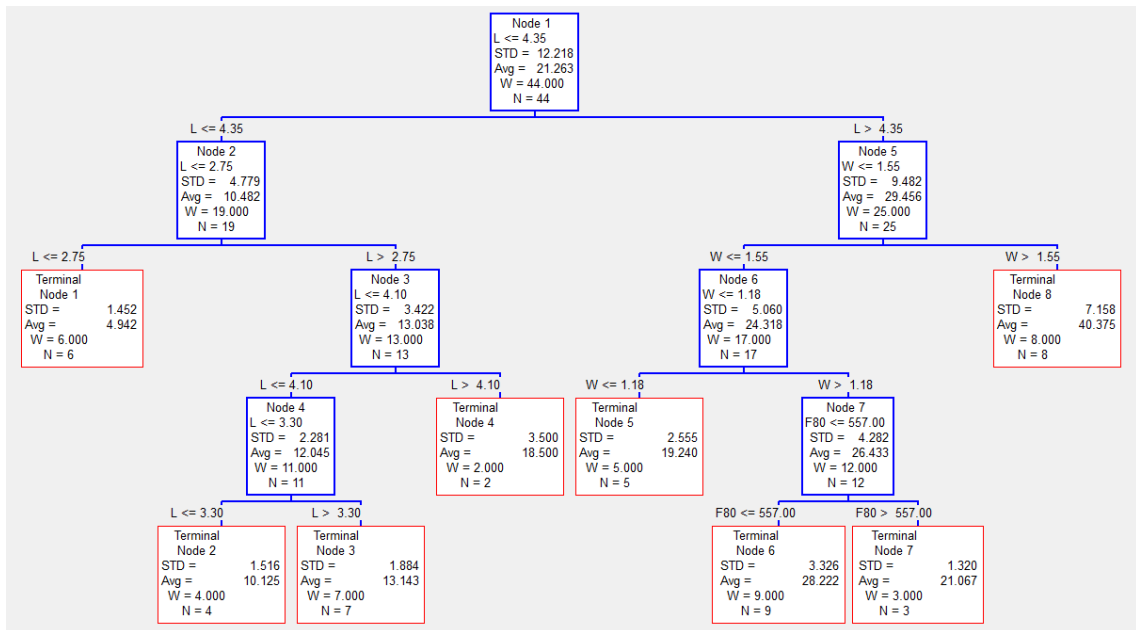


Figure 2. CART decision tree.

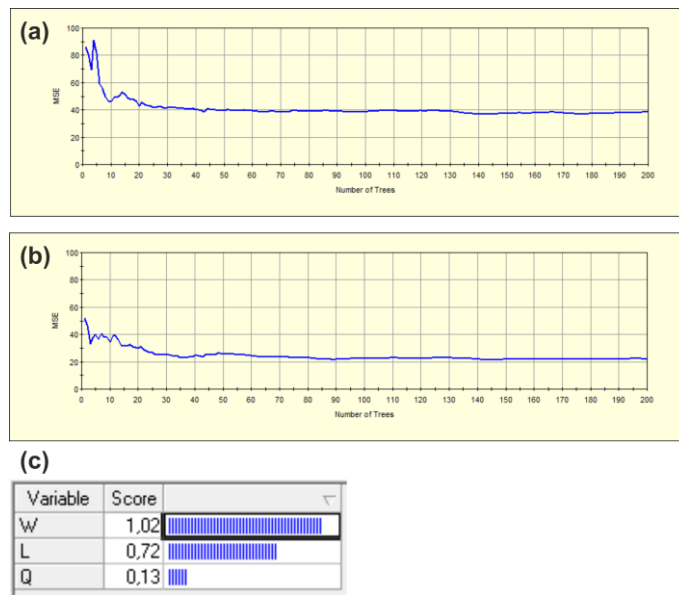


Figure 3. RF outputs a) Training process b) Testing process c) Relative importance of the input parameters.

The input parameters in the developed ANFIS model were W, L, F₈₀, and Q (Figure 4a). During the training process, ANFIS analyses continued until the minimum relative error was achieved (Figure 4b). Similar to what has been done previously, the dataset was divided into training (70/100) and testing (30/100) datasets. The ANFIS model structure is given in Figure 4c. For each input parameter, four Gaussian membership functions were defined (Figure 4d), and based on four if-then rules, P values were estimated.

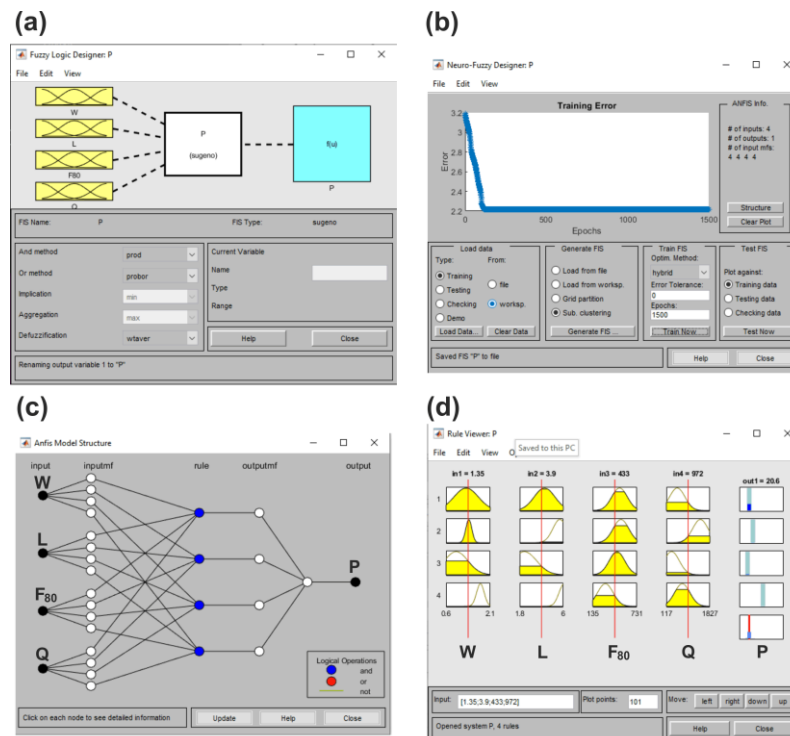


Figure 4. ANFIS outputs a) Input parameters, b) Training process c) ANFIS model structure d) Rule viewer.

The performance of the proposed models was visualized through scatter plots (Figure 5).

Accordingly, the ANFIS model was found to be the best predictive tool with a correlation of determination value (R^2) of 0.97. When compared to the performance of the CART and RF models, there is no superiority in estimating varying P values. Nevertheless, these models (CART and RF) gave undulating results when considering grizzly feeders with higher capacity ($P > 37$ kW). This phenomenon was not observed in the ANFIS model.

Moreover, the performance of the proposed predictive models was also revealed by a comprehensive performance evaluation table (Table 3) based on some performance indicators such as R^2 and root means square error (RMSE). Accordingly, for the training data ($n=31$), the R^2 and RMSE values were found to be between 0.887 – 0.966 and 2.136 – 4.223 kW, respectively. Based on the testing data ($n=13$), these values were better than the ones found in the training data. Based on this performance evaluation table, different statistical indicators suggest that the best predictive model in this study is based on the ANFIS methodology.

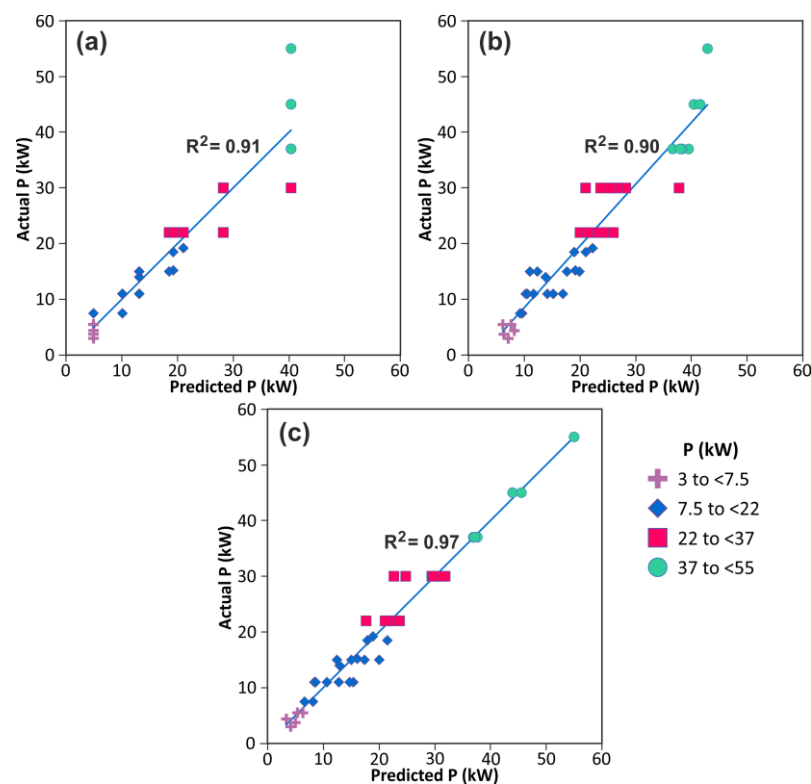


Figure 5. Scatter plots of the proposed models (a) CART (b) RF (c) ANFIS

Table 3. Statistical indicators of the proposed models.

Statistical indicator	Methodology	Training Data (70/100, n = 31)	Testing Data (30/100, n = 13)	All data (n=44)
R^2	CART	0.887	0.960	0.908
	RF	0.897	0.937	0.905
	ANFIS	0.966	0.972	0.968
RMSE (kW)	Methodology	Training Data (70/100, n = 31)	Testing Data (30/100, n = 13)	All data (n=44)
	CART	4.223	2.245	3.749
	RF	4.148	3.429	3.949
	ANFIS	2.316	1.949	2.214

It was also found that the proposed ANFIS method acts differently based on varying P classes. In this study, four different P classes were defined based on a k-means clustering algorithm.

For example, the average relative error (ARE) decreases with increasing the capacity of the grizzly feeders (e.g., $37\text{kW} \leq P < 55\text{kW}$). The ARE values for these classes were found to be as follows:

- Class I (3 to < 7.5 kW), ARE = 22.65%
- Class II (7.5 to < 22 kW), ARE = 15.30%
- Class III (22 to < 37 kW), ARE = 6.39%
- Class IV (37 to < 55 kW), ARE = 0.88%

To the best of the corresponding author's knowledge, there is no investigation in the literature on the P of grizzly feeders. In this context, the findings obtained from the present study can guide one willing to design a proper grizzly feeder in a crushing-screening plant. Nonetheless, the number of case studies should be increased to improve the CART and RF models.

For this purpose, additional input parameters, such as the flow characteristics of the materials being conveyed, might also be necessary. In addition, a continuous material flow on grizzly feeders, which means a fixed H value, should also be required to sustain and select proper engines in material transportation.

Finally, in order to implement the ANFIS methodology, a design chart was also developed based on the typical working conditions of grizzly feeders. In this design chart (Figure 6), different P values can be easily estimated by considering the parameters of W, L, and Q. It is worth remembering that this design table is based on some assumptions, such as $H \leq 0.5W$ and $F_{80} = 250$ mm. These assumptions are typical for most grizzly feeders operating in crushing-screening plants from the database specified.

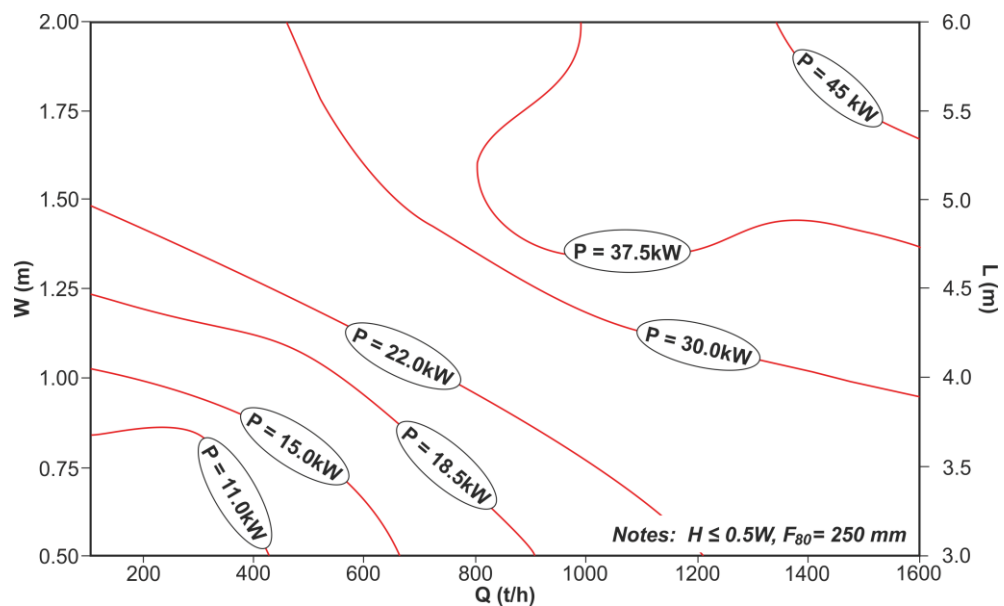


Figure 6. Proposed design chart to estimate the P based on different design parameters.

4. CONCLUSIONS

The present study introduces robust predictive models to estimate the P of different grizzly feeders. For this purpose, a comprehensive field survey is conducted to collect quantitative data on the grizzly feeders used in several crushing-screening plants in Turkey (Table 1).

Several soft computing analyses were performed based on the collected data. As a result of these analyses, three predictive models were obtained to evaluate varying P values. The R^2 values for the models are between 0.90 and 0.97, showing their relative success (Figure 5). The best predictive model to estimate the P values is based on the ANFIS methodology. Nevertheless, there is no significant difference between the performance of the CART and RF models.

In order to implement the proposed ANFIS methodology, a design chart is also provided in this study (Figure 6). Different P values can be easily estimated by using this design chart based on various parameters of W, L and Q. In this manner, the present study is believed to be beneficial to those who want to design proper grizzly feeders applicable for crushing – screening plants.

Declaration of Competing Interest

The author declares that he has no known competing financial interests or personal relationships that could have influenced the work reported in this paper.

Funding

This research paper did not receive any specific grant from public, commercial, or not-for-profit funding agencies.

Data Availability

Enquiries about data availability should be directed to the corresponding author.

REFERENCES

- [1] R.L. Attridge, "New mine developments-The Navachab Gold Mine." *Journal of the Southern African Institute of Mining and Metallurgy*, vol 91(3), 104-107, 1991
- [2] S.K. Singh, S.G. Nair, "Stochastic modeling and analysis of stone crushing system used in Iron ore mines." *Journal of Ravishankar University*, vol 8(1), 101-114, 1995
- [3] B.P. Numbi, J. Zhang, X. Xia, "Optimal energy management for a jaw crushing process in deep mines." *Energy*, 68, 337-348, 2014
- [4] F.A. Munandar, S. Sriyanti, Y. Yuliadi, "Evaluasi Kinerja Unit Crushing Plant Batu Andesit pada PT Silva Andia Utama di Desa Giri Asih, Kecamatan Batujajar, Kabupaten Bandung, Provinsi Jawa Barat." *Prosiding Teknik Pertambangan*, 486-494, 2018
- [5] M.R.E. Trisna, S. Widayati, P. Pramusanto, "Kajian Teknis Unit Crushing Plant Batu Andesit di PT Panghegar Mitra Abadi, Desa Lagadar, Kecamatan Marga Asih, Kabupaten Bandung, Provinsi Jawa Barat." *Prosiding Teknik Pertambangan*, 41-48, 2018
- [6] G. Antarfallah, S. Widayati, S. Rancangan Crushing Plant Tambang Sirtu di CV Barokah Laksana Jaya, Desa Margaluyu, Kecamatan Leles, Kabupaten Garut, Provinsi Jawa Barat. In *Bandung Conference Series: Mining Engineering* vol 3(1), 203-209, 2023
- [7] J.W. Carson, "Step-by-step process in selecting a feeder." *Chem. Process., Powder Solids Annu*, 38-41, 2000
- [8] A. Fakhry, L. Pulungan, S. Widayati, S. "Studi Perancangan Stone Crushing Plant di PT Cahaya Baru Madani, Desa Giriasih Kecamatan Batujajar, Kabupaten Bandung Barat Provinsi Jawa Barat." *Prosiding Teknik Pertambangan*, 287-296, 2020
- [9] E.O. Elgendi, K. Shawki, "Automated process control system of Jaw crusher production." In *Journal of Physics: Conference Series* (Vol. 2128, No. 1, p. 012034). IOP Publishing, 2021
- [10] G. Harbort, G. Cordingley, M. Phillips, "The Integration of Geometallurgy with Plant Design", In *metallurgical plant design and operating strategies*, Perth, Australia, 2011
- [11] Metso, *Crushing and Screening Handbook*, sixth edition (eds. Keijo Viilo), Metso Corporation, 2011
- [12] V.I. Lyashenko, V.Z. Dyatchin, V.P. Franchuk, "The Improvement in the Efficiency and Reliability of the Operation of the GPK Type Vibrating Grizzly Feeder for the Mining Industry." *Ferrous Metallurgy. Bulletin of Scientific, Technical and Economic Information*, (3), 28-33, 2015
- [13] R. Timofeev, *Classification and regression trees (CART) theory and applications*, Master Thesis

- (unpublished), Humboldt University, Berlin, 2004
- [14] W.Y. Loh, "Classification and regression trees" Wiley interdisciplinary reviews: data mining and knowledge discovery, 1(1), 14-23, 2011
- [15] M. Hasanipanah, R.S. Faradonbeh, H.B. Amnieh, D.J. Armaghani, M. Monjezi, Forecasting blast-induced ground vibration developing a CART model. *Engineering with Computers*, 33, 307-316, 2017
- [16] A. Salimi, R.S. Faradonbeh, M. Monjezi, C. Moormann, "TBM performance estimation using a classification and regression tree (CART) technique." *Bulletin of Engineering Geology and the Environment*, 77, 429-440, 2018
- [17] J.P. Bharti, P. Mishra, U. Moorthy, V.E. Sathishkumar, Y. Cho, P. Samui, "Slope stability analysis using Rf, gbm, cart, bt and xgboost." *Geotechnical and Geological Engineering*, 39, 3741-3752, 2021
- [18] L. Breiman, "Random forests." *Machine learning*, 45, 5-32, 2001
- [19] L. Collins, G. McCarthy, A. Mellor, G. Newell, L. Smith, L. "Training data requirements for fire severity mapping using Landsat imagery and random forest". *Remote Sensing of Environment*, 245, 111839, 2020
- [20] S.S. Matin, L. Farahzadi, S. Makaremi, S.C. Chelgani, G.H. Sattari, "Variable selection and prediction of uniaxial compressive strength and modulus of elasticity by random forest". *Applied Soft Computing*, 70, 980-987, 2018
- [21] D. Zhao, Q. Wu, "An approach to predict the height of fractured water-conducting zone of coal roof strata using random forest regression." *Scientific Reports*, 8(1), 10986, 2018
- [22] H. Gu, M. Yang, C.S. Gu, X.F. Huang, "A factor mining model with optimized random forest for concrete dam deformation monitoring." *Water Science and Engineering*, 14(4), 330-336, 2021
- [23] N. Yesiloglu-Gultekin, C. Gokceoglu, E.A. Sezer, "Prediction of uniaxial compressive strength of granitic rocks by various nonlinear tools and comparison of their performances." *International Journal of Rock Mechanics and Mining Sciences*, 62, 113-122, 2013
- [24] L.K. Sharma, V. Vishal, T.N. Singh, "Developing novel models using neural networks and fuzzy systems for the prediction of strength of rocks from key geomechanical properties." *Measurement*, 102, 158-169, 2017
- [25] D.G. Roy, T.N. Singh, "Predicting deformational properties of Indian coal: Soft computing and regression analysis approach." *Measurement*, 149, 106975, 2020
- [26] E. Köken, T. Kadağcı Koca, "Evaluation of soft computing methods for estimating tangential young modulus of intact rock based on statistical performance indices." *Geotechnical and Geological Engineering*, 40(7), 3619-3631, 2022.
- [27] J.S Jang, "Neuro-fuzzy modeling: architecture, analyses and applications", Dissertation (unpublished), Department of Electrical Engineering and Computer Science, University of California, Berkeley, USA, 1992.

A COMMERCIAL TURBOFAN ENGINE MODELING AND EXERGY ANALYSIS

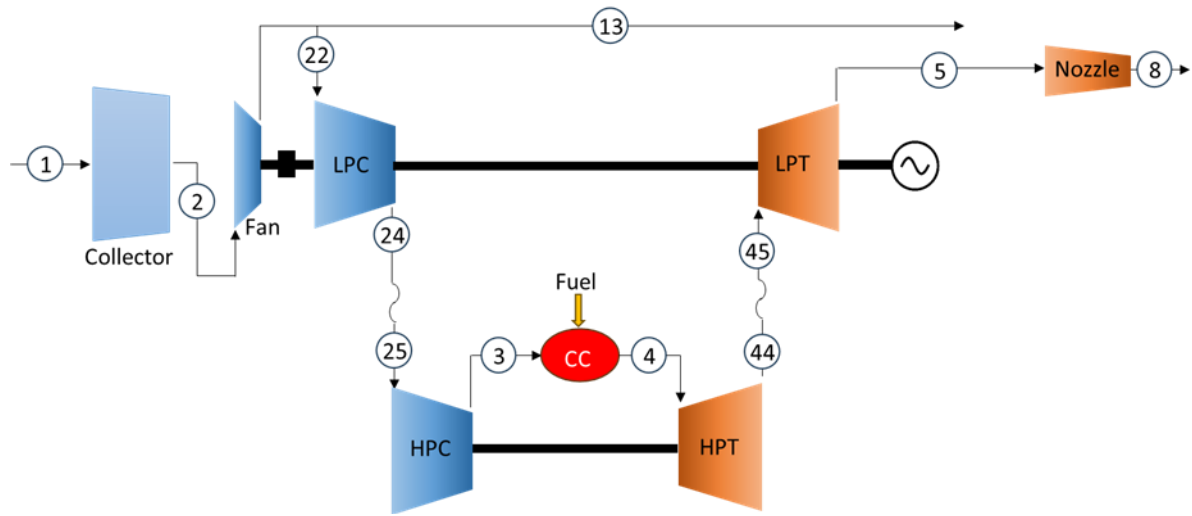
*Orhan KALKAN 

*Erzincan Binali Yıldırım University, Engineering-Architecture Faculty, Mechanical Engineering Department,
Erzincan, TÜRKİYE
orhan.kalkan@erzincan.edu.tr*

Highlights

- Thermodynamic modeling of a commercial turbofan engine.
- Performing exergy analysis to evaluate the performance criteria of engine components.
- Evaluation of how the bypass ratio affects net thrust and specific fuel consumption.

Graphical Abstract (Optional)



Thermodynamic schematic of the modelled engine



A COMMERCIAL TURBOFAN ENGINE MODELING AND EXERGY ANALYSIS

*Orhan KALKAN

*Erzincan Binali Yıldırım University, Engineering-Architecture Faculty, Mechanical Engineering Department,
Erzincan, TÜRKİYE*

orhan.kalkan@erzincan.edu.tr

(Received: 24.07.2023; Accepted in Revised Form: 08.01.2024)

ABSTRACT: Turbofan engines are one of the most common types of engines used in modern commercial and military aircraft due to their efficiency and performance characteristics. In this study, a thermodynamic model is generated using GasTurb 14 software for a commercial two-spool, unmixed flow, and booster turbofan engine (CFM56-5A3) used in Boeing A320-212. Besides, an exergy analysis of the modeled turbofan engine is performed. Exergy performance criteria such as exergy efficiency, exergy development potential, exergy destruction ratio, productivity lack ratio, and fuel depletion ratio are evaluated for the engine components. In addition, how bypass ratio (BPR) affects net thrust and specific fuel consumption (SFC) for the modeled turbofan engine is investigated. As a result, the net thrust and SFC values of the modeled engine and the actual engine are overlapped with 14.0% and 7.2% deviation, respectively. The maximum exergy efficiency occurs at the high-pressure turbine as 0.992. When the bypass ratio is minimum, the maximum net thrust and SFC occur as 62.24 kN and 24.08 g kN⁻¹ s⁻¹, respectively. High pressure turbine has the minimum exergy development potential of 1528.5 kW.

Keywords: *Bypass ratio, Exergy analysis, Thermodynamic model, Turbofan engine*

1. INTRODUCTION

A turbofan engine is a type of aircraft engine that is commonly used in commercial airliners. It is a variation of the basic gas turbine engine, which is also known as a jet engine. Turbofan engines are designed to provide efficient propulsion by generating thrust through the combination of two main components: the core engine and the fan [1]. Exergy analysis, also known as the second law analysis, is a method used in thermodynamics to assess the quality of energy and the efficiency of energy conversion processes. While traditional thermodynamic analysis focuses on the quantities of energy and heat transfer, exergy analysis considers the quality of energy and the potential for useful work [2-4]. Exergy analysis can be employed to assess the performance of gas turbine engines, such as turbofan engines used in commercial aircraft. By analyzing the exergy flows within the engine, it is possible to identify the locations and causes of energy losses and inefficiencies. This information can help in optimizing engine design, improving fuel efficiency, and reducing emissions [5-7].

Some of the studies conducted by researchers on modeling and exergy analysis of jet engines are summarized as follows. Akdeniz et al. [8] performed a comprehensive exergoeconomic and environmental analysis of a turbofan engine. The lowest and highest exergy efficiency of the system components were calculated for the combustion chamber (CC) and high pressure turbine (HPT) as 49.8% and 98.8%, respectively. Turan [9] carried out an exergoeconomic analysis of the commercial CFM56-7B turbofan engine used in Boeing 737. The results of the study show that the maximum exergy flow and maximum exergy cost of the turbofan engine are around 289.8 GJ/h and 5366 \$/h, respectively, at HPT. Besides, the total cost of the examined engine was calculated as 394 \$/h. Balli [10] studied the sustainability calculations of the high bypass ratio PW4056 turbofan engine based on exergy analysis. When the sustainability indices for the engine's maximum power mode and running power mode were compared, it was emphasized that more sustainable results are obtained in the maximum power mode. In another study, the energy and exergy analysis of a turbofan engine were performed parametrically, as well as the environmental effects of the exhaust gas were evaluated by Aygun and Turan et al. [11]. As a result, CO₂

*Corresponding Author: Orhan KALKAN, orhan.kalkan@erzincan.edu.tr

emission values were calculated between 1.88 kg/s and 1.5 kg/s according to different altitude cruise conditions. Koruyucu et al. [12] determined the performance parameters of a two-spool turbojet engine model using thermodynamic analysis. As a result of the study, it was stated that when the engine thrust is 516 daN, and the thrust specific fuel consumption (TSFC) rate is about 19.7 g/kN.s. In addition, the authors emphasized that due to high exergy destruction, it is necessary to focus on the CC component to improve the first law and second law efficiency ratios. Dinc et al. [13] analyzed a turboprop engine using environmental, economic and thermodynamic perspective. Exergy recovery potentials were calculated in different flight scenarios. Additionally, it was evaluated how much carbon dioxide emissions were released when maximum SFC occurred. As a result, it was evaluated how environmentally friendly the turboprop engine was and how much exergy efficiency it had in which flight stages. Şöhret et al. [14] examined a three-spool turboprop engine used in a cargo aircraft according to thermal, environmental, and ecological criteria. The engine of the cargo airplane was found to have an exergy efficiency of between 29 and 32%. Additionally, it has been observed that the ecological function is inversely correlated with engine power and energy efficiency. Ekici [15] studied thermodynamic analysis of a turboshaft engine using in agricultural spraying. Performance metrics for each turboshaft engine component were determined and presented. It was stated that the production of entropy rises as the temperature of the turboshaft's parts rises. Coban et al. [16] performed exergy and economic analysis for a turbojet engine using jet fuel and biofuel. As a result, the exergy efficiency for HPT decreased from 99% to 98.44% when using biofuel. On the other hand, the exergy efficiency of the compressor increased from 74.52% to 75.22%. Besides, the cost rate of thrust is increased by about 16%. Ekici et al. [17] carried out a thermodynamic analysis of an experimental turbojet engine to determine exergy destruction in terms of endogenous and exogenous variables. Endogenous and exogenous exergy destruction rates were calculated as 13.55 kW and 1.59 kW, respectively. Additionally, it has been emphasized that exogenous exergy destruction occurs in the compressor component.

Considering the studies in the literature, it can be seen that exergy analysis has been performed for many turbojet engine models and their efficiency has been examined. The motivation of this study is to thermodynamically analyze the effect of bypass ratio on performance parameters and a commercial turbofan model whose exergy analysis has not been examined before in the literature. In this study, a thermodynamic model is generated for a commercial turbofan engine (CFM56-5A3) used in Boeing A320-212. In addition, an exergy analysis is performed using some exergy performance tools. Exergy performance criteria for engine components are evaluated. Also, how bypass ratio (BPR) affects net thrust and specific fuel consumption (SFC) for the modeled turbofan engine is investigated. The results obtained provide preliminary ideas for the optimization of design parameters for turbofan engine companies.

2. CFM56-5A3 TURBOFAN ENGINE MODELLING

The trial version of the GasTurb 14 software is used for modeling the considered turbofan engine. The software includes models for many types of jet engines. With a user-friendly graphical interface, simple terminology, and no obscure abbreviations, GasTurb is a robust and versatile gas turbine cycle tool for simulating the most popular types of aircraft and power generating gas turbines [18]. A two-spool, unmixed flow, and booster turbofan engine similar to the CFM56-5A3 are selected as the component configuration. The characteristics of the CFM56-5A3 used in Boeing A320-212 are given in Table 1 [19-21].

Table 1. The characteristics of CFM56-5A3

Parameter	Value
Thrust [dry]	117.88 kN
Thrust [cruise]	22.24 kN
Specific fuel consumption (SFC) [cruise]	15.18 g kN ⁻¹ s ⁻¹
Airflow [static]	397.3 kg s ⁻¹
Overall pressure ratio (OPR) [static]	27.8
Bypass ratio (BPR) [static]	6
Fan pressure ratio (FPR)	1.55
Cruise altitude	10668 m
Cruise speed	0.8 Mach
Spool number	2
Fan stages	1
Low pressure compressor (LPC) stage	3
High pressure compressor (HPC) stage	9
High pressure turbine (HPT) stage	1
Low pressure turbine (LPT) stage	4
Fan radius	0.865 m
Length	2.423 m
Width	1.829 m
Weight	2266 kg

Figure 1 shows the cycle components of the modeled turbofan engine and station numbers. The turbofan engine consists of a collector, 1 stage fan, 3 stage LPC, 9 stage HPC, 1 stage HPT, 4 stage LPT, a CC, and an exhaust nozzle.

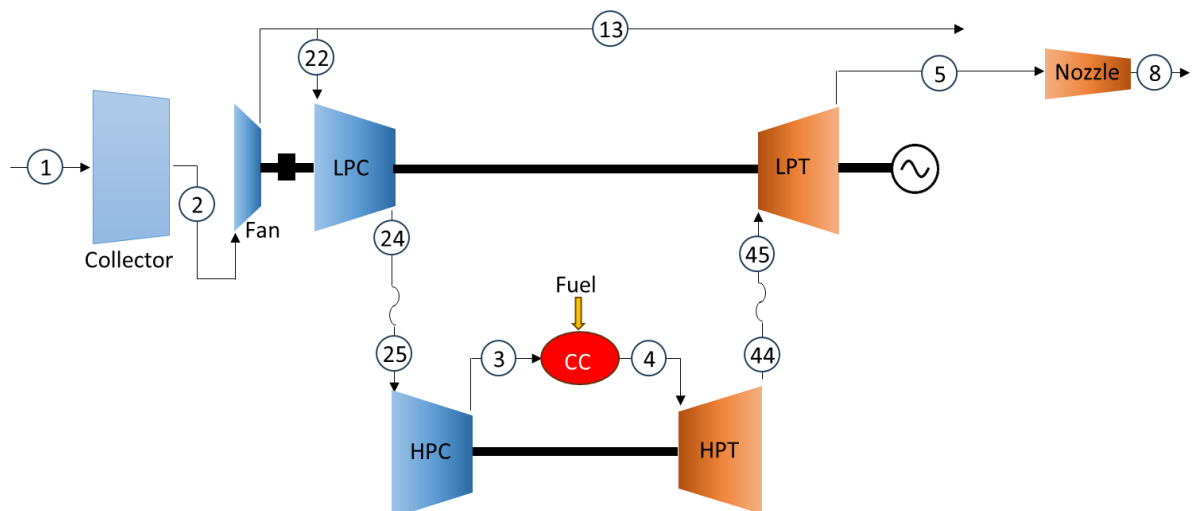
**Figure 1.** Thermodynamic schematic of the modeled engine

Figure 2 shows the geometric schematic and stations of the modeled turbofan engine. Output parameters are calculated by integrating many input parameters into the model within the framework of catalog information and some assumptions.

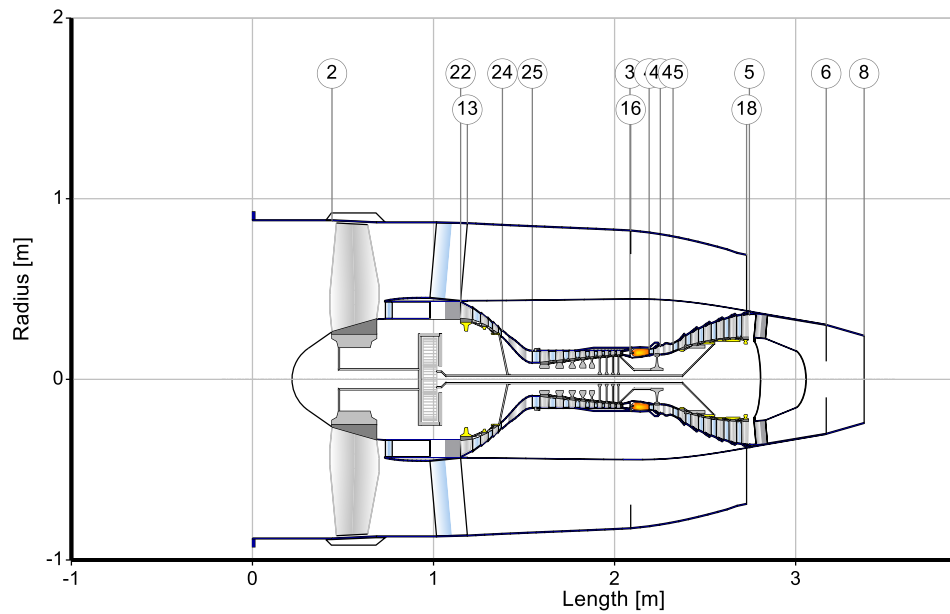


Figure 2. Modelled engine schematic

The following assumptions are taken into account when modeling the turbofan engine.

- Thermodynamic cycle is in a steady state.
- All compressions and expansions are isentropic.
- The ambient air temperature is 218.8 K at an altitude of 10668 m.
- Complete combustion in CC is provided by kerosene fuel with a lower heating value (LHV) of 42800 kJ/kg.
- Assuming no bleed air.
- The modelled engine is adiabatic.
- Engine cooling systems are not considered.

3. ENERGY, EXERGY BASED GOVERNING EQUATIONS

Exergy analysis focuses on the quality of energy and identifies the irreversibilities or losses within a system. The magnetic, electrical, nuclear, potential, and kinetic energy changes for the considered system are ignored while performing the exergy analysis. The physical exergy for all stations, as well as the chemical exergy for CC only, are included in the calculations. When ambient air and exhaust gas are considered as an ideal gas and assuming specific heat is constant, the physical exergy can be written as follows [23-26].

$$\dot{E}_{phy} = \dot{m} \left(c_p (T - T_o) - T_o \left[c_p \ln \left(\frac{T}{T_o} \right) - R \ln \left(\frac{P}{P_o} \right) \right] \right) \quad (1)$$

The exergy expression of jet fuel is considered as the sum of the physical and chemical exergy values as follows.

$$\dot{E}_f = \dot{E}_{phy,f} + \dot{E}_{chm,f} \quad (2)$$

Considering the fuel as an incompressible fluid, the physical exergy of the fuel is as follows [23-26].

$$\dot{E}_{phy,f} = \dot{m}_f c_{p,f} \left[T - T_o - T_o \ln \left(\frac{T}{T_o} \right) \right] \quad (3)$$

The chemical exergy of the considered jet fuel ($C_{12}H_{23}$) can be expressed as an equation dependent on the LHV of fuel and a parameter defined as the exergy degree factor (σ) as follows.

$$\dot{E}_{chm,f} = \dot{m}_f LHV \sigma \quad (4)$$

σ for $C_{12}H_{23}$ was calculated as 1.0616 by many researchers [8, 10].

The mass, energy, exergy balances for control volumes with steady state flow is as follows [25, 26].

Mass balance equation:

$$\sum \dot{m}_i - \sum \dot{m}_o = 0 \quad (5)$$

Energy balance equation:

$$\sum \dot{m}_i h_i - \sum \dot{m}_o h_o + \dot{Q} - \dot{W} = 0 \quad (6)$$

Exergy balance equation:

$$\sum \left(1 - \frac{T_0}{T_k}\right) \dot{Q}_k - \dot{W} + \sum_i \dot{m} \psi - \sum_o \dot{m} \psi - \dot{X}_d = 0 \quad (7)$$

Mass, energy and exergy balance for Fan:

$$\dot{m}_2 - \dot{m}_{22} - \dot{m}_{13} = 0 \quad (8)$$

$$-\dot{W}_{fan} + \dot{m}_2 h_2 - \dot{m}_{22} h_{22} - \dot{m}_{13} h_{13} = 0 \quad (9)$$

$$\dot{W}_{fan} + \dot{E}_2 - \dot{E}_{22} - \dot{E}_{13} - \dot{E}_{D,fan} = 0 \quad (10)$$

Mass, energy and exergy balance for LPC:

$$\dot{m}_{22} - \dot{m}_{24} = 0 \quad (11)$$

$$-\dot{W}_{LPC} + \dot{m}_{22} h_{22} - \dot{m}_{24} h_{24} = 0 \quad (12)$$

$$\dot{W}_{LPC} + \dot{E}_{22} - \dot{E}_{24} - \dot{E}_{D,LPC} = 0 \quad (13)$$

Mass, energy and exergy balance for HPC:

$$\dot{m}_{25} - \dot{m}_3 = 0 \quad (14)$$

$$-\dot{W}_{HPC} + \dot{m}_{25} h_{25} - \dot{m}_3 h_3 = 0 \quad (15)$$

$$\dot{W}_{HPC} + \dot{E}_{25} - \dot{E}_3 - \dot{E}_{D,HPC} = 0 \quad (16)$$

Mass, energy and exergy balance for CC:

$$\dot{m}_3 + \dot{m}_f - \dot{m}_4 = 0 \quad (17)$$

$$\dot{m}_3 h_3 + \dot{m}_f LHV \eta_f - \dot{m}_4 h_4 = 0 \quad (18)$$

$$\dot{E}_3 + \dot{E}_f - \dot{E}_4 - \dot{E}_{D,CC} = 0 \quad (19)$$

Mass, energy and exergy balance for HPT:

$$\dot{m}_4 - \dot{m}_{44} = 0 \quad (20)$$

$$\dot{W}_{HPT} + \dot{m}_4 h_4 - \dot{m}_{44} h_{44} = 0 \quad (21)$$

$$-\dot{W}_{HPT} + \dot{E}_4 - \dot{E}_{44} - \dot{E}_{D,HPT} = 0 \quad (22)$$

Mass, energy and exergy balance for LPT:

$$\dot{m}_{45} - \dot{m}_5 = 0 \quad (23)$$

$$\dot{W}_{LPT} + \dot{m}_{45}h_{45} - \dot{m}_5h_5 = 0 \quad (24)$$

$$-\dot{W}_{LPT} + \dot{E}_{45} - \dot{E}_5 - \dot{E}_{D,LPT} = 0 \quad (25)$$

Many metric parameters have been defined in the open literature to measure the exergy performance of a system. Of these, the exergy efficiency, exergy development potential, exergy destruction ratio, productivity lack ratio, and fuel depletion ratio are selected for the modeled system [27-29].

First of all, the sum of the exergy inlet flows to any component of the system is considered as the fuel exergy (\dot{E}_F), and the sum of the exergy outlet flows is considered as the product exergy (\dot{E}_P). The exergy efficiency (ψ) is expressed as:

$$\psi = \frac{\dot{E}_P}{\dot{E}_F} \quad (26)$$

The exergy development potential (ϕ) depending on the exergy destruction rate (\dot{E}_D), and the exergy efficiency is expressed as follows.

$$\phi = \dot{E}_D(1 - \psi) \quad (27)$$

The exergy destruction ratio (χ) is expressed as the ratio of the exergy destruction rate at a component to the overall exergy destruction rate as follows.

$$\chi = \frac{\dot{E}_D}{\sum \dot{E}_D} \quad (28)$$

The productivity lack ratio (Ω) can be calculated using the following expression to evaluate how much of the product exergy potential is lost due to exergy destruction.

$$\Omega = \frac{\dot{E}_D}{\sum \dot{E}_P} \quad (29)$$

The fuel depletion ratio (φ) is determined using following equation. The equation is calculated as the ratio of the exergy destruction rate of a component to the overall exergy product ratio.

$$\varphi = \frac{\dot{E}_D}{\sum \dot{E}_F} \quad (30)$$

4. RESULTS AND DISCUSSION

4.1. Exergetic Performance Analysis

Thermodynamic modeling is performed for the CFM56-5A3 engine within the framework of the specified assumptions and boundary conditions. The net thrust and SFC values of the modeled engine and the actual engine are compared in Table 2. 14.0% and 7.2% errors occur for net thrust and SFC selected for validation parameters, respectively. Accordingly, the values of the parameters in the model can be used in exergy calculations with an acceptable deviation.

Table 2. Verification of the modeled engine

Components	Net thrust (cruise), [kN]	SFC (cruise), [g kN ⁻¹ s ⁻¹]
The modeled engine	25.86	16.35
The actual engine	22.24	15.18
Error rate (%)	14.0%	7.2%

The sum of the exergy inlet flows to any component of the system is considered as the fuel exergy (\dot{E}_F), the sum of the exergy outlet flows is considered as the product exergy (\dot{E}_P), and the exergy destruction (\dot{E}_D), are calculated for Fan, LPC, HPC, CC, HPT, and LPT as given in Table 3.

Table 3. The exergy rates of the components

Components	\dot{E}_F (W)	\dot{E}_P (W)	\dot{E}_D (W)
Fan	9893705.8	9352643.0	541062.8
LPC	5957677.2	5621098.8	336578.3
HPC	13349251.3	13013100.2	336151.1
CC	32714282.6	26627567.2	6086715.4
HPT	26627567.2	26425821.9	201745.3
LPT	19949752.4	19638881.3	310871.2

Figure 3 represents the variation of the temperature and pressure values at the component stations. The temperature and pressure values at various component stations of a turbofan engine are critical for understanding its performance and efficiency. While the air inlet temperature is -38.5 °C, it reached its maximum value of 1265 °C at the CC outlet. Then it decreased to 517 °C at the LPT outlet. On the other hand, while the air inlet total pressure is 36.4 kPa, it reaches its maximum value of 1742 kPa at the CC outlet. Then it decreased to 92.2 kPa at the LPT output.

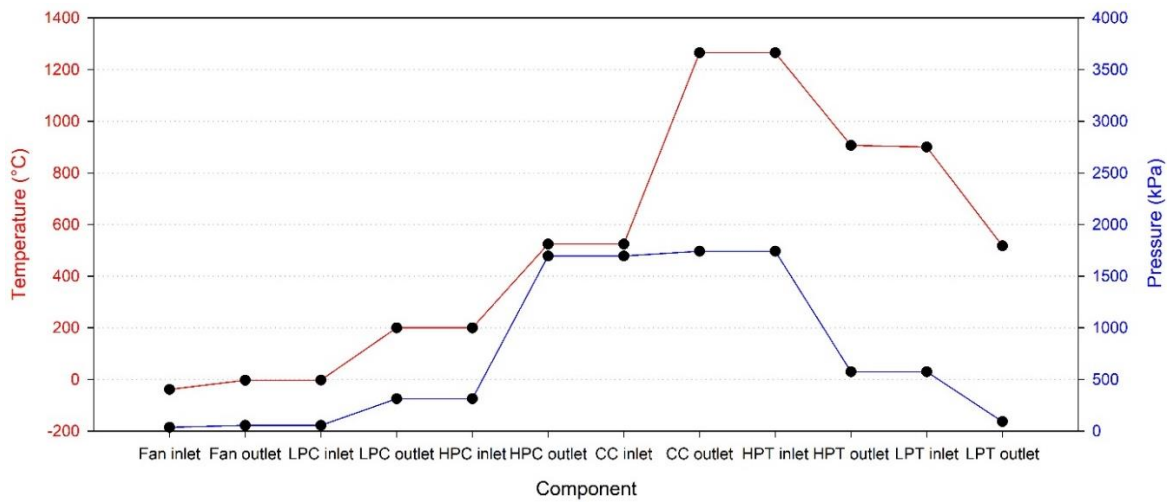


Figure 3. Temperature and pressure values of the components

Exergy efficiency, also known as second-law efficiency, is a measure of how effectively an energy conversion process or system utilizes the available energy, taking into account both the quantity and quality of the energy. The exergy efficiencies of Fan, LPC, HPC, CC, HPT, and LPT components are calculated as illustrated in Figure 4. The maximum exergy efficiency occurs at HPT as 0.992. The calculated minimum exergy efficiency is 0.814 for CC.

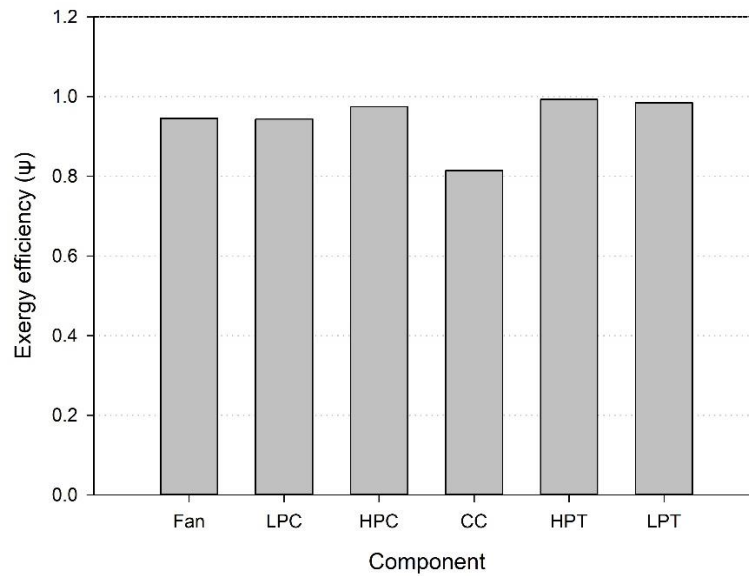


Figure 4. Exergy efficiencies of the components

The exergy development potentials of a turbofan engine represent the opportunities for improving the engine's efficiency by reducing exergy losses and enhancing the useful work output. Analyzing these potentials is a critical aspect of the ongoing efforts to make jet engines more energy-efficient and environmentally friendly. Figure 5 shows the calculated exergy development potentials of Fan, LPC, HPC, CC, HPT, and LPT. CC with a $\dot{\phi}$ of 1132 kW appears to have much more exergy development than other components. HPT has the minimum exergy development potential of 1528.5 kW.

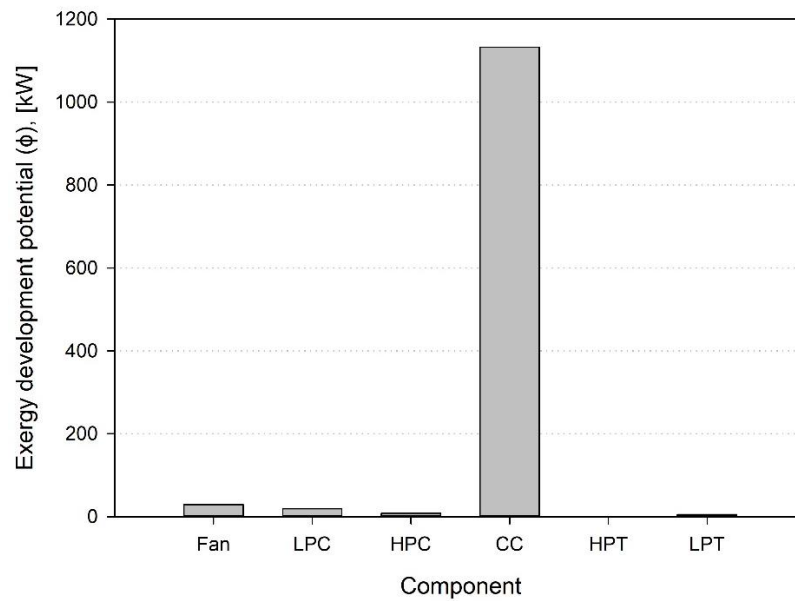


Figure 5. Exergy development potentials of the components

The exergy destruction ratio of a turbofan engine is a measure of how efficiently the engine converts the available energy into useful work while minimizing exergy losses or destruction. Exergy destruction, also known as exergy loss, refers to the wasted energy in a system that cannot be converted into useful work and is typically associated with irreversibilities within the system. Figure 6 depicts the exergy destruction ratios of Fan, LPC, HPC, CC, HPT, and LPT. CC has an exergy destruction value of 0.779. The exergy destruction rates of other components vary between 0.026 and 0.069. These values show that there is much more exergy destruction in CC than in other components.

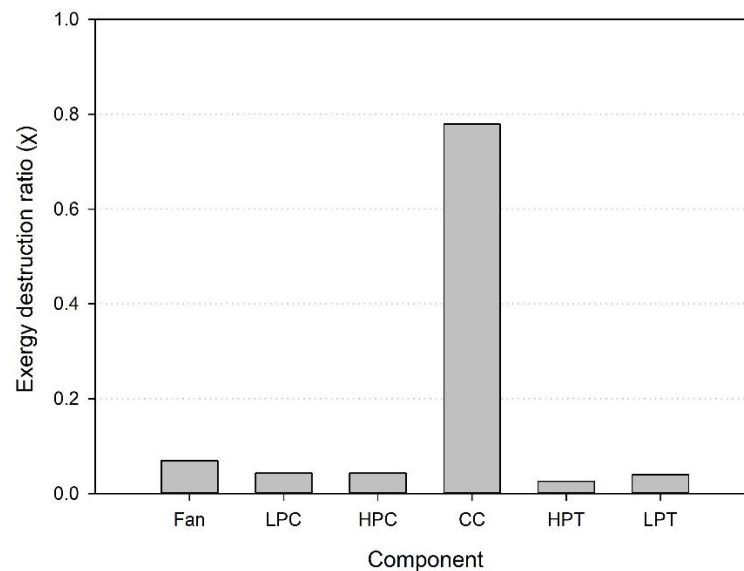


Figure 6. Exergy destruction ratios of the components

The productivity lack ratios are determined for Fan, LPC, HPC, CC, HPT, and LPT as shown in Figure 7. CC has a productivity lack ratio of 0.06. The productivity lack ratios of LPC, HPC, and LPT are approximately 0.003 and are very close to each other. It is understood that HPT has the minimum rate.

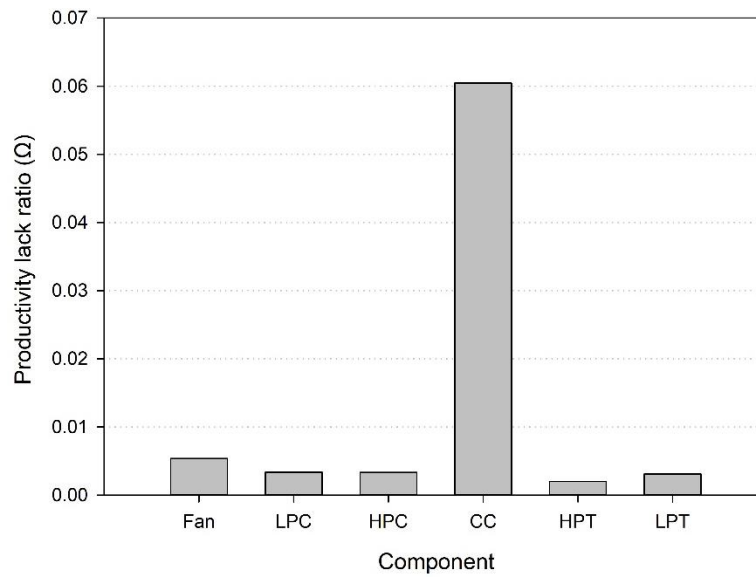


Figure 7. Productivity lack ratios of the components

Figure 8 represents the fuel depletion ratios of Fan, LPC, HPC, CC, HPT, and LPT. CC with a maximum fuel depletion ratio of 0.056 appears to have much greater fuel depletion ratio than other components. The minimum fuel depletion ratio is about 0.002 calculated for HPT. It is seen that Fan has the highest fuel depletion ratio of components other than CC.

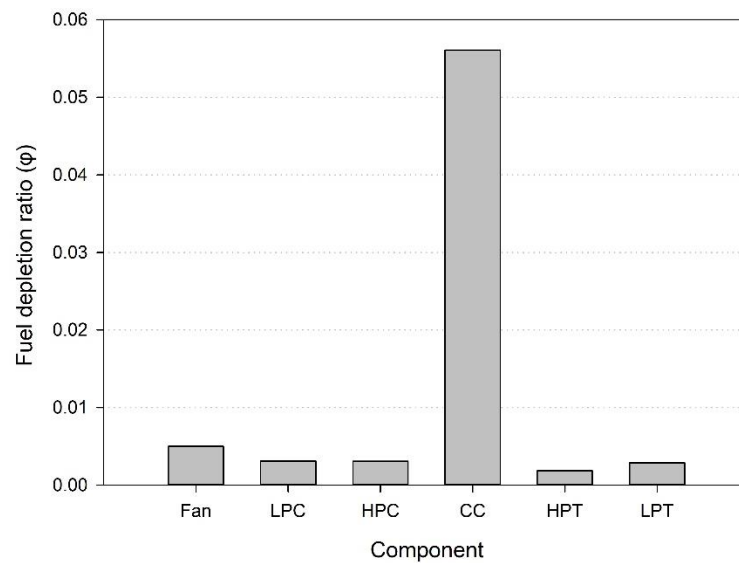


Figure 8. Fuel depletion ratios of the components

4.2. Effect of BPR on Engine Performance

Net thrust and specific fuel consumption (SFC) are indeed critical parameters in the field of aviation and aerospace engineering [30]. These parameters play a crucial role in determining the performance and efficiency of aircraft and other propulsion systems. The net thrust is a crucial performance parameter as it directly affects the aircraft's acceleration, climb rate, and maximum speed. Higher net thrust values generally result in better aircraft performance. On the other hand, SFC is a measure of the fuel efficiency of an aircraft's engine or propulsion system. It represents the amount of fuel consumed per unit of thrust or power produced. A lower SFC value indicates higher fuel efficiency, as it means the engine is producing more thrust or power with less fuel consumption. Fuel efficiency is a critical factor in the aviation industry due to its impact on operating costs and environmental considerations. Figure 9 depicts the net thrust and SFC variation according to BPR for CFM56-5A3 turbofan engine model. As the engine design, which is normally BPR= 6, decreases towards BPR=1, it is seen that the net thrust increases significantly. As the BPR increases towards 10, a less rapid decrease in net thrust is observed. It is also clear that while BPR decreases, SFC also increases parabolically. When BPR is reduced by 1 from 6, net thrust and SFC increases by 141% and 45%, respectively. When BPR increases from 6 to 10, net thrust and SFC decreases by 28% and 12%, respectively.

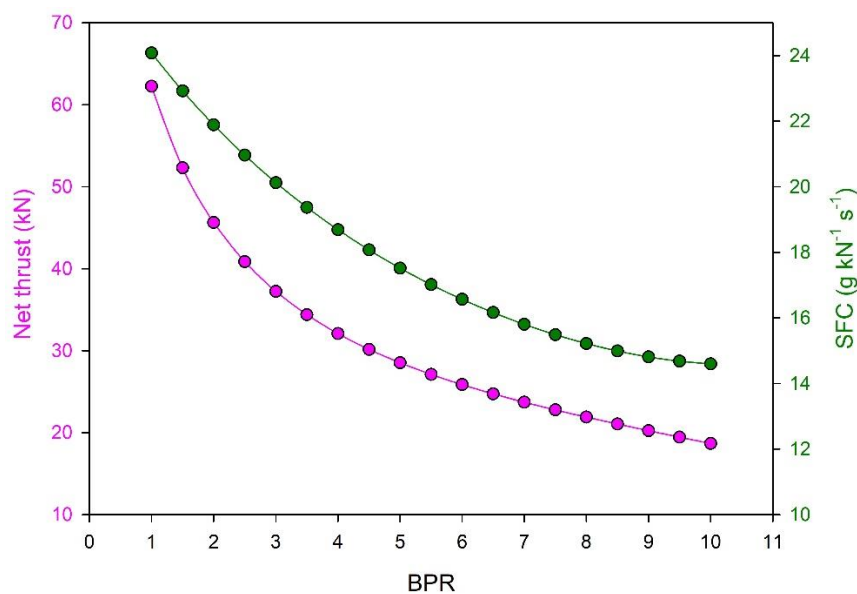


Figure 9. Net thrust and SFC variation relative to BPR

5. CONCLUSIONS

This study presents a thermodynamic model, and exergy analysis for a commercial turbofan engine (CFM56-5A3). Besides, a parametric study is conducted to show how the bypass ratio affects net thrust and specific fuel consumption. The concluding remarks can be summarized as follow,

- The net thrust and SFC values of the modeled engine and the actual engine are compared. 14.0% and 7.2% errors occur for net thrust and SFC selected for validation parameters, respectively.
- The fuel exergy, the product exergy, and the exergy destruction are calculated for Fan, LPC, HPC, CC, HPT, and LPT.
- The air inlet temperature reached its maximum value of 1265 °C at the CC outlet. On the other hand, the air total pressure reaches its maximum value of 1742 kPa at the CC outlet.
- The maximum exergy efficiency occurs at HPT as 0.992.
- HPT has the minimum exergy development potential of 1528.5 kW.

- The productivity lack ratios of LPC, HPC, and LPT are approximately 0.003 and are very close to each other.
- CC with a maximum fuel depletion ratio of 0.056 appears to have much greater fuel depletion ratio than other components.
- When BPR is reduced by 1 from 6, net thrust and SFC increases by 141% and 45%, respectively. When BPR increases from 6 to 10, net thrust and SFC decreases by 28% and 12%, respectively.

The modeling and exergy analysis discussed can be applied to many different jet engines. The effects of many parameters used in the design of jet engines on engine performance can be evaluated in different studies. Optimization studies that evaluate the effects of these parameters on engine performance can also be performed.

Declaration of Ethical Standards

The author declares that the study complies with all applicable laws and regulations and meets ethical standards.

Credit Authorship Contribution Statement

The author contributed to the design and modelling of the system, the analysis of the results and the writing of the manuscript.

Declaration of Competing Interest

The author declares that he has no known competing financial interests or personal relationships that could have appeared to influence the work reported in this paper.

Funding / Acknowledgements

The author declares that he has no financial support.

Data Availability

Research data has not been made available in a repository.

REFERENCES

- [1] S. Gudmundsson, "Thrust Modeling for Gas Turbines," in *General Aviation Aircraft Design*, UK: Butterworth-Heinemann, 2022, pp. 573-595.
- [2] R. Sangi and D. Müller, "Application of the second law of thermodynamics to control: A review," *Energy*, vol. 174, pp. 938-953, May 2019.
- [3] C. E. Keutenedjian Mady, C. Reis Pinto, and M. Torelli Reis Martins Pereira, "Application of the Second Law of Thermodynamics in Brazilian Residential Appliances towards a Rational Use of Energy," *Entropy*, vol. 22, no. 6, p. 616, Jun. 2020.
- [4] T. K. Ibrahim et al., "Thermal performance of gas turbine power plant based on exergy analysis," *Applied Thermal Engineering*, vol. 115, pp. 977-985, Mar. 2017.
- [5] C. T. Yucer, "Thermodynamic analysis of the part load performance for a small scale gas turbine jet engine by using exergy analysis method," *Energy*, vol. 111, pp. 251-259, Sep. 2016
- [6] S. Manigandan, A. E. Atabani, V. K. Ponnusamy, and P. Gunasekar, "Impact of additives in Jet-A fuel blends on combustion, emission and exergetic analysis using a micro-gas turbine engine," *Fuel*, vol. 276, p. 118104, Sep. 2020.
- [7] C. Cai, Q. Zheng, J. Fang, H. Chen, C. Chen, and H. Zhang, "Performance assessment for a novel supersonic turbine engine with variable geometry and fuel precooled: From feasibility, exergy,

- thermo-economic perspectives," *Applied Thermal Engineering*, vol. 225, p. 120227, May 2023.
- [8] H. Y. Akdeniz, O. Balli, and H. Caliskan, "Energy, exergy, economic, environmental, energy based economic, exergoeconomic and enviroeconomic (7E) analyses of a jet fueled turbofan type of aircraft engine," *Fuel*, vol. 322, p. 124165, Aug. 2022.
- [9] O. Turan, "Exergo-economic analysis of a CFM56-7B turbofan engine," *Energy*, vol. 259, p. 124936, Nov. 2022.
- [10] O. Balli, "Exergy modeling for evaluating sustainability level of a high by-pass turbofan engine used on commercial aircrafts," *Applied Thermal Engineering*, vol. 123, pp. 138–155, Aug. 2017.
- [11] H. Aygun and O. Turan, "Analysis of cruise conditions on energy, exergy and NO_x emission parameters of a turbofan engine for middle-range aircraft," *Energy*, vol. 267, p. 126468, Mar. 2023.
- [12] E. Koruyucu, S. Ekici, and T.H. Karakoc, "Performing thermodynamic analysis by simulating the general characteristics of the two-spool turbojet engine suitable for drone and UAV propulsion," *Journal of Thermal Analysis and Calorimetry*, vol. 145, no. 3, p. 1303-1315, Jan. 2021.
- [13] A. Dinc, H. Caliskan, S. Ekici, and Y. Sohret, "Thermodynamic-based environmental and enviroeconomic assessments of a turboprop engine used for freight aircrafts under different flight phases," *Journal of Thermal Analysis and Calorimetry*, vol. 147, pp. 12693–12707, Jul 2022.
- [14] Y. Şöhret, S. Ekici, and A. Dinc, "Investigating the green performance limits of a cargo aircraft engine during flight: a thermo-environmental evaluation," *Energy Sources, Part A: Recovery, Utilization, and Environmental Effects*, pp. 1-16, Dec 2021.
- [15] S. Ekici, "Design of Unmanned Helicopter Equipped with Turboshift Engine for Agriculture Spraying Mission Based on Thermodynamic Analysis," *Journal of the Institute of Science and Technology*, vol. 10, no. 1, pp. 532-546, Mar. 2020.
- [16] K. Coban, Y. Şöhret, C. O. Colpan, and T. H. Karakoç, "Exergetic and exergoeconomic assessment of a small-scale turbojet fuelled with biodiesel," *Energy*, vol. 140, pp. 1358–1367, Dec. 2017.
- [17] S. Ekici, İ. Orhan, Y. Şöhret, Ö. Altuntaş, T. H. Karakoç, "Calculating Endogenous and Exogenous Exergy Destruction for an Experimental Turbojet Engine," *International Journal of Turbo & Jet-Engines*, vol. 39, no. 2, pp. 233-240, May 2022.
- [18] P. Jeschke, J. Kurzke, R. Schaber, and C. Riegler. "Preliminary gas turbine design using the multidisciplinary design system moped," *J. Eng. Gas Turbines Power*, vol. 126, no. 2, Apr. 2004.
- [19] EASA, "TYPE-CERTIFICATE DATA SHEET," 2018. [Online]. Available: <https://www.easa.europa.eu/en/downloads/7689/en>. [Accessed: 17-Jul-2023].
- [20] Jet-Engine, "Civil turbojet/turbofan specifications." [Online]. Available: <https://www.jet-engine.net/civtfspec.htm>. [Accessed: 17-Jul-2023].
- [21] D. N. M. P. Paulo, "Exergy Analysis of a Turbofan Engine," MSc, Aerospace Sciences of the University of Beira Interior, 2018.
- [22] GasTurb, "Design and Off-Design Performance of Gas Turbines," [Online]. Available: <https://www.gasturb.com/Downloads/Manuals/GasTurb14.pdf>. [Accessed: 17-Jul-2023].
- [23] T. J. Kotas, *The exergy method of thermal plant analysis*. Oxford, England: Butterworth-Heinemann, 1985.
- [24] O. Balli, "Advanced exergy analyses of an aircraft turboprop engine (TPE)," *Energy*, vol. 124, pp. 599–612, Apr. 2017.
- [25] Y. A. Çengel and M. A. Boles. "Thermodynamics: an engineering approach," Eighth edition. New York: McGraw-Hill Education, 2015.
- [26] A. Bejan and D. L. Siems, "The need for exergy analysis and thermodynamic optimization in aircraft development," *Exergy, An International Journal*, vol. 1, no. 1, pp. 14–24, Jan. 2001.
- [27] C. T. Yucer, "Thermodynamic analysis of the part load performance for a small scale gas turbine jet engine by using exergy analysis method," *Energy*, vol. 111, pp. 251–259, Sep. 2016.
- [28] H. Caliskan, S. Ekici, and Y. Sohret, "Advanced exergy analysis of a turbojet engine main components considering exogenous, endogenous, exogenous, avoidable and unavoidable exergy destructions," *Propulsion and Power Research*, Aug. 2022.

- [29] R. Atilgan and Onder Turan, "Economy and exergy of aircraft turboprop engine at dynamic loads," *Energy*, vol. 213, p. 118827, Dec. 2020.
- [30] M. Vera-Morales, and C.A. Hall, "Modeling performance and emissions from aircraft in the aviation integrated modelling project," *Journal of Aircraft*, vol. 47, no. 3, pp. 812-819, 2010.



ENERGY, ENVIRONMENTAL, AND EXERGOECONOMIC (3E) ANALYSIS OF TRANSCRITICAL CO₂ BOOSTER AND PARALLEL COMPRESSION SUPERMARKET REFRIGERATION CYCLES IN CLIMATE ZONES OF TÜRKİYE

^{1,*}Oğuz ÇALIŞKAN , ²H. Kürşad ERSOY 

^{1,2}Konya Technical University, Engineering and Natural Sciences Faculty, Mechanical Engineering Department,
Konya, TÜRKİYE

¹ocaliskan@ktun.edu.tr, ²hkersoy@ktun.edu.tr

Highlights

- Two CO₂ supermarket refrigeration cycle configurations were investigated.
- Bin-hour data of 11 provinces in Türkiye were derived using hourly temperatures.
- Up to 5.6% energy consumption reduction was obtained using parallel compression.
- The contribution of CO₂ to direct emissions is negligible.
- Parallel compression cycle has up to 18% less unit product cost.



ENERGY, ENVIRONMENTAL, AND EXERGOECONOMIC (3E) ANALYSIS OF TRANSCRITICAL CO₂ BOOSTER AND PARALLEL COMPRESSION SUPERMARKET REFRIGERATION CYCLES IN CLIMATE ZONES OF TÜRKİYE

^{1,*}Oğuz ÇALIŞKAN , ²H. Kürşad ERSOY 

^{1,2}Konya Technical University, Engineering and Natural Sciences Faculty, Mechanical Engineering Department,
Konya, TÜRKİYE

¹ocaliskan@ktun.edu.tr, ²hkersonoy@ktun.edu.tr

(Received: 20.11.2023; Accepted in Revised Form: 19.01.2024)

ABSTRACT: Legal restrictions on high-GWP refrigerants lead to the widespread use of carbon dioxide in commercial refrigeration, where there is a high energy consumption. Although CO₂ has many benefits, its lower critical temperature and higher operation pressure compared to other refrigerants lead to performance reduction. For this reason, studies have been conducted by researchers for performance enhancement. This paper presents energy, environmental impact, and exergoeconomic (3E) analysis of transcritical CO₂ booster and parallel compression supermarket refrigeration cycles based on meteorological data of 11 provinces in Türkiye as samples of different climatic regions. Parallel compression cycle achieved up to 18.4% higher coefficient of performance than booster cycle between the investigated ambient temperatures. Up to 5.6% annual energy consumption and environmental impact reduction were obtained using parallel compression. Unit product costs of the parallel compression cycles were calculated between 8.2% and 18% lower than booster cycle in investigated provinces. Developing energy-efficient systems that use environmentally friendly refrigerants will contribute to a sustainable future.

Keywords: Bin-hour, Carbon dioxide, Environmental impact, Exergoeconomic analysis, Supermarket

1. INTRODUCTION

Global warming is a serious issue around the world and therefore, legal authorities are taking action to avoid it. Commercial refrigerators contribute to 25-60% of the electricity used in stores and the highest CO₂ emission of all refrigerators [1], [2]. Because the European Commission has prohibited using refrigerants with global warming potential (GWP) values higher than 150 for newly installed central refrigeration systems starting from 2022 [3], using low-GWP refrigerants has gained importance. Carbon dioxide (CO₂) is a non-toxic, non-flammable, and cheap refrigerant with a GWP value of only 1 [4]. However, CO₂ has a lower critical temperature and a higher operation pressure compared to other common refrigerants. This case leads to lower performance. There have been improvements made to increase the performance of transcritical CO₂ refrigeration cycles including parallel compression, adiabatic gas cooling, subcooling, and ejector expansion [5]. There are also studies using CO₂ in cascade and secondary loop cycles in the literature [6], [7].

Sharma et al. [8] conducted a theoretical comparison of various supermarket refrigeration systems including transcritical CO₂ and cascade/secondary loop for various climate zones in the US resulting in that transcritical CO₂ system with parallel compressor is the most efficient in northern and central regions among investigated systems. Fritschi et al. [9] determined that a low evaporation temperature and high gas cooler outlet temperature have a positive effect on the parallel compression circuit. Chesi et al. [10] found that an ideal cycle with parallel compressor may improve the coefficient of performance (COP) and cooling capacity by over 30% and 65%, respectively, provided that there is no pressure loss along piping, superheat is constant, and liquid-vapor separation is perfect in the flash tank.

The use of transcritical CO₂ systems in commercial refrigeration is spreading worldwide. International supermarket chain Carrefour has installed two CO₂ systems in İstanbul. The one installed

*Corresponding Author: Oğuz ÇALIŞKAN, ocaliskan@ktun.edu.tr

in Bahçelievler is an R404A/CO₂ cascade system while the other one in Kurtköy is transcritical CO₂ booster system with adiabatic gas cooler [11], [12]. The company continues to install transcritical CO₂ refrigeration systems around the world such as Poland, Romania, Italy, and Belgium [13]–[15]. UK-based grocery retailer Tesco has installed transcritical CO₂ systems at about 1000 stores, with plans to be HFC-free by 2035 [16]. Longo Brothers Fruit Markets in Canada uses transcritical CO₂ systems in 44% of its grocery stores, with plans to install CO₂ systems in all new stores [17]. It is reported that 6960 locations in Japan (including 300 large retail stores, 6330 convenience stores, and 330 industrial facilities) use transcritical CO₂ refrigeration systems as of the end of December 2022 [18].

This paper presents energy, environmental impact, and exergoeconomic analysis of transcritical booster and parallel compression CO₂ supermarket refrigeration cycles based on meteorological data of 11 provinces in Türkiye.

2. MATHEMATICAL MODELS OF THE CYCLES

Transcritical CO₂ booster refrigeration cycle (BRC) is a baseline for supermarket refrigeration systems as shown in Figure 1. The cycle consists of two evaporators for frozen and fresh food. No phase change occurs above the critical point in the gas cooler, contrary to the condenser. High-pressure refrigerant coming from the gas cooler is expanded to intermediate pressure in the high-pressure expansion valve (HPXV). In the flash tank, liquid and vapor separation occurs. Vapor is expanded to chiller pressure via the flash-gas-bypass (FGB) valve while liquid is sent to the low-pressure expansion valve (LPXV) and medium-pressure expansion valve (MPXV). Refrigerant gaining heat in the freezer is compressed to chiller pressure via the low-pressure compressor (LPC). Three refrigerant streams are mixed in the suction line of the high-pressure compressor (HPC) and compressed to the gas cooler pressure.

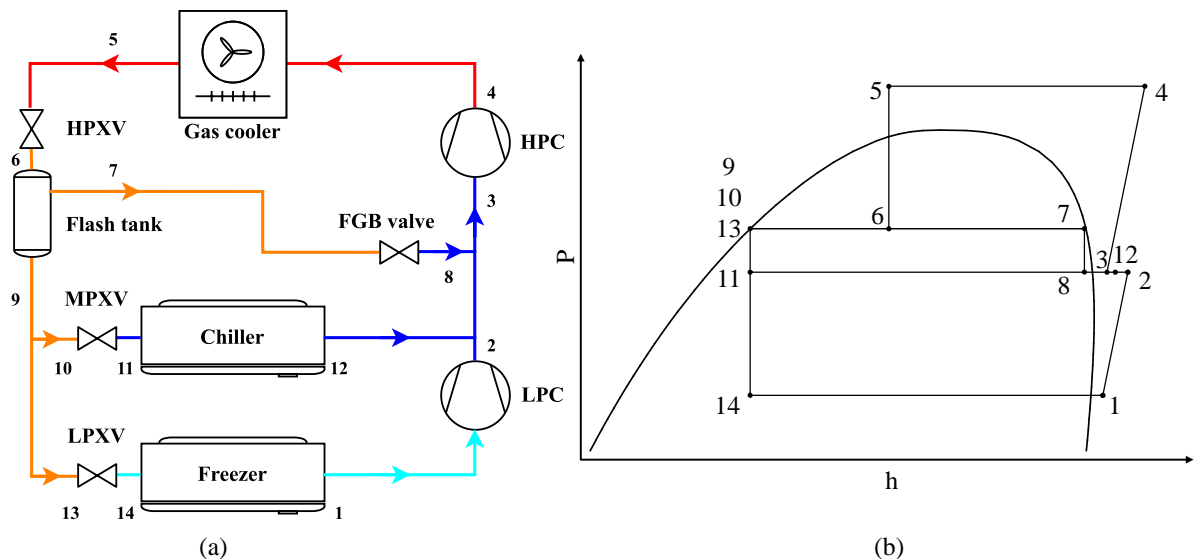


Figure 1. Transcritical CO₂ booster refrigeration cycle (BRC) (a) Plant layout, (b) P-h diagram

Transcritical CO₂ parallel compression refrigeration cycle (PRC) is an improvement made to BRC as shown in Figure 2. Vapor coming from the flash tank is separately compressed to the gas cooler pressure via a separate parallel compressor (PC). There is no expansion loss caused by the flash vapor. There is also a bypass circuit in case of insufficient mass flow rate in the PC at lower ambient temperatures. It works exactly the same as BRC in this case.

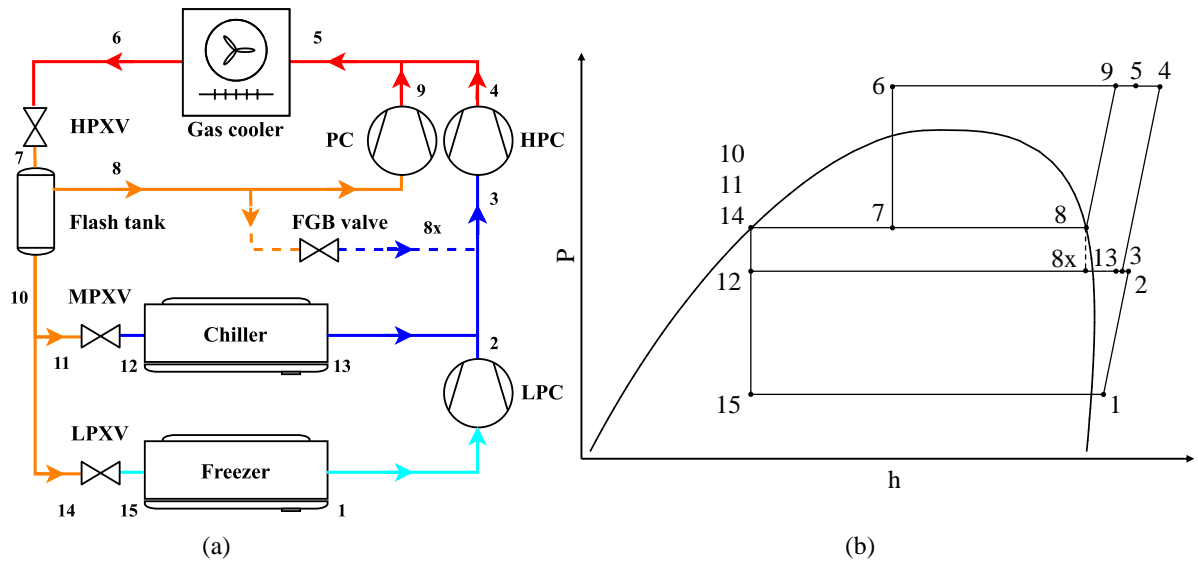


Figure 2. Transcritical CO₂ parallel compression refrigeration cycle (PRC) (a) Plant layout, (b) P-h diagram

The cycles were modeled in Engineering Equation Solver (EES) software [19] and the following assumptions were made:

- Cycles are operating in steady-state conditions.
- Expansion processes in the valves were assumed to be isenthalpic.
- Heat losses in the piping were neglected.
- Pressure losses in the piping and evaporators were neglected.
- Flash tank phase separation efficiency was taken as 100%.
- Freezer temperature and capacity were taken as -35 °C and 25 kW, respectively [20], [21].
- Chiller temperature and capacity were taken as -10 °C and 120 kW, respectively [20], [21].
- 5 K of useful superheat was applied to evaporators [21].
- Power consumptions of the evaporator and gas cooler fans were taken as 3% of the heat transfer ratio of the respective component [21], [22].
- Eq. (1) for used for compressor isentropic efficiency ($\eta_{comp,is}$) calculations [23] while global efficiency correlations were used for energy consumption calculations [21].

$$\eta_{comp,is} = -0.04478 \frac{P_{comp,out}}{P_{comp,in}} + 0.9343 \quad (1)$$

Energy analysis of the cycles was made using Eqs. (2-4) [21].

$$\sum \dot{Q}_{in} + \sum \dot{m}_{in} h_{in} + \sum \dot{W}_{in} = \sum \dot{Q}_{out} + \sum \dot{m}_{out} h_{out} + \sum \dot{W}_{out} \quad (2)$$

$$COP_{BRC} = \frac{\dot{Q}_{LT} + \dot{Q}_{MT}}{\dot{W}_{HPC} + \dot{W}_{LPC}} \quad (3)$$

$$COP_{PRC} = \frac{\dot{Q}_{LT} + \dot{Q}_{MT}}{\dot{W}_{HPC} + \dot{W}_{LPC} + \dot{W}_{PC} + \dot{W}_{fan,LT} + \dot{W}_{fan,MT}} \quad (4)$$

Where \dot{Q} is the heat transfer ratio, \dot{m} is the mass flow rate of the refrigerant, h is the specific enthalpy, and \dot{W} is the power consumption. Condenser/gas cooler conditions were determined based on Table 1. The cycles operate under transcritical conditions at ambient temperatures above 27 °C.

Table 1. Evaporator/gas cooler conditions [24]

T_{amb} (°C)	$T_{cond/GC,out}$ (°C)	$P_{cond/GC}$ (bar)
$T_{amb} \leq 5$	11	$P_{sat}@ (13 \text{ °C})$
$5 < T_{amb} \leq 14$	$T_{amb} + 6$	$P_{sat}@ (T_{amb} + 8 \text{ °C})$
$14 < T_{amb} \leq 27$	$0.7692T_{amb} + 9.23$	$1.397T_{GC,out} + 32.09$
$T_{amb} > 27$	$T_{amb} + 3$	Optimized

Evaporator loads vary between the minimum and design values based on the ambient temperature as shown in Table 2. This is because when ambient temperature deviates from the design point, the indoor air temperature and relative humidity will change and this will cause refrigeration loads to deviate from the design loads defined by the store refrigeration schedule [25].

Table 2. Evaporator load fractions [25]

T_{amb} (°C)	\dot{Q}_{MT} (kW)	\dot{Q}_{LT} (kW)
$T_{amb} < 5$	$0.66\dot{Q}_{MT,design}$	$0.80\dot{Q}_{LT,design}$
$5 \leq T_{amb} \leq 30$	$\left[1 - (1 - 0.66)\left(\frac{30 - T_{amb}}{30 - 5}\right)\right]\dot{Q}_{MT,design}$	$\left[1 - (1 - 0.80)\left(\frac{30 - T_{amb}}{30 - 5}\right)\right]\dot{Q}_{LT,design}$
$T_{amb} > 30$	$\dot{Q}_{MT,design}$	$\dot{Q}_{LT,design}$

The Total Equivalent Warming Impact (TEWI) method based on the EN378 standard was used for environmental impact calculations. Direct, indirect, and total TEWI were calculated using Eqs. (5-7). Emission caused by refrigerant leakage during the system lifetime and disposal contributes to direct TEWI while the one caused by energy production to operate the system contributes to indirect TEWI [26].

$$TEWI_{Direct} = GWP \times m \times [L \times n + (1 - \alpha)] \quad (5)$$

$$TEWI_{Indirect} = E \times K \times n \quad (6)$$

$$TEWI_{tot} = TEWI_{Direct} + TEWI_{Indirect} \quad (7)$$

Where E is the annual energy consumption. GWP, annual leakage loss (L), operation lifetime (n), recovery factor (α), refrigerant charge (m), and CO₂ emission coefficient (K) were taken as 1, 15%, 10 years, 90%, 435 kg, and 0.551 kg CO₂/kWh, respectively [22], [27]–[30].

Exergy calculations of the cycles were made using Eqs. (8-12) [31].

Exergy rate of the mass flow:

$$\dot{E}_{mass} = \dot{m}[h - h_0 - T_0(s - s_0)] \quad (8)$$

Exergy transfer rates from the evaporators and gas cooler:

$$\dot{E}_{MT}^Q = \dot{Q}_{MT} \left(\frac{T_0}{T_{L,MT}} - 1 \right) \quad (9)$$

$$\dot{E}_{LT}^Q = \dot{Q}_{LT} \left(\frac{T_0}{T_{L,LT}} - 1 \right) \quad (10)$$

$$\dot{E}_{GC}^Q = \dot{Q}_{GC} \left(1 - \frac{T_0}{T_{H,GC}} \right) \quad (11)$$

Exergy balance throughout the cycle:

$$\sum \dot{E}_{mass,in} + \sum \dot{W} = \sum \dot{E}_{mass,out} + \sum \dot{E}_{out}^Q + \dot{E}_D \quad (12)$$

Dead state temperature and pressure were taken as $T_{amb}+273$ K, and 1.01325 bar, respectively. Source temperatures for freezer, chiller, and gas cooler were taken as 249 K, 272 K, and $T_{amb} + 275.5$ K, respectively while air inlet and outlet temperatures were taken as -23 °C and -25 °C for freezer, 2 °C and 0 °C for chiller, T_{amb} and $T_{amb}+5$ °C for gas cooler, respectively [32], [24], [30].

The Specific Exergy Costing (SPECOC) method was used for exergoeconomic calculations. Capital investment and operation and maintenance costs are the non-exergy costs. Hourly capital investment (\dot{Z}_k^{CI}) and operation and maintenance (\dot{Z}_k^{OM}) costs of the components were calculated using Eqs. (13-15) considering purchased equipment cost (PEC), lifetime (n), operation hours (H), and interest rate of money (i_{eff}) [33], [34]. Table 3 presents PEC calculations of each component.

$$\dot{Z}_k = \dot{Z}_k^{CI} + \dot{Z}_k^{OM} \quad (13)$$

$$\dot{Z}_k^{CI} = PEC \times \frac{CRF}{H} \quad (14)$$

$$CRF = \frac{i_{eff}(1+i_{eff})^n}{(1+i_{eff})^n - 1} \quad (15)$$

Taxes, operation, and maintenance costs were not considered. 15% was added to the capital investment cost of each component for piping, automation, control instruments, and installation [35]. Annual interest rate and operation lifetime were taken as 2% and 10 years, respectively [27], [28], [36].

Table 3. Purchased equipment cost (PEC) values of the components

Component	Purchased equipment cost (€)	Reference
Compressor	$10167.5W_{el,comp}^{0.46}$	[35], [37]
Gas cooler	$1397A_{GC}^{0.89} + 629.05W_{fan,GC}^{0.76}$	[35], [38]
	$A_{GC} = \frac{\dot{Q}_{GC}}{U \times LMTD}$	
	$LMTD = \frac{(T_{GC,in} - T_{air,out}) - (T_{GC,out} - T_{air,in})}{\ln\left(\frac{T_{GC,in} - T_{air,out}}{T_{GC,out} - T_{air,in}}\right)}$	
	$U = 0.575 \text{ kW/m}^2\text{K}$	
Evaporator	19226 € for chiller 3243 € for freezer	[39]
Expansion valve	$114.5\dot{m}_{exp}$	[40]
Flash tank	$280.3\dot{m}_{flash}^{0.67}$	[40]

Unit electricity price was multiplied by the constant escalation levelization factor (CEL)

considering inflation (r_n) and interest (i_{eff}) rates using Eqs. (16-18) [33], [34].

$$c_{el} = \text{Electricity cost per kWh} \times CELF \quad (16)$$

$$CELF = \frac{k(1 - k^n)}{1 - k} \times CRF \quad (17)$$

$$k = \frac{1 + r_n}{1 + i_{eff}} \quad (18)$$

Where k is the cost correction factor. Annual inflation rate (r_n) and electricity price (c_{el}) were taken as 9.2% and 0.2104 €/kWh, respectively according to Eurostat [41], [42].

Eqs. (19-23) were used as cost balance equations of the components [33], [34].

$$c_{comp,in} \dot{E}_{comp,in} + c_{el} \dot{W}_{comp,el} + \dot{Z}_{comp} = c_{comp,out} \dot{E}_{comp,out} \quad (19)$$

$$c_{ev,in} \dot{E}_{ev,in} + c_{Q_{ev}} \dot{Q}_{ev} \left(1 - \frac{T_0}{T_L}\right) + c_{el} \dot{W}_{fan,ev} + \dot{Z}_{ev} = c_{ev,out} \dot{E}_{ev,out} \quad (20)$$

$$c_{GC,in} \dot{E}_{GC,in} + c_{el} \dot{W}_{fan,GC} + \dot{Z}_{GC} = c_{GC,out} \dot{E}_{GC,out} + c_{Q_{GC}} \dot{Q}_{GC} \left(1 - \frac{T_0}{T_H}\right) \quad (21)$$

$$c_{exp,in} \dot{E}_{exp,in} + \dot{Z}_{exp} = c_{exp,out} \dot{E}_{exp,out} \quad (22)$$

$$c_{flash,in} \dot{E}_{flash,in} + \dot{Z}_{flash} = c_{flash,out,l} \dot{E}_{flash,out,l} + c_{flash,out,g} \dot{E}_{flash,out,g} \quad (23)$$

Where c is the hourly exergy cost, \dot{E} is the exergy rate, \dot{Z} is the hourly non-exergy cost of the component. Eqs. (24-26) were used as auxiliary equations [43].

$$c_{ev,in} = c_{ev,out} \quad (24)$$

$$c_{GC,in} = c_{GC,out} \quad (25)$$

$$c_{flash,out,l} = c_{flash,out,g} \quad (26)$$

3. RESULTS AND DISCUSSION

As temperature and pressure are independent of each other above the critical point, gas cooler outlet pressure needs to be optimized for maximum performance. Optimum gas cooler pressures for each gas cooler outlet temperature were obtained using the Golden Section Search method and Eqs. (27-28) were derived with curve-fitting. Intermediate pressure was taken as $P_{MT} + 5$ bar for BRC, and 55 bar under transcritical conditions for PRC [30]. Intermediate pressure for PRC, however, was taken as 45 bar under subcritical conditions.

$$P_{GC,opt,BRC} = 2.6529T_{GC,out} - 4.80083 \quad (27)$$

$$P_{GC,opt,PRC} = 2.35073T_{GC,out} + 1.85568 \quad (28)$$

Figure 3 shows COP comparison of the modeled cycles with the study done by Gullo et al. [21] under the same evaporator and gas cooler conditions. The results exhibited a satisfactory agreement

with the literature.

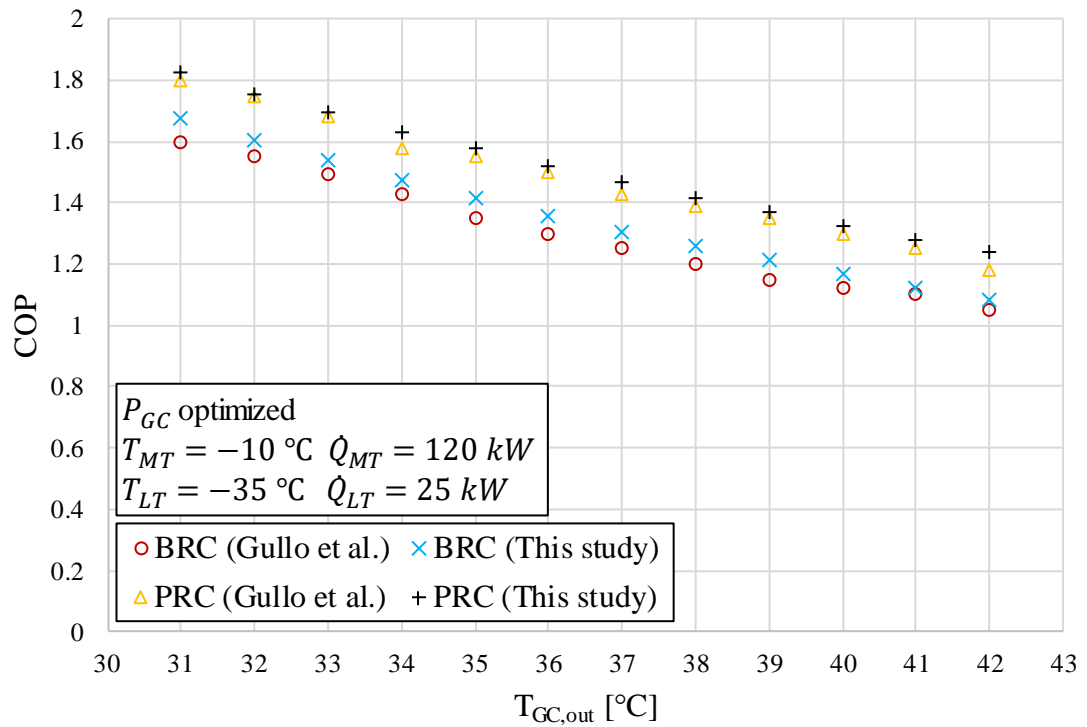


Figure 3. COP comparison of the investigated cycles with the literature

Figure 4 presents COP and total power consumption values of the cycles under different ambient temperatures. PRC was modeled as the same as BRC at ambient temperatures below 14 °C due to the insufficient mass flow rate in the PC. The cycles perform similarly under subcritical conditions. The performance difference increases under transcritical conditions with the increase in the ambient temperature. COP improvement and total power consumption reduction of PRC are up to 14.8% and up to 12.9%, respectively within the investigated ambient temperatures.

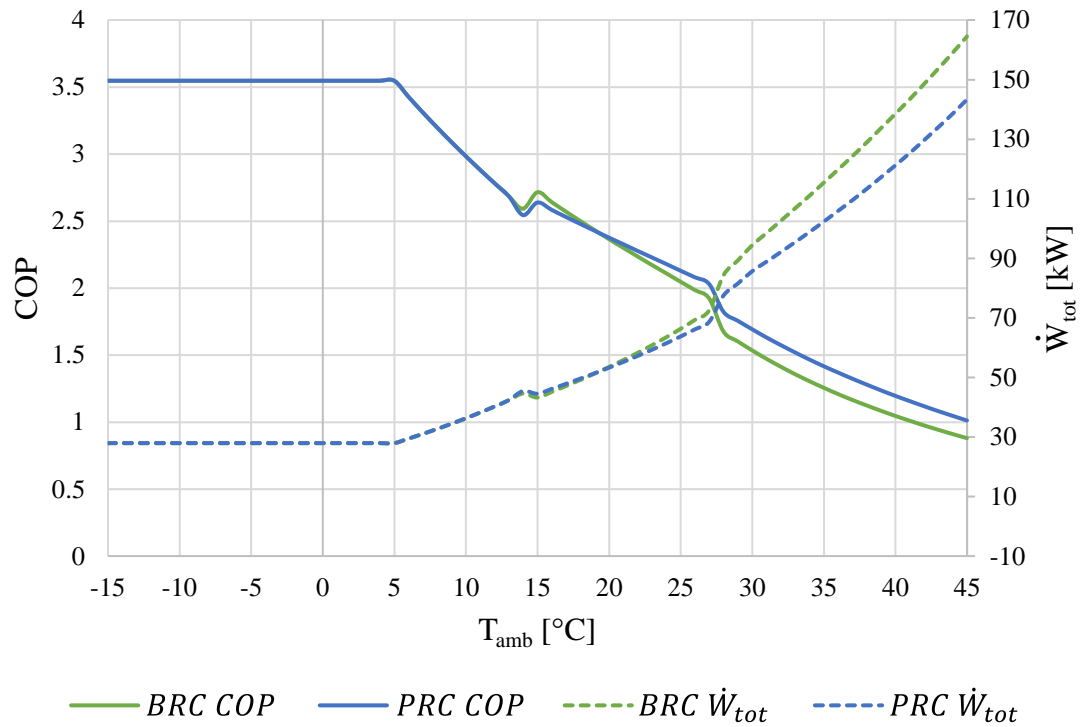


Figure 4. COP and total power consumption comparison of the cycles

Figure 5 presents bin-hour data for 11 provinces of Türkiye, which are in different climate zones. Bin-hours were derived using hourly dry-bulb temperatures of the provinces for the years 2016-2020 gathered from the Meteorological Data Information, Presentation and Sales System of Türkiye [44]. Temperature values were grouped into temperature bins with 3 °C increments and then the number of occurrence hours for each temperature bin was calculated. Power consumptions at the mid-point of each temperature bin were multiplied by the occurrence hours, and then these values were summed to calculate annual energy consumptions of the cycles.

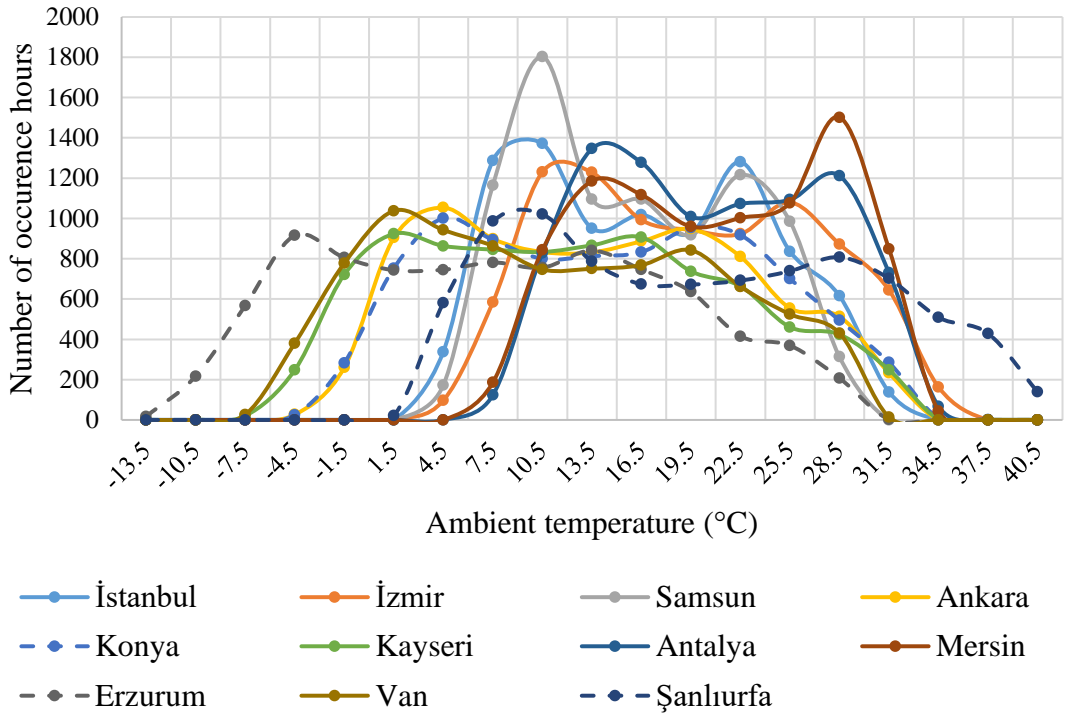


Figure 5. Bin-hour data for 11 provinces of Türkiye

Figure 6 shows the number of occurrence hours of the temperatures below and above 14 °C, which is the operating threshold of PC, for 11 provinces as well as annual mean temperatures. Erzurum and Van have the lowest annual mean temperatures while Antalya, Mersin, and Şanlıurfa have the highest. PC has the highest operation hours in Mersin and lowest in Erzurum.

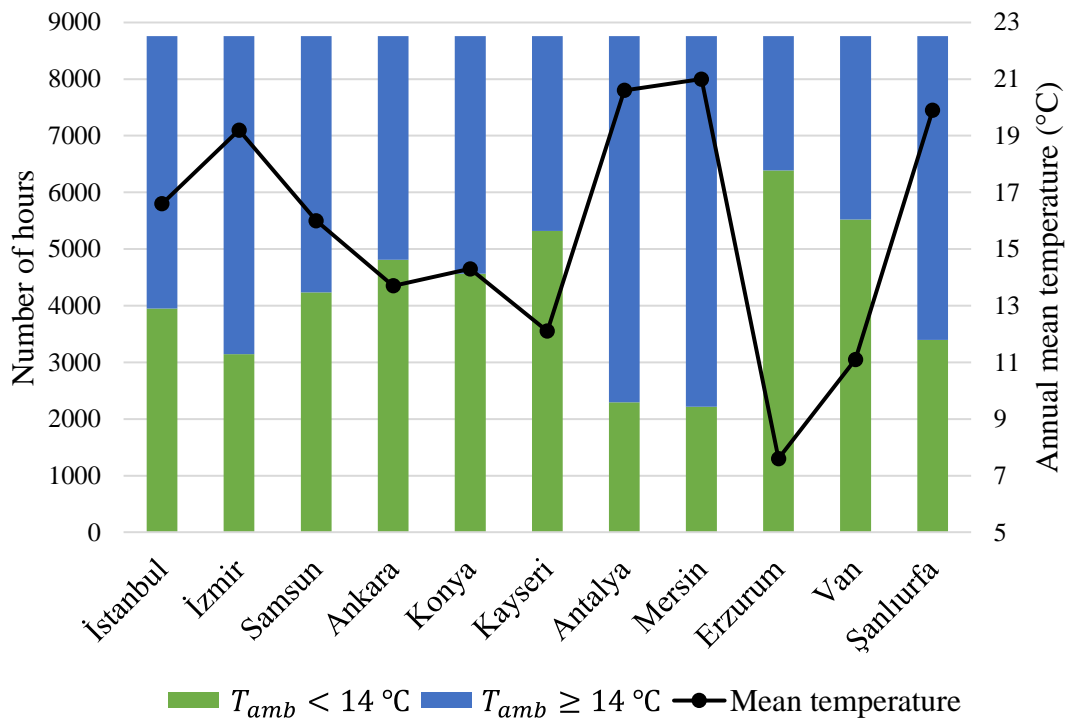


Figure 6. Number of hours at ambient temperatures below and above 14 °C, and annual mean temperatures of 11 provinces

Annual energy consumption values of the cycles for 11 provinces are presented in Figure 7. PRC outperforms BRC in all provinces. The difference is more identical in İzmir, Antalya, Mersin, and Şanlıurfa, which have warm climates. An increase in the ambient temperature increases the mass flow rate of PC which has a lower pressure difference compared to HPC. This results in higher performance compared to BRC in warmer provinces. In Erzurum and Van, which are cooler provinces, there is a small amount of difference as PC operation hours are low. Consumption for Erzurum and Van is below 400 MWh while it exceeds 500 MWh for Antalya, Mersin, and Şanlıurfa. PRC consumed 5.6% less energy than BRC in Şanlıurfa. Since GWP value of CO₂ is 1, direct TEWI of CO₂ cycles is negligible and total TEWI highly depends on the energy consumption. Figure 8 shows 10-year TEWI values of the cycles for 11 provinces. TEWI for Erzurum is below 2000 tons while it is above 2500 tons for İzmir, Antalya, Mersin, and Şanlıurfa.

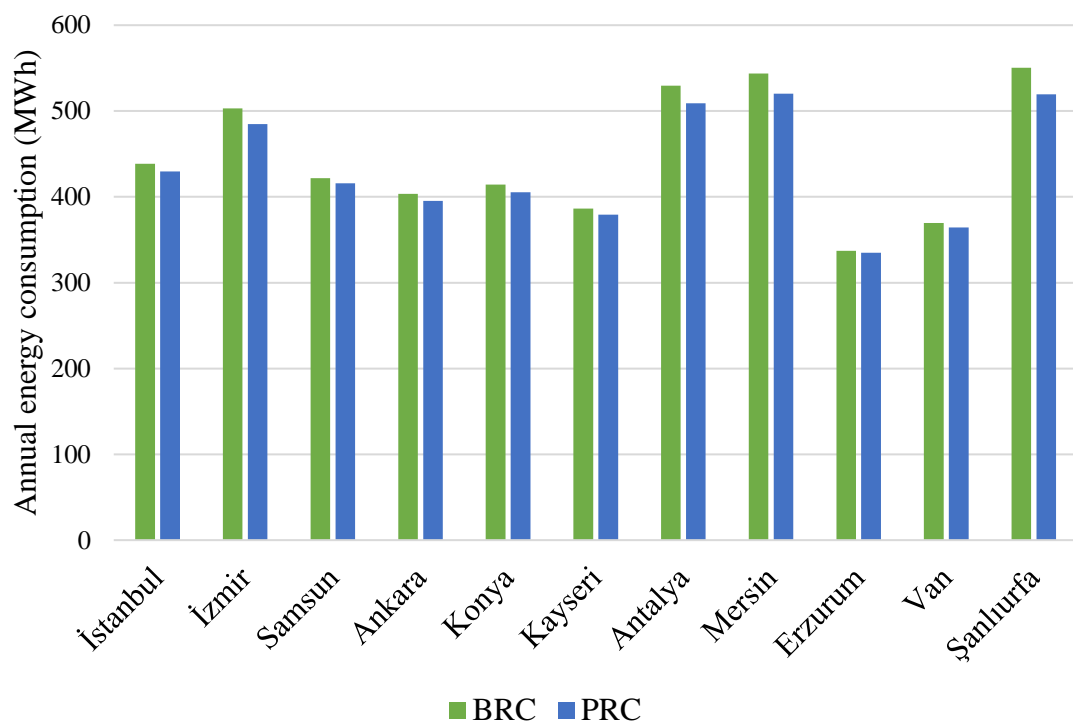


Figure 7. Annual energy consumption of the cycles for 11 provinces

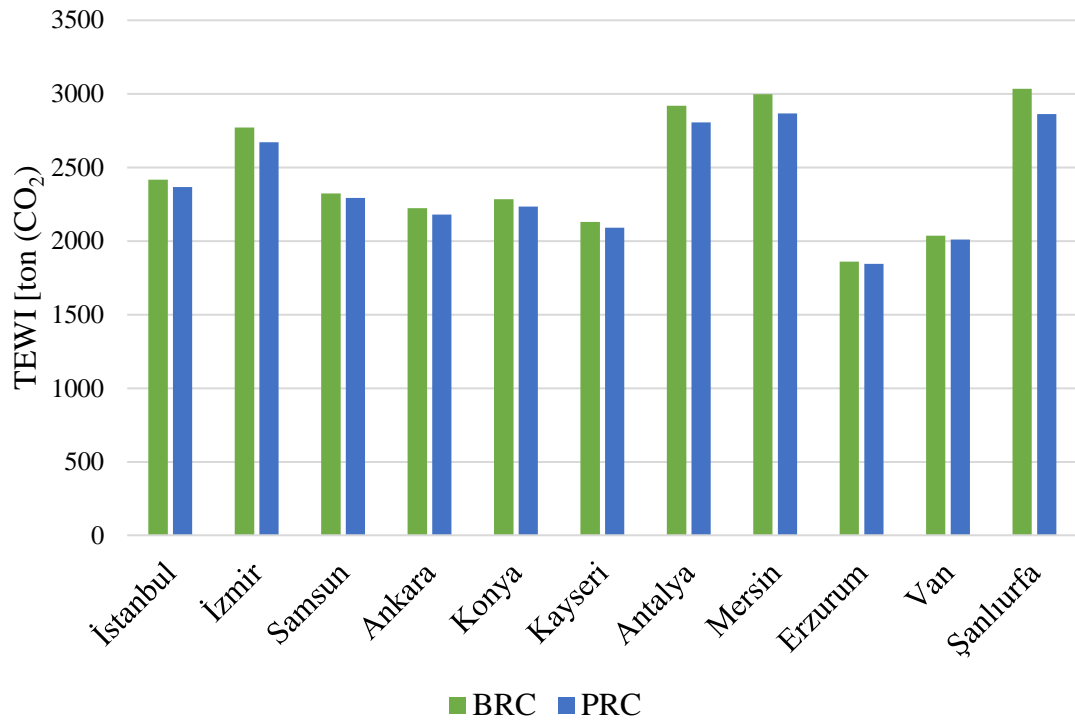


Figure 8. 10-year TEWI values of the cycles for 11 provinces

Figure 9 presents PEC values of the cycles for 11 provinces. Maximum ambient temperatures for the provinces were considered to ensure the proper operation of the cycles. The cost of PRC is higher than BRC as compressors are expensive components.

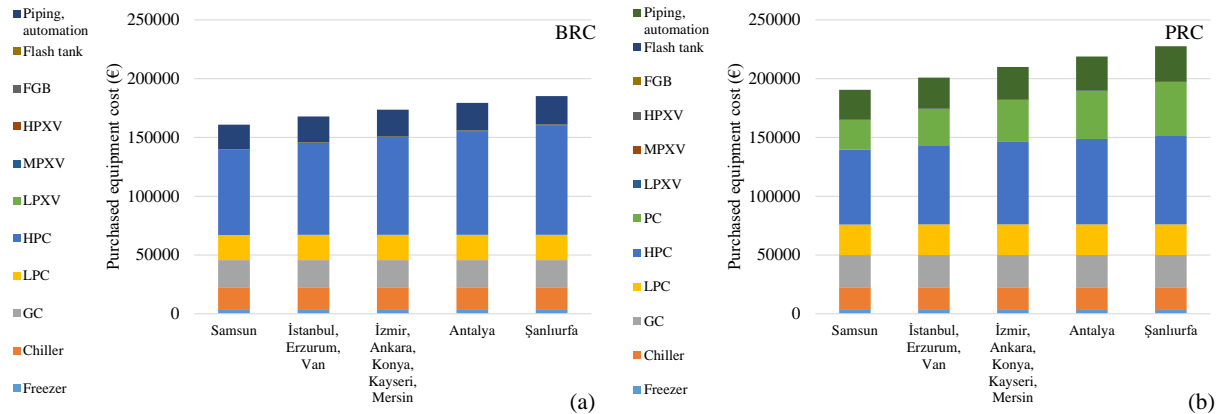


Figure 9. Purchased equipment costs of (a) BRC, (b) PRC

Unit product exergy costs of the cycles for 11 provinces at maximum ambient temperatures are presented in Table 4. Levelized electricity price was calculated as 0.3474 €/kWh. Although the equipment cost of PRC is higher than BRC, reduced energy consumption leads to lower product cost. Cost reduction in PRC varies between 8.2% and 18%. Provinces that have higher ambient temperatures have higher product costs due to higher energy consumption.

Table 4. Unit product exergy costs of the cycles for 11 provinces

Province	$T_{amb,max}$ (°C)	Unit product exergy cost (€/kWh)		
		BRC	PRC	Reduction
İstanbul	31.5	1.957	1.748	10.7%
İzmir	34.5	2.021	1.75	13.4%
Samsun	28.5	1.894	1.739	8.2%
Ankara	34.5	2.021	1.77	12.4%
Konya	34.5	2.021	1.766	12.6%
Kayseri	34.5	2.021	1.779	12%
Antalya	37.5	2.088	1.752	16.1%
Mersin	34.5	2.021	1.743	13.8%
Erzurum	31.5	1.957	1.796	8.2%
Van	31.5	1.957	1.77	9.6%
Şanlıurfa	40.5	2.159	1.77	18%

4. CONCLUSIONS

In this paper, transcritical CO₂ booster (BRC) and parallel compression (PRC) supermarket refrigeration cycles were modeled in EES software and annual energy, TEWI, and exergoeconomic analysis were made deriving bin-hour data of 11 provinces in Türkiye. Up to 14.8% higher COP was obtained with PRC compared to BRC between the investigated ambient temperatures. Annual energy consumption in Erzurum and Van is below 400 MWh while It is above 500 MWh in Antalya, Mersin, and Şanlıurfa. Similarly, TEWI value in Erzurum is below 2000 tons while it is above 2500 tons in İzmir, Antalya, Mersin, and Şanlıurfa. PRC has lower energy consumption and TEWI values between 0.7% and 5.6% compared to BRC in the investigated provinces. The equipment cost of PRC is higher than BRC between 18% and 23% due to the additional compressor. Unit product exergy cost difference at the maximum ambient temperatures is between 8.2% and 18%. It was seen that since parallel compressor operates above the ambient temperatures of 14 °C, there is no significant annual consumption reduction in cooler provinces such as Erzurum and Van. The advantage of the use of parallel compressor is more significant in warmer provinces such as Antalya, Mersin, and Şanlıurfa. The performance of the cycles can be improved more by applying more advanced solutions such as ejector expansion, which is used for expansion work recovery, especially in warm climates [30]. Performance enhancement of the cycles using environmentally friendly refrigerants will contribute to a sustainable future.

Declaration of Ethical Standards

The authors of this article declare that the materials and methods used in this study do not require ethical committee permission and/or legal-special permission.

Credit Authorship Contribution Statement

Oğuz ÇALIŞKAN: Conceptualization, Methodology, Formal analysis, Software, Resources, Writing - original draft, Visualization.

H. Kürşad ERSOY: Conceptualization, Methodology, Formal analysis, Resources, Writing - review & editing, Supervision.

Declaration of Competing Interest

The authors declare that they have no known competing financial interests or personal relationships that could have appeared to influence the work reported in this paper.

Funding / Acknowledgements

This work was supported by Konya Technical University Academic Staff Training Program (Grant No. 2016-ÖYP-046). In addition, the present paper constitutes part of the Ph.D. thesis of Oğuz Çalışkan. Also, the authors thank the anonymous reviewers for their constructive comments and suggestions in improving the quality of this paper.

Data Availability

The data used to support the findings of this study are included within the article.

REFERENCES

- [1] EPA, "Putting energy into profits: Energy Star guide for small business," *U.S. Environmental Protection Agency*, 2007. [Online]. Available: <https://nepis.epa.gov/Exe/ZyPURL.cgi?Dockkey=P100FCSW.txt>. [Accessed: Dec. 02, 2022].
- [2] IPCC/TEAP, "Safeguarding the ozone layer and the global climate system: Issues related to hydrofluorocarbons and perfluorocarbons," Intergovernmental Panel on Climate Change Technology and Economic Assessment Panel, 2005.
- [3] M. Schulz and D. Kourkoulas, "Regulation (EU) No 517/2014 of the European Parliament and of the Council of 16 April 2014 on fluorinated greenhouse gases and repealing Regulation (EC) No 842/2006," 517/2014, 2014. Available: <http://eur-lex.europa.eu/eli/reg/2014/517/oj>.
- [4] ASHRAE, "ANSI/ASHRAE Standard 34-2019: Designation and Safety Classification of Refrigerants," *American Society of Heating, Refrigerating and Air-Conditioning Engineers*, 2019.
- [5] B. Yu, J. Yang, D. Wang, J. Shi, and J. Chen, "An updated review of recent advances on modified technologies in transcritical CO₂ refrigeration cycle," *Energy*, vol. 189, p. 116147, Dec. 2019, doi: 10.1016/j.energy.2019.116147.
- [6] F. Yılmaz and R. Selbaş, "Energy and Exergy Analyses of CO₂/HFE7000 Cascade Cooling System," *Süleyman Demirel Univ. J. Nat. Appl. Sci.*, vol. 21, no. 3, pp. 854–860, Oct. 2017, doi: 10.19113/sdufbed.58140.
- [7] S. Zong, X. Yin, T. Miao, S. Zhang, X. Yang, and F. Cao, "Experimental investigation on the cooling performance of direct and secondary loop CO₂ air conditioning systems for electric vehicles," *Int. J. Refrig.*, vol. 152, pp. 376–386, Aug. 2023, doi: 10.1016/j.ijrefrig.2023.05.019.
- [8] V. Sharma, B. Fricke, and P. Bansal, "Comparative analysis of various CO₂ configurations in supermarket refrigeration systems," *Int. J. Refrig.*, vol. 46, pp. 86–99, 2014, doi: 10.1016/j.ijrefrig.2014.07.001.
- [9] H. Fritschi, F. Tillenkamp, R. Löhner, and M. Brügger, "Efficiency increase in carbon dioxide refrigeration technology with parallel compression," *Int. J. Low-Carbon Technol.*, vol. 12, no. 2, pp. 171–180, Jun. 2017, doi: 10.1093/ijlct/ctw002.
- [10] A. Chesi, F. Esposito, G. Ferrara, and L. Ferrari, "Experimental analysis of R744 parallel compression cycle," *Appl. Energy*, vol. 135, pp. 274–285, Dec. 2014, doi: 10.1016/j.apenergy.2014.08.087.
- [11] C. Papazahariou, "Natural refrigerants faster to market, commercial refrigeration with low gwp alternatives," presented at the Joint Meeting of the Regional Ozone Networks for Europe & Central Asia and South Asia, Istanbul: Shecco, 2010.
- [12] W. Chakroun, *Lower-GWP Alternatives in Commercial and Transport Refrigeration: An expanded compilation of propane, CO₂, ammonia and HFO case studies*. Paris: United Nations Environment Programme, 2016.
- [13] M. Garry, "Carrefour Poland Retrofits 46 Stores with R744," *r744.com*, Oct. 22, 2019. Available: <https://r744.com/carrefour-poland-retrofits-46-stores-with-r744/>. [Online], [Accessed: Nov. 18, 2022].

- [14] R744.com, "Carrefour Timisoara: New CO2 multi-ejector refrigeration system is major success," *R744.com*, Dec. 16, 2015. [Online], Available: <https://r744.com/carrefour-timisoara-new-co2-multi-ejector-refrigeration-system-is-major-success/>. [Accessed: Nov. 18, 2022].
- [15] A. Rubatto, "Carrefour using ejectors in CO2 transcritical system in Italy," *R744.com*, Mar. 12, 2018. [Online], Available: <https://r744.com/carrefour-using-ejectors-in-co2-transcritical-system-in-italy/>. [Accessed: Nov. 18, 2022].
- [16] M. Garry, "Tesco Has Transcritical CO2 Refrigeration at 1,000 Stores.," *r744.com*, Oct. 19, 2022. [Online], Available: <https://r744.com/tesco-has-transcritical-co2-refrigeration-at-1000-stores-one-third-of-its-estate/>. [Accessed: Nov. 11, 2022].
- [17] J. O. Haroldsen, "Canadian Longo's Commits to CO2 in New Stores and Renovations," *R744.com*, May 22, 2023. [Online], Available: <https://r744.com/with-44-of-stores-using-co2-refrigeration-canadian-retailer-longos-commits-to-co2-in-new-stores-and-renovations/>. [Accessed: Aug. 22, 2023].
- [18] J. O. Haroldsen, "Japanese C-Store Operator Lawson Operates 5,028 Stores – Over 34% of Its Chain – With CO2 Refrigeration," *R744.com*, Jun. 21, 2023. [Online], Available: <https://r744.com/japanese-c-store-operator-lawson-operates-5028-stores-over-34-of-its-chain-with-co2-refrigeration/>. [Accessed: Aug. 22, 2023].
- [19] S. A. Klein, "Engineering Equation Solver." F-Chart Software, 2020.
- [20] S. Girotto, S. Minetto, and P. Neksa, "Commercial refrigeration system using CO2 as the refrigerant," *Int. J. Refrig.*, vol. 27, no. 7, pp. 717–723, 2004, doi: 10.1016/j.ijrefrig.2004.07.004.
- [21] P. Gullo, A. Hafner, and G. Cortella, "Multi-ejector R744 booster refrigerating plant and air conditioning system integration – A theoretical evaluation of energy benefits for supermarket applications," *Int. J. Refrig.*, vol. 75, pp. 164–176, 2017, doi: 10.1016/j.ijrefrig.2016.12.009.
- [22] M. Karampour and S. Sawalha, "State-of-the-art integrated CO2 refrigeration system for supermarkets: A comparative analysis," *Int. J. Refrig.*, vol. 86, pp. 239–257, Feb. 2018, doi: 10.1016/j.ijrefrig.2017.11.006.
- [23] J. S. Brown, S. F. Yana-Motta, and P. A. Domanski, "Comparitive analysis of an automotive air conditioning systems operating with CO2 and R134a," *Int. J. Refrig.*, vol. 25, no. 1, pp. 19–32, Jan. 2002, doi: 10.1016/S0140-7007(01)00011-1.
- [24] D. Tsimpoukis *et al.*, "Energy and environmental investigation of R744 all-in-one configurations for refrigeration and heating/air conditioning needs of a supermarket," *J. Clean. Prod.*, vol. 279, Jan. 2021, doi: 10.1016/j.jclepro.2020.123234.
- [25] M. Zhang, "Energy Analysis of Various Supermarket Refrigeration Systems," in *International Refrigeration and Air Conditioning Conference*, Purdue, 2006.
- [26] A. Zottl, M. Lindahl, R. Nordman, P. Rivière, and M. Miara, "Evaluation method for comparison of heat pump systems with conventional heating systems, D4.3. Concept for evaluation of CO2-reduction potential," *European Commission*, 2011.
- [27] J. A. Shilliday, "Investigation and optimisation of commercial refrigeration cycles using the natural refrigerant CO2," Ph.D. dissertation, Brunel University, London, 2012. Available: <http://bura.brunel.ac.uk/handle/2438/7454>.
- [28] P. Gullo, "Thermodynamic and environmental comparison of R744 booster supermarket refrigeration systems operating in Southern Europe," Ph.D. dissertation, University of Udine, Udine, Italy, 2016. Available: https://air.uniud.it/retrieve/handle/11390/1132962/251100/10990_827_PhD_thesis_GULLO.pdf.
- [29] H. Dulkadiroğlu, "Türkiye'de elektrik üretiminin sera gazı emisyonları açısından incelenmesi," *Niğde Ömer Halisdemir Univ. J. Eng. Sci.*, vol. 7, no. 1, pp. 67–74, 2018, doi: 10.28948/ngumuh.369948.
- [30] O. Caliskan and H. K. Ersoy, "Energy analysis and performance comparison of transcritical CO2 supermarket refrigeration cycles," *J. Supercrit. Fluids*, vol. 189, p. 105698, Oct. 2022, doi: 10.1016/j.supflu.2022.105698.

- [31] T. J. Kotas, *The exergy method of thermal plant analysis*. London; Boston: Butterworths, 1985.
- [32] P. Gullo, A. Hafner, and K. Banasiak, "Thermodynamic Performance Investigation of Commercial R744 Booster Refrigeration Plants Based on Advanced Exergy Analysis," *Energies*, vol. 12, no. 3, p. 354, Jan. 2019, doi: 10.3390/en12030354.
- [33] A. Bejan, G. Tsatsaronis, and M. J. Moran, *Thermal design and optimization*. in A Wiley-Interscience publication. New York: Wiley, 1996.
- [34] A. Lazzaretto and G. Tsatsaronis, "SPECO: A systematic and general methodology for calculating efficiencies and costs in thermal systems," *Energy*, vol. 31, no. 8–9, pp. 1257–1289, Jul. 2006, doi: 10.1016/j.energy.2005.03.011.
- [35] F. Fazelpour and T. Morosuk, "Exergoeconomic analysis of carbon dioxide transcritical refrigeration machines," *Int. J. Refrig.*, vol. 38, pp. 128–139, Feb. 2014, doi: 10.1016/j.ijrefrig.2013.09.016.
- [36] ECB, "Official interest rates," *European Central Bank*, May 04, 2023. [Online]. Available: https://www.ecb.europa.eu/stats/policy_and_exchange_rates/key_ecb_interest_rates/html/index.en.html. [Accessed: May 10, 2023].
- [37] O. Rezayan and A. Behbahaninia, "Thermoeconomic optimization and exergy analysis of CO₂/NH₃ cascade refrigeration systems," *Energy*, vol. 36, no. 2, pp. 888–895, 2011, doi: 10.1016/j.energy.2010.12.022.
- [38] Id. M. C. Santosa, K. M. Tsamos, B. L. Gowreesunker, and S. A. Tassou, "Experimental and CFD investigation of overall heat transfer coefficient of finned tube CO₂ gas coolers," *Energy Procedia*, vol. 161, pp. 300–308, Mar. 2019, doi: 10.1016/j.egypro.2019.02.096.
- [39] Friterm, "Friterm Product Selection Software." 2022.
- [40] A. H. Mosaffa, L. G. Farshi, C. A. Infante Ferreira, and M. A. Rosen, "Exergoeconomic and environmental analyses of CO₂/NH₃ cascade refrigeration systems equipped with different types of flash tank intercoolers," *Energy Convers. Manag.*, vol. 117, pp. 442–453, Jun. 2016, doi: 10.1016/j.enconman.2016.03.053.
- [41] Eurostat, "Inflation in the euro area," 2023. [Online]. Available: https://ec.europa.eu/eurostat/statistics-explained/index.php?title=Inflation_in_the_euro_area. [Accessed: Apr. 13, 2023].
- [42] Eurostat, "Electricity price statistics," 2023. [Online]. Available: https://ec.europa.eu/eurostat/statistics-explained/index.php?title=Electricity_price_statistics. [Accessed: May 10, 2023].
- [43] P. Gullo, B. Elmegaard, and G. Cortella, "Energetic, Exergetic and Exergoeconomic Analysis of CO₂ Refrigeration Systems Operating in Hot Climates," in *ECOS 2015 28th International Conference on Efficiency, Cost, Optimization, Simulation and Environmental Impact of Energy Systems*, Pau, France, Jul. 2015.
- [44] O. Çalışkan, "CO₂ akışkanlı ejektör genleştiricili süpermarket soğutma sistemlerinin Türkiye iklim şartlarında termodinamik, çevresel ve termoeconomik analizi," Ph.D. dissertation, Konya Technical University, Konya, Türkiye, 2022. Available: <https://tez.yok.gov.tr/UlusalTezMerkezi/TezGoster?key=sELqXHtIFGAjsbjOuuYCEpA0yENEpzFQC8tfkzv2-m2Bn7L1xI9fWYroF97Gvpj>.



ESTIMATIONS OF GREEN HOUSE GASES EMISSIONS OF TURKEY BY STATISTICAL METHODS

¹Suat ÖZTÜRK , ^{2,*}Ahmet EMİR 

¹Zonguldak Bulent Ecevit University, Zonguldak Vocational School, Electronic and Automation Department, Zonguldak, TÜRKİYE

²Zonguldak Bulent Ecevit University, Engineering Faculty, Computer Engineering Department, Zonguldak, TÜRKİYE

¹suatozturk@beun.edu.tr, ²ahmet.emir@beun.edu.tr

Highlights

- Estimations of CH₄, N₂O and CO₂ Emissions of Turkey are aimed.
- Predictions are evaluated by of GM, ARIMA and DES methods.
- Prediction performance is decided by mean absolute percentage error (MAPE).



ESTIMATIONS OF GREEN HOUSE GASES EMISSIONS OF TURKEY BY STATISTICAL METHODS

¹Suat ÖZTÜRK^{ID}, ^{2,*}Ahmet EMİR^{ID}

¹ Zonguldak Bulent Ecevit University, Zonguldak Vocational School, Electronic and Automation Department, Zonguldak, TÜRKİYE

² Zonguldak Bulent Ecevit University, Engineering Faculty, Computer Engineering Department, Zonguldak, TÜRKİYE

¹suatozturk@beun.edu.tr, ²ahmet.emir@beun.edu.tr

(Received: 17.03.2023; Accepted in Revised Form: 22.01.2024)

ABSTRACT: The way of life, consumption habits, urbanization rate, type of energy production and increasing energy need with growing economies and population progressively promote the GHGs emissions to Earth's atmosphere. GHGs consisting of CH₄, N₂O, CO₂, H₂O and HFCs cause the climate change, disrupting ecological balance, melting glaciers with global warming in the last decades. Therefore, the issues of future prediction and reduction of GHGs emissions became crucial for policy makers of Turkey and other countries under the international protocols and agreements. This article aims to present the prediction and 8-year future forecasting of CH₄, N₂O and CO₂ emissions of Turkey using past annual data between years 1970 and 2018 with grey, autoregressive integrated moving average and double exponential smoothing models. Based on the results, the best prediction performance is reached by DES model followed by ARIMA and GM for all the emissions. MAPEs calculated from the available data and prediction by DES model from 1970 to 2018 are 0.285, 0.355 and 0.408 for CH₄, N₂O and CO₂ in turn. DES future estimations of CH₄, N₂O and CO₂ at 2026 year are determined as 50700 kiloton of CO₂ eq., 38100 thousand metric ton of CO₂ eq., and 512000 kilotons.

Keywords: Greenhouse gases, Emission, Forecasting, Environment, Turkey

1. INTRODUCTION

Green House Gases (GHGs) causes global warming as a serious factor that changes the earth's climate [1]. The emissions of GHGs, such as methane (CH₄), carbon dioxide (CO₂), and nitrous oxide (N₂O) have a great effect on anthropogenic climate warming phenomena according to the assessment of Intergovernmental Panel on Climate Change in 2013 [2]. Although CO₂ emission is higher than other GHG emissions, CH₄ and N₂O emissions are more effective 28 and 256 times than CO₂ emissions on global warming [3]. On the other hand, if no action is taken to reduce these hazardous emissions, annual median temperature will be expected to increase by 4 to 5 degrees Celsius by 2100 [4].

GHGs are emitted to the atmosphere by both human-based and natural ways [5]. From these gases, N₂O emerges from the reaction of NO and O₃ in atmosphere air and depletes O₃ [6]. NO and CO₂ are mostly produced at the end of combustion by vehicle's engines, heating and electricity energy production systems using hydrocarbon-based fuels as natural gas, diesel, gasoline, and coal, etc [7, 8]. CH₄ emission comes from agriculture activity, farm animals, organic decays, and gas leakages from underground and volcanos [9, 10].

To combat the predictable effects of GHGs over bios, atmosphere and climate of earth, Kyoto Protocols and Paris Agreement were signed in both 1997 and 2015. However, GHG emissions have been desperately increased by great demand of countries to hydrocarbon-based energy consumption. For this reason, the countries led by the G7 have increased their GHGs forecasting studies related to the decrease of energy consumption [11]. Moreover, the usage of renewable energy types as wind, solar, wave, waste recycle and combustion systems emitting less GHGs are to be recommended for energy production [12, 13].

Turkey is a developing country as a terrestrial bridge among Europe, Asia and Africa continents.

*Corresponding Author: Ahmet EMİR, ahmet.emir@beun.edu.tr

GHGs emissions of Turkey has been increasing since 1980s [14] because the growing trend of Turkey has a deep impact on its energy consumption. After Turkey joined Kyoto in 2009 and signed Paris Agreement in 2015, Turkey was expected to decrease its GHGs emissions to 21 %. Even though Turkey aimed not to exceed 929 million tone (MT) CO₂ equivalent emissions by 2030 [15], its GHGs emissions have risen up to 520.9 MT in 2018 [16]. Because of this reason, studies about the forecasting GHGs emissions of Turkey has begun to gain significance more and more.

Time series data of GHGs emissions of countries are able to be obtained in hourly, daily, monthly and annual terms. Forecasting techniques on past univariate or multivariate data generally include methods of artificial neural networks [17], fuzzy logic [18] support vector machine [19], machine learning [20] and classic statistical models as regression [21], autoregressive integrated moving average [22] and grey [23], etc. Statistical methods are more appropriate for future predictions of short univariate time series in regard to other methods preferred more for long univariate and multivariate data.

In this study, CH₄, N₂O and CO₂ greenhouse gas emissions of Turkey are predicted by grey, autoregressive integrated moving average, and double exponential smoothing models from statistical techniques using past annual univariate time series data [24] of CH₄, N₂O and CO₂ between 1970 and 2018 years. Besides, next 8-year data are forecasted up to 2026. The calculations of train, test, and prediction of models are realized using Python codes.

In the literature, according to authors knowledge, the studies about the estimation of Turkey's green gas emissions are presented less. Main contribution of this study is to forecast future greenhouse gases emissions by statistical methods. Besides, the study is suitable for future planning of decreasing GHGs emissions because new arrangements and regulations to minimize GHGs are forced by developed countries in the world. In addition, EU countries have been planning to put new restrictions to countries where they import goods and services from. For realizing this purpose, real data and statistical results are compared by error criterion (MAPE). Error criterion increases the reliability of future emission data for the next years and thus, more accurate results are obtained.

2. LITERATURE OVERVIEW

Prediction is an important issue for determination of the reduction targets of GHGs emissions because countries have been scheduling annual GHGs emissions using predictions to achieve the aimed limits. There are many studies that include estimation methods forecasting future data from former time series data in literature. [4] forecasted total GHGs emission between 2018 and 2050 in Romania. [7] estimated heavy-duty vehicle emissions (CO₂) for future 9 years of Semarang City, Indonesia. Şahin [8] predicted Turkey's GHGs emission between years 2017 and 2025 using Grey methods. [9] used machine learning method with regression models, shallow learning, and deep learning for predicting greenhouse gas emissions from agricultural soils. [11] predicted CO₂ emissions in the G7 countries. [12] utilized a recursive structural vector autoregression method to forecast GHGs in Montenegro. [13] constructed a novel multi-variable grey forecasting model based on the smooth generation of independent variable sequences with variable weights and new multivariable grey prediction model with structure compatibility for forecasting of CO₂ with the effect of renewable energy in Turkey. [14] predicted the energy-related CO₂ emission between years 2013 and 2025. [15] estimated GHGs in Turkey with grey wolf optimizer algorithm-optimized artificial neural networks. [16] forecasted of GHGs caused by electricity production in Turkey with deep learning, support vector machine and artificial neural network algorithms. [17] compared actual and predicted GHGs emissions by artificial neural networks of Bulgaria and Serbia. [19] applied Support Vector Regression, Artificial Neural Networks, and Box-Jenkins method to model CO₂ emissions. [21] studied on CH₄ emissions for Tibetan Plateau between years 2006 and 2100. [22] used autoregressive integrated moving average to model and forecast CO₂ emissions in Bangladesh. [23] used generalized accumulative grey model to predict GHGs emissions in China. [25] forecasted methane emissions from tropical and subtropical areas by using artificial neural networks. Ammar et. al. [26] predicted Tunisian greenhouse gas emissions from different species. [27] forecasted the methane percentage in the air for the future 10 years using autoregressive integrated moving average model, self-existing threshold

autoregressive model, and smooth logistic transition autoregressive model for the methane data of Pakistan, China, and India from 1970 to 2012. [28] estimated CO₂ emissions in the eight Asian countries between years 2019 and 2023 by grey model. [29] compared actual and predicted CO₂ emission values by grey method between years 1995 and 2009. [30] studied the controlling and monitoring of CO₂ in Oman by linear regression prediction. [31] predicted the CO₂ emissions of the developed countries by using multi-layer artificial neural networks. [32] analyzed total GHGs emission between years 1990 and 2016. [33] forecasted total CO₂ emission from paddy crops in India for coming next six years by using prediction methods. [34] predicted the effect on GHGs emissions of the end-of-life vehicles (ELV). [35] estimated CH₄ emissions by combining wavelet transform and artificial neural networks on the Bely Island, Russia. [36] studied GHGs emissions in Turkey consistent with energy, industrial products, agribusiness, and barren sectors by using time series models as moving average, exponential smoothing, exponential smoothing with trend. [37] predicted GHGs during the period at LTO (landing /take off) of aircrafts at Kahramanmaraş Airport in Turkey. [38] forecasted CO₂ emissions in China between years 2011 and 2020. [39] estimated direct and indirect total CO₂ eq. emissions of a family in Turkey. [40] studied with purpose of the evolution of GHGs emissions in 12 developed economies by using time series data between 1970 and 2018 years applying the exponential smoothing state-space model (ETS), the Holt–Winters model (HW), the TBATS model, the ARIMA model, the structural time series model (STS), and the neural network autoregression model (NNAR). [41] predicted CO₂ eq. emissions reaching 728.3016 metric tons in the year 2030. [42] predicted a 30% increase in the total CO₂ emissions of Iran by 2030 with multiple linear regression (MLR) and multiple polynomial regression (MPR) analysis. [43] proposed multi-agent intertemporal optimization model (MIOM) based on forecasting trends of 13 products in Liaoning Province, China from 2018 to 2030. [44] compared ARIMA and Verhulst model predicting CO₂ emissions in Russia and China. [45] studied the forecasting of CO₂ emissions based on energy planning in Shanxi Province from 2019 to 2035.

3. METHOD

There is no only one forecasting model that is appropriate in the same time for all of data. The determination of model is a very significant step for prediction and future estimation with past univariate or multivariate time series data. Classical statistical models are mostly able to present better solutions in acceptable limits for short time series data according to models as machine learning, artificial neural network, deep learning, etc. In the present study, statistical models preferred for annual estimations of CH₄, N₂O and CO₂ from greenhouse gases emitted by Turkey are as follows: Grey, autoregressive integrated moving average, and double exponential smoothing models.

3.1. Grey Model

Grey theory is compatible with the discrete small number data series and incomplete information [46]. Beyond of this, easily it can be applied to forecast future series f for a time interval. GM (1,1) is a kind of Grey model that first “1” specifies that this model is a first order Grey model, and corresponding “1” shows that Grey model depends on univariate time series.

$x^{(0)} = x^{(0)}(1), x^{(0)}(2), \dots, x^{(0)}(n)$ is a representation of non-negative original sequence where n represents length of data. $x^{(1)} = x^{(1)}(1), x^{(1)}(2), \dots, x^{(1)}(n)$ represents new accumulated sequence. Accumulated generating operator (AGO) of $x^{(0)}$ is calculated as [47]:

$$x^{(1)}(k) = \sum_{i=1}^k x^{(0)}(i) \quad (1)$$

Adjacency mean generating sequence of $x^{(1)}(1)$ is $z^{(1)} = z^{(1)}(1), z^{(1)}(2), \dots, z^{(1)}(n)$ and $z^{(1)}(1)$ is defined as $z^{(1)}(1) = z^{(1)}(1), x^{(1)}(k) = 0.5[x^{(1)}(k) - x^{(1)}(k-1)]$ where k denotes $2, 3, \dots, n$. First-order grey differential equation model is calculated as [48]:

$$\frac{dx^{(1)}(t)}{dt} + ax^{(1)}(t) = b \tag{2}$$

where t is independent variables, a represents grey developed coefficient and b is named as grey controlled variable.

Basically grey difference equation of GM(1,1) model is given by,

$$x^{(0)}(k) + az^{(1)}(k) = b \tag{3}$$

[a,b]^T (T is transpose of the inner brackets matrix) parameter satisfies least square equation and is estimated as [49]:

$$[a, b]^T = (B^T B)^{-1} B^T Y \tag{4}$$

where B is denoted as:

$$B = \begin{bmatrix} z^{(1)}(2) & 1 \\ z^{(1)}(3) & 1 \\ \vdots & \vdots \\ z^{(1)}(n) & 1 \end{bmatrix} \tag{5}$$

and Y is given by,

$$Y = \begin{bmatrix} x^{(0)}(2) \\ x^{(0)}(3) \\ \vdots \\ x^{(0)}(n) \end{bmatrix} \tag{6}$$

AGO sequence is predicted by Eq(7) and AGO sequence is denoted as [50]:

$$\hat{x}^{(1)}(k + 1) = \left(x^{(0)}(1) - \frac{b}{a}\right) e^{-ak} + \frac{b}{a}, k = 1,2,3, \dots \tag{7}$$

Similarly predicted original sequence is defined as:

$$\hat{x}^{(0)}(k + 1) = \hat{x}^{(1)}(k + 1) - \hat{x}^{(1)}(k) \tag{8}$$

3.2. Autoregressive Integrated Moving Average Model (ARIMA)

ARIMA methodology is an appropriate technology which is progressed by Box and Jenkins for short series and forecasting. [51]. The ARIMA(p,q,d) is based on the autoregressive (AR), moving average (MA), and the combination of AR and MA (ARMA) models [52]. Future value variable is as a kind of function that has a property of linearity and depends on several past observations and random errors. Nonseasonal time series are composed of past values and errors so nonseasonal time series are defined by [53]:

$$X_t = \theta_0 + \phi_1 X_{t-1} + \phi_2 X_{t-2} + \dots + \phi_p X_{t-p} + e_t + \theta_1 e_{t-1} + \theta_2 e_{t-2} + \dots + \theta_q e_{t-q} \tag{9}$$

where X_t, e_t re value and random error at time t respectively. θ_i(i=1,2,..,p) and φ_j (j=1,...,q) are model parameters. p is named as order of autoregressive polynomial and q is denoted as order of moving average polynomial. d is the difference process that converts non-stationary times series to stationary time series. d can be selected as 0,1 and 2 [54]. If q is equal to zero, X_t becomes an autoregressive (AR) model of order p. Besides if p is equal to zero, X_t becomes a moving average (MA) model of order q. In this study p,q,d are selected as 0,1 and 2 respectively. As a result, ARIMA(0,1,1) is used.

3.3. Double Exponential Smoothing Model (DES)

Another naming of double exponential smoothing (DES) model is Holt's linear exponential model that is used to forecast time series of which trend is known. DES is based on three equations: Equations (10), (11) and (12) [55]:

$$L_i = \alpha X_i + (1 - \alpha)(L_{i-1} + b_{i-1}) \quad (10)$$

$$b_i = \beta(L_{i-1} + b_{i-1}) + (1 - \beta)b_{i-1} \quad (11)$$

$$Y_{i+m} = L_i + mb_i \quad (12)$$

Where X_i is the input raw data of original times series at sample i , L_i is an estimation of the data series at the sample number i and b_i is estimation of the data series trend at the sample number i . α and β are weighting coefficients that could be selected between 0 and 1. Finally, Y_{i+m} is used for forecasting for specific interval ($m > 0$). To specify initial L_i and b_i . Equations (13), (14), (15) and (16) are applied.

$$L_1 = X_1 \quad (13)$$

$$b_1 = 0 \quad (14)$$

$$b_1 = X_2 - X_1 \quad (15)$$

$$b_1 = (X_n - X_1)/(n - 1) \quad (16)$$

For b_i which minimum forecast error is obtained, is selected.

3.4. Mean Absolute Percentage Error (MAPE)

To evaluate the performance of statistical forecasting models is used MAPE equation as follows:

$$MAPE = \frac{1}{n} \sum_{i=1}^n \left| \frac{X[i] - P[i]}{X[i]} \right| \times 100\% \quad (17)$$

where $X[i]$ is present data, $P[i]$ is the forecasted data and n is the test length.

4. RESULTS AND DISCUSSION

The prediction results of GM, ARIMA and DES methods for observed emissions of CH_4 , N_2O and CO_2 between years 1970 and 2018 are presented in Figure 1-3. ARIMA and DES predictions are able to track the observed time data better. The prediction performance is to be mostly decided by MAPE in literature. The best MAPEs are achieved with DES model following by ARIMA and GM given in Table 1. MAPEs calculated for GM, ARIMA and DES methods after train, test and prediction processes are 6.426%, 3.167% and 0.285% for CH_4 ; 7.304%, 3.829% and 0.355% for N_2O ; 7.503%, 5.503% and 0.408% for CO_2 emission in turn

Table 1. MAPEs for predictions obtained between years 1970 and 2018.

	CH ₄			N ₂ O			CO ₂		
	GM	ARIMA	DES	GM	ARIMA	DES	GM	ARIMA	DES
MAPE %	6.426	3.167	0.285	7.304	3.829	0.355	7.503	5.503	0.408

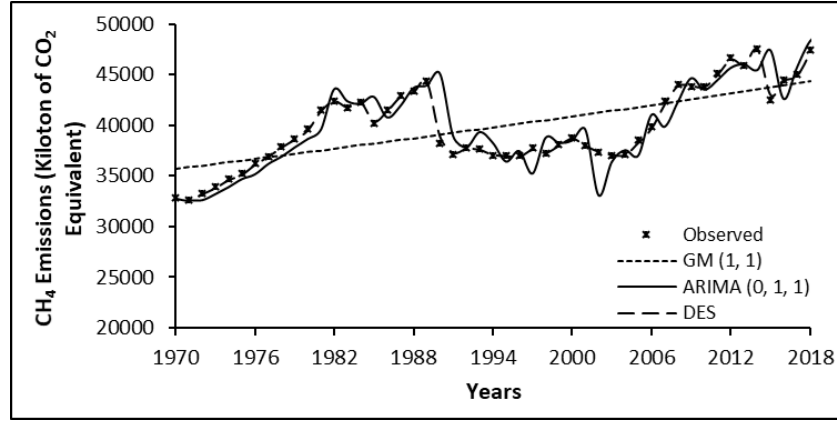


Figure 1. CH₄ Emissions versus Time

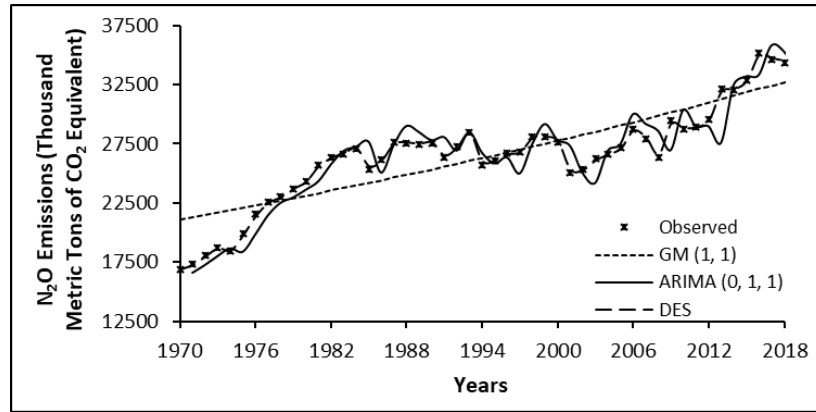


Figure 2. N₂O Emissions versus Time

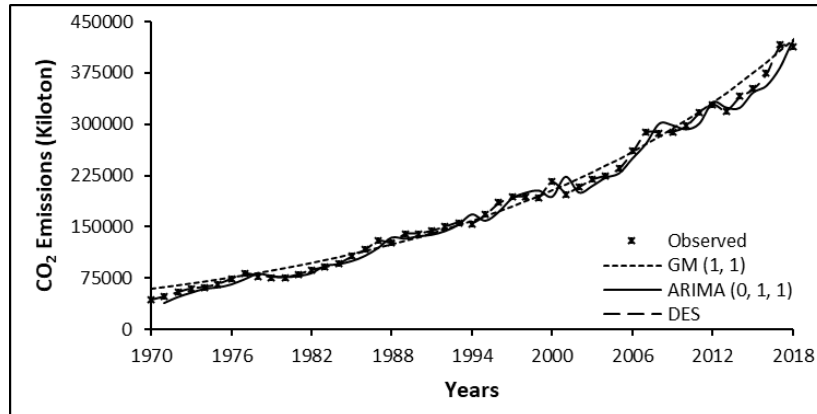


Figure 3. CO₂ Emissions versus Time

Table 2 presents the forecasted values for future 8 years based on the past time data of the 49-year emissions between years 1970 and 2018. The estimated emission values for CH₄, N₂O and CO₂ at year 2026 are 50700 kiloton of CO₂ eq., 38100 thousand metric ton of CO₂ eq., and 512000 kilotons. An upward trend goes on for all the emissions. According to forecasting figures of DES model, it is clarified that the

emissions of CH₄, N₂O and CO₂ ascend 6.9%, 10.8% and 23.9% between years 2019 and 2026. The increments between years 1970 and 2026 are found as 54.6%, 125.5% and 1100.7%, respectively. From these results, it is concluded that CO₂ emission indicates a bigger increasing rate in years and has a significant share in the emissions of the other greenhouse gases. Moreover, the forecasted values for next 8 years are also illustrated in Figure 4-6.

Table2. Future 8-year forecasted values between years 2019 and 2026

YEAR	CH ₄ (CO ₂ equivalent in kt)			N ₂ O (CO ₂ equivalent in kt)			CO ₂ in kt		
	GM	ARIMA	DES	GM	ARIMA	DES	GM	ARIMA	DES
2019	44600	49137.1	47600	33000	33604.3	34900	441000	433373	427000
2020	44800	50474.6	48100	33300	32282.3	35400	459000	436016	439000
2021	45000	50162.5	48500	33700	34367.3	35800	479000	440277	451000
2022	45200	50319.4	49000	34000	33813.4	36300	498000	448828	463000
2023	45400	51447.7	49400	34300	34301.7	36700	519000	464220	476000
2024	45600	52662.6	49800	34600	34847.3	37200	541000	472634	488000
2025	45800	52251.0	50300	34900	37353.9	37700	563000	465039	500000
2026	46000	53035.4	50700	35200	37248.7	38100	587000	481444	512000

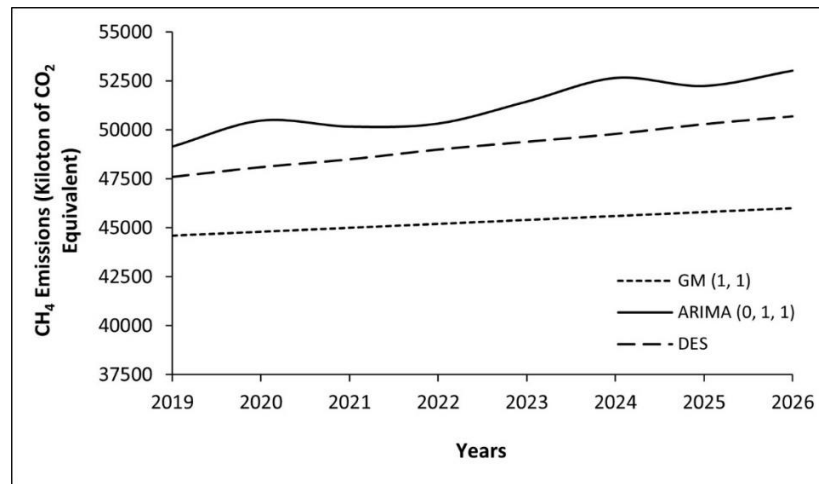


Figure 4. Future CH₄ Emissions versus Time.

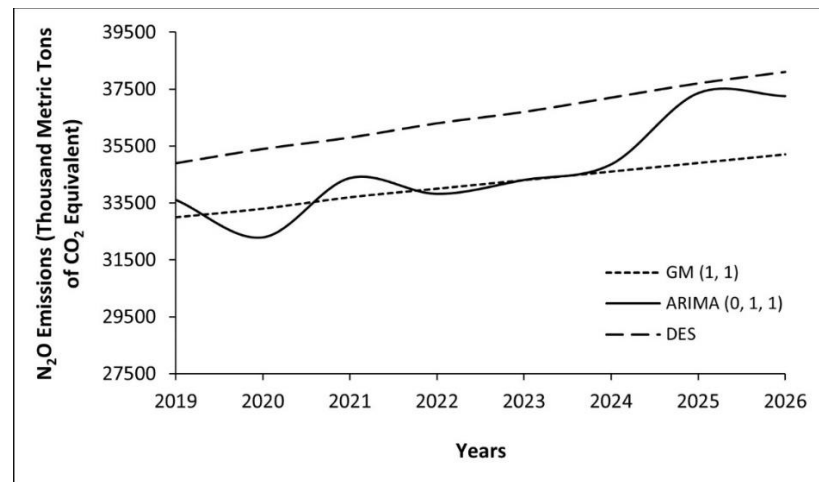


Figure 5. Future N₂O Emissions versus Time.

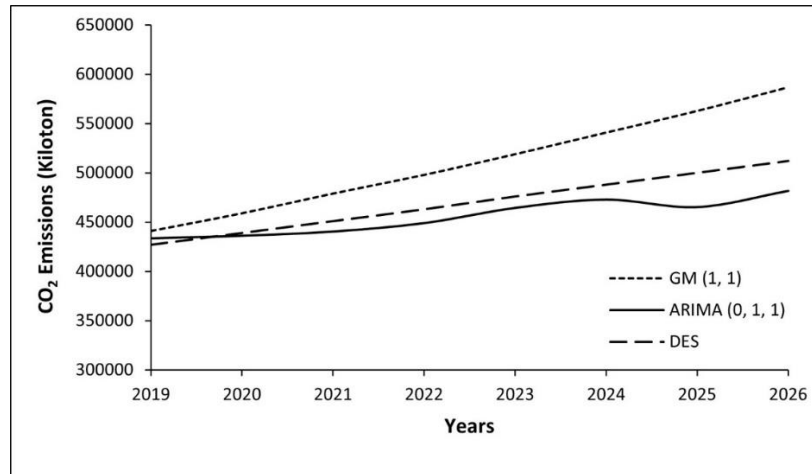


Figure 6. Future CO₂ Emissions versus Time.

CO₂ can substantially be reduced by using cleaner fuels as hydrogen in present transportation, heating and energy production systems based on combustion in Turkey. Both CO₂ and N₂O linked with NO largely formed by fuel combustion can be diminished by the use of renewable energy production systems as wind, solar, wave in place of combustion-based systems. The decrease of CH₄ emitted by livestock, manure and agriculture activities can be realized by building the methane gas aggregation and transformation facilities on location with the technique of mass production.

5. CONCLUSION

GHGs emissions are serious factors over environmental pollution and global warming. Turkey signed the Paris Climate Agreement and Kyoto protocols to decrease greenhouse gas emissions in compliance with the termed rates. Predictions of GHGs emissions are very crucial for policy makers of Turkey to reach the targeted annual emission values by establishing the balance between the environmental policies and sustainable economic development. Furthermore, the forecasting studies of GHGs gases are able to present contributions to organize and to predict the national inventory of GHGs emissions.

In this study, the estimations of annual emissions of CH₄, N₂O and CO₂ greenhouse gases in Turkey are realized by three statistical models: GM, ARIMA and DES. The univariate time series data between years 1970 and 2018 are used for trains, tests and predictions of models. with the aim of evaluating the performance of models, MAPE values are calculated between annual observed and predicted emissions of 49 years. Finally, 8-year future forecasting is determined from 2019 to 2026. The following results are obtained by the study: DES model represents the best prediction performance according to ARIMA and GM models above available emission data of greenhouse gases. MAPE values for DES prediction is 0.285, 0.355 and 0.408 for CH₄, N₂O and CO₂. GHGs emissions continues to rise in the near future. The emissions of CH₄, N₂O and CO₂ increase 6.9%, 10.8% and 23.9%, respectively between years 2018 and 2026. The forecasted values of CH₄, N₂O and CO₂ for 2026 year are 50700 kiloton of CO₂ eq., 38100 thousand metric ton of CO₂ eq., and 512000 kilotons, respectively.

CO₂ holds an important place in GHGs emissions and its emission is relatively easier to be reduced by not using fossil fuel based combustion systems. The usage of hydrocarbon based fuels can gradually be decreased and be replaced with cleaner hydrogen fuels. Policy makers can increase the investments for renewable energy production types such as wind, solar, geothermal and biomass. Nuclear energy is still appropriate option for intense energy production with minimum GHGs emissions. In addition, other statistical methods, forecasting approaches of machine learning or hybrid models can also be utilized to achieve more accurate estimations in future studies.

Declaration of Ethical Standards

Authors declare to comply with all ethical guidelines, including authorship, citation, data reporting and original research publication.

Credit Authorship Contribution Statement

Suat ÖZTÜRK: The author has done research, analyzed and written the article.

Ahmet EMİR: The author has analyzed, written and edited the article.

Declaration of Competing Interest

The authors declare that they have no known competing financial interests or personal relationships that could have appeared to influence the work reported in this paper.

Funding / Acknowledgements

The authors declare that they have not received any funding or research grants during the review, research or assembly of the article.

Data Availability

Research data has not been made available in a repository.

REFERENCES

- [1] Ü. Ağbulut, İ. Ceylan, A. E. Gürel, and A. Ergün, "The history of greenhouse gas emissions and relation with the nuclear energy policy for Turkey," *International Journal of Ambient Energy*, vol. 42, no. 12, pp. 1447–1455, 2021, doi: 10.1080/01430750.2018.1563818.
- [2] B. Wu and C. Mu, "Effects on greenhouse gas (CH₄, CO₂, N₂O) emissions of conversion from over-mature forest to secondary forest and Korean pine plantation in Northeast China," *Forests*, vol. 10, no. 9, 2019, doi: 10.3390/f10090788.
- [3] K. Kumaş ve A. Ö. Akyüz, "Theoretical nitrous oxide, methane, carbon dioxide emissions calculations to the atmosphere in Niğde, Turkey," *Dicle Üniversitesi Fen Bilimleri Enstitüsü Dergisi*, c. 10, sayı. 2, ss. 209-220, Ara. 2021
- [4] G. Moiceanu and M. N. Dinca, "Climate change-greenhouse gas emissions analysis and forecast in Romania," *Sustain.*, vol. 13, no. 21, 2021, doi: 10.3390/su132112186.
- [5] R. Sivaprasada, B. Meenakshi, Amruta R, Kowsalya S, Nivetthini Ag, "Forecasting of greenhouse gases and air quality prediction using matlab analytics," *Turkish Journal of Computer and Mathematics Education*, 12, 13, 7226-7231, 2021.
- [6] Q. R. Ollivier, D. T. Maher, C. Pitfield, and P. I. Macreadie, "Winter emissions of CO₂, CH₄, and N₂O from temperate agricultural dams: fluxes, sources, and processes," *Ecosphere*, 10 (11), e02914, 2019.
- [7] M. A. Budihardjo, I. Faadhilah, N. G. Humaira, M. Hadiwidodo, I. W. Wardhana and B. S. Ramadan, "Forecasting greenhouse gas emissions from heavy vehicles: a case study of Semarang city," *Vol 18, Jurnal Presipitasi*, 2, 254-260, 2021.
- [8] U. Şahin, "Forecasting of Turkey's greenhouse gas emissions using linear and nonlinear rolling metabolic grey model based on optimization," *Journal of Cleaner Production*, 239, 118079, 2019, doi: 10.1016/j.jclepro.2019.118079.
- [9] A. Hamrani, A. Akbarzadeh and C. A. Madramootoo, "Machine learning for predicting greenhouse gas emissions from agricultural soils," *Science of the Total Environment*, 741, 140338, 2020, doi: 10.1016/j.scitotenv.2020.140338.

- [10] Ö. Eren, O. Gökdoğan and M. F. Baran, "Determination of greenhouse gas emissions (GHG) in the production of different aromatic plants in Turkey," *Türk Tarım ve Doğa Bilimleri Dergisi*, 6(1), 90–96, 2019.
- [11] Sadorsky, P., "Renewable energy consumption, CO2 emissions and oil prices in the G7 countries. *Energy Economics*," 31(3), 456–462, 2009).
- [12] M. Muhadinovic, G. Djurovic, M. M. Bojaj, "Forecasting greenhouse gas emissions and sustainable growth in montenegro: a SVAR approach", *Pol. J. Environ. Stud.*, 30, 5, 4115–4129, 2021, doi: 10.15244/pjoes/132625.
- [13] Ö. K. Albayrak, "Forecasting of CO2 with the effect of renewable energy, non-renewable energy, gdp and population for Turkey: Forecasting with Nmgm (1, N) gray forecasting model", *KAUJEASF*, 12, 24, 2021, doi: 10.36543/kauibfd.2021.033.
- [14] C. Hamzacebi and I. Karakurt, "Forecasting the energy-related CO2 emissions of Turkey using a grey prediction model," *Energy Sources, Part A Recover. Util. Environ. Eff.*, vol. 37, no. 9, pp. 1023–1031, 2015, doi: 10.1080/15567036.2014.978086.
- [15] E. Uzlu, "Estimates of greenhouse gas emission in Turkey with grey wolf optimizer algorithm-optimized artificial neural networks," *Neural Comput. Appl.*, vol. 33, no. 20, pp. 13567–13585, 2021, doi: 10.1007/s00521-021-05980-1.
- [16] M. S. Bakay and Ü. Ağbulut, "Electricity production based forecasting of greenhouse gas emissions in Turkey with deep learning, support vector machine and artificial neural network algorithms," *J. Clean. Prod.*, vol. 285, 2021, doi: 10.1016/j.jclepro.2020.125324.
- [17] D. Radojević, V. Pocajt, I. Popović, A. Perić-Grujić, and M. Ristić, "Forecasting of greenhouse gas emissions in serbia using artificial neural networks," *Energy Sources, Part A Recover. Util. Environ. Eff.*, vol. 35, no. 8, pp. 733–740, 2013, doi: 10.1080/15567036.2010.514597.
- [18] Mardani, A., Streimikiene, D., Nilashi, M., Arias Aranda, D., Loganathan, N., & Jusoh, A., "Energy consumption, economic growth, and CO2 emissions in G20 countries: application of adaptive neuro-fuzzy inference system," *Energies*, 11(10), 2771, 2018.
- [19] F. Çemrek ve Ö. Demir , "Estimating CO2 emission time series with support vector machines regression, artificial neural networks, and classic time series analysis," *Turkish Journal of Forecasting*, c. 05, sayı. 2, ss. 36–44, Ara. 2021, doi:10.34110/forecasting.1035912.
- [20] M. Akhshik, A. Bilton, J. Tjong, C. V. Singh, O. Faruk, and M. Sain, "Prediction of greenhouse gas emissions reductions via machine learning algorithms: Toward an artificial intelligence-based life cycle assessment for automotive lightweighting", *Sustainable Materials and Technologies*, 31, e00370, 2022, doi: 10.1016/j.susmat.2021.e00370.
- [21] T. Li et al., "Prediction of CH4 emissions from potential natural wetlands on the Tibetan Plateau during the 21st century," *Sci. Total Environ.*, vol. 657, pp. 498–508, 2019, doi: 10.1016/j.scitotenv.2018.11.275.
- [22] A. Rahman and M. M. Hasan, "Modelling and Forecasting of Carbon Dioxide Emissions in Bangladesh Using Autoregressive Integrated Moving Average (ARIMA) Models," *Open J. Stat.*, vol. 07, no. 04, pp. 560–566, 2017, doi: 10.4236/ojs.2017.74038.
- [23] K. Li, P. Xiong, Y. Wu, and Y. Dong, "Forecasting greenhouse gas emissions with the new information priority generalized accumulative grey model," *Sci. Total Environ.*, vol. 807, 2022, doi: 10.1016/j.scitotenv.2021.150859.
- [24] World Bank Open Data, <http://data.worldbank.org>, 12.03.2022.
- [25] T. Abbasi, T. Abbasi, C. Luithui, and S. A. Abbasi, "A model to forecast methane emissions from tropical and subtropical reservoirs on the basis of artificial neural networks," *Water (Switzerland)*, vol. 12, no. 1, 2020, doi: 10.3390/w12010145.
- [26] H. Ammar et al., "Estimation of Tunisian greenhouse gas emissions from different livestock species," *Agric.*, vol. 10, no. 11, pp. 1–17, 2020, doi: 10.3390/agriculture10110562.
- [27] S. U. Rehman, I. Husain, M. Z. Hashmi, E. E. Elashkar, J. A. Khader, and M. Ageli, "Forecasting and modeling of atmospheric methane concentration," *Arab. J. Geosci.*, vol. 14, no. 16, 2021, doi:

- 10.1007/s12517-021-07998-0.
- [28] H. T. H. Xuyen, N. T. M. Tram, N. T. H. Tram and N. T. H. Quyen, "Forecasting carbon dioxide emissions, total energy consumption and economic growth in Asian countries based on grey theory," *International Research Journal of Advanced Engineering and Science*, Volume 6, Issue 2, pp. 77-81, 2021
- [29] H. Yilmaz and M. Yilmaz, "Forecasting CO2 emissions for Turkey by using the grey prediction method," *J. Eng. Nat. Sci.*, vol. 31, pp. 141–148, 2013.
- [30] J. H. Yousif, N. N. Alattar, and M. A. Fekihal, "Forecasting models based CO2 emission for sultanate of Oman," *Int. J. Appl. Eng. Res.*, vol. 12, no. 1, pp. 95–100, 2017.
- [31] P. R. Jena, S. Managi, and B. Majhi, "Forecasting the CO2 emissions at the global level: A multilayer artificial neural network modelling," *Energies*, vol. 14, no. 19, 2021, doi: 10.3390/en14196336.
- [32] F. Cemrek. Modelling of CO2 emission statistics in turkey by fuzzy time series analysis, 17 January 2022, Preprint (Version 1) available at Research Square, doi: 10.21203/rs.3.rs-1261965/v1.
- [33] P. K. Singh, A. K. Pandey, S. Ahuja, and R. Kiran, "Multiple forecasting approach: a prediction of CO2 emission from the paddy crop in India," *Environ. Sci. Pollut. Res.*, vol. 29, no. 17, pp. 25461–25472, 2022, doi: 10.1007/s11356-021-17487-2.
- [34] Ü. A. Şahin, B. Onat, N. Sivri, and E. Yalçın, "The potential effect of the regulation for the end of life vehicles (ELV) on greenhouse gas emission sourced from cars," *J. Fac. Eng. Archit. Gazi Univ.*, vol. 26, no. 3, pp. 677–682, 2011.
- [35] A. Rakhmatova, A. Sergeev, A. Shichkin, A. Buevich, and E. Baglaeva, "Three-day forecasting of greenhouse gas CH4 in the atmosphere of the Arctic Belyy Island using discrete wavelet transform and artificial neural networks," *Neural Comput. Appl.*, vol. 33, no. 16, pp. 10311–10322, 2021, doi: 10.1007/s00521-021-05792-3.
- [36] S. Akcan, Y. Kuvvetli, and H. Koçyigit, "Time series analysis models for estimation of greenhouse gas emitted by different sectors in Turkey," *Hum. Ecol. Risk Assess.*, vol. 24, no. 2, pp. 522–533, 2018, doi: 10.1080/10807039.2017.1392233.
- [37] Özgünoğlu, K. and Uygur, N., "Kahramanmaraş havalimanı için uçaklardan kaynaklanan emisyonların belirlenmesi," *Kahramanmaraş Sütçü İmam Üniversitesi Mühendislik Bilimleri Dergisi*, 20 (3), 24-30, 2017, doi: 10.17780/ksujes.335226.
- [38] Y. Yang, J. Zhang, and C. Wang, "Forecasting China's carbon intensity: Is China on track to comply with its copenhagen commitment?," *Energy J.*, vol. 39, no. 2, pp. 147–171, 2018, doi: 10.5547/01956574.39.2.yyan.
- [39] M. M. Yatarkalkmaz and M. B. Özdemir, "The calculation of greenhouse gas emissions of a family and projections for emission reduction," *J. Energy Syst.*, vol. 3, no. 3, pp. 96–110, 2019, doi: 10.30521/jes.566516.
- [40] C. Tudor and R. Sova, "Benchmarking ghg emissions forecasting models for global climate policy," *Electron.*, vol. 10, no. 24, 2021, doi: 10.3390/electronics10243149.
- [41] M. Akyol and E. Uçar, "Carbon footprint forecasting using time series data mining methods: the case of Turkey," *Environ. Sci. Pollut. Res.*, vol. 28, no. 29, pp. 38552–38562, 2021, doi: 10.1007/s11356-021-13431-6.
- [42] S. M. Hosseini, A. Saifoddin, R. Shirmohammadi, and A. Aslani, "Forecasting of CO2 emissions in Iran based on time series and regression analysis," *Energy Reports*, vol. 5, pp. 619–631, 2019, doi: 10.1016/j.egy.2019.05.004.
- [43] X. Pan, H. Xu, M. Song, Y. Lu, and T. Zong, "Forecasting of industrial structure evolution and CO2 emissions in Liaoning Province," *J. Clean. Prod.*, vol. 285, 2021, doi: 10.1016/j.jclepro.2020.124870.
- [44] M. Tong, H. Duan, and L. He, "A novel Grey Verhulst model and its application in forecasting CO2 emissions," *Environ. Sci. Pollut. Res.*, vol. 28, no. 24, pp. 31370–31379, 2021, doi: 10.1007/s11356-020-12137-5.
- [45] G. Moiceanu and M. N. Dinca, "Climate change-greenhouse gas emissions analysis and forecast

- in Romania," *Sustain.*, vol. 13, no. 21, 2021, doi: 10.3390/su132112186.
- [46] Z. X. Wang, Q. Li, and L. L. Pei, "A seasonal GM(1,1) model for forecasting the electricity consumption of the primary economic sectors," *Energy*, 2018, doi: 10.1016/j.energy.2018.04.155.
- [47] K. Li and T. Zhang, "Forecasting electricity consumption using an improved grey prediction model," *Inf.*, vol. 9, no. 8, 2018, doi: 10.3390/info9080204.
- [48] M. Cheng and G. Shi, "Improved methods for parameter estimation of gray model GM(1,1) based on new background value optimization and model application," *Commun. Stat. Simul. Comput.*, vol. 51, no. 2, pp. 647–669, 2022, doi: 10.1080/03610918.2019.1657450.
- [49] J. Guo, X. Xiao, J. Yang, and Y. Sun, "GM(1,1) model considering the approximate heteroscedasticity," *J. Grey Syst.*, vol. 29, no. 2, pp. 53–66, 2017.
- [50] Z. X. Wang, D. D. Li, and H. H. Zheng, "Model comparison of GM(1,1) and DGM(1,1) based on Monte-Carlo simulation," *Phys. A Stat. Mech. its Appl.*, vol. 542, 2020, doi: 10.1016/j.physa.2019.123341.
- [51] Box GEP, Jenkins GM (1976) *Times series analysis-forecasting and control*. Prentice-Hall, Englewood Cliffs.
- [52] Box GEP, Jenkins GM, Reinsel GC (1994) *Time series analysis: forecasting and control*, 3rd edn. Prentice Hall, Englewood Cliffs.
- [53] L. Wang, H. Zou, J. Su, L. Li, and S. Chaudhry, "An ARIMA-ANN hybrid model for time series forecasting," *Syst. Res. Behav. Sci.*, vol. 30, no. 3, pp. 244–259, 2013, doi: 10.1002/sres.2179.
- [54] W. C. Wang, K. W. Chau, D. M. Xu, and X. Y. Chen, "Improving forecasting accuracy of annual runoff time series using ARIMA based on EEMD decomposition," *Water Resour. Manag.*, vol. 29, no. 8, pp. 2655–2675, 2015, doi: 10.1007/s11269-015-0962-6.
- [55] T. Booranawong and A. Booranawong, "Simple and double exponential smoothing methods with designed input data for forecasting a seasonal time series: In an application for lime prices in Thailand," *Suranaree J. Sci. Technol.* 2017,24(3):301-310.



ADSORPTION OF MALACHITE GREEN INTO POTATO PEEL: NONLINEAR ISOTHERM AND KINETIC

¹İlhan KÜÇÜK , ²Halil BİÇİCİ 

¹ Muş Alparslan University, Rektorship, Muş, TÜRKİYE

² Muş Alparslan University, Applied Sciences Faculty, Muş, TÜRKİYE

¹i.kucuk@alparslan.edu.tr, ²hbicici17@gmail.com

Highlights

- Potato peel can be used as an effective material for the adsorption of harmful substances such as Malachite Green.
- The adsorption isotherm reveals a nonlinear relationship between Malachite Green and potato peel, indicating its effective adsorption.
- Kinetic studies demonstrate that the adsorption of Malachite Green onto potato peel is fast and efficient.



ADSORPTION OF MALACHITE GREEN INTO POTATO PEEL: NONLINEAR ISOTHERM AND KINETIC

¹İlhan KÜÇÜK^{ID}, ²Halil BİÇİÇİ^{ID}

¹ Muş Alparslan University, Rektorship, Muş, TÜRKİYE

² Muş Alparslan University, Applied Sciences Faculty, Muş, TÜRKİYE

¹i.kucuk@alparslan.edu.tr, ²hbicici17@gmail.com

(Received: 23.10.2023; Accepted in Revised Form: 01.02.2024)

ABSTRACT: Potato peels (PPs) were utilized for removal of malachite green (MG) from aqueous solutions. The adsorbent underwent characterization through attenuated total reflection fourier transform infrared spectroscopy (ATR-FTIR), Scanning electron microscope (SEM), point zero charge (pH_{PZC}) X-Ray diffraction (XRD), and Energy dispersive X-ray spectroscopy (EDX). The removal of MG was found to be significantly influenced by pH, temperature, contact time, and initial concentration. Temperature and particle size were determined to have lesser influence compared to other factors. The adsorption process lasted for 120 minutes, with rapid removal occurring within the first 60 minutes. Adsorption kinetics were analyzed using the Elovich, pseudo first order, and pseudo second order models. The pseudo second order model was found to be more suitable for the kinetic study. Isotherm modeling was conducted using the Temkin, Freundlich, and Langmuir isotherms. Due to the exothermic nature of the study, the Freundlich and Langmuir models were found to be highly compatible. The maximum adsorption capacity was determined as 37.8 mg/g at 41°C. ATR-FTIR analysis revealed the involvement of hydroxide and carbonyl groups in the adsorption process. Overall, this study concluded that PPs is promising adsorbent for removal of MG from aqueous solutions.

Keywords: Raw adsorbent, Malachite green, Adsorption, Nonlinear isotherm-kinetic models, Potato peel

1. INTRODUCTION

The effluent waste stream from dyeing processes alters water chemistry, damaging aquatic ecosystems. In the past few years, significant damage has been caused by this untreated discharge, which comprises 10-15% of the dyes in the effluent from paper, textile production, leather tanning, food processing industries, and various dyes used in hair colouring products [1]. Dyes are dangerous contaminants as they are toxic, mutagenic, carcinogenic, and non-degradable, and they tend to remain stable in the environment for an extended period [2].

MG is a synthetic triphenylmethane dye that is classified as cationic dye and has the feature of being very water-soluble. MG is often used as a disinfectant in the fish farming sector and in animal husbandry, as an antiseptic and fungicidal agent in humans, and to suppress fungal assaults and protozoan diseases in aquaculture [3]. MG is also frequently used in the cotton, silk, wool, paper, and leather dyeing industries [4]. Despite being widely used in both medicinal and industrial settings, MG has negative impacts on human health and harms the environment. The harmful effects of MG include teratogenesis, carcinogenesis, and mutagenesis, which result in reproductive, immunological, and brain system damage as well as respiratory illnesses [5]. Additionally, the release of MG into the hydrosphere alters photosynthetic activity and lowers sunlight penetration while producing noticeable colouration even at low MG concentrations. The removal of MG from industrial effluents before release into the aquatic environment is therefore becoming an increasing problem [6].

Different methods have been proposed and tested to treat water and remove toxic compounds, including adsorption, ozonation, ultrafiltration, flocculation and oxidation [7]. Among these techniques, adsorption is considered the best approach as it offers several advantages compared to others. It is an effective method with low energy consumption, simple operation, and capable of reducing the

*Corresponding Author: İlhan KÜÇÜK, i.kucuk@alparslan.edu.tr

concentrations of dye and pharmaceuticals in polluted streams. Using materials with functionalized surfaces is alternative to improve removal efficiency of adsorption for water treatment and purification [8].

There are many studies in the literature related to potato peel [9-11]. These studies generally focus on various industrial applications of potato peel. However, research on the adsorption of malachite green dye by raw potato peel is quite limited. In particular, there is a lack of kinetic studies on the adsorption of malachite green by raw potato peel [12]. Therefore, more detailed and comprehensive studies are needed in this area. The results of these studies can reveal the potential of using potato peel in an environmentally friendly way for the treatment of dyes. Research in this area is of great importance in terms of the disposal of industrial waste and the reduction of environmental pollution.

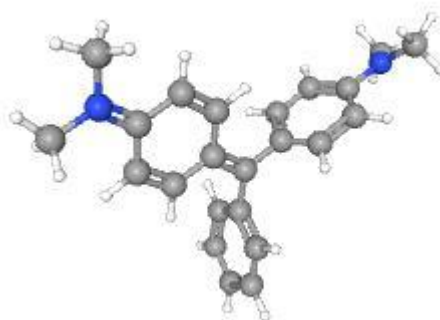
The objective of this study was to determine capacity of raw adsorbent to adsorb MG. PPs with varying pore sizes were used as the adsorbent. The study investigated various parameters such as particle size, pH, temperature, contact time, and initial concentration. The data obtained from the study were applied to different kinetic and isotherm models to determine results.

2. MATERIAL AND METHODS

Potatoes were purchased from the market located in the Eastern Anatolia Region of Turkey. After being washed multiple times, they were peeled and left to dry in open air. The dried peels were then cut into pieces by hand and shredded with a laboratory blender. The biosorbent was characterized using ATR-FTIR, SEM, pH_{PZC} , XRD and EDX.

During the experiment, we tested the adsorption isotherm at three distinct temperatures: 21°C, 31°C, and 41°C. To conduct the test, we shook 0.05 g of PP (Particle size=0.5<PP<0.425). adsorbent with 50 mL of MG (Figure 1) solution with varying initial concentrations (ranging from 10 to 50 mg/L). After three hours of reaching equilibrium, we analyzed the concentration of MG via UV-Vis (616 nm). The adsorption capacity of adsorbent was calculated through following equation:

Figure 1. Malachite green structure



$$q_t = \frac{(C_0 - C_t)V}{w} \quad (1)$$

During the experiment, we conducted a kinetic study to determine the effects of varying initial MG concentrations, temperatures, and particle sizes. To begin with, we mixed a constant adsorbent dose of 0.2 g/L with 200 mL of the MG solution at the desired initial concentration. The resulting mixture was then agitated at a constant speed of 200 rpm for a set amount of time.

The particle size distribution analysis was performed on 100 grams of PP. The PP was washed, dried

in open area, and then ground using a laboratory blender. Six types of Laboratory Test Sieves (ISO 3310-1) ranging from 0.250 mm to 1 mm were used to pass the PP through. The weight of different particle sizes was measured, and a graph was plotted to show the particle size versus the particle amount. The PP was analyzed using ATR-FTIR analysis in Agilent Cary 630 Infrared Spectrophotometer equipped with a spectrum range of 4000-500 cm^{-1} , resolution of 2 cm^{-1} , and particle size of 0.5<PP<0.425 mm to observe different functional groups. The XRD spectrum of the PP was analyzed in a PANalytical Empyrean with a spectrum range of 10-80 2θ , X-ray generator of 4 kW, and particle size of 0.5<PP<0.425 mm to observe crystallization. The SEM (scanning electron microscope model LEO-EVO 40) and EDX (energy dispersive X-ray analysis model Bruker-125 eV) were used to determine the surface morphologies of raw and MG adsorbed PP (particle size = 0.5<PP<0.425 mm).

3. RESULTS AND DISCUSSION

3.1. Characterization of PP

The functional groups in PP adsorbent were identified by analyzing its ATR-FTIR spectrum and its characteristic vibrations. The analysis further supported the adsorption mechanism by demonstrating that the vibrations of functional groups in adsorbents can change when they come into contact with cation ions in dye through various interactions such as covalent bonding, complexation, electrostatic interactions, or hydrogen bonding. The infrared spectra of PP adsorbent before and after adsorption are presented in Figure 2 A.

The ATR-FTIR spectrum in Figure 2 A shows broad peak at 3270 cm^{-1} , confirming presence of free and O-H stretching vibrations of hydroxyl group within the hemicellulose, lignin, and cellulose in adsorbent structure. The vibration observed at 2918 cm^{-1} is attributed to stretching of the C-H bonds in methylene groups and methyl found in adsorbent's polymers such as hemicellulose, lignin, and cellulose [2]. The peak at 1618 cm^{-1} indicates the presence of aromatic compounds in lignin components of adsorbent, and is associated with C-O stretching vibration of ketones and aldehydes, as well as C=C stretching vibration of benzene ring [13]. The peaks at 1021 cm^{-1} and 1318 cm^{-1} correspond to stretching vibrations of hydroxyl and carboxylate group's C-O bonds, respectively, in hemicellulose, cellulose and lignin [14]. The 1409 cm^{-1} peak corresponds to the OH bending vibration, whereas the peak at 1236 cm^{-1} is attributed to stretching vibration of the C-O-C bonds in aryl-alkyl ether linkages and deformation of phenolic OH plane in hemicellulose and cellulose components of lignocellulosic structure of the adsorbent [15]. The 1021 cm^{-1} vibrations can be attributed to primary amine functional groups present on the adsorbent surface, whereas the vibration observed at 1137 cm^{-1} may be linked to stretching of tertiary amine groups. [16]. Lignocellulosic materials contain hydroxyl and carboxylate groups that have been reported to interact with metal ions during adsorption. There are noticeable changes in the frequency spectrum of the adsorbent following adsorption. Some of the bands have an increase in intensity, with one of the most prominent being the O-H, C-O stretching and bending vibrations. This observation provides further evidence that these groups on the surface of the residue are indeed involved in the adsorption interactions [17].

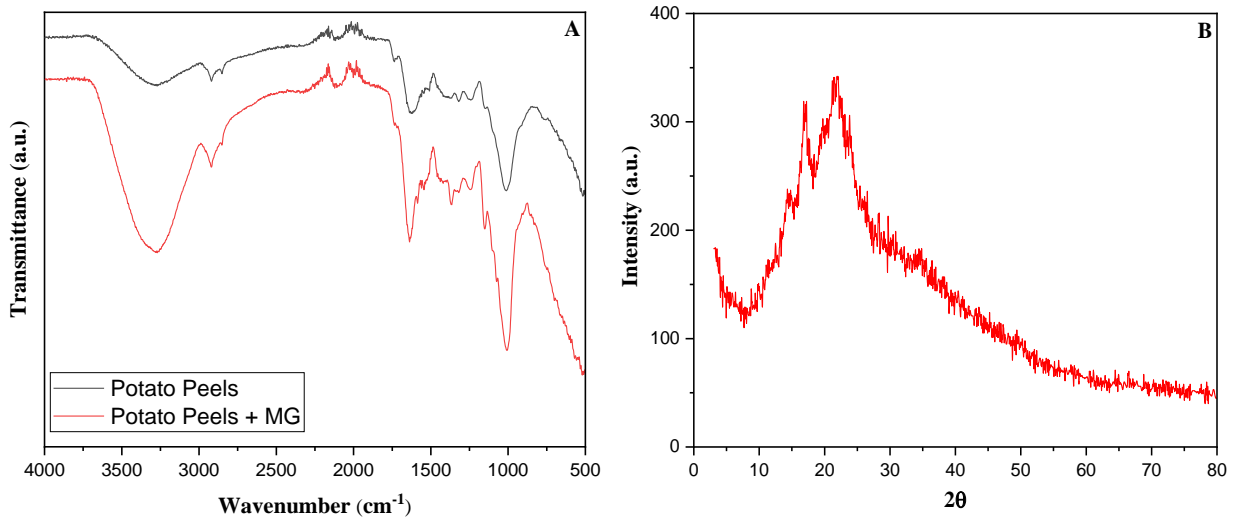


Figure 2. A. ATR-FTIR spectrum of PPs B. XRD spectrum of PPs

XRD patterns of PPs are shown in Figure 2 B, which display the characteristic peaks of cellulosic materials. The absence of sharp peaks confirms the amorphous nature of PPs. There are only four peaks observed at approximately 14°, 18°, 21°, and 34°, corresponding to the reflection from the 101, 101, 200, and 004 planes, respectively. These peaks indicate the structure's presence of hemicellulose, lignin, and cellulose [18].

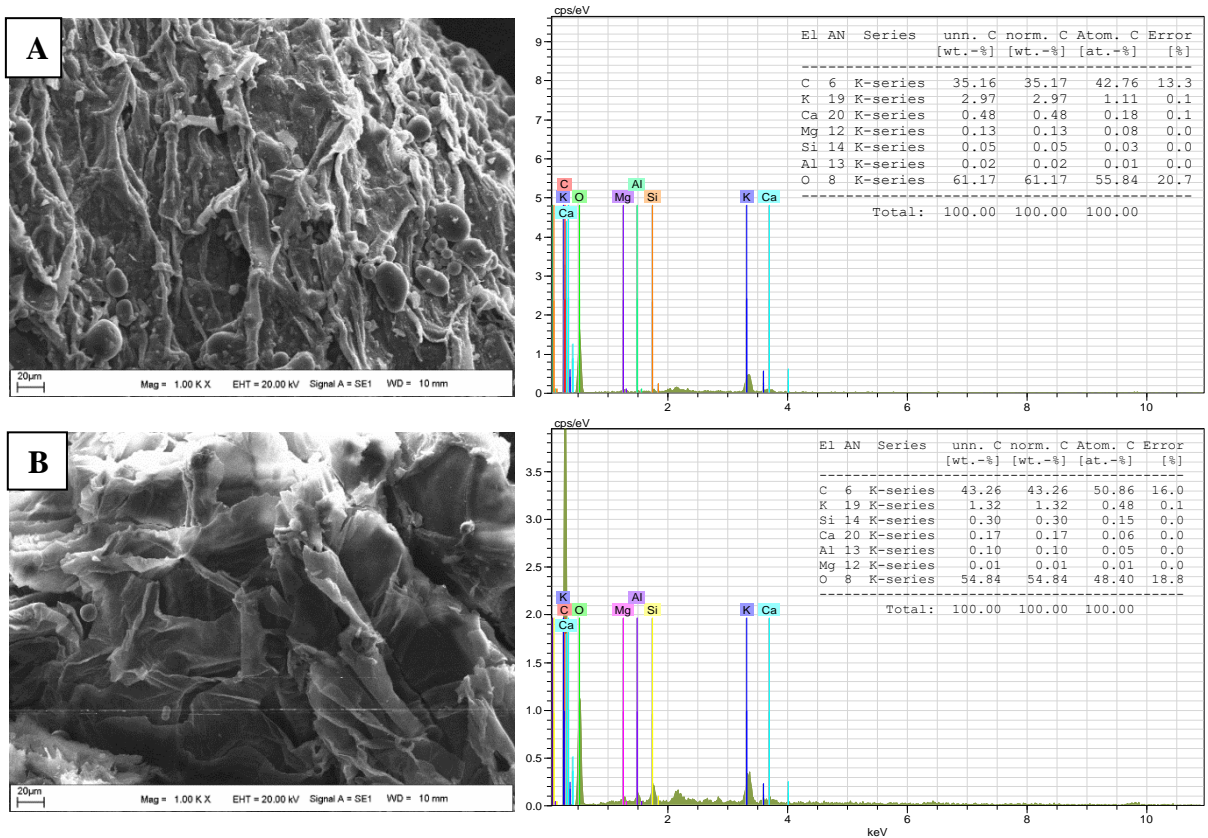


Figure 3. A. Before MG adsorption of PPs B. After MG adsorption of PPs

Figure 3 A shows SEM micrograph of PP adsorbent, indicating presence of uneven crevices that likely play significant role in transport of MG during adsorption. Figure 3 B illustrates the morphology of the

structure following adsorption. It is evident that the structure, which previously had cracks, becomes flatter after adsorption. The relative compositions of chemical elements present in an adsorbent can be analyzed by utilizing energy-dispersive X-ray coupled with the SEM instrument. After analysis, the carbon level has increased from 35.16 to 43.26, while the oxygen level has decreased from 61.17 to 54.84. Furthermore, the changes in other elements are shown in Figure 3. EDX results provide evidence of increased carbon, indicating that the structure effectively adsorbs MG.

3.2. Adsorption of MG

Figure 4 A illustrates the distribution of particle sizes. The weight of each class is depicted in relation to the diameter of the particles. Three specific ranges of particle sizes have been chosen: < 0.25 , $0.5-0.425$, and $1-0.85$. The pH of aqueous solution is crucial factor that affects sorption of dyes. It influences speciation of ions in the solution and, consequently, determines types of ions present at specific concentrations of hydroxyl or hydrogen ions [19]. This, in turn, determines the effectiveness of adsorbents in removing these ions. At a higher pH, PP was more effective in removing MG, as shown in Figure 4 C. When the pH value of the aqueous solution is acidic, the removal efficiency was lower. This is because the positively charged CV ions are repelled by the protonation of hydroxyl and carbonyl groups on the surface of lignocellulosic material, which negatively affects the removal efficiency. However, as the pH increases, the negatively charged surface of the lignocellulosic material changes its charge, making it easier to remove positively charged CV ions from the water. This claim is supported by the analysis of pH_{pzc} , which

was determined to be 6.35 (Figure 4 B, $T=21^{\circ}\text{C}$, $\text{PP}=0.05\text{g}$, $C_0 \text{ NaCl}=0.1 \text{ M}$, Particle size= $0.5 < \text{PP} < 0.425$), indicating that surface of this adsorbent is positively charged below this pH.

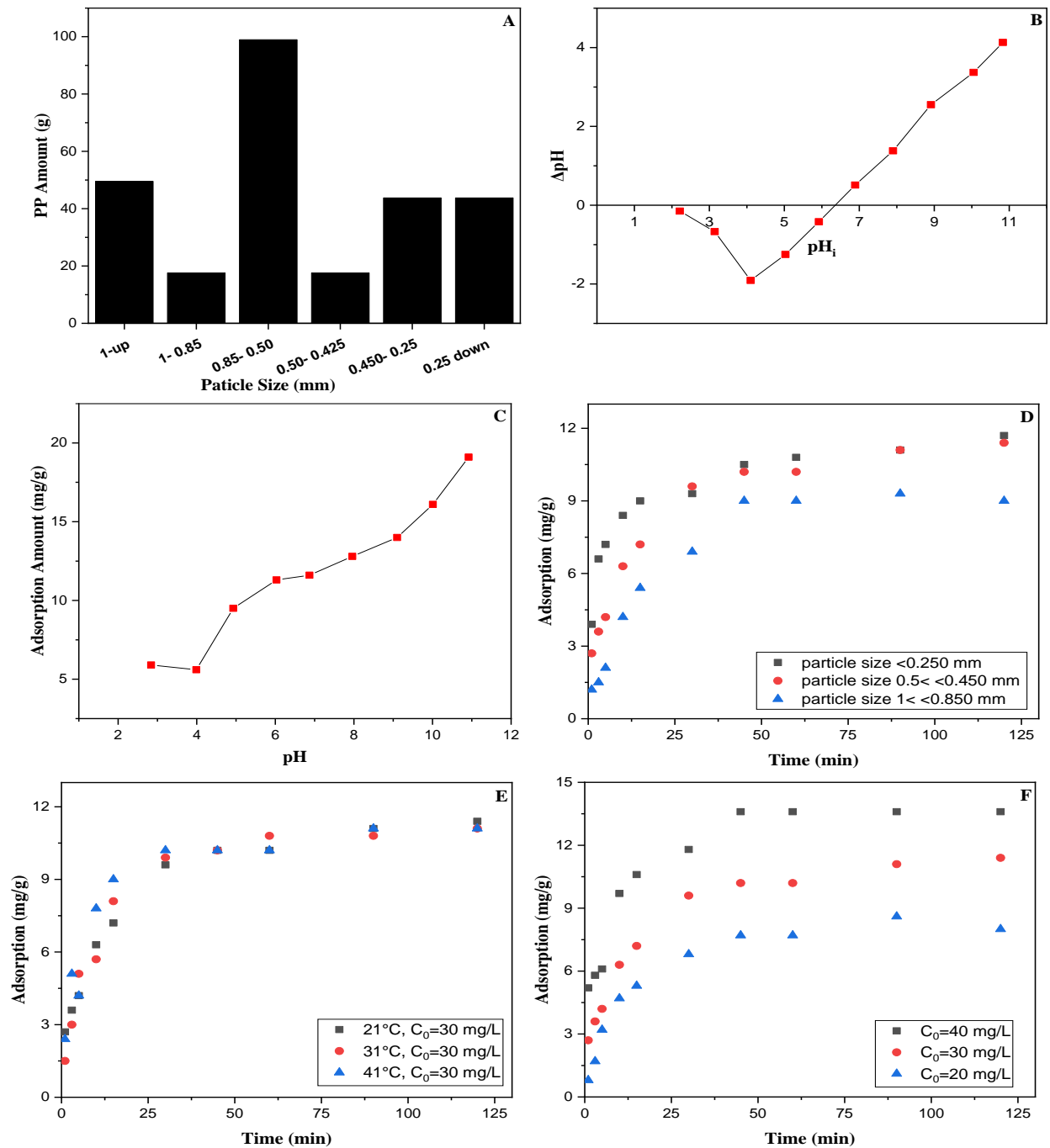


Figure 4. A. Particle size of PPs B. pH_{pzc} of PPs C. Effect of pH on MG adsorption D. Effect of particle size on MG adsorption E. Effect of temperature on MG adsorption F. Effect of contact time and initial concentration on MG adsorption

Size of adsorbent particles greatly affects their capacity to adsorb pollutants. Increasing the particle size usually leads to a decrease in adsorptive properties due to a reduced surface area. Conversely, decreasing the particle size enhances adsorptive properties by increasing the surface area. However, significantly reducing particle size may result in less efficient and environmentally friendly remediation techniques. Drawbacks of extremely small particle sizes include reduced adsorbent yield and rigidity, as

well as increased adsorption process costs [20]. Therefore, optimizing particle size is necessary for each unique remediation case. To investigate this, MG batch adsorption experiments were conducted using three particle sizes (1.00–0.850, 0.50–0.450, and 0.250–down mm). Figure 4 D ($T=21^{\circ}\text{C}$, $\text{pH}=5$, $C_0=30\text{ mg/L}$, $\text{pp}=0.05\text{ g}$) displays removals of MB by three adsorbents at different particle sizes. It was observed that the adsorption decreases as the particle size increases, compared to the adsorption at smaller particle sizes. The removal efficiency of PP for MG from aqueous solutions was investigated at three different temperatures: 21, 31, and 41°C . Figure 4 E shows the variation in adsorption capacity of PP for MG over time at these temperatures ($\text{pH}=5$, $C_0=30\text{mg/L}$, Particle size= $0.5 < \text{PP} < 0.425$). Initially, adsorption tended to decrease as temperature increased. The adsorption capacity at low temperature in the first minute was 2.7 mg/g. However, it decreased to 1.5 mg/g with increasing temperature. Although the adsorption values equalize over time, there are partial decreases in adsorption observed after 120 minutes at higher temperatures. At 21°C , the adsorption amount was 11.4 mg/g, while at 41°C , it was 11.1 mg/g. This indicates that the system undergoes an exothermic adsorption [21]. The decrease in adsorption at higher temperatures may be attributed to increased thermal energy of system. As the temperature rises, the kinetic energy of the adsorbate molecules also increases, leading to a greater tendency for desorption to occur. This phenomenon is commonly observed in exothermic adsorption processes, where the release of heat during adsorption can result in a decrease in adsorption capacity over time.

The adsorption of MG dye over time is shown in Figure 4 F. Initially, the adsorption was rapid, with around 50% of the dye being adsorbed within the first 5 minutes. As the contact time between the adsorbent and adsorbate increased, uptake of MG gradually increased up to 45 minutes, reaching a maximum removal rate. This initial fast adsorption rate may be attributed to abundance of active sites and pores on surface of adsorbent [22]. However, as the adsorption process continued, the accumulation of dye molecules on surface hindered diffusion into pores, resulting in slower adsorption rate. The effect of initial metal concentration on adsorption capacity of PGP was investigated for concentration values of 20, 30, and 40 mg/L, as illustrated in Figure 4 F ($T=21^{\circ}\text{C}$, $\text{pH}=5$, $\text{PP}=0.05\text{g}$, Particle size= $0.5 < \text{PP} < 0.425$). Adsorption capacity rises from 8 mg/g to 13.6 mg/g as initial MG concentration increases from 20 mg/L to 40 mg/L, until it reaches a constant value where no more MG can be eliminated. The increase in adsorption capacity is attributed to high concentration of MG ions in the concentrated solution. The saturation point is reached when concentration of MG ions in solution becomes too high for further adsorption onto PP. At this point, the adsorption capacity remains constant since no more MG can be removed from the solution. This observation indicates that the adsorption process relies on the initial MG concentration. Higher initial MG concentrations provide a larger quantity of MG ions accessible for adsorption, resulting in an enhanced adsorption capacity of PP. Understanding the relationship between initial MG concentration and adsorption capacity is crucial in assessing the effectiveness of PP as a potential adsorbent for MG removal.

3.2.1. Adsorption isotherm and kinetic

Adsorption is the binding or adherence of a substance or molecule to a surface, a process that plays a crucial role in various industrial applications such as catalysis, water and gas purification, and pharmaceutical production. Adsorption isotherms, which are mathematical models of the adsorption process, are used to describe the adsorption equilibrium state [23].

The Temkin, Freundlich, and Langmuir models are commonly used adsorption isotherm models. These models provide a mathematical expression of the adsorption process and are used to determine its agreement with experimental data.

The Langmuir model describes monolayer adsorption, relating the number of adsorbed molecules on surface of adsorbent, the number of vacant places on surface, and the equilibrium state of adsorption. The Langmuir isotherm equation calculates the adsorption capacity and rate [24]. The Freundlich model explains multilayer adsorption by expressing the relationship between the number of active sites on surface of adsorbent and concentration of adsorbent. The Freundlich isotherm equation is non-linear expression of adsorption process and is used to calculate the adsorption capacity and rate [25]. The

Temkin model explains the interaction of the adsorption process with chemical reactions. It expresses the relationship between the interaction of adsorbate molecules on surface of adsorbent and equilibrium state of adsorption. The Temkin isotherm equation is also non-linear expression of the adsorption process and is used to calculate the adsorption capacity and rate [26]. These three models mathematically express the adsorption isotherms while addressing different aspects of the adsorption process and their interactions. The use of these models helps to understand and optimize the adsorption process. The nonlinear equations for these models are presented in equations 2, 3, and 4.

$$q_e = \frac{Q_0 b C_e}{1 + b C_e} \quad (2)$$

$$q_e = K_F C_e^{\frac{1}{n}} \quad (3)$$

$$q_e = \frac{RT}{b_T} \ln A_T C_e \quad (4)$$

The function and plot of the isotherms are shown in Figure 5 A, and Table 1, respectively.

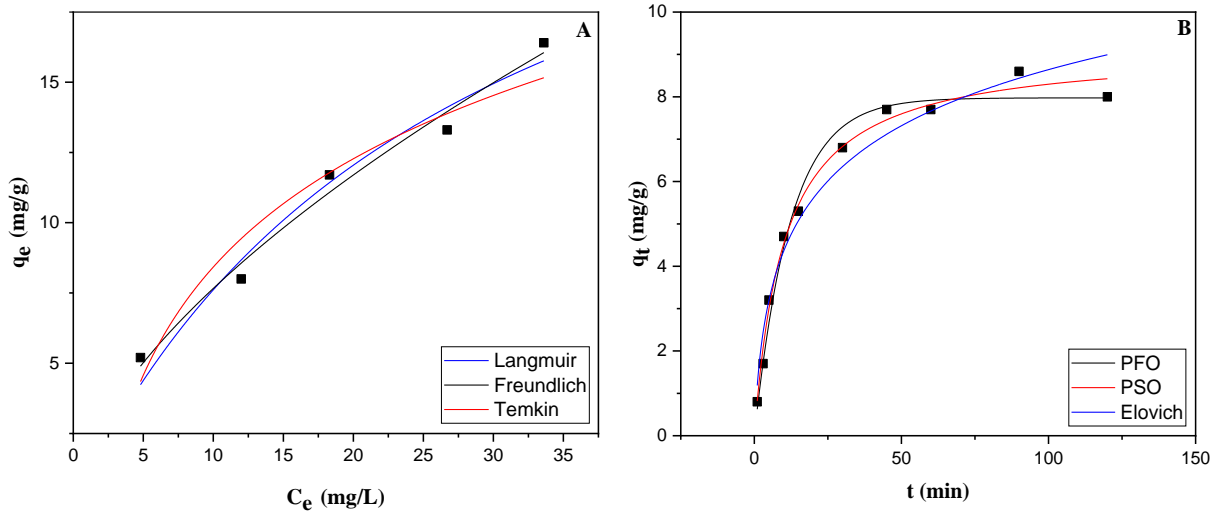


Figure 5. A. Non-linear isotherms plots B. Non-linear kinetics plots

Table 1 shows that at 41°C, langmuir isotherm model yielded maximum monolayer adsorption capacity (q_m) of 37.8 mg/g. Langmuir isotherm constant (K_L) was found to be 0.02 L/mg, with R^2 value of 0.99. From Freundlich model, K_F is an approximate indicator of adsorption capacity, while $1/n$ represents the strength of adsorption in the process. If $n = 1$, the partition between the phases does not depend on the concentration. Value of $1/n$ below one indicates normal adsorption, while a value above one indicates cooperative adsorption. At a temperature of 21°C, the K_F value was determined to be 1.88, the n value was found to be 1.63, and the R^2 value was calculated to be 0.982. According to the Temkin model, A_T represents equilibrium binding constant (L/g). Maximum A_T value was computed to be 0.45 at a temperature of 21°C, with an R^2 value of 0.939.

Adsorption kinetics are mathematical models that describe speed of adsorbate molecules on surface of adsorbent and change of adsorption process over time. These models are used to calculate rate of the adsorption process and the adsorption capacity [27].

Table 1. Adsorption isotherm constant

°C	Langmuir			Freundlich			Temkin		
	q_m	K_L	R^2	K_F	n	R^2	b_T	A_T	R^2
21	28.8	0.03	0.967	1.88	1.63	0.982	439.9	0.45	0.939
31	35.4	0.02	0.985	1.33	1.41	0.978	378.8	0.28	0.983
41	37.8	0.02	0.990	1.22	1.36	0.980	373.5	0.26	0.996

The pseudo first order model is kinetic model that describes rate of adsorption process. In this model, adsorption rate is proportional to concentration of molecules adsorbed to surface of the adsorbate. This model is used to calculate initial rate and rate constant in adsorption process [28]. The second order model is another kinetic model that explains speed of adsorption process. In this model, adsorption rate is proportional to square of concentration of molecules adsorbed to the surface of the adsorbate. This model is used to calculate rate constant and adsorption capacity in the adsorption process [29]. The Elovich model is another kinetic model that explains the speed of adsorption process. In this model, adsorption rate is expressed as a function of number of molecules adsorbed to surface of adsorbate and activation energy in the adsorption process. The Elovich model is used to calculate rate constant and adsorption capacity in the adsorption process [30]. These three models mathematically express the rate in the adsorption process and are used to calculate the adsorption capacity. The pseudo first order model is used to calculate initial rate and rate constant in the adsorption process, while second order model is used to calculate rate constant and adsorption capacity in the adsorption process. The Elovich model is used to calculate activation energy and rate constant in the adsorption process. The nonlinear equations for these models are presented in equations 5, 6, and 7.

$$q_t = q_e(1 - e^{-k_1 t}) \quad (5)$$

$$q_t = (k_2 q_e^2 t) / (1 + k_2 q_e t) \quad (6)$$

$$q_t = (1/b) \ln(abt + 1) \quad (7)$$

The function and plot of the isotherms are shown in Figure 5 B, and Table 2, respectively

Table 2. Adsorption kinetic constant

Particle size	°C	C_0	Pseudo-First Order			Pseudo-Second Order			Elovich		
			k_1	q_e	R^2	k_2	q_e	R^2	a	b	R^2
0.5>PP>0.425	21	20	0.08	7.97	0.983	0.01	9.14	0.990	1.63	0.51	0.965
0.5>PP>0.425	21	30	0.09	10.6	0.938	0.01	11.9	0.971	3.48	0.43	0.977
PP>0.25	21	30	0.29	10.2	0.817	0.03	11.0	0.942	29.8	0.65	0.976
1>PP>0.85	21	30	0.05	9.23	0.987	0.01	10.9	0.979	1.07	0.38	0.954
0.5>PP>0.425	21	40	0.14	13.1	0.845	0.01	14.1	0.910	13.6	0.45	0.935
0.5>PP>0.425	31	30	0.09	10.6	0.977	0.01	12.0	0.985	3.11	0.41	0.956
0.5>PP>0.425	41	30	0.14	10.5	0.938	0.01	11.5	0.957	6.82	0.50	0.925

In general, chemisorption processes can be described using the pseudo-second-order and Elovich models. The pseudo-second-order model accounts for the involvement of valency forces, such as covalent forces and ion exchange, through the sharing or exchange of electrons between the adsorbate and adsorbent. On the other hand, the Elovich model explains the kinetics of chemisorption on a heterogeneous surface of the adsorbent. After analyzing the fitted models (Figure 5B) and their corresponding parameters (Table

2), it was observed that the pseudo-second-order and Elovich models exhibited a better fit with a higher coefficient of determination (R^2) compared to the pseudo-first-order model. This suggests that chemisorption mechanisms play a significant role in the adsorption of the MG dye.

4. CONCLUSIONS

An experimental study was conducted to investigate the efficacy of PPs - a common agricultural residue - in removing MG dye from aqueous solutions. The study examined various parameters, including temperature, pH, particle size, contact time, and initial concentration, to determine their effect on the adsorption of MG onto the adsorbent. Results indicated that the loading of MG onto PP increased with initial concentration, time, and pH. The optimal contact time was found to be 120 min, with adsorption kinetics showing an initial fast phase followed by a slower equilibrium phase. Kinetic modeling of MG adsorption was performed using pseudo-first-order (PFO), pseudo-second-order (PSO), and Elovich models. PSO was found to describe the kinetics better than the other models. Based on this model, the highest R^2 value was found to be 0.99 at 21°C. The physical, chemical, elemental, and spectroscopic characteristics of the PP residue adsorbent were studied, and the findings indicate that the loading of MG may involve ion exchange and adsorption-complexation mechanisms. Equilibrium sorption studies were modeled using Temkin, Langmuir, and Freundlich isotherms, with the Langmuir model providing the best fit. Based on this model, the maximum adsorption capacity (q_{\max}) at 21°C was determined to be 25.8 mg/g. However, adsorption was found to be non-endothermic in temperature experiments. Thus, while the Freundlich model was suitable at low temperatures, the Temkin model was deemed more appropriate at higher temperatures. In summary, the findings of this study demonstrate the promising capability of utilizing agricultural waste residue as a viable adsorbent for efficient removal of MG dye.

Declaration of Ethical Standards

The authors state that the materials and methods employed in this study do not necessitate ethical committee approval.

Credit Authorship Contribution Statement

All authors made equal contributions to this study.

Declaration of Competing Interest

The authors state that they do not have any known conflicting financial interests or personal relationships.

Funding / Acknowledgements

The authors acknowledge the financial support of The Scientific and Technological Research Council of Türkiye under (TUBITAK) 2209-A Research Project Support Programme for Undergraduate Students.

Data Availability

The study's supporting data is included in the article.

REFERENCES

- [1] S. Sharma, A. Hasan, N. Kumar, and L. M. Pandey, "Removal of methylene blue dye from aqueous solution using immobilized agrobacterium fabrum biomass along with iron oxide nanoparticles as biosorbent," *Environmental Science and Pollution Research*, vol. 25, no. 22, pp. 21605–21615,

2018. doi:10.1007/s11356-018-2280-z
- [2] M. T. Yagub, T. K. Sen, S. Afroze, H.M. Ang, "Dye and its removal from aqueous solution by adsorption: A review," *Advances in Colloid and Interface Science*, vol. 209, pp. 172-184, 2014. doi:10.1016/j.cis.2014.04.002
- [3] K.Y.A. Lin, H.A. Chang, "Ultra-high adsorption capacity of zeolitic imidazole framework-67 (ZIF-67) for removal of malachite green from water," *Chemosphere*, vol. 139, pp. 624-631, 2015. doi:10.1016/j.chemosphere.2015.01.041
- [4] A. Elhalil, H. Tounsadi, R. Elmoubarki, F.Z. Mahjoubi, M. Farnane, M. Sadiq, M. Abdennouri, S. Qourzal, N. Barka, "Factorial experimental design for the optimization of catalytic degradation of malachite green dye in aqueous solution by Fenton process," *Water Resour Ind.*, vol. 15, pp. 41-48, 2016. doi:10.1016/j.wri.2016.07.002.
- [5] R. Selvasembian, P. Balasubramanian, "Utilization of unconventional lignocellulosic waste biomass for the biosorption of toxic triphenylmethane dye malachite green from aqueous solution," *International Journal of Phytoremediation*, vol. 20 no. 6, pp. 624-633, 2018. doi:10.1080/15226514.2017.1413329.
- [6] M. Liu, Z. Liu, T. Yang, Q. He, K. Yang, H. Wang, "Studies of malachite green adsorption on covalently functionalized Fe₃O₄@SiO₂-graphene oxides core-shell magnetic microspheres," *J Solgel Sci Technol.*, vol. 82, pp. 424-431, 2017. doi: 10.1007/s10971-017-4307-1.
- [7] H. A. Al-Yousef, B. M. Alotaibi, M. M. Alanazi, F. Aouaini, L. Sellaoui, A. Bonilla-Petriciolet, "Theoretical assessment of the adsorption mechanism of ibuprofen, ampicillin, orange G and malachite green on a biomass functionalized with plasma," *Journal of Environmental Chemical Engineering*, vol. 9, no. 1, pp 104950, 2021. doi: 10.1016/j.jece.2020.104950.
- [8] B. Takam, J. B. Tarkwa, E. Acayanka, S. Nzali, D. M. Chesseu, G. Y. Kamgang, S. Laminsi, "Insight into the removal process mechanism of pharmaceutical compounds and dyes on plasma-modified biomass: the key role of adsorbate specificity." *Environ. Sci. Pollut. Res.*, vol. 27, pp. 20500-20515, 2020. doi: 10.1007/s11356-020-08536-3.
- [9] Sharma, Neetu, D. P. Tiwari, S. K. Singh, "The efficiency appraisal for removal of malachite green by potato peel and neem bark: isotherm and kinetic studies." *International Journal*, vol.5, no.2, pp. 84-88 2014.
- [10] A. Stavrinou, C.A. Aggelopoulos, C.D. Tsakiroglou, "Exploring the adsorption mechanisms of cationic and anionic dyes onto agricultural waste peels of banana, cucumber and potato: Adsorption kinetics and equilibrium isotherms as a tool." *Journal of Environmental Chemical Engineering*, vol.6, no.6, pp. 6958-6970, 2018. doi: 10.1016/j.jece.2018.10.063.
- [11] Ioannis Anastopoulos, George Z. Kyzas, "Agricultural peels for dye adsorption: A review of recent literature." *Journal of Molecular Liquids*, vol. 200, Part B, pp. 381-389, 2014. doi:10.1016/j.molliq.2014.11.006.
- [12] G. El-Khamsa, H. Oualid, "Sorption of malachite green from aqueous solution by potato peel: Kinetics and equilibrium modeling using non-linear analysis method," *Arabian Journal of Chemistry*, vol. 9, pp. S416-S424, 2016. doi: 10.1016/j.arabjc.2011.05.011.
- [13] U. Farooq, M. A. Khan, M. Athar, J. A. Kozinski, "Effect of modification of environmentally friendly biosorbent wheat (*Triticum aestivum*) on the biosorptive removal of cadmium (II) ions from aqueous solution," *Chemical Engineering Journal*, vol. 171, no. 2, pp. 400-410, 2011. doi: 10.1016/j.cej.2011.03.094.
- [14] T.K. Naiya, B. Singha, S.K. Das, "FTIR study for the Cr(VI) removal from aqueous solution using rice waste," *International Conference on Chemistry and Chemical Process-IPCBE*, vol. 10 pp114-119, 2011.
- [15] H. Yang, R. Yan, H. Chen, D.H. Lee, C. Zheng, "Characteristics of hemicellulose, cellulose and lignin pyrolysis," *Fuel*, vol. 86, pp. 1781-1788, 2007.
- [16] M. J. K. Ahmed, M. Ahmaruzzaman, R. A. Reza, "Lignocellulosic-derived modified agricultural waste: Development, characterisation and implementation in sequestering pyridine from aqueous

- solutions," *Journal of Colloid and Interface Science*, vol. 428, pp. 222-234, 2014. doi: 10.1016/j.jcis.2014.04.049.
- [17] E. D. Asuquo, A. D. Martin, "Sorption of cadmium (II) ion from aqueous solution onto sweet potato (*Ipomoea batatas* L.) peel adsorbent: Characterisation, kinetic and isotherm studies," *Journal of Environmental Chemical Engineering*, vol. 4, no. 4, pp. 4207-4228, 2016. doi: 10.1016/j.jece.2016.09.024.
- [18] Z. Zhezi, Z. Mingming, Z. Dongke, "A Thermogravimetric study of the characteristics of pyrolysis of cellulose isolated from selected biomass," *Applied Energy*, vol. 220, pp. 87-93, 2018. doi: 10.1016/j.apenergy.2018.03.057.
- [19] W. Qu, T. Yuan, G. Yin, S. Xu, Q. Zhang, H. Su, "Effect of properties of activated carbon on malachite green adsorption," *Fuel*, vol. 249, pp. 45-53, 2019. doi: 10.1016/j.fuel.2019.03.058.
- [20] M.A. Al-Ghouti, R.S. Al-Absi, "Mechanistic understanding of the adsorption and thermodynamic aspects of cationic methylene blue dye onto cellulosic olive stones biomass from wastewater," *Sci. Rep.*, vol. 10, pp. 15928, 2020. doi: 10.1038/s41598-020-72996-3.
- [21] C. Silva, B. Gama, A. Gonçalves, J. Medeiros, A. Abud, "Basic-dye adsorption in albedo residue: effect of pH, contact time, temperature, dye concentration, biomass dosage, rotation and ionic strength," *J. King Saud. Univ. Eng. Sci.* vol. 32 no. 6, pp. 351-359 2019. doi: 10.1016/j.jksues.2019.04.006.
- [22] S. Ben-Ali, I. Jaouali, S. Souissi-Najar, A. Ouederni, "Characterization and adsorption capacity of raw pomegranate peel biosorbent for copper removal, *Journal of Cleaner Production*," vol. 142, no. 4, pp. 3809-3821, 2017. doi: 10.1016/j.jclepro.2016.10.081.
- [23] M. A. Al-Ghouti, D. A. Da'ana, "Guidelines for the use and interpretation of adsorption isotherm models: A review," *Journal of Hazardous Materials*, vol. 393, pp. 122383, 2020. doi: 10.1016/j.jhazmat.2020.122383.
- [24] H. Swenson, N. Stadie, "Langmuir's theory of adsorption: a centennial review," *Langmuir*, vol. 35 no. 16, pp. 5409-5426, 2019. doi: 10.1021/acs.langmuir.9b00154.
- [25] N. Ayawei, A. N. Ebelegi, D. Wankasi, "Modelling and Interpretation of Adsorption Isotherms," *Hindawi Journal of Chemistry*, vol. 11 pp. 3039817, 2017. doi: 10.1155/2017/3039817.
- [26] M. Vadi, A. Mansoorabad, M. Mohammadi, N. Rostami, "Investigation of Langmuir, Freundlich and temkin adsorption isotherm of tramadol by multi-wall carbon nanotube," *Asian J. Chem.*, vol. 25 no. 10, pp. 5467-5469, 2013. doi: 10.14233/ajchem.2013.14786.
- [27] J. Wang, X. Guo, "Adsorption kinetic models: Physical meanings, applications, and solving methods," *Journal of Hazardous Materials*, vol. 390, pp. 122156, 2020. doi: 10.1016/j.jhazmat.2020.122156.
- [28] G. Ersan, Y. Kaya, M.S. Ersan, O.G. Apul, T. Karanfil, "Adsorption kinetics and aggregation for three classes of carbonaceous adsorbents in the presence of natural organic matter," *Chemosphere*, vol. 229, pp. 514-524, 2019. doi: 10.1016/j.chemosphere.2019.05.014.
- [29] G. Sabarinathan, P. Karuppasamy, C.T. Vijayakumar, T. Arumuganathan, "Development of methylene blue removal methodology by adsorption using molecular polyoxometalate: kinetics, thermodynamics and mechanistic Study," *Microchem. J.*, vol. 146, pp. 315-326, 2019. doi: 10.1016/j.microc.2019.01.015.
- [30] C. Lin, W. Luo, T. Luo, Q. Zhou, H. Li, L. Jing, "A study on adsorption of Cr (VI) by modified rice straw: characteristics, performances and mechanism," *J. Clean. Prod.*, vol. 196, pp. 626-634, 2018. doi: 10.1016/j.jclepro.2018.05.279.



ASSESSMENT OF URBAN FLOOD RISKS OF THE CITIES USING ENTROPY-VIKOR METHODS IN TÜRKİYE

^{1,*} Onur DERSE , ²Elifcan GÖÇMEN POLAT 

¹ Tarsus University, Faculty of Engineering, Department of Industrial Engineering, Mersin, TÜRKİYE

² Munzur University, Faculty of Engineering, Department of Industrial Engineering, Tunceli, TÜRKİYE

¹onurderse@tarsus.edu.tr, ²elifcangocmen@munzur.edu.tr

Highlights

- Exposure, hazard, vulnerability are effective for urban flood risk.
- The risks of the areas should be evaluated by different methods.
- The study results are effective.



ASSESSMENT OF URBAN FLOOD RISKS OF THE CITIES USING ENTROPY-VIKOR METHODS IN TÜRKİYE

^{1,*} Onur DERSE , ² Elifcan GÖÇMEN POLAT 

¹ Tarsus University, Faculty of Engineering, Department of Industrial Engineering, Mersin, TÜRKİYE

² Munzur University, Faculty of Engineering, Department of Industrial Engineering, Tunceli, TÜRKİYE

¹ onurderse@tarsus.edu.tr, ² elifcangocmen@munzur.edu.tr

(Received: 12.04.2023; Accepted in Revised Form: 01.02.2024)

ABSTRACT: In recent years, there is growing interest for evaluation of urban flood risks of cities over the past decade due to rapid urbanization and climate change. The optimal flood risk assessment is strategically achieved not only with classical risk modelling approaches but also with holistic and comprehensive framework. This paper focuses on a detailed flood assessment providing risk database for policymakers and urban planners to decide the flood prone areas in Turkey. In this context, the Entropy based VIKOR (VIseKriterijumska Optimizacija Kompromisno Resenje) was provided to evaluate a range of flood risk criteria named number of floods, population density and number of buildings, flood protection area which are under the concept of risk dimension including “hazard, exposure and vulnerability” aspects. Computational results demonstrate that the provinces of Şanlıurfa, Ordu, Zonguldak and Van are assigned with higher urban risk values, respectively and the ranking of the cities was presented with different q values. The findings should support practitioners and researchers for land use planning and risk reduction works as the detailed flood risk evaluation was presented in terms of the flood management.

Keywords: Entropy-VIKOR, Exposure, Hazard, Urban flood risks, Vulnerability

1. INTRODUCTION

The raising awareness of disaster management is of great significance to protect the earth, human health. Flooding is one of the most prominent disasters which bring about catastrophic effects [1]. Flood is defined as overflowing of water due to watercourses and the generation of storm water [2]. With increasing severity of the floods, more regions are affected by floods [3]. Given this, how can urban flood management deal with this crisis? As the disaster rates which threaten the sustainable world increase with the climate change, new management shifts are urgently required to overcome these disasters. This new shift is optimal urban flood management understanding the risks at the local level. It represents the shift from classical risk management models to holistic systems and visionary methods. Urban flood management is an integrated vision that requires multi-dimensional evaluation. With the growth of cities, urban flood risks have become increasing problems for regional and national government. The devastating impacts of flood are exacerbated in cities. In Mediterranean, large floodable regions highly destructive are generated and the population has affected due to intense population, wrong perception of risk, required short reaction time [4]. Turkey is a vulnerable country in which natural disasters cause large number of victims and affected people [5]. Accurate urban flood management models are required to reduce this mitigation and building resilience in regions. In the flood management of cities, first, cities with high risk should be identified. To determine the risk situations of cities, an evaluation including various parameters of the risk ensures the accuracy of the analysis. While most studies are evaluated based on vulnerability criteria, studies that include other criteria should be prioritized in the flood assessment. Vulnerability is considered as the low ability to cope with the environmental threats [6] and a tool for the severity and climate change [7]. The main contribution of this study is the integration of multi-criteria decision-making (MCDM) tools in urban flood risk assessment regarding hazard, exposure, and vulnerability dimensions of the risk. First, we identified the most important flood

*Corresponding Author: Onur DERSE, onurderse@tarsus.edu.tr

conditioning factors. Second, we ranked the cities to identify hazardous areas in a flood-prone city in Turkey. Although most papers have focused on flood management, there is a great gap of evaluation of cities and flood risk criteria at the national scale in Turkey.

This paper mainly uses the hierarchical analysis method to evaluate the cities to comprehensively assess the important influencing factors of flood management processes. Main contribution of this paper is to determine the weights of number of floods, population density and number of buildings, flood protection area and to evaluate them with the developed methodology in the context of flood management. Novelties of this study are presented as follows:

- Integrating Entropy and VIKOR method and various criteria were first incorporated to decide the importance weights of the criteria and ranking the cities in Turkey.
- Three basic components of risk; hazard, exposure, and vulnerability, are first considered for measuring urban flood risk. Flood disasters considering the hazard parameter, population density and the number of buildings discussed within the scope of exposure, flood protection area within the scope of vulnerability were incorporated into the study.
- Ranking the city's urban flood risks was validated with different q values and this ensures the comparison of the results.

2. LITERATURE REVIEW

Although few studies are available on flood risk evaluations in Turkey, not enough discussion has been presented at the national scale using MCDM methods. However, MCDM is widely used for the disaster studies [8] – [9]. Especially, TOPSIS has been applied for ranking the regions on flood risk assessments [10] – [12]. Sørensen et al. [13] identified regions which require improvements for urban flood management. They evaluated the water systems, reducing energy-usage, land usage, climate change effects, etc. Yang et al. [14] addressed the flood risk evaluation and prediction using fuzzy AHP. They predicted risk factors and presented the measures. Developed evaluation index could ensure more reasonable results for the flood risk management. Radmehr and Araghinejad [15] presented decisions for urban flood management with multi-criteria decision making and a geographic information system. Also, artificial neural network (ANN) model was used to weight the criteria of flood management strategies are discussed in Iran. Moghadas et al. [16] developed an index regarding social, economic, institutional, and environmental aspects using MCDM. The methodology integrates AHP and TOPSIS for ranking cities in Tahrán. Data were mostly from the Statistical Center of Iran and Tehran Municipality's accessible data sources. The study resulted with most resilient districts. Sun et al. [17] presented a comprehensive analysis to decide the regional risk size. They used three MCDM methods to compare the units of Jiangsu Province and criteria including agriculture, population, drainage etc. Shah et al. [18] discussed the vulnerability to flood in Pakistan regions. They assigned weights to the criteria such as exposure, susceptibility using expert decisions. The results revealed the vulnerable and low resilience regions. Liu et al. [19] assessed the flood risks of regions of China using an index. The areas with high, moderate, and low levels of flood risk were obtained in the paper. Xu et al. [20] integrated an entropy weight method and analytic hierarchy process (AHP) method to weight the criteria. K-means cluster for flood risk map and TOPSIS for ranking were used to present the high-risk zones. Liu et al. [21] discussed the agricultural drought and flood disasters in the three provinces of Yangtze River. They used three MCDM methods and sensitivity analysis to decide the flood disaster. The results showed that the region was affected by drought and flooding. Danumah et al. [22] used MCDM to assess the flood risk in Abidjan. They evaluated the criteria, hazard, and vulnerability. Results of MCDM showed the areas under high and very high flood risk. Xie et al. [23] addressed the meteorological disasters to evaluate the provinces of China. They used a grey cluster model. They provided the serious and lighter grey classes. Camarasa-Belmonte and Soriano-García [4] assessed the flood risks in Spain. They evaluated the hazards and exposure and created a map that shows the floodable areas. Doorga et al. [24] proposed GIS based MCDM to model the flood risks. The vulnerable areas were identified based on the physical, social, and economical metrics. The regions highly vulnerable were considered to design the

urban landscape. Garrote et al. [25] proposed a flood risk analysis regarding the relation of cultural heritage and the flow-prone areas. Developed risk matrix included hazard and vulnerability. Risk levels obtained showed the high flood risks to eliminate these risks. Souissi et al. [26] prepared a flood map with MCDM. They considered eight factors regarding their weights using AHP. The results showed the most prominent flood zones. Hadian et al. [27] analysed the flood risks using TOPSIS and Additive Border Approximation Area Comparison (MABAC). They also developed a map showing distribution of high-risk regions.

3. MATERIAL AND METHODS

Climate changes reveal the risk of flooding in urban areas. In the study, urban flood risks are evaluated considering the “hazard, exposure and vulnerability” parameters. Real data for each parameter was used to assign the weights of the criteria. ENTROPY-based VIKOR method is applied to ranking the of the provinces in Turkey. In Figure 1, the risk parameters of natural events including combination of “hazard, exposure and vulnerability” are demonstrated in Figure 1.

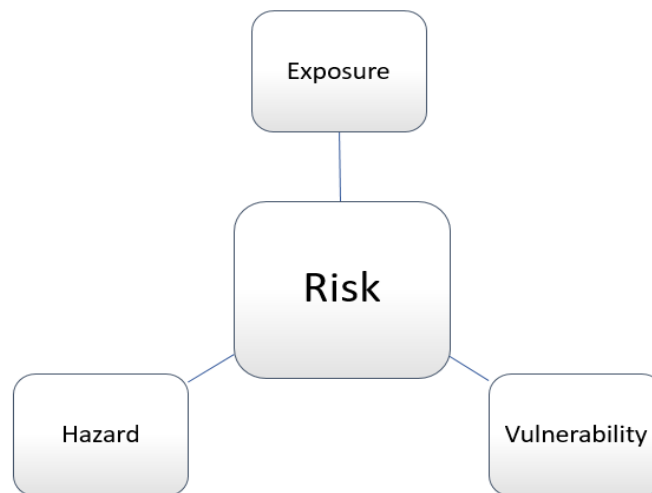


Figure 1. Conceptual framework of urban flood risk [28].

In the risk analysis, risk definition, measurement, evaluation and control stages are applied and probability and the effect are the basically used parameters to define the risk factors [29]. This paper deals with three risk factors including hazard indicates the frequency of the risks, vulnerability indicates the possibility of predicting risks before they occur, and exposure is the seriousness of the risk to the system.

This approach is derived from the FMEA (failure mode and effects analysis) method including occurrence, detectability, and severity parameters [30]. These FMEA parameters are part of the systematic method to examine the risks and reduce the highest risk factors [31] – [32].

3.1. Material

There are three basic components for measuring urban flood risk. In the study, these three components, hazard, exposure, and vulnerability, are considered. Flood risks were evaluated regarding number of floods, population density and number of buildings, flood protection area. In preliminary works, flood durations, depth-velocity were considered [33]; population, capacity, exposure [34]; only flood vulnerability [35]; mortality, economical and agricultural issues [36]; social and economical metrics [37], resilience [38].

Within the scope of hazard, flood disasters in Turkey in 2019, 2020 and 2021 are considered. In this context, distribution of Heavy Rain/Flood Disasters in Turkey in 2019 [39] by Meteorological Disasters

Assessment report of the T.C. Republic of Türkiye Ministry of Agriculture and Forestry, Distribution of Heavy Rain/Flood Disasters in Turkey in 2020 [40] by Meteorological Disasters Evaluation report of T.R. Ministry of Environment, Urbanization and Climate Change General Directorate of Meteorology, the Distribution of Heavy Rain/Flood Disasters in Turkey in 2021 [41] by Meteorological Disasters Assessment report of the Ministry of Environment, Urbanization and Climate Change General Directorate of Meteorology is taken into account. By evaluating the data published on the map, the average of the years 2019-2020-2021 was taken and in Table 1 is figured.

Table 1. Average values obtained by examining the maps for the years 2019-2020-2021

Provinces	Average values
Balıkesir	12.17
Bursa	12.5
İzmir	13
Antalya	11.33
Muğla	10.83
Ordu	9.33
Van	10.83
Giresun	11.83
Zonguldak	8
Manisa	9
Şanlıurfa*	5.33

*Taken into account due to severe flooding in 2023.

In the study, population density and the number of buildings are discussed within the scope of exposure. The data discussed contains the data in the "Annual growth rate of population and population density of provinces by years, 2007-2022" [42] and the "Households by provinces and ownership status of the dwelling 2021" [43] data shared by the Turkish Statistical Institute (TURKSTAT).

Table 2. Population density and number of households of provinces

Provinces	Population Density	Number of households by province
Balıkesir	88	456,193
Bursa	307	966,765
İzmir	371	1,053,086
Antalya	130	858,107
Muğla	82	362,287
Ordu	128	265,344
Van	58	241,504
Giresun	66	164,548
Zonguldak	178	199,841
Manisa	112	475,046
Şanlıurfa	116	411,421

Within the scope of Vulnerability, data of the year 2021 in the "Flood Protection Facilities by Province" shared by the General Directorate of State Hydraulic Works are used [44]. In this context, Flood Protection Facility Protection Area (ha) data are taken into consideration. In Table 3, protection area percentages are calculated by considering the area of the provinces and the 2021 Flood Protection Facility Protected Area data.

Table 3. Flood protection area percentages of provinces

Provinces	Surface Area of the Province (km ²)	2021 Flood Protection Area (ha)	%Flood Protection Area
Balıkesir	14,583	39,932	2.738
Bursa	10,813	15,262	1.411
İzmir	11,891	55,733	4.687
Antalya	20,177	69,296	3.434
Muğla	12,654	31,543	2.493
Ordu	5,861	24	0.004
Van	20,921	290	0.014
Giresun	7,025	4,114	0.586
Zonguldak	3,342	647	0.194
Manisa	13,339	32,642	2.447
Şanlıurfa	19,242	5,615	0.292

3.2. Methods

Preliminary works evaluate the vulnerability of the regions to the flood using curve method [45] and probability [46]. In this study, MCDM methods were used due to potentially relevance to analyze the current data in Turkey. The presented study contains a new approach integrating Entropy and VIKOR methods. To the best of our knowledge, this integrating method named Entropy based VIKOR is first applied to decide the vulnerable cities to flood in the national scale.

3.2.1. ENTROPY method

Entropy method is one of the preferred MCDM methods although it is new for the flood assessment [47]. The method consists of 5 basic steps as follows:

Step 1: Creating the decision matrix

$$X = [x_{ij}]_{m \times n} = \begin{bmatrix} x_{11} & x_{12} & \dots & x_{1n} \\ x_{21} & x_{22} & \dots & x_{2n} \\ \dots & \dots & \dots & \dots \\ x_{m1} & x_{m2} & \dots & x_{mn} \end{bmatrix}; i = 1, 2, \dots, m; j = 1, 2, \dots, n \quad (1)$$

Step 2: Performing normalization to eliminate measurement outliers

$$v_{ij} = \frac{x_{ij}}{\sum_{i=1}^m x_{ij}} \quad (2)$$

Step 3: Finding Entropy (E_j) values

$$e_j = -k \sum_{i=1}^m v_{ij} \ln(v_{ij}) = -\frac{1}{\ln(m)} \sum_{i=1}^m v_{ij} \ln(v_{ij}) \quad (3)$$

Step 4: Calculation of (D_j) and weight (W_j) values

$$D_j = 1 - e_j, j \in [1, \dots, n]$$

$$W_j = \frac{d_j}{\sum_{j=1}^n d_j} \quad (4)$$

3.2.2. VIKOR method

VIKOR method are less complex, ensuring accurate results, widely preferred [48]. The VIKOR method consists of 6 basic steps.

Step 1: Creating the decision matrix and determining the best/worst values

For each criterion, the best (f_i^+) and worst (f_i^-) values are determined.

Step 2: Performing the normalization

Step 3: Weighting the normalized decision matrix

Step 4: Finding (S_i) and (R_i) values

$$S_i = w_i (f_i^+ - f_{ij}) / (f_i^+ - f_i^-) \quad (5)$$

$$R_i = \max (w_i (f_i^+ - f_{ij}) / (f_i^+ - f_i^-)) \quad (6)$$

Step 5: Calculating (Q_i) values, v : weight of the strategy

$$Q_i = v (S_i - S_i^+) / S^- - S_i^+ + (1 - v) (R_i - R_i^+) / R^- - R_i^+ \quad (7)$$

Step 6: Ranking the alternatives and examining the conditions

4. RESULTS and DISCUSSIONS

In Türkiye, many cities face flood disasters due to climate change and local authorities try to make great efforts to deal with this disaster. Therefore, it is critical to identify the cities where the risk of flooding is most intense and to take measures for the optimal land use planning. Evaluating this issue with a multidimensional approach enable a very important database for decision makers or stakeholders. In this context, this paper mainly presents the hierarchical analysis method to evaluate the cities to comprehensively assess the important influencing factors. The evaluation is based on the number of floods, population density and number of buildings, flood protection area. In addition, urban risks for each q levels (0, 0.25, 0.5, 0.75, 1) are presented in this section. This approach also enables the sensitivity analysis for the results.

4.1. Results of the ENTROPY method

Step 1: Creating the decision matrix

The criteria values for the 11 provinces discussed are demonstrated in Table 4.

Table 4. The decision matrix

Provinces	Number of floods	Population Density	Number of households by province	%Flood Protection Area
Balıkesir	12.17	88	456,193	2.738
Bursa	12.5	307	966,765	1.411
İzmir	13	371	1,053,086	4.687
Antalya	11.33	130	858,107	3.434
Muğla	10.83	82	362,287	2.493
Ordu	9.33	128	265,344	0.004
Van	10.83	58	241,504	0.014
Giresun	11.83	66	164,548	0.586
Zonguldak	8	178	199,841	0.194
Manisa	9	112	475,046	2.447
Şanlıurfa	5.33	116	411,421	0.292

Step 2: Performing normalization according to Benefit/Cost indices

Since the number of floods, population density and number of buildings will increase due to the investigation of the urban flood risk, and the low % protection area will increase the risk, the number of floods, population density and number of buildings are taken into consideration as max and % protection area as min.

Table 5. Calculation of Benefit/Cost criteria

Provinces	Number of floods	Population Density	Number of households by province	%Flood Protection Area
Balıkesir	0.936	0.237	0.433	0.001
Bursa	0.962	0.827	0.918	0.003
İzmir	1.000	1.000	1.000	0.001
Antalya	0.872	0.350	0.815	0.001
Muğla	0.833	0.221	0.344	0.002
Ordu	0.718	0.345	0.252	1.000
Van	0.833	0.156	0.229	0.286
Giresun	0.910	0.178	0.156	0.007
Zonguldak	0.615	0.480	0.190	0.021
Manisa	0.692	0.302	0.451	0.002
Şanlıurfa	0.410	0.313	0.391	0.014

Step 3: Performing normalization to eliminate measurement outliers

Table 6 shows the normalized decision matrix.

Table 6. Normalized decision matrix

Provinces	Number of floods	Population Density	Number of households by province	%Flood Protection Area
Balıkesir	0.107	0.054	0.084	0.001
Bursa	0.110	0.188	0.177	0.002
İzmir	0.114	0.227	0.193	0.001
Antalya	0.099	0.079	0.157	0.001
Muğla	0.095	0.050	0.066	0.001
Ordu	0.082	0.078	0.049	0.748
Van	0.095	0.035	0.044	0.214
Giresun	0.104	0.040	0.030	0.005
Zonguldak	0.070	0.109	0.037	0.015
Manisa	0.079	0.068	0.087	0.001
Şanlıurfa	0.047	0.071	0.075	0.010

Step 4: Finding Entropy (E_j) values

Step 5: Calculation of (D_j) and weight (W_j) values

Step 4 and Step 5 results are obtained as in Table 7.

Table 7. Calculation of (E_j), (D_j) and (W_j) values

Values	Number of floods	Population Density	Number of households by province	%Flood Protection Area
(E_j)	0.990	0.925	0.927	0.306
(D_j)	0.010	0.075	0.073	0.694
(W_j)	0.01182171	0.087633039	0.085918076	0.81462718

4.2. Results of the VIKOR method

Step 1: Creating the decision matrix and determining the best/worst values

At this stage, the description of Step 1 and Step 2 in the Application of the ENTROPY method section is handled similarly.

Step 2: Performing the normalization in Table 8.

Table 8. Normalization results.

Provinces	Number of floods	Population Density	Number of households by province	%Flood Protection Area
Balıkesir	0.108	0.904	0.672	0.584
Bursa	0.065	0.204	0.097	0.300
İzmir	0.000	0.000	0.000	1.000
Antalya	0.218	0.770	0.219	0.732
Muğla	0.283	0.923	0.777	0.531
Ordu	0.478	0.776	0.887	0.000
Van	0.283	1.000	0.913	0.002
Giresun	0.153	0.974	1.000	0.124
Zonguldak	0.652	0.617	0.960	0.041
Manisa	0.522	0.827	0.651	0.522
Şanlıurfa	1.000	0.815	0.722	0.061

Step 3: Weighting the normalized decision matrix

In this study, the weighting was done with the values obtained from the Entropy method results. Table 9 shows the weighted normalized matrix.

Table 9. Weighted normalized decision matrix

Provinces	Number of floods	2022 Population Density	Number of households by province	%Flood Protection Area
Balıkesir	0.001	0.079	0.058	0.476
Bursa	0.001	0.018	0.008	0.245
İzmir	0.000	0.000	0.000	0.815
Antalya	0.003	0.067	0.019	0.597
Muğla	0.003	0.081	0.067	0.433
Ordu	0.006	0.068	0.076	0.000
Van	0.003	0.088	0.078	0.002
Giresun	0.002	0.085	0.086	0.101
Zonguldak	0.008	0.054	0.083	0.033
Manisa	0.006	0.073	0.056	0.425
Şanlıurfa	0.012	0.071	0.062	0.050

Step 4: Finding S_i and R_i values

S_i values define row averages, R_i values define the max element in the row. Table 10 shows the values.

Table 10. Values of S_i and R_i

Provinces	S_i	R_i
Balıkesir	0.614	0.476
Bursa	0.272	0.245
İzmir	0.815	0.815
Antalya	0.686	0.597
Muğla	0.584	0.433
Ordu	0.150	0.076
Van	0.171	0.088
Giresun	0.274	0.101
Zonguldak	0.177	0.083
Manisa	0.560	0.425
Şanlıurfa	0.195	0.071

S^* : 0.150; S_- : 0.815; R^* : 0.071; R_- : 0.815

Step 5: Calculating Q_i values

The q value represents the maximum group utility. In this study, q values were taken as (0; 0.25; 0.5; 0.75; 1). Table 10 shows the Q_i values.

Table 11. Q_i values

q values	0	0.25	0.5	0.75	1
Balıkesir	0.543835	0.582359	0.620882	0.659405	0.697928
Bursa	0.23325	0.220791	0.208332	0.19587	0.183414
İzmir	1	1	1	1	1
Antalya	0.706735	0.731514	0.756294	0.781073	0.805853
Muğla	0.486493	0.528147	0.569802	0.611456	0.653111
Ordu	0.006428	0.004821	0.003214	0.001607	0
Van	0.021849	0.024409	0.026969	0.029529	0.032088
Giresun	0.040158	0.076937	0.113716	0.150495	0.187274
Zonguldak	0.01495	0.02153	0.028111	0.034691	0.041272
Manisa	0.475727	0.510865	0.546003	0.581141	0.61628
Şanlıurfa	0	0.017111	0.034222	0.051332	0.068443

In this section, ranking of the cities were presented and all conditions were examined.

Step 6: Ranking the alternatives and examining the conditions

In Table 12, the alternatives are shown respectively. Table 13 shows the examination of the conditions.

Condition 1: Acceptable advantage condition and defined as $Q(A2) - Q(A1) \geq DQ$ ($DQ = 1 / (\text{number of alternatives} - 1)$).

Condition 2: It is an acceptable stability condition, and the minimum values are the best alternative when the Q_i values are ordered from smallest to largest, from smallest to largest, according to S and/or R values.

Table 12. Ranking of alternatives

<i>q</i> values	0	0.25	0.5	0.75	1
Balıkesir	9	9	9	9	9
Bursa	6	6	6	6	5
İzmir	11	11	11	11	11
Antalya	10	10	10	10	10
Muğla	8	8	8	8	8
Ordu	2	1	1	1	1
Van	4	4	2	2	2
Giresun	5	5	5	5	6
Zonguldak	3	3	3	3	3
Manisa	7	7	7	7	7
Şanlıurfa	1	2	4	4	4

Table 13. Examination of conditions

<i>q</i> values	0	0.25	0.5	0.75	1
Q(A2)	0.006428	0.017111	0.026969	0.029529	0.032088
Q(A1)	0	0.004821	0.003214	0.001607	0
Q(A2)-Q(A1)	0.006428	0.01229	0.023755	0.027922	0.032088
DQ	0.1	0.1	0.1	0.1	0.1
Condition 1	False	False	False	False	False
Condition 2	True	True	True	True	True

The *q* value should be selected when both conditions are met. However, since condition 1 is not met in the results, the relationship $Q(A11) - Q(A1) < DQ$ is checked up to the upper limit value.

This examination was conducted again for each *q* in Table 14. According to the table, for $q = 0$, the provinces of Şanlıurfa, Ordu, Zonguldak, Van and Giresun, respectively, were assigned with more urban risks. For $q = 0.25$, the provinces of Ordu, Şanlıurfa, Zonguldak, Van and Giresun, respectively, were assigned with more urban risks. For $q = 0.5$, Ordu, Van, Zonguldak and Şanlıurfa provinces were assigned with more urban risks, respectively. For $q = 0.75$, Ordu, Van, Zonguldak and Şanlıurfa provinces were assigned with more urban risks, respectively. For $q = 1$, Ordu, Van, Zonguldak and Şanlıurfa provinces, respectively, were assigned with more urban risks.

Table 14. Alternatives according to *q* values

<i>q</i> values	0	0.25	0.5	0.75	1
Q(A2)-Q(A1)	0.006428	0.01229	0.023755	0.027922	0.032088
Q(A3)-Q(A1)	0.01495	0.01671	0.024897	0.033085	0.041272
Q(A4)-Q(A1)	0.021849	0.019588	0.031008	0.049726	0.068443
Q(A5)-Q(A1)	0.040158	0.072117	0.110502	0.148888	0.183414
Q(A6)-Q(A1)	0.23325	0.21597			
Provinces with Urban Flood Risk	Şanlıurfa, Ordu, Zonguldak, Van, Giresun	Ordu, Şanlıurfa, Zonguldak, Van, Giresun	Ordu, Van, Zonguldak, Şanlıurfa	Ordu, Van, Zonguldak, Şanlıurfa	Ordu, Van, Zonguldak, Şanlıurfa

Discussions of the study are presented in the following:

In this study, Entropy based VIKOR was used to define the flood risks although most papers have used geographic information system (GIS) [49] – [51], developed index method [52] – [53]. VIKOR was used for hazard, exposure, and vulnerability while risk mapping was addressed for the first time regarding both hazard and vulnerability [54].

Performance of developed Entropy based VIKOR was analyzed to compare the alternatives using q values.

This paper used the conceptual framework of urban flood risk dimensions including hazard, exposure, vulnerability [28] although some papers address the flood management based on PESTEL Analysis, SWOT Analysis [55].

5. CONCLUSION

The current cities are over consuming and overpopulated, and thus they are faced with enormous disasters environmentally damaging. All cities are facing this crisis and trying to control the disasters. Therefore, holistic strategies are required to transform existing cities to more sustainable. To understand the dynamics of the city in terms of the flood management concept, the presented paper provided various criteria to evaluate the cities. Integrated methodology involving the detailed evaluation of key strategies could ensure for long-term sustainability. In this article, flood risk is assessed using a combination of two decision-making methods. The data supporting the analysis consists of 11 flood points and various derived factors: number of floods, population density and number of buildings, flood protection area. Next, we used the VIKOR decision making method to analyse the urban flood risk vulnerability. The results showed that population density is the most critical factor in urban flood risk modelling. Given this, provinces with higher or very higher population density values have the most vulnerable flood risk. For each q value, the provinces with the highest urban flood risk were Ordu, Van, Zonguldak, and Şanlıurfa, respectively. In some q values, it was concluded that in addition to these provinces, Giresun province also has a high risk of urban flooding. The computational result showed that flood risk management provides recommendations to plan the flood risk management and urban disaster controlling. Some implications are presented for the cities which have high risks of urban flooding as follows:

- Flood warning system should be improved in these cities.
- Stakeholders should use a holistic approach for the land use planning.
- City planners should design the cities regarding water sensitive urban modeling systems or sponge city construction.
- City authorities raise the flood awareness providing information and risk maps.

The integrated approach provided in this study could be addressed as the first stage to manage flood risks in areas where there are no meteorological stations. The results could be evaluated by stakeholders and policy makers for guiding urban development, planning drainage systems, provide flood walls and other engineering structure, and protecting building. Urban floods cannot be only managed at the city scale but also with regarding political, economic, and environmental plans. Novel methods for urban flood management should be integrated among stakeholders and authorities that ensure resilience to climate change [13].

Declaration of Ethical Standards

Authors declare to comply with all ethical guidelines, including authorship, citation, data reporting, and original research publication.

Declaration of Competing Interest

There is no conflict of interest.

Funding / Acknowledgements

The authors declare that they have not received any funding or research grants during the review, research or assembly of the article.

Data Availability

Research data has not been made available in a repository.

REFERENCES

- [1] W. Qi, C. Ma, H. Xu, K. Zhao, and Z. Chen, "A comprehensive analysis method of spatial prioritization for urban flood management based on source tracking," *Ecological Indicators*, vol. 135, no. 108565, 2022. <https://doi.org/10.1016/j.ecolind.2022.108565>
- [2] M. Gimenez-Maranges, J. Breuste, and A. Hof, "Sustainable Drainage Systems for transitioning to sustainable urban flood management in the European Union: A review," *Journal of Cleaner Production*, vol. 255, no. 120191, 2020. <https://doi.org/10.1016/j.jclepro.2020.120191>
- [3] T. Wu, (2021). "Quantifying coastal flood vulnerability for climate adaptation policy using principal component analysis," *Ecological Indicators*, vol. 129, no. 108006, 2021. <https://doi.org/10.1016/j.ecolind.2021.108006>
- [4] A. M. Camarasa-Belmonte, and J. Soriano-García, "Flood risk assessment and mapping in peri-urban Mediterranean environments using hydrogeomorphology. Application to ephemeral streams in the Valencia region (eastern Spain)," *Landscape and Urban Planning*, vol. 104, no. 2, pp. 189-200, 2012. <https://doi.org/10.1016/j.landurbplan.2011.10.009>
- [5] E. G. Polat, "Distribution centre location selection for disaster logistics with integrated goal programming-AHP based TOPSIS method at the city level," *Afet ve Risk Dergisi*, vol 5, no. 1, pp. 282-296, 2022. <https://doi.org/10.35341/afet.1071343>
- [6] F. Fatemi, A. Ardalan, B. Aguirre, N. Mansouri, and I. Mohammadfam, "Social vulnerability indicators in disasters: Findings from a systematic review," *International Journal of Disaster Risk Reduction*, vol. 22, pp. 219-227, 2017. <https://doi.org/10.1016/j.ijdr.2016.09.006>
- [7] N. Etinay, C. Egbu, and V. Murray, "Building urban resilience for disaster risk management and disaster risk reduction," *Procedia Engineering*, vol. 212, pp. 575-582, 2018. <https://doi.org/10.1016/j.proeng.2018.01.074>
- [8] M. M. de Brito, and M. Evers, "Multi-criteria decision-making for flood risk management: a survey of the current state of the art," *Natural Hazards and Earth System Sciences*, vol. 16, no. 4, pp. 1019-1033, 2016. <https://doi.org/10.5194/nhess-16-1019-2016>
- [9] O. Derse, "A new approach to the Fine Kinney method with AHP based ELECTRE I and math model on risk assessment for natural disasters," *J Geogr*, vol. 42, pp. 155-164, 2021. Doi: 10.26650/JGEOG2021-875427
- [10] K. S. Jun, E. S. Chung, J. Y. Sung, and K. S. Lee, "Development of spatial water resources vulnerability index considering climate change impacts," *Science of The Total Environment*, vol. 409, no. 24, pp. 5228-5242, 2011. <https://doi.org/10.1016/j.scitotenv.2011.08.027>
- [11] G. Lee, K. S. Jun, and E. S. Chung, "Robust spatial flood vulnerability assessment for Han River using fuzzy TOPSIS with α -cut level set," *Expert Systems with Applications*, vol. 41, no. 2, pp. 644-654, 2014. <https://doi.org/10.1016/j.eswa.2013.07.089>
- [12] S. M. H. Mojtahedi, and B. L. Oo, "Coastal buildings and infrastructure flood risk analysis using multi-attribute decision-making," *Journal of Flood Risk Management*, vol. 9, no. 1, pp. 87-96, 2016. <https://doi.org/10.1111/jfr3.12120>
- [13] J. Sörensen, A. Persson, C. Sternudd, H. Aspegren, J. Nilsson, J. Nordström, ... and S. Mobini, "Re-thinking urban flood management—Time for a regime shift," *Water*, vol. 8, no. 8, pp. 332, 2016. <https://doi.org/10.3390/w8080332>

- [14] X. L. Yang, J. H. Ding, and H. Hou, "Application of a triangular fuzzy AHP approach for flood risk evaluation and response measures analysis," *Natural Hazards*, vol. 68, pp. 657-674, 2013. <https://doi.org/10.1007/s11069-013-0642-x>
- [15] A. Radmehr, and S. Araghinejad, "Developing strategies for urban flood management of Tehran city using SMCDM and ANN," *Journal of Computing in Civil Engineering*, vol. 28, no. 6, 05014006, 2014.
- [16] M. Moghadas, A. Asadzadeh, A. Vafeidis, A. Fekete, and T. Kötter, "A multi-criteria approach for assessing urban flood resilience in Tehran, Iran," *International Journal of Disaster Risk Reduction*, vol. 35, no. 10106, 2019. <https://doi.org/10.1016/j.ijdr.2019.101069>
- [17] R. Sun, Z. Gong, G. Gao, and A. A. Shah, "Comparative analysis of Multi-Criteria Decision-Making methods for flood disaster risk in the Yangtze River Delta," *International Journal of Disaster Risk Reduction*, vol. 51, no. 101768, 2020. <https://doi.org/10.1016/j.ijdr.2020.101768>
- [18] A. A. Shah, J. Ye, M. Abid, J. Khan, and S. M. Amir, "Flood hazards: household vulnerability and resilience in disaster-prone districts of Khyber Pakhtunkhwa province, Pakistan," *Natural Hazards*, vol. 93, pp. 147-165, 2018.
- [19] D. Liu, Y. Li, X. Shen, Y. Xie, and Y. Zhang, "Flood risk perception of rural households in western mountainous regions of Henan Province, China," *International Journal of Disaster Risk Reduction*, vol. 27, pp. 155-160, 2018. <https://doi.org/10.1016/j.ijdr.2017.09.051>
- [20] H. Xu, C. Ma, J. Lian, K. Xu, and E. Chaima, "Urban flooding risk assessment based on an integrated k-means cluster algorithm and improved entropy weight method in the region of Haikou, China," *Journal of Hydrology*, vol. 563, pp. 975-986, 2018. <https://doi.org/10.1016/j.jhydrol.2018.06.060>
- [21] Y. Liu, M. You, J. Zhu, F. Wang, and R. Ran, "Integrated risk assessment for agricultural drought and flood disasters based on entropy information diffusion theory in the middle and lower reaches of the Yangtze River, China," *International Journal of Disaster Risk Reduction*, vol. 38, no. 101194, 2019. <https://doi.org/10.1016/j.ijdr.2019.101194>
- [22] J. H. Danumah, S. N. Odai, B. M. Saley, J. Szarzynski, M. Thiel, A. Kwaku, F. K. Kouameand, and L. Y. Akpa, "Flood risk assessment and mapping in Abidjan district using multi-criteria analysis (AHP) model and geoinformation techniques, (cote d'ivoire)," *Geoenvironmental Disasters*, vol. 3, pp. 1-13, 2016.
- [23] N. Xie, J. Xin, and S. Liu, "China's regional meteorological disaster loss analysis and evaluation based on grey cluster model," *Natural Hazards*, vol. 71, pp. 1067-1089, 2014.
- [24] J. R. Doorga, L. Magerl, P. Bunwaree, J. Zhao, S. Watkins, C. G. Staub,... and R.Boojhawon, "GIS-based multi-criteria modelling of flood risk susceptibility in Port Louis, Mauritius: Towards resilient flood management," *International Journal of Disaster Risk Reduction*, vol. 67, no. 102683, 2022. <https://doi.org/10.1016/j.ijdr.2021.102683>
- [25] J. Garrote, A. Díez-Herrero, C. Escudero, and I. García, "A framework proposal for regional-scale flood-risk assessment of cultural heritage sites and application to the Castile and León Region (Central Spain)," *Water*, vol. 12, no. 2, page 329, 2020. <https://doi.org/10.3390/w12020329>
- [26] D. Souissi, L. Zouhri, S. Hammami, M. H. Msaddek, A. Zghibi, and M. Dlala, "GIS-based MCDM-AHP modeling for flood susceptibility mapping of arid areas, southeastern Tunisia," *Geocarto International*, vol. 35, no. 9, pp. 991-1017, 2020. <https://doi.org/10.1080/10106049.2019.1566405>
- [27] S. Hadian, H. Afzalimehr, N. Soltani, E. Shahiri Tabarestani, and Q. B. Pham, "Application of MCDM methods for flood susceptibility assessment and evaluation the impacts of past experiences on flood preparedness," *Geocarto International*, pp. 1-24, 2022. <https://doi.org/10.1080/10106049.2022.2107714>
- [28] H. M. Lyu, S. L. Shen, A. Zhou, and J. Yang, "Perspectives for flood risk assessment and management for mega-city metro system," *Tunnelling and Underground Space Technology*, vol. 84, pp. 31-44, 2019.

- [29] E. G. Polat, "Medical waste management during coronavirus disease 2019 pandemic at the city level," *International Journal of Environmental Science and Technology*, vol. 19, no. 5, pp. 3907-3918, 2020. <https://doi.org/10.1007/s13762-021-03748-7>
- [30] C. Dağsuyu, E. Göçmen, M. Narlı, and A. Kokangül, "Classical and fuzzy FMEA risk analysis in a sterilization unit," *Computers & Industrial Engineering*, vol. 101, pp. 286-294, 2016. <https://doi.org/10.1016/j.cie.2016.09.015>
- [31] M. Narlı, E. Göçmen, and O. Derse, "Risk assessment using a novel hybrid method: a case study at the biochemistry department," *Hacettepe Sağlık İdaresi Dergisi*, vol. 24, no. 3, pp. 571-588, 2021.
- [32] C. Dagsuyu, O. Derse, and M. Oturakci, "Integrated risk prioritization and action selection for cold chain," *Environmental Science and Pollution Research*, vol. 28, no. 13, pp. 15646-15658, 2021.
- [33] T. Tingsanchali, and Y. Keokhumcheng, "A method for evaluating flood hazard and flood risk of east Bangkok plain, Thailand," *Proceedings of the Institution of Civil Engineers-Engineering Sustainability*, Thomas Telford Ltd. vol. 172, no. 7, pp. 385-392, 2018.
- [34] T. Tingsanchali, and T. Promping, "Comprehensive assessment of flood hazard, vulnerability, and flood risk at the household level in a municipality area: A case study of Nan Province, Thailand," *Water*, vol. 14, no. 2, page 161, 2022. <https://doi.org/10.3390/w14020161>
- [35] M. P. Mohanty, and S. P. Simonovic, "Understanding dynamics of population flood exposure in Canada with multiple high-resolution population datasets," *Science of The Total Environment*, vol. 759, no. 143559, 2021. <https://doi.org/10.1016/j.scitotenv.2020.143559>
- [36] M. M. A. Khan, N. A. B. Shaari, A. M. A. Bahar, M. A. Baten, and D. B. Nazaruddin, "Flood impact assessment in Kota Bharu, Malaysia: a statistical analysis," *World Applied Sciences Journal*, vol. 32, no. 4, pp. 626-634, 2014.
- [37] D. Ma, J. Chen, W. Zhang, L. Zheng, and Y. Liu, "Farmers' vulnerability to flood risk: a case study in the Poyang Lake Region," *Journal of Geographical Sciences*, vol. 17, pp. 269-284, 2007. <https://doi.org/10.1007/s11442-007-0269-5>
- [38] M. I. Mahmood, N. A. Elagib, F. Horn, and S. A. Saad, "Lessons learned from Khartoum flash flood impacts: An integrated assessment," *Science of the Total Environment*, vol. 601, pp. 1031-1045, 2017. <https://doi.org/10.1016/j.scitotenv.2017.05.260>
- [39] T.R. Ministry of Agriculture and Forestry, General Directorate of Meteorology, 2019 Meteorological Disasters Evaluation, "The Distribution of Heavy Rainfall/Flood Disasters in Turkey in 2019 by Provinces", Ankara, 2020.
- [40] T.R. Ministry of Environment, Urbanization and Climate Change General Directorate of Meteorology, 2020 Meteorological Disasters Assessment, "The Distribution of Heavy Rainfall/Flood Disasters in Turkey in 2020 by Provinces", Ankara, 2021.
- [41] T.R. Ministry of Environment, Urbanization and Climate Change, General Directorate of Meteorology, Assessment of Meteorological Disasters for 2021, "The Distribution of Heavy Rain/Flood Disasters in Turkey in 2021 by Provinces", Ankara, 2022.
- [42] Turkish Statistical Institute (TUIK), "Annual growth rate of population and population density of provinces by years, 2007-2022", [Accessed: 03.04.2023].
- [43] Turkish Statistical Institute (TÜİK), "Households by provinces and ownership status of the dwelling, 2021", [Accessed: 03.04.2023].
- [44] General Directorate of State Hydraulic Works (DSI), "Flood Protection Facilities by Province, 2013-2021", <https://www.dsi.gov.tr/Sayfa/Detay/1622>, [Accessed: 01.04.223].
- [45] A. Godfrey, R. L. Ciurean, C. J. Van Westen, N. C. Kingma, and T. Glade, "Assessing vulnerability of buildings to hydro-meteorological hazards using an expert-based approach—An application in Nehoiu Valley, Romania," *International Journal of Disaster Risk Reduction*, vol. 13, pp. 229-241, 2015. <https://doi.org/10.1016/j.ijdr.2015.06.001>
- [46] Z. E. Yin, J. Yin, S. Xu, and J. Wen, "Community-based scenario modelling and disaster risk assessment of urban rainstorm waterlogging," *Journal of Geographical Sciences*, vol. 21, pp. 274-284, 2011. <https://doi.org/10.1007/s11442-011-0844-7>

- [47] K. Khosravi, H. R. Pourghasemi, K. Chapi, and M. Bahri, "Flash flood susceptibility analysis and its mapping using different bivariate models in Iran: a comparison between Shannon's entropy, statistical index, and weighting factor models," *Environmental Monitoring and Assessment*, vol. 188, pp. 1-21, 2016.
- [48] Y. Ma, S. Guga, J. Xu, X. Liu, Z. Tong, and J. Zhang, "Assessment of maize drought risk in Midwestern Jilin Province: A comparative analysis of TOPSIS and VIKOR models," *Remote Sensing*, vol. 14, no. 10, page 2399, 2022. <https://doi.org/10.3390/rs14102399>
- [49] L. A. Hadi, W. M. Naim, N. A. Adnan, A. Nisa, and E. S. Said, "GIS based multi-criteria decision making for flood vulnerability index assessment," *Journal of Telecommunication, Electronic and Computer Engineering (JTEC)*, vol. 9, no. 1-2, pp. 7-11, 2017.
- [50] H. Desalegn, and A. Mulu, "Flood vulnerability assessment using GIS at Fetam watershed, upper Abbay basin, Ethiopia," *Heliyon*, vol. 7, no. 1, page e05865, 2021. <https://doi.org/10.1016/j.heliyon.2020.e05865>
- [51] E. Feloni, I. Mousadis, and E. Baltas, "Flood vulnerability assessment using a GIS-based multi-criteria approach—The case of Attica region," *Journal of Flood Risk Management*, vol. 13, page e12563, 2020. <https://doi.org/10.1111/jfr3.12563>
- [52] K. Garbutt, C. Ellul, and T. Fujiyama, "Mapping social vulnerability to flood hazard in Norfolk, England," *Environmental Hazards*, vol. 14, no. 2, pp. 156-186, 2015. <https://doi.org/10.1080/17477891.2015.1028018>
- [53] L. Rygel, D. O'sullivan, and B. Yarnal, "A method for constructing a social vulnerability index: an application to hurricane storm surges in a developed country," *Mitigation and Adaptation Strategies for Global Change*, vol. 11, pp. 741-764, 2006. <https://doi.org/10.1007/s11027-006-0265-6>
- [54] Ö. Ekmekcioğlu, K. Koc, and M. Özger, "Towards flood risk mapping based on multi-tiered decision making in a densely urbanized metropolitan city of Istanbul," *Sustainable Cities and Society*, vol. 80, no. 103759, 2022. <https://doi.org/10.1016/j.scs.2022.103759>
- [55] C. Sawangnate, B. Chaisri, and S. Kittipongvises, "Flood hazard mapping and flood preparedness literacy of the elderly population residing in Bangkok, Thailand," *Water*, vol. 14, no. 8, page 1268, 2022. <https://doi.org/10.3390/w14081268>



COMPARISON OF CLASSICAL AND FUZZY EDGE DETECTION METHODS

Gülcihan ÖZDEMİR 

Istanbul Technical University, Informatics Institute, Applied Informatics, Istanbul, TÜRKİYE
ozdemir@itu.edu.tr

Highlights

- To find the optimum methodology for edge detection in image processing, eight distinct approaches those are four classical edge detection methods—Sobel, Prewitt, Roberts, and Canny and four fuzzy-logic-based inference systems - type-1, type-2, hybrid-1, hybrid-2 are investigated.
- The performance of each approach is evaluated against three error metrics - Mean Square Error (MSE), Peak Signal Noise Ratio (PSNR), and Structural Similarity Index (SSIM) using two distinct data sets one is street images (three different data sets are utilized in this category) the other is blood vessel recognition in retinal images with varied attributes.
- The BIPED data set contains street images. The methods are presented in the order of best to worst; Roberts > Hybrid-1 Fuzzy > Prewitt > Sobel > Type-2 Fuzzy ...
- The STARE data set contains medical images of blood vessels in the retina.
The methodological success order operates as follows:
Type-2 Fuzzy > Hybrid-1 Fuzzy > Prewitt > Hybrid-2 Fuzzy > Roberts ...
- The hybrid-1 fuzzy inference methodology can be applied effectively for edge detection in most types of image-processing tasks.



COMPARISON OF CLASSICAL AND FUZZY EDGE DETECTION METHODS

*Gülcihan ÖZDEMİR

Istanbul Technical University, Informatics Institute, Applied Informatics, Istanbul, TÜRKİYE
ozdemir@itu.edu.tr

(Received: 15.05.2022; Accepted in Revised Form: 02.02.2024)

ABSTRACT: Edge detection is one of the challenging problems in image processing. Four different classical edge detection methods—Sobel, Prewitt, Roberts, and Canny—and type-1 and type-2 fuzzy logic-based edge detection methods are applied to analyze two separate datasets with various properties. The datasets are STARE which contains medical images of the retina and BIPED which contains images of the street. Furthermore, two separate hybrid fuzzy logic methods are implemented. The type-1 and type-2 fuzzy inference techniques are combined to produce the hybrid-1 and hybrid-2 approaches, using the "AND" and "OR" logic operators. We compare the simulation results for each technique using three different image quality metrics. These are Mean Square Error (MSE), Peak Signal Noise Ratio (PSNR), and Structural Similarity Index (SSIM). The type-2 fuzzy technique outperformed the hybrid-1 fuzzy method in visual quality metrics comparison, demonstrating superior blood vessel recognition on the STARE retinal image dataset—a dataset that more closely resembles the human visual system. Using the BIPED street image dataset, the hybrid-1 fuzzy approach outperformed the Roberts method. The hybrid-1 fuzzy technique showed good results in the second order for both kinds of datasets. Any data and general applications can take advantage of it.

Keywords: Edge detection, Fuzzy inference system, Hybrid fuzzy inference system, Image processing, Type-1 fuzzy inference system, Type-2 fuzzy inference system

1. INTRODUCTION

Edge detection is among the most significant topics in computer vision. The study of medical images [1] and object recognition [2] are two common uses of edge detection. The focus of edge detection techniques in the past has been on grayscale images. Today, RGB (Red, Green, and Blue) images are frequently used for edge detection instead of grayscale images because they can provide more information. Despite taking more time, processing RGB images is more efficient than processing grayscale images [3]. Techniques for recognizing edges are improved using type-1 fuzzy logic [4].

In [5] a 3x3 kernel is employed to determine the derivative for four different directions. This technique yields four distinct inputs. Zero-order Sugeno Inference System is utilized for the fuzzy inference system. Triangle membership functions are available for inputs. There are 20 rules altogether set for the system, with 5 rules being applied to each input. The system produces 4 outputs, which are collected and added together to provide the edge image as the end result. According to [5], the proposed method produces results that are comparable to those of conventional methods.

The study in [6] uses fuzzy if-then rules to implement the suggested strategy for detecting the edges. The maximum entropy principle is used in the proposed algorithm to define the initial membership function. The suggested approach figures out gray-level differences. There are two defined trapezoidal membership functions for this. Fuzzy rules are then used to obtain the edges. In the suggested method, 16 fuzzy rules are defined. The output is then retrieved after applying defuzzification. The pixel is known as an edge pixel if its value is greater than a certain threshold and a non-edge pixel in all other cases. The proposed method, according to the publication, performs effectively even when there is image noise [6].

A new neuro-fuzzy (NF) operator for edge recognition in digital images which is distorted by impact noise is presented in [7]. Edge detection provides details about objects in the image. For instance, procedures like object recognition and classification in the image. Edge identification was carried out on

*Corresponding Author: Gülcihan ÖZDEMİR, ozdemir@itu.edu.tr

noisy digital images using the Neuro-fuzzy method without the use of pre-filtering, and it was found that the results were superior to those of traditional edge detection methods [7].

A new edge detection approach is introduced in [8]. Grayscale and RGB images can be used with this technique. The study makes use of a 3x3 mask. To determine the edge density and orientation of the pixels in the mask, the values of the target function are used as a guide. Thus, the direction map and the edge map are obtained. Edge points are found using the Non-Maximum Suppression approach on these maps. The results of the method were compared with those of traditional edge detection techniques like Sobel and Canny [8].

The grayscale image in [9] has been modified using 3x3 Sobel masks. Then, a fuzzy inference system (FIS) was created by applying the Gaussian membership function to both the inputs and the output in the low, medium, and high linguistic variables. There are seven fuzzy inference rules used. The suggested method performed better than conventional edge detection techniques [9].

Various camera systems, including rotating and fisheye camera systems utilized for Omnidirection, are mentioned along with the challenges these systems face [10]. Omnidirectional vision is frequently used in the imaging industry nowadays. However, there are significant radial distortions in these images. Because traditional edge detection techniques are inadequate for these images, fuzzy edge detection techniques are used in this study. The Prewitt method, one of the traditional edge detection techniques, was utilized to examine the effectiveness of the fuzzy edge detection technique [10].

The proposed approach in the study [4] uses fuzzy logic and morphological gradient. Four inputs representing various orientations for the fuzzy system are obtained using morphological gradients. There are three linguistic variables in these inputs: low, medium, and high. Fuzzy systems of type-1 and interval type-2 are employed for detection. Images are used as input membership function parameters in the method. Images with different gray scales can be processed using this method. The input membership function for the type-1 system is the Gaussian membership function. Calculating the minimum, middle, and maximum values of each input gives the center of the Gaussian membership functions for that input. The system produces a single output with three linguistic variables—black, gray, and white. The output range is set to be between 0 and 255. The main modification in the architecture of the interval type-2 fuzzy system is the addition of a footprint of uncertainty (FOU) for the membership functions. Several sizes are used to calculate the FOU's value. As a consequence, interval type-2 systems outperformed type-1 systems by retaining greater visual details [4].

Image processing steps like edge detection, object recognition, and classification are carried out [11]. This study made edge detection in MRI (magnetic resonance imaging) images easier using the Mamdani fuzzy inference method. The cancerous area in MR images can be found utilizing the edge detection technique. The Mamdani fuzzy inference system was utilized to achieve this judgment, and the K-means clustering technique was used as the input. The Sobel edge detector then receives these threshold values. In comparison to the traditional Sobel edge detector, it was shown that the results were better [11].

A method for edge detection that makes use of general type-2 fuzzy logic has been presented by [3]. The technique is applied to colored images. For the suggested algorithm, two methods are combined. These methods use picture gradients and general type-2 fuzzy logic. This method is considered helpful when there is image noise. The system receives 12 inputs from the 4 different gradients that are utilized for gradient images, each of which is applied to a separate channel of a color image. The system employs 12 inputs and produces 3 outputs for each of the image's channels. For inputs and outputs, Gaussian membership functions are employed. Every input uses low, middle, and high linguistic variables. As linguistic variables for the outputs, background, and edge are employed. The nine fuzzy rules are set up to process inputs. To demonstrate how well the approach performs in comparison to grayscale images, color images are used for evaluation.

The edges of blood vessels are derived from retinal images using the proposed method [12]. The method employs only the green channels from RGB images. Four separate image gradients are produced using filters and supplied to the type-2 Mamdani fuzzy inference system after the contrast enhancement and background extraction are implemented. Each input has two Gaussian membership variables and the

output has two triangle membership functions. The parameters needed to define these membership variables are obtained using the Otsu threshold method. Two fuzzy rules are defined for the proposed approach. After fuzzy edge detection has been performed, the final output is produced using postprocessing. Multiple datasets are used to evaluate the method and obtain positive findings [12].

Our contribution to this research is the application of two fuzzy logic-based edge detection methods as well as various classical edge detection methods from the literature to two different datasets, and the comparison of the results using various metrics like PSNR, SSIM, and MSE. In addition, we have suggested two hybrid fuzzy approaches (hybrid 1 and hybrid 2) that combine type-1 fuzzy and type-2 fuzzy methods using the "AND" and "OR" operators, respectively. As classical techniques Sobel, Prewitt, Roberts, and Canny are utilized. As fuzzy logic-based techniques type-1, type-2, hybrid-1, and hybrid-2 fuzzy inference systems are utilized. The BIPED data set contains street images. The STARE data set contains medical images. We concluded that Roberts's methodology performs best for street images while type-2 fuzzy methodology works best for medical images detecting blood vessel edges in the retina. Hybrid-1 fuzzy methodology ranks the second best follows Robert's methodology for the street images and type-2 fuzzy for the medical images. Lastly, the Hybrid-1 fuzzy approach can be applied to image recognition problems for general-purpose edge detection.

2. IMAGE QUALITY METRICS

2.1. Peak signal-to-noise ratio, Mean-square error

Image compression quality is compared using the mean-square error (MSE) and peak signal-to-noise ratio (PSNR). The PSNR represents a measure of the peak error, whereas the MSE represents the total squared error between the original and compressed image. The error decreases as the MSE value decreases. The higher the PSNR, the better the quality of the compressed, or reconstructed image [13], [14]. First, use the following equation to determine the mean-squared error before computing the PSNR:

Given a noise-free $m \times n$ monochrome image I and corresponding noise image K . MSE is defined as in Equation 1:

$$MSE = \frac{1}{m * n} \sum_{i=1}^m \sum_{j=1}^n [I(i, j) - K(i, j)]^2 \quad (1)$$

Here, m and n denote the size, which is the number of rows and columns in the input images.

The PSNR measurement is typically converted from MSE [13]. Even with noise and corruption present, PSNR is utilized to evaluate the quality of an image. The degree of representation fidelity depends on the ratio between the maximal power of a signal and the power of corrupting noise. The PSNR, represented in decibel (dB) scale, is defined as Equation 2:

$$PSNR = 10 * \log_{10} \left(\frac{MAX_I^2}{MSE} \right) \quad (2)$$

Here, MAX_I is the maximum possible pixel intensity value of the image.

2.2. Structural Similarity Index

When comparing images, MSE may not be a very reliable measure of how similar two images are, despite being easy to compute [13].

The Structural Similarity Index (SSIM) seeks to fix this weakness by considering texture and assigning a higher score to images that may appear similar.

Since SSIM collects important data including brightness (l), contrast (c), and structure (s), it is more analogous to the human visual system. It can be utilized to assess noise reduction and structure preservation. Based on the computation of these three components, the SSIM Index quality assessment index is created. These three elements are multiplicatively combined to form the overall index (Wang et al., 2004) is given in Equations 3 and 4:

$$SSIM(x, y) = [l(x, y)]^\alpha \cdot [c(x, y)]^\beta \cdot [s(x, y)]^\gamma \quad (3)$$

where

$$l(x, y) = \frac{2\mu_x\mu_y + C_1}{\mu_x^2 + \mu_y^2 + C_1}$$

$$c(x, y) = \frac{2\sigma_x\sigma_y + C_2}{\sigma_x^2 + \sigma_y^2 + C_2} \quad (4)$$

$$s(x, y) = \frac{\sigma_{xy} + C_3}{\sigma_x\sigma_y + C_3}$$

where $\mu_x, \mu_y, \sigma_x, \sigma_y,$ and σ_{xy} are the local means, standard deviations, and cross-covariance for images $x, y.$

A block diagram of the SSIM measurement process is shown in Figure 1.

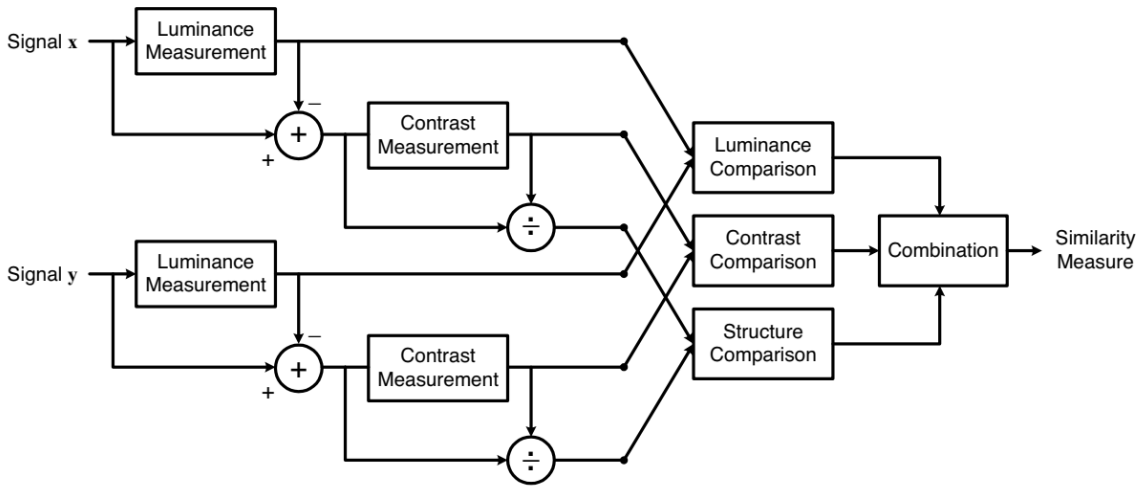


Figure 1. Structural similarity (SSIM) measurement diagram [15].

The images to be used for quality measurement are supplied as a numeric array and could be a 2-D grayscale image or 3-D grayscale volume, such as an RGB image or stack of grayscale images.

Input Arguments:

- Signal x— Image for quality measurement, numeric array
- Signal y— Reference image, numeric array

Output Arguments:

- Similarity measure — SSIM index, numeric scalar

As expected from identical images, an SSIM score of 1.00 indicates perfect structural similarity.

3. A BRIEF SUMMARY OF CLASSICAL EDGE DETECTION METHODS

Image edge detection has drawn a lot of interest from researchers since it was first introduced. Edge detection operators can be categorized under two groups [16]:

- Gradient-based operators which compute first-order derivatives such as;
 - Robert operator
 - Prewitt operator
 - Sobel operator
- Gaussian-based operators which compute second-order derivatives such as;
 - Canny edge detector
 - Laplacian of Gaussian

The Robert operator [17], also known as the cross-differential algorithm as the simplest operator, was the first edge detection operator and was proposed by Lawrence Roberts in 1963. Its basic idea is to locate the image contour with the aid of a local difference operator.

The Prewitt operator, followed it in 1970, which is frequently used on high-noise, pixel-value fading images [18].

Then, in the 1980s, the Sobel operator introduced the concept of weights [19], and the Laplacian operator used second-order differentiation [20].

Later, the best operator for detection in the area of edge detection at the time was the optimal Canny operator [21], which constantly optimized the image contour information through filtering, enhancing, and detecting processes.

4. MODELLING

First, the method that is proposed by [12] is implemented. In this method, a fuzzy edge detection method is presented to obtain blood vessels from retinal images. In the method, the RGB image is taken as input. Operations for edge detection are continued on the green channel of the image. Then, contrast enhancement is applied to the extracted green channel. After contrast enhancement, to remove the background of the image, the contrast-enhanced version of the image is subtracted from the median filtered image. The median-filtered image is obtained by applying a median filter to contrast the enhanced image. After the background is removed from the image, the fuzzy edge detection part of the method is applied. In this part, first, a Gaussian kernel is applied for blurring. Then, 8 gradients given in Figure 2 are applied and 4 gradients with the highest value are chosen by comparing mirror kernels [12].

These four gradients are used as input to the fuzzy inference system. For each input, two Gaussian membership functions named *BP* (Black Pixel) and *WP* (White Pixel) are defined. Some of the parameters of these functions are obtained from the Otsu thresholding technique. For the output of the system, two triangle functions named *EO* (Edge Output) and *NEO* (Not Edge Output) are defined. Two fuzzy rules are defined for the proposed system as given below:

1. IF I_x is *BP* AND I_y is *BP* AND I_z is *BP* AND I_k is *BP* THEN *EO*
2. IF I_x is *WP* AND I_y is *WP* AND I_z is *WP* AND I_k is *WP* THEN *NEO*

Pixel values of the fuzzy inference system's output are checked and if the pixel value is higher than some threshold, that pixel is assigned as 0 otherwise it is assigned as 255.

Even though edges are detected using the method explained, there is noise in the output. In the article a morphological operation called erosion is applied but, in our implementation, we have applied a 4x4

median filter because when erosion is used, some of the edge parts of the output are affected. Flowcharts of the type-2 fuzzy edge detection method and the fuzzy edge detection part of the flowchart are given in Figures 3 and 4, respectively [12].

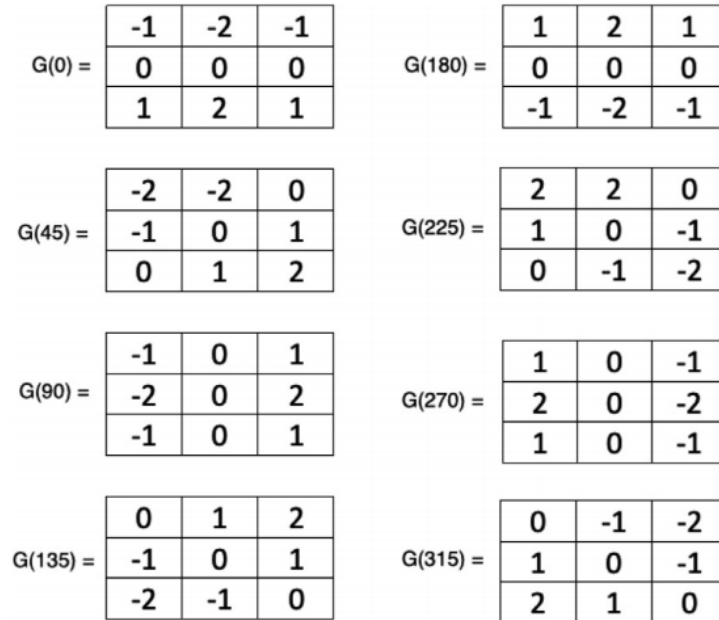


Figure 2. Mirrored kernels [12].

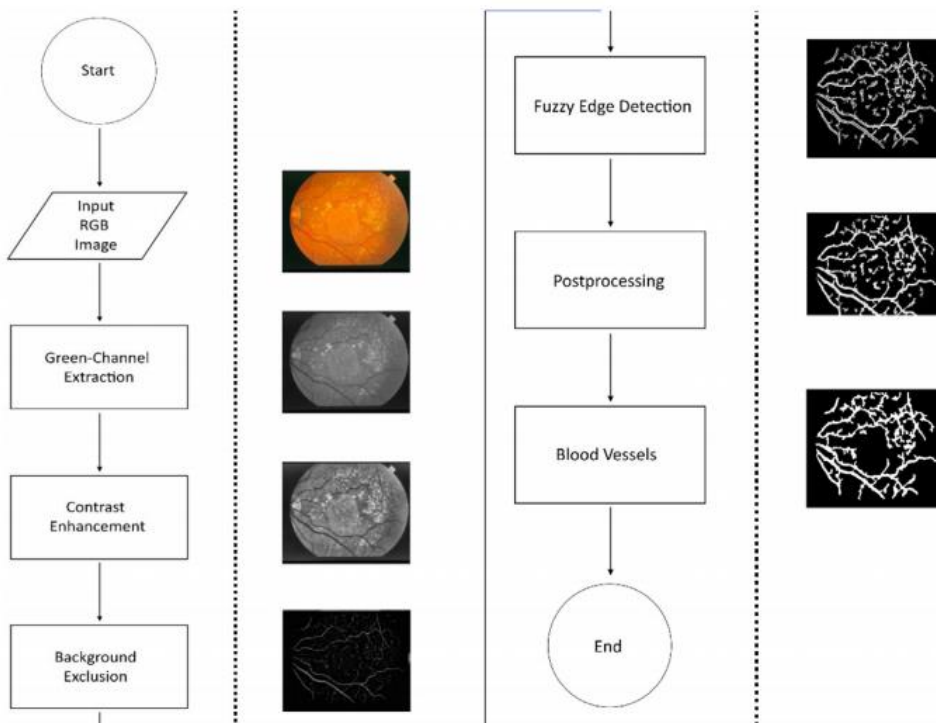


Figure 3. Flowchart of the type-2 fuzzy edge detection method [12].

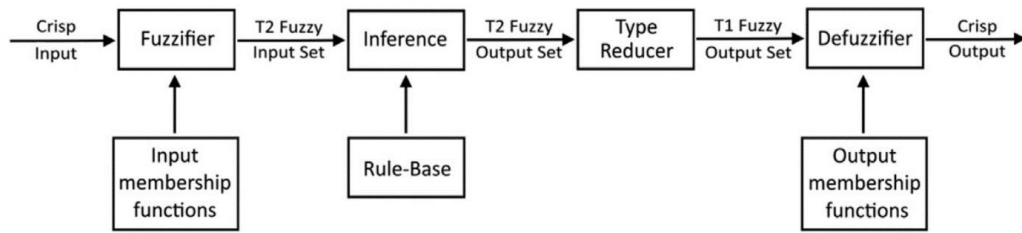


Figure 4. Fuzzy system of the type-2 fuzzy edge detection method [12].

The method in [9] is the second method that we have implemented. In this method, RGB images are first converted to grayscale images. To obtain the inputs for the fuzzy inference system four different kernels are used. These kernels are Sobel in the x direction, Sobel in the y direction, and high-pass and low-pass filters. They are given in Equations 5 through 8:

$$Sobel_x = \begin{bmatrix} -1 & 0 & 1 \\ -2 & 0 & 2 \\ -1 & 0 & 1 \end{bmatrix} \quad (5)$$

$$Sobel_y = \begin{bmatrix} 1 & 2 & 1 \\ 0 & 0 & 0 \\ -1 & -2 & -1 \end{bmatrix} \quad (6)$$

$$hHP = \begin{bmatrix} \frac{-1}{16} & \frac{-1}{8} & \frac{-1}{16} \\ \frac{-1}{8} & \frac{3}{4} & \frac{-1}{8} \\ \frac{-1}{16} & \frac{-1}{8} & \frac{-1}{16} \end{bmatrix} \quad (7)$$

$$hMF = \frac{1}{25} * \begin{bmatrix} 1 & 1 & 1 & 1 & 1 \\ 1 & 1 & 1 & 1 & 1 \\ 1 & 1 & 1 & 1 & 1 \\ 1 & 1 & 1 & 1 & 1 \\ 1 & 1 & 1 & 1 & 1 \end{bmatrix} \quad (8)$$

Inputs S_x , S_y , H and L are obtained by applying $Sobel_x$, $Sobel_y$, hHP and hMF filters, respectively. After obtaining inputs by applying filters, mamdani fuzzy inference system is defined. For each input, three gaussian membership functions called low, medium and high are defined. An example is given in the Figure 5.

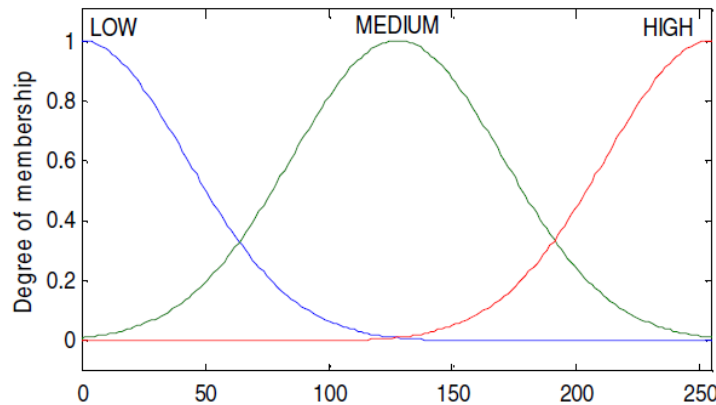


Figure 5. One of the four input membership functions [9].

In the same way, one output named E (Edge) with three gaussian membership functions is defined. Then seven fuzzy rules are defined as follows:

1. (E is LOW) If (S_x is LOW) and (S_y is LOW)
2. (E is HIGH) If (S_x is MEDIUM) and (S_y is MEDIUM)
3. (E is HIGH) If (S_x is HIGH) and (S_y is HIGH)
4. (E is HIGH) If (S_x is MEDIUM) and (H is LOW)
5. (E is HIGH) If (S_y is MEDIUM) and (H is LOW)
6. (E is LOW) If (L is LOW) and (S_y is MEDIUM)
7. (E is LOW) If (L is LOW) and (S_x is MEDIUM)

By applying these rules output of the system is obtained and to get the final result, a threshold is applied. The threshold is calculated as mean + 2*standard deviation in both methods.

5. RESULTS AND DISCUSSIONS

Methods in [9] and [12] are implemented and they are evaluated using two datasets. These datasets are STARE (Structured Analysis of the Retina) [22] and BIPED (Barcelona Images for Perceptual Edge Detection) [23] datasets. STARE (available at <https://cecas.clemson.edu/~ahoover/stare/probing/index.html>) is a dataset for blood vessel segmentation in retinal images. Twenty images were selected and labeled by hand. Labels provided by Valentina Kouznetsova were chosen as ground truth for this work. Each image is an RGB retinal image with a dimension of 605 x 700. BIPED (available at <https://github.com/xavysp/MBIPED>) is another dataset that includes street and car images for edge detection. The dataset contains 250 RGB outdoor images with a dimension of 1280 x 720. Ground truths for these images were obtained by experts. Fifty images from this dataset are used for validation and the rest is used for training. In this work, we only use validation images for testing since we do not use deep-learning approaches.

These images have been thoroughly examined by computer vision experts, hence no redundancy has been considered. These datasets are available for free and serve as a benchmark for evaluating edge detection techniques.

Three image quality metrics were used to evaluate and compare the results for the fuzzy and classical edge detection methods, Sobel, Prewitt, Roberts, and Canny. These are PSNR, SSIM, and MSE; their details are given in section 2. Results of evaluations and example visual outputs are given below. Images were converted to grayscale before using classical methods. Edge results obtained using type-1 and type-2 fuzzy methods were connected with “AND” and “OR” operators. These results are given as hybrid 1 fuzzy method and hybrid 2 fuzzy methods, respectively.

Table 1. PSNR, SSIM, and MSE results of the fuzzy and classical methods for the STARE dataset.

Method/Metric	PSNR	SSIM	MSE
Sobel	9.2358	0.5818	7980.3
Prewitt	9.6734	0.5951	7269.5
Roberts	9.5697	0.5910	7462.8
Canny	8.3984	0.4399	9542.5
Type-1 Fuzzy Method	9.3015	0.5752	7816.8
Type-2 Fuzzy Method	10.475	0.6557	6005.3
Hybrid 1 Fuzzy Method	10.040	0.6558	6700.5
Hybrid 2 Fuzzy Method	9.5334	0.5713	7343.4

Table 1 shows that the type-2 fuzzy method has the highest PSNR and SSIM values and the lowest MSE value, indicating that it gives the best solution among these methods for detecting the blood vessel edges from retinal images according to the image quality metrics given in Equation 1, 2 and 3. The hybrid 1 fuzzy method has the second highest PSNR value, the best SSIM value, and the second lowest MSE value for STARE dataset. From the classical methods Prewitt is the best and Canny is the worst numerically. For an image from STARE dataset, original image, ground truth and visual results of the methods are given in Figure 6. From visual results, it can be seen that Canny, type-2 fuzzy method and hybrid 2 fuzzy method perform well. Rest of the methods perform poorly. We can put the methods in an order from the best to worst value quantitatively in terms of quality metrics used above as follows:

Type-2 Fuzzy > Hybrid 1 Fuzzy > Prewitt > Hybrid 2 Fuzzy > Roberts>...

From Table 2, it seems that Roberts from classical methods gave the best result regarding all three metrics PSNR, SSIM, and MSE. The hybrid 1 fuzzy method has the second best of all the methods and the best result with higher PSNR and SSIM values and the lowest MSE value among all fuzzy methods. In Figure 7, a visual comparison of the methods is provided for an image from the BIPED dataset. Between type-1 and type-2 fuzzy methods, in terms of PSNR and SSIM, the type-2 fuzzy method has a higher value and in terms of MSE error, it has a lower value. Results of fuzzy methods for STARE and BIPED datasets are different which is understandable since the type-2 fuzzy method has pre-process and post-process designed for retinal images. Also, the number of fuzzy rules used in these methods is different. Even though the type-2 fuzzy method is designed for retinal images, it also works well on other images but the same thing cannot be said for type-1 fuzzy method since it performed poorly on retinal images. The methods in an order from the best to worst value quantitatively in terms of quality metrics used are as follows:

Roberts > Hybrid 1 Fuzzy > Prewitt > Sobel > Type-2 Fuzzy > ...

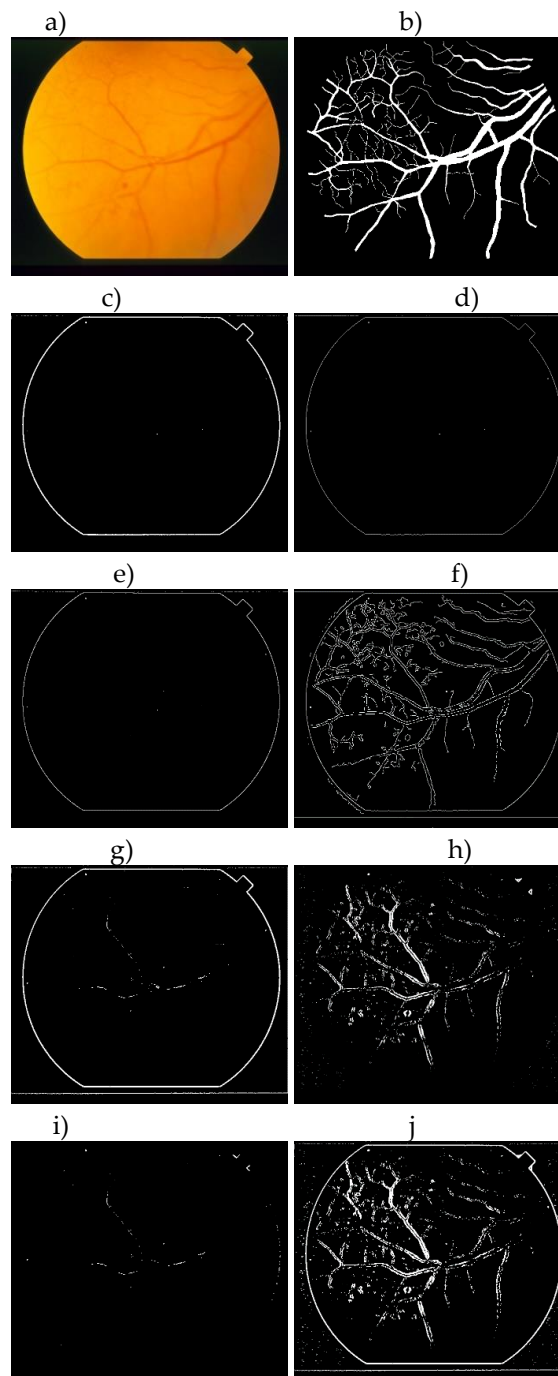


Figure 6. A visual comparison of different methods is given for an image from the STARE dataset. The original image and the ground truth for the image are given in a and b, respectively. Outputs of both classical and fuzzy methods are given as follows: c) Sobel filter, d) Prewitt filter, e) Roberts filter, f) Canny filter, g) Type-1 fuzzy method, h) Type-2 fuzzy method i) Hybrid 1 fuzzy method j) Hybrid 2 fuzzy method.

We concluded that Type-2 fuzzy method is the best for the STARE dataset with the retinal images, Roberts is the best for the BIPED dataset with the street and car images. Hybrid 1 fuzzy method is in the second best for the two distinct dataset used. It can be utilized for general purpose-all kinds of images.

Two different images from the BIPED dataset are simulated again to verify the results of the various methods used in Figure 7. As seen from both Figure 8 and Figure 9 the results confirm the argument made.

Table 2. PSNR, SSIM and MSE results of the fuzzy and classical methods for the BIPED dataset.

Method/Metric	PSNR	SSIM	MSE
Sobel	12.876	0.6649	3470.9
Prewitt	13.230	0.6499	3171.7
Roberts	13.487	0.6621	2997.6
Canny	9.1863	0.3731	7898.9
Type-1 Fuzzy Method	10.442	0.5267	5947.7
Type-2 Fuzzy Method	12.601	0.5899	3620.1
Hybrid 1 Fuzzy Method	13.154	0.6310	3222.7
Hybrid 2 Fuzzy Method	9.2007	0.4870	7897.6

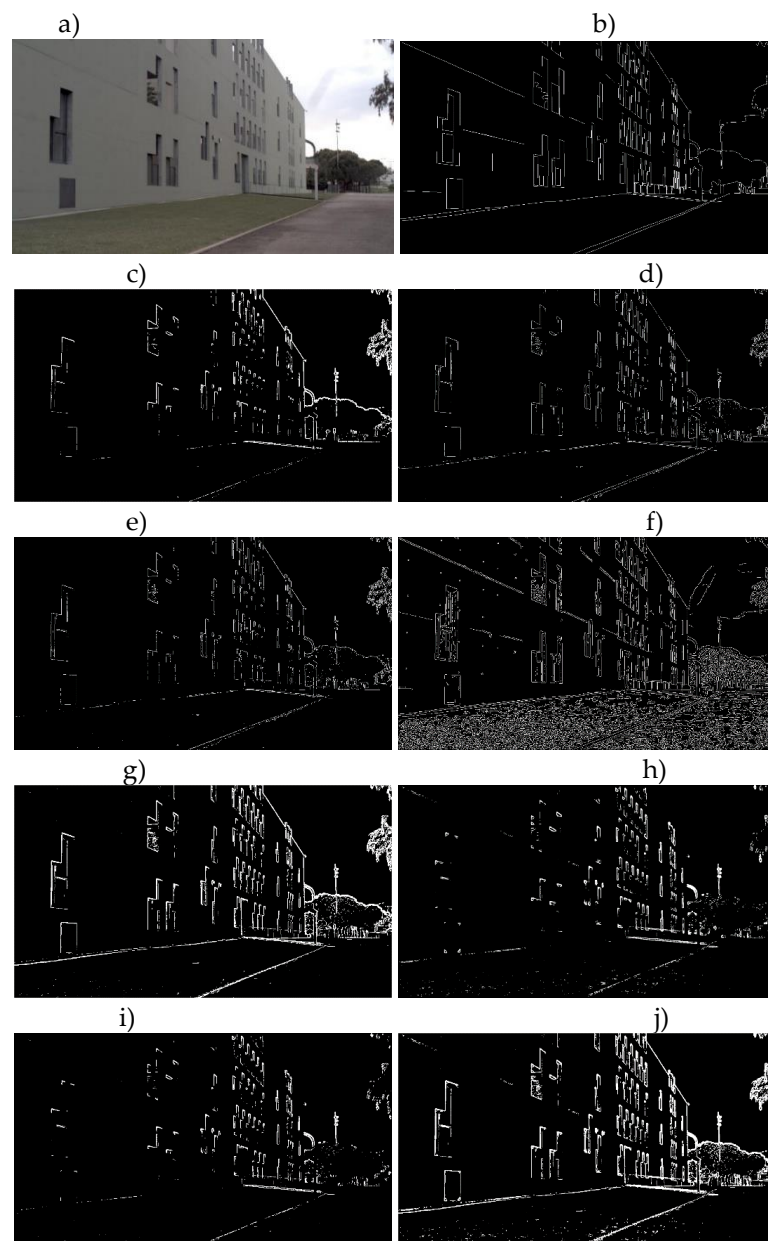


Figure 7. A visual comparison of different methods is given for an image from BIPED dataset. Original image and the ground truth for the image is given in a and b, respectively. Outputs of both classical and fuzzy methods are given as follows: c) Sobel filter, d) Prewitt filter, e) Roberts filter, f) Canny filter, g) Type-1 fuzzy method, h) Type-2 fuzzy method i) Hybrid 1 fuzzy method j) Hybrid 2 fuzzy method.

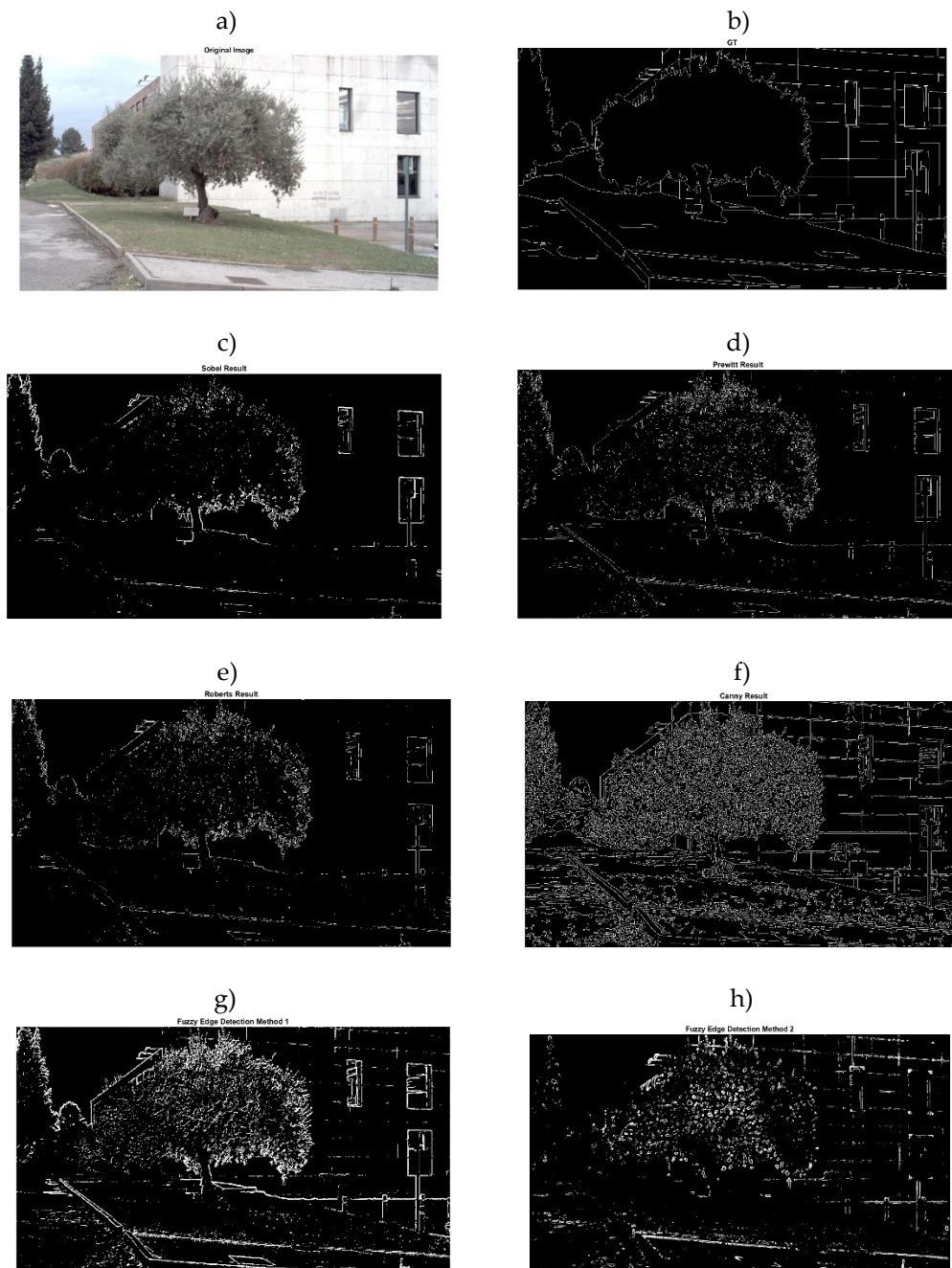


Figure 8. A visual comparison of the second image from BIPED dataset. The original image is provided in a, the ground truth image is provided in b. The following are the results of the fuzzy and classical methods: Type-1 fuzzy method (c), Sobel filter (d), Prewitt filter (e), Roberts filter (f), Canny filter (g), and Type-2 fuzzy method (h).

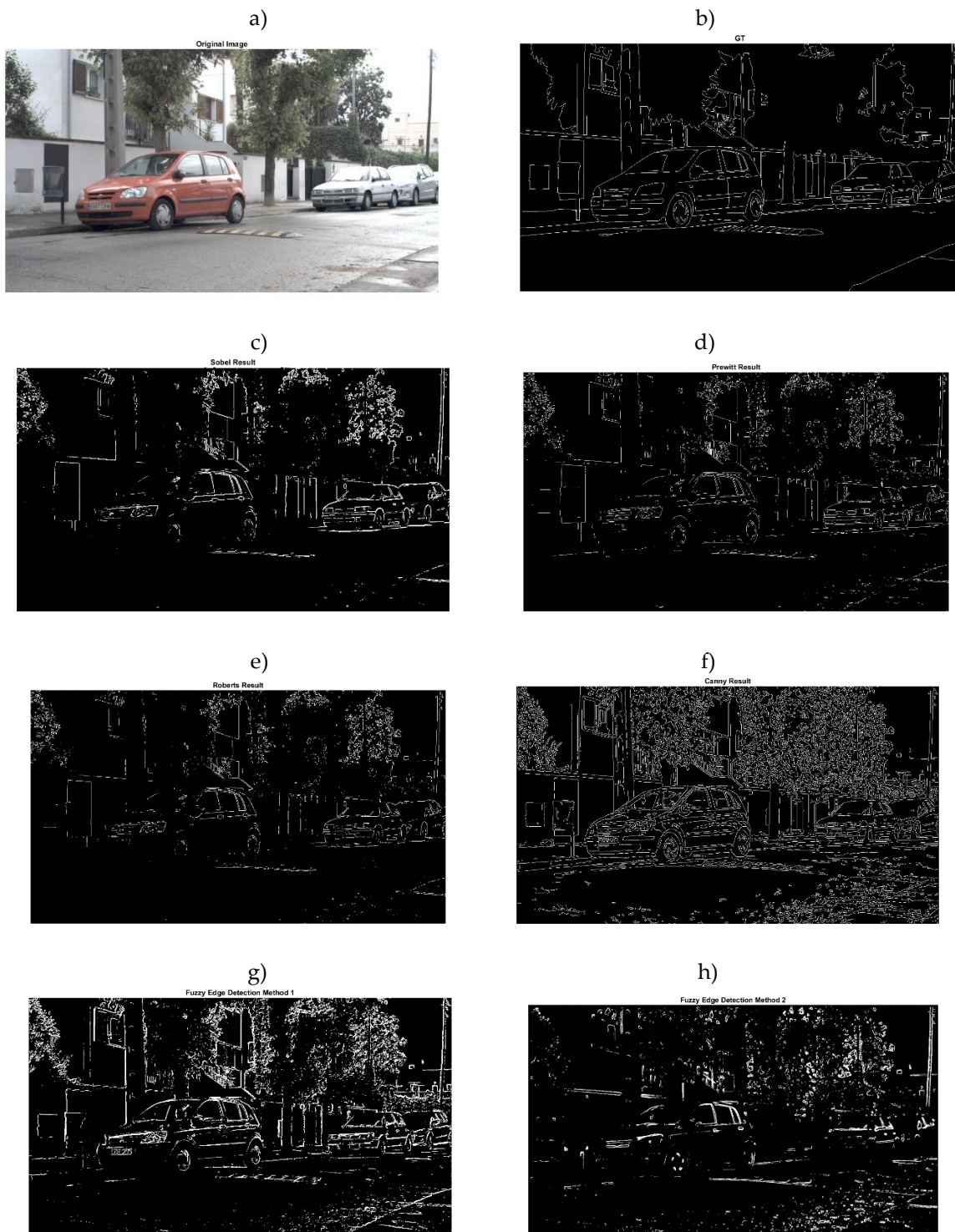


Figure 9. A visual comparison of the third image from the BIPED dataset. The original image is provided in a, the ground truth image is provided in b. The following are the results of the fuzzy and classical methods: Type-1 fuzzy method (c), Sobel filter (d), Prewitt filter (e), Roberts filter (f), Canny filter (g), and Type-2 fuzzy method (h).

6. CONCLUSION

Edge detection is one of the critical subjects in computer vision and has many application areas such as object detection. In this paper, several classical methods that are Sobel, Prewitt, Roberts, and Canny, and two of the fuzzy logic-based edge detection methods that use the type-1 fuzzy inference system and type-2 fuzzy inference system were implemented. Also, results of hybrid fuzzy methods which are obtained with “AND” and “OR” operators using outputs of type-1 and type-2 fuzzy methods are provided. The results were compared by using two datasets which are STARE blood vessels from retinal images and BIPED street and car images. Results were analyzed quantitatively and qualitatively. For quantitative assessment, PSNR, SSIM, and MSE image metrics were calculated for each method on both datasets. The type-2 fuzzy method outperformed on the STARE retinal image dataset while the Roberts method outperformed the BIPED street image dataset. In terms of visual quality, the hybrid-1 fuzzy method worked well on the BIPED data set following the Roberts method then the type-2 fuzzy method comes after the hybrid-1 fuzzy method.

For medical images, we choose the type-2 fuzzy approach, which may also be applied to street images. For more general images, the hybrid-1 fuzzy technique was adopted. Conclusion: Based on the selected image quality measures, we have discovered that the type-2 fuzzy approach is the best for identifying blood vessels, and Robert is the best for street images.

Declaration of Competing Interest

There is no competing interest.

Funding / Acknowledgements

There is no funding for the research.

Acknowledgments

I would like to thank Ismail Yener and Dursun Ali Ekinici for their contributions.

REFERENCES

- [1] S. Yunhong, Y. Shilei, Z. Xiaojing, and Y. Jinhua, “Edge Detection Algorithm of MRI Medical Image Based on Artificial Neural Network,” in *Procedia Computer Science*, Elsevier B.V., 2022, pp. 136–144. doi: 10.1016/j.procs.2022.10.021.
- [2] M. C. Shin, D. B. Goldgof, and K. W. Bowyer, “Comparison of edge detector performance through use in an object recognition task,” *Computer Vision and Image Understanding*, vol. 84, no. 1, pp. 160–178, 2001, doi: 10.1006/cviu.2001.0932.
- [3] C. I. Gonzalez, P. Melin, and O. Castillo, “Edge detection method based on general type-2 fuzzy logic applied to color images,” *Information (Switzerland)*, vol. 8, no. 3, Aug. 2017, doi: 10.3390/info8030104.
- [4] P. Melin, O. Mendoza, and O. Castillo, “An improved method for edge detection based on interval type-2 fuzzy logic,” *Expert Syst Appl*, vol. 37, no. 12, pp. 8527–8535, 2010, doi: 10.1016/j.eswa.2010.05.023.
- [5] Y. Becerikli and T. M. Karan, “LNCS 3512 - A New Fuzzy Approach for Edge Detection,” in *LNCS*, Springer-Verlag, 2005, pp. 943–951.
- [6] L. Hu, H. D. Cheng, and M. Zhang, “A high performance edge detector based on fuzzy inference rules,” *Inf Sci (N Y)*, vol. 177, no. 21, pp. 4768–4784, Nov. 2007, doi: 10.1016/j.ins.2007.04.001.

- [7] M. E. Yüksel, "Edge detection in noisy images by neuro-fuzzy processing," *AEU - International Journal of Electronics and Communications*, vol. 61, no. 2, pp. 82–89, Feb. 2007, doi: 10.1016/j.aeue.2006.02.006.
- [8] C. C. Kang and W. J. Wang, "A novel edge detection method based on the maximizing objective function," *Pattern Recognit*, vol. 40, no. 2, pp. 609–618, Feb. 2007, doi: 10.1016/j.patcog.2006.03.016.
- [9] O. Mendoza, P. Melin, and G. Licea, "A New Method for Edge Detection in Image Processing Using Interval Type-2 Fuzzy Logic," Institute of Electrical and Electronics Engineers (IEEE), Apr. 2008, pp. 151–151. doi: 10.1109/grc.2007.115.
- [10] F. Jacquy, F. Comby, and O. Strauss, "Fuzzy edge detection for omnidirectional images," *Fuzzy Sets Syst*, vol. 159, no. 15, pp. 1991–2010, Aug. 2008, doi: 10.1016/j.fss.2008.02.022.
- [11] N. Mathur, S. Mathur, and D. Mathur, "A Novel Approach to Improve Sobel Edge Detector," in *Procedia Computer Science*, Elsevier B.V., 2016, pp. 431–438. doi: 10.1016/j.procs.2016.07.230.
- [12] F. Orujov, R. Maskeliūnas, R. Damaševičius, and W. Wei, "Fuzzy based image edge detection algorithm for blood vessel detection in retinal images," *Applied Soft Computing Journal*, vol. 94, Sep. 2020, doi: 10.1016/j.asoc.2020.106452.
- [13] Z. Wang and A. C. Bovik, "Mean squared error: Lot it or leave it? A new look at signal fidelity measures," *IEEE Signal Process Mag*, vol. 26, no. 1, pp. 98–117, 2009, doi: 10.1109/MSP.2008.930649.
- [14] J. Erfurt, C. R. Helmrich, S. Bosse, H. Schwarz, D. Marpe, and T. Wiegand, "A Study of The Perceptually Weighted Peak Signal-To-Noise Ratio (Wpsnr) For Image Compression," in *2019 IEEE International Conference on Image Processing (ICIP): September 22-25, 2019, Taipei International Convention Center (TICC), Taipei, Taiwan*, IEEE Signal Processing Society, 2019.
- [15] Z. Wang, A. C. Bovik, H. R. Sheikh, and E. P. Simoncelli, "Image quality assessment: From error visibility to structural similarity," *IEEE Transactions on Image Processing*, vol. 13, no. 4, pp. 600–612, Apr. 2004, doi: 10.1109/TIP.2003.819861.
- [16] R. Sun *et al.*, "Survey of Image Edge Detection," *Frontiers in Signal Processing*, vol. 2, Mar. 2022, doi: 10.3389/frsip.2022.826967.
- [17] D. Ziou and S. Tabbone, "Edge detection techniques: An overview' Article .," 1998. [Online]. Available: <https://www.researchgate.net/publication/312890367>
- [18] G. T. Shrivakshan and C. Chandrasekar, "A Comparison of various Edge Detection Techniques used in Image Processing," 2012. [Online]. Available: www.IJCSI.org
- [19] D. Ma, "Theory of edge detection," 1980. [Online]. Available: <https://royalsocietypublishing.org/>
- [20] X. Wang, "Laplacian operator-based edge detectors," *IEEE Trans Pattern Anal Mach Intell*, vol. 29, no. 5, pp. 886–890, May 2007, doi: 10.1109/TPAMI.2007.1027.
- [21] J. Canny, "A Computational Approach to Edge Detection," *IEEE Trans Pattern Anal Mach Intell*, no. 6, 1986.
- [22] A. Hoover, V. Kouznetsova, and M. Goldbaum, "Locating Blood Vessels in Retinal Images by Piecewise Threshold Probing of a Matched Filter Response," *IEEE Trans Med Imaging*, vol. 19, no. 3, 2000.
- [23] X. Soria, E. Riba, and A. Sappa, "Dense Extreme Inception Network: Towards a Robust CNN Model for Edge Detection." [Online]. Available: <https://github.com/xavysp/DexiNed>



ENCAPSULATION OF VITAMIN D IN THE EXINE-ALGINATE-CHITOSAN MICROCAPSULE SYSTEM

¹Gülnur DUYSAK , ^{2,*}İdris SARGIN 

Selcuk University, Science Faculty, Biochemistry Department, Konya, TÜRKİYE
¹duysakg@gmail.com, ²idris.sargin@selcuk.edu.tr

Highlights

- Exine microcapsules are obtained from *C. libani* pollen using a microwave-assisted chemical process.
- Microwaved exine microcapsules remain structurally intact.
- Vitamins D₂ and D₃ could be loaded in exine microcapsules using ethanol.
- Alginate and chitosan are capable of effectively stabilising D₂ and D₃ loaded-exine microcapsules.
- Vitamins D₂ and D₃ release depends on time and temperature in the microcapsule system.



ENCAPSULATION OF VITAMIN D IN THE EXINE-ALGINATE-CHITOSAN MICROCAPSULE SYSTEM

¹Gülnur DUYSAK^{ID}, ^{2,*}İdris SARGIN^{ID}

Selcuk University, Science Faculty, Biochemistry Department, Konya, TÜRKİYE

¹duysakg@gmail.com, ²idris.sargin@selcuk.edu.tr

(Received: 12.09.2023; Accepted in Revised Form: 06.02.2024)

ABSTRACT: The insufficiency of vitamin D, resulting from inadequate exposure to sunlight and/or insufficient dietary intake, remains a major public health concern on a global scale. In this study, vitamin D₂ and D₃ were microencapsulated using sporopollenin exine microcapsules extracted from *Cedrus libani* pollens. After loading vitamin D into the microcapsules, they were coated with chitosan, an edible, biocompatible, and mucoadhesive polysaccharide, and alginate (a food additive agent coded E401). Exine microcapsules were extracted by microwave irradiation-assisted chemical method, and structural and morphological examination of exine structures was performed by FT-IR, TGA, SEM, and SEM-EDX analyses. After loading vitamin D into microcapsules in an ethanol medium, the loaded microcapsules were immobilised into the alginate matrix in a calcium chloride solution. D₂ and D₃ were loaded into 100 mg of sporopollenin exine microcapsules, resulting in loading efficiencies of 31.5 mg and 16.0 mg, respectively. The vitamin D release performance of the microcapsules was examined depending on time and temperature after they were coated with a thin chitosan layer. The release of the highest amount of vitamin D₂ and D₃ occurred at a temperature of 37°C. Encapsulating vitamin D molecules in chitosan and alginate creates a barrier against degrading environmental conditions, which helps prevent the loss of vitamin D biological activity. This can improve vitamin D dietary supplements' storage, preservation, and marketing requirements.

Keywords: Alginate, *Cedrus libani*, Chitosan, Encapsulation, Sporopollenin, Vitamin D

1. INTRODUCTION

Vitamin D is a fat-soluble vitamin that can be found in both plants and animals. It comes in two forms, ergocalciferol (D₂) in plants and cholecalciferol (D₃) in animals [1-3]. Vitamin D is crucial in many bodily functions such as calcium metabolism, bone health, and cellular and metabolic cycles [4].

Vitamin D deficiency is common due to its low presence in foods and resistance to heat and cooking. For this reason, it is essential to enrich foods with vitamin D and make supplements available [5]. Microencapsulation processes enhance vitamin D's bioavailability, as it is easily absorbed in the intestine and suitable for food preservation and processing [6]. Since the chemical molecules used during microencapsulation may cause health problems when taken into the body, it has been observed that more natural molecules can be preferred in the processes.

Plant pollen's exine shells are ideal microcarriers for drug delivery [7]. Sporopollenin is a substance on the outer surface of spores and pollen grains. It is an abundant and edible material with a porous morphology and can maintain its structural integrity during extraction. Due to its thermal stability, sporopollenin grains, also known as exine capsules, are resistant to chemical and biological attacks [8]. It is challenging to microencapsulate sporopollenin microcapsules due to their complex microstructure and poor solubility [9].

Alginate has a unique property of selectively binding with multivalent cations to form a gel, and CaCl₂ is commonly used to create calcium alginate gel. Sodium alginate (NaC₆H₇O₆) is a linear polysaccharide derivative of alginic acid composed of 1,4-β-d-mannuronic and α-1,4-guluronic acids. Alginates have the unique property of turning into a gel form when dissolved in water. This transformation occurs almost instantaneously by replacing monovalent ions (e.g., Na⁺) with divalent

***Corresponding Author:** İdris SARGIN, idris.sargin@selcuk.edu.tr

ions (specifically, Ca^{2+}), leading to the formation of a gel structure from a low-viscosity solution. The resulting gel is a copolymer composed of two different monomer units [10]. Alginate is a type of biocompatible polymer that is degradable and has the advantage of being low-cost [10, 11]. It is a non-toxic component that protects the upper gastrointestinal mucous membranes [10]. The dry alginate can absorb water and release the drug in a controlled manner. Studies indicate high compatibility between core and shell materials in alginate encapsulations [12]. However, alginate capsules alone are insufficient for successful encapsulation [10].

Chitosan is a copolymer produced by partially or entirely deacetylating chitin under alkaline conditions with either sodium hydroxide or chitin deacetylase enzyme [13, 14]. Chitosan is a commonly used excipient in the pharmaceutical industry for direct tablet compression and as a tablet integrator for producing controlled-release dosage forms. This is due to its non-toxic, biocompatible, and biodegradable properties. In recent years, chitosan microspheres have been developed for site-specific drug delivery, including intestinal selective drugs, anticancer agents, and mucoadhesive drug delivery systems [15].

Studies have been conducted on microencapsulation of Vitamin D, with one study using Vitamin D₂ as a model drug. The study found that using spray drying, the chitosan micronuclei efficiently trapped the Vitamin D₂. The microcapsules were then coated with ethylcellulose. Tests on the morphology and release properties of the microcapsules were carried out. *In vitro* release results showed that the microcapsules could achieve sustained release in the intestinal environment [15]. A recent study involved the synthesis of a new amphiphilic chitosan derivative of N, N-dimethyl hexadecyl carboxymethyl chitosan, followed by the loading of vitamin D₃. The study found that the vitamin was loaded at a rate of 53.2%. The *in vitro* release process of the loaded vitamin D₃ was initially rapid and then followed by a sustained release [16]. In another study, the process of encapsulating vitamin D by complex coacervation was studied. The encapsulation was done using a carbohydrate, specifically cress seed mucilage and gelatin protein. The study found that the efficiency and payload of encapsulation were significantly affected by the core-to-shell ratio and the mucilage/gelatin ratio. The best microcapsules had 67.93% and 50.9% efficiency and loading capacity, respectively [17].

This study was conducted to create a microencapsulated form of vitamin D using sporopollenin exine microcapsules extracted from *Cedrus libani* pollens. Both forms of vitamin D, D₂ and D₃, were loaded into the exine microcapsules, which were then coated with alginate (a food additive, E401) and chitosan, an edible and biocompatible polysaccharide that is also mucoadhesive. The release profile of vitamin D from the microencapsulation system was studied at different temperatures and durations.

2. MATERIAL AND METHODS

2.1. Materials

Harvesting of *C. libani* pollens: The pollen samples used in this study were collected from Selcuk University Alaeddin Keykubad Campus in October 2022 (coordinates of the pollen collection site: 38.025663N, 32.504256E) (Konya, Türkiye). To collect the pollen, the cones were first dried, and then the pollen was shaken off. The collected pollen was then sieved to remove dust or other unwanted particles.

Chemicals: Ergocalciferol (D₂) (95220-1G, ≥98.0, Sigma-Aldrich), cholecalciferol (D₃) (C9756-1G, ≥98.0, Sigma-Aldrich), hydrochloric acid (Sigma-Aldrich), sodium hydroxide (Merck), methanol (≥99.7, GC, Sigma-Aldrich), chloroform (CAS: 67-66-3, HPLC, Loba Chemie), calcium chloride (Merck), ethanol (Emsure, ACS, ISO, Reag. Ph Eur, absolute, Merck), chitosan (448877, medium molecular weight, Sigma-Aldrich), acetic acid (Merck) and sodium alginate (W201502-1KG, Sigma-Aldrich) were used in the study.

2.2. Extraction of Exin Microcapsules from *C. Libani* Pollens

Extraction of exin microcapsules from *C. libani* pollens involved a three-step process to remove minerals, proteins, and pigments from the pollens. Firstly, 1.0 g of pollen was treated with 4.0 M 20.0 mL HCl solution in a microwave oven at 400 watts for three minutes to demineralise. The samples were then filtered with a Whatman filter paper and washed with pure water until neutral pH. Secondly, deproteinisation was done by treating the samples with 4.0 M NaOH 20.0 mL solution in a microwave oven at 400 watts for three minutes. Once again, the samples were filtered with a Whatman filter paper and washed with pure water until neutral pH. Lastly, the acid and base-treated pollen samples were incubated at room temperature in chloroform/methanol/water solution (4:2:1 by volume) at 400 watts for three minutes to remove pigments. Finally, the sporopollenin samples were washed thoroughly with distilled water and left to dry at room temperature.

2.3. Loading of Vitamin D₂ Or D₃ Molecules into The Exine Microcapsules

For each encapsulation process, 100.0 mg of sporopollenin was mixed with 2.0 mL of ethanol and 40.0 mg of vitamin D₂ or D₃ solution (20 mg/mL) to form a homogeneous mixture, which was then loaded into exine microcapsules. The product was mixed on a vortex for about 10 minutes to help the vitamin penetrate through the porous wall of the microcapsules.

The loading efficiencies of vitamin D₂ and D₃ into exine microcapsules were calculated based on mass measurements. The microcapsules were weighed before and after the vitamin loading to calculate the loading efficiency. Three repetitions were made, and the average weight was calculated to obtain a result closer to reality.

2.4. Coating of Vitamin D-Loaded Exine Microcapsules with Alginate and Chitosan

The process began by stirring 2.5 grams of sodium alginate in 50 mL of pure water at room temperature for 30 minutes, with the mixer set at 1000 rpm. Next, vitamins D₂ and D₃ were added separately to the alginate solution and mixed for another 30 minutes to ensure that they were evenly distributed. The mixing was carried out in a closed container to minimise air exposure. Capsules were formed by transferring the mixture into a burette and dropping it into a solution containing 100 mL of water and 5 grams of CaCl₂. The mixture was added drop by drop to the solution containing calcium ions, resulting in the formation of spherical gel structures [10].

The microcapsules immersed in calcium chloride solution were filtered using Whatman filter paper, washed with pure water, and then dried at room temperature. Later, vitamin D-loaded sporopollenin exine alginate microcapsules were added to the chitosan solution (2.0 g chitosan in 100 mL 2% acetic acid solution) and left for an hour. Using a needle under a light microscope, the microcapsules were carefully separated to avoid sticking together. To avoid vitamin loss and preserve their structure, the microcapsules were washed with a solution prepared by dissolving 5.0 g CaCl₂ in 100 mL water. However, it was observed that the presence of CaCl₂ prevented the release of vitamins. Therefore, the vitamin D-loaded sporopollenin exine alginate microcapsules were dried at room temperature after being immersed in a chitosan solution. Finally, they were stored in glass bottles.

2.5. The Release Profiles of Vitamin D₂ and D₃-Exine-Alginate-Chitosan System

To carry out release tests, calibration graphs were initially created. To prepare these graphs, specific amounts of vitamin D₂ or D₃ were added to ethyl alcohol and mixed using a vortex. The mixtures were then subjected to absorbance measurements (at 265 nm for vitamin D₂ and D₃) on a UV-Vis spectrophotometer (Fig. 1), and calibration curves were drawn [15]. These curves were then used to calculate the releases of the microcapsules.

The release tests for the vitamin D-microcapsule system were performed at different temperatures

(4, 20, and 37°C). A mixture of 15.0 mg of vitamin D loaded-exine-alginate-chitosan microcapsules and 3.0 mL of ethyl alcohol was shaken at 100 rpm for 120 minutes. The release of vitamin D was recorded at different temperatures. To study the effects of duration on the release of vitamin D from the vitamin D loaded-exine-alginate-chitosan microcapsule system, the release tests were repeated at different durations. A mixture of 15.0 mg of vitamin D loaded-exine-alginate-chitosan microcapsules and 3.0 mL of ethyl alcohol was shaken at 100 rpm at 37°C.

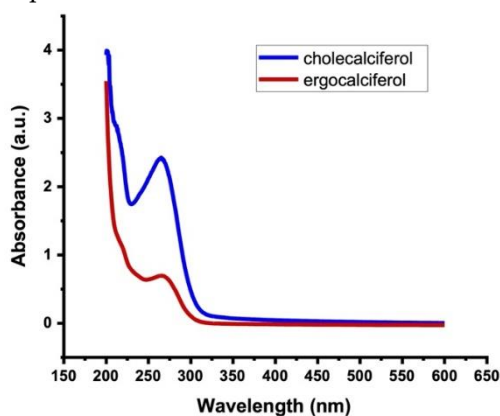


Figure 1. UV-vis spectra of ergocalciferol (D₂) and cholecalciferol (D₃).

3. RESULTS AND DISCUSSION

3.1. Extraction of Exine Microcapsules from *C. Libani* Pollens

Exine microcapsules were extracted using a microwave-assisted chemical method, and their structural and morphological characteristics were examined by FT-IR, TGA, SEM, and SEM-EDX analyses.

3.1.1. FT-IR Spectroscopy analysis

FT-IR spectra of untreated pollen were taken before and after the application of chemical treatments. The first spectrum was taken before any treatment, and the second spectrum was taken after the pollen grains were treated with acid. As a result of the acid treatment, there were noticeable differences and shifts in absorption band values in the pollen spectrum. An alkaline treatment was applied after the acid treatment, but no significant difference in the spectra was observed. This suggests that alkali treatment does not create any observable difference in the surface functional groups of the pollen. Finally, microwave irradiation was used to isolate exine structures in the last processing step by exposing the samples to a mixture of chloroform, methanol, and water. After this step, differences were observed in the FT-IR spectrum, as shown in Figure 2 (a-d).

The spectrum of *C. libani* pollen showed an intermolecular OH bond peak at 3359 cm⁻¹. Two peaks were recorded at 2920 and 2851 cm⁻¹, which are attributed to aliphatic C-H stretching vibrations. Furthermore, the absorption peak of -CNH bonds was observed at 2851 cm⁻¹, while the peak at 1112 cm⁻¹ was due to C-O-C stretching vibration.

Compared with the spectrum of untreated *C. libani* pollen, changes in some peak values were observed in the spectrum of the extracted *C. libani* sporopollenin (Figure 1 d). Additionally, new peaks appeared in the spectrum of the exine (sporopollenin). The broad OH bond peak in the pollen spectrum shifted to 3365 cm⁻¹. The band at 1447 cm⁻¹ can be associated with the C-O-H deformation vibration. The sharp peaks at 2922 and 2854 cm⁻¹ can be interpreted as resulting from aliphatic C-H stretching of unsaturated fatty acids. The aliphatic C=C stretch band of sporopollenin structures was detected at 1604 cm⁻¹ [18]. Literature comparisons show that structures isolated from *C. libani* pollen consist of sporopollenin [19].

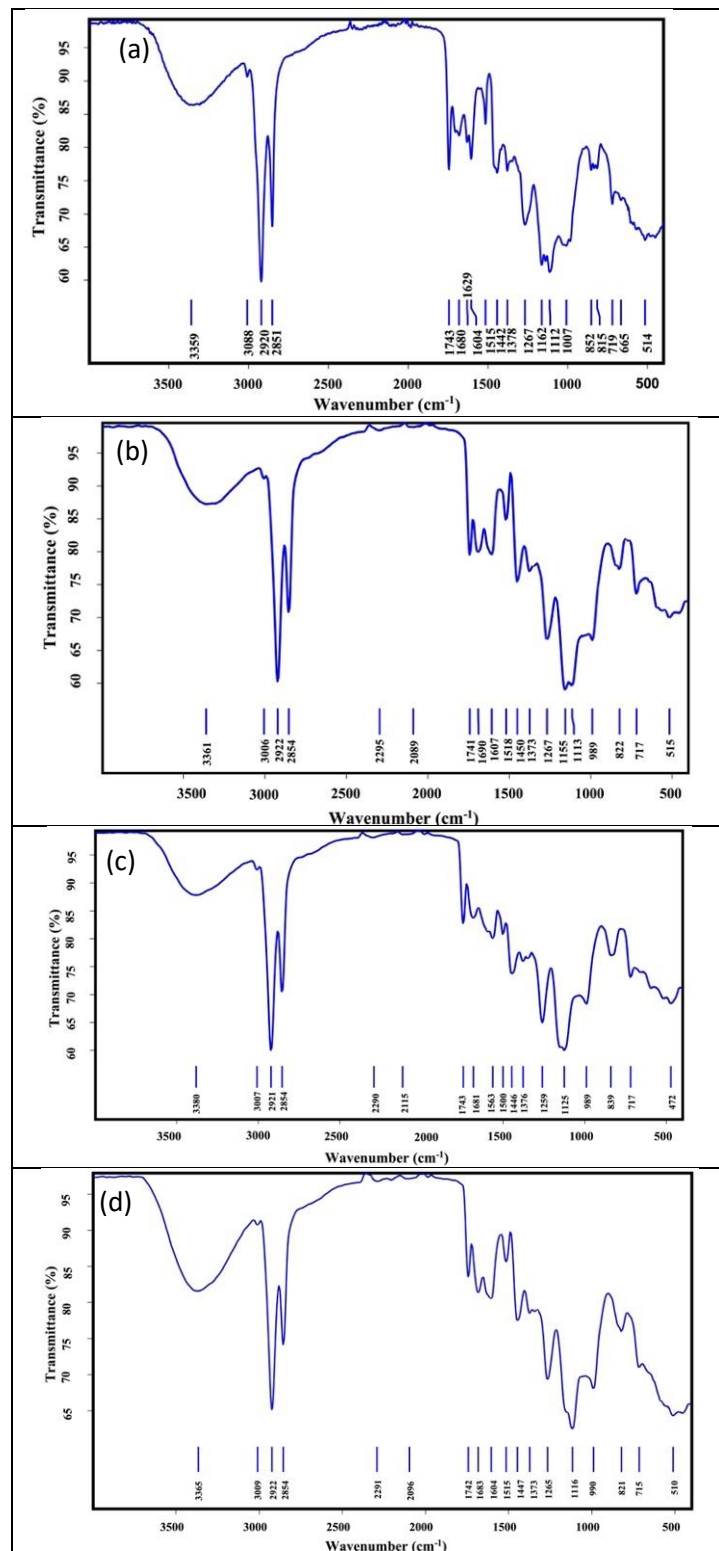


Figure 2. (a) FT-IR spectra of pristine *C. libani* pollens, (b) the pollens treated with a hydrochloric acid solution, (c) the pollens treated with a sodium hydroxide solution following the acid treatment, and (d) the pollens undergone the acid, the base, and the chloroform/methanol/water treatments (the exine microcapsules, the final product)

3.1.2. Thermal gravimetric analysis

Thermal gravimetric analysis (TGA) was used to evaluate the thermal stability of both pollen and isolated exine capsules. The untreated pollen retained its mass up to around 250°C, after which mass loss occurred and continued until approximately 450°C. When treated with acid during exine isolation, the mass loss of the pollen began after 300°C. This suggests that pure pollen contains organic structures that can decompose at low temperatures, and the acid treatment removes these structures. After treatment with base and chloroform/methanol/water, mass loss began at higher temperatures due to the loss of an organic compound (Figure 3). Numerous studies have reported that exine microcapsules show higher thermal stability than the pollen from which they are extracted [7, 20]. Studies indicate that sporopollenin is the primary component of the exine structure. Sporopollenin is a highly stable polymer that is resistant to thermal, mechanical, chemical, and biological effects [9, 21].

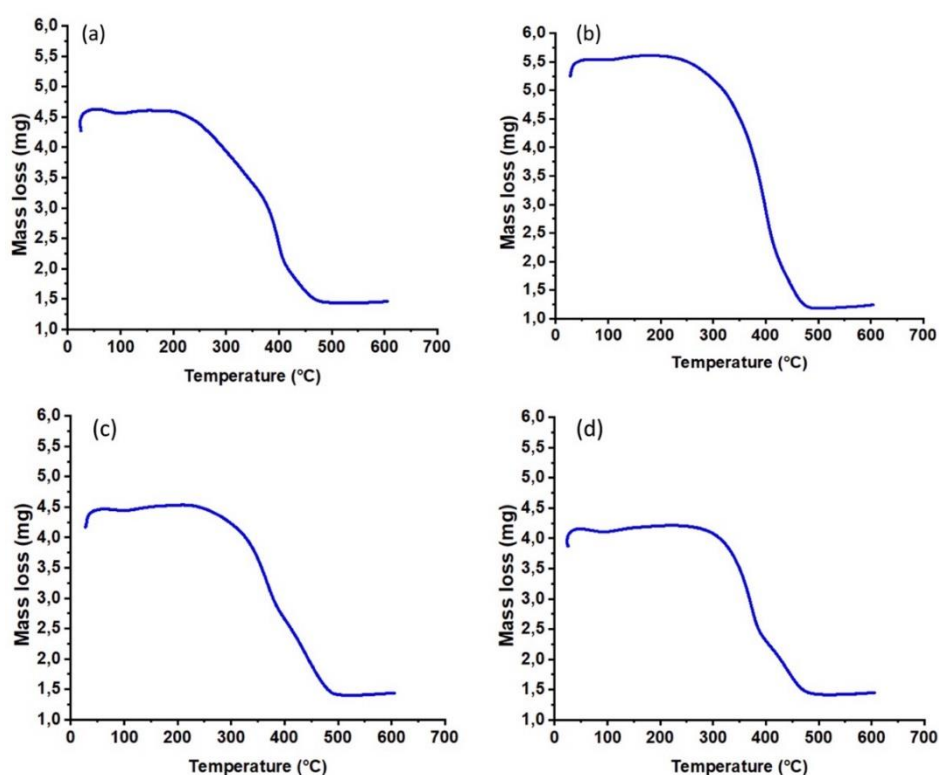


Figure 3. (a) TGA profiles of pristine *C. libani* pollens, (b) the pollens treated with a hydrochloric acid solution, (c) the pollens treated with a sodium hydroxide solution following the acid treatment, and (d) the pollens undergone the acid, the base, and the chloroform/methanol/water treatments (the exine microcapsules, the final product)

3.1.3. Analysis of the SEM images of the exine microcapsules

Pollens from *C. libani* were observed under a scanning electron microscope (SEM), along with the extracted exine structures (Figures 4 a–d). The aim was to examine the effect of a chemical extraction process on the pollen's morphological properties. To begin with, the pollen was treated with acid under microwave irradiation. This caused the removal of minerals and the formation of protrusions on the pollen's surface (Figure 4 b). Next, an alkaline treatment was applied, resulting in an increase in the number of protrusions on the pollen (Figure 4 c). This demonstrated that the alkaline treatment effectively removed protein-like structures within the pollen structure. Finally, a mixture of methanol, chloroform, and water was used to remove pigments and oily molecules from the completely empty

structure of the pollen (Figure 4 d).

Exine microcapsules were extracted from *C. libani* pollens using a modified version of chemical processes reported in the literature. The microcapsules were then emptied, and their structural integrity was preserved, so they could be loaded with vitamins for the study [7, 20]. It is noteworthy that no external heat source was utilised in the procedures outlined in the study. Rather, the experiment was conducted in a microwave oven at an energy level of 400W, with exposure to microwave radiation for a duration of 3 minutes. The study revealed that microwave radiation could significantly reduce the length of the extraction procedures, as opposed to the lengthy processes documented in previous literature.

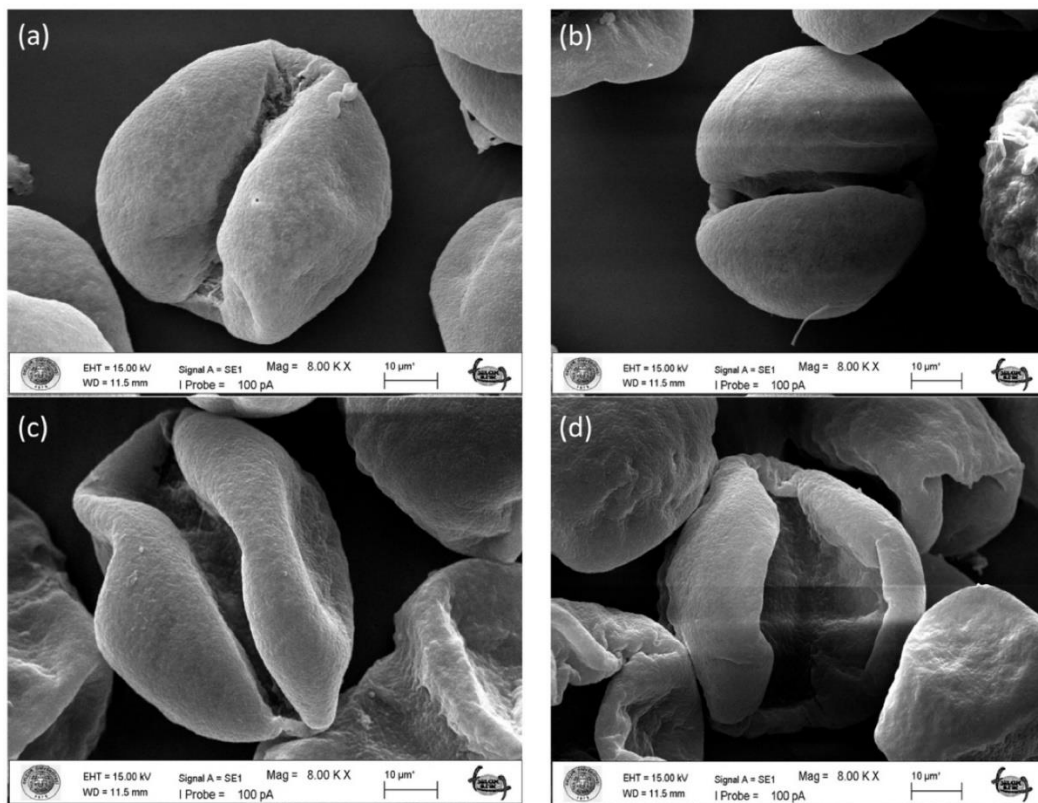


Figure 4. (a) SEM images of pristine *C. libani* pollens, (b) the pollens treated with a hydrochloric acid solution, (c) the pollens treated with a sodium hydroxide solution following the acid treatment, and (d) the pollens undergone the acid, the base, and the chloroform/methanol/water treatments (the exine microcapsules, the final product)

3.1.4. Analysis of the SEM-EDX profiles of vitamin D-exine-alginate-chitosan microcapsule system

The surface chemical compositions of microcapsules containing vitamin D, exine, chitosan, and alginate were analysed using SEM-EDX (Figure 5). The analysis revealed that microcapsules coated only with alginate (vitamin D-exine-alginate microcapsule) contained O, Ca, Cl, C, and Na. They had a higher mass of O, as presented in Tables 1 and 3. Na content was from alginate since the sodium salt of alginate was used in the study. The Ca and Cl contents were from the calcium chloride solution that was used to form alginate gel beads. After being coated with chitosan, the microcapsules (vitamin D-exine-chitosan-alginate microcapsule) contained N. Since sporopollenin, the material that forms the exine microcapsules doesn't contain N but C and O [22], the presence of N detected is due to chitosan, as presented in Tables 2 and 4. The SEM-EDX analysis results demonstrate that exine-alginate microcapsules with vitamin D₂ or D₃ are coated with chitosan.

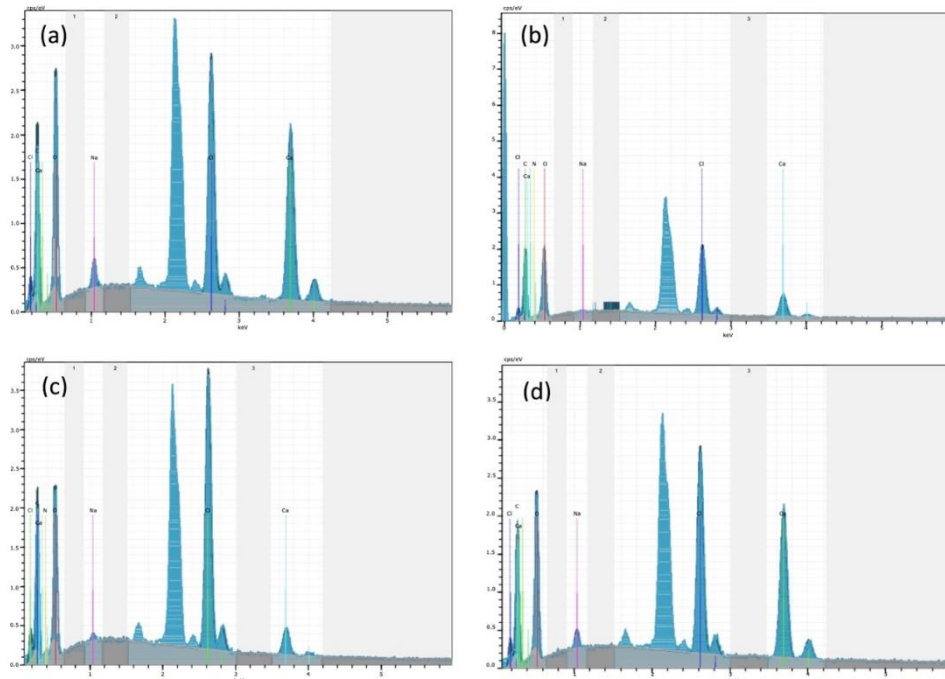


Figure 5. SEM-EDX profiles of vitamin D₂/D₃-exine-alginate-chitosan microcapsule system. (a) D₂-exine-alginate microcapsules, (b) D₂-exine-alginate-chitosan microcapsules, (c) D₃-exine-alginate microcapsules, (d) D₃-exine-alginate-chitosan microcapsules

Table 1. SEM-EDX results of D₂-exine-alginate microcapsules

Element	Mass [%]	Atomic [%]	Error [%]
Oxygen	65.92	65.41	21.3
Calcium	6.39	2.53	0.2
Chlorine	4.83	2.16	0.2
Carbon	22.37	29.56	7.9
Sodium	0.49	0.34	0.1

Table 2. SEM-EDX results of D₂-exine-alginate-chitosan microcapsules

Element	Mass [%]	Atomic [%]	Error [%]
Oxygen	65.77	62.16	21.2
Calcium	2.01	0.76	0.1
Chlorine	3.61	1.54	0.1
Carbon	26.07	32.83	9.0
Sodium	0.06	0.04	0.0
Nitrogen	2.47	2.67	1.8

Table 3. SEM-EDX results of D₃-exine-alginate microcapsules

Element	Mass [%]	Atomic [%]	Error [%]
Oxygen	65.28	64.48	21.3
Calcium	5.98	2.36	0.2
Chlorine	5.07	2.26	0.2
Carbon	23.28	30.63	8.4
Sodium	0.39	0.27	0.1

Table 4. SEM-EDX results of D₃-exine-alginate-chitosan microcapsules

Element	Mass [%]	Atomic [%]	Error [%]
Oxygen	63.80	60.82	20.6
Calcium	1.10	0.42	0.1
Chlorine	6.12	2.63	0.2
Carbon	25.56	32.46	8.9
Sodium	0.13	0.09	0.0
Nitrogen	3.29	3.58	2.2

3.2. Loading of Vitamin D Molecules into The Exine-Alginate-Chitosan Microcapsule System

The loading efficiencies of vitamin D₂ and D₃ into exine microcapsules were calculated based on mass measurements. The average weight of vitamin D₂-loaded exine microcapsules was 131.5 mg, while that of vitamin D₃ was 116.0 mg. It was concluded that 40.0 mg of vitamins D₂ and D₃ were initially loaded into 100 mg of microcapsules, resulting in loading efficiencies of 31.5 mg and 16.0 mg, respectively.

The process involved loading vitamins into the microcapsules of the exine, which were then coated with alginate. The surface of the microcapsules was analysed under a scanning electron microscope (SEM) at 100x, 350x, and 1000x dimensions (Figure 6). The study revealed that the exine particles loaded with vitamin D₂ and D₃ were embedded in the alginate matrix, and the exine capsules showed a non-uniform distribution on the microspheres. Additionally, the exine-alginate microcapsules were almost spherical in shape, and their dimensions were similar to each other. The dimensions of the D₂-exine-alginate spheres and D₃-exine-alginate spheres were approximately 1.3 μ m (Figures 6 b–e).

Further analysis revealed the presence of cracks on the surfaces of the microcapsules at high magnifications (Figures 6 c–f). It was determined that the cracks were formed during the drying phase. As a result, the release properties of the microcapsules may not be predictable when D₂ or D₃-loaded exine microcapsules are used only with an alginate matrix, limiting their use as a vitamin supplement.

In the study, alginate microcapsules were prepared to contain vitamin D supplements. These microcapsules were then coated with chitosan, as shown in Figure 7. The chitosan-coated microcapsules were spherical in shape, with similar sizes and a thin chitosan layer. The microcapsules' size was approximately 1.3 μ m, which did not change much after the coating process. During the drying phase, excess chitosan leaked from the microcapsules spread on the ground and dried there, as shown in Figures 7 b and e. The chitosan coating effectively closed the cracks on the microcapsules' surface, as shown in Figures 7 c and f. However, the vitamin D-loaded exine microcapsules on the surface were still visible even after the chitosan coating.

3.3. Vitamin D Release Profiles of The Exine-Alginate-Chitosan Microcapsule System

The release of vitamins D₂ and D₃ from microcapsules was studied over a period of time (30, 60, 120, and 240 min.) at 37°C. Table 5 presents the time-dependent release percentages calculated from the absorbance values. The results showed that the longer the duration of both vitamins, the higher the release rate.

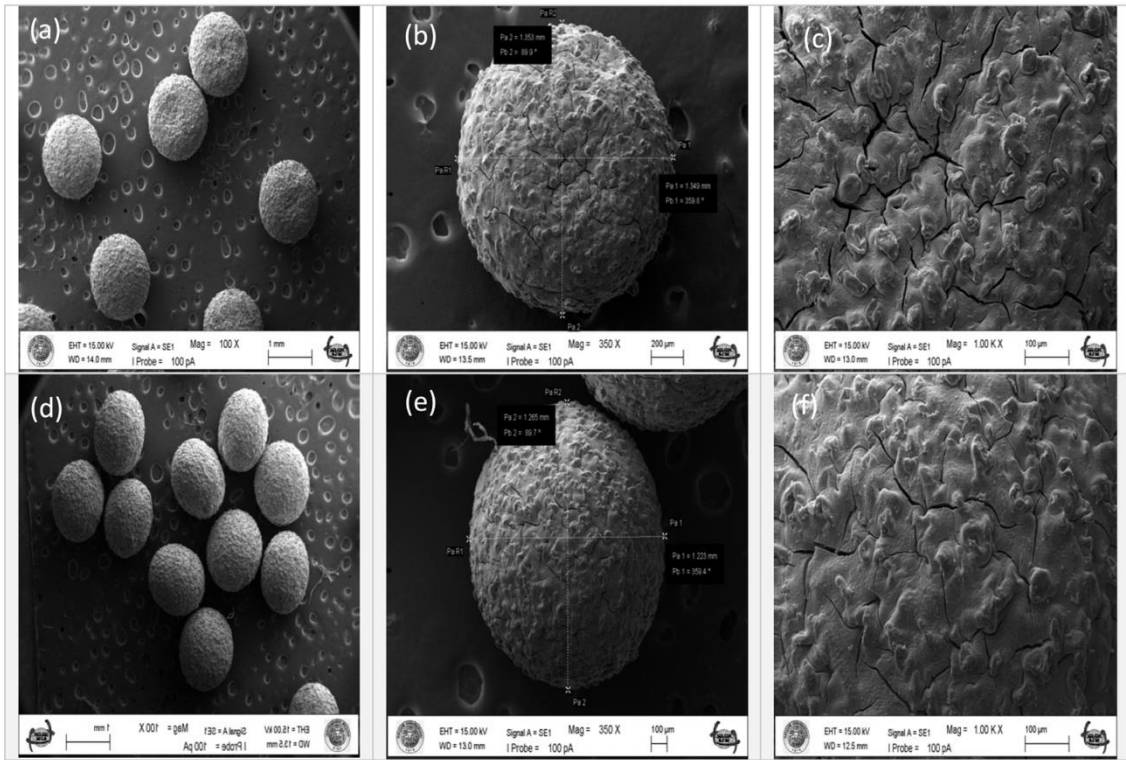


Figure 6. SEM images of the vitamin D-exine-alginate microcapsule system; (a-c): D₂ and (d-e): D₃

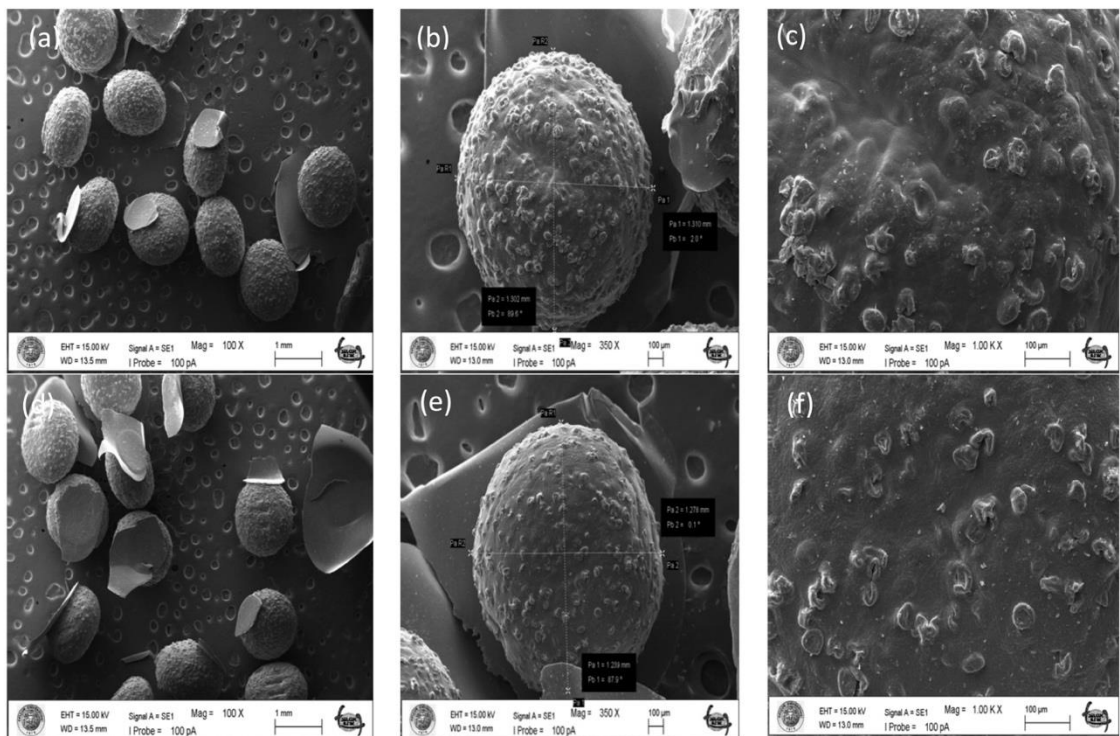


Figure 7. SEM images of the vitamin D-exine-alginate-chitosan microcapsule system; (a-c): D₂ and (d-e): D₃

Table 5. Time-dependent D₂ and D₃ release rates of the exine-alginate-chitosan microcapsule system

Time [min.]	D ₂ release [%]	D ₃ release [%]
30	2.6	1.8
60	3.1	2.3
120	4.3	4.4
240	4.9	5.0

The study examined the release of vitamins at different temperatures (4, 20, and 37°C) over a period of 120 minutes (Table 6). The results indicated that the highest release occurred at 37°C for both vitamins.

During the study, D₂ and D₃ vitamins were loaded into exine microcapsules, which were then distributed and encapsulated in an alginate matrix. The surface of the microcapsules was coated with chitosan, a biopolymer that dissolves easily in aqueous media, especially at low pH. However, since the release studies were conducted in alcohol, the chitosan coating and alginate matrix remained undissolved, preventing the solvent from reaching the microcapsules and releasing the vitamins. As a result, low release rates were observed for both vitamins. In a previous study, it was found that the release rate of vitamin D₂ from chitosan/ethylcellulose complex microcapsules was influenced by the chitosan coating layer, which caused a delay in its release [15]. The resistance of drug diffusion increased with an increase in the coating layer. The release of microcapsules in artificial gastric juice was very limited, indicating that the coating of vitamin D₂ could effectively delay drug release in gastric juice.

Table 6. Temperature-dependent D₂ and D₃ release rates of the exine-alginate-chitosan microcapsule system (in 120 min.)

Temperature [°C]	D ₂ release [%]	D ₃ release [%]
4	3.2	0.8
20	4.0	0.9
37	4.3	4.4

4. CONCLUSIONS

Herein the presented study demonstrated that it is possible to obtain sporopollenin exine microcapsules from *C. libani* pollens through a chemical process that involves the use of a microwave. This method is significantly faster and more energy efficient than traditional methods that use external heat sources. The structural integrity of the exine microcapsules remains intact even after undergoing microwave treatment. In this study, vitamins D₂ and D₃ were successfully loaded into the exine microcapsules using an ethanol medium. Alginate was found to be a suitable matrix for encapsulating the loaded exine microcapsules, and chitosan was used to coat them, thus increasing their structural stability. The study also revealed that the release of vitamins D₂ or D₃ from the exine-alginate-chitosan microcapsule system was dependent on both temperature and time. Further studies are required to evaluate the performance of vitamin D₂ or D₃-the exine microcapsule-alginate-chitosan microcapsule system in *in vitro* and *in vivo* studies.

Declaration of Ethical Standards

No ethical committee approval was required for the materials and methods used in the study.

Credit Authorship Contribution Statement

GD: Benchwork, experimental design, and data collection. IS: Conceptualization, study design, analysis and interpretation of data, manuscript writing, funding acquisition, and work supervision.

Declaration of Competing Interest

The authors state no financial or personal conflicts of interest.

Funding / Acknowledgements

The study was funded by the Selcuk University Research Foundation, Konya, Turkey (BAP-23201018).

Data Availability

Data will be made available on request.

REFERENCES

- [1] E. Erbay, S. Mersin, and Ö. İbrahimoglu, "D Vitamini ve vücut sistemleri üzerine etkisi," *Sağlık Akademisyenleri Dergisi*, vol. 6, no. 3, pp. 201-206, 2019.
- [2] E. Avşar and D. L. Şahiner, "D Vitamini? ne Genel Bir Bakış," *Akdeniz Tıp Dergisi*, vol. 6, no. 2, pp. 168-174, 2020.
- [3] M. B. Y. Çimen and Ö. B. Çimen, "Obezite ve D vitamini," *Mersin Üniversitesi Sağlık Bilimleri Dergisi*, vol. 9, no. 2, pp. 102-112, 2016.
- [4] Y. Doğan, "D vitaminin Kognisyon, Fiziksel Fonksiyon ve Ultrasonografik Cilt, Cilt Altı Yağ Dokusu ve Kas Ölçümleri Üzerine Etkilerinin Değerlendirilmesi," 2021.
- [5] Z. Tarakçı and M. Dervişoğlu, "Vitamin D, Beslenmede Önemi ve Gıdalarda Zenginleştirilmesi," *Türkiye*, vol. 9, pp. 24-26, 2009.
- [6] C. Bilbao-Sainz *et al.*, "Vitamin D-fortified chitosan films from mushroom waste," *Carbohydrate polymers*, vol. 167, pp. 97-104, 2017.
- [7] M. Mujtaba, I. Sargin, L. Akyuz, T. Ceter, and M. Kaya, "Newly isolated sporopollenin microcages from *Platanus orientalis* pollens as a vehicle for controlled drug delivery," *Materials Science and Engineering: C*, vol. 77, pp. 263-270, 2017/08/01/ 2017, doi: <https://doi.org/10.1016/j.msec.2017.02.176>.
- [8] T. Baran, I. Sargin, M. Kaya, A. Menteş, and T. Ceter, "Design and application of sporopollenin microcapsule supported palladium catalyst: Remarkably high turnover frequency and reusability in catalysis of biaryls," *Journal of Colloid and Interface Science*, vol. 486, pp. 194-203, 2017/01/15/ 2017, doi: <https://doi.org/10.1016/j.jcis.2016.09.071>.
- [9] F.-S. Li, P. Phyo, J. Jacobowitz, M. Hong, and J.-K. Weng, "The molecular structure of plant sporopollenin," *Nature plants*, vol. 5, no. 1, pp. 41-46, 2019.
- [10] İ. Gökbulut and F. S. Öztürk, "Gıda mikrokapsülasyonunda aljinat kullanımı," *Batman Üniversitesi Yaşam Bilimleri Dergisi*, vol. 8, no. 1/2, pp. 16-28, 2018.
- [11] B. Demir and A. Demirdöven, "Aljinat ve Meyve-Sebze Ürünlerindeki Uygulamaları," *Journal of New Results in Engineering and Natural Sciences*, no. 9, pp. 20-34, 2019.
- [12] K. Y. Lee and D. J. Mooney, "Alginate: Properties and biomedical applications," *Progress in Polymer Science*, vol. 37, no. 1, pp. 106-126, 2012/01/01/ 2012, doi: <https://doi.org/10.1016/j.progpolymsci.2011.06.003>.
- [13] N. K. Kuzgun and A. G. İnanlı, "Kitosan üretimi ve özellikleri ile kitosanın kullanım alanları," *Türk Bilimsel Derlemeler Dergisi*, no. 2, pp. 16-21, 2013.
- [14] Z. Yıldırım, N. Öncül, and M. Yıldırım, "Kitosan ve antimikrobiyal özellikleri," *Niğde Ömer Halisdemir Üniversitesi Mühendislik Bilimleri Dergisi*, vol. 5, no. 1, pp. 19-36, 2015.
- [15] X.-Y. Shi and T.-W. Tan, "Preparation of chitosan/ethylcellulose complex microcapsule and its application in controlled release of Vitamin D2," *Biomaterials*, vol. 23, no. 23, pp. 4469-4473, 2002.

- [16] W. Li *et al.*, "Amphiphilic chitosan derivative-based core-shell micelles: Synthesis, characterisation and properties for sustained release of Vitamin D3," *Food chemistry*, vol. 152, pp. 307-315, 2014.
- [17] N. Jannasari, M. Fathi, S. J. Moshtaghian, and A. Abbaspourrad, "Microencapsulation of vitamin D using gelatin and cress seed mucilage: Production, characterization and in vivo study," *International journal of biological macromolecules*, vol. 129, pp. 972-979, 2019.
- [18] L. Akyuz, I. Sargin, M. Kaya, T. Ceter, and I. Akata, "A new pollen-derived microcarrier for pantoprazole delivery," *Materials Science and Engineering: C*, vol. 71, pp. 937-942, 2017.
- [19] M. Mujtaba *et al.*, "Newly isolated sporopollenin microcages from Cedrus libani and Pinus nigra as carrier for Oxaliplatin; xCELLigence RTCA-based release assay," *Polymer Bulletin*, pp. 1-22, 2022.
- [20] I. Sargin *et al.*, "Controlled release and anti-proliferative effect of imatinib mesylate loaded sporopollenin microcapsules extracted from pollens of Betula pendula," *International Journal of Biological Macromolecules*, vol. 105, pp. 749-756, 2017/12/01/ 2017, doi: <https://doi.org/10.1016/j.ijbiomac.2017.07.093>.
- [21] F. E. Atalay, A. A. Culum, H. Kaya, G. Gokturk, and E. Yigit, "Different plant sporopollenin exine capsules and their multifunctional usage," *ACS Applied Bio Materials*, vol. 5, no. 3, pp. 1348-1360, 2022.
- [22] E. Grienberger and T. D. Quilichini, "The toughest material in the plant kingdom: an update on sporopollenin," *Frontiers in Plant Science*, vol. 12, p. 703864, 2021.



ESTIMATING THE HARDNESS AND ABRASION PROPERTIES OF IGNEOUS ROCKS FROM CERCHAR INDENTATION DEPTH (CID)

*Ahmet TEYMEN 

Niğde Ömer Halisdemir University, Engineering Faculty, Mining Engineering Department, Niğde, TÜRKİYE
ateymen@ohu.edu.tr

Highlights

- A new experimental data was obtained by calculating the average depth of the scratch that emerged in the CAI test.
- The CID parameter is directly related to the hardness and abrasiveness of the rocks.
- The strongest statistical relationships with the CID parameter belong to Bohme Abrasion Resistance.
- Carefully prepared core samples are needed to measure the CID parameter.



ESTIMATING THE HARDNESS AND ABRASION PROPERTIES OF IGNEOUS ROCKS FROM CERCHAR INDENTATION DEPTH (CID)

*Ahmet TEYMEN

Niğde Ömer Halisdemir University, Engineering Faculty, Mining Engineering Department, Niğde, TÜRKİYE
ateymen@ohu.edu.tr

(Received: 10.08.2023; Accepted in Revised Form: 06.02.2024)

ABSTRACT: The most known and applied method for determining the abrasivity of rocks is the Cerchar Abrasivity Index (CAI). Properties of rocks such as abrasive mineral content, density, strength, and degree of cementation are the main factors affecting abrasivity, and these parameters likewise control their hardness properties. In this study, the average scratch depth formed on the rock surface after the CAI test was determined and it was investigated whether this calculated new parameter had the properties to represent the rock. Measurements were taken from four points along the scratch line formed on the surface with the help of a comparator and the average value was defined as the Cerchar Indentation Depth (CID). Measurements have shown that igneous rocks have CID values in the range of 0.01 mm-0.68 mm. Apart from the CID parameter, nine different properties (hardness, abrasivity, and physical) of fifty igneous rocks were tested. Statistically significant results were obtained by establishing relationships between CID and other rock mechanics tests. In CAI tests, it has been shown that CID measurements can be determined very sensitively if well-leveled core samples with parallel lower and upper surfaces are used. It has been determined that the CID value is directly related to the investigated rock properties and can be used as very useful experimental data in estimation studies.

Keywords: *Cerchar indentation depth, Cerchar abrasivity index, Abrasion, Hardness, Regression*

1. INTRODUCTION

In mining works, excavation is carried out either by the drilling-blasting method or by mechanized methods. All tools used in mining are subject to abrasion because they interact with the rock. In the meantime, deformation and fragmentation occur in the rock. Especially in mining operations, increased tunnel advancement rates or increased production rates require more rock abrasion information. By predicting rock abrasivity according to changing geology and rock type, project budgets can be controlled by preventing unexpected tool abrasion. Rock abrasion can be defined as the detachment of particles from the material surface, while tool abrasion can be defined as the loss of tool material interacting with the rock. The CAI is an index determination method for the abrasivity of rock and is frequently used in academic research as well as industry. The CAI test method is highly preferred due to its fast and simple applicability and the use of a small number of rock samples.

Hardness is defined as a rock's resistance to an object impacting or submerging on a rock's surface. Rock hardness is a function of the hard mineral composition and the strength and bonding capacity of the matrix material. Applications, where hardness is important, are engineering studies where rock-metal interaction is intense. Mining operations such as ripping, drilling, crushing, transportation, grinding, and excavation can be shown among these engineering applications. The most widely used rock hardness methods are Schmidt hammer hardness (SHH) and Shore scleroscope hardness (SSH) due to the advantage of being applicable in the field. Hardness methods such as Brinell hardness (HB) and Vickers hardness (HV) are designed for metal. It requires special tools with certain characteristics and their use in rock engineering applications is limited. Among these methods, the Indentation hardness index (IHI) is the newest proposed method for determining rock hardness. Determining the hardness and excavability of rocks can be defined as the main objectives of the CAI test. At the Montreal meeting of the International Society of Rock Mechanics, it was suggested that the CAI test be used as a

*Corresponding Author: Ahmet TEYMEN, ateymen@ohu.edu.tr

standard rock mechanics test on the cuttability, drillability, and excavability of rocks [1]. The American Society for Testing and Materials has published a standard for CAI testing [2]. Many aspects of the original design and modified CAI have been studied by various researchers.

Using in-situ measurements, Johnson and Fowell [3] showed that the cutter consumption of excavators is directly related to the CAI values of the rocks. Çopur and Eskikaya [4] determined some physical and mechanical properties of marls in the TKİ Eynez region and made a classification in the direction of workability with the mechanized method. Al-Ameen and Waller [5] investigated the relationship between rock strength and CAI. The authors determined that some high-strength rocks with low abrasive mineral content may have a high abrasivity index, while some low-strength rocks with high abrasive mineral content may have a low abrasivity index. Plinninger et al. [6] determined correlations between CAI and Modulus of Elasticity (E), equivalent quartz content.

Yaralı and Akçın [7] determined the hardness of the rocks with the help of a modified experimental setup and drill bits with two different tip angles and revealed the relationships between the drill bit angle and CAI. Tercan and Ozcelik [8] investigated the relationships between the mechanical and hardness properties of andesites and their mechanical and abrasion properties and obtained strong correlations. Mateus et al. [9] developed correlations between IHI values (248 samples) and mechanical properties of Colombian sandstones. Tumac et al. [10] calculated two different SSH values and deformation coefficient (K) for 30 different rocks. Using these values, they determined the relationship between SSH values, K, and Roadheader cutting speed for different rock types. Regression analysis results showed satisfactory correlations.

Kahraman et al. [11] focused on the predictability of E and Uniaxial compressive strength (UCS) values of Misis fault breccia from some indirect methods such as unit volume weight (UW), CAI, and P-wave velocity (Vp) using neural network analysis and regression analysis. In his study, Deliormanli [12] used simple and multiple regression methods to determine the strength values of rocks such as UCS, direct shear strength (DSS), and abrasion properties such as BSA, Wide-Wheel Abrasion (WWA) with the help of CAI. The first chart they created according to the results of the study shows the relationship between CAI-UCS-DSS, while the second chart shows the relationship between CAI-BSA-WWA.

Dipova [13] investigated the relationships between CAI data and strength properties of weak limestones by testing rock samples from the inner city tunnel of Austin (Texas, USA). Considering the abrasion of rock and steel together, wear on the steel and indentation on the rock that occurred at the same time were measured and tried to be correlated. As a result of statistical studies, the researcher determined that there is a relationship between CAI and UCS and Brazilian tensile strength (BTS) values, and also between CAI and CID and between CID and UCS and BTS values.

Boutrid et al. [14] showed that there are significant correlations between HB and the strength properties of rocks, according to the results of the Hassi Messaoud field study. Yaralı [15] conducted Point load index (Is), CAI, SSH, UCS, and BTS experiments on 29 coal-surrounding rocks, all of which are sandstones. Then, CAI evaluated the strength and index test results with regression analysis methods. Teymen [16] conducted a statistical study to estimate difficult and time-consuming bedrock mechanics tests with CAI. Apart from the parameters that are frequently researched in the literature, the relationships between parameters such as BSA, rate of penetration (ROP), block punch index (BPI), fracture toughness (K_{IC}), and CAI have been investigated in detail.

In this study, new experimental data was obtained by measuring the depth of the scratch formed on the surface of the rocks in the CAI test. Depth measurements were made at four points along the one-centimeter scratch line using a comparator. The mean value is defined as the CID. Abrasivity and hardness tests were applied to fifty igneous rocks and the relationships between these parameters and CID were investigated. Statistically significant results were obtained with the CID parameter. In addition to simple regression analyses (SRA), nonlinear multiple regression analyses (NMRA) were performed by including the physical properties of rocks such as unit volume weight (UW) and porosity (Pg) into the models. Performance indices were used to measure the estimation capacity of the equations produced by regression analysis and to determine their reliability.

As it is known, the CAI test is a practical abrasivity test method that can be applied in the field and is designed to be measured on rough rock surfaces. This study was carried out to estimate some properties of many igneous rocks under standard conditions. In such prediction studies, it is of great importance to test the rocks under the same conditions. Core samples with regular geometry were used to determine the CAI values of the rocks under the same conditions. It has been determined that accurate measurements can be made on the surfaces of the cores cut with a rough cutting machine, provided that no polishing is done. The fact that the test samples used had a shaped geometry allowed data to be obtained from the scratches formed on the rock surface after the CAI test. By measuring the average scratch depth, it was possible to obtain a new/additional data set in addition to the CAI data. The measurement method presented in this study is experimental and open to improvement/updating. While the data obtained by the CAI test is an indicator of the wear occurring in the excavation tools used in mining, the CID value represents the deformation/wear occurring in the rock in contact with the excavation tools. It is thought that the CID value can be considered as a new rock property in this respect.

2. MATERIAL AND METHODS

19 of the igneous rocks used in the study are of volcanic origin, 15 of them are of plutonic, 9 of them are pyroclastic and 7 of them are of subvolcanic origin. Laboratory experiments were carried out on block and core samples taken from fresh parts of 50 rocks. Rocks types, geological origins, and average test results are given in Table 1. The test devices used in the study are shown in Figure 1.

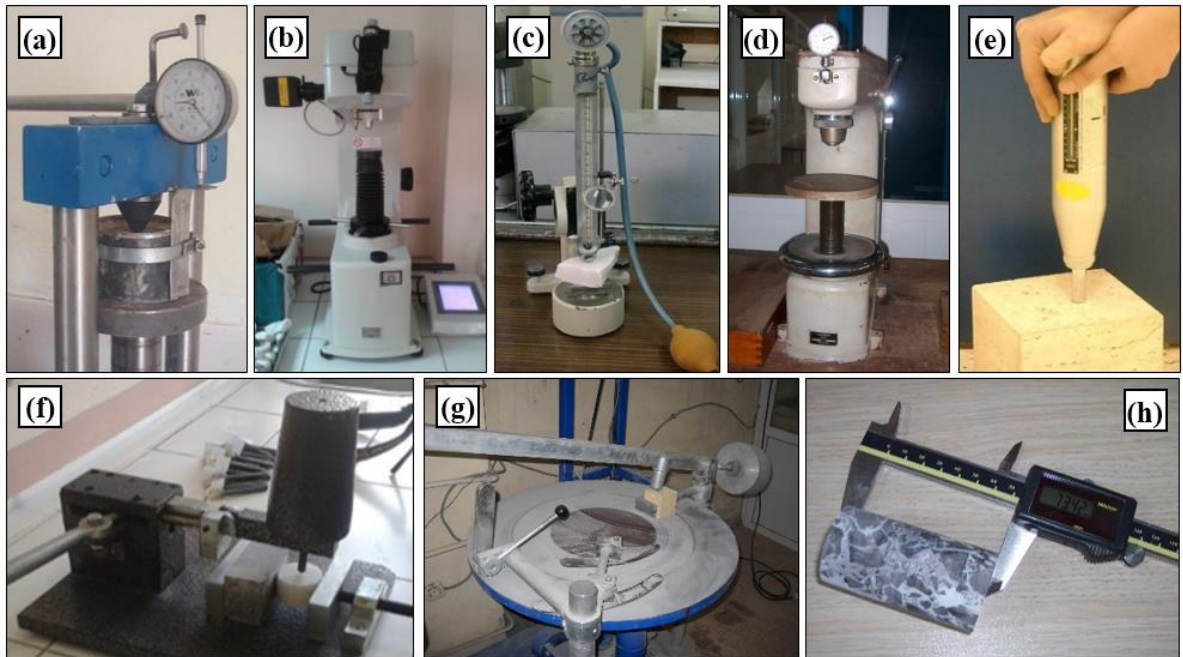


Figure 1. Test devices a) IHI, b) HV, c) SSH, d) HB, e) SHH, f) CAI, g) BSA, and h) UW-Pg

2.1. Cerchar Abrasivity Index (CAI)

The standard Cerchar test [17] instrument was used in the CAI test (Fig. 1f). The steel inserts used in the experiment had a Rockwell HRC 54-56 hardness, 2000 MPa tensile strength, and a 90° apex angle. This conical steel tip was pulled for 10 mm at a speed of 1 mm/s on the rock sample surface with a pressing force of 70 N and the size of the abrasion surface formed on the tip of the tip was measured. Abrasivity measurements were carried out on core samples with a diameter of 42-54 mm and a length of 30-50 mm. The cores were cut on a rough cutting machine and no sanding/polishing process was

specifically applied to their surfaces. If the surface to be worn is completely polished, the steel tip does not sink into the rock and slides easily along the surface. If the rock surface on which the process will be applied is completely polished, the steel tip does not sink into the rock and slides easily along the surface. This makes a reliable measurement impossible. Tip wear was detected using a high-resolution camera and a calibrated digital caliper program.

2.2. Schmidt Hammer Hardness (SHH)

An N-type Schmidt hammer was used for the SHH hardness test (Fig. 1e). Measurements were made from smooth surfaces of core rock blocks [18]. 20 hits were applied to the block surfaces and the average of the 10 highest values was calculated. A correction factor was used to correct the measured SHH values.

2.3. Shore Schlerescope Hardness (SSH)

SSH is a method of measuring the surface hardness of any rock in terms of elasticity. The test was carried out with a C-2 model device on rock samples with a surface area of approximately 14 cm² and a thickness of 2 cm [18]. The measurements were repeated 20 times with at least 5 mm intervals and the mean of the ten highest measurements was determined as the SSH value (Figure 1c).

2.4. Brinell Hardness (HB)

HB is a commonly used test method for metals but is generally not preferred for rocks due to its brittle nature. A 30 mm thick and 42 mm diameter core and a 10 mm diameter spherical steel ball were used for the experiment. By applying a load of up to 3000 kg on the steel ball, the pressure was applied to the rock surface of the ball for 30 seconds (Figure 1d). The HB value was determined by dividing the load applied to the rock by the calculated indentation surface area [19].

2.5. Vickers Hardness (HV)

The large-scale HV tester shown in Figure 1b was developed as an alternative to the HB method. For the experiment, loads varying between 1-50 kg, depending on the type of rock, were applied to the rock surface for 10-15 seconds. The trace formed on the rock surface was measured under the microscope and the average of the two diagonal values was calculated. Similar to the HB test, the ratio of the applied load to the calculated sinking area gives the HV value [20].

2.6. Indentation Hardness (IHI)

Tests were performed with a 30 kN capacity point load tester (Fig. 1a). Smooth core specimens (42 mm diameter and 30 mm thickness) placed in a steel frame with resin were used in the experiment. Penetration amounts were monitored with a manual comparator. IHI values for rocks loaded up to 20 kN were calculated by dividing the maximum load by the maximum penetration values.

2.7. Bohme Surface Abrasion (BSA)

This test is a test defined in [21] to determine the surface abrasion resistance of the rocks used as building and covering stones. After drying in the oven, the cube samples with a side length of 71 mm prepared for the experiment were measured and recorded with the help of a caliper. A pressure of 0.6 kg/cm² was created on the friction strip by applying a load of 30 kg on the sample with a steel lever. 20 abrasion periods (total 440 cycles) were applied for each sample and approximately 20 g of abrasive dust was used for each cycle. After the test, the dimensions were re-measured and the amount of abrasion

was determined volumetrically (Figure 1g).

2.8. Unit Weight (UW), Apparent Porosity (Pg)

Laboratory tests described in the ISRM [22] standard have been used to determine the physical properties of the rocks. The core samples were dried at 105°C for 24 hours, cooled to room temperature in a desiccator, and their dry weights were determined. Samples were kept in water for 24 hours and their saturation weights were determined. UW and Pg values were calculated with the help of the volumes, and saturated-dry weights of the samples whose dimensions were measured with 0.1 mm precision with the help of calipers (Figure 1h).

2.9. Cerchar Indentation Depth (CID)

The CAI test, the details of which are given in Section 2.1, was applied to the disc-shaped specimens prepared by cutting the cores in a rough stone-cutting machine. The samples used in the CAI experiment and with 1 cm long scratches on them were taken to the measurement setup shown in Figure 2 for CID measurements. The setup is formed by mounting a needle thick enough to penetrate the scratches formed on the rock surface to the tip of a comparator with 100 times magnification. The device to which the comparator is connected was measured and fixed in contact with the rock surface at an angle of 90 degrees. The average of the depth measurements taken from four points along the one cm-long scratch line on the rock surface with the help of a comparator is called the CID. The details and constraints to be considered to make these measurements can be summarized as follows.

The test can be applied to core or prismatic specimens. For the measurements to be carried out reliably and precisely, samples with their lower and upper surfaces cut parallel to each other must be prepared. Cores should be cut with a rough cutting machine at a very low speed. Samples with saw marks on the surface after cutting or with roughness at a level that would affect measurements should not be used in the test. The measured surfaces of core samples without polishing reflect the structure and texture of the rock. As it is known, all rocks contain pores, although they vary depending on their formation mechanism. The steel tip used during the CAI test, with the help of the weight, sinks into these pores to a certain extent, allowing the test to be carried out healthily.

A precise measurement will be made by determining the level difference between the point where the measurement is made within the scratch and the flat area at the edge of this point (as close as possible). Average sample thickness should not be used in calculations. Possible errors will be avoided by making the measurements as described. It should be noted that all rocks were cut using the same cutting machine and the experiments were carried out under the same conditions. The CID value, which is the subject of this study, is not an absolute rock property but is proposed as a new parameter that will enable us to compare different rocks relatively. Therefore, negligible measurement errors resulting from possible roughness on the rock surface will be valid for all rocks compared.

Table 1. Tested rocks and average test results.

No	Rock Type	Rock Class	CID mm	CAI *	BSA cm ³ /50cm ²	SSH rebound	SHH rebound	HB kg/mm ²	HV kg/mm ²	IHI kN/mm	UW g/cm ³	Pg %
1	Andesite-1-	Volcanic	0.142	2.75	22.11	77.25	53.40	101.27	127.30	20.01	2.35	6.50
2	Andesite-2-	Volcanic	0.038	3.20	16.98	72.00	52.92	384.68	237.30	21.60	2.64	0.33
3	Andesite-3-	Volcanic	0.045	2.79	16.86	71.50	54.12	203.00	136.20	18.12	2.60	2.60
4	Andesite-4-	Volcanic	0.242	2.32	28.00	53.67	42.30	8.12	59.78	7.89	2.15	10.58
5	Aplite	Subvolcanic	0.017	4.23	7.86	88.80	58.23	450.96	415.40	22.99	2.63	0.30
6	Basalt-1-	Volcanic	0.055	3.09	12.03	65.75	59.28	108.49	131.50	14.08	2.69	4.22
7	Basalt-2-	Volcanic	0.045	4.10	9.28	74.80	57.28	269.86	134.30	26.65	2.56	1.58
8	Basalt-3-	Volcanic	0.024	4.38	13.53	84.60	53.82	304.35	231.20	22.85	2.71	0.60
9	Basalt-4-	Volcanic	0.042	3.75	13.50	72.00	57.45	194.40	128.45	23.24	2.64	2.29
10	Basalt-5-	Volcanic	0.151	3.30	18.02	67.20	50.31	245.36	125.40	19.81	2.62	2.42
11	Basalt-6-	Volcanic	0.051	3.14	11.25	65.30	52.47	115.89	109.45	18.67	2.69	2.48
12	Basalt-7-	Volcanic	0.156	2.45	18.09	64.86	42.15	72.70	70.45	10.84	2.61	1.82
13	Basalt-8-	Volcanic	0.180	2.80	22.75	65.33	46.12	99.29	33.40	14.39	2.51	3.97
14	Dacite-1-	Volcanic	0.226	2.45	26.07	62.20	40.80	40.96	72.23	14.29	2.26	12.74
15	Dacite-2-	Volcanic	0.083	3.24	33.85	68.75	44.00	115.70	106.74	15.81	2.42	6.80
16	Dacite-3-	Volcanic	0.105	3.05	24.09	62.67	44.12	116.76	66.47	15.99	2.27	9.40
17	Diabase-1-	Subvolcanic	0.087	4.12	17.23	71.60	56.80	351.08	161.50	19.15	2.81	0.70
18	Diabase-2-	Subvolcanic	0.030	4.13	8.86	87.33	60.12	446.54	463.00	22.73	2.83	0.71
19	Diabase-3-	Subvolcanic	0.135	2.95	15.60	63.00	45.26	115.89	78.36	12.15	2.54	2.71
20	Diabase-4-	Subvolcanic	0.112	3.25	16.30	68.00	55.12	108.49	132.26	17.12	2.54	3.13
21	Diorite-1-	Plutonic	0.021	3.29	12.96	82.60	53.71	170.34	181.70	18.08	2.62	0.45
22	Diorite-2-	Plutonic	0.039	2.90	21.68	75.75	52.20	152.66	136.70	10.98	2.67	0.60
23	Dunite-1-	Plutonic	0.117	2.57	29.30	59.67	51.20	140.25	69.50	15.12	2.53	1.83
24	Dunite-2-	Plutonic	0.136	2.38	28.60	58.50	46.00	103.32	100.46	13.43	2.57	0.95
25	Gabbro-1-	Plutonic	0.030	3.32	10.84	88.40	52.20	360.18	250.20	17.47	2.84	1.18
26	Gabbro-2-	Plutonic	0.025	4.14	11.43	85.10	54.00	257.99	282.35	19.76	2.88	0.21
27	Gabbro-3-	Plutonic	0.019	4.49	13.13	85.50	60.24	317.30	390.00	22.19	2.96	0.73
28	Gabbro-4-	Plutonic	0.091	2.96	20.28	77.50	51.59	321.14	157.90	23.54	2.69	1.27
29	Granite-1-	Plutonic	0.056	3.88	11.29	72.75	56.00	196.06	135.60	26.94	2.71	0.86
30	Granite-2-	Plutonic	0.017	3.91	12.98	96.00	50.96	243.32	150.50	21.98	2.58	1.21
31	Granite-3-	Plutonic	0.058	3.62	10.29	92.00	54.15	175.03	152.80	16.95	2.59	0.99
32	Granite-4-	Plutonic	0.031	3.77	16.80	88.20	52.00	254.45	122.00	18.40	2.57	0.91
33	Granite-5-	Plutonic	0.030	4.18	12.50	91.00	60.40	255.52	119.60	19.92	2.59	0.49
34	Granodiorite	Plutonic	0.021	3.44	8.50	75.20	61.78	241.15	160.45	15.87	2.61	1.12
35	Ignimbrite-1-	Pyroclastic	0.680	0.75	139.13	9.17	16.85	1.89	7.45	1.08	1.34	37.48
36	Ignimbrite-2-	Pyroclastic	0.634	0.68	130.00	15.89	22.82	2.22	11.12	1.15	1.52	31.65
37	Ignimbrite-3-	Pyroclastic	0.413	0.97	113.13	15.13	17.78	2.69	9.45	1.21	1.50	30.26
38	Microdiorite-1-	Subvolcanic	0.014	4.86	5.00	85.12	57.33	614.25	511.10	21.14	2.85	0.27
39	Microdiorite-2-	Subvolcanic	0.020	4.30	11.12	93.20	55.00	232.70	232.10	22.90	2.61	1.07
40	Rhyolite-1-	Volcanic	0.098	2.89	22.10	75.10	44.14	95.42	72.10	14.57	2.42	2.91
41	Rhyolite-2-	Volcanic	0.023	4.21	12.06	95.10	58.12	220.93	184.20	22.85	2.56	1.86
42	Spilite	Volcanic	0.050	4.14	13.09	79.75	56.30	207.35	248.10	24.46	2.77	2.01
43	Syenite	Plutonic	0.033	3.02	10.93	88.29	59.85	107.67	166.30	13.79	2.54	0.53
44	Trachyte	Volcanic	0.079	2.45	16.75	55.50	45.60	109.11	50.12	8.90	2.48	6.18
45	Tuff-1-	Pyroclastic	0.421	0.92	63.70	31.75	22.60	15.63	19.40	2.74	1.61	26.85
46	Tuff-2-	Pyroclastic	0.484	1.40	65.59	40.00	23.91	12.00	25.00	6.26	1.89	18.18
47	Tuff-3-	Pyroclastic	0.407	1.27	58.61	37.00	36.50	18.05	9.30	3.57	1.83	25.77
48	Tuff-4-	Pyroclastic	0.563	0.46	70.23	29.50	31.50	6.42	14.00	2.08	1.57	28.14
49	Tuff-5-	Pyroclastic	0.460	0.95	67.00	19.20	22.00	7.48	11.00	3.12	1.70	21.46
50	Tuff-6-	Pyroclastic	0.386	1.31	68.25	32.00	26.15	16.65	30.46	4.23	1.77	18.22

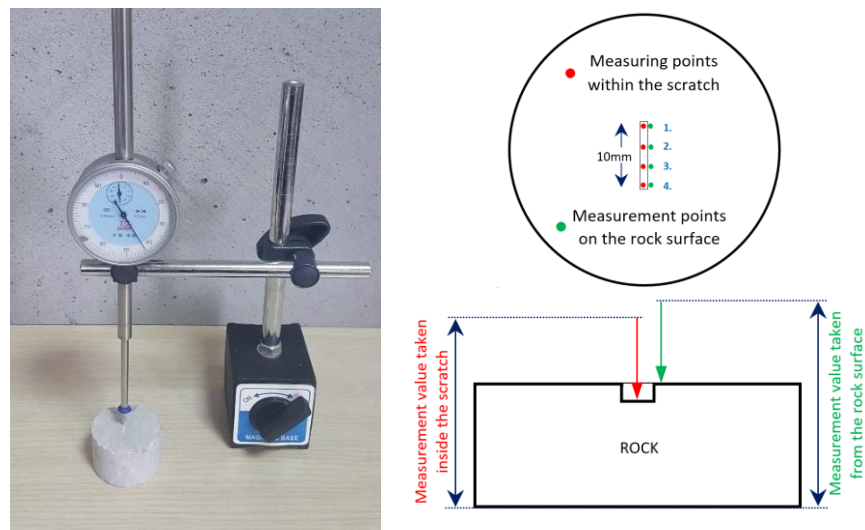


Figure 2. Cerchar indentation depth (CID) measuring device and schematic representation of CID measurement.

3. RESULTS AND DISCUSSION

SRA is frequently used to model the relationships between rock properties. SPSS computer software was used for all statistical analysis. For SRA, all models (Linear, power, logarithmic, cubic, inverse, quadratic, logistic, compound, s-curve, exponential, and growth) in the "Curve Estimation" menu were tried. While choosing the most suitable model for each parameter, attention was paid to ensuring that the models meet all validity/reliability conditions within the 95% confidence interval, as well as having a high coefficient of determination. The equations obtained from SRA using the data set consisting of 50 rocks, the details of which are given in Table 2, are given in Equations 1-7.

SRA

$$SSH = 104.7CID^2 - 178.5CID + 87.7 \quad (1)$$

$$CAI = 4.13 \times 0.05^{CID} \quad (2)$$

$$SHH = 60.5CID^2 - 99.5CID + 59.1 \quad (3)$$

$$HB = 0.0004 \times 303.9^{CID} \quad (4)$$

$$IHI = 0.011 \times 23.87^{CID} \quad (5)$$

$$HV = 10.46CID^{-0.086} \quad (6)$$

$$BSA = 173.2CID^2 - 61.0CID + 10.6 \quad (7)$$

CID values showed significant correlations with the hardness and abrasion values of the rocks, and the coefficients of determination obtained from the equations ranged from 0.81 to 0.91. Detailed graphs of SRA are given in Figures 3-9. Correlation graphs (Figures 3a-9a) were drawn to include the maximum and minimum confidence intervals calculated according to the 95% confidence interval and the maximum and minimum estimation limits. In Figures 3b-9b, it is possible to see the differences (residuals) between the test values of the parameters and the predicted values in detail.

The validity of the equations was determined with the help of F and t-tests at the 95% confidence interval. All of the calculated t-values according to the t-test used to determine the significance level of the R-values of the equations are greater than the table t-values (Table 2). Likewise, the significance coefficients (sig.) of all t-values are less than 0.05, so the established models are valid. Analysis of variance was performed to determine the significance of the regressions. Accordingly, the calculated F values are considerably higher than the tabulated F values. Since the importance of the equations is confirmed by the tests mentioned above, they can be used safely in predictive studies. Since the

equations with SRA are estimated with a single independent variable, they are more practical than equations with more than one independent variable.

Table 2. Validity of derived simple regression models (F-test and t-test).

Equation number	Independent variable	B (Coeff.)	Std. Error	R ²	t value	p value	t value	F value	p value	F value			
1 (SSH)	CID	-178.5	24.3	0.875	7.34	0.000	2.01	165.1	0.000	3.19			
	Quadratic	CID ²	104.7								40.5	2.59	0.013
	(Constant)	87.7	2.0								43.55	0.000	
2 (CAI)	CID	0.05	0.007	0.906	7.25	0.000	2.01	464.1	0.000	3.19			
	Compound	(Constant)	4.13								0.131	31.51	0.000
3 (SHH)	CID	-99.46	13.3	0.875	7.47	0.000	2.01	164.7	0.000	3.19			
	Quadratic	CID ²	60.48								22.2	2.73	0.009
	(Constant)	59.14	1.1								53.65	0.000	
4 (HB)	CID	0.0004	0.000	0.906	2.42	0.019	2.01	355.0	0.000	3.19			
	Compound	(Constant)	303.9								28.8	10.54	0.000
5 (IHI)	CID	0.011	0.003	0.868	3.97	0.000	2.01	315.8	0.000	3.19			
	Compound	(Constant)	23.87								1.38	17.27	0.000
6 (HV)	ln (CID)	-0.86	0.06	0.812	14.41	0.000	2.01	207.6	0.000	3.19			
	Power	(Constant)	10.46								1.73	6.05	0.000
7 (BSA)	CID	61.0	29.9	0.897	2.04	0.047	2.01	204.8	0.000	3.19			
	Quadratic	CID ²	173.2								49.8	3.48	0.001
	(Constant)	10.6	2.5								4.27	0.000	

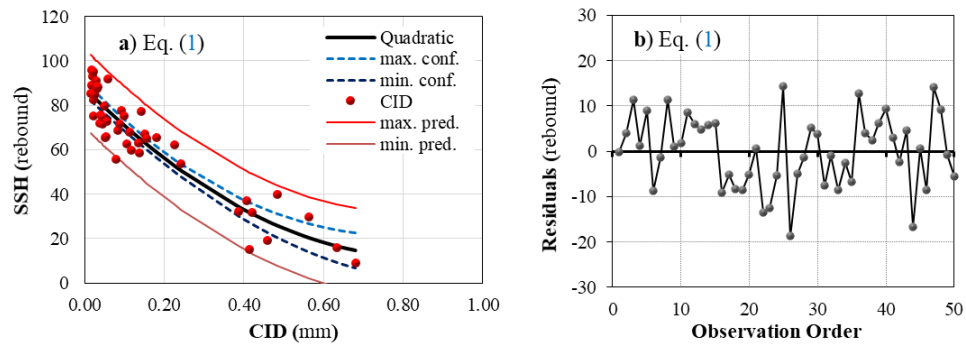


Figure 3. a) SSH-CID correlation graph b) residual graph

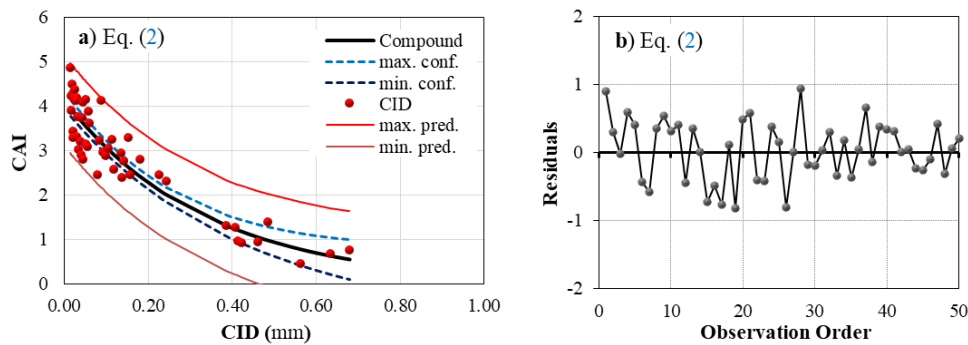


Figure 4. a) CAI-CID correlation graph b) residual graph

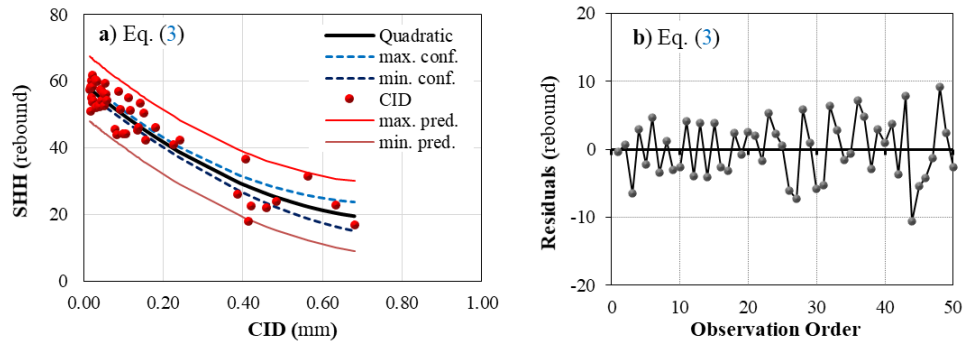


Figure 5. a) SHH-CID correlation graph b) residual graph

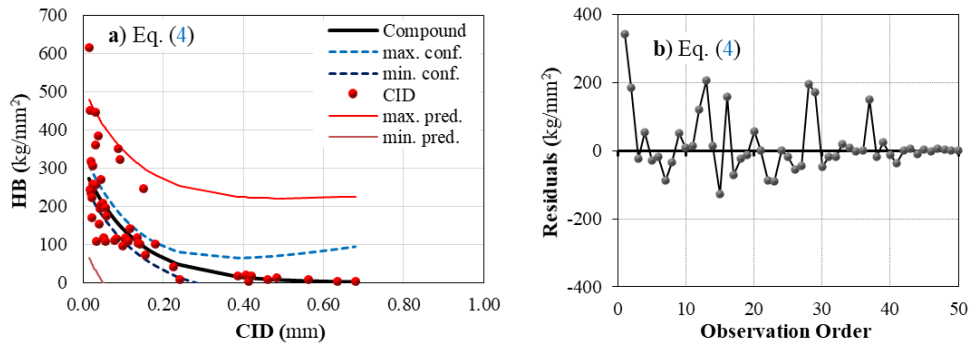


Figure 6. a) HB-CID correlation graph b) residual graph

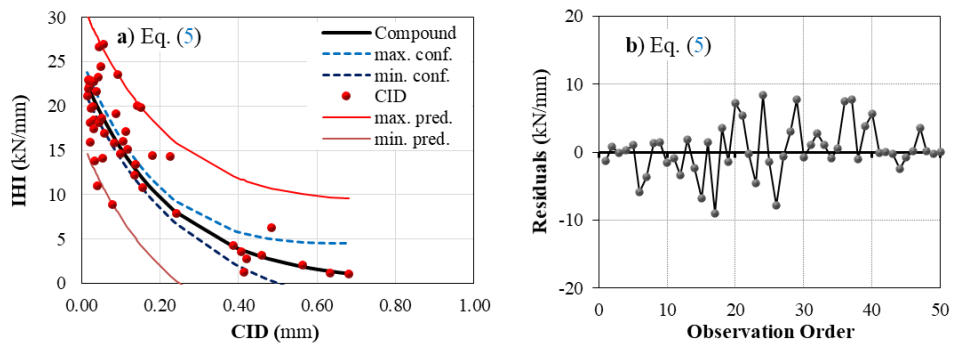


Figure 7. a) IHI-CID correlation graph b) residual graph

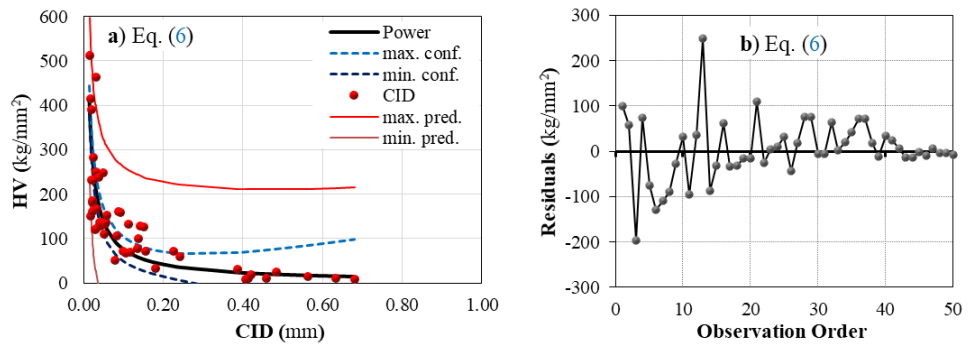


Figure 8. a) HV-CID correlation graph b) residual graph

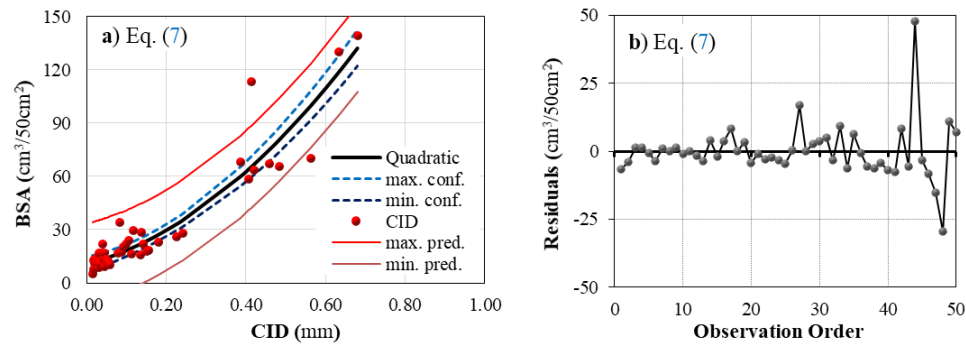


Figure 9. a) BSA-CID correlation graph b) residual graph

Equations with a high coefficient of determination were obtained from SRA. All of these equations are equations whose validity has been proven by F and t-tests, as presented in Table 2. However, as can be seen from the residual graphs given in Figures 3-9, there are points outside the estimation range in some of these equations. To eliminate this handicap, an NMRA study was carried out, in which physical properties of rocks such as UW and Pg were used as independent variables, as well as CID. In this context, two models were constructed. In the first model (NMRA-1), CID and UW were used as independent variables (Eqs. 8-14). In the second model (NMRA-2), the abrasion and hardness properties of the rocks were tried to be estimated with the help of CID, UW, and Pg independent variables (Eqs. 15-21).

Nonlinear regression is a method used to find a nonlinear model of the relationship between a feature determined as the dependent variable and a set of independent variables. Unlike traditional regression, which is limited to the estimation of only linear models, a model with arbitrary relationships between dependent and independent variables can be obtained with the help of nonlinear regression [23]. Multiple nonlinear regression is one of the methods in which Y-dependent values are estimated based on given independent values [24]. In this study, the twin logarithmic method was used in multivariate nonlinear regression analysis for BSA estimation [25]. The parameters used in simple regressions were analyzed in various combinations using the equation described below, and the process was performed using an iterative estimation algorithm. $Y = aX_1^{b_1}X_2^{b_2} \dots X_n^{b_n}$. Where Y is the dependent variable, a is the intercept, X_1 , X_2 , and X_n are independent variables and b_1 , b_2 , and b_n are the regression equation constants. Again, the 95% confidence interval was used to check the validity of the equations obtained from the NMRA studies. The procedure for SRA is also considered here. All of the equations presented are equations with the highest coefficient of determination satisfying the F and t-test conditions.

NMRA-1

$$SSH = 15.97 \times CID^{-0.013} \times UW^{1.2} \quad (8)$$

$$CAI = 0.47 \times CID^{-0.014} \times UW^{1.61} \quad (9)$$

$$SHH = 14.18 \times CID^{-0.06} \times UW^{1.18} \quad (10)$$

$$HB = 1.43 \times CID^{-0.36} \times UW^{4.0} \quad (11)$$

$$IHI = 1.54 \times CID^{-0.1} \times UW^{2.26} \quad (12)$$

$$HB = 0.22 \times CID^{-0.49} \times UW^{5.25} \quad (13)$$

$$BSA = 324.2 \times CID^{0.25} \times UW^{-2.45} \quad (14)$$

NMRA-2

$$SSH = 15 \times CID^{-0.14} \times UW^{1.24} \times P_g^{0.01} \quad (15)$$

$$CAI = 0.43 \times CID^{-0.15} \times UW^{1.68} \times P_g^{0.02} \quad (16)$$

$$SHH = 12.45 \times CID^{-0.07} \times UW^{1.27} \times P_g^{0.02} \quad (17)$$

$$HB = 4.22 \times CID^{-0.25} \times UW^{3.28} \times P_g^{-0.17} \quad (18)$$

$$IHI = 1.21 \times CID^{-0.12} \times UW^{2.41} \times P_g^{0.04} \tag{19}$$

$$HV = 0.45 \times CID^{-0.42} \times UW^{4.75} \times P_g^{-0.11} \tag{20}$$

$$BSA = 419.6 \times CID^{0.3} \times UW^{-2.53} \times P_g^{-0.06} \tag{21}$$

Comparison graphs of the estimated and measured values of the three equations produced for each rock feature are given in Figures 10-16. It is very clear that the CID parameter alone is a strong variable in the estimation of the SSH parameter (Figure 10a). The SSH parameter can be strongly estimated by the CID parameter without the need for any physical testing. This situation can be interpreted similarly for the SHH parameter, which is another rock hardness test (Figure 12). Although the CID parameter alone has very high predictive power in the estimation of CAI and IHI parameters, with the inclusion of physical tests in the model, partially stronger estimation equations were obtained (Figures 11 and 14). The positive effect of physical tests in the prediction equations is clearly prominent in the prediction of metal hardness tests such as HB and HV. The low estimation capacities of the regression equations obtained only with CID in the estimation of both parameters can be seen in Figure 13a and Figure 15a. It can be said that the prediction capacities of the models increased in the NMRA equations created with CID and UW in the estimation of these two parameters, but a real significant increase was obtained with the NMRA equations created with CID, UW, and P_g (Figure 13c and Figure 15c). It can be easily said that the rock mechanics property most closely related to the CID parameter is BSA. In the estimation of this parameter, equations with very high predictive power were obtained with both SRA and NMRA models.

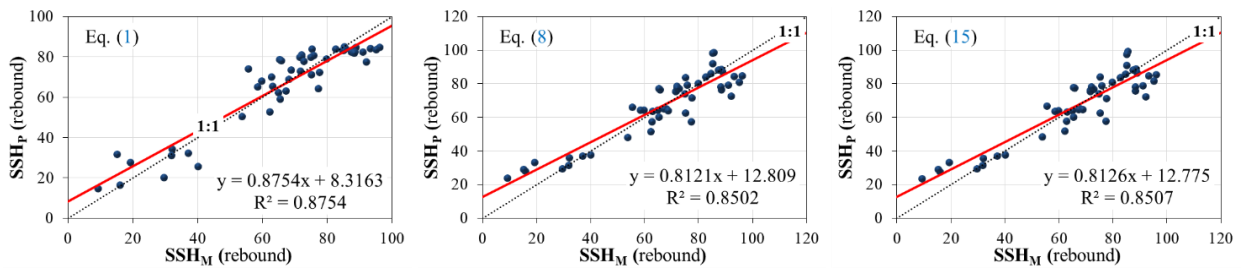


Figure 10. Comparison graphs of measured SSH-predicted SSH.

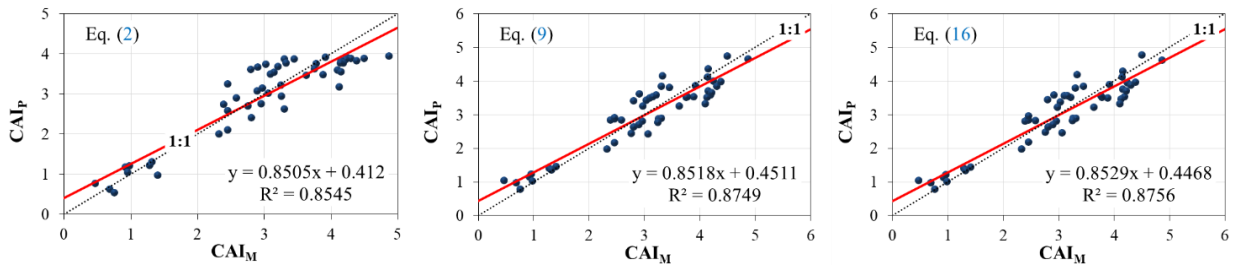


Figure 11. Comparison graphs of measured CAI-predicted CAI.

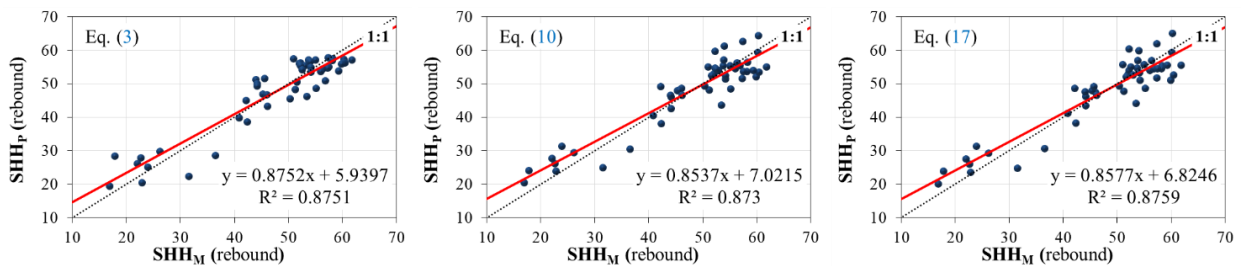


Figure 12. Comparison graphs of measured SHH-predicted SHH.

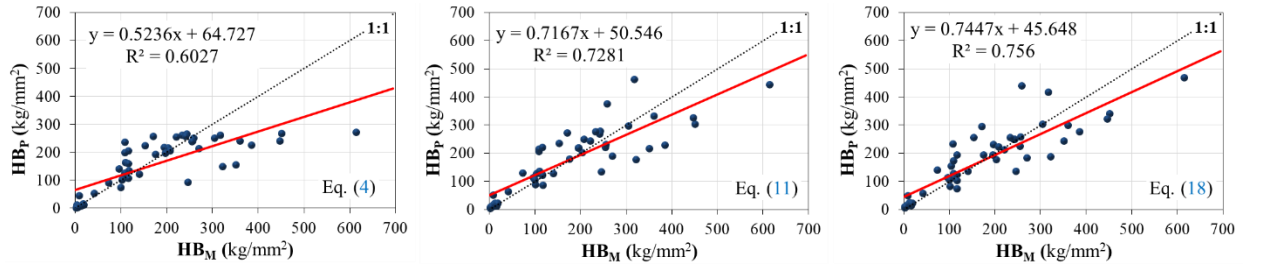


Figure 13. Comparison graphs of measured HB-predicted HB.

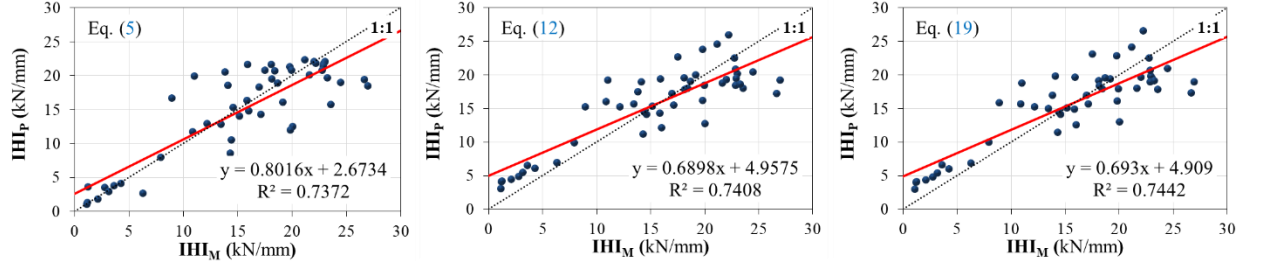


Figure 14. Comparison graphs of measured IHI-predicted IHI.

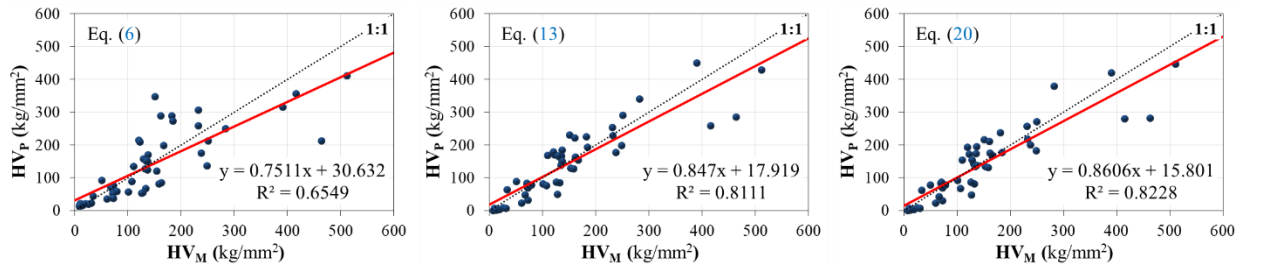


Figure 15. Comparison graphs of measured HV-predicted HV.

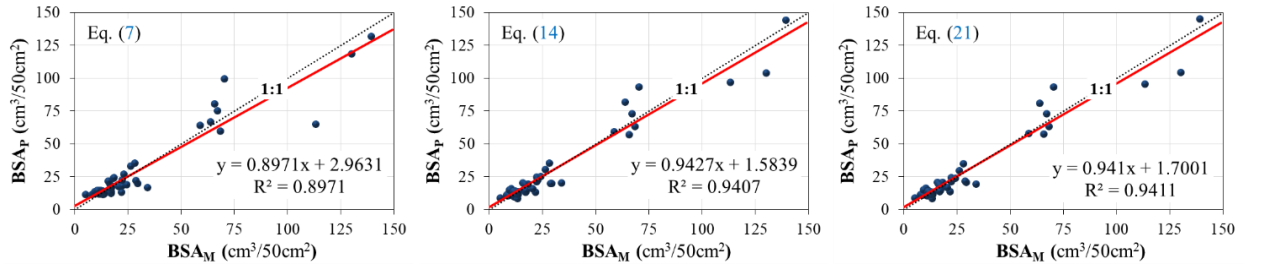


Figure 16. Comparison graphs of measured BSA-predicted BSA.

4. PERFORMANCE ANALYSES OF DERIVED MODELS

To compare the capacity performances of all forecasting models, some statistical performance indices such as RSR, VAF, E, and Adj.R² were calculated separately for each model. E is the efficiency coefficient, VAF is the variance calculation factor, and Adj.R² is the corrected coefficient of determination. RSR is the root square error rate of the prediction values relative to the standard deviation ratio. PI_{at} is the performance index value developed by the author [26] within the scope of this study. This new performance index given in Equation 22 was created by using four of the above-mentioned performance indexes in the same formula.

$$PI_{at} = \left[Adj.R^2 + \left(\frac{VAF}{100} \right) + E - RSR \right] \quad (22)$$

The theoretical perfection of the performance index given in Eq. 22 depends on the condition that the RSR value is "0", the E and Adj.R² value is "1" and the VAF value is "100". As it can be understood from here, the perfect PI_{at} value should theoretically be equal to 3, and the equations with the highest predictive power are those with the highest PI_{at} value (Table 3).

Within the scope of this study, estimation equations were developed for a total of seven parameters, with CID being the main independent variable. For each parameter; three equations were generated, one SRA (Eqs. 1-7), one NMRA-1 (Eqs. 8-14), and one NMRA-2 (Eqs. 15-21). According to the calculated average PI_{at} values, the rock properties estimated with the CID parameter in the most reliable way and with the highest estimation capacity are as follows; BSA (2.51), SHH (2.26), CAI (2.23), SSH (2.19), HV (1.78), IHI (1.69), and HB (1.51). The equations with the highest estimation capacity for each rock feature are as follows; Eq. 21 (BSA); Eq. 3 (SHH); Eq. 16 (CAI); Eq. 1 (SSH); Eq. 20 (HV); Eq. 19 (IHI); Eq. 18 (HB).

Table 3. Calculated statistical performance indices for derived simple regression models.

Equation number	Adj.R ²	VAF	E	RSR	PI _{at}
Eq. (1)	0.873	87.54	0.875	0.353	2.27
Eq. (2)	0.851	85.45	0.854	0.383	2.18
Eq. (3)	0.873	87.51	0.875	0.353	2.27
Eq. (4)	0.594	59.23	0.574	0.653	1.11
Eq. (5)	0.732	73.16	0.729	0.521	1.67
Eq. (6)	0.648	64.07	0.639	0.601	1.33
Eq. (7)	0.895	89.71	0.897	0.321	2.37
Eq. (8)	0.844	84.85	0.848	0.389	2.15
Eq. (9)	0.869	87.42	0.874	0.355	2.26
Eq. (10)	0.868	87.25	0.872	0.357	2.26
Eq. (11)	0.717	72.79	0.728	0.522	1.65
Eq. (12)	0.730	73.73	0.737	0.513	1.69
Eq. (13)	0.803	80.95	0.809	0.438	1.98
Eq. (14)	0.938	94.07	0.941	0.244	2.58
Eq. (15)	0.841	84.90	0.849	0.389	2.15
Eq. (16)	0.867	87.49	0.875	0.354	2.26
Eq. (17)	0.868	87.55	0.875	0.353	2.27
Eq. (18)	0.740	75.59	0.756	0.494	1.76
Eq. (19)	0.727	74.06	0.740	0.510	1.70
Eq. (20)	0.811	82.11	0.820	0.424	2.03
Eq. (21)	0.937	94.11	0.941	0.243	2.58

5. CONCLUSIONS

In this study, it is planned to make depth measurements along the scratch line formed on the rock surface with the CAI experiment and thus create a new experimental data set. Detection of this parameter, called CID, requires the use of a specially prepared sample. The determination of CID values is dependent on the condition that the CAI test is applied on well-sized core or prismatic rocks. The fact that mostly irregularly shaped samples are used for CAI experiments is the main reason why the CID parameter is not commonly found in the literature. In this study, which was carried out with test data of a large number of rocks, hardness, abrasion, and physical properties, which are thought to be directly related to the CID parameter, were tried to be correlated. The results obtained from SRA and NMRA have been tried to be summarized in the following items.

- When a general evaluation is made, it is seen that the determination coefficients of the equations obtained with igneous rocks are quite high. The general uniformity of mineral distribution in igneous rocks is the main reason for obtaining these stable results.

- According to the average performance index (PI_{at}) analysis, it is clear that the BSA, SHH, CAI, and SSH tests have a high level of reliability, respectively. The common feature of these parameters is that they are common methods that are frequently applied to rocks. The estimation equations of methods developed to measure metal hardness, such as HB and HV, did not give reliable results as in classical methods.
- The equations with the highest coefficient of determination and performance index value for all data sets in the estimation of the CID parameter were obtained by the BSA test.
- It should be underlined that all of the 30 equations presented in the study meet the reliability test conditions. Equations that fail to meet the F and t-test conditions, although giving a higher coefficient of determination, are not included. The results revealed that the CID parameter has a very significant relationship with the properties of the rocks, especially the surface properties such as abrasion and hardness.
- Within the scope of the study, tests such as BSA, CAI, SHH, SSH, HB, HV, and IHI were carried out. Elements such as abrasive mineral content, porosity, density, degree of cementation, cement (matrix) material, and structure texture affect the abrasion/hardness properties listed above more than mechanical properties. Similarly, CID is controlled by the same parameters. Based on this determination, it is recommended to researchers that the CID values should be determined in case the CAI tests are to be carried out with well-sized core or prismatic samples.
- It is thought that the CID parameter will provide an important data set to the researchers thanks to the sensitive measurements to be made by paying attention to the conditions detailed in the text. This study revealed that a significant data set can be obtained from the scratches on the rock surface as well as the wear on the steel tips used in the CAI test. New studies can be carried out in the future by making the experimental set created in this study more professional/standard. A digital comparator and a more rigid-thin steel tip can be used. In addition to depth, the width of the scratch along the measurement line can also be measured. It is thought that if high-resolution photographs are processed with the help of computer programs, the average scratch width will reveal meaningful relationships with other rock properties.

Declaration of Ethical Standards

The study was conducted in accordance with ethical standards.

Credit Authorship Contribution Statement

Ahmet TEYMEN Conceptualization, Methodology, Designed the Experiments, Writing original draft, Supervision, and Writing review and Editing.

Declaration of Competing Interest

The author declares no conflict of interest.

Funding / Acknowledgements

The author declares that she has no financial support.

Data Availability

Data will be made available on request.

REFERENCES

- [1] ISRM "Suggested methods for determining hardness and abrasiveness of rocks," *International Journal of Rock Mechanics and Mining Science & Geomechanics Abstracts*, 1978, vol. 15, p. 89–97.
- [2] ASTM D7625-10 "Standard test method for laboratory determination of abrasiveness of rock using the CERCHAR Method" *ASTM International, West Conshohocken, PA*, 2010.
- [3] S.T. Johnson, and R.J. Fowell, "Compressive strength is not enough (Assessing pick wear for drag tool-equipped machines)," In Proc. 27th US Symp Rock Mechanics, Tuscaloosa, Alabama, USA, 1986, pp. 23-25.
- [4] H. Çopur, and Ş. Eskikaya, "ELI Eyzek Bölgesi M2 marnının fiziksel ve mekanik özelliklerinin mekanize kazı bakımından incelenmesi," In Proc. Türkiye 8. Kömür Kongresi, TMMOB Maden Mühendisleri Odası Yayını, Zonguldak, Türkiye, Mayıs 1992, pp. 4-8. (in Turkish)
- [5] S.L. Al-Ameen and M.D. Waller, "The influence of rock strength and abrasive mineral content on the Cerchar abrasive index," *Engineering Geology*, vol. 36, p. 293-301, 1994. [Online]. Available: [https://doi.org/10.1016/0013-7952\(94\)90010-8](https://doi.org/10.1016/0013-7952(94)90010-8)
- [6] R. Plinninger, H. Kasling and K. Thuro, "Wear prediction in hardrock excavation using the Cerchar abrasivity index (CAI)" in: *Schubert, editor. Proc. EUROCK 2004 and 5rd Geomechanics Colloquium VGE*. Germany: Essen, 2004, pp- 599–604.
- [7] O. Yaralı, and N.A. Akçın, "Kayaçların Cerchar sertlik indeks değerleri ile dayanım özellikleri arasındaki ilişkilerin belirlenmesi," In Proc. Türkiye 19. Uluslararası Madencilik Kongresi ve Fuarı, IMCET2005. İzmir, Türkiye, Haziran 2005, pp. 9-12. (in Turkish)
- [8] A.E. Tercan and Y. Ozcelik, "Canonical ridge correlation of mechanical and engineering index properties," *International Journal of Rock Mechanics and Mining Sciences*, vol. 43, no. 1, p. 58-65, 2006. [Online]. Available: <https://doi.org/10.1016/j.ijrmms.2005.04.002>
- [9] J. Mateus, N. Saavedra, Z.C. Carrillo, and D. Mateus, "Correlation development between indentation parameters and uniaxial compressive strength for Colombian sandstones," *CT&F-Ciencia, Tecnología y Futuro*, vol. 3, no. 3, p. 125-136, 2007. [Online]. Available: <https://doi.org/10.29047/01225383.481>
- [10] D. Tumac, N. Bilgin, C. Feridunoglu, and H. Ergin, "Estimation of rock cuttability from shore hardness and compressive strength properties," *Rock Mechanics and Rock Engineering*, vol. 40, no. 5, p. 477-490, 2007. [Online]. Available: <https://doi.org/10.1007/s00603-006-0108-5>
- [11] S. Kahraman, M. Alber, M. Fener and O. Gunaydin, "The usability of Cerchar abrasivity index for the prediction of UCS and E of Misis Fault Breccia: Regression and artificial neural networks analysis," *Expert Systems with Applications*, vol. 37, p. 8750–8756, 2010. [Online]. Available: <https://doi.org/10.1016/j.eswa.2010.06.039>
- [12] A. H. Deliormanli, "Cerchar abrasivity index (CAI) and its relation to strength and abrasion test methods for marble stones," *Construction and Building Materials*, vol. 30, p. 16-21, 2012. [Online]. Available: <https://doi.org/10.1016/j.conbuildmat.2011.11.023>
- [13] N. Dipova, "Bir tünel güzergâhındaki zayıf kireçtaşlarının aşınma ve dayanım özellikleri arasındaki ilişkilerin araştırılması," *Jeoloji Mühendisliği Dergisi*, vol. 36, no. 1, p. 23-34, 2012 (in Turkish)
- [14] A. Boutrid, S. Bensehamdi, and R. Chaib, "Investigation into Brinell hardness test applied to rocks," *World Journal of Engineering*, vol. 10, no. 4, p. 367-380, 2013. [Online]. Available: <https://doi.org/10.1260/1708-5284.10.4.367>
- [15] O. Yaralı, "Kayaçların mekanik özelliklerinin Cerchar aşınma indeksine olan etkilerinin araştırılması," *Karaelmas Fen ve Mühendislik Dergisi*, vol. 6, no. 1, p. 218-229, 2016 (in Turkish)
- [16] A. Teymen, "The usability of Cerchar abrasivity index for the estimation of mechanical rock properties," *International Journal of Rock Mechanics and Mining Sciences*, vol. 128, no. 104258, 2020. [Online]. Available: <https://doi.org/10.1016/j.ijrmms.2020.104258>

- [17] ISRM "Suggested method for determining the abrasivity of rock by the Cerchar abrasivity test" R. Ulusay (edt.), *The ISRM Suggested Method for Rock Characterization, Testing and Monitoring: 2007-2014*, Springer, USA, 101-106p., 2015.
- [18] ISRM "The complete ISRM suggested methods for rock characterization, testing and monitoring: 1974–2006" R. Ulusay and J.A. Hudson (eds.), *Suggested Methods Prepared by the Commission on Testing Methods, International Society for Rock Mechanics, Compilation Arranged by the ISRM Turkish National Group, Kozan Ofset, Ankara, Turkey*, 628p., 2007.
- [19] ASTM E10-01 "Standard test methods for Brinell Hardness of metallic materials" ASTM International, West Conshohocken, PA, 1995.
- [20] ASTM E92-82 "Standard test methods for Vickers Hardness of metallic materials" ASTM International, West Conshohocken, PA, 2003.
- [21] TS EN 14157, "Aşınma direncinin tayini – Böhme" *Türk Standartları Enstitüsü, Ankara*, 2005.
- [22] ISRM "Rock characterization, testing and monitoring – Commission on standardization laboratory and field results" *Suggested methods for determining hardness and abrasiveness of rocks*, Pergamon, Oxford, p. 102-103, Part 4, 1981.
- [23] SPSS Inc. SPSS regression models (version 17.0). Available from: <http://www.spss.com>.
- [24] B. Tiryaki, "Application of artificial neural networks for predicting the cuttability of rocks by drag tools," *Tunnelling and Underground Space Technology*, vol. 23, no. 3, p. 273-280, 2008. [Online]. Available: <https://doi.org/10.1016/j.tust.2007.04.008>
- [25] S. Choi, *Introductory Statistics in Science*. New Jersey:, Prentice-Hall Inc., 1978.
- A. Teymen and E.C. Mengüç, "Comparative evaluation of different statistical tools for the prediction of uniaxial compressive strength of rocks," *International Journal of Mining Science and Technology*, vol. 30, no. 8, p. 785-797, 2020. [Online]. Available: <https://doi.org/10.1016/j.ijmst.2020.06.008>



PRODUCTION OF CuO/ZrO₂ NANOCOMPOSITES IN POWDER AND FIBER FORMS

Zeynep ÇETİNKAYA 

*Konya Technical University, Engineering and Natural Sciences Faculty, Metallurgical and Materials Engineering
Department, Konya, TÜRKİYE*
zcetinkaya@ktun.edu.tr

Highlights

- Investigating the production of CuO/ZrO₂ nanoparticles and composite fibers using a hydrothermal and electrospinning method.
- For the first time, the drop-casting method used for the production of CuO particles onto ZrO₂ fibers.
- Alternative production method for the production of CuO/ZrO₂ composites.



PRODUCTION OF CuO/ZrO₂ NANOCOMPOSITES IN POWDER AND FIBER FORMS

Zeynep ÇETİNKAYA 

*Konya Technical University, Engineering and Natural Sciences Faculty, Metallurgical and Materials Engineering
Department, Konya, TÜRKİYE
zcetinkaya@ktun.edu.tr*

(Received: 26.12.2023; Accepted in Revised Form: 07.02.2024)

ABSTRACT: CuO/ZrO₂ composite systems were synthesized in two different ways and comprehensively characterized with X-ray diffraction(XRD), Fourier transform infrared spectroscopy(FTIR), scanning electron microscopy(SEM), transmission electron microscopy(TEM), and energy dispersive X-ray spectroscopy(EDX). These metal oxide samples were prepared by hydrothermal synthesis and electrospinning process. In these methods, the same metal salts were used as precursors. Separately produced ZrO₂ nanoparticles(NPs) and CuO particles have spherical and cube-like shapes, and both morphologies have monoclinic structures. However, ZrO₂ and CuO particles do not have uniform diameters, and the average size of these particles ranges between 6–17 and 215–847 nm, respectively. Moreover, CuO/ZrO₂ nanocomposite particles(NCPs) were synthesized using a facile and one-pot hydrothermal technique. They have uniform, spherical, and monoclinic structures with a 15nm average diameter. Furthermore, ZrO₂ fibers were produced with the electrospinning process as highly crystalline structures after annealing, with a 230 nm average fiber diameter. In addition, ZrO₂ fibers were doped with hydrothermally synthesized CuO particles with a drop-casting method for the first time. This study clearly shows that particle-fiber structure allows the development of the efficiency of p-type counterparts by using only 0.5-1.5wt.% n-type. With these results, two methods can be used to produce heterostructure CuO/ZrO₂ composite particles/fibers and as potential for photocatalytic degradation.

Keywords: Composite fibers, Electrospinning process, Hydrothermal synthesis, Nanoparticles, Fibers, CuO/ZrO₂

1. INTRODUCTION

There has been significant progress in the production of nanoscale materials in the last decades, and these materials are becoming essential in applications such as photocatalytic [1], adsorption [2], drug carriers [3], fuel cells [4], etc. Nanoscale materials with different structures and dimensions (i.e., zero, one, two, and three) have been prepared with their unique chemical and physical properties. Among these, one-dimensional materials which are nanowires, nanofibers, nanorods, and nanotubes, are used in many industrial fields, especially in the biomedical and chemical sectors [5]-[7]. Different production methods are developed since nanoparticles' physicochemical and morphological properties are affected by the initial material characteristics. These methods show partial changes with respect to the nanomaterial production which is preferred bottom-up or top-down production method. The main bottom-up production methods are ultrasonic spray pyrolysis, hydrothermal, sol-gel, chemical vapor condensation, inert gas condensation, and electrospinning. Hydrothermal synthesis is the most common method for producing nanomaterials among these techniques. In this method, temperature can be changed for controlling the particle morphology of the materials, either in low- or high-pressure conditions. Another technique used in this study is the electrospinning process for producing metal oxide nanofibers due to the advantage of high performance, simplicity, low expense, and excellent reproducibility [8]. Electrospun nanomaterials have a large surface area and better pore interconnectivity than the nanostructures synthesized by other methods mentioned above. With this fabrication method, nano to micron-sized fibers can be produced with various structures and morphologies such as hallow [9], core-shell [10], and porous structures [11] by modifying process parameters such as feed rate, collector type, applied voltage, tip to collector distance, and nozzle design. Today, ceramic, metal, metal

*Corresponding Author: Zeynep ÇETİNKAYA, zcetinkaya@ktun.edu.tr

alloy, and polymer-based nanoparticles with different morphologies such as spherical, rod-like, core-shell, doped, hollow, or their mixture can be prepared with the desired properties via electrospinning.

In transition metals of Mo, Ti, Zr, and Hf, wide band gaps between 3.0 and 7.0 eV are commonly used with an n-type semiconductor in several industries [12]. ZrO₂ has been investigated for various chemical applications such as physical, optical, and mechanical properties, including high melting point, high resistivity, excellent chemical stability, low electrical conductivity, and biocompatibility, which can be used as a catalyst by doping with other elements. Scientists have often investigated the effect of secondary metal oxides added to ZrO₂, such as Tb, Au, Al, Ti, Ag, Cu, etc. [12]-[16].

Copper oxide (CuO) is a p-type semiconductor oxide with a band gap between 1.2 and 2.1 eV [8]. At the nanoscale, it possesses distinct features such as nontoxicity, low cost, easy production in various morphologies, electrochemical activity, high surface area, and excellent stability. With these features, CuO has shown fascinating properties for applications in various areas, such as solar cells, gas sensors, catalysis, batteries, etc. Moreover, CuO can be coupled with well-known n-type photocatalytic materials (i.e., TiO₂, ZrO₂, and SnO₂) using various methods for heterostructure p-n type photocatalysts with their efficiencies [15], [17], [18].

CuO/ZrO₂ composites is one of the most significant CuO-based nanostructures widely produced and mostly applied to photocatalytic activities with ZrO₂ [19]. Furthermore, the physical and chemical properties of ZrO₂ NPs and fibers are also very suitable for this composite material synthesis. This approach leads to candidates for photodegradation via CuO/ZrO₂ nanocomposites being chosen for this study to investigate their production.

Various techniques have been used to enhance the photocatalytic properties of materials by forming nanocomposites, such as binary and ternary heterojunctions and different metal ion dopants [1], [6], [20], [21]. Based on these observations, in this work, at pH 9.4, CuO/ZrO₂ composite materials were produced in powder and fiber forms by hydrothermal synthesis and electrospinning process using the same precursors with various side chemicals. Thus, samples can be utilized in various or the same applications. p-type CuO was produced by the hydrothermal method with well-crystallized particles as cube-like morphology. Then, n-type ZrO₂ fibers were produced using an electrospinning process and employed as a template for the drop-casting method to couple the two phases *for the first time* in this material system. This system successfully obtained heterostructure samples with different amounts of CuO. The shape and size features of the CuO/ZrO₂ composite materials were investigated via XRD, FTIR, SEM, and TEM analysis. CuO/ZrO₂ is a well-known composite product for photocatalytic reduction studies and was successfully produced by both methods. This study differs from similar studies because it produces composite materials using electrospinning with one-step hydrothermal synthesis and drop-casting on the fiber.

2. MATERIAL AND METHODS

2.1. Chemicals

Zirconium (IV) nitrate pentahydrate (Zr(NO₃)₄·5H₂O, China) and copper (II) nitrate hydrate (Cu(NO₃)₂·2.5H₂O, Sigma Aldrich) were employed as a precursor. Urea (Co(NH₂)₂, Sigma Aldrich) and sodium oleate (CH₃(CH₂)₇CH, China) were commercially acquired to synthesize CuO and ZrO₂ NPs, respectively. Ammonia was used to adjust the pH value of both CuO and ZrO₂ NPs. Polyvinyl pyrrolidone (PVP, M_w = 1.3 × 10⁶, Sigma Aldrich), acetic acid, and ethanol were used to prepare the electrospinning solution. Deionized water (DI) was present for the production of NPs.

2.2. Synthesis of CuO/ZrO₂ NPs

In the first step of preparing the CuO/ZrO₂ NPs, Zr(NO₃)₄·5H₂O (metal source, 0.117 M) was dissolved in 30 ml DI water. In a different beaker, surfactant CH₃(CH₂)₇CH (NaOL, 0.233 M) was dissolved in 15 ml DI water and stirred for 15 minutes at room temperature. The solution in two

separate beakers (metal source and surfactant) was added to each other and mixed on a magnetic stirrer for 10 minutes. When the pH of 9.4 with NH₃ is adjusted, the white precipitate becomes homogeneous. Then, in the different beakers, Cu(NO₃)₂·2.5H₂O (0.1 M) and Co(NH₂)₂ (0.1 M) were mixed well with 50 mL DI water under continuous stirring for 15 minutes. After mixing two beakers, a few drops of NH₃ were added to adjust the pH to 7. The two solution's half-volume were mixed. The final solution's pH was fixed to 9.4. Then, a sufficient volume of distilled water was added to complete the total solution volume to 80 mL, and stirring was continued for another 10 minutes. After, the solution was transferred to the hydrothermal unit and heated at 200 °C for 13 hours. Furthermore, the same procedure can prepare each NP/particle solution separately.

In the second step of the hydrothermal process after 13 hours, the autoclave was cooled at room temperature and opened. Black color precipitation was washed sequentially with water, ethanol, and acetone and dried at 55 °C for 3 hours (Fig. 1).

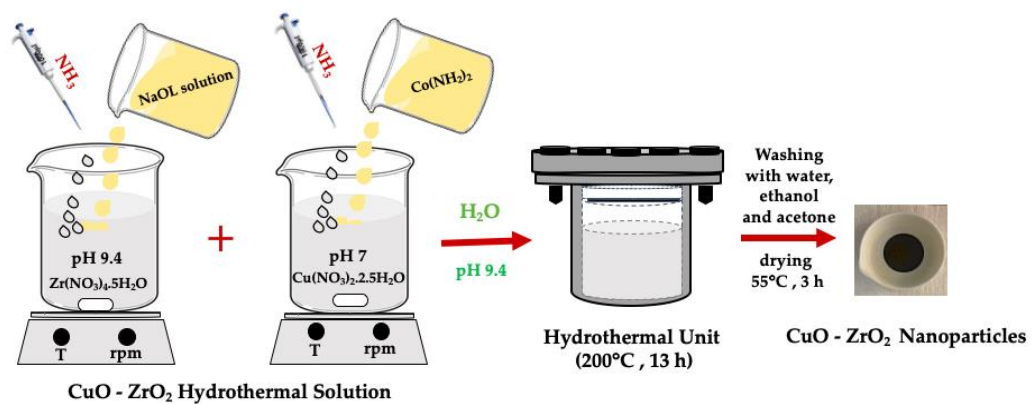


Figure 1. Scheme of the hydrothermal preparation of the CuO/ZrO₂ NPs

2.3. Preparations of The Heterostructure CuO/ZrO₂ CFs

As detailed in the previous study, ZrO₂ fibers were fabricated using the electro-spinning method [12]. Briefly, 0.15 g PVP was dissolved in 2.5 ml ethanol and 1 ml acetic acid at 50 °C for 20 minutes. Then, 1.5 g Zr(NO₃)₄·5H₂O was added to the vial at 50 °C for 20 minutes, and the transparent solution was turned white and cooled to room temperature (Fig. 2).

The precursor was transferred into the syringe for electrospinning. The tip was electrified under an applied voltage of 18 kV using a DC power supply (Spellman SL30). Between the tip of the needle and the collector, it was set to 15 cm. The viscous solution's feeding rate was adjusted to 1 mL/h (Fig. 2). The collected fibers were dried at room temperature overnight, then annealed at 550 °C with a heating rate of 3 °C/min and kept at this temperature for 5 h under atmospheric conditions to remove any organics.

The production of CuO particles was carried out as described in section 2.2. Then, different amounts of CuO particles/ethanol ratios (0.5, 1, 1.5 wt.%) were dispersed with ethanol in an ice bath by mixing with sonication for 15 minutes. Afterward, CuO particle dispersions were used to produce heterostructures of CuO/ZrO₂ with a drop-casting method on the annealed ZrO₂ CFs. These samples were dried at room temperature and then annealed at 300 °C for 1 hour to obtain partially merged heterostructures with individually dispersed CuO on the ZrO₂ fibers (Fig.2).

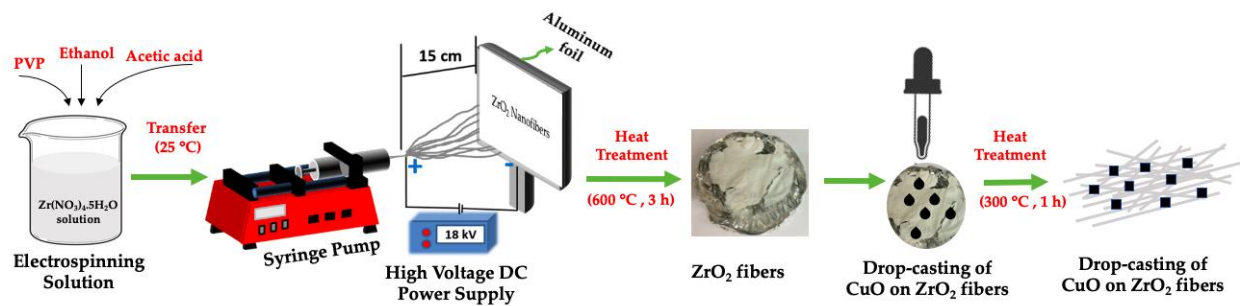


Figure 2. Scheme of the preparation of the ZrO₂ fibers and drop-casting method for producing CuO/ZrO₂ CFs

2.4. Characterization

Following characterization techniques were carried out to characterize the powder of CuO/ZrO₂ NCPs. Phase identification was done with XRD (Bruker D8 Advance, Cu-K α , $\lambda = 1.54 \text{ \AA}$). The scanning speed was determined to be $2^\circ/\text{min}$ from 10 to 80° . FTIR (PerkinElmer GX Spectrometer) was recorded in the range of $4000\text{-}400 \text{ cm}^{-1}$ using the ATR method with a wavenumber resolution of 1 cm^{-1} . The morphologies of the CuO/ZrO₂ NCPs and CuO particles were examined by TEM (JEOL-Jem 2100) and SEM (SM-Zeiss LS-10). The size of the CuO/ZrO₂ NCPs, CuO particles, ZrO₂ fibers, and ZrO₂ CFs were calculated using *Image J* software.

3. RESULTS AND DISCUSSION

Figure 3 shows the XRD pattern of ZrO₂ NPs at pH 9.4. As a result of the investigations, it was observed that all diffraction peaks in this pattern were compatible with ZrO₂ in cubic, monoclinic, and tetragonal with mixed phase structures (JCPDS card no: 49-1642) [18]. This observation shows that the ZrO₂ phase can be obtained in pure form in the prepared solution at pH 9.4, 200°C , and 20 h hydrothermal cycle. In addition, the low intensity of the peaks in the pattern and the narrow-angle of the peaks indicate that the nanoparticle formation is complete with smaller particle size distribution. Using the peaks belonging to the (111) and (220) planes at $2\theta = 30.15^\circ$ and 50.27° , respectively, the crystallite size of ZrO₂ NPs in pure cubic structure was found to be 9 and 10.5 nm, respectively, calculated by the Debye-Scherrer formula:

$$D = \frac{k\lambda}{\beta\cos\theta} \quad (1)$$

In this equation, where D is the grain size, λ is the wavelength of X-ray diffraction ($\lambda = 1.5405 \text{ \AA}$), $K = 0.9$ which is the correction factor, β is FWHM of the most intense diffraction factor, and θ is the Bragg angle.

The peaks at $2\theta = 30.15^\circ; 34.95^\circ; 50.27^\circ; 59.74^\circ; 62.69^\circ; 73.84^\circ; 74.72^\circ$ are shown on the XRD diffraction pattern shown in Figure 3a. The crystal structures of ZrO₂ NPs are indicated using the abbreviations c; cubic, m; monoclinic, and t; tetragonal concerning JCPDS card numbers (80-0965, 37-1484, 49-1642) [12], [18] (Fig.3b).

The crystallinity of the CuO particles was examined with XRD and TEM. Fig. 3a shows the typical XRD pattern of the CuO. The sharp peaks imply the high crystallinity of the monoclinic phase of the CuO crystals. This pattern was matched with the JCPDS Card 048-1548 [15]. Two dominant and sharp peaks diffraction in the pattern at $2\theta = 35.6$ and 38.8° as proof of the monoclinic CuO phase. No impurity-related products such as Cu₂O or Cu(OH)₂ were observed, confirming the purity of the CuO particles [15].

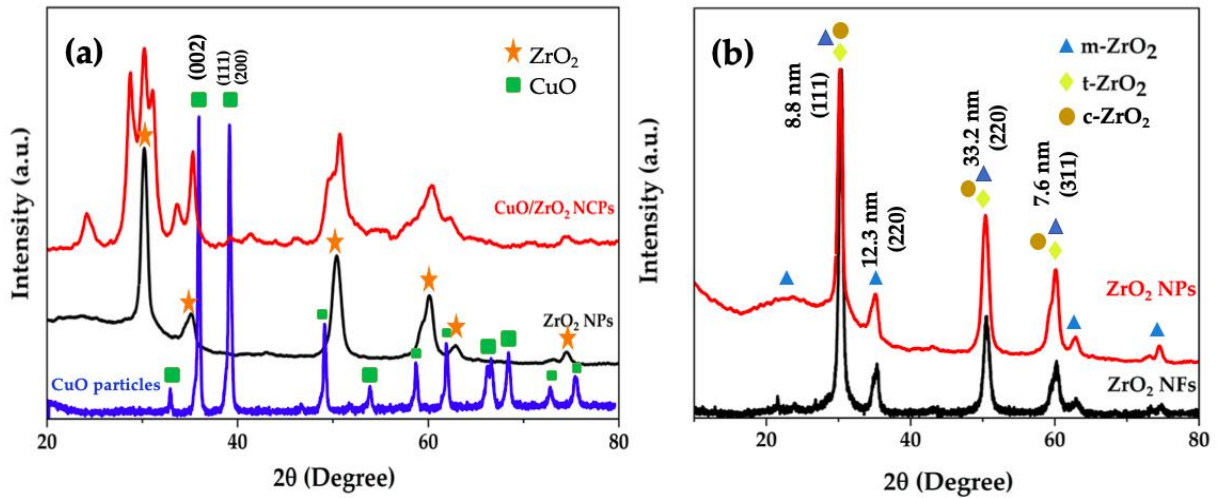


Figure 3. XRD patterns of the a) pure ZrO₂ NPs, CuO particles, and CuO/ZrO₂ NCPs and b) ZrO₂ NFs and ZrO₂ NPs

The crystallite size of the CuO-doped ZrO₂ NPs was calculated as 12.3 nm. These results confirm that the crystallite size of ZrO₂ NPs is larger than the CuO-doped ZrO₂ NPs (8.8 nm). Besides, this size difference can be attributed to the constraint of the motion of crystallites at the interaction between host and dopant crystallites due to stress formation [15]. Incorporating Cu into Zr atoms decreases the energy band gap [19].

As for the preparation of TEM samples, each sample was ultrasonically dispersed in ethanol, and a drop of ethanol containing ZrO₂ NPs or CuO particles was placed in the TEM grids; hence, samples were also seen one on top of another or sparsely dispersed in TEM micrographs. ZrO₂ NPs and CuO particles were characterized with TEM and shown in Fig.4. According to TEM images, ZrO₂ NPs' diameter is between 6 and 17 nm; however, particles are not uniform, and the particle shapes are round-like (Fig.4a). Fig.4b clearly shows the shapes of CuO particles in cubes and in various sizes between 215 and 847 nm.

The chemical compositions of the ZrO₂ NPs, CuO/ZrO₂ NCPs, as-collected and annealed ZrO₂ CFs were examined by FTIR (Fig.5). ZrO₂ NPs peaks matches with CuO/ZrO₂ NCPs various adsorption bands at 487, 502.6, 627, 1651 and 3466 cm⁻¹. The first three peaks are characteristic of the monoclinic of CuO nanocrystals. The peaks between 750 and 1600 cm⁻¹ appear to be small absorption bands, probably nitrate groups [12]. Absorption bands at 3466 and 3414 cm⁻¹ are associated with the bending vibration of absorbed water and O–H stretching mode [1], [2]. For a deeper understanding of CuO particles, the Raman spectrum was examined. CuO particles show three characteristic peaks of the cubic phase at 288, 327, and 627 cm⁻¹ (Fig. 5a). Further, XRD, FTIR, and SEM analysis proved that the sample mainly comprised the CuO phase.

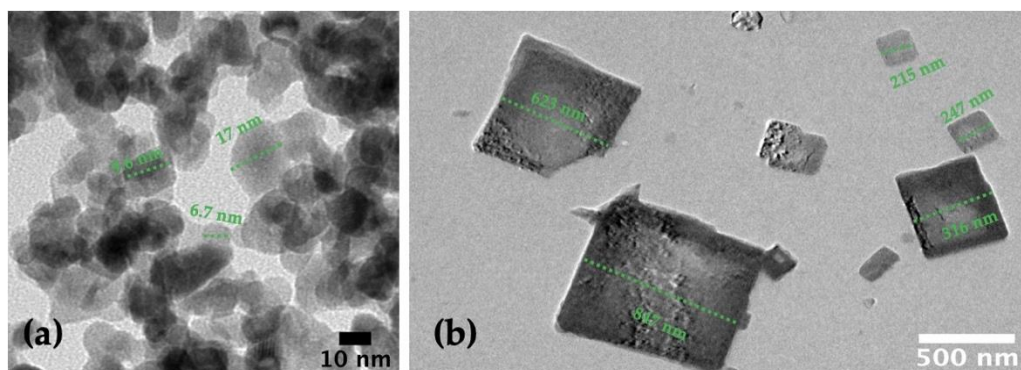


Figure 4. TEM images of a) ZrO₂ NPs and b) CuO particles

FTIR was examined the structure morphology of the as-collected fibers and annealed ZrO₂ CFs as illustrated in Fig. 5b. All fibers were annealed at 550 °C to remove all polymers. Then, the bands became stronger and supported the formation of the Zr–O. PVP has characteristic peaks at 3187, 1650, 1424, and 1290 cm⁻¹, defined as the CH₂ unsymmetrical stretching, C=O stretching, CH₂ bending, and C–N stretching vibration bands, respectively [22]. PVP peaks disappeared after heat treatment at 550 °C, and pure ZrO₂ fibers displayed two peaks at 502.6 and 635 cm⁻¹. The peak can be assigned to the Zr–O and Zr–OH stretching mode of surface-bridging oxygen formed by condensation of adjacent surface oxide groups. The peak at 1635 cm⁻¹ represents the –OH band's vibration [12], [22].

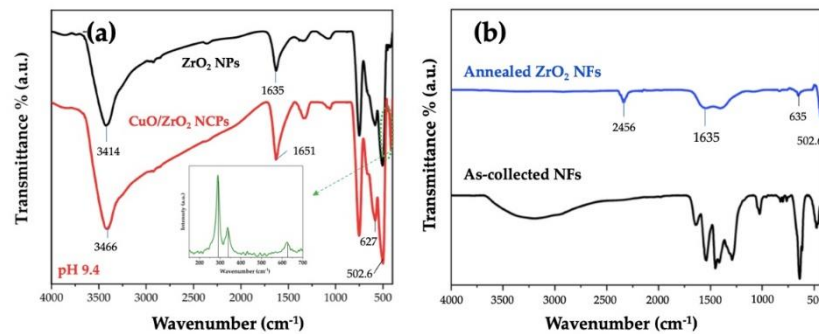


Figure 5. FTIR analysis of a) ZrO₂ NPs and CuO/ZrO₂ NCPs (Raman spectrum of CuO particles is given inset) and b) as-collected and annealed ZrO₂ fibers

SEM, EDX, and TEM analysis of the CuO/ZrO₂ NCPs have been carried out to measure the synthesized samples' particle size and morphology (Fig.6). SEM examination was carried out on the morphology of the samples. A hydrothermal process obtained SEM studies of CuO/ZrO₂ NCPs at 200 °C, showing the spherical formation of NCPs with an average diameter of 20 nm. High and low magnifications were also added in the detailed formation of NCPs. In Fig. 6b, EDX and elemental area map analysis demonstrated the presence of Cu and Zr oxides. In the inset images in Figure 6a, the particles cannot be clearly observed even though they are as close to 100 nm. For this reason, TEM analysis was performed to get closer to the NCPs (Fig. 6c). As seen from these images of CuO/ZrO₂ NCPs, CuO particles and ZrO₂ NPs were successfully assembled. The average diameter was calculated to be 15 nm from Fig. 6c. The HR-TEM image in the inset of Fig.6c reveals that the perfect NCPs were produced with this procedure. The figure exhibits that the interplanar spaces are measured as 1.8 Å. In addition, CuO-doped ZrO₂ NPs are more uniform and have lower diameters than ZrO₂ NPs.

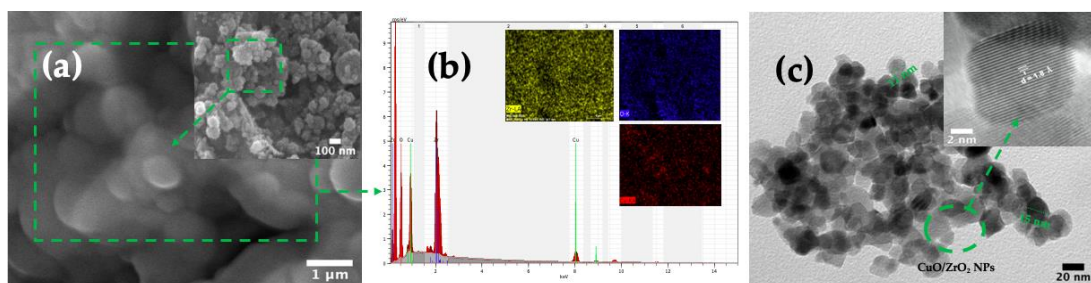


Figure 6. a) SEM images, b) elemental mapping analysis (Cu, Zr, and O elements are given as inset images), c) TEM images (HR-TEM is given inset images) of CuO/ZrO₂ NCPs

The morphology of as-collected and annealed ZrO₂ fibers structures were examined via SEM in Fig. 7. As-collected ZrO₂ fibers' average diameters were found ~540 nm. According to the SEM images, after annealing at 550 °C, all ZrO₂ fibers have bead-free, smooth, and wire-like structures, and fibers are still continuous. These results indicate that the fibers preserved their uniform structure and had average diameters of 232 and 207 nm (Fig. 7b).

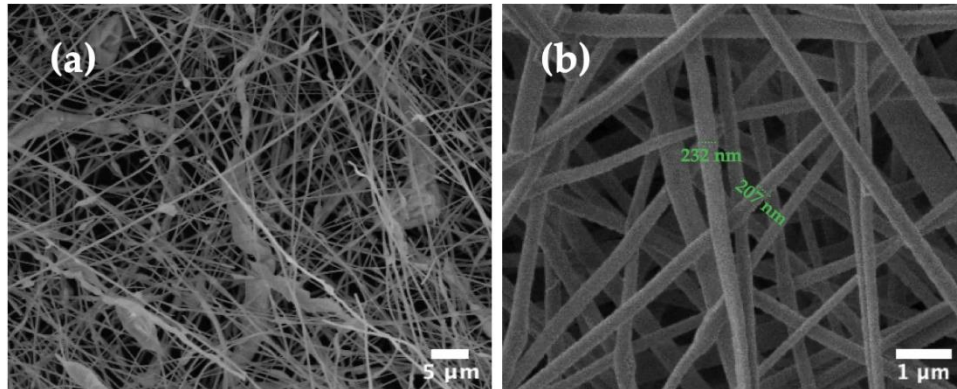


Figure 7. SEM images a) as-collected, b) annealed of ZrO₂ fibers

CuO/ZrO₂ heterostructure CFs were prepared having 0.5, 1.0, and 1.5 wt.% CuO, which were shown in Figure 8a, 8b, and 8c, respectively. Figure 8a presents the SEM analysis of 0.5 wt.% CuO doped ZrO₂ fibers. Before the dope process, the diameters of the fibers were ~230 nm; after the dope process, the CuO particles were attached to the fibers' surface; thus, fiber diameters increased. As a result of the dope process, fiber diameters varied between 300 and 700 nm. Furthermore, similar processes with other ratios were applied to the doping process, and similar segregations to the fibers' interstices and surfaces were observed. After 1 wt.% CuO doping, the fiber diameters varied between 384 and 844 nm. Moreover, CuO was successfully attached between the individual ZrO₂ fiber surfaces. In Figure 8c, the average fiber diameter increased to 619 nm by doping 1.5 wt.% CuO and deposited to the fiber surface. In addition, in Figures 8a, 8b, and 8c, the large CuO particles located between the fibers are marked with a green line color in Fig. 8. The EDX pattern in Fig.8d belongs to the 1.5 wt.% CuO doped ZrO₂ fibers (Zr, O, and Cu elemental area analysis is given in inset images), proving green line marked areas are copper. Therefore, these results indicate that nanopowder and fiber forms of CuO/ZrO₂ have been successfully produced and can be candidates for photocatalysts and gas sensor applications.

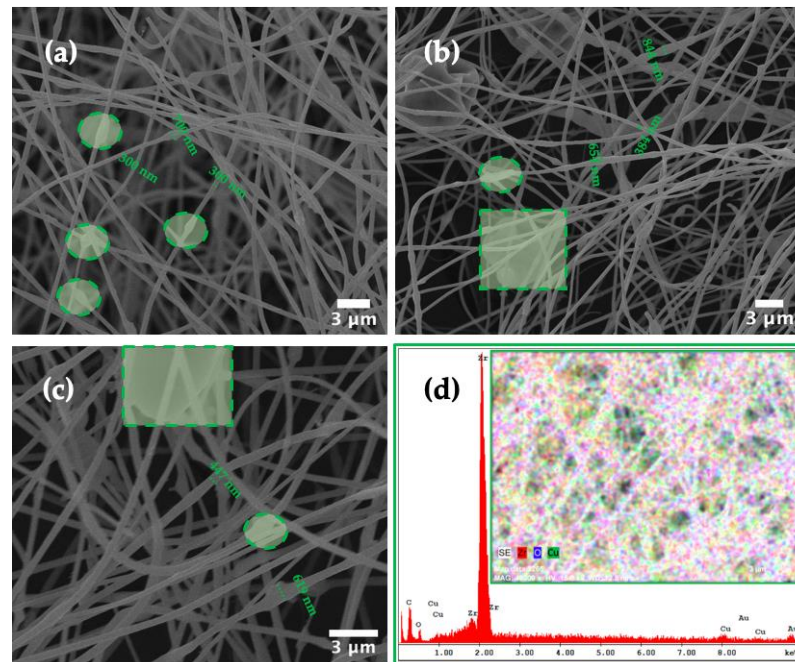


Figure 8. SEM images a) 0.5 wt.%, b) 1 wt.%, c) 1.5 wt.% NFs, and d) EDX analysis of 1.5 wt.% of heterostructure CuO/ZrO₂ fibers

4. CONCLUSIONS

In this study, 2 different production routes were followed to obtain the pure phase of CuO/ZrO₂. Undoped (ZrO₂ NPs and CuO particles) and CuO-doped ZrO₂ NPs with ZrO₂ fibers were produced by hydrothermal and electrospinning systems, respectively. XRD, FTIR, SEM, and TEM techniques were applied to examine the samples. The structural analysis shows that undoped and doped NP samples have monoclinic crystallinity besides spherical and cube-like morphology. Furthermore, CuO-doped ZrO₂ compositions were produced by using the electrospinning method. CuO/ZrO₂ heterostructure CFs were carried out with the drop-casting method to produce p-n-type heterostructure photocatalyst candidates consisting of n-type cube-like CuO particles and p-type ZrO₂ fibers. As mentioned in the introduction, CuO/ZrO₂ composites are mainly used for the photocatalytic organic removal process in the literature. In this study, heterostructure CuO/ZrO₂ CFs production successfully improved the high surface area for the photocatalytic removals by using electrospinning for the first time. Finally, this study clearly shows that particle-fiber structure allows the development of the efficiency of p-type counterparts by using very few amounts (only 0.5-1.5 wt.%. n-type).

Declaration of Ethical Standards

The author followed all ethical guidelines, including authorship, citation, data reporting, and publishing original research.

Declaration of Competing Interest

The author declares that they have no known competing financial interests or personal relationships that could have appeared to influence the work reported in this paper.

Funding / Acknowledgements

The authors gratefully acknowledge the financial support provided by the Scientific Research Projects Coordination Unit of Konya Technical University (Contract # BAP- 211019030).

Data Availability

No data was used for the research described in the article.

REFERENCES

- [1] A. Turki Jalil, H. Emad Al Qurabiy, S. Hussain Dilfy, S. Oudah Meza, S. Aravindhan, M. M Kadhim, A. M Aljeboree, "CuO/ZrO₂ nanocomposites: facile synthesis, characterization and photocatalytic degradation of tetracycline antibiotic", *Journal of Nanostructures*, vol. 11, no. 2, pp. 333-346, 2021, doi: 10.22052/JNS.2021.02.014.
- [2] Y. Wang and R. A. Caruso, "Preparation and characterization of CuO-ZrO₂ nanopowders", *Journal of Materials Chemistry*, vol. 12, no. 5, pp. 1442-1445, 2002, doi: 10.1039/B110844A.
- [3] Z. Chen, N. Meng, C. Gen, W. Qiong, T. Longfei, F. Changhui, R. Xiangling, Z. Hongshan, X. Ke, and Xianwei Meng, "Oxygen production of modified core-shell CuO@ZrO₂ nanocomposites by microwave radiation to alleviate cancer hypoxia for enhanced chemo-microwave thermal therapy", *ACS nano*, vol. 12, no. 12, pp. 12721-12732, 2018, doi: 10.1021/acsnano.8b07749.
- [4] J. Baneshi, M. Haghghi, N. Jodeiri, M. Abdollahifar, and H. Ajamein, "Homogeneous precipitation synthesis of CuO-ZrO₂-CeO₂-Al₂O₃ nanocatalyst used in hydrogen production via methanol steam reforming for fuel cell applications", *Energy Conversion and Management*, vol. 87, pp. 928-937, 2014, doi: /10.1016/j.enconman.2014.07.058.

- [5] J. Liu, J. Shi, D. He, Q. Zhang, X. Wu, Y. Liang, and Q. Zhu, "Surface active structure of ultra-fine Cu/ZrO₂ catalysts used for the CO₂+ H₂ to methanol reaction", *Applied Catalysis A: General*, vol. 218, no. 1-2, pp. 113-119, 2001, doi: 10.1016/S0926-860X(01)00625-1.
- [6] S. F. Zakeritabar, M. Jahanshahi, and M. Peyravi, "Photocatalytic Behavior of Induced Membrane by ZrO₂-SnO₂ Nanocomposite for Pharmaceutical Wastewater Treatment", *Catalysis Letters*, vol. 148, no. 3, pp. 882-893, 2018, doi: 10.1007/s10562-018-2303-x.
- [7] S. Naz, A. Gul, M. Zia, and R. Javed, "Synthesis, biomedical applications, and toxicity of CuO nanoparticles", *Applied Microbiology and Biotechnology*, vol. 107, no. 4, pp. 1039-1061, 2023, doi: 10.1007/s00253-023-12364-z.
- [8] S. F. Shaikh ve Z. A. Shaikh, "Electrospinning of metal oxide nanostructures", *Solution Methods for Metal Oxide Nanostructures*, Elsevier, pp. 125-152, 2023, doi: 10.1016/B978-0-12-824353-4.00009-9.
- [9] T. Zhao, Y. Zheng, X. Zhang, D. Teng, Y. Xu, and Y. Zeng, "Design of helical groove/hollow nanofibers via tri-fluid electrospinning", *Materials & Design*, vol. 205, pp. 109705, 2021, doi: 10.1016/j.matdes.2021.109705.
- [10] A. Yarin, "Coaxial electrospinning and emulsion electrospinning of core-shell fibers", *Polymers for Advanced Technologies*, vol. 22, no. 3, pp. 310-317, 2011, doi: 10.1002/pat.1781.
- [11] Y. Zhang, Y. Feng, Z. Huang, S. Ramakrishna, and C. Lim, "Fabrication of porous electrospun nanofibres", *Nanotechnology*, vol. 17, no. 3, pp. 901, 2006, doi: 10.1088/0957-4484/17/3/047.
- [12] Z. Çetinkaya, E. Güneş, and İ. Şavkliyildiz, "Investigation of biochemical properties of flash sintered ZrO₂-SnO₂ nanofibers", *Materials Chemistry and Physics*, vol. 293, pp. 126900, 2023, doi: 10.1016/j.matchemphys.2022.126900.
- [13] R. O. İjeh, C. O. Ugwuoke, E. B. Ugwu, S. O. Aisida, and F. I. Ezema, "Structural, optical and magnetic properties of Cu-doped ZrO₂ films synthesized by electrodeposition method", *Ceramics International*, vol. 48, no. 4, pp. 4686-4692, 2022, doi: 10.1016/j.ceramint.2021.11.0041.
- [14] K. V. Özdokur, Ç. C. Koçak, Ç. Eden, Z. Demir, Ç. Çirak, E. Yavuz, B. Çağlar, "Gold-Nanoparticles-Decorated ZrO₂-CuO Nanocomposites: Synthesis, Characterization and A Novel Platform for Electrocatalytic Formaldehyde Oxidation", *Chemistryselect*, vol. 7, no 28, pp. e202201411, 2022, doi: 10.1002/slct.202201411.
- [15] E. S. Borovinskaya, S. Trebbin, F. Alscher, and C. Breitkopf, "Synthesis, modification, and characterization of CuO/ZnO/ZrO₂ mixed metal oxide catalysts for CO₂/H₂ conversion", *Catalysts*, vol. 9, no. 12, pp. 1037, 2019, doi: 10.3390/catal9121037.
- [16] A. Figini Albisetti, C. A. Biffi, and A. Tuissi, "Synthesis and structural analysis of Copper-Zirconium oxide", *Metals*, vol. 6, no. 9, pp. 195, 2016, doi: 10.3390/met6090195.
- [17] S. Azhar, K. S. Ahmad, I. Abrahams, W. Lin, R. K. Gupta, and A. El-marghany, "Synthesis of phyto-mediated CuO-ZrO₂ nanocomposite and investigation of their role as electrode material for supercapacitor and water splitting studies", *Journal of Materials Research*, vol. 38, pp. 4937-4950, 2023, doi: 10.1557/s43578-023-01204-5.
- [18] T. Athar, S. K. Vishwakarma, A. Bardia, R. Alabass, A. Alqarlosy, and A. A. Khan, "Green approach for the synthesis and characterization of ZrSnO₄ nanopowder", *Applied Nanoscience*, vol. 6, no. 5, pp. 767-777, 2016, doi: 10.1007/s13204-015-0488-5.
- [19] N. Scotti, F. Bossola, F. Zaccheria, and N. Ravasio, "Copper-zirconia catalysts: Powerful multifunctional catalytic tools to approach sustainable processes", *Catalysts*, vol. 10, no. 2, pp. 168, 2020, doi: 10.3390/catal10020168.
- [20] K. Kaviyarasu, L. Kotsedi, Aline Simo, Xolile Fuku, Genene T. Mola, J. Kennedy, M. Maaza, "Photocatalytic activity of ZrO₂ doped lead dioxide nanocomposites: Investigation of structural and optical microscopy of RhB organic dye", *Applied Surface Science*, vol. 421, pp. 234-239, 2017, doi: 10.1016/j.apsusc.2016.11.149.

- [21] A. K. Arora, V. S. Jaswal, K. Singh, and R. Singh, "Applications of metal/mixed metal oxides as photocatalyst:(A review)", *Oriental Journal of Chemistry*, vol. 32, no. 4, pp. 2035, 2016, doi: 10.13005/ojc/320430.
- [22] V. Anitha, S. S. Lekshmy, and K. Joy, "Effect of annealing temperature on optical and electrical properties of ZrO₂-SnO₂ nanocomposite thin films", *Journal of Materials Science: Materials in Electronics*, vol. 24, pp. 4340-4345, 2013, doi: 10.1007/s10854-013-1408-7.



DETERMINATION BY NUMERICAL MODELING OF STRESS-STRAIN VARIATIONS RESULTING FROM GALLERY CROSS-SECTION CHANGES IN A LONGWALL TOP COAL CAVING PANEL

^{1,*} Mehmet MESUTOĞLU , ¹ İhsan ÖZKAN , ² Alfonso RODRIGUEZ-DONO 

¹ Konya Technical University, Engineering and Natural Sciences Faculty, Mining Engineering Department,
Konya, TÜRKİYE

² Universitat Politècnica de Catalunya (UPC), Civil and Environmental Engineering Department, Barcelona,
SPAIN

¹ mmesutoglu@ktun.edu.tr, ¹ iozkan@ktun.edu.tr, ² alfonso.rodriquez@upc.edu

Highlights

- Significance of sustainability and efficiency in global coal mining.
- Transition to deeper underground mining due to increased coal demand.
- Numerical modeling crucial for understanding and addressing gallery cross-sectional variation.
- Understanding the impact of gallery cross-sectional variation is crucial for safe and efficient mining operations.



DETERMINATION BY NUMERICAL MODELING OF STRESS-STRAIN VARIATIONS RESULTING FROM GALLERY CROSS-SECTION CHANGES IN A LONGWALL TOP COAL CAVING PANEL

^{1,*} Mehmet MESUTOĞLU , ¹ İhsan ÖZKAN , ² Alfonso RODRIGUEZ-DONO 

¹ Konya Technical University, Engineering and Natural Sciences Faculty, Mining Engineering Department,
Konya, TÜRKİYE

² Universitat Politècnica de Catalunya (UPC), Civil and Environmental Engineering Department, Barcelona,
SPAIN

¹ mmesutoglu@ktun.edu.tr, ¹ iozkan@ktun.edu.tr, ² alfonso.rodriguez@upc.edu

(Received: 27.12.2023; Accepted in Revised Form: 07.02.2024)

ABSTRACT: As a major pillar of global energy production, coal mining requires continuous advancements in efficiency to contribute to the broader goal of energy sustainability, all the while the shift towards more sustainable energy sources is underway. Mechanized excavation systems employed in underground coal mines, particularly within the longwall mining method, enable high-tonnage coal production. The Longwall Top Coal Caving (LTCC) method, one of the longwall mining techniques, has been developed for the effective extraction of coal from thick coal seams. However, as mining operations delve deeper, various complex issues, such as gallery cross-sectional variation, emerge. Gallery cross-sectional variation can increase the risk of collapse by affecting the stress distribution in the rock mass, posing a threat to worker safety. This study centers on the numerical modeling and analysis of gallery cross-sectional variation in the Ömerler underground mine, operated by the Turkish Coal Enterprises (TKI), West Lignite Enterprise (GLI). To achieve this objective, an extensive database was established through field and laboratory rock mechanics studies. This database was then utilized in the Fast Lagrangian Analysis of Continua 3D (FLAC3D) (v6.0) program to simulate the cross-sectional variations of the A6 panel in the Ömerler underground mine. The numerical simulation results provide valuable insights into the secondary stress-deformation changes associated with gallery cross-sectional variation.

Keywords: Gallery cross-section, FLAC 3D, Longwall mining, Numerical modeling, Strata control

1. INTRODUCTION

As coal mining remains a crucial component of global energy production, the significance of sustainability and efficiency in this sector is continuously on the rise [1,2]. In 2022, global coal consumption experienced a notable surge of 3.3%, reaching a total of 8.3 billion tons [3]. The ongoing increase in global coal demand has led to a necessity for a shift toward deeper underground mining practices due to diminishing open-pit reserves [4]. This transition imposes a compelling demand on the coal mining industry to improve both sustainability and operational efficiency.

In recent years, the implementation of mechanized excavation systems, particularly in the longwall mining method within underground coal mines, has facilitated high-tonnage coal production [5,6,7]. The Longwall Top Coal Caving (LTCC) method, one of the longwall mining techniques, has been specifically developed for underground coal mining, enabling the effective and efficient extraction of thick coal seams [8,9,10,11,12].

LTCC is considered a safer alternative compared to traditional longwall mining methods [11,13,14]. The controlled collapse process enhances worker safety. However, as mining operations employing the LTCC method delve deeper, they bring forth various complex challenges. One of these challenges is the increasingly significant gallery cross-sectional variation as mining progresses to deeper levels. Gallery cross-sectional variation refers to the alteration of dimensions, shape, or position of the mine gallery as it advances into the depths. It can significantly influence the stress distribution of rock masses and also can

*Corresponding Author: Mehmet MESUTOĞLU, mmesutoglu@ktun.edu.tr

increase the risk of collapse, jeopardizing the safety of mine workers. Additionally, gallery cross-sectional variation has the potential to escalate mining operational costs and negatively impact productivity. Miners seek innovative and secure solutions to overcome this challenge and extract coal reserves as efficiently as possible.

The numerical modeling and analysis of gallery cross-sectional variation can play a crucial role in understanding and addressing these issues. Furthermore, such analyses can serve as a critical tool in finding ways to make mining operations more efficient and safer [15, 16]. Therefore, gallery cross-sectional variation has become an important topic to be addressed in the context of modern coal mining.

An example of the mentioned problem occurred during the implementation of the LTCC method in the Ömerler underground mine, operated by the West Lignite Enterprise (GLI), a subsidiary of Turkish Coal Enterprises (TKI). During coal production and advancement in the production direction within the mine, a situation arises where the transition support units, in the sizing of the gallery, require scanning and widening operations, essentially being unable to pass through the horseshoe gallery sections. As a result, pressures within the face increase during production, often necessitating additional reinforcement. This condition, along with scanning operations, leads to time loss and creates problems for the smooth progress of the waiting coal face.

This paper presents the establishment of a comprehensive database through in-situ and laboratory rock mechanics studies to facilitate the numerical modeling of potential cross-sectional variations in the trackways in the existing conditions of the Ömerler underground mine. Utilizing this extensive database, the FLAC3D (v6.0) program is employed to accurately simulate the secondary stress-deformation alterations that could arise during the transition from a horseshoe cross-section to a trapezoidal cross-section for the A6 panel. The outcomes of these numerical simulations provide valuable insights into the anticipated changes in secondary stress-deformation characteristics.

2. STUDY SITE

TKI-GLI Ömerler Underground coal mine is located in the town of Tunçbilek, (Tavşanlı district of Kütahya province) in Turkey (Fig. 1).

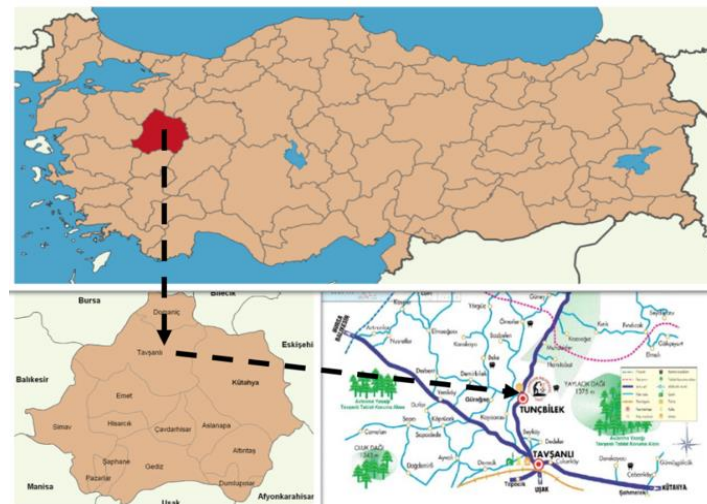


Figure 1. Location of study site

The rock units within the Tunçbilek series are grouped into three main categories, namely Shale, Calcareous Marl, and Marl. The Shale formation, which surrounds the coal seam, is also subdivided into three subgroups. These subgroups consist of the soft shale layer located immediately above the coal seam with a thickness ranging from 20 to 50 cm, the roof shale forming the main roof rock of this formation, and the floor shale formations situated beneath the coal seam (Fig 2).

In the GLI Tunçbilek coal basin, underground coal production has been carried out in the Ömerler-A field. In this underground mine, a fully mechanized mining system is used, and coal extraction is performed using the LTCC method. The thick coal seam, averaging 8 m in thickness, is excavated using a single-pass method for the lower 3.5 m, while the remaining approximately 5 m at the roof level is extracted through the backfilling process, (controlled caving operation), (Fig 2).

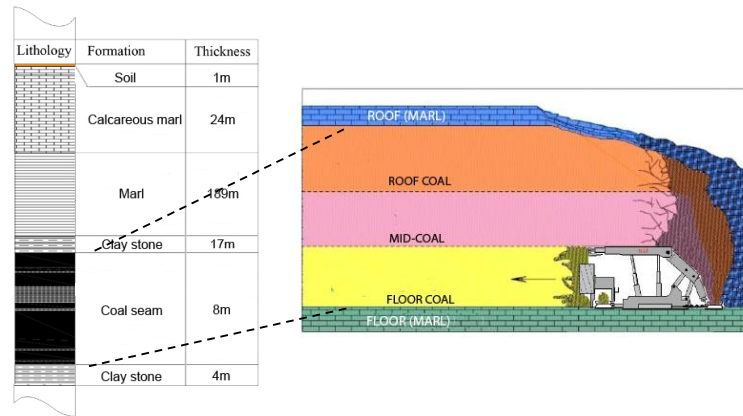


Figure 2. Lithology of geological structure

In the basin, strata have generally dip angles ranging from 5 to 20° toward the northeast. The coal reserve within the study area is estimated to be around 18 million tons. The coal seam thickness varies between 5-12 m, with an average thickness of 8 m [17]. The coal seam contains clay partings of approximately 15-30 cm thickness at various levels. The deepest working section in the underground mine is located at a sea level elevation of +469, and the thickness of the overlying strata is approximately 330 m. The study area is the A6 longwall panel in the Tunçbilek Ömerler underground coal mine (Fig 3) in this research. Rock mass and material property determination studies for coal and surrounding rocks were carried out in the A1, A2, and A6 panels.

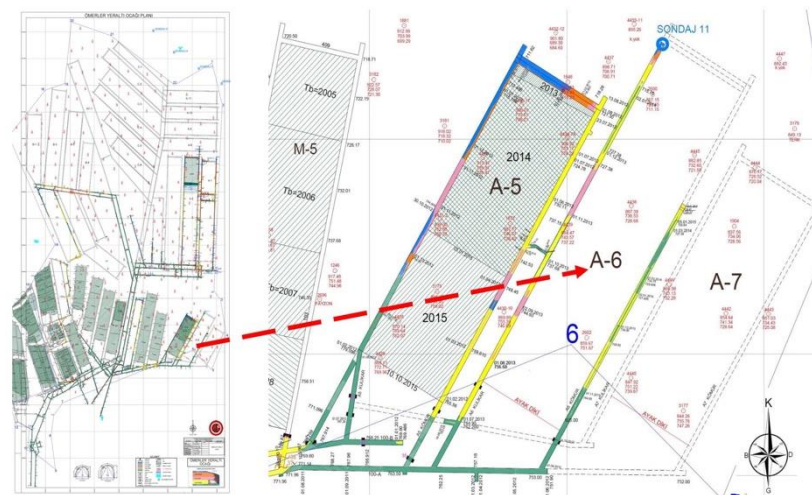


Figure 3. The view of the A6 longwall panel considered in gallery cross-section design studies on the mine layout

3. DETERMINATION OF ROCK MASS AND ROCK MATERIAL PROPERTIES

In the design studies aiming to analyze the cross-sectional variation of the A6 longwall panel galleries

in the Ömerler underground coal mine, on-site and laboratory investigations were conducted to determine rock mass and material properties. These studies encompassed not only the A6 longwall panel where the implementation occurred but also the A1 and A2 longwall panels, where preparatory and production activities are currently in progress.

Underground drilling operations and block extraction studies were carried out in specific underground areas to determine rock mass and material properties, contributing to classification studies. Drilling activities were conducted in the production panel in four directions. Additionally, 50 blocks were extracted from the A1 and A2 panels and transported to the laboratory for sample collection (Fig 4). Moreover, Schmidt hammer rebound hardness tests, point load strength index tests, and plate loading tests were conducted in the A1, A2, and A6 panels.



Figure 4. Typical images from the drilling and block extraction operations conducted in the Ömerler underground mine

All rock mechanics tests were performed on the rock material samples obtained from the blocks transported to the laboratory and the drilling cores. The resulting database is presented in Table 1 [18,19]. Field-based GSI classification studies were conducted in the A1 preparatory gallery for rock mass classifications. The determined values, along with results from other rock mass classification systems, were calculated and presented in Table 2 [18,19].

Table 1. Rock material properties of Ömerler underground mine

Data	Symbol, Unit	Coal	Roof Rock	Floor Rock
Uniaxial compressive strength (UCS)	σ_{ci} (MPa)	8.84	10.66	12.04
Tensile strength (Indirect-Brazilian)	σ_t (MPa)	2.30	8.31	8.91
Cohesion	c (MPa)	0.401	0.487	0.419
Friction angle	φ (°)	31.03	24.32	25.44
Modulus of elasticity	E (MPa)	2663	3198	3612
Poisson ratio	ν (-)	0.18	0.264	0.27
Bulk density	ρ (gr/cm ³)	1.26	2.00	2.12
Natural unit weight	γ (kN/m ³)	12.40	19.60	21.7
Slake durability index	I_{d2} (%)	91.00	98.89	98.55
Point load strength index	$I_{s(50)}$ (MPa)	0.51	0.70	2.38

The rock mechanics studies revealed that the material and mass properties of the coal unit were weaker compared to the roof and floor units. It was determined that the floor unit exhibited better mechanical properties.

Table 2. Rock mass properties of the Ömerler underground mine

Data	Symbol, Unit	Coal	Roof Rock	Floor Rock
Geological Strength Index	GSI	35	43	47
Rock Mass Rating	RMR	32	44	47
Rock Quality Designation	RQD	50	60	70
Quantitative Rock Mass Rating	Q	0.37	0.99	1.16
Uniaxial compressive strength	σ_{cm} (MPa)	1.481	1.244	1.543
Tensile strength	σ_{tm} (MPa)	0.004	0.024	0.037
Cohesion	c_m (MPa)	0.401	0.487	0.419
Friction angle	φ_m (°)	31.03	24.32	25.44
Modulus of elasticity	E_m (MPa)	302	625.99	920.07
Poisson ratio	ν	0.18	0.264	0.27
Bulk modulus ($K = [E/3(1-2\nu)]$)	K (MPa)	157.29	442.08	666.72
Shear modulus ($G = [E/2(1+\nu)]$)	G (MPa)	127.97	247.62	362.23

To make accurate predictions for the stability of underground openings, the mechanical properties of the rock mass and measurements of the primary stresses in the environment are necessary [20]. In this context, primary stress analysis studies were conducted within the A1 longwall panel of the Ömerler underground coal mine (Fig 5). Following the approach proposed by Aydan [21] for determining the primary in-situ stresses using the fault slip method, the analysis results indicated that the maximum horizontal stress is approximately oriented in the north-south direction. Furthermore, it was determined that at a depth of 300 meters, the largest horizontal primary stress ($P_H = 6.74$ MPa) in the A1 panel is oriented parallel to the gate axis.

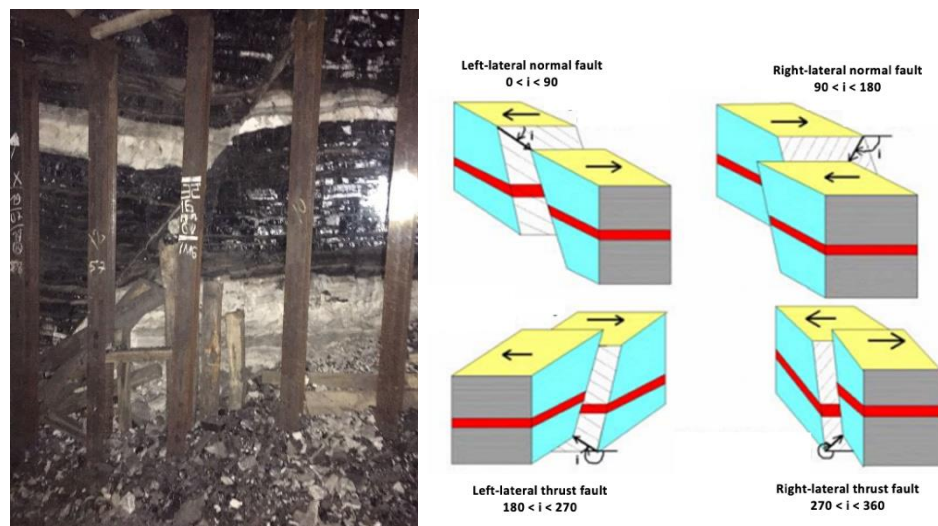


Figure 5. (a) Measurement of primary in-situ stress in a coal seam fault example (b) Definition and measurement of fault lines [21]

3.1. Dimensioning Studies for Gallery Cross-Sectional Change

TKI-GLI operation plans to open new galleries in trapezoidal section in the Ömerler underground mine. The reason for this is that the horseshoe section is not suitable for the comfortable execution of the support units, especially at the foot beginnings in the production panels. The second reason is that the useful cross-sectional area of the horseshoe gallery section is not satisfactory for the operations in the mine. For these reasons, the gallery cross-sectional design studies for the A6 panel of the Ömerler underground coal mine have been modeled in three dimensions for both horseshoe and trapezoidal sections. The stress-

deformation variations occurring in the A6 headgate between the trapezoidal and horseshoe sections have been examined.

Figure 6 presents the existing gallery section of the Ömerler underground coal mine operated by TKI-GLI. According to the dimensions specified here, the width of the gallery is 4600 mm, and the gallery height is 3970 mm. Accordingly, the current gallery section is 18.26 m². However, due to closures occurring in the gallery opening, this gallery section can drop to approximately 13 m² in some areas of the mine.

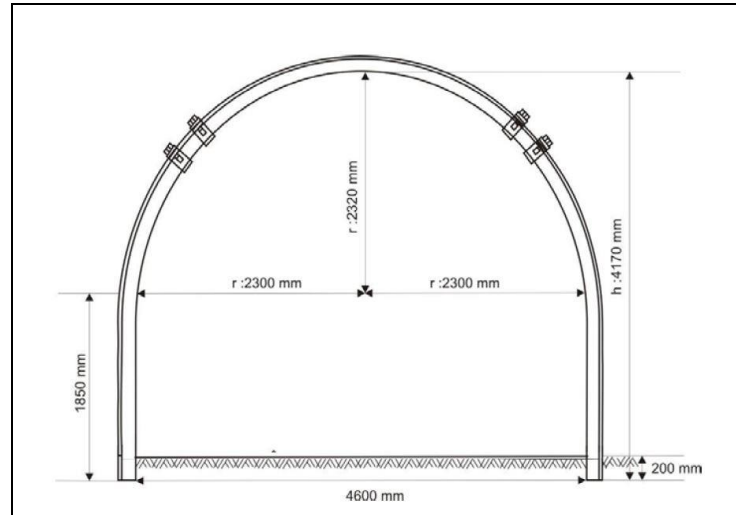


Figure 6. Dimensions of the existing horseshoe gallery section at the Ömerler coal mine

During the dimensioning studies for the trapezoidal gallery section, the opinions of the operation officials were taken, and the situation of the openings in the trapezoidal section opened in some parts of the existing base roads was considered. In addition, the optimum expansion of the useful cross-sectional area has also been a determining factor in the dimensioning of the trapezoidal gallery section to be opened.

In the dimensioning process of the gallery section in underground openings, it is obvious that the mine must be subjected to ventilation in an optimum manner. Therefore, in the dimensioning studies of the gallery section, a ventilation project carried out in the Ömerler underground mine in 2017 was considered. In the ventilation project conducted by Fişne et al. [22], it was stated that the required air velocity for the Ömerler underground mine was 0.5 m/s in the base roads and 1.0 m/s inside the foot. It was also mentioned that the calculated required air volume for the mine is 2591 m³/min, and the 4040 m³/min of clean air entering the mine would be sufficient for the mine. Therefore, it is seen that the newly dimensioned trapezoidal section added to the bottom row of Table 3 is in accordance with the calculated clean air (required) volume for the mine.

Figure 7 presents the trapezoidal opening dimensions designed during the transition from the existing horseshoe section to the trapezoidal section for the base roads of the Ömerler underground mine. As seen in Figure 7, the gallery width was determined as 6000 mm, gallery height as 4000 mm, and trapezoidal section upper width as 5000 mm to expand the useful cross-sectional area of the gallery opening. In this case, the gallery section is calculated as 22 m². The opening dimensions considered in the empirical and numerical analysis studies for the trapezoidal section are presented as shown in Figure 7.

Table 3. Air requirements according to air velocity limits for the Ömerler coal mine [22]

Location	Gallery Section (m ²)	Min. Air Velocity (m/s)	Req. Air Volume (m ³ /min)
A1 Headgate	16.00	1.0	870
A1 Tailgate	13.75	0.5	480
A2 Coal Face	14.50	0.5	413
A6 Headgate	13.80	0.5	414
A6 Tailgate	13.80	0.5	414
Trapezoidal Section	22.00	0.5	660

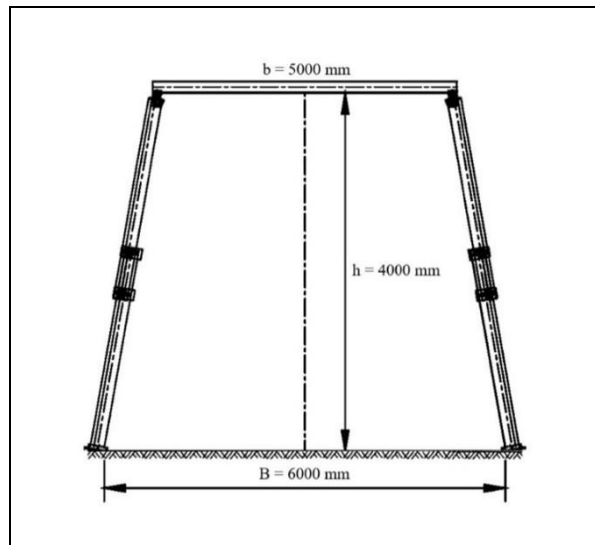


Figure 7. Dimensioning of the trapezoidal gallery section designed for numerical modeling studies

4. NUMERICAL MODELING STUDIES

4.1. Modeling Procedure

The three-dimensional numerical model of the A6 longwall panel of the Ömerler underground coal mine, where the steel set support system is applied to the main roadways and gateroads of the panels, has been created using FLAC 3D software. Two different scenarios were considered in the analysis of the models. The first scenario involves the opening of the gateroads and the implementation of support system in the A6 longwall panel's tunnel position. The second scenario involves the modeling of the coal production position, including the opening of the face, placement of face support units (self-advancing hydraulic roof support units), advancement of the face, and caving coal from the back of the face. For both positions in the created models, stress and deformation variations were examined for both trapezoidal and horseshoe sections due to the load imposed by the gateroad support units.

The coal seam in the region where the A6 longwall panel is located is approximately 161 m deep from the surface. The underlying shale, which is the base rock unit beneath the coal seam with a thickness of about 11 m, is defined in the model geometry as 39 m. The model geometry is defined as 200 m in the z-direction. The limestone unit, defined as tuffstone immediately above the coal seam with a thickness of about 140 m, is considered based on drilling logs obtained from the mine. The marl formation, consisting of limestone shale interbedded with sandstone siltstone bands, and the limestone shale roof, which together make up a large part of the 140 m layers above the coal seam, are defined in the model as the same unit due to similar mass and material properties. No separate boundary is defined for the 6 m dolerite rock unit, which constitutes approximately 4.2% of the 140 m roof unit. The 10 m topsoil fill material above the layers in the coal roof is also defined in the models.

The actual length of the A6 longwall panel is approximately 450 m. In the model, the geometry

representing the length of the panel is defined in the +y direction as 500 m. In the initial stage of modeling, which involves the opening of galleries and the implementation of support units, the gateroads were driven for 500 m. The face of the panel is defined at the 450th m in the +y direction in the model geometry, and the remaining 50 m behind it are designated as the compressed caved zone to be defined after the stages of face excavation and supporting, for the determination of the effects of the compressed caved zone and the dynamic caved zone resulting from the advancement of the face.

The other regions of the model geometry are divided into 5m and 10 m grids according to the sensitivity of the regions where stress and deformation are to be examined. The created model, in its final form, includes a total of 361,665 zones and 376,320 grid points. The model geometry created in the FLAC 3D program for the A6 longwall panel, with detailed information provided above, is generally illustrated in Figure 8.

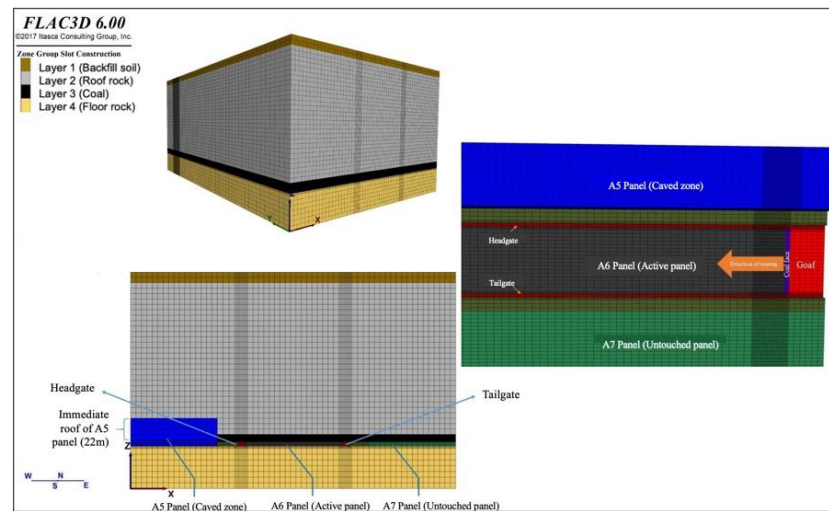


Figure 8. The geometry and details of the model created in FLAC 3D

The boundary conditions in a numerical model consist of the values of field variables (e.g., stress and displacement) that are prescribed at the boundary of the numerical grid. Boundaries are of two categories: real and artificial. Real boundaries exist in the physical object being modeled (e.g., a tunnel surface or the ground surface). Artificial boundaries do not exist in reality, but they must be introduced to enclose the chosen number of zones.

While determining the boundary conditions of the Ömerler underground coal mine model, roller boundaries are placed on the left, right, front, and rear boundaries of the grid. The bottom of the grid is fixed. The results obtained from the primary stress analyses carried out in the in-situ were defined in the model and $K_0 = 0.473$ (σ_h / σ_v) was assigned as the initial condition and gravity effect was also defined in the model.

In the model which was created by using FLAC 3D program of Ömerler underground quarry A6 longwall panel, properties of gob materials were defined and some equations were used in literature. The mechanical behavior of the gob is defined by the double-yield model in which the gob is simulated in FLAC 3D. Pappas and Mark [23] examined the behavior of longwall gob material by laboratory tests and stated that the equation presented by Salamon [24] in the gob model (1990) gave the closest results to laboratory tests. In the Salamon gob model [24], the following equation is presented (Equation 1).

$$\sigma = \frac{E_0 \varepsilon}{1 - \varepsilon / \varepsilon_m} \quad (1)$$

In Equation 1, σ ; the uniaxial stress (MPa) over the material ε ; unit deformation of the material under stresses; E_0 ; represents the initial tangent module (MPa); ε_m represents the maximum unit deformation

that can occur in the compacted rock material.

In the modeling studies, the equation given above were used to determine the mechanical behavior of the gob. Depending on the face advancement, the A6 panel is assigned a double-yield constitutive model after every 1m advance to the 1m section behind the coal face. Thus, in the model, in the early stages of face advancement, the gob region would represent a region that was broken and collapsed, unable to withstand the pressure from the roof. In this region, the gob will squeeze slowly, leading to an increase roof stress.

In the A6 longwall panel model, the resulting equation of the volumetric unit deformation behavior, deformation change values and FLAC 3D program output are determined in Table 5 and Equation 2.

$$\sigma = \frac{29.2\varepsilon}{1-6.25\varepsilon} \tag{2}$$

Table 5. Cap pressure for the double-yield model

Strain (m/m)	Stress (MPa)	Strain (m/m)	Stress (MPa)
0.00	0	0.08	4.67
0.01	0.31	0.09	6.01
0.02	0.67	0.10	7.79
0.03	1.08	0.11	10.28
0.04	1.56	0.12	14.02
0.05	2.12	0.13	20.25
0.06	2.80	0.14	32.70
0.07	3.63	0.15	70.08

In the modeling studies, when modeling the steel set for gateroads support, a beam structural element was used. In the models, the support element input parameters used the properties of the GI profile used in the Ömerler underground mine (Table 6).

Table 6. The model's input parameters for steel set support

Profile type	GI 140	
Section weight	41.6 kg/m	
Dimensions	h=140 mm b=110 mm	
Section area	0.0154 m ²	
I _x - I _y	1586 cm ⁴ 315cm ⁴	
Density	2701.3 kg/m ³	

4.2. Identifying Monitoring Points in the Model

Two separate models have been prepared for three-dimensional analyses of gateroads opened in horseshoe and trapezoidal sections. In both prepared models, varying stress-deformation values were obtained for both trapezoidal and horseshoe-section gateroads at the tunnel position where the gateroads are opened (Stage-1) and at the face advancement positions where coal production is carried out (Stage-2). For monitoring the stresses and deformations generated in the model, a total of 120 monitoring points has been set up. In the evaluation of numerical analysis results, two station points located above the headgate adjacent to panels A5 and A6 have been considered. These station points are U9 located at 300 m and U3 positioned at 429 m along the material gallery (Fig. 9).

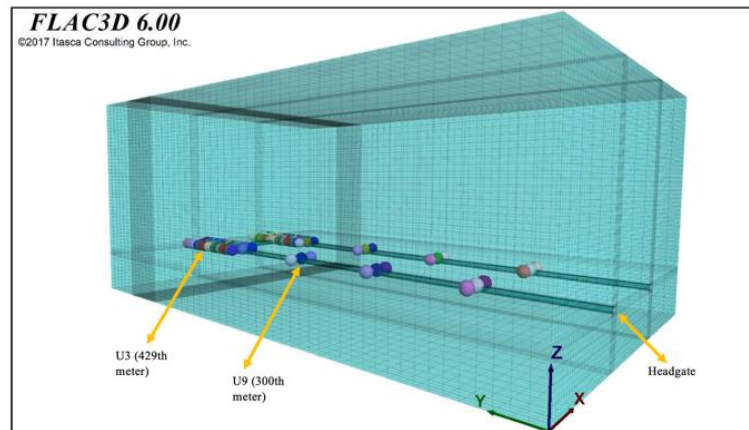


Figure 9. Location of the monitoring points on the numerical models

4.3. Assumptions and Constraints in the Model

During the modeling process, certain assumptions and constraints were considered. These are as follows:

- i. In the model studies, σ_1 is assumed to be vertical (in the $-z$ direction), and σ_2 and σ_3 are assumed to be horizontal (in the x and y directions).
- ii. The length of the A6 longwall panel, which is actually between 400 m- 450 m, was taken as 500 m in the y -direction in the model.
- iii. Material properties related to subsidence were determined using some equations available in the literature.
- iv. For defining the support units in the model, the self-advancing hydraulic roof support units were represented with shell structural elements, and the steel set support system with beam structural elements.
- v. The dip angle of the coal seam where the A6 longwall panel is located was assumed to be 0° in the model.
- vi. The groundwater was neglected in the underground water modeling studies

5. RESULT AND DISCUSSION

The gateroads of the TKI-GLI Ömerler underground mine A6 longwall panel were numerically modeled separately in horseshoe and trapezoidal sections. The results obtained for both gallery sections, contingent upon the gateroad excavation (Stage-1) and the excavation of a total of 18 m of coal of 1 m inside the coal face and the removal of the back coal (Stage-2) are presented separately below.

5.1. Numerical Analysis Results for the Horseshoe Cross Section

Throughout the process from the beginning of the excavation in the A6 gateroad with a horseshoe section until the completion of all excavation and support operations in the gateroad (Stage-1), the vertical displacement and secondary stress values at monitoring point U9, positioned at the 300th meter of the upper gateroad as schematically shown in Figure 9, were determined using FLAC 3D.

The model outputs for this condition are presented in Figure 10. Additionally, the vertical displacement and secondary stress values observed in the model outputs are presented in Table 6.

The vertical displacement and secondary stress values at monitoring point U3, located at the 429th meter of the upper gateroad and shown schematically in Figure 9, were determined using FLAC 3D for Stage-2 (Figure 11 and Table 7).

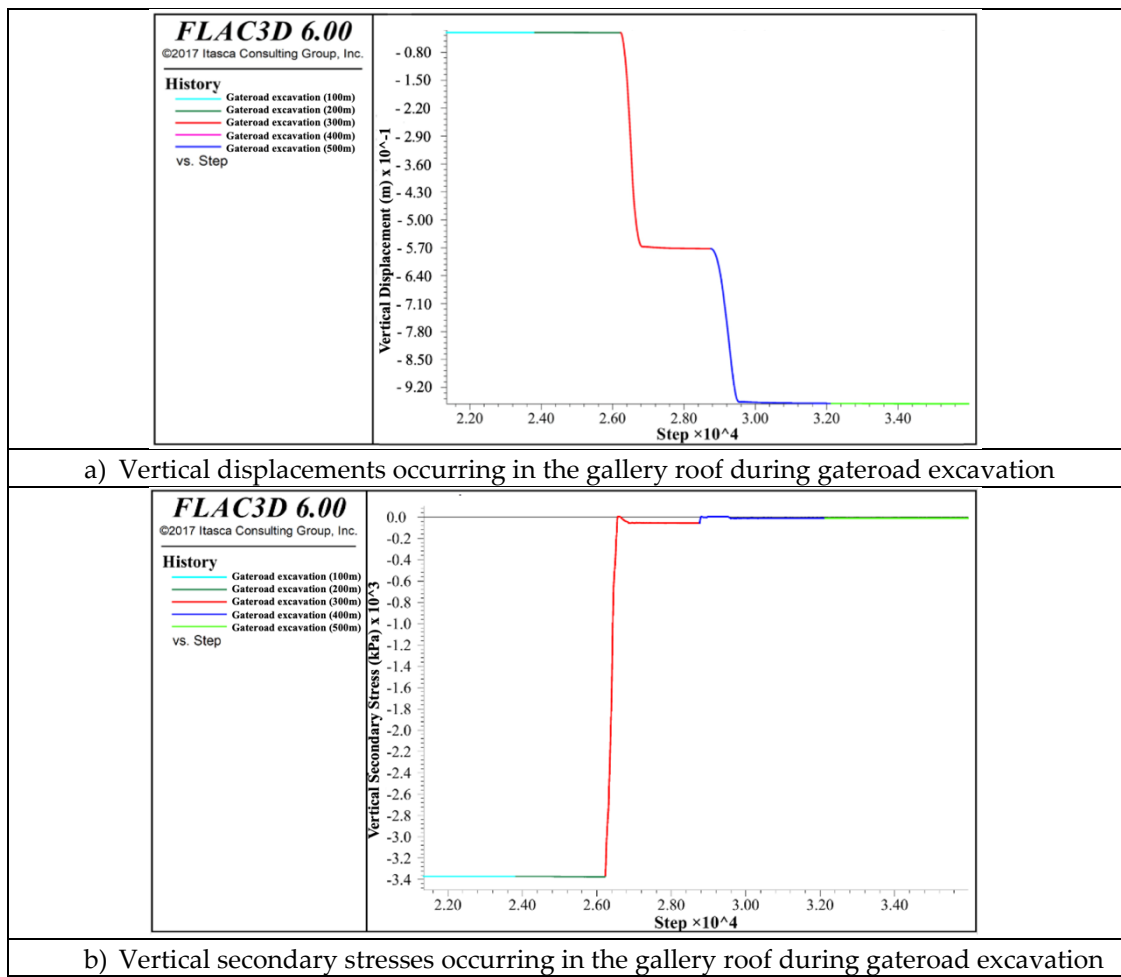


Figure 10. Vertical displacements and vertical secondary stresses for the horseshoe cross-section excavation model (U9)

Table 6. Vertical displacements and vertical secondary stress values of U9 for the horseshoe cross-section

Gallery Excavation	Monitoring Point U9	Monitoring Point U9
L (m)	U (mm)	P (kPa)
0	-6.5*	-3370.00*
50	-6.5	-3367.50
100	-6.5	-3365.00
150	-6.5	-3362.50
200	-6.5	-3360.00
250	-30	-1600.00
300**	-57	-40.00
350	-76.6	-30.00
400	-96.2	-20.00
450	-96.2	-15.00
500	-96.2	-10.00

* The amount of vertical displacement and secondary stress resulting from initial conditions, in monitoring point U9.
 ** U9 monitoring point is located at the 300th meter of excavation.

As seen in Table 6 and Figure 10, it is observed that the vertical displacement and secondary stress values remain very low up to the first 200 m as the excavation face approaches the U9 monitoring point

located at the 300th meter of the gateroad. In this situation, with still 100 m remaining to reach the U9 monitoring point, the values remain close to the initial primary values in the field. However, as the excavation face approaches the U9 monitoring point at the 300th meter, vertical displacements and secondary stresses begin to change rapidly, reaching values of $U=57$ mm and $P=-40$ kPa when the excavation face reaches the U9 monitoring point (Table 6 and Figure 10).

The numerical outputs of FLAC 3D, illustrating the vertical displacement and secondary stress values at point U3 during the progress of the gateroad excavation up to the 18th meter (Stage-2) from the start of excavation in the A6 longwall panel are presented in Figure 11. Additionally, the vertical displacement and secondary stress values observed in the model outputs are provided in Table 7.

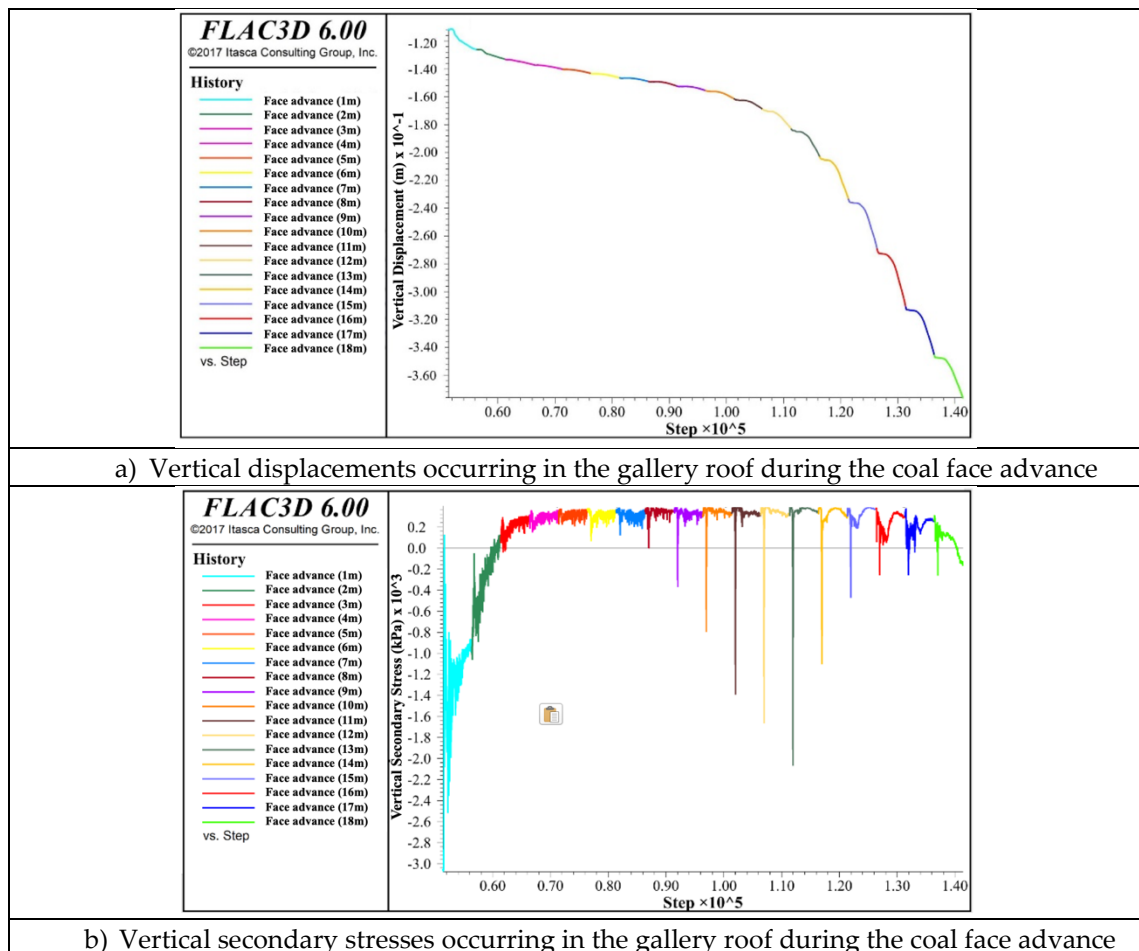


Figure 11. Vertical displacements and vertical secondary stresses for the horseshoe cross-section excavation model (U3)

As seen in Table 7 and Figure 11, the longwall advancement in the model was carried out in one-meter increments. The monitored point U3 is located at the 429th m of the gateroad. At the initial moment, this point is 18 m behind the coal face. As excavation activities progress in the longwall, displacements and stresses at the U3 monitoring point start to change. While displacements are relatively small in the first 10 m, they rapidly increase in the last 8 (Figure 11). When the longwall face advances 18 m and reaches the U3 monitoring point, the total displacement is $U=376$ mm. Stress changes initially exhibit tensile stresses and later evolve into compressive stresses. When the excavation face reaches the U3 monitoring point, the stress value in the gallery roof is $P=-1.8$ kPa (Table 7 and Figure 11).

Table 7. Vertical displacements and vertical secondary stress values of U3 for the horseshoe cross-section

Longwall Coal Face Advancement	Monitoring Point U3	Monitoring Point U3
L (m)	U (mm)	P (kPa)
0	-112.000	-30.800
1	-126.000	8.800
2	-132.000	2.800
3	-138.000	1.400
4	-140.000	0.800
5	-143.000	0.800
6	-145.000	0.800
7	-148.000	0.800
8	-152.000	0.700
9	-156.000	0.700
10	-162.000	0.700
11	-168.000	0.700
12	-184.000	0.700
13	-204.000	0.600
14	-238.000	1.200
15	-262.000	0.400
16	-312.000	1.200
17	-348.000	1.600
18*	-376.000	-1.800

* U3 monitoring point is located at the 429th meter of excavation.

5.2. Numerical Analysis Results for the Trapezoidal Cross Section

The gateroad with a trapezoidal cross-section for the TKI-GLI Ömerler underground coal mine A6 panel has been modeled. The vertical displacement and secondary stress values resulting from the gateroad excavation at the monitoring point U9, as shown in Figure 9, were determined using FLAC 3D for Stage-1. The FLAC 3D outputs depicting the vertical displacement and secondary stress values at the U9 monitoring point throughout the entire process, from the moment when no excavation activities have yet started in the gateroad to the completion of all excavation and support operations in the gateroad, are presented in Figure 12. The vertical displacement and secondary stress values seen in the model outputs in Figure 12 are provided in Table 8.

As seen in Table 8 and Figure 12, it is observed that, in the model, the vertical displacement and vertical secondary stress values remain very low for the first 200 meters as the excavation face approaches the monitoring point U9, located at the 300th meter of the gateroad. In this situation, where there is still 100 meters to U9 monitoring point, the values can be stated to be close to the initial primary values in the field. However, as the excavation face approaches the U9 monitoring point at the 300th meter, vertical displacements and secondary stresses rapidly increase, reaching U=161.1 mm and P=-53.38 kPa when the excavation face reaches the U9 monitoring point (Table 8 and Figure 12).

After the excavation face passes the U9 (300th meter) monitoring point in the gateroad, the vertical displacement continues to rapidly change up to 400 meters. When the gateroad excavation face reaches from 400 meters to 500 meters, it is understood that the vertical displacement values at the U9 point in the remaining part of the gateroad almost remain constant, reaching U=271.6 mm (Table 8 and Figure 12). Similarly, after the gateroad excavation face passes the U9 (300th meter) monitoring point, the vertical stress values continue to change very little up to 500 meters. When the gateroad excavation face reaches 500 meters, it is observed that the vertical stress values at the U9 point in the remaining part of the gateroad almost remain constant, reaching P=-8.93 kPa.

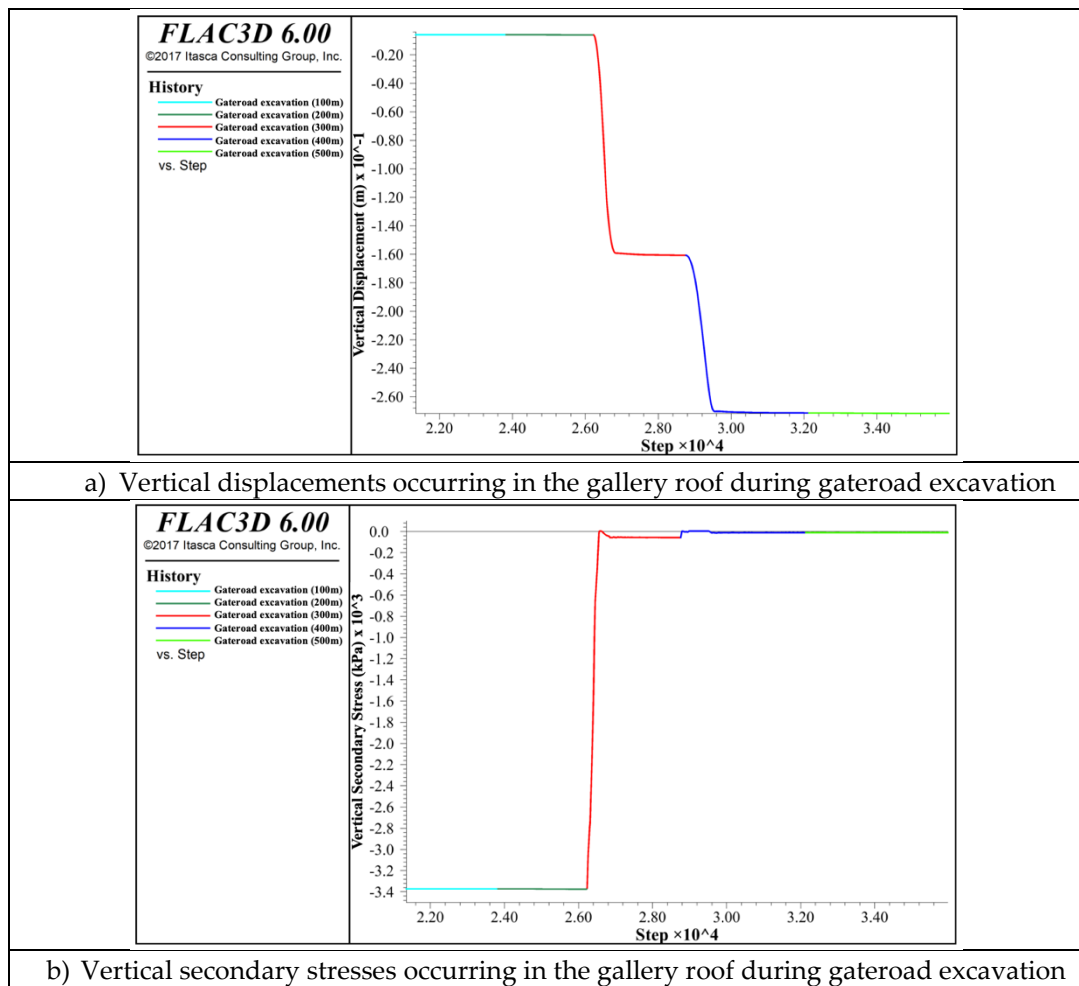


Figure 12. Vertical displacements and vertical secondary stresses for the trapezoidal cross-section excavation model(U9)

Table 8. Vertical displacements and vertical secondary stress values of U9 for the trapezoidal cross-section.

Gallery Excavation	Monitoring Point U9	Monitoring Point U9
L (m)	U (mm)	P (kPa)
0	-5.6*	-3371.26*
50	-5.7	-3371.68
100	-5.9	-3371.96
150	-6	-3373.66
200	-6.1	-3375.08
250	-84.4	-1574.55
300**	-161.1	-53.3806
350	-216.9	-8.93721
400	-270.85	-8.93725
450	-271.4	-8.9275
500	-271.6	-8.9275

* The amount of vertical displacement and secondary stress resulting from initial conditions, in monitoring point U9.

** U9 monitoring point is located at the 300th meter of excavation

The vertical displacement and secondary stress values at the U3 monitoring point, as shown schematically in Figure 9 and located at the 429th meter of the upper gateroad, were determined by FLAC

3D. The FLAC 3D outputs depicting the vertical displacement and secondary stress values at the U3 point during the process of gateroad excavation and the advancement of the 18-meter coal cutting within the longwall face in Stage-2, starting from the moment the preparatory activities were completed, are presented in Figure 13. The vertical displacement and secondary stress values observed in the model outputs are provided in Table 9.

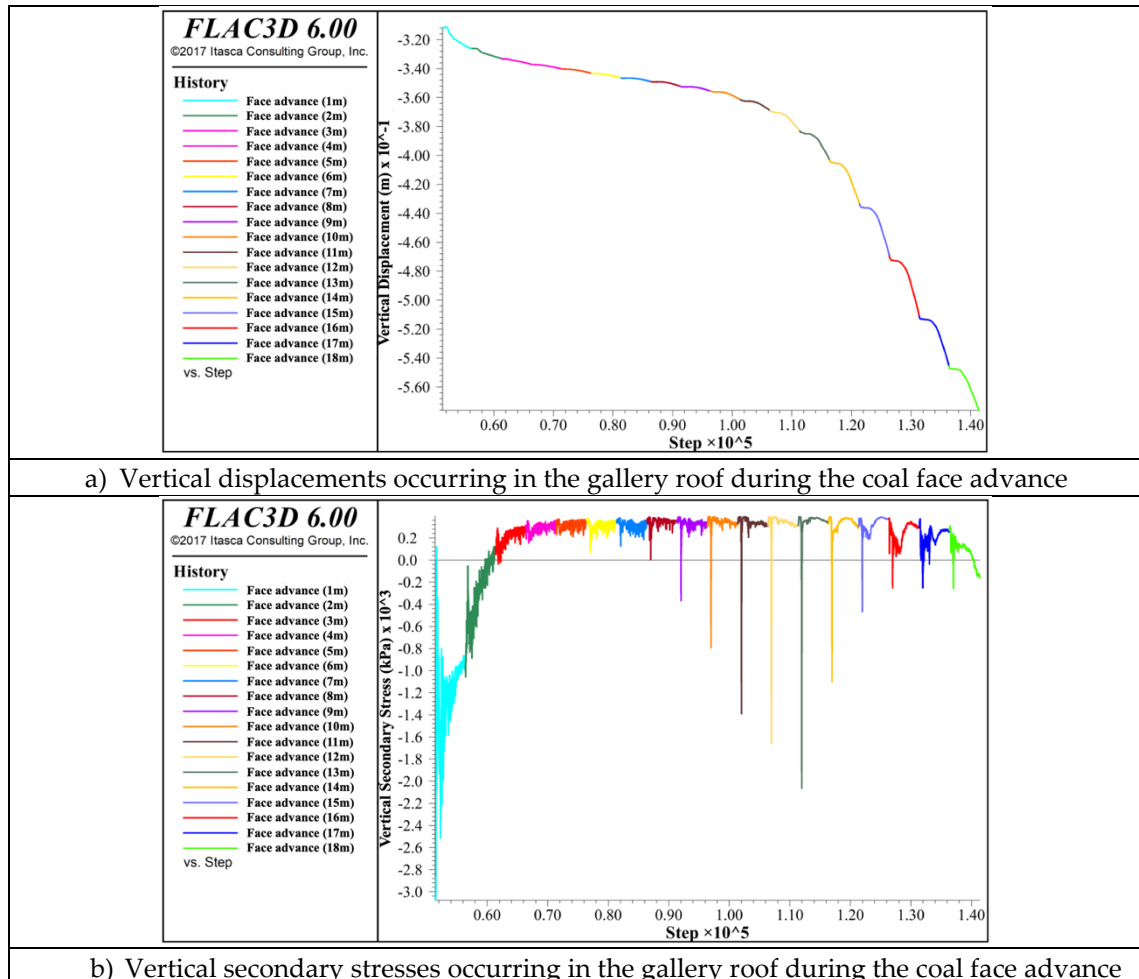


Figure 13. Vertical displacements and vertical secondary stresses for the trapezoidal cross-section excavation model (U3)

As seen in Table 9 and Figure 13, the longwall advancement in the model was carried out in one-meter increments. The monitored point U3 is located at the 429th m of the gateroad. At the initial moment, this point is 18 m behind the coal face. As excavation activities progress in the longwall, displacements and stresses at the U3 monitoring point start to change. While displacements are relatively small in the first 10 m, they rapidly increase in the last 8 (Figure 13). When the longwall face advances 18 m and reaches the U3 monitoring point, the total displacement is $U=575.77$ mm. Stress changes initially exhibit tensile stresses and later evolve into compressive stresses. When the excavation face reaches the U3 monitoring point, the stress value in the gallery roof is $P=-1.59$ kPa (Table 9 and Figure 13).

In the models prepared for the excavation of the gateroads of A6 panel, considering both horseshoe and trapezoidal cross-sections, it is assumed that Stage-1 precedes Stage-2, as indicated by their names. For Stage-1 in the model, the U9 monitoring point (300th m) has been tracked from the initiation of headgate excavation (0th m) until the completion of the gallery (500th m). Subsequently, for Stage-2, involving the top coal caving excavation, the U3 monitoring point is positioned just 18 meters ahead of the coal face (429th m). The process of approaching the coal face with 1-meter advancements and the time

until the caving is observed. Figures 14 and 15 were constructed using data from monitoring points U3 and U9 on the headgates.

Table 9. Vertical displacements and vertical secondary stress values of U3 for the trapezoidal cross-section

Longwall Coal Face Advancement	Monitoring Point U3	Monitoring Point U3
L (m)	U (mm)	P (kPa)
0	-311.345	-30.440
1	-325.976	-8.9457
2	-333.113	1.2661
3	-337.038	2.9086
4	-340.25	3.2656
5	-343.461	3.6941
6	-346.316	3.5513
7	-348.814	3.337
8	-352.026	3.348
9	-355.237	3.194
10	-361.304	3.265
11	-368.441	3.265
12	-382.714	3.194
13	-402.698	3.551
14	-433.03	2.980
15	-468.715	3.690
16	-510.466	2.980
17	-544.723	2.694
18	-575.769	-1.590

* U3 monitoring point is located at the 429th meter of excavation.

5.3. Comparison of Results obtained from Numerical Analysis for both Gallery Cross Sections

The graphs presented in Figures 14 and 15 analyze all processes covering Stage-1 and Stage-2 in three sections. The first section covers Stage-1 progress (excavation advancement stage: 0-10), the second section represents the initial 50 meters of excavation for the first coal caving on the panel (excavation advancement stage: 10-11), and the third section indicates activities during Stage-2 (excavation advancement stage: 11-29). These processes are sequentially defined independently of time.

In the first part of the prepared graphs, representing Stage-1, when the gallery excavation reached the 200th m, displacements and changes in original field stresses at the yet unexcavated U3 point (300th m) are observed in Figure 14 and Figure 15. It is evident that the change of displacements is significantly higher when the headgate is excavated in a trapezoidal cross-section compared to a horseshoe cross-section. Displacement values are 161.1 mm in the trapezoidal cross-section and 57 mm in the horseshoe cross-section. Similarly, the change in secondary stresses is -53.38 kPa for the trapezoidal section and -40 kPa for the horseshoe section. It is observed that less displacement occurs in the horseshoe cross-section for Stage-1, requiring less reinforcement for the excavation (excavation advancement stage: 0-10).

For the second part of the graphs, it is assumed that the first expected collapse occurred behind the panel, and the coal face on the backside of the collapse relaxed (excavation advancement stages: 10-11).

In the third part of the prepared graphs, representing Stage-2, it is observed that displacements on the gallery ceiling rapidly increase after the coal face advance total of 10 m at 1-m intervals (excavation advancement stage: 21). This increase is much greater in the trapezoidal cross-section. Displacement values are 575.77 mm in the trapezoidal section and 376 mm in the horseshoe section. Similarly, the change

in secondary stresses is -1.59 kPa for the trapezoidal cross-section and -1.8 kPa for the horseshoe cross-section (excavation advancement stage: 11-29).

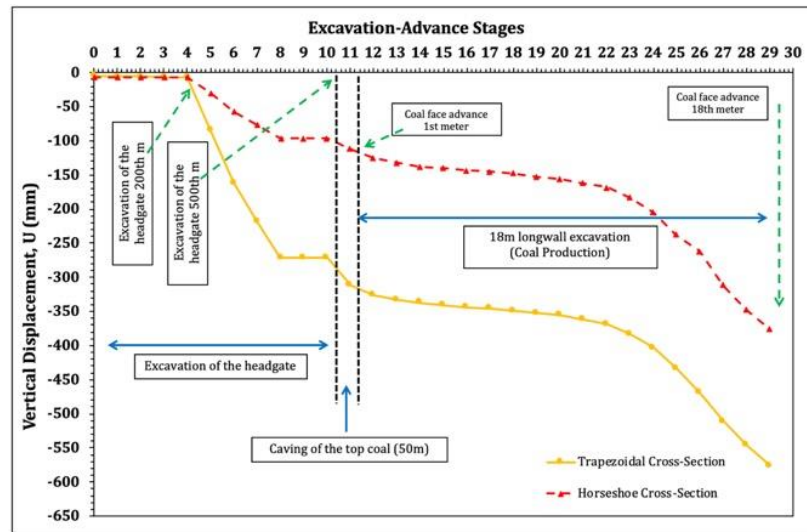


Figure 14. Vertical displacement changes in trapezoidal and horseshoe gallery cross-sections for all steps of Stage-1 and Stage-2 scenarios

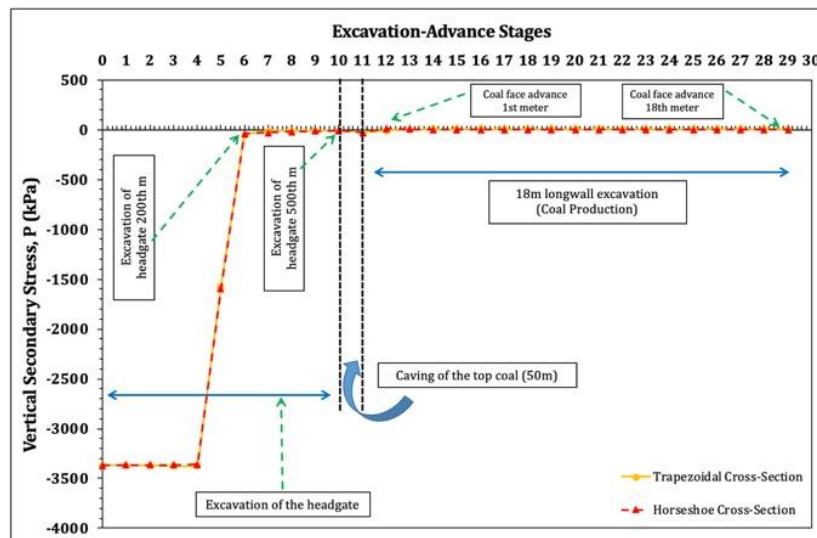


Figure 15. Vertical secondary stress changes in trapezoidal and horseshoe gallery cross-sections for all steps of Stage-1 and Stage-2 scenarios

6. CONCLUSIONS

The numerical modeling and analysis of gallery cross-sectional variation in the Ömerler underground mine, operated by the TKI-GLI, provided valuable insights into the stress-strain variations resulting from gallery cross-section changes in a LTCC panel. The study focused on the A6 panel and utilized the FLAC3D for numerical simulations. In the study, extensive field and laboratory rock mechanics studies were conducted to establish a comprehensive database. Rock mass and material properties were determined through drilling, block extraction, and various rock mechanics tests. Numerical simulations were performed using FLAC3D to model the A6 panel's gallery cross-sectional changes. Two scenarios were considered: Stage-1 involved gateroad excavation, and Stage-2 focused on coal production. Key findings and conclusions from the study include:

- i. Gallery cross-sectional variation significantly influences stress distribution in the rock mass.
- ii. Trapezoidal cross-sections showed higher vertical displacements and secondary stresses compared to horseshoe cross-sections.
- iii. The change in displacements and stresses was more pronounced in trapezoidal sections during both gateroad excavation and coal production stages.
- iv. Trapezoidal sections, while providing increased useful cross-sectional area, may lead to higher displacements and stresses.
- v. The study highlights the need for careful consideration in designing gallery cross-sections to minimize stress-induced risks.
- vi. Continuous monitoring of stress-strain variations during mining operations can inform real-time adjustments to ensure worker safety.
- vii. The study contributes to the understanding of stress-strain variations in LTCC mining and provides a basis for improving safety measures and operational efficiency.

In conclusion, the numerical modeling of stress-strain variations resulting from gallery cross-section changes in the Ömerler underground mine contributes essential insights to the field of mining engineering. It emphasizes the delicate balance between achieving operational efficiency and ensuring the safety of mining operations, shedding light on the complex dynamics of underground coal mining, particularly in the context of LTCC mining methods. In addition, it would be appropriate to compare the rock bolts design results obtained from using numerical methods for two different cross sections.

Declaration of Ethical Standards

The authors declare that the study complies with all applicable laws and regulations and meets ethical standards.

Declaration of Competing Interest

The authors declare that they have no known competing financial interests or personal relationships that could have appeared to influence the work reported in this paper.

Funding / Acknowledgements

This work was supported by the TUBITAK (The Scientific and Technological Research Council of Turkey) with a 1001 project (Project No: 116M698). The authors thanks to Turkish Coal Enterprises (TKI) and West Lignite Enterprise (GLI) staff for their help in field studies .

Data Availability

Data will be made available on request.

REFERENCES

- [1] G. Li, Z. Hu, P. Li, D. Yuan, Z. Feng, W. Wang and Y. Fu, "Innovation for sustainable mining: Integrated planning of underground coal mining and mine reclamation," *Journal of Cleaner Production*, 351, 131522, 2022.
- [2] Z. Hu, G. Li, J. Xia, Z. Feng, J. Han, Z. Chen, W. Wang and G. Li, "Coupling of underground coal mining and mine reclamation for farmland protection and sustainable mining," *Resources Policy*, 84, 103756, 2023.
- [3] International Energy Agency (IEA), *World Energy Outlook*. (2022). Accessed: July, 19, 2023. [Online]. Available: <https://www.iea.org/reports/world-energy-outlook-2022>.
- [4] A. Çelik and Y. Özçelik, "Investigation of the effect of caving height on the efficiency of the longwall top coal caving production method applied in inclined and thick coal seams by physical

- modeling," *International Journal of Rock Mechanics and Mining Sciences*, 162, 105304, 2023.
- [5] M. Shabanimashcool, and C. C. Li, "Numerical modelling of longwall mining and stability analysis of the gates in a coal mine," *International Journal of Rock Mechanics and Mining Sciences*, 51, 24-34, 2012.
- [6] M. Mesutoğlu, and İ. Özkan, "Büyük Ölçekli Kömür Arınında Gerçekleştirilen Schmidt Sertlik İndeksi ve Nokta Yükleme Dayanımı Deney Sonuçlarının Değerlendirilmesi," *Konya Mühendislik Bilimleri Dergisi*, v.7, n.4, pp. 681-695, 2019.
- [7] L. Zhou, X. Li, Y. Peng, B. Xia, and B. Fang, "Material point method with a strain-softening model to simulate roof strata movement induced by progressive longwall mining," *International Journal of Rock Mechanics and Mining Sciences*, 170, 105508, 2023.
- [8] N.E. Yaşitlı, and B. Unver, "3D numerical modeling of longwall mining with top-coal caving," *International Journal of Rock Mechanics and Mining Sciences*, v.42, i.2, pp. 219-235, 2005.
- [9] F. Şimşir, and M. K. Özfirat, "Determination of the most effective longwall equipment combination in longwall top coal caving (LTCC) method by simulation modelling," *International Journal of Rock Mechanics and Mining Sciences*, v.45, pp. 1015-1023, 2008.
- [10] T. D. Le, and J. Oh, "Longwall face stability analysis from a discontinuum-Discrete Fracture Network modelling," *Tunnelling and Underground Space Technology*, 124, 104480, 2022.
- [11] H. Wang, J. Wang, D. Elmo, M. He, Z. Ma, and C. Gao, "Ground response mechanism of entries and control methods induced by hard roof in longwall top coal caving panel," *Engineering Failure Analysis*, 144, 106940, 2023.
- [12] A. Çelik and Y. Özçelik, "Investigation of the efficiency of longwall top coal caving method applied by forming a face in horizontal thickness of the seam in steeply inclined thick coal seams by using a physical model," *International Journal of Rock Mechanics and Mining Sciences*, 148, 104917, 2021.
- [13] T. D. Le, J. Oh, B. Hebblewhite, C. Zhang, and R. Mitra, "A discontinuum modelling approach for investigation of Longwall Top Coal Caving mechanisms," *International Journal of Rock Mechanics and Mining Sciences*, 106, pp.84-95, 2018.
- [14] J. Wang, W. Wei, J. Zhang, B. Misra, and A. Li, "Numerical investigation on the caving mechanism with different standard deviations of top coal block size in LTCC," *International Journal of Mining Science and Technology*, 30, 583-591, 2020.
- [15] F. Song, A. Rodriguez-Dono, S. Olivella, Z. Zhong "Analysis and modelling of longitudinal deformation profiles of tunnels excavated in strain-softening time-dependent rock masses," *Computers and Geotechnics*, 125, 103643, 2020.
- [16] F. Song, A. Rodriguez-Dono, "Numerical solutions for tunnels excavated in strain-softening rock masses considering a combined support system," *Applied Mathematical Modelling*, 92, 905-930, 2021.
- [17] R. Çelik, "Developing of Moving Procedure for Powered Supports in Ömerler Coal Mine," Ph. D. dissertation, Osmangazi Univ. Dep. of Mining Eng., Eskişehir, 2005.
- [18] M. Mesutoğlu, "Determination of rock bolt and steel set behaviors used in control of longwall tailgate roof strata by numerical analysis," PhD dissertation, Konya Tech. Univ., Dep. of Mining Eng., Konya, 2019.
- [19] İ. Özkan, M. Geniş, Ö. Uysal and M. Mesutoğlu "New technology for roof support of coal roadways in our national underground coal mining: Design of roof bolt systems," TÜBİTAK Project No. 116M698 Final Report, Ankara, 430p. 2022.
- [20] M. Geniş, and Ö. Aydan, "Static and dynamic stability of a large underground opening," Proceedings of the second symposium on Underground excavations for Transportation (in Turkish), TMMOB, Istanbul, 2007, pp. 317-326.
- [21] Ö. Aydan, "A new stress inference method for the stress state of Earth's crust and its application," *Bulletin of Earthscience*, v.22, pp. 223-236, 2000.
- [22] A. Fişne, "Türkiye Kömür İşletmeleri Kurumu Garp Linyitleri İşletmesi Müdürlüğü Ömerler-A

- Yeraltı Kömür Ocağı Havalandırma Sisteminin Deęerlendirilmesi” Project Report. 2017.
- [23] D.M. Pappas, and C. Mark, “Behavior of simulated longwall gob material,” *Report of Investigation No: 9458*, United States Department of the Interior, Bureau of Mines, 1993.
- [24] M. Salamon, “Mechanism of caving in longwall coal mining, Rock mechanics contributions and challenges” Proceedings of the 31st US symposium, 1990, pp. 161-168.



MACHINE WHELL EDGE DETECTION MORPHOLOGICAL OPERATIONS

Pınar KARAKUŞ 

Osmaniye Korkut Ata University, Engineering and Natural Sciences Faculty, Geomatic Engineering, Osmaniye,
TÜRKİYE
pinarkarakus@osmaniye.edu.tr

Highlights

- Canny and Sobel edge detection algorithms were applied to determine the edges of different milling cutters used in machinability.
- According to MSE and PSNR results, the Canny algorithm gave better results than the Sobel algorithm.
- it was concluded that the images obtained from the applied morphological operations provided better performance than those not applied for both Canny and Sobel algorithms.



MACHINE WHELL EDGE DETECTION MORPHOLOGICAL OPERATIONS

Pınar KARAKUŞ 

Osmaniye Korkut Ata University, Engineering and Natural Sciences Faculty, Geomatic Engineering, Osmaniye, TÜRKİYE

pinarkarakus@osmaniye.edu.tr

(Received: 12.01.2023; Accepted in Revised Form: 09.02.2024)

ABSTRACT: One of the critical issues of image processing, defined as obtaining useful information from the image and improving the quality of the image, is edge detection. How edge detection performance will be affected by adding morphological operators to edge detection algorithms is among the issues that have not been fully resolved. In the study, Canny and Sobel edge detection algorithms were applied to different milling cutters used in machinability. Morphological operators were applied to the determined edges, and their effects on the edges were examined. Mean Square Error (MSE) and Peak Signal Noise Ratio (PSNR) values were used to compare the performances of edge detection algorithms. According to MSE and PSNR results, it was seen that the Canny algorithm gave better results than the Sobel algorithm. In addition, it was concluded that the images obtained as a result of the applied morphological operations provided better performance than the images that were not applied for both Canny and Sobel algorithms.

Keywords: Canny, Edge detection, Sobel, Morphological operations

1. INTRODUCTION

The process of enhancing image quality and/or obtaining valuable information from an image is known as image processing. Image processing consists of three stages: pre-processing, enhancement, and information extraction [1]. Edge detection algorithms applied in extracting information from the stages used are one of the critical issues of digital image processing. Edge detection is defined as determining sharp discontinuities in an image and includes image segmentation, registration, feature recognition, and extraction operations. The edge, which has many definitions, is generally discontinuities that indicate sudden changes in pixel densities that characterize the boundaries between objects in a scene and/or between an object and its background [2]. In other words, it is a feature of the high-density pixel and the close neighborhood in the images. In this way, the object's shape in the image is formed by the edges, and the edge is used in image analysis to determine the region boundaries. In these analyses, the image's brightness is the main feature of calculating its edges [3]. The edge detection algorithms consist of a series of steps to obtain a digital image, calculate its density, and emphasize the boundaries of the zones [4]. In addition, many edge detection algorithms are used, such as Canny, Log, Zero Cross, Sobel, Roberts, and Prewitt [5-8]. One of these algorithms, the Canny algorithm, is ideal for determining complex shapes by accurately determining the edges of the object to be processed [9]. Therefore, the Canny algorithm has been used in applications in the field of medicine [10] and in applications in the field of aviation was used [11]. The Canny algorithm has the advantage of faster edge detection than operators such as Sobel, Prewitt, and Roberts [12].

Determining the edge detection performance by adding morphological operators to edge detection algorithms is among the issues still not fully clarified. In a study, they examined edge detection using mathematical morphological operators. They used erosion and dilation processes simultaneously. Their algorithm was applied to the grayscale image but could not obtain accurate results [13].

The study examined the effects of the operations performed to detect and improve the edge information in the image to understand the image and its information. For this purpose, images of different milling cutters used in machinability were converted to black and white and then median filtered. The edges were determined by applying Canny and Sobel edge detection algorithms to the

*Corresponding Author: Pınar KARAKUŞ, pinarkarakus@osmaniye.edu.tr

median filtered images. The effects on the edges were examined by adding morphological operators, and images were obtained. Afterward, to numerically express which image achieved the best result from the images obtained, Mean Square Error (MSE) and Peak Signal Noise Ratio (PSNR) values were calculated, and the edge detection performances of the edge detection algorithms and applied processes were evaluated.

2. MATERIAL AND METHODS

2.1. Material

In the study, milling cutters with different sizes, given in Figure 1, were used. To avoid confusion, the milling cutters are named as shown in Figure 1. Images of milling cutters were obtained with a Nikon digital DSLR digital camera with 300 dpi, 500 ISO, and 32mm focal length [14]. While the images were being obtained, only the milling cutters were focused on, and the background was blurred.



Figure 1. The milling cutters used in the examinations are a) milling cutters No. 1, b) milling cutters No. 2, and c) milling cutters No. 3

2.2. Methodology

2.2.1. Pre-processing

Pre-processing was the first stage in obtaining edges from the images obtained from milling cutters. At the pre-processing stages, the images obtained in RGB were first converted to black and white. In edge detection, the density of grayscale images is sufficient for the operation. Grayscale is called the value that represents the intensity of each pixel. The conversion from RGB to black and white image is given in Equality (1) [15].

$$Gray = Rx0.299 + Gx0.587 + Bx0.114 \quad (1)$$

As the second stage in image preprocessing, the Median filtering process, which is used to improve the quality of the image and eliminate the noise present in the image, was performed. With this process, the element in the middle of the list formed by sorting the grayscale values of the pixels in the neighborhood of a pixel from small to large and called the median is taken as the output value [16]. The most important feature of the median filter is that it protects the edges while eliminating noise. The process makes the image smoother, intensifying its pixels, mainly the background pixels close to each other [17].

2.2.2. Edge detection

2.2.2.1. Canny algorithm

First, The Canny algorithm eliminates noise by softening the black and white image. The results of the Canny algorithm vary depending on the specified threshold values. Appropriate threshold values should be determined depending on the study performed. The Canny edge detection algorithm has five stages, as indicated below [18-19];

- Using a Gaussian filter to improve the quality of the image by smoothing the image
- To find the gradients with the maximum response, use an edge detector.
- Suppressing non-maximal ones to mark locally maximum-valued edges by thinning the edges found in the previous step.
- Applying the double thresholding technique for more accurate determination of actual edges.
- The pixel merging process was used to determine the final edges by removing the weak edge pixels in the last step.

The Canny edge detection algorithm is based on some criteria. The first and most obvious is the low error rate. It is essential that the edges found in the images are not overlooked and those not edges are eliminated. Another criterion is that the edge points are well localized. For this process, the distance between the edge pixels found by the detector and the real edge pixels must be minimum [20].

2.2.2.2. Sobel algorithm

The Sobel operator is based on convolving the image in horizontal and vertical directions, as seen in Figure 2. a), b), and c) with a small, separable, and integer-valued filter. For this reason, there is also an ease of calculation [21]. One could think of this as an approximation of the first Gaussian derivative. This is the same as the first derivative of the Gaussian blurred image produced when applied with a 3x3 mask.

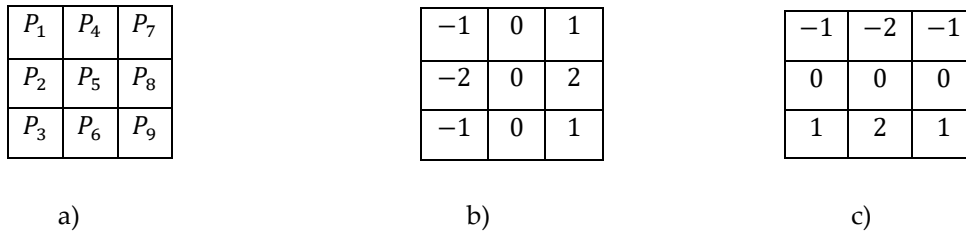


Figure 2. a) Pixel matrix representation of the Sobel operator. b) A convolution matrix of 3*3 dimensions in the X-direction. c) A convolution matrix of 3*3 dimensions in the Y-direction.

The first derivative of the density in the horizontal and vertical directions is,

$$G_x = \frac{\partial f(x,y)}{\partial x} = P_9 + 2P_8 + P_7 - P_1 - 2P_2 - P_3 \quad (2)$$

$$G_y = \frac{\partial f(x,y)}{\partial y} = P_9 + 2P_6 + P_3 - P_1 - 2P_4 - P_7 \quad (3)$$

(2) and (3) are shown in the equation. The gradient size is;

$$G = \sqrt{G_x^2 + G_y^2} \quad (4)$$

It is calculated by.

2.2.3. Morphological operations

2.2.3.1. Dilation and erosion

The basic mathematical morphological operators are dilation and erosion. Other morphological processes are the synthesis of these two essential processes. Specifically, morphological processes enable the identification of geographical details and the determination of the boundaries of objects. Looking at the mathematical structure of morphological operations [20],

Let $f(x, y)$ show the configuration element C of a black-and-white two-dimensional image. Dilation of a black-and-white image $F(x, y)$ by a black-and-white configuration element $C(s, t)$

$$(F \oplus C)(x, y) = \max\{F(x - s, y - t) + C(s, t)\} \quad (5)$$

It is indicated by.

Erosion of a black-and-white image $F(x, y)$ by a black-and-white configuration element $C(s, t)$

$$(F \ominus C)(x, y) = \min\{F(x + s, y + t) - C(s, t)\} \quad (6)$$

It is indicated by.

The opening and closing of the grayscale image $F(x, y)$ by the grayscale configuration element $C(s, t)$ are indicated by the equations (7) and (8), respectively.

$$F \circ C = (F \ominus C) \oplus C \quad (7)$$

$$F \cdot C = (F \oplus C) \ominus C \quad (8)$$

Erosion is a reduction transformation that reduces the grayscale value of the image, while dilation is an expansion transformation that increases the grayscale value of the image. Both of them are sensitive to image edges whose grayscale value changes. Erosion filters the inner image, while expansion filters the outer image [22]. To achieve better morphological results, the dilation process is followed by the erosion process, which fills the gaps inside the objects whose edges are to be determined without any change in size and combines the isolated ones to form smooth boundaries [23]. Opening can be defined as first narrowing and then expanding; it eliminates noise and disconnected sections on the image. The closing process applied later can be defined as first expanding and then contracting; it is a morphological process that combines the remaining large parts and allows the disconnections to be combined [24,25].

3. RESULTS AND DISCUSSION

As a result of the image processing stages performed on the images of milling wheels given in Figure 1, the edges were tried to be determined. In the preliminary procedures carried out as the first stage of the investigations, RGB images were converted into black and white images (Figure 3). After that, a median filter was passed through the images converted to black and white to eliminate the salt and pepper noise effect and improve the image quality. It is stated in the studies that the median filter process does not cause any damage to the edges while eliminating noise [24,26,27]. In addition, the median filter is a linear filtering method that is more successful than linear filtering [28,29].

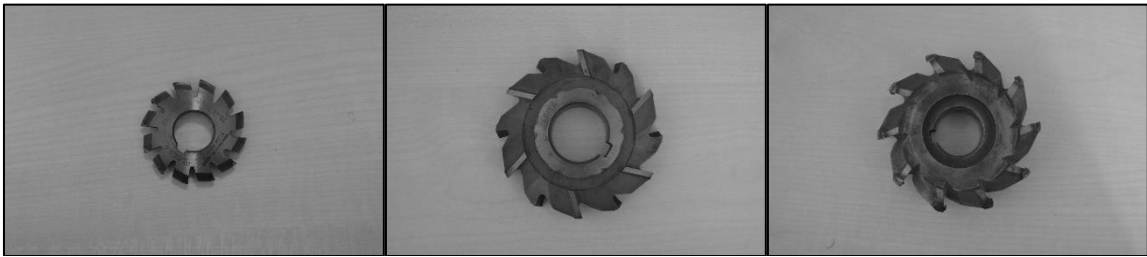


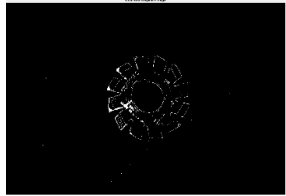
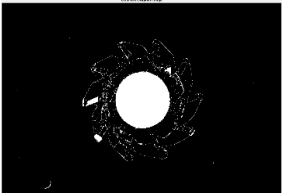
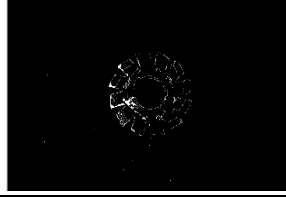
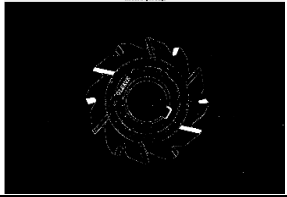
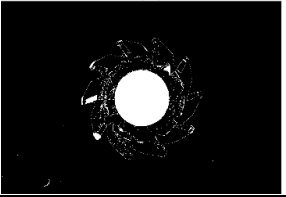
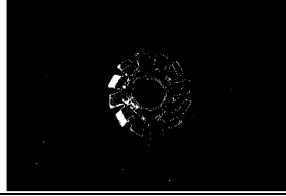
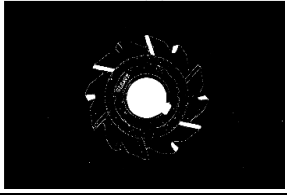
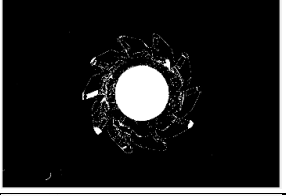
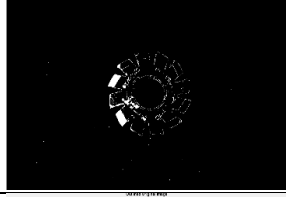
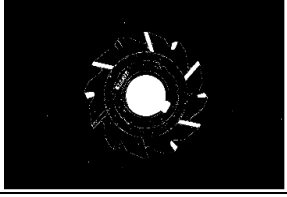
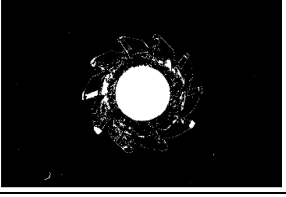
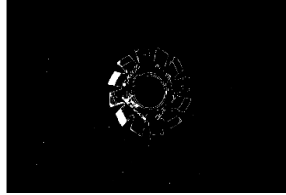
Figure 3. Black and white images

After the preprocessing operations were performed to obtain better results in edge detection operations, Canny and Sobel edge detection techniques were applied to the images, and an attempt was made to determine the edges. During these processes, Canny and Sobel detection techniques and more accurate determination of the edges [30-32] and the effect of providing threshold values were also examined. Due to the nature of the algorithms used [30,31], two threshold values, Low and High, in the interval $0 < \text{Low} < \text{High} < 1$ for Canny [33,34] and the single threshold value for Sobel [35] has been applied. After all the different threshold values were applied, the morphological operator determined the edges. As a result of these operations, the effects of different threshold values and the processing ends of edge detection algorithms on edge detection have been observed. In the operations performed with the Canny algorithm, first of all, the Low value was selected as 0.075 to determine the High value that would give the best result and different High values. Then morphological operators were applied to this value. When the obtained images were examined, it was observed that a clear edge did not form on the three pocket knives until the 0.475 High value for the 0.075 low value, and the edges became more apparent with the decreasing High value. However, it has been determined that the edges deteriorate after a certain reduction value from the High value for each milling cutter, and different High values for each milling cutter give good results. After that, different Low values were selected according to the determined High value, and the most appropriate Low value was determined. The images obtained from these operations and the morphological operators applied are given in Tables 1 and 2. When the images were examined, it was determined that different threshold values gave better results for each milling cutter. The threshold values that provide the best results in the Canny algorithm and behind the applied morphological operations are from milling cutter No. 1 to milling cutter No. 3, respectively. [0.045,0.095], [0.065,0.105], [0.045,0.085] The conclusion has been reached that it is.

Table 1. The results for different High values of 0.075 and Low value selected in determining the edges of different milling cutters with the Canny algorithm

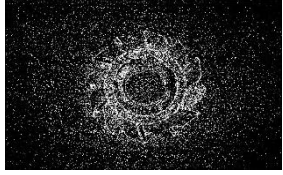
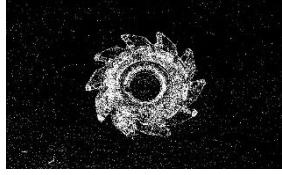
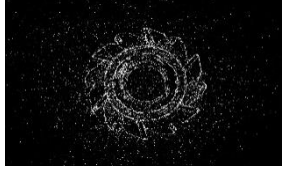
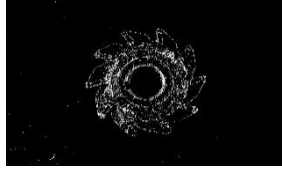
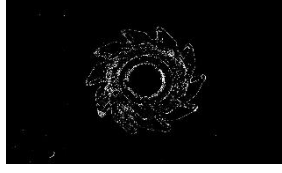
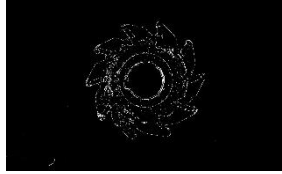
Canny			
Low value: 0.075			
High values	Milling cutter No.1	Milling cutter No.2	Milling cutter No.3
0.975			
0.875			
0.575			
0.475			
0.175			
0.105			
0.095			
0.085			

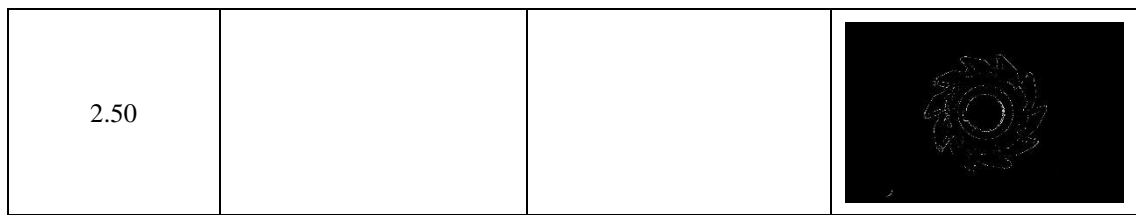
Table 2. The results obtained for different Low values at the High value determined by the Canny algorithm of different milling cutters

Canny					
Milling cutter No.1		Milling cutter No.2		Milling cutter No.3	
High value:0.095		High value:0.105		High value:0.085	
0.085		0.095		0.075	
0.075		0.085		0.065	
0.065		0.075		0.055	
0.055		0.065		0.045	
0.045					

After the edges are determined as a result of the Canny algorithm and threshold values applied in the study, a single threshold value is used in the Sobel operator, and the other edge determination algorithm is applied after the edges are determined as a result of threshold values applied [36]. Different values have been applied for the Sobel operator by starting from the threshold values of [0.5] and increasing them at certain rates. The threshold values applied and the images obtained as a result of the morphological operations applied after are given in Table 3. When the obtained images were examined, it was determined that the optimal threshold value for the images belonging to each milling cutter was [1.75]. However, after that, it was tested on the images of milling cutter No. 3 to examine how increasing the threshold value by a little more would affect determining the edges. When the images were examined, it was observed that the edges began to deteriorate when the threshold value rose above the value of [1.75]. Compared to the Sobel algorithm, it can be seen that the Canny operator can provide clear edges and that there are more object details in the images [37,22,38]. [22] showed that the Canny algorithm can determine smoother and thinner edges than Sobel. [39] in their studies, they stated that the Canny edge detection method is better in terms of performance than other edge detection methods, but it contains complex processing steps.

Table 3. The results obtained in the Sobel algorithm for different Threshold values of different milling cutters

Sobel			
Threshold values	Milling cutter No.1	Milling cutter No.2	Milling cutter No.3
0.50			
0.75			
1.00			
1.25			
1.50			
1.75			
2.0			
2.25			



In the threshold values determined in the study, the edge detection algorithms and the morphological processing applied to MSE and PSNR regression models were used to compare the image edge detection quality of the images obtained. In these models, MSE refers to the average value of the sum of squares of the difference between the processed and original image pixels. The magnitude of the MSE represents the difference between the original grayscale image and the processed grayscale image. The higher value of MSE means better edge detection results [3,7]. The term PSNR refers to the maximum possible error of an image. In addition, it is seen that the smaller the obtained PSNR value, the better the edge detection operator is [3,7].

The study calculated MSE and PSNR for images obtained from Canny and Sobel algorithms at the threshold values that give the best image, both with and without morphological operators applied. For this purpose, the effect of both the Canny and Sobel algorithms and the morphological operator have been observed. Accordingly, the MSE and PSNR equations used are given in Equation (9) and Equation (10). MSE and PSNR results obtained from the equations used are given in Table 4 and Table 5.

MSE [40]

$$MSE = \frac{1}{M \times N} \sum_{i=1}^M (f'(i, j) - f(i, j))^2 \quad (9)$$

Here, $f'(i, j)$ and $f(i, j)$ are the image to be evaluated and the original grayscale image, respectively. "M" and "N" represent the length and width of the image, respectively. The symbol " Σ " means addition.

PSNR [41];

$$PSNR = 10 \log_{10} \frac{255^2}{MSE} \quad (10)$$

Here, 255 is the maximum pixel value of the image, and MSE is the mean square error.

Table 4. Without morphological processing

Sobel			Canny		
	MSE	PSNR		MSE	PSNR
Milling cutter No.3	19791.28	5.17	Milling cutter No.3	19852.47	5.15
Milling cutter No.2	19592.35	5.21	Milling cutter No.2	19611.89	5.21
Milling cutter No.1	18699.80	5.41	Milling cutter No.1	18728.23	5.41

Table 5. Morphologically processed version

Sobel			Canny		
	MSE	PSNR		MSE	PSNR
Milling cutter No.3	19997.8688	5.12	Milling cutter No.3	20117.2846	5.10
Milling cutter No.2	19734.6844	5.18	Milling cutter No.2	19750.0511	5.18
Milling cutter No.1	18818.3281	5.38	Milling cutter No.1	18873.8014	5.37

When the results given in Tables 4 and 5 are examined, the effect of applying morphological processing on edge detection was observed in both Canny and Sobel algorithms. In both methods, the results with and without morphological processing were examined. It was observed that the MSE value

obtained after the morphological process was applied was higher, and the PSNR value was lower. It was determined that the morphological process gave better results in edge detection [3,7]. In addition, when the results were examined in terms of the algorithms used, it was observed that they gave almost similar results in terms of PSNR values, regardless of the morphological operations. Still, the Canny algorithm was lower in some cases. It was determined that the MSE values obtained for the Canny algorithm were more significant than those obtained for the Sobel algorithm, regardless of the morphological operations. These results show that the Canny algorithm is better than the Sobel algorithm in edge detection [3,7]. Many studies have similarly observed that the Canny algorithm gives better results in edge detection than the Sobel algorithm [37,22, 38,39].

4. CONCLUSIONS

The study examined the effects of the commonly used Canny and Sobel edge detection algorithms on image performance and the morphological operations applied to these methods. Images belonging to three different milling cutters were used in the investigations. The determination of the edges and the MSE and PSNR calculations were performed in the Matlab program. According to the MSE and PSNR results obtained, it has been determined that the Canny algorithm gives more results than the Sobel algorithm. In addition, it has been concluded that the images obtained from the applied morphological operations in both Canny and Sobel algorithms provide better performance than the unapplied images.

Funding / Acknowledgements

There is no funding for this study

REFERENCES

- [1] R. Choudhary, S. Gawade, "Survey on Image Contrast Enhancement Techniques", *International Journal of Innovative Studies in Sciences and Engineering Technology*, vol. 2, is. 3, 2016.
- [2] C. R., Gonzalez, & R. E. Woods, "Digital Image Processing". Pearson Education International, 2008.
- [3] D. Poobathy, & R. M. Chezian, "Edge detection operators: Peak signal to noise ratio based comparison", *IJ Image, Graphics and Signal Processing*, 10, 55-61, 2014.
- [4] D. Poobathy and R. ManickaChezian, "Recognizing and Mining Various Objects from Digital Images", *Proceedings of 2nd International Conference on Computer Applications and Information Technology (CAIT 2013)*, pp. 89-93, 2013.
- [5] C. Gentsos, C. Sotiropoulou, S. Nikolaidis, N. Vassiliadis, "Real-time canny edge detection parallel implementation for FPGAs", *IEEE international Conference On Electronics, Circuits and Systems*, 2010.
- [6] P. Acharjya, R. Das, D. Ghoshal, "Study and comparison of different edge detectors for image segmentation", *Global Journal of Computer Science and Technology Graphics & Vision*, 12 (13) (2012).
- [7] S. Kumar, M. Singh, D. Shaw, "Comparative analysis of various edge detection techniques in biometric application", *International Journal of Engineering and Technology (IJET)*, 8 (6) 2452-2459, 2016.
- [8] M. Hagar, P. Kubince, "About edge detection in digital images", *Radio engineering*, 27 (4), 2018. 919-929.
- [9] Z. Stosic, , & P. Rutesic, "An improved canny edge detection algorithm for detecting brain tumors in MRI images". *International Journal of Signal Processing*, 3, 2018.
- [10] Ravikumar, R., & Arulmozhi, V. "Digital Image Processing-A Quick Review", *International Journal of Intelligent Computing and Technology (IJICT)*, 2(2), 11-19, 2019.
- [11] S. S. Al-Amri, N. V.Kalyankar, , & S. D. Khamitkar, "Image segmentation by using edge detection". *International journal on computer science and engineering*, 2(3), 804-807, 2010.
- [12] B. M. Chandra, D. Sonia, A. R. Devi, C. Y. Saraswathi,, K. M. Rathan, , & K. Bharghavi,

- "Recognition of Vehicle NumberPlate Using Matlab", *J. Univ. ShanghaiSci. Technol*, 23(2), 363-370, 2021.
- [13] S. Rani, DeeptiBansal, and B. Kaur, "Detection of Edges Using Mathematical Morphological Operators," *Open Transactions On Information Processing*, vol. 1, No. 1, pages 17- 26, may 2014.
- [14] https://www.nikon.com.tr/tr_TR/product/discontinued/digital-cameras/2015/d3100-black
- [15] F. Liu, et al. "Low computation and high efficiency Sobel edge detector for robot vision." 2021 IEEE International Conference on Real-time Computing and Robotics (RCAR). IEEE, 2021.
- [16] U. Qidwai, and C.H. Chen, "Digital image processing: an algorithmic approach with MATLAB", CRC Press, 2010.
- [17] F. S. Ning, & Y. C. Lee, "Combining Spectral Water Indices and Mathematical Morphology to Evaluate Surface Water Extraction in Taiwan". *Water*, 13(19), 2774, 2021.
- [18] Moeslund T. "Canny Edge detection". Denmark: Laboratory of Computer Vision and Media Technology, Aalborg University. (http://www.cvmt.dk/education/teaching/f09/VGIS8/AIP/canny_09gr820.pdf), March 2009.
- [19] D. Rana, & S. Dalai, "Review on traditional methods of edge detection to morphological based techniques", *International Journal of Computer Science and Information Technologies*, 5(4), 5915-5920, 2014.
- [20] S. Sridhar, "Digital Image Processing", Oxford University Press, 2012.
- [21] W. Kangtai & D. Wenzhan, "Approach of Image Edge Detection Based on Sobel Operator and Grayrelation", *Computer Applications*, 26(5), 1035-1036, 2006.
- [22] R. Rana, & A. Verma, "Comparison and Enhancement of Digital Image by Using Canny Filter and Sobel Filter". *IOSR Journal of Computer Engineering*, 16(1), 06-10, 2014.
- [23] H. Dong, "Comparison of Edge Detection Techniques and Mathematical Morphology in Car Plate Detection Application". In *2021 7th International Conference on Computer and Communications (ICCC)* (pp. 775-781). IEEE, 2021.
- [24] S. M. Abid Hasan, & K. Ko, "Depth edge detection by image-based smoothing and morphological operations", *Journal of Computational Design and Engineering*, 3(3), 191-197, 2016.
- [25] N. G. Korkusuz, "Otomatik hedef tanıma (ATR)", Yıldız Teknik Üniversitesi Fen Bilimleri Enstitüsü, Elektronik ve Haberleşme Mühendisliği Anabilim Dalı, Yüksek Lisans Tezi, 2008.
- [26] K. C. Liao, H. Y. Wu, & H. T. Wen, "Using Drones for Thermal Imaging Photography and Building 3D Images to Analyze the Defects of Solar Modules", *Inventions*, 7(3), 67, 2022.
- [27] O. Appiah, M. Asante, & J. B. Hayfron-Acquah, "Improved approximated median filter algorithm for real-time computer vision applications". *Journal of King Saud University-Computer and Information Sciences*, 34(3), 782-792, 2022.
- [28] T. Chen, K. K. Ma and L. H. Chen, Tri-state median filter for image denoising. *IEEE Transactions on Image processing*, 8(12), 1834-1838, 1999.
- [29] İ. Kayadibi, G. E. Güraksin, & U. Ergün, "ESA tabanlı göz durumu tespitinde görüntü önilem yöntemlerinin etkisi", *Niğde Ömer Halisdemir Üniversitesi Mühendislik Bilimleri Dergisi*, 1-1, 2022.
- [30] Jae S. Lim, "Two-Dimensional Signal and Image Processing, Englewood Cliffs", NJ, *Prentice Hall*, pp. 478-488, 1990.
- [31] James R. Parker, "Algorithms for Image Processing and Computer Vision", New York, John Wiley & Sons, Inc., pp. 23-29, 1997.
- [32] Z. Xu, X. Baojie, & W. Guoxin, " Canny edge detection based on Open CV". In *2017 13th IEEE international conference on electronic measurement & instruments (ICEMI)*, pp. 53-56, 2017.
- [33] Y. Lu, L. Duanmu, Z. J. Zhai, & Z. Wang, "Application and improvement of Canny edge-detection algorithm for exterior Wall hollowing detection using infrared thermal images". *Energy and Buildings*, 274, 112421. IEEE, 2022.
- [34] D. Dhillon, & R. Chouhan, "Enhanced edge detection using SR-guided threshold maneuvering and window mapping: Handling broken edges and noisy structures in canny edges". *IEEE Access*, 10, 11191-11205, 2022.

- [35] W. Kong, J. Chen, Y. Song, Z. Fang, X. Yang, & H. Zhang, "Sobel edge detection algorithm with adaptive threshold based on improved genetic algorithm for image processing", *International Journal of Advanced Computer Science and Applications*, 14(2),2023.
- [36] L. Berus, P. Skakun, D. Rajnovic, P. Janjatovic, L. Sidjanin, & M. Ficko, "Determination of the grain size in single-phase materials by edge detection and concatenation", *Metals*, 10(10), 1381, 2020.
- [37] S. Vijayarani, & M. Vinupriya, "Performance analysis of canny and sobel edge detection algorithms in image mining". *International Journal of Innovative Research in Computer and Communication Engineering*, 1(8), 1760-1767,2013.
- [38] Malbog, Mon Arjay F., et al. "Edge detection comparison of hybrid feature extraction for combustible fire segmentation: a Canny vs Sobel performance analysis." 2020 11th IEEE Control and System Graduate Research Colloquium (ICSGRC). IEEE, 2020.
- [39] Remya Ajai, AS, and Gopalan Sundararaman. "Comparative Analysis of Eight Direction Sobel Edge Detection Algorithm for Brain Tumor MRI Images." *Procedia Computer Science*, 201, 487-494, 2022.
- [40] Q. Wu, & J. An, "An active contour model based on texture distribution for extracting inhomogeneous insulators from aerial images". *IEEE Transactions on Geoscience and Remote Sensing*, 52(6), 3613-3626, 2013.
- [41] D. Vilimek, J. Kubicek, M. Golian, R. Jaros, R. Kahankova, P. Hanzlikova, & M.Buzga, "Comparative analysis of wavelet transform filtering systems for noise reduction in ultrasound images". *Plos one*, 17(7), 2022.



GIS-AHP APPROACH FOR A COMPREHENSIVE FRAMEWORK TO DETERMINE THE SUITABLE REGIONS FOR GEOTHERMAL POWER PLANTS IN IZMIR, TÜRKİYE

¹Kemal KOCA , ^{2,*}Fatih KARİPOĞLU , ³Emel Zeray ÖZTÜRK 

¹ Abdullah Gül University, Engineering Faculty, Mechanical Engineering Department, Kayseri, TÜRKİYE

¹ Abdullah Gül University, KOCA Research Group, Kayseri, TÜRKİYE

² Izmir Institute of Technology, Energy Systems Engineering Department, Izmir, TÜRKİYE

³ Konya Technical University, Engineering and Natural Sciences Faculty, Geomatics Engineering Department, Konya, TÜRKİYE

¹ kemalkoca@agu.edu.tr, ² fatihkaripoglu@iyte.edu.tr, ³ ezozturk@ktun.edu.tr

Highlights

- GIS-AHP approach to determine the suitable region for Geothermal Power Plants is used under physical (C1), environmental (C2), and technical (C3) main criteria.
- To construct the AHP structure, experts' opinions were taken from Geothermal DHC Summer School which was carried out in Slovenia July 2021 (CA18129).
- İzmir Province has highly suitable regions of 1037 km² for potential GPP.
- Based on the comparing process, Dikili power plant was determined as the non-suitable score while Balçova power plant had the highly suitable score.



GIS-AHP APPROACH FOR A COMPREHENSIVE FRAMEWORK TO DETERMINE THE SUITABLE REGIONS FOR GEOTHERMAL POWER PLANTS IN IZMIR, TÜRKİYE

¹Kemal KOCA , ^{2,*}Fatih KARİPOĞLU , ³Emel Zeray ÖZTÜRK 

¹ Abdullah Gül University, Engineering Faculty, Mechanical Engineering Department, Kayseri, TÜRKİYE

¹ Abdullah Gül University, KOCA Research Group, Kayseri, TÜRKİYE

² Izmir Institute of Technology, Energy Systems Engineering Department, Izmir, TÜRKİYE

³ Konya Technical University, Engineering and Natural Sciences Faculty, Geomatics Engineering Department, Konya, TÜRKİYE

¹ kemalkoca@agu.edu.tr, ² fatihkaripoglu@iyte.edu.tr, ³ ezozturk@ktun.edu.tr

(Received: 26.10.2023; Accepted in Revised Form: 15.02.2024)

ABSTRACT: Geothermal energy is gaining more reputation and importance around the world. Correspondingly, suitable location selection is a critical step and has become necessary for the successful installation and operation of geothermal power plants. This study investigated suitability of İzmir region, located in the Aegean part of Türkiye, in terms of geothermal power plants applications by using the combination of Geographical Information System and Analytic Hierarchy Process. Based on the request of power plants, thirteen important criteria were evaluated under three main categories named as physical (C₁), environmental (C₂) and technical (C₃). Moreover, expert's opinions were taken into consideration to calculate the importance of these criteria. Key results showed that İzmir was suitable for geothermal power plants. The final suitability map layer pointed out that %8.73 (1.037 km²) of total area were determined as highly suitable regions in terms of installation. In addition, the obtained suitability map layer was compared with actual geothermal power plants. Based on the comparison study, power plants in Seferihisar were moderately suitable for geothermal power plants while the location of Balçova power plant was highly suitable. Regarding the suitability assessment in the present study, the location of Dikili power plants had the least suitability score.

Keywords: Analytic hierarchy process, Geographical information system, Geothermal energy, İzmir, Suitable site selection

1. INTRODUCTION

Since energy is staminal for daily life activities such as heating, fabricating, cooking and transportation, energy sources have enormously influenced the strategic policies of both developed and developing countries. These activities have been provided by different energy sources such as natural gas, fuel oil, solar, wind, geothermal, etc. Given that certain energy resources are finite while others are sustainable, the source from which energy is derived becomes of utmost significance. Hence, supplying energy from non-renewables has lagged the renewable energy sources, especially over the last two decades. In this respect, renewable energy sources such as wind, solar, geothermal, hydropower and biomass as seen in Figure 1 have been started to substitute with conventional energy sources such as coal, natural gas, and fuel oil because of increasing sustainability issues and environmental threat such as atmospheric emissions, solid waste, and water consumption [1]. These threats which will be seen in the near future have proved why utilizing appropriate renewable energy resources is important. Renewable energies provide a reduction in secondary waste and environmental impacts, the mitigation of greenhouse gas emissions, and the promotion of sustainability [2].

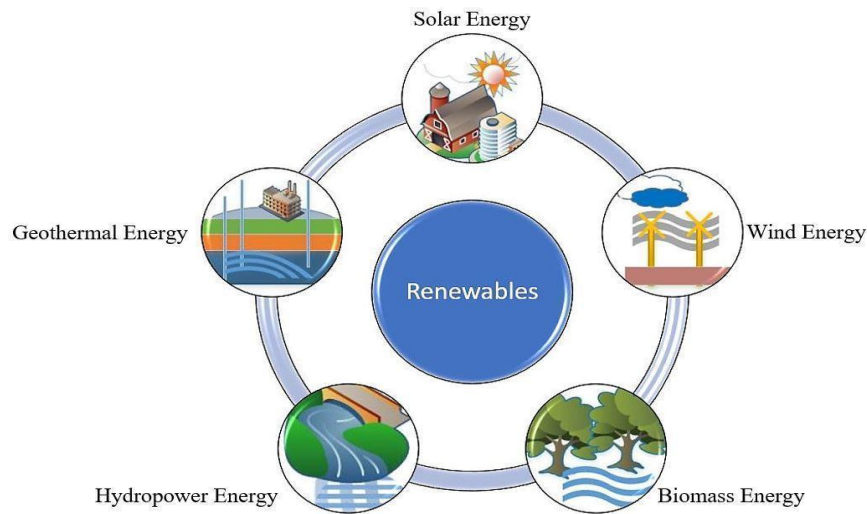


Figure 1. The types of renewable energy resources

Among renewable energies, energy production with wind and solar power could be problematic because of their intermittent nature [3-4]. Energy supply could be ensured via hydropower [5]. However, it is not continuous especially in the drought period of summer seasons. Biomass can also provide energy production. However, since a continuous biomass supply cannot be made during drought periods, the same problem arises here as well. On the other hand, geothermal energy is different. Because it is the only renewable resource which is not affected by natural events and weather conditions [5].

Hostility to renewable energies was not uncommon. Hence, the geothermal power industry tends to categorize such behavior as a social acceptance issue [6]. On the other hand, hostility should be thought of as being part of more general energy management and environmental issues than social acceptance. Those issues may be classified as local pollution, economic considerations, water conservation concerns, energy policy, quality of life, and employment effects. In such situations, finding a straightforward and unambiguous resolution is difficult. Therefore, acceptable compromise solutions to geothermal power may be ensured by suitable planning processes [7].

Recently, the territorial planning and suitable site selections for the installation of those renewable energies have enormously gained popularity in the literature. Some researchers have studied the suitable site selections for onshore wind farms [8-10] and offshore wind power [4], [11-12], whilst some of them have tended to investigate the territorial planning for PV power plants [3] and biomass power plants [10], [13-14]. Unlike those renewable energies, the suitable site selection for geothermal power plants was rare in the literature [15-17]. Coles et al. studied the spatial decision analysis for geothermal resource to provide a guideline selecting the best locations as a case study [15]. For the investigation of the detected criteria, nine exploratory wells were drilled to select the suitable locations. Coro and Trumpy carried out the novel research which was predicted the geographical suitability for geothermal power plants by considering lots of criteria [16]. The study presented the first suitability map of globally geothermal power plants. Mostafaeipour et al. studied an interesting topic which ranked the locations for geothermal power plants integrated hydrogen production in Afghanistan [17]. In the scope of study, nine criteria were assessed to evaluate the 17 provinces in Afghanistan regards with suitability locations for hybrid system. According to results, the number of refineries and distance from distribution centers were determined as the most important criteria for the geothermal based hydrogen production systems [17].

The process of determining the best location for installation has been detected deficient even though Türkiye has huge geothermal energy potential. In order to assess this huge geothermal energy potential, an accepted roadmap is not available currently. Within the renewable energy policies and targets of Türkiye, the mentioned gap must be filled with the best method. The main objective of the present study was to provide a suitable site for the installation of a geothermal power plant in Izmir and to compare it

with the locations of current geothermal power plants in order to understand if they were installed in a reliable region. In addition, this study aimed to fill the detected gap in assessing the huge geothermal potential in Türkiye. To select the best suitable regions, the multi-criteria should be assessed and suitable locations should be selected with suitable methods. Based on the literature, necessary and crucial criteria were detected and ranked by relevant experts. Hence, the obtained information and experience from experts provided guidance for creating a successful roadmap. The rest of this study was categorized into four main sections. In Section 2, a preliminary definition of materials and methods including the Analytical Hierarchy Method (AHP) and Geographical Information Systems (GIS) was performed. In section 3, the case study for selected areas and multi-criteria was evaluated. In Section 4, the results that emerged from the analysis was discussed. In Section 5, the conclusions with the key findings were put forward.

2. MATERIAL AND METHODS

The present study analyzed the suitable site selection of geothermal power plants in İzmir province of Türkiye. This section revealed the study area, methods and tools, expert panel analysis by means of AHP.

2.1. Study Area

The most suitable topography for geothermal power plants depends on a number of factors that ensure the most efficient use of geothermal resources. Project planning and location selection is a process that requires many details, taking into account all of those factors. İzmir province, which was chosen as the study area, is located in the west of Türkiye within an area of 11.891 km². It is one of the important regions with geothermal energy potential in Türkiye and has suitable geothermal resources to evaluate this potential. At first glance, some factors that provide geothermal energy potential in Izmir can be listed as follows:

- **Geothermal Resources:** Izmir has huge potential in geothermal resources and hosts many geothermal resource areas. These sources support the production of hot water and steam.
- **High Temperature:** Most of the geothermal resources in Izmir have high temperatures, which provides an advantage in terms of energy efficiency.
- **Climate Factors:** Izmir's climate is suitable for geothermal energy production. The temperature values are above average values which are 14 °C. It is sunny and mild throughout the year, which supports solar and geothermal energy.
- **Infrastructure:** Izmir has a developed region in terms of energy transmission and infrastructure, which is important for energy production and distribution.

Fault line densities for İzmir are classified as second degree [18]. There are also a few geothermal plants for different purposes. As a result of those factors, İzmir was selected as a pilot region due to its high utilization potential of geothermal energy. Aydın and İzmir could be named as geothermal capitals because of existing plants and continuing research activities. Therefore, the selection of the most suitable region for geothermal power plants could be very useful for researchers and investors. Another main reason is to check the accuracy of existing plants' position. The study area was illustrated in Figure 2.

2.2. Data Collection and Preparation

As seen in Figure 3, 13 criteria that were important for the installation of a geothermal power plant in Izmir province were determined and they were evaluated by an expert group including hydrogeologists, geologists, power engineers, geotechnical engineers, geoscience engineers and energy systems engineers.

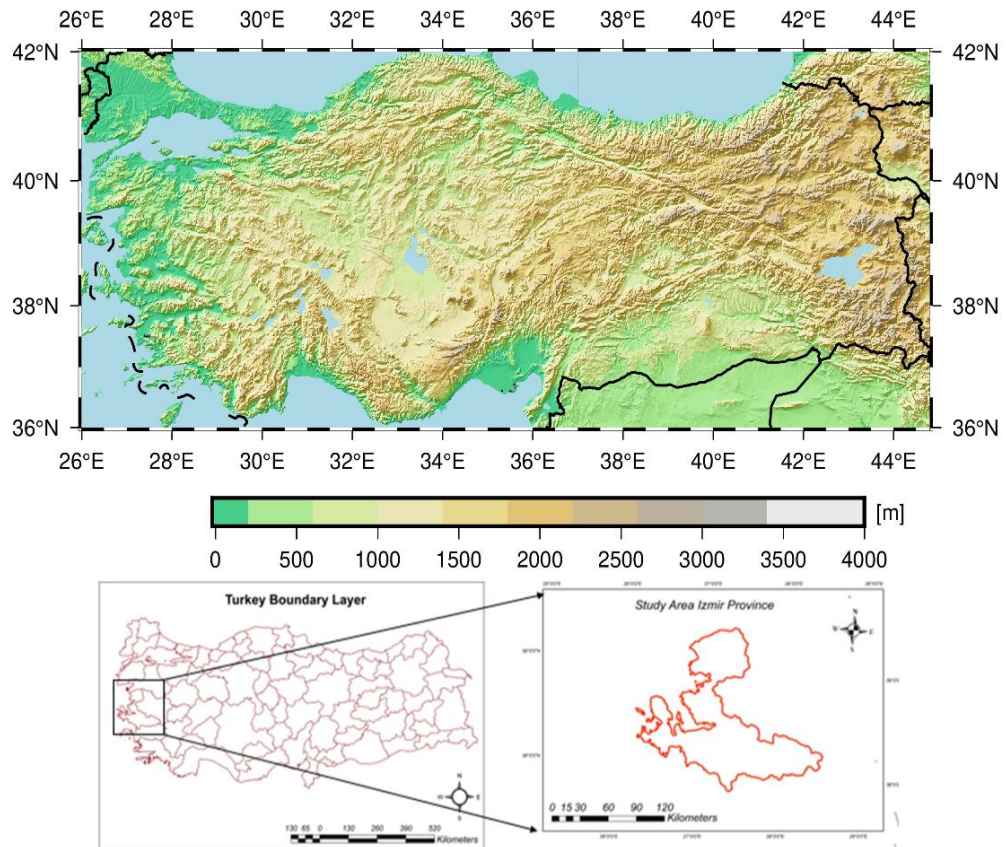


Figure 2. Geographical location of study area

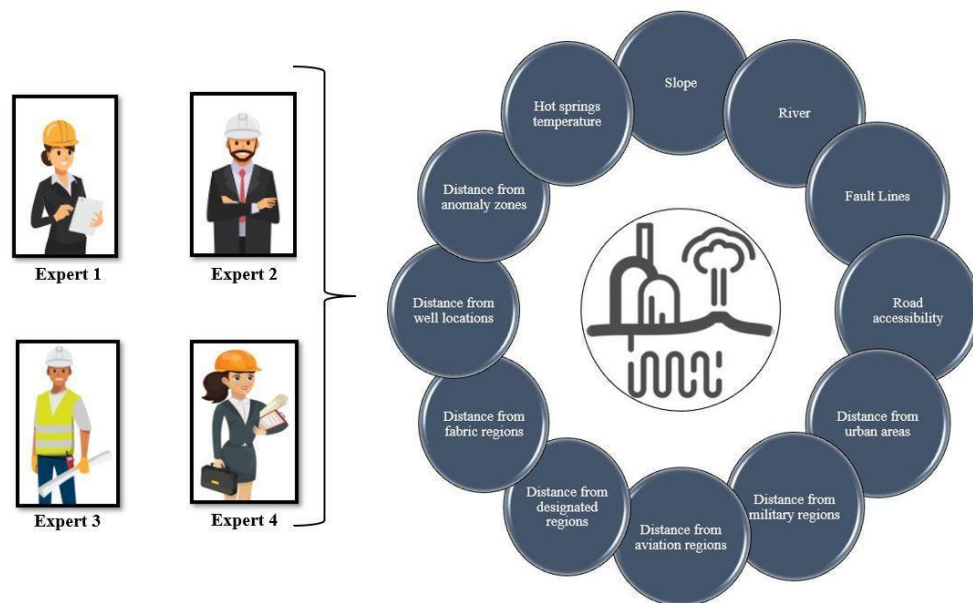


Figure 3. Criteria for suitable location of geothermal power plant installation

2.3. Geographical Information System (GIS)

The geographic information system (GIS) is a system that creates, manages, analyzes, and maps all types of data. GIS connects data to a map, integrating location data with all types of descriptive

information. This provides a foundation for mapping and analysis that is used in science and almost every industry. GIS helps researchers understand patterns, relationships, and geographic context. The benefits include improved communication and efficiency as well as better management and decision making. In this study, the creation of visual map layers was performed by utilizing GIS tools.

2.3. Multi-attribute Decision Making Techniques

So far, different techniques including the Additive Ratio Assessment (ARAS) method [19], technique for order preference by similarity to an ideal solution (TOPSIS) [20], Stepwise Weight Assessment Ratio Analysis (SWARA) method [17] have been employed for several purposes in the literature of renewable energy. It can be foreseen that multi-attribute decision making (MADM) technique is the most popular one. Because MADM can select between potential alternatives and evaluate them under multiple criteria even though some of them conflicted with each other. It may also be said that determination of the most appropriate energy resources, assessment of energy resources performance and identification of the most optimal location of energy facilities could be performed with these methods. Moreover, MADM techniques are immensely effective in order to achieve the solutions since these problems have different factors including social, environmental, financial, etc., which must be taken into consideration. In this study, AHP as a MADM method was employed for the installation of a geothermal power plant.

2.3.1. Analytic Hierarchy Process (AHP)

Analytic Hierarchy Process (AHP) is an additive weighting technique among MADM methods in order to solve the renewable and sustainable energy problems. Complicated problems in a hierarchical structure form the core of AHP. Essential aim is at the top of hierarchy, whilst decision alternatives are positioned at the bottom [21]. The implementation of AHP method applies under three main principles: (i) determining the problem and creating the hierarchy, (ii) creating a comparative decision-making preference matrix and (iii) determining the factor weights for each criterion [3]. The AHP uses a pairwise comparison of criteria to determine which criteria is more important than other criteria [22]. Firstly, each criterion must be compared as a binary value using the pairwise comparison method and the relative values must be assessed based on the level of importance among themselves to each other. Afterwards, a matrix, showing the paired comparison value of criteria, is formed easily. Level of importance value was shown in Table 1.

Table 1. AHP binary comparison scale

Importance level	Meaning
1	Indifferent (equal)
3	Weak preference (moderately more important)
5	Preference (more important)
7	Strong preference (strongly more important)
9	Very strong preference (extremely more important) (Intermediate values 2,4,6 and 8 are also possible)

After obtaining comparison matrices, the weighted vectors are normalized. The normalized weight vector values are obtained according to the level of importance value of the used criteria. With the resulting vector values, the consistency ratio (CR) values are calculated, and these calculated values are

used in the application to determine whether it is valid. CR formula is given in Equation 1. CC represents the consistency index and RI represents the random consistency index.

$$CR=CC/RI \quad (1)$$

Because of the best solution research, an upper limit of CR is determined. If the CR value is less than 0.1, it can be said that the binary comparisons are acceptable [13]. If not, the binary comparisons contradict each other. The factor weights were analyzed for use in practice in accordance with the CR and the spatial analysis performed. The results obtained from surveys from 20 experts were provided the proper consistency ratio.

3. RESULTS AND DISCUSSION

The present study discussed the required criteria and roadmap for suitable site selection of Geothermal Power Plants (GPP) in İzmir province, Türkiye. Combination of GIS and MCDM has been determined as the most preferable method [23]. According to the MCDM results, environmental concerns have the highest degree of importance, while both other criteria have similar rankings. For any energy investment, it was expected that the technical criteria must have the most critical impact [4], [24]. However, this study revealed that environmental issues could need to be analyzed in detail. In the literature, some studies have not included the environmental criterion for suitable site selection of GPP [25-27]. Thus, the present study filled the vital lack area in the literature by assessing the possible environmental issues. Furthermore, GPP did some significant environmental damage and gathered negative impacts on social acceptance [28-29]. However, this objective and scientific site selection process will cause social acceptance positively. It clearly makes comments that biodiversity, groundwater sources, and agricultural production will not be jeopardized. The factors selected for suitable location were obtained as a result of a wide literature review and experts' opinions. For this study, 20 experts provided the pairwise value for AHP analysis. As a result of provided values, importance values of main and sub-criteria were calculated, and they were shown in Table 2. Furthermore, twelve different map layers were made ready for use in the GIS. These map layers consisted of slope, river, fault lines, road accessibility, urban areas, military regions, aviation regions, designated regions, fabric regions, well locations, anomaly zones and hot springs temperature. For all those criteria, the buffer zones were carefully determined. In this study, all restrictive regions based on buffer zones of criteria were excluded from the analysis. Therefore, visual pollution and confusion that occurs in the reader's brain were prevented in analysis map layers. The datasets and determined criteria set were taken into account in determining the optimum location for geothermal power plants shown in Table 2.

Table 2. Factors, sub-factors, and factor weights for geothermal power plants

Criteria/ Data sources	Sub-Criteria	Buffer Zone	Unit	Suitability Score/Ranking *	Importance Weights	
C1. Physical - Earth Data - Copernicus Land Monitoring CLC2000 - General Directorate of Mineral Exploration and Research	Slope	<15°	%	(1) 12-15 (2) 6-12 (3) 0-6	0,065	0,34
	Water Bodies	outside	m	(1) 0-500 (2) 500-1500 (3) 1500-3500	0,075	
	Fault Lines	<200	m	(1)200-500 (2) 500-1000 (3) 1000-2000	0,12	
	Road Accessibility	<100	m	(1)100-200 (2) 200-1000 (3) 1000-2000	0,074	
C2. Environmental - Copernicus Land Monitoring Service - Earth Data	Dist. from urban areas	<500	m	(1) 500-700 (2) 700-1500 (3) 1500-3000	0,086	0,35
	Dist. from military regions	<5	km	(1)5-7 (2) 7-12 (3) 12-20	0,062	
	Dist. from aviation regions	<3	km	(1)3-5 (2) 5-15 (3) 15-30	0,058	
	Dist. from designated regions	<3	km	(1)3-4 (2) 4-5 (3) 5-6	0,072	
C3. Technical -Earth Data - (MTA, 2020). -Copernicus Land Monitoring CLC2000	Dist. from well locations	<200	m	(1) 200-500 (2) 500-1000 (3) 1000-2000	0,107	0,31
	Dist. from anomaly zones	<3	km	(1) 5-7 (2) 4-5 (3) 3-4	0,109	
	Hot springs temperature	<10	°C	(1) 10-13 (2) 13-18 (3) 18-25	0,097	

*(1) Lowest suitable/ (2) moderately suitable/ (3) most suitable

A comparison of the importance level of sub-criteria in conjunction with their standard deviation was illustrated as seen in Fig. 4. The blue dashed line demonstrated the mean values of sub-criteria, while the red solid line showed their standard deviation. As seen in the Figure, there were weak fluctuations in the sub-criteria including slope, river, road access, military regions, aviation distance, designated regions, and fabric regions. However, there were bigger peaks at the sub-criteria including fault lines, urban areas, wells, anomalies, and hot springs. This revealed that four sub-criteria which had bigger peaks were more important than other criteria in terms of installation of a geothermal power plant.

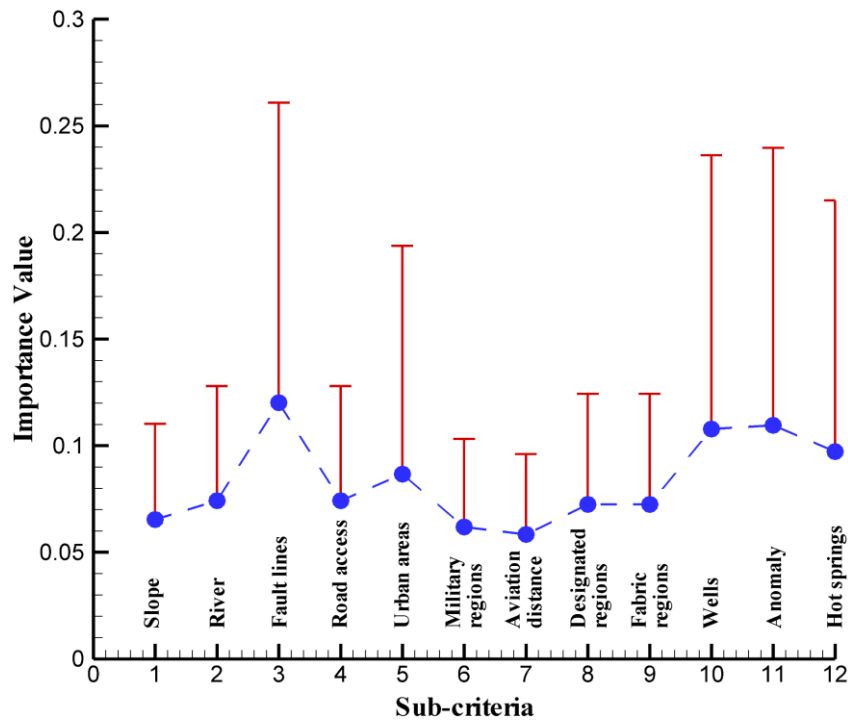


Figure 4. The importance level of sub-criteria with their standard deviations, blue dashed line: mean values, red solid line: standard deviation

3.1. Physical Factors

Physical factors which were one of the main factors consist of slope, river, fault lines and road accessibility. These sub-factors could define almost all geological feasibility and technical infrastructure for power plants. The weight of physical factors was calculated in 0,34 as a result of experts' opinions. Based on the literature review and other research studies the buffer zones of sub-criteria were determined and ranking processes were created between 1 (most suitable) and 3 (low suitable). Afterwards, the suitability score was assigned according to the distance from buffer zones of criteria. Obtained map layers based on buffer zones and ranking were shown in Figure 5.

- **Slope:** Slope is a very important and principal criterion for installing any energy power plant. If the selected land does not meet the requirement, excavation in the area causes losses in terms of both time and cost [3]. Also, for the accessibility requirement of power plants, slope is a key factor. Even though there is no regulation related to the maximum slope range, areas with a slope of less than 15 were assumed as suitable for geothermal power plants [30]. In this analysis, areas with land slopes of more than 15 were evaluated as unsuitable regions. In addition, areas with land slopes less than 15 were classified shown in Table 2 and were analyzed to obtain the optimal regions.
- **Rivers:** Rivers are carrying importance for the next generation due to the lack of water supply. Therefore, these water sources should not be used for different purposes. Also, regions maintaining a maximum water level should not be used to avoid negative effects from stronger river flowing when precipitation is high during the year [2]. Finally, in this study, relevant buffer zones were expected outside of river regions and ranking was classified based on this assumption.

- ***Fault lines:*** One of the key components to analyze a region of geothermal potential is to understand the role of fault lines [13]. Noorollahi et al. [26] determined the dominant distance between fault lines and geothermal wells. According to the results, 95% of the existing wells are located in a zone within a 6000 m distance to active fault lines. However, another study [4] showed the optimal maximum distance should be 2000 m from fault lines. Therefore, this study deemed regions with far above 2000 m are unsuitable regions. Fault lines have the highest importance weight among all sub-criteria shown in Table 2 and Fig 4.
- ***Road accessibility:*** Road accessibility is the one criterion of the technical infrastructure. Distance to main roads is very important for every energy power plant. The buffer zone for maintenance and other activities of the roads was accepted as 100 m and the ranking was classified according to a maximum distance of 2000 m [3].

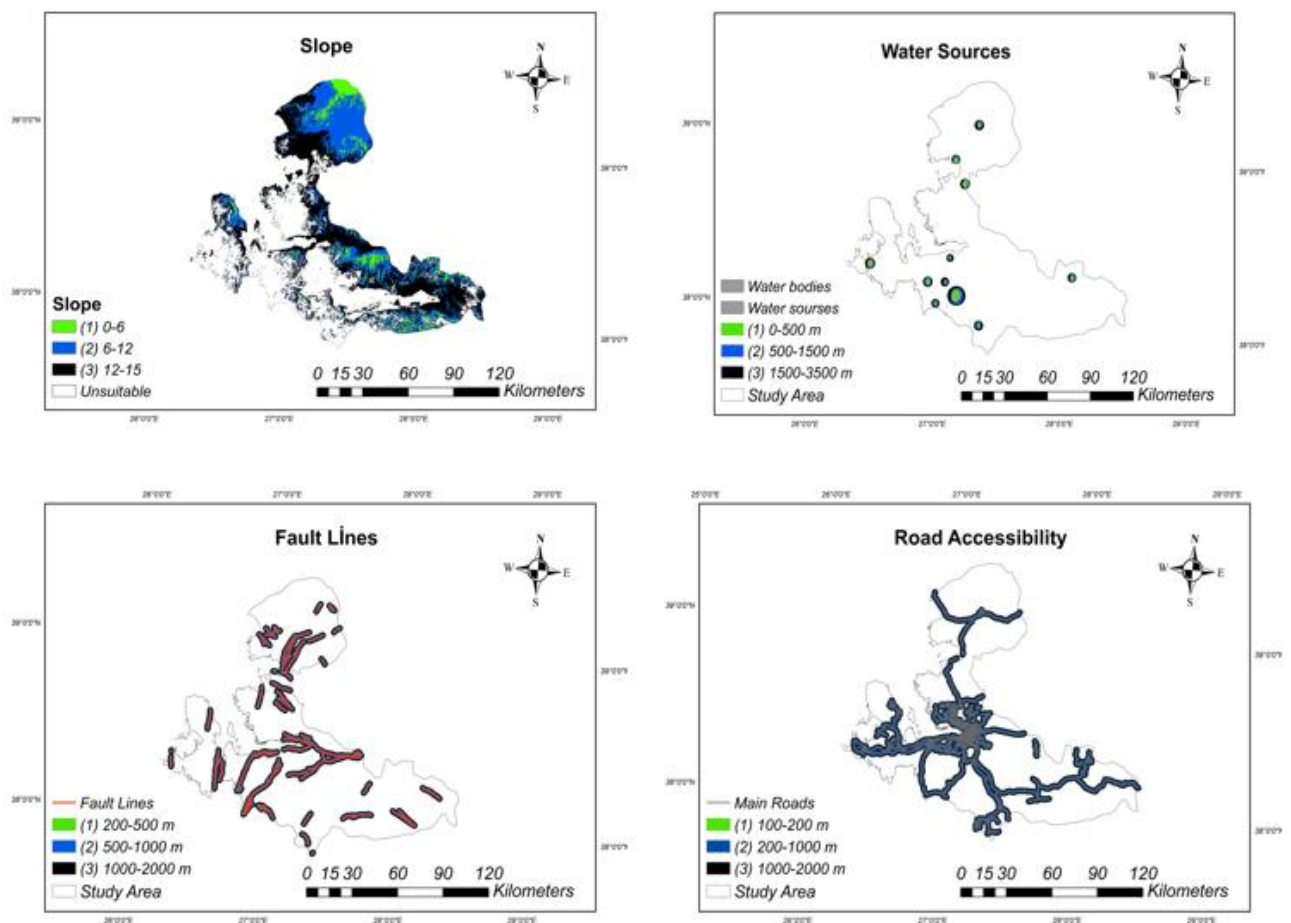


Figure 5. The map layers belonging to the physical factors

3.2. Environmental Factors

The analysis of environmental factors is a basic requirement for optimal location selection of energy power plants such as wind, solar energy [4]. It can be useful and accurate to analyze too many factors related to directly or indirectly environmental issues. According to the expert's opinion, the environmental factors have gained a 0.35 weight score which is the highest score among the main factors. Therefore, this study represents important and necessary factors which consist of distance from urban areas, military regions, aviation facilities, designated regions, and fabric regions. It was determined that

there were no special criteria or restrictions for the study area. CLC 2018 and Earth Data sources were used to analyze the determined environmental criteria. The buffer zones of sub-criteria can be seen in Table 2. Reclassified environmental map layers were shown in Figure 6.

- ***Distance from urban areas:*** Using land is a very important criterion for geothermal power plants. Although the analysis of existing urban areas is important, the prediction of future settlement directions must be taken into consideration in detail [30]. Also, energy demand, and energy costs of regions must be taken into consideration under urban areas criteria. The spatial data of urban areas used in this study was determined by CLC 2018 and Earth Data. To prevent any negative effect, the buffer zone of urban areas was determined as 500 m and was classified based on distance from urban areas [30].
- ***Distance from military regions:*** Military regions are carrying the secret and special value for countries. Therefore, military exercise, training, storing or other regions should not be used for different purposes [24]. In the study area, there are some critical military ports, hence this study is accepted as 5 km in the buffer zone of military regions.
- ***Distance from aviation regions:*** Aviation regions that consist of civil, military or load airports are very important points like military regions. Therefore, these regions cannot be used for different purposes because of their value. To determine the location of airports, CLC 2018 airport data sources were used and proceeded in GIS. There were 2 airports in the study area. Based on aviation rules, energy power plants have to be 3 km far from aviation points [30].
- ***Distance from designated regions:*** Designated regions are identified and protected by national or international institutes. The study area has some natural and historical places protected by UNESCO. To protect the natural and historical places, the buffer zone of designated regions was determined as 3 km. Based on the determined buffer zone, ranking was classified between 3 km and 6 km so as not to narrow the fields [31].
- ***Distance from fabric regions:*** The study area is a very important commercial center because of its location. Therefore, 30 fabric regions exist in the study area dispersedly. To predict the location of the future residential area, it is necessary to analyze the growth of factory areas and determine buffer zones. For this opinion, the buffer zone of the fabric region was determined as 500 m and ranking values were classified based on these opinions [32].

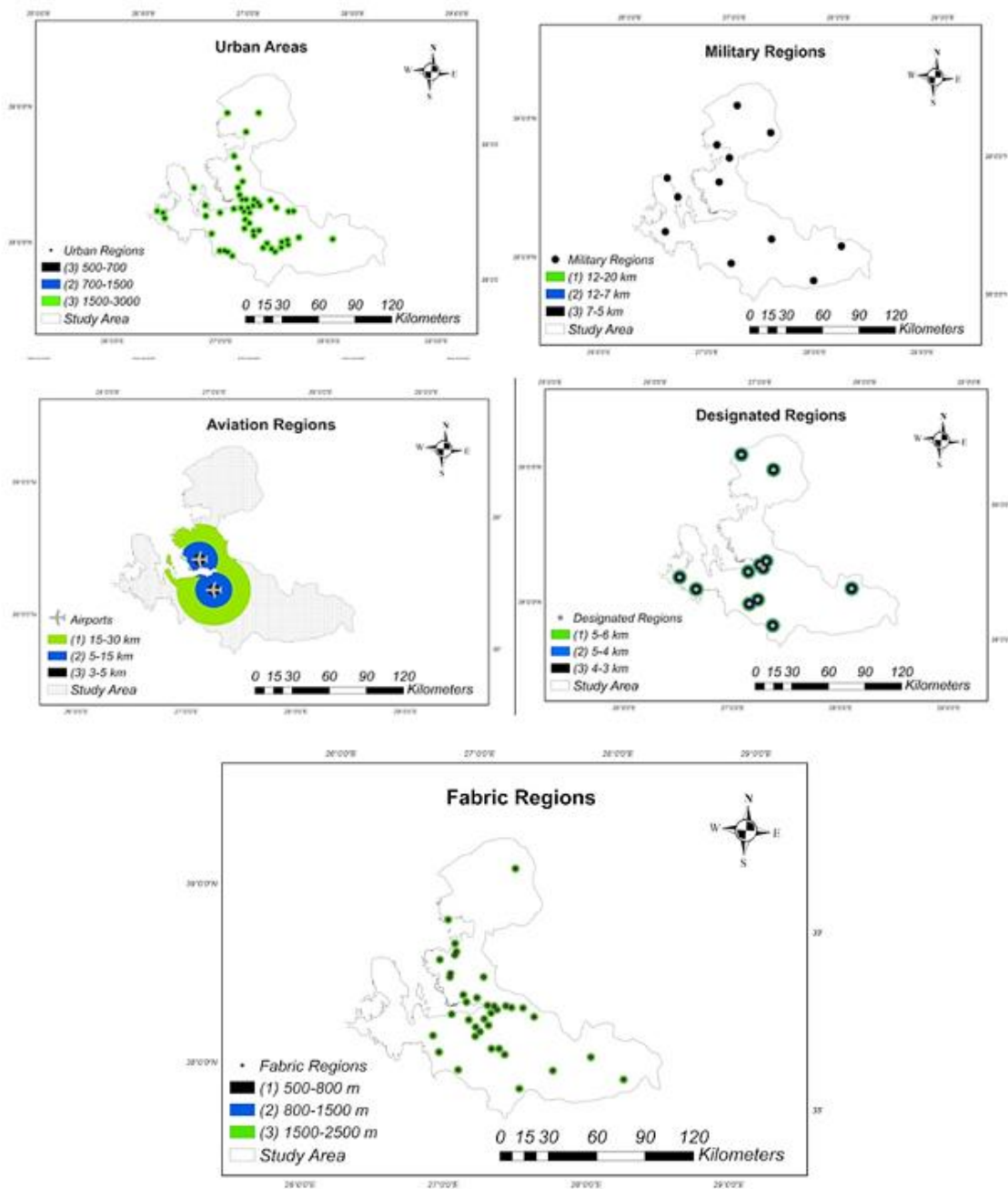


Figure 6. The map layers belonging to Environmental factors analysis

3.3. Technical Factors

Technical factors were categorized under three sub-criteria which were distance from well location, distance from anomaly zones and hot springs temperature. In the geothermal energy potential assessment could be evaluated to measure the temperature of underground waters. Thus, existing wells could be useful and guide to selecting the optimal location. In the scope of this study although general information will be obtained, potential measures must be taken certainly for the determined suitable regions. Used datasets, determined sub-criteria and then buffer zones shown in Table 2. Also, reclassified map layers for technical factors were created in Figure 7.

- ***Distance from well location:*** Existing well locations can give information to researchers, investors, and energy planners about potential locations. Analyzing well locations is a rather vital step for

technical factors. General Directorate Mineral Research and Exploration Institution measures underground water temperature and determines well locations. This study used General Directorate Mineral Research and Exploration [34] map layers which are in “.TIFF” format and these map layers were processed in GIS. In the study, the buffer zone of the well location was determined as 200 m [13]. When geothermal power plants must be near the well location, a distance from well with between 200 and 500 m was classified as the most suitable region in Table 2.

- ***Distance from anomaly zone:*** Geothermal fluids can be transported easily and economically by pipelines to a few kilometers [27]. Therefore, consumption facilities or generating plants should be located near anomaly zones. To determine the suitable regions, a buffer zone of 3 km was applied in the study area. Reclassified ranking distance was given in Table 2. Additionally, the distance from the anomaly zone was identified as the most important criterion among technical factors with a 0.109 weight score.
- ***Hot springs:*** Hot springs are the basic evidence of the hot waters and subsurface heat source [33]. The location of hot springs can give information about geothermal potential. As hot springs can be used for commercial facilities, geothermal power plants must be located at a certain distance because of noise and visual impacts. Also, the minimum hot spring temperature must be 10 °C. According to this information, the ranking section was edited between the minimum and maximum temperature of the study area.

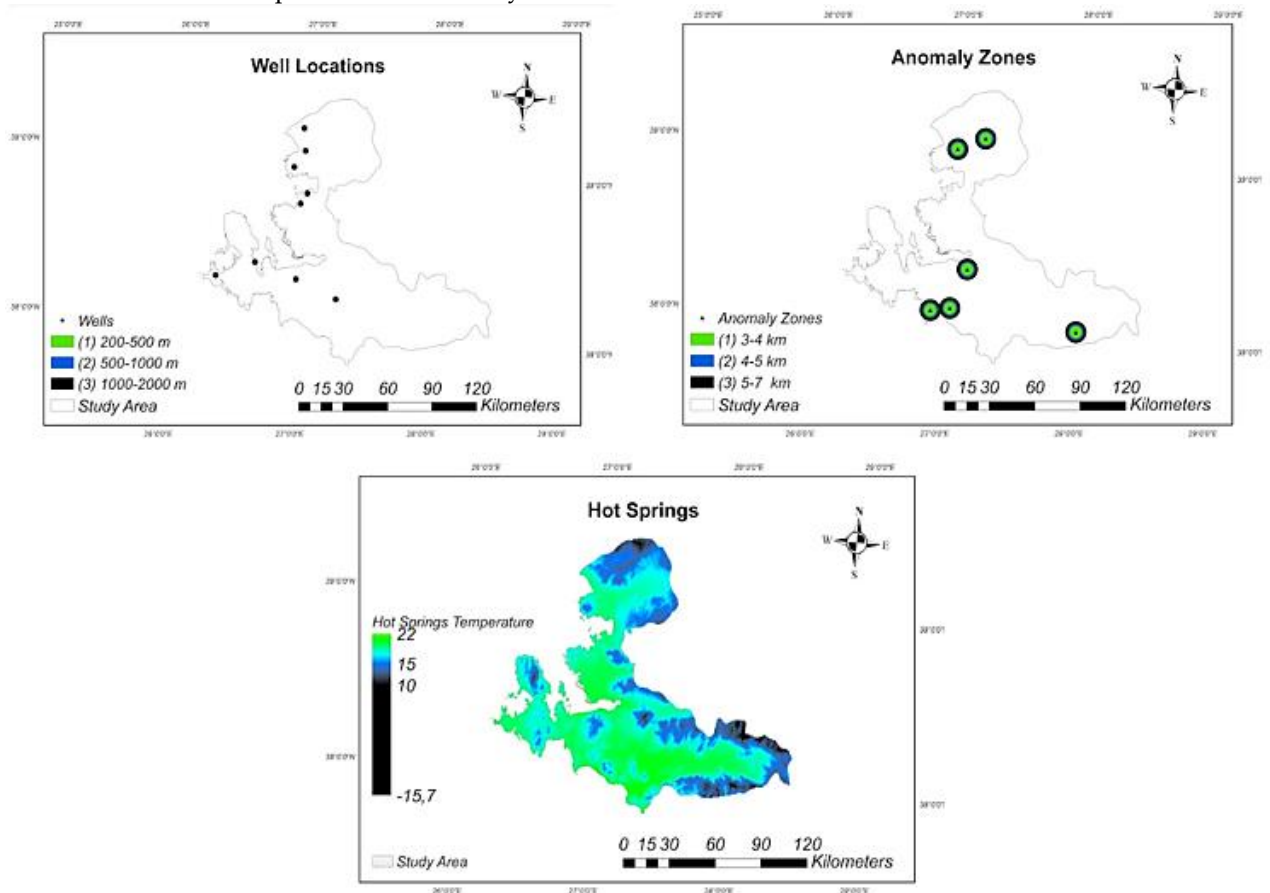


Figure 7. The map layers belonging to technical factors analysis

3.4. Determination of Suitable Location and Comparison

Fig. 8 shows the suitable regions which were determined in this comprehensive analysis study. Intensive black points were presented in the non-suitable regions where there were restrictions or buffer zones. Green points demonstrate the suitable regions based on the experts' opinions. The south direction of the study area could be a new geothermal region center in order to produce geothermal energy. Although the north of Izmir Bay had huge potential and was a suitable region, these regions were utilized intensively for settlement and residential facilities. In addition, the Balçova region which was located on the Izmir Bay had the suitable region although it was a small region. Furthermore, the sensitive areas including lakes and rivers were identified in the detailed study [35]. According to the study, those sensitive areas were found especially at the center of the region which was far away from the suitable areas of desired geothermal power plants. This proved that the suitable sites for geothermal power plants indicated as green color would not disturb the areas of wetlands, drinking water and fertile agricultural lands. It was also found that Türkiye's agricultural activity including wild and cultivated olives which were too crucial for export was studied [36]. The desired geothermal power plant with green color did not jeopardize the lands of wild and cultivated olives.

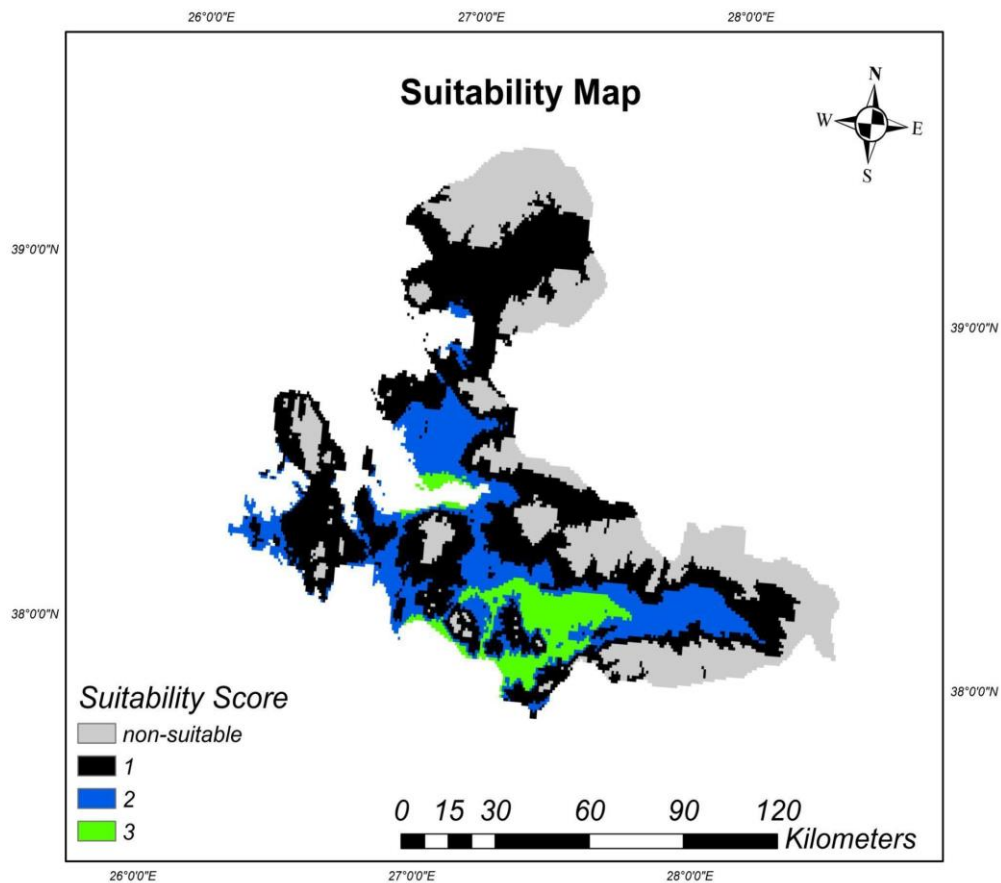


Figure 8. Suitability map layer in the study area

In terms of comparison of the key findings, Fig. 9 pointed out the actual geothermal energy power plants in the Aegean region obtained from the General Directorate of Mineral Exploration and Research [34]. Geothermal power plants were shown with temperature values and locations. It was seen that the Balçova region, which was determined as a highly suitable region, had an energy power plant. Moreover, Seferihisar, situated in the southwestern part of the area, was identified as a region of moderate suitability in both of the conducted studies. It is clear that the two existing geothermal power plants are closely aligned with the findings shown in Figure 8 of this paper. Apart from the existing geothermal power plants, the results clearly indicated that the areas in the northwest of Balçova (near the shore) and the

eastern section of Seferihisar are enormously well-suited for the establishment of geothermal power plants. On the other hand, there was an actual geothermal power plant in the Dikili region even though there was not any suitable region in that area to the findings. The study also proved that the South and South-west parts of the region were the most suitable areas.

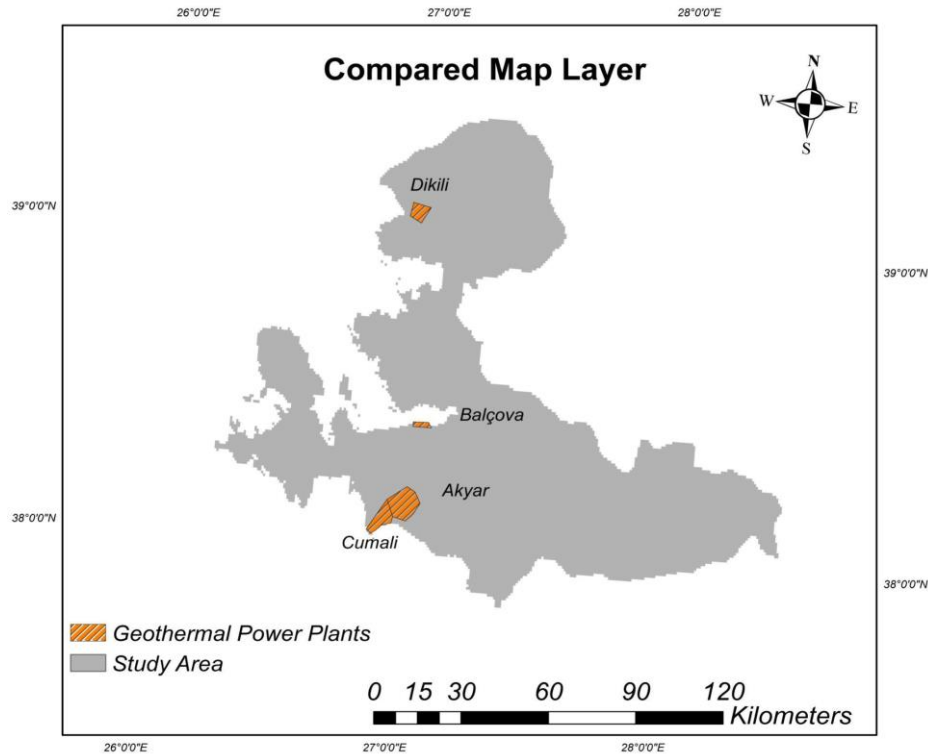


Figure 9. Current geothermal energy power plant in the study area

4. CONCLUSIONS

For any country, it was obvious that possessing and governing a high geothermal energy potential makes the transition from fossil fuels to renewable energies easier. In the present study, a comprehensive framework was performed to determine the suitable sites for the installation of a geothermal power plant under three main criteria by evaluating twelve sub-criteria. So as to calculate the suitability and show the criteria effectiveness for the study area, the combination of GIS-AHP was conducted. For the AHP structure, experts' opinions were ensured. Türkiye could be a leader in geothermal energy with correct and effective new projects. Therefore, the installation of new applications requires a comprehensive feasibility study. This study investigated the İzmir province which had high geothermal energy potential. Based on the results, the presence of fault lines was calculated as the most important criterion while the distance from aviation regions was the slightly unimportant criterion. In addition, the obtained suitability map layer discussed the locations of the existing geothermal power plants in terms of the determined criteria. The study can give important information and may be a vital guideline for energy planners, investors, policymakers, etc. For future studies, the use of geothermal potential for district heating and cooling processes will be discussed. Besides, a social multi criteria decision will be taken into consideration.

Declaration of Ethical Standards

Authors declare that all ethical standards have been complied with.

Declaration of Competing Interest

The authors declare that there are no declarations of interest.

Acknowledgement

The authors would like to acknowledge the experts' opinion from Summer School in Slovenia "Coupling technologies to use low and medium depth hydro-geothermal energy" funded by CA18219 EU COST Research Network for Including Geothermal Technologies into Decarbonized Heating and Cooling Grids (Geothermal DHC) supported by COST (European Cooperation in Science and Technology), www.cost.eu.

Data Availability

The all presented data used in the present study is available online.

REFERENCES

- [1] D. A. Haralambopoulos and H. Polatidis, "Renewable energy projects: structuring a multi-criteria group decision-making framework," *Renewable Energy*, vol. 28, no. 6, pp. 961–973, May 2003, doi: [https://doi.org/10.1016/s0960-1481\(02\)00072-1](https://doi.org/10.1016/s0960-1481(02)00072-1).
- [2] N. L. Panwar, S. C. Kaushik, and S. Kothari, "Role of renewable energy sources in environmental protection: A review," *Renewable and Sustainable Energy Reviews*, vol. 15, no. 3, pp. 1513–1524, Apr. 2011, doi: <https://doi.org/10.1016/j.rser.2010.11.037>.
- [3] H. E. Colak, T. Memisoglu, and Y. Gercek, "Optimal site selection for solar photovoltaic (PV) power plants using GIS and AHP: A case study of Malatya Province, Turkey," *Renewable Energy*, Dec. 2019, doi: <https://doi.org/10.1016/j.renene.2019.12.078>.
- [4] M. S. Genç, F. Karipoğlu, K. Koca, and Ş. T. Azgın, "Suitable site selection for offshore wind farms in Turkey's seas: GIS-MCDM based approach," *Earth Science Informatics*, May 2021, doi: <https://doi.org/10.1007/s12145-021-00632-3>.
- [5] M. Melikoglu, "Geothermal energy in Turkey and around the World: A review of the literature and an analysis based on Turkey's Vision 2023 energy targets," *Renewable and Sustainable Energy Reviews*, vol. 76, pp. 485–492, Sep. 2017, doi: <https://doi.org/10.1016/j.rser.2017.03.082>.
- [6] A. C. D. JESUS, "Environmental Sustainability of Geothermal Development," *Energy Sources*, vol. 19, no. 1, pp. 35–47, Jan. 1997, doi: <https://doi.org/10.1080/00908319708908830>.
- [7] G. Munda, P. Nijkamp, and P. Rietveld, "Qualitative multicriteria evaluation for environmental management," *Ecological Economics*, vol. 10, no. 2, pp. 97–112, Jul. 1994, doi: [https://doi.org/10.1016/0921-8009\(94\)90002-7](https://doi.org/10.1016/0921-8009(94)90002-7).
- [8] F. KARİPOĞLU, S. ÖZTÜRK, and M. S. GENÇ, "Determining Suitable Regions for Potential Offshore Wind Farms in Bandırma Bay using Multi-criteria-Decision-Making Method," *Mühendislik Bilimleri ve Araştırmaları Dergisi*, Apr. 2021, doi: <https://doi.org/10.46387/bjesr.900204>.
- [9] J. M. Sánchez-Lozano, M. S. García-Cascales, and M. T. Lamata, "GIS-based onshore wind farm site selection using Fuzzy Multi-Criteria Decision Making methods. Evaluating the case of Southeastern Spain," *Applied Energy*, vol. 171, pp. 86–102, Jun. 2016, doi: <https://doi.org/10.1016/j.apenergy.2016.03.030>.
- [10] X. Shi *et al.*, "Using spatial information technologies to select sites for biomass power plants: A case study in Guangdong Province, China," *Biomass and Bioenergy*, vol. 32, no. 1, pp. 35–43, Jan. 2008, doi: <https://doi.org/10.1016/j.biombioe.2007.06.008>.

- [11] A. Fetanat and E. Khorasaninejad, "A novel hybrid MCDM approach for offshore wind farm site selection: A case study of Iran," *Ocean & Coastal Management*, vol. 109, pp. 17–28, Jun. 2015, doi: <https://doi.org/10.1016/j.ocecoaman.2015.02.005>.
- [12] J.-Y. Kim, K.-Y. Oh, K.-S. Kang, and J.-S. Lee, "Site selection of offshore wind farms around the Korean Peninsula through economic evaluation," *Renewable Energy*, vol. 54, pp. 189–195, Jun. 2013, doi: <https://doi.org/10.1016/j.renene.2012.08.026>.
- [13] C.-N. Wang, T.-T. Tsai, and Y.-F. Huang, "A Model for Optimizing Location Selection for Biomass Energy Power Plants," *Processes*, vol. 7, no. 6, p. 353, Jun. 2019, doi: <https://doi.org/10.3390/pr7060353>.
- [14] Y. Wu, X. Sun, Z. Lu, J. Zhou, and C. Xu, "Optimal site selection of straw biomass power plant under 2-dimension uncertain linguistic environment," *Journal of Cleaner Production*, vol. 212, pp. 1179–1192, Mar. 2019, doi: <https://doi.org/10.1016/j.jclepro.2018.12.091>.
- [15] D. Coles *et al.*, "Spatial decision analysis of geothermal resource sites in the Qualibou Caldera, Saint Lucia, Lesser Antilles," *Geothermics*, vol. 33, no. 3, pp. 277–308, Jun. 2004, doi: <https://doi.org/10.1016/j.geothermics.2003.07.012>.
- [16] G. Coro and E. Trumpy, "Predicting geographical suitability of geothermal power plants," *Journal of Cleaner Production*, vol. 267, p. 121874, Sep. 2020, doi: <https://doi.org/10.1016/j.jclepro.2020.121874>.
- [17] A. Mostafaeipour, S. J. Hosseini Dehshiri, and S. S. Hosseini Dehshiri, "Ranking locations for producing hydrogen using geothermal energy in Afghanistan," *International Journal of Hydrogen Energy*, vol. 45, no. 32, pp. 15924–15940, Jun. 2020, doi: <https://doi.org/10.1016/j.ijhydene.2020.04.079>.
- [18] I. K. Koukouvelas and A. Aydin, "Fault structure and related basins of the North Aegean Sea and its surroundings," *Tectonics*, vol. 21, no. 5, pp. 10–110–17, Oct. 2002, doi: <https://doi.org/10.1029/2001tc901037>.
- [19] E. K. Zavadskas and Z. Turskis, "A NEW ADDITIVE RATIO ASSESSMENT (ARAS) METHOD IN MULTICRITERIA DECISION-MAKING / NAUJAS ADITYVINIS KRITERIJŲ SANTYKIŲ ĮVERTINIMO METODAS (ARAS) DAUGIAKRITERINIAMS UŽDAVINIAMS SPREŠTI," *Technological and Economic Development of Economy*, vol. 16, no. 2, pp. 159–172, Jun. 2010, doi: <https://doi.org/10.3846/tede.2010.10>.
- [20] Hwang, C. L., Yoon, K. "Methods for multiple attribute decision making. In Multiple attribute decision making", Springer, Berlin, Heidelberg, 1981.
- [21] E. W. Stein, "A comprehensive multi-criteria model to rank electric energy production technologies," *Renewable and Sustainable Energy Reviews*, vol. 22, pp. 640–654, Jun. 2013, doi: <https://doi.org/10.1016/j.rser.2013.02.001>.
- [22] H. A. Donegan, F. J. Dodd, and T. B. M. McMaster, "A New Approach to AHP Decision-Making," *The Statistician*, vol. 41, no. 3, p. 295, 1992, doi: <https://doi.org/10.2307/2348551>.
- [23] S. Ozturk and Fatih Karipoglu, "Investigation of the best possible methods for wind turbine blade waste management by using GIS and FAHP: Turkey case," *Environmental Science and Pollution Research*, vol. 30, no. 6, pp. 15020–15033, Sep. 2022, doi: <https://doi.org/10.1007/s11356-022-23256-6>.
- [24] Mustafa Serdar Genç, "Determination of the most appropriate site selection of wind power plants based Geographic Information System and Multi-Criteria Decision-Making approach in Develi, Turkey," Feb. 2021, doi: <https://doi.org/10.5278/ijsepm.6242>.
- [25] S. Chokchai *et al.*, "A Pilot Study on Geothermal Heat Pump (GHP) Use for Cooling Operations, and on GHP Site Selection in Tropical Regions Based on a Case Study in Thailand," *Energies*, vol. 11, no. 9, p. 2356, Sep. 2018, doi: <https://doi.org/10.3390/en11092356>.
- [26] Y. Noorollahi, H. Yousefi, and M. Mohammadi, "Multi-criteria decision support system for wind farm site selection using GIS," *Sustainable Energy Technologies and Assessments*, vol. 13, pp. 38–50, Feb. 2016, doi: <https://doi.org/10.1016/j.seta.2015.11.007>.

- [27] Y. Noorollahi, H. Yousefi, R. Itoi, and S. Ehara, "Geothermal energy resources and development in Iran," *Renewable and Sustainable Energy Reviews*, vol. 13, no. 5, pp. 1127–1132, Jun. 2009, doi: <https://doi.org/10.1016/j.rser.2008.05.004>.
- [28] M. Günther and T. Hellmann, "International environmental agreements for local and global pollution," *Journal of Environmental Economics and Management*, vol. 81, pp. 38–58, Jan. 2017, doi: <https://doi.org/10.1016/j.jeem.2016.09.001>.
- [29] Z.I. González Acevedo, M.A. Sánchez Vázquez, J.C. González Troncoso, S. Lee Sánchez, and M.A. García Zarate, "SOCIAL ACCEPTANCE/RESISTANCE OF GEOTHERMAL POWER PLANTS IN MEXICO," Jan. 2021, doi: <https://doi.org/10.3997/2214-4609.202182033>.
- [30] M. A. Günen, "A comprehensive framework based on GIS-AHP for the installation of solar PV farms in Kahramanmaraş, Turkey," *Renewable Energy*, vol. 178, pp. 212–225, Nov. 2021, doi: <https://doi.org/10.1016/j.renene.2021.06.078>.
- [31] "Law No. 102 of 1983 on Natural Protected Areas.," www.ecolex.org. <https://www.ecolex.org/details/legislation/law-no-102-of-1983-on-natural-protected-areas-lex-faoc020777/> (accessed Feb. 26, 2024).
- [32] "General Directorate of Mineral Research and Exploration," www.mta.gov.tr. <https://www.mta.gov.tr/en/>
- [33] M. Gozen, "License applications based on solar energy (legislation and Practice)" *Energy Market Regulatory Authority Solarex*, Istanbul 2014.
- [34] G. Najafi and B. Ghobadian, "Geothermal resources in Iran: The sustainable future," *Renewable and Sustainable Energy Reviews*, vol. 15, no. 8, pp. 3946–3951, Oct. 2011, doi: <https://doi.org/10.1016/j.rser.2011.07.032>.
- [35] S. Ayaz *et al.*, "An approach for determining the nutrient sensitive areas: a case study for Gediz River Basin, Turkey," *Environmental Monitoring and Assessment*, vol. 193, no. 5, Apr. 2021, doi: <https://doi.org/10.1007/s10661-021-09017-x>.
- [36] B. Yoruk and V. Taskin, "Genetic diversity and relationships of wild and cultivated olives in Turkey," *Plant Systematics and Evolution*, vol. 300, no. 5, pp. 1247–1258, Feb. 2014, doi: <https://doi.org/10.1007/s00606-014-1002-3>.